

Electrochemical
N₂-splitting and functionalisation
in the coordination sphere of Rhenium

Dissertation

for the award of the degree
"Doctor rerum naturalium" (Dr.rer.nat.)
of the Georg-August-Universität Göttingen

within the doctoral program of the
Georg-August University School of Science (GAUSS)

submitted by
Richt Sieteke van Alten

from Dokkum (Dongeradeel), the Netherlands

Göttingen, 2021

Thesis Committee

Prof. Dr. Sven Schneider
Institute for Inorganic Chemistry, Georg-August-Universität, Göttingen

Prof. Dr. Inke Siewert
Institute for Inorganic Chemistry, Georg-August-Universität, Göttingen

Dr. Markus Finger
Institute for Inorganic Chemistry, Georg-August-Universität, Göttingen

Members of the Examination Board

First Reviewer: Prof Dr. Sven Schneider
Institute for Inorganic Chemistry, Georg-August-Universität, Göttingen

Second Reviewer: Prof Dr. Inke Siewert
Institute for Inorganic Chemistry, Georg-August-Universität, Göttingen

Further Reviewers: Prof Dr. Franc Meyer
Institute for Inorganic Chemistry, Georg-August-Universität, Göttingen

Prof Dr. Manuel Alcarazo
Institute for Organic and Biomolecular Chemistry, Georg-August-Universität,
Göttingen

Dr. Christian Sindlinger
Institute for Inorganic Chemistry, Georg-August-Universität, Göttingen

Dr. Lisa Vondung
Institute for Inorganic Chemistry, Georg-August-Universität, Göttingen

Date of the oral examination: 21.06.2021

*Wat is leafde foar jins bertegrûn, in beaken yn 'e tiid?
Is it ljocht yn tsjustere dagen, in hâldfest yn soarch en striid?*

*Foar elk dy't soms himsels ferliest op fier en frjemde grûn
In bân mei 't plakje dêr't de reis begûn*

(Wat is leafde', de Kast, Simmertime 2, 2000)

Acknowledgments

I am very thankful to my supervisor Prof. Dr. Sven Schneider, for various reasons: for welcoming me in the group, for (somewhat accidentally) putting me on such an exciting electrochemical project and giving me the accordingly required tools & trust, for being a good and challenging supervisor, for having such a well-equipped lab and allowing me to go to several conferences, and for doing so intriguing research within your group that gathers an exciting mix of people that makes it fun to come to work (almost) every day. Thank you very much!

I sincerely thank Prof. Dr. Inke Siewert for being my second supervisor. Your support throughout this project has been very essential. I highly appreciate how often I could pop by your office to ask (many) questions, and to have your friendly guidance during these years.

I thank Prof. Dr. Franc Meyer, Prof. Dr. Manuel Alcarazo, Dr. Christian Sindlinger, and Dr. Lisa Vondung for taking time to be in my examination board.

Furthermore, I am truly grateful for many people that I have worked with or that helped me during the past years:

- Dr. Markus Finger and Dr. Christian Würtele for guidance and support throughout the years, both from a scientific as personal point of view. Off course also for DFT-calculations and Xray-diffractometry, and for the latter I also thank Dr. Matthias Otte for taking over during the last year.

- To the whole of AK Schneider, I am very indebted from both a scientific and personal point of view. Ranging from my first lab & office colleagues for helping me find my way and having extremely good times in the lab, to the crew as it is now: despite the current circumstances, it still operates as a tight team. It was an absolute blast! Some became very dear friends over the past years and I am grateful for the experiences we shared (and will share in the future).

- My direct co-workers: Dr. Ekatarina Yu Yuzik-Klimova, and Manuel Oelschlegel and Maj Grit Kruse (both master interns) and especially my bachelor students Philipp Wieser, Ciara Kiene and Charlotte von Petersdorff-Campen. Your contributions to this work are very valuable and I cherish the great time we had in the lab; it is always better & more fun to work together.

- Kai Sebastian Kopp for the synthesis of the ligand and all the (technical) help in the lab.

- Everybody of the Siewert group for (electrochemical) support and for being so welcoming. I'd like to especially emphasise initial guidance from Dr. Mona Wilken for potentiostat troubleshooting tips, Dr. Sebastian Nestke and Dr. Jia-Pei Du for long glovebox hours entertainment, and Lucas Paul for being so helpful.

- Dr. Michael John and Ralf Schöne for performing and assisting with NMR measurements.

- Cooperation partners Dr. Brian Lindley and Prof. Dr. Alex Miller for a challenging but fun project of Chapter II.1; the many teleconferences were a kick-start for my PhD.

- Dr. Markus van Alten, Dr. Bastian Schluschaß, Max Fritz, and Dr. Daniel Delony for proofreading.

- The mechanic and electric workshop for (last-minute) repairs and 'Neubau' projects. Especially making the PTFE flow-cell on short notice for Charlotte was very helpful.

- Petra Gaugel, Frau Stückl and Dalila Griffin for administrative support, and additionally Dalila for having our (ir)regular fun chats.

- The past years would not have been so valuable (and enjoyable) without the teaching part. Here I would like to especially thank Frau Stückl, Jörg Schöne, and Angelika Wraage for good times within the geology course.

- The Hausi's, for maintaining a crazy good mood within the building.

- Beyond science, I'd like to highlight the excellent distraction offered by 'JC Caramba', and I am sure we manage our long-distance relationship for many more years to come. I thank Filip Savic, and especially Maxime van Wiggen for their warm friendship.

- Finally, I am deeply thankful to my family, especially for the exceptional support from my 'mem'.

-I am – so much – looking forward to all that life will bring with Markus in it.

List of Abbreviations

AEM	- Anion Exchange Membrane
BAR ^F ₂₄	- Tetrakis(3,5-bis(trifluoromethane)phenylborate anion
CE	- Counter Electrode
CEM	- Cation Exchange Membrane
COSY	- Correlated spectroscopy
Cp	- Cyclopentadienyl anion
Cp*	- Pentamethylcyclopentadienyl anion
CPE	- Controlled Potential Electrolysis
CPVC	- Chlorinated Polyvinylchloride
CV	- Cyclovoltammetry
D	- Diffusion coefficient [cm ² s ⁻¹]
DBU	- 1,8-diazabicyclo[5,4,0]undec-7-en
DCM	- Dichloromethane
DOSY	- Diffusion Ordered Spectroscopy
dppe	- di(bisphenylphosphino)ethylene
E.A.	- Elemental Analysis
EPDM	- Ethylene Propylene Diene Monomer
EPR	- Electron Paramagnetic Resonance
ESI	- Electron Spray Ionization
f	- frequency [cm ⁻¹]
Fc	- Ferrocene
Fc*	- Decamethylferrocene
FE	- Faradaic efficiency
HER	- Hydrogen Evolution Reaction
HMBC	- Heteronuclear Multiple Bond Correlation
HSQC	- Heteronuclear Single Quantum Coherence
IR	- Infrared
iR	- internal resistance
KHMDS	- Potassium hexamethyldisilylazide
LIFDI	- Liquid Injected Field Desorption Ionization
LWHH	- Linewidth at half height
MeCN	- acetonitrile
NCS	- N-chlorosuccinimide
NMR	- Nuclear Magnetic Resonance
OTf	- Triflate anion
PCET	- Proton Coupled Electron Transfer
PNP	- (N(CH ₂ CH ₂ PtBu ₂) ₂) ⁻
PNP ^{iPr}	- (N(CH ₂ CH ₂ PiPr ₂) ₂) ⁻
P=NP	- (N(CH ₂ CH ₂ PtBu ₂)(CHCHPtBu ₂) ⁻
P=N=P	- (N(CHCHPtBu ₂) ₂) ⁻
ppm	- Parts per million
PTFE	- Polytetrafluoroethylene
Re	- Reynolds Number
RE	- Reference Electrode
RT	- Room temperature (298K)
SEC	- Spectro-electro
SQUID	- Superconducting Quantum Interference Device
TBP	- 2,4,6-tri- <i>tert</i> -butylphenoxy radical
(TD-)DFT	- (Time Dependent) Density Functional Theory
THF	- Tetrahydrofuran
TIP	- Temperature Independent Paramagnetism
TMG	- 1,1,3,3-Tetramethylguanidine
TMS	- Trimethylsilyl
UV-vis	- Ultra Violet visible light
VT	- Variable Temperature
WE	- Working Electrode
XRD	- X-ray diffraction spectroscopy
δ	- Chemical shift [ppm]
v	- Scan rate [Vs ⁻¹]

I. Introduction

I.1. Dinitrogen coordination and splitting.....	12
1.1. Properties of Dinitrogen.....	12
1.2. Industrial and biological conditions for N ₂ -activation.....	12
1.3. Dinitrogen as ligand for coordination complexes.....	14
1.4. N ₂ -splitting into terminal nitrides.....	22
I.2. Dinitrogen functionalisation.....	36
2.1. Ammonia formation.....	36
2.1.1. Ammonia formation using chemical reagents	36
2.1.2. Ammonia formation by means of electrochemistry	40
2.1.3. Ammonia formation in an electrochemical flow cell.....	43
2.2. N-Element Bond formation.....	45
2.2.1. N-X bond formation	45
2.2.2. N-C bond formation	47
2.2.3. Nitrile generation from N ₂	53
I.3. Research scope	60

II. Results and Discussion

II.1: Mechanism of (electro)chemical N ₂ -splitting from [ReCl ₂ (PNP)].....	64
1.1. Dinuclear N ₂ -bridged intermediate and its splitting into nitrides	64
1.2. Electrochemical N ₂ -splitting from [ReCl ₂ (PNP)]	69
1.3. CV study of [ReCl ₂ (PNP)] under Ar	71
1.4. CV study of [ReCl ₂ (PNP)] under N ₂ towards a N ₂ -splitting mechanism	73
1.5. Discussion of the N ₂ -splitting mechanism	77
II.2: Influence of halide substitution on N ₂ -splitting.....	84
2.1. Synthesis of the bromide and iodide starting platforms.....	84
2.2. (Electro)chemical N ₂ -splitting of 1 ^{Br} and 1 ^I	87
2.3. Synthesis of nitride reference species	90
2.4. Characterisation of dinuclear N ₂ -bound intermediate.....	92
2.5. Initial electrochemical analysis of the 1 ^X platforms	101
2.6. CV Study of [ReBr ₂ (PNP)] under Ar and N ₂	102
2.7. CV Study of [ReI ₂ (PNP)] under Ar and N ₂	107
2.8. Halide Comparisons and trends.....	116
II.3: The influence of ligand oxidation on N ₂ -splitting.....	124
3.1. Synthesis attempts towards the partially unsaturated chloride platform	124
3.2. Electrochemical N ₂ -splitting from the unsaturated chloride platform	128
3.3. CV Study of [ReCl ₂ (P=N=P)].....	134
3.4. (Electro)chemical N ₂ -splitting from [ReI ₂ (P=N=P)].....	138
3.5. Initial attempts to form ammonia from the iodide platform	144
3.6. Discussion of the (electro)chemical N ₂ -splitting yields	146

II.4: Electrochemical MeCN release	148
4.1. Electrochemical MeCN release from [Re(NCHCH ₃)Cl(PNP)].....	148
4.2. Platform modifications to the unsaturated ligand	155
4.3. Electrochemical MeCN release of [ReCl(NCHCH ₃)(P=N=P)]	162
4.4. Chemical MeCN release of [ReCl(NCHCH ₃)(P=N=P)]	167
4.5. Synthesis and CV analysis of [ReCl ₃ (PNP)] and [ReCl ₃ (P=N=P)].....	168
4.6. Electrochemical N ₂ -splitting from the Re(IV)-platform	172
II.5: N ₂ -splitting in a flow cell.....	176

III. Conclusion and Outlook

III.1. Conclusion	182
III.2. Outlook.....	186

IV. Experimental Section

IV.1. General working techniques	190
IV.2. Chemicals and purification methods.....	190
IV.3. Analytical methods	192
Cyclic voltammetry (CV)	192
Cyclic voltammetry (CV).....	193
Controlled Potential Electrolysis (CPE).....	193
Elemental analysis	195
Gas Chromatography	195
IR-spectroscopy	195
EPR-spectroscopy	196
Karl-Fischer Titration.....	196
Mass Spectroscopy.....	196
NMR Spectroscopy	196
³¹ P{ ¹ H} NMR quantification method	196
UV-vis Spectroscopy	197
UV-vis Spectroelectro (UV-vis SEC).....	197
IV.4. Special equipment.....	197
4.1 High-pressure electrochemical equipment.....	197
4.2 Flow Cell.....	199
4.2.1 Flow Cell modifications.....	199
4.2.2 Electrodes.....	200
4.2.3 Membranes.....	201
4.2.4 Flow rates	201
IV.5. Syntheses of Rhenium compounds	203
[ReBr ₂ (PNP)] (1 ^{Br})	203
[ReI ₂ (PNP)] (1 ^I)	203

[ReBrCl(PNP)] (1^{BrCl}) (as spectroscopically found)	204
[ReCl(PNP)] (1^{Cl}) (as spectroscopically found).....	204
Synthesis attempts to [ReCl ₂ (P=NP)] (1^{Cl}).....	204
[{ReCl(PNP)} ₂ (μ -N ₂)] (2^{Cl})	205
[{ReBr(PNP)} ₂ (μ -N ₂)] (2^{Br})	205
[{ReI(PNP)} ₂ (μ -N ₂)] (2^{I})	206
[ReNCl(PNP)] (3^{Cl})	206
[ReNCl(P=N=P)] ($=3^{\text{Cl}}$)	207
[ReNBr(PNP)] (3^{Br})	208
[ReNI(PNP)] (3^{I})	209
[ReNI(P=N=P)] ($=3^{\text{I}}$)	211
[ReNBr(^H PNP)]Br ($4^{\text{Br-Br}}$)	212
[ReNI(^H PNP)]I ($4^{\text{I-I}}$).....	212
[Re(NCH ₂ CH ₃)Cl(P=N=P)] ($=5$).....	212
[Re(NCHCH ₃)Cl(PNP)] (6).....	213
[Re(NCHCH ₃)Cl(P=N=P)] ($=6$).....	213
[ReCl ₃ (PNP)] (8).....	214
[ReCl ₃ (P=N=P)] ($=8$)	215
[ReNI(N(CHCH ₂ PtBu ₂)(CHCHPtBu ₂))OTf] ($9^{\text{I-OTf}}$).....	215
[ReNI(N(CHCHPtBu ₂)(CHCHPHtBu)) (10)	215
[ReN(OTf)(P=N=P)] (11).....	216
12.....	216
IV.6. Electrochemical, kinetic and various experiments.....	217
6.1 Chapter II.1.	217
NMR kinetic measurement for N ₂ splitting of 2^{Cl} into 3^{Cl}	217
NMR experiments of 1^{Cl} at high pressures and with added chloride	217
Electrochemical experiments for 1^{Cl} and 3^{Cl}	218
6.2 Chapter II.2:	219
UV-vis Spectroelectrochemistry of 1^{Cl} , 1^{Br} , 1^{I}	219
Electrochemical experiments for 1^{Br}	219
NMR experiments of 1^{I} at high pressures and with added iodide and electrolyte.....	220
Electrochemical experiments for 1^{I}	221
6.3 Chapter II.3	222
(Electro)chemical stability tests	222
Electrochemical experiments for $=1^{\text{Cl}}$	222
6.4 Chapter II.4.	224
Electrochemical MeCN release from 6.....	224
Electrochemical MeCN release from 5.....	224
Electrochemical MeCN release from $=6$	224
Chemical MeCN release from $=6$	225
Attempts to quantify $=8$ electrochemically upon oxidation of ($=6$).....	225

Chloride titration of 8	225
Chloride titration of 8	226
Stability of 8 in presence of electrolyte and chloride source	226

V. Appendix

A1. Graphical overview of all <i>used</i> or <i>aimed for</i> rhenium complexes.....	228
A2. pKa-values and Redox potentials of reagents/solvents used in this work	229
A3. Figures and Tables of chapter II.1.....	230
A4. Figures and Tables of chapter II.2.....	235
A5. Figures and Tables of chapter II.3.....	253
A6. Figures and Tables of chapter II.4.....	258
A7. Crystallographic Details	264
A7.1 General crystallographic experimental details.....	264
A7.2 Crystallographic Details of 1^{Br}	265
A7.3 Crystallographic Details of 3^{Br}	266
A7.4 Crystallographic Details of 3^I	267
A7.5 Crystallographic Details of 4^I	268
A7.6. Crystallographic Details of 5	269
A7.7. Crystallographic Details of 6	270
A7.7 Crystallographic Details of 12	271

VI. References

VII. Curriculum Vitae

I Introduction

I.1. Dinitrogen coordination and splitting

1.1. Properties of Dinitrogen

Dinitrogen (N_2) is an abundant diatomic molecule (present in circa 78 % in the atmosphere) and represents therefore an accessible building block for nitrogen atoms. Its activation is also strongly required for today's society relying on the industrial Haber-Bosch (HB) process to convert N_2 into NH_3 mainly for agricultural industry, yet also as building block for all nitrogen containing (fine) chemicals and pharmaceuticals. Unfortunately, it is a very inert molecule, as reflected in various properties: i.e. a high HOMO-LUMO gap (10.82 eV), a low proton affinity (5.1 eV, even lower compared to CH_4 5.3 eV), and a high ionisation energy (15.8 eV), combined with the absence of a dipole moment. An electron affinity is basically non-present (-1.9 eV), also expressed in the very negative reduction potential of $N_2 + 1e^- \rightarrow [N_2]^-$ of -4.16 V vs. NHE. Notably, turning this reduction in a multi-electron reduction combined with protonation via proton-coupled electron transfer (PCET) makes the reaction substantially milder.^{1,2} The molecule's high bond dissociation energy (226 kcal mol⁻¹) is not outstanding compared to other diatomic triple bonded molecules.³ Yet, the distribution of this energy over the three NN bonds (1 σ and 2 π bonds) is rather uneven: the first (π -)bond is exceptionally strong (≈ 100 kcal mol⁻¹), compared to the first (π -)bond of acetylene (53 kcal mol⁻¹).⁴

1.2. Industrial and biological conditions for N_2 -activation

Despite its inertness, it is possible to utilise dinitrogen and to transform it to ammonia. In nature this is done enzymatically on nitrogenases and on a large scale, the HB process was developed to account for agricultural needs. Both will be briefly addressed.

Nitrogenase enzymes are found in certain bacteria and provide all N-containing molecules for plants required via atmospheric N_2 -uptake. The active site for N_2 -reduction is a metal-sulfur cluster located at the enzyme, of which three types are known: a Fe, FeV, and FeMo co-factor. The latter has the highest selectivity for N_2 -reduction over the competing hydrogen evolution reaction (HER), and is therefore extensively examined. Its structure and especially the central ligand has long been a topic of debate, but high-resolution X-ray spectroscopy confirmed a $[Fe_7MoS_9C]$ -structure with an interstitial carbon atom, see Figure 1. Upon coordination to an all iron-based reductase, a multi-step and still partly unknown mechanism takes place including

ATP as energy source to allow electron and proton transfer from reductase to nitrogenase to reduce the co-factor and perform the overall 6-electron transformation of N₂. The currently hypothesised mechanism is initiated by a number of 1 e⁻/1 H⁺ transfers (3 or 4) to the co-factor before it coordinates N₂ either at an Fe or Mo centre. Then, NH₃-formation can be rationalised via two pathways: either both N-atoms are alternately functionalised in an “alternating” mechanism. Alternatively, first the terminal N_β is functionalised to its full extent, and subsequently the remaining nitride N_α, following a “distal” pathway. It is to date unclear whether one of these pathways or hybrid forms of it occur.^{5,6} The enzymatic involvement of iron and molybdenum has inspired many inorganic chemists to use these metals in their development of (bio-inspired) molecular N₂-reduction complexes (*vide infra*).

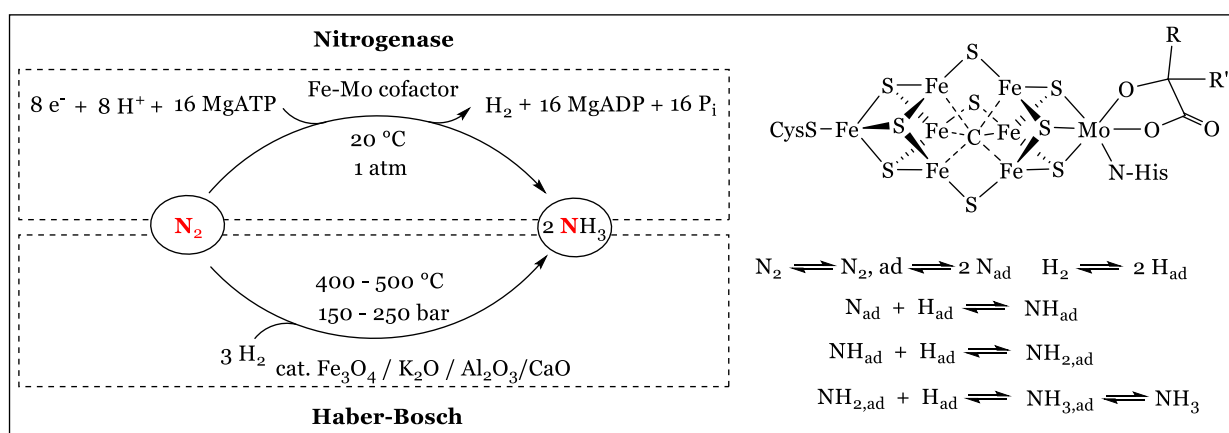


Figure 1. Schematic representation of N₂-fixation by nitrogenase and the FeMo co-factor (top) and via the Haber-Bosch process including a schematic representation of its dissociative mechanism (bottom).^{5,7} Visualisation idea from Mougel.⁸

The industrial revolution ignited the increase of the world population, and towards the end of the 19th century, it was foreseen that nutritional demands would go beyond what natural sources for fertiliser could offer. Therefore, many research efforts were put into transformation of atmospheric dinitrogen. In the early 1910's, Haber invented the direct reaction of N₂ with H₂ to form NH₃, which reaction set up was optimised by Bosch: the HB process operates since 1913 and produces ammonia over 100·10⁶ ton per year. As catalyst, a heterogeneous mixture is used of iron oxides, promoted and stabilised with potassium-, aluminium-, and calcium oxides.^{7,9} High reaction temperatures are required (400 - 500 °C), to overcome the high activation barrier as a result of N₂ inertness. As the reaction is exergonic, high pressures of roughly 200 bars are required to still achieve good yields. The HB process is often associated with circa 1-2 % of the

world's energy consume. Yet, the majority of this demand lies in the synthesis and purification of H_2 , which relies on energy-intensive steam reforming of methane and coal.¹⁰ Due to this high energy consume, the development of alternative ammonia formation strategies, especially by means of electrochemistry, gained a lot of attention in recent years: a brief overview thereof is provided in Section I.2.1.2. The HB mechanism was elucidated by Ertl, who found that the initial elementary step is the dissociative chemisorption on N_2 on the iron surface into nitrides (Figure 1). Note how this is distinctly different from the current proposed mechanism of nitrogenase where the N-N bond is initially retained. Subsequent reaction with chemisorbed hydrogen atoms forms ammonia, which is then released.⁷

1.3. Dinitrogen as ligand for coordination complexes

Beyond the heterogeneous nature of the N_2 -activating compounds in the HB process, lies N_2 -fixation on molecular defined complexes. A first characterised example of dinitrogen as ligand was found by Allen and Senoff in 1965, in form of $[Ru(NH_3)_5(N_2)]^{2+}$, see Figure 2.¹¹ As highlighted in interesting background narratives by Leigh and Jones,^{12,13} the original purpose of the work was to synthesize the hexa-ammine ruthenium complex via reaction of $[RuCl_3(H_2O)_3]$ and hydrazine as reduction agent and ammonia source. Yet without the addition of an ammonium salt, the penta-ammine dinitrogen complex was formed, where the N_2 originates from hydrazine. Especially the appearance of a stretching frequency at 2100 cm^{-1} by IR spectroscopy was indicative for coordinated N_2 , even though it was first interpreted as a metal-hydride. Later, it was shown that the N_2 ligand can also originate from atmospheric uptake via reduction of a Ru(III) precursor under a dinitrogen atmosphere. The original work was welcomed with a lot of criticism, that was first tempered by the publication of the crystal structure of $[Ru(NH_3)_5(N_2)]Cl_2$. This showed a N-N bond length of 1.12 \AA , which is only moderately activated compared to free N_2 (1.10 \AA , see Table 1).¹⁴

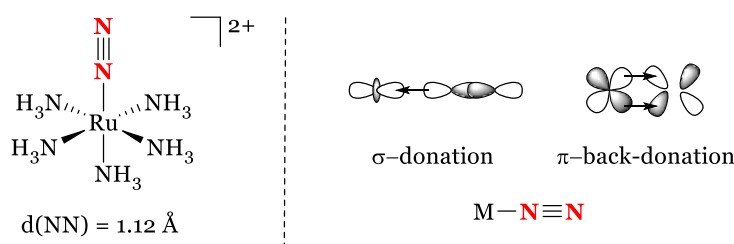


Figure 2. Left: first characterised N_2 -bound complex by Allen.¹¹ Right: qualitative σ - and π -interactions in an end-on M- N_2 fragment.

Thereafter, and with the realisation how to identify a possible N_2 -complex, many complexes were developed. The metal-dinitrogen interaction relies on a σ -donation from N_2 to the metal, and a π -backdonation from the metal into the π^* -orbital of N_2 (Figure 2). Both interactions will decrease the bond-order in dinitrogen. The reminiscence with a carbonyl ligand is evident and from the early complexes the same basic rules for N-N bond elongation were found, i.e. a shorter N-N bond is found upon oxidation of the metal centre or the coordination of π -accepting ancillary ligands, and *vice versa*. The degree of activation can be expressed by N-N bond lengths or stretching frequencies, as listed for various oxidation states of N_2 in Table 1. Weak orbital overlap between N_2 and the metal only results in weak bond activation compared to CO, as reflected in typical N-N bond lengths in M- N_2 complexes usually in the range of 1.10-1.12 Å.¹⁵

Table 1. Bond lengths and stretching frequencies of coordinated N_2 and free N_2 , H_2N_2 and H_4N_2 .¹⁶

Free $N\equiv N$	1.10 Å	2331 cm^{-1}
$N\equiv N$	$\approx 1.10\text{-}1.20$ Å	$\approx 1700\text{-}2331$ cm^{-1}
$[N\equiv N]^-$	n.a.	n.a.
Free H_2N_2	1.25 Å	1583/1529 cm^{-1}
$[N=N]^{2-}$	$\approx 1.20\text{-}1.35$ Å	$\approx 1200\text{-}1700$ cm^{-1}
$[N=N]^{3-}$	1.40 Å	989-1040 cm^{-1}
Free H_4N_2	1.45 Å	885 cm^{-1}
$[N-N]^{4-}$	$\approx 1.40\text{-}1.60$ Å	$\approx 700\text{-}1100$ cm^{-1}

A higher degree of activation can be reached when a multi-metallic approach is pursued. Within this strategy, the coordination modes of N_2 are various, and an overview of common binding motives is given in Figure 3. Evolving from mononuclear, end-on coordination, the binding to a second metal centre leads to an end-on N_2 -bridge ($= \mu\text{-}\eta^1:\eta^1$), which is a well-known motif. Additionally, dinitrogen can be coordinated in a side-on bridging $\mu\text{-}\eta^2:\eta^2$ mode, or a mixed side-on end-on $\mu\text{-}\eta^1:\eta^2$ mode. Considering the relevance for the research as performed within this work, the focus in the next sections will be on end-on bridging complexes.

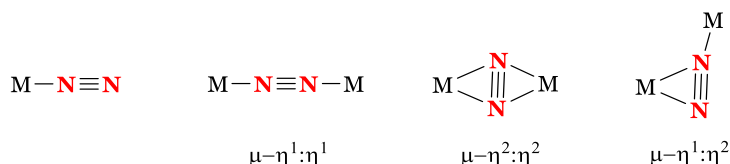
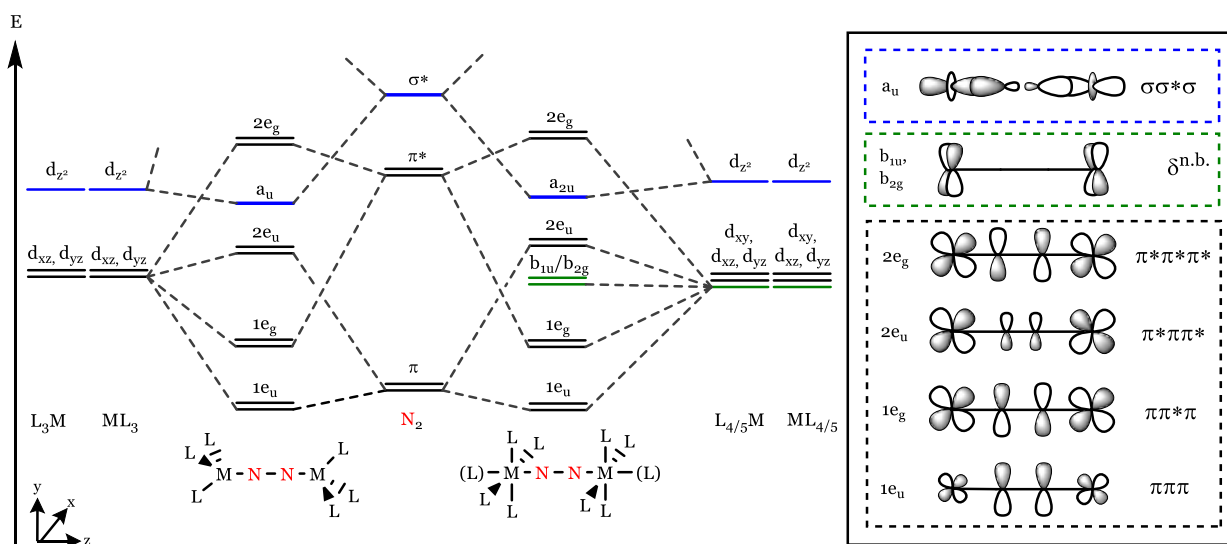


Figure 3. Common binding motives for dinitrogen as ligand.

Continuing from $[Ru(NH_3)_5(N_2)]^{2+}$, Taube and co-workers isolated in 1969 the first example of a bimolecular end-on N_2 -complex, in form of $[Ru(NH_3)_5]_2(\mu\text{-}\eta^1:\eta^1\text{-}N_2)]^{4+}$,¹⁷ which was right thereafter crystallised by Gray and co-workers.¹⁸ Many N_2 -bridging complexes followed and less

than ten years later, Chatt reviewed the over 30 (more or less well characterised) examples reported within that short time frame.¹⁵ More recent reviews give an overview of the circa 50 years of research.^{1,19,20} To rationalise the bonding situation of these dinuclear end-on complexes, the orbital interactions between the metal and the N₂-ligand were considered, as initiated by Gray and Richards.^{18,21} As frontier orbitals, a π -orbital dominated manifold was found, based on the interaction between the metal d_{xz}/d_{yz} and the N₂ π/π^* -orbitals, see Scheme 1. This constructs four MO's ranging from fully bonding ($1e_u, \pi\pi\pi$), to fully anti-bonding ($2e_g, \pi^*\pi^*\pi^*$), with respect to the {MNNM}-manifold. A second degenerate set is oriented orthogonally. Within the same energy range, the combination between the metal d_{z^2} - and the N₂ σ^* -orbital to a $\sigma\sigma^*\sigma$ MO is found, which has a strong NN anti-bonding character and will be relevant for N₂-splitting (*vide infra*). If the ancillary ligand arrangement on the metal centre is threefold, the ligand-metal interactions raise the energy of the remaining metal orbitals (d_{xy} and $d_{x^2-y^2}$). In a fourfold coordination, the orthogonal ancillary ligands interact differently with the d-orbitals, and the d_{xy} orbitals appear within the relevant energy level for the {MNNM} manifold. Without finding interaction with N₂, they remain non-bonding, metal centred orbitals, as highlighted in green in Scheme 1. It was found by calculations that the fully π -bonding set ($1e_u$) is mainly N₂-centred and the $\pi\pi^*\pi$ set ($2e_u$) is mainly metal-centred in nature. Depending on the nature of the ancillary ligands or the metal centres, the energy levels or degeneracy of the orbitals as sketched in Scheme 1 can be different.



Scheme 1. Schematic qualitative orbital interaction scheme for end-on dinuclear {MNNM} fragments, as originating between N₂ and two 'ML₃' fragments in a threefold coordination (left) or N₂ and two 'ML_{4/5}' fragments in a fourfold coordination (right), where L represents an ancillary ligand. The orbitals are drawn with the following colour code: π orbitals (black, only the set in the y,z-direction is visualised), δ non-bonding (n.b.) orbitals (green) and σ orbital (blue).

Based on the metal valence d-electrons and the population of the orbitals, this model can be used to rationalise the N-N bond orders as found by XRD or vibrational spectroscopy. For pioneering $\text{Ru}^{\text{II}} [\{\text{Ru}(\text{NH}_3)_5\}_2(\mu\text{-}\eta^1\text{:}\eta^1\text{-N}_2)]^{4+}$, the N-N bond length (1.124 Å) is barely activated, compared to free N_2 (Table 1). This is in line with occupation of 16 available electrons (4 from the dinitrogen, and two times 6 valence electrons from Ru^{II}) up to and including the $2e_g$ set (in a so-called ‘ $\delta^4\pi^{12}$ ’ configuration). Since this latter π -orbital is N-N bonding in nature, its population will strengthen the N-N bond. A contrary example is the paramagnetic heteronuclear $\text{Re}^{\text{I}}/\text{Mo}^{\text{V}} [\{\text{ReCl}(\text{PMe}_2\text{Ph})_4\}\{\text{MoCl}_4(\text{OMe})\}(\mu\text{-}\eta^1\text{:}\eta^1\text{-N}_2)]$ as found by the group of Richards, with an elongated N-N bond of 1.18(3) Å. This elongation is in line with its $\delta^3\pi^8$ configuration, where the N_2 π -bonding orbital $\pi^*\pi\pi^*$ remains unpopulated.^{22,23}

In addition to these isolated examples that illustrate the use of this MO description to rationalise the N-N bond metrics, various redox-series of end-on N_2 -bridged complexes were prepared, of which some will be discussed herein. Dinuclear $[\{\text{Mo}(\text{NAr}t\text{Bu})_3\}_2(\mu\text{-}\eta^1\text{:}\eta^1\text{-N}_2)]$ (Ar = 3,5-dimethylphenyl) is the pioneering example for N_2 -bond splitting into terminal nitrides (*vide infra*), as characterised by Cummins. Cyclic voltammetry (CV) of this compound suggested synthetic access to both mono- and di-cationic congeners at mild potentials and both complexes were synthesised (Figure 4, left). Upon oxidation, the N-N bond order decreases as shown by XRD and vibrational spectroscopy. This initially seems a paradox: in a classical mononuclear binding situation electron removal decreases the metal to ligand backdonation, which strengthens the N-N bond. Yet, by considering the π^{10} configuration within the $\{\text{MNNM}\}$ manifold of the neutral complex, it gives a coherent picture: subsequent removal of electrons from the N-N bonding $\pi^*\pi\pi^*$ -orbital to a π^9 and π^8 configuration gradually elongated the NN bond. In addition, both the absence of a N_2 -stretching band in the IR spectrum or a typical mixed-valent electronic absorption band for $[\{\text{Mo}(\text{NAr}t\text{Bu})_3\}_2(\mu\text{-}\eta^1\text{:}\eta^1\text{-N}_2)]^+$, highlights the high covalency within the $\{\text{MNNM}\}$ core for this $S = 1/2$ compound.²⁴

Another example of a redox-series comes from our group: $[\{\text{WCl}(\text{PNP})\}_2(\mu\text{-}\eta^1\text{:}\eta^1\text{-N}_2)]$ was characterised by Dr. B. Schlusshass within our group, assigned to a $\delta^4\pi^8$ configuration. Electron removal towards either the one- or two-fold oxidised products has no influence on the dinitrogen bond order as the bond length and stretching frequency are basically invariant within this series (see Figure 4, middle). The HOMO orbital of $[\{\text{WCl}(\text{PNP})\}_2(\mu\text{-}\eta^1\text{:}\eta^1\text{-N}_2)]$ consist of the metal-based δ -orbitals, and oxidation to the $\delta^3\pi^8$ and $\delta^2\pi^8$ configuration does indeed not interfere with the $\{\text{MNNM}\}$ core. For the di-cationic product, two weakly anti-ferromagnetically coupled $S=1/2$ ions indicate a $\delta^1\delta^1\pi^8$ configuration, as substantiated by SQUID magnetometry and DFT calculations.²⁵ Recently, the analogue Mo series was isolated and characterised, showing the

same invariant behaviour. When going from W to Mo, the potentials are circa 0.25 V milder to access these oxidised analogues highlighting the decreased reducing properties of Mo vs. W.²⁶

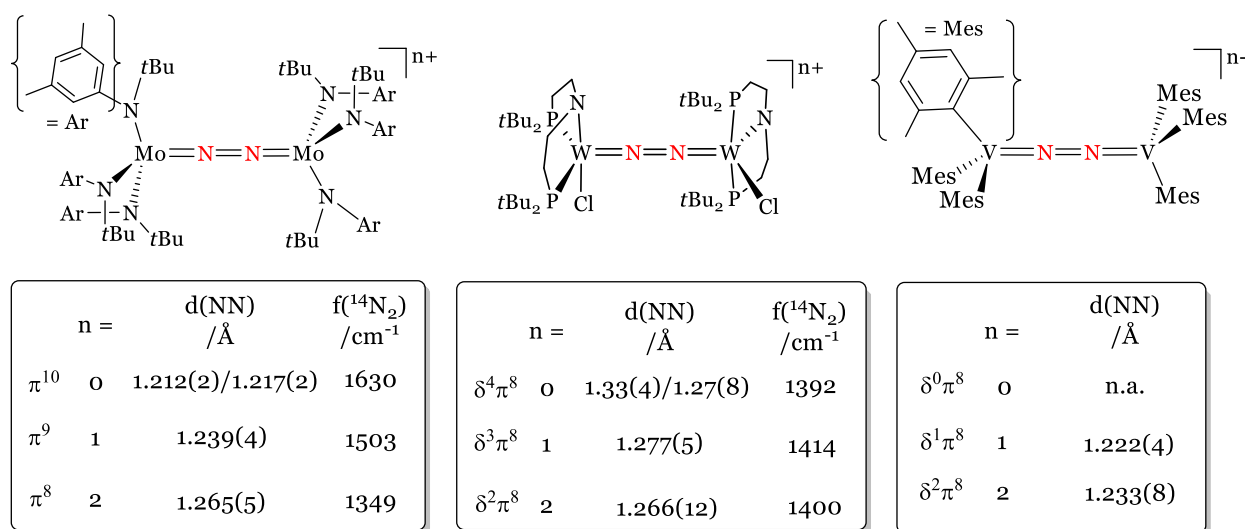


Figure 4. Selected end-on bridging N₂-complexes of Mo, W and V and their N-N bond order characteristics (bond length by XRD and stretching frequency by Raman spectroscopy).^{24–27}

Floriani decided to apply pure σ-donating carbon-based ancillary ligands; the lack of metal to ligand back-bonding was envisioned to access electron-rich metal centres favoured for N₂-fixation. Their vanadium based end-on dinuclear complex [$\{VMes_3\}_2(\mu-\eta^1:\eta^1-N_2)$] could be isolated as neutral, mono-anionic and di-anionic series (Figure 4, right). Unfortunately, no crystal structure of the neutral compound was obtained, but the one or two-fold reduction has virtually no effect on the N-N bond. DFT corroborated that the LUMO orbitals proved low-lying δ-symmetric metal-based orbitals, and their population upon reduction does not affect the N₂-bond metrics. The neutral complex has interesting magnetic behaviour: the low-lying vacant δ-orbitals mix into the singlet (π⁸) ground state causing temperature-independent paramagnetism (TIP).^{27–29}

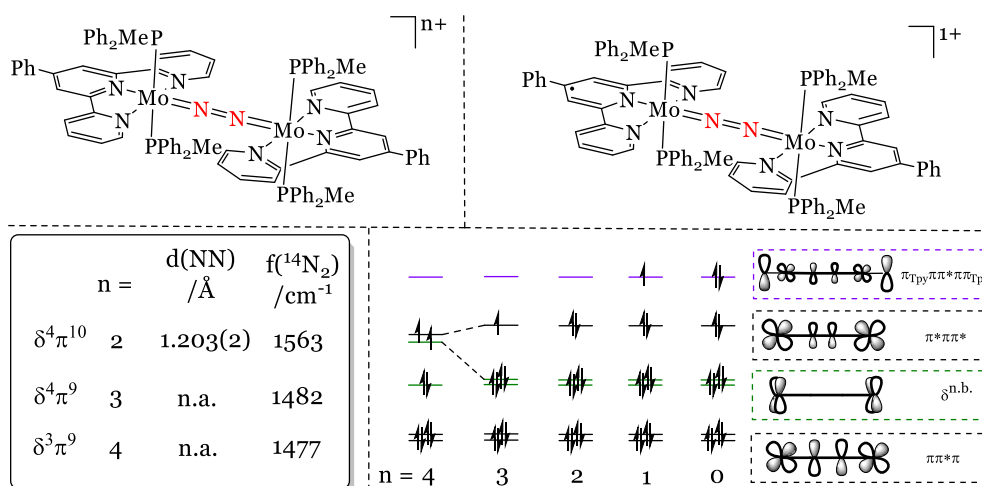


Figure 5. An end-on bridging N₂ complex from Chirik in different redox states and its N-N bond metrics upon oxidation (left), the ligand-based mono-reduced compound (top right), and the corresponding scheme of the frontier orbitals (bottom right).³⁰

The work by Chirik represents a remarkable example of an end-on bridging N₂ complex with a redox-active ligand, which is stable over five redox states (Figure 5). The complex $[\{\text{Mo}(\text{PPh}_2\text{Me})_2(\text{PhTpy})\}_2(\mu\text{-}\eta^1\text{:}\eta^1\text{-N}_2)]^{2+}$ (PhTpy = 4'-Ph-2,2':6',2''-terpyridine) shows a moderately activated N₂-bridge (1.203(2)Å), in line with the population of the $\pi^*\pi\pi^*$ orbital in a $\delta^4\pi^{10}$ configuration. Due to interactions with the π -manifold of the terpyridine ligand, which is in the similar energy range, the degeneracy of the $\pi^*\pi\pi^*$ -orbitals is lifted. Oxidation to the tricationic complex ($\delta^4\pi^9$) leads to a more activated N-N bond. Yet, the subsequent oxidation does not induce further bond elongation, as one of the δ -orbitals is raised in energy and a S=1 ground state is found for $[\{\text{Mo}(\text{PPh}_2\text{Me})_2(\text{PhTpy})\}_2(\mu\text{-N}_2)]^{4+}$ with a $\delta^3\pi^9$ configuration (see Figure 5). Reduction of the two-fold oxidised compound populates the LUMO, which has mainly terpyridine π^* character with a small contribution of the $\pi\pi^*\pi$ set. Consequently, the first reduction is accompanied by a slight decrease in N-N bond order ($f(\text{N}_2) = 1530 \text{ cm}^{-1}$), yet the electron density is mainly located on the ligand. The two-fold reduced neutral species was synthesised, but unfortunately its N-N bond metrics could not be characterised. It is a diamagnetic species, in analogy to the MO-scheme in Figure 5.³⁰

Sita prepared an extensive dataset of dinuclear N₂-bridging complexes with various early transition metals all with virtually the same ligands, from which the metal influence on the N₂ bond can be examined. For M = Ti, V, Nb, Ta, Mo, and W, end-on N₂-bridging complexes were found of the general formula $[\{\text{M}(\text{Cp}^*)(\text{NiPrC}(\text{Me})\text{NiPr})\}_2(\mu\text{-}\eta^1\text{:}\eta^1\text{-N}_2)]$.³¹⁻³³ As shown in Figure 6, all N-N bonds are elongated and are within the diazenido (N₂)²⁻ range. Within a group (e.g. V – Nb – Ta of group 5) a gradual elongation of the N-N bond is observed, as assigned to the more

electron donating properties for the heavier metals. Notably, for $M = \text{Zr}$ and Hf , a side-on coordination mode was found $[\{M(\text{Cp}^*)(\text{NiPrC}(\text{NMe}_2)\text{NiPr})\}_2(\mu\text{-}\eta^2\text{:}\eta^2\text{-N}_2)]$,³⁴ attributed to the larger covalent radius for these metals ($\approx 1.75 \text{ \AA}$ (Zr/Hf)). The N-N bond for these compounds is extraordinarily elongated, and upon decreasing the steric demand on the amidinate substituents, N-N bonds up to $1.635(5) \text{ \AA}$ are found. Therefore, these complexes are best described as two $\text{Zr}^{\text{IV}}/\text{Hf}^{\text{IV}}$ with a bridging $(\text{N}_2)^{4-}$ moiety. The contrasting description of two Ti^{III} bridging a diazenido ligand for the first-row analogue is attributed to its low oxidation potential inhibiting the Ti^{IV} state.

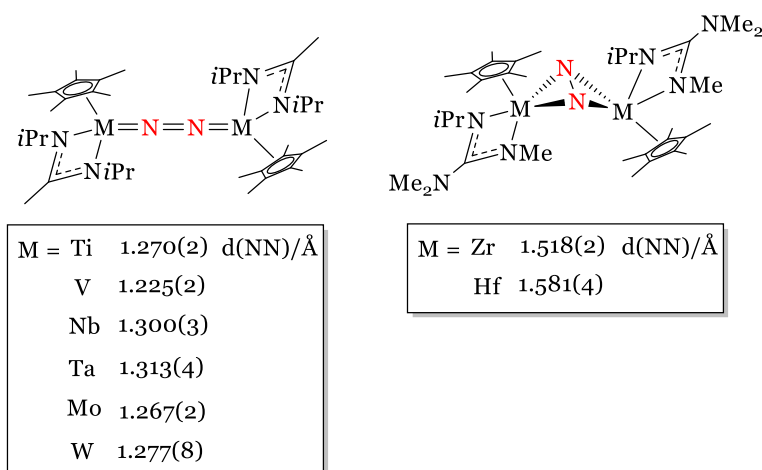
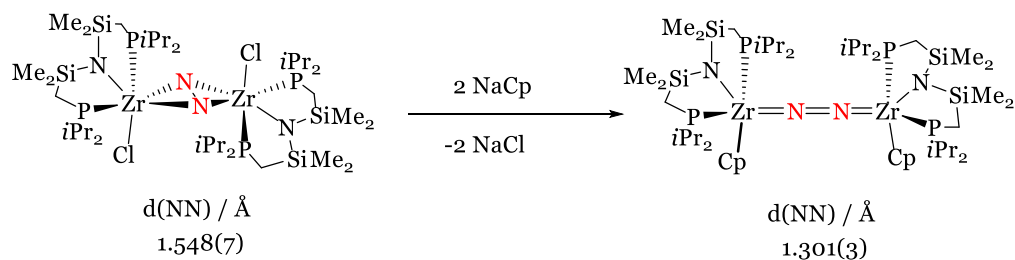


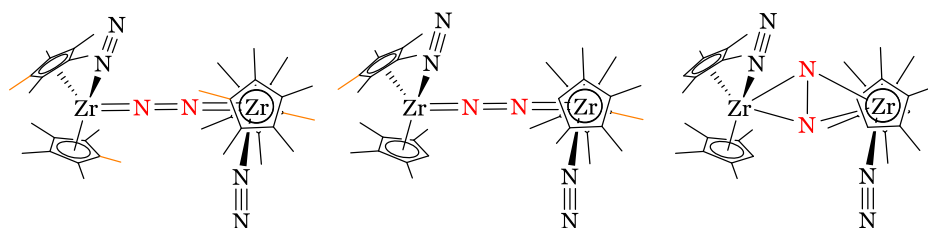
Figure 6. Dinuclear N_2 -bound series of early transition metals by Sita and co-workers. For $M = \text{Mo}$, the C of the amidinate bears a dimethylamide substituent. For $M = \text{Nb}$, the C of the amidinate bears a phenyl substituent.³¹⁻³⁴

Controlling the coordination mode of N_2 upon ligand-exchange was found by Fryzuk, for the side-on N_2 -bridging $[\{\text{ZrCl}(\text{N}(\text{SiMe}_2\text{CH}_2\text{P}i\text{Pr}_2))\}_2(\mu\text{-}\eta^2\text{:}\eta^2\text{-N}_2)]$. When replacing the ancillary chloride ligand for a cyclopentadienyl ring, a rearrangement takes place to the end-on N_2 -bridging analogue (Scheme 2). The latter is associated with a π^8 configuration, in agreement with a significant elongated N-N bond ($1.301(3)\text{\AA}$). These different bridging modes were rationalised by considering the different MO-schemes for side-on versus end-on bridging. For the side-on bridging mode, interaction between the metal d- and the $\text{N}_2 \pi^*$ -orbitals result in a π - and δ -symmetric MO (in contrast to two π symmetric MOs for end-on bridging, see Scheme 2). When a Cp-ligand is coordinated, the required metal d-orbital for this δ -symmetric orbital is involved in the bond with the Cp ring instead, which enforces an end-on N_2 -bridging mode where this d-orbital remains metal-centred. In order to rule out that the altered steric shielding play a role, a similar compound with a smaller metal (Ta) and a smaller ancillary ligand (neopentylidene) is synthesised. This compound is assumed to also adopt the end-on mode, yet without the indicative prove of XRD analysis.^{35,36}



Scheme 2. Side-on to end-on bridging N_2 isomerisation upon ligand exchange by Fryzuk.^{35,36}

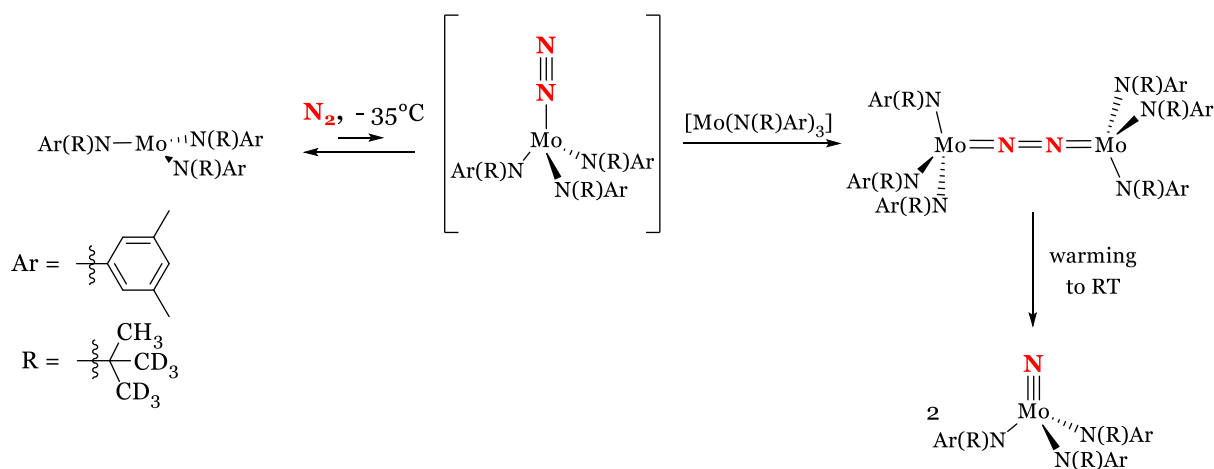
Bercaw and Chirik systematically addressed increased steric demand on the same ligand. It was found that different N_2 -bridging modes were adapted depending on the number of Me-substituents on the ancillary Cp-ligand. $[\{\text{Zr}(\text{Cp}^*)_2(\text{N}_2)_2\}_2(\mu-\eta^1:\eta^1-\text{N}_2)]$ and $[\{\text{Zr}(\text{Cp}^*)(\text{Cp}')(\text{N}_2)_2\}_2(\mu-\eta^1:\eta^1-\text{N}_2)]$ ($\text{Cp}' = \text{C}_5\text{Me}_4\text{H}^-$) are in an end-on N_2 -bridging mode, whereas $[\{\text{Zr}(\text{Cp}')_2(\text{N}_2)_2\}_2(\mu-\eta^2:\eta^2-\text{N}_2)]$ bridges N_2 in a side-on coordination (Scheme 3). Computations suggested that the side-on coordination is in principle preferred. Yet, when more than 4 methyl groups are present at the Cp ring, the end-on mode is enforced because of steric repulsion (in the end-on mode the ancillary ligands are substantially further apart). All complexes adapt a twisted structure with regard to the four $\text{Cp}'^*/$ rings, that allow both appropriate (orthogonal) metal d-orbitals to overlap with the orthogonal π^* -orbitals of N_2 , which induces a stronger bond activation of the latter.³⁷⁻⁴¹



Scheme 3. Dinuclear zirconium N_2 -complexes by Bercaw and Chirik with Cp-ligands bearing from left to right reduced steric demand; the successive -Me for -H replacement is highlighted in orange.³⁸⁻⁴¹

1.4. N₂-splitting into terminal nitrides

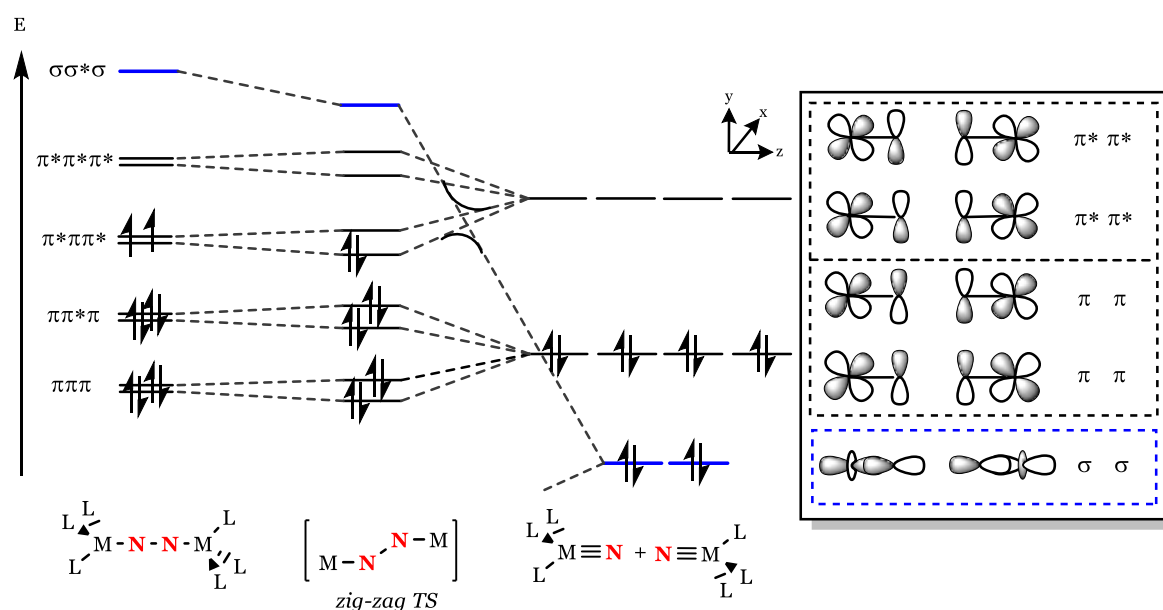
In 1995, Cummins and Laplaza showed the pioneering example of direct cleavage of a N-N bond into terminal, well-defined, molecular nitrides for the first time. Starting Mo(III) precursor $[\text{Mo}(\text{N}(\text{R})\text{Ar})_3]$ ($\text{R} = \text{C}(\text{CD}_3)_2\text{CH}_3$, $\text{Ar} = 3,5\text{-(CH}_3)_2\text{C}_6\text{H}_3$) under a N₂-atmosphere at low temperatures for prolonged time (3 days) and successive warming to RT, revealed formation of pale yellow Mo(VI) nitride $[\text{MoN}(\text{N}(\text{R})\text{Ar})_3]$ in good yields (Scheme 4). Fortunately, they were able to isolate the dinuclear end-on N₂ bridging intermediate $[\{\text{Mo}(\text{N}(\text{R})\text{Ar})_3\}_2(\mu\text{-N}_2)]$ (from here on, only 'μ' is used when an end-on 'μ-η¹:η¹' mode is implied). It forms the fundament for an in-depth mechanistic understanding of this overall 6-electron activation.^{42,43} As elemental step for the assembly of this dinuclear intermediate, they propose formation of end-on N₂ bound $[\text{Mo}(\text{N}(\text{R})\text{Ar})_3(\text{N}_2)]$ that reacts with a second precursor molecule. This is substantiated by the isolation of anionic $[\text{Mo}(\text{N}(\text{R})\text{Ar})_3(\text{N}_2)]^-$ when quantitatively reducing the precursor under N₂ with a strong reductant (Na/Hg), and the fact that the Mo(III) precursor cannot be reduced under Ar as verified from CV measurements. In general, sub stoichiometric amounts of Na/Hg accelerate the formation of the dinuclear intermediate via redox-catalysis. The steric demand of the amide ligand turned out to be a crucial parameter. Changing the *tert*-butyl groups for either adamantyl or *iso*-propyl has a dramatic effect: in the former case, no N₂-splitting could be established.²⁴ In the latter case, a bridging nitride linkage between two monomers was found as only product, presumably going through the terminal nitride.⁴⁴ Smaller substituents form dimeric Mo-Mo structures without incorporation of N₂.⁴⁵



Scheme 4. Pioneering example of N₂-splitting into terminal nitrides by Cummins.⁴³

This pioneering example (and the isolation of the dinuclear intermediate therein) allowed to construct the orbital considerations for splitting, and to rationalise successful requirements for

the further systems that were developed since. Considering two closed shell Mo^{VI} nitrides, 4 σ -, and 8 π -electrons are required to construct the formal triple bond between M and N (1 σ - and 2 π -bonds). [$\{\text{Mo}(\text{N}(\text{R})\text{Ar})_3\}_2(\mu\text{-N}_2)$] has 10 π -electrons within its {MNNM}-framework. 2 σ -electrons are additionally present lower in energy, in a MO mainly comprised of the σ -orbital of N₂ (visualised in ref 46). Therefore, re-distribution of two electrons must occur from the {MNNM} π -manifold into the $\sigma\sigma^*\sigma$ -orbital to form stable, closed-shell nitrides. To accommodate this electron transfer, this latter orbital should be lowered in energy during splitting. By calculations, a transition state (TS) was proposed with a zig-zag nature regarding the {MNNM} core, which stabilises the σ -orbital (Scheme 5). Furthermore, adopting this TS lowers the symmetry, leveraging the degeneracy of the π -manifold and allowing the highest filled π -orbital to correlate with the σ -orbital for electron transfer. Parallel, a triplet to singlet spin flip occurs. In this zig-zag TS, the N-N bond is elongated and the M-N bonds are shortened, *en route* to splitting.⁴⁷ Cummins determined the activation parameters for this pioneering N₂-splitting platform, confirming a sizeable barrier ($\Delta G^\ddagger_{\text{exp., 25 }^\circ\text{C}} = +22.4 \text{ kcal mol}^{-1}$). The activation entropy ($\Delta S^\ddagger = +2.9 \text{ cal mol}^{-1} \text{ K}^{-1}$) is in line with a similarly ordered transition state compared to the N₂-bridging starting compound. With these considerations and MO-scheme in hand, several experimental observations can be explained. First of all, it was shown that from the redox series [$\{\text{Mo}(\text{N}(\text{R})\text{Ar})_3\}_2(\mu\text{-N}_2)$]ⁿ⁺ (Figure 5), the π^9 (n = 1) and π^8 (n = 2) configurations do not split N₂ despite their more elongated N-N bond. No stable closed-shell nitrides can be formed from these configurations, underlining the importance of a π^{10} configuration.



Scheme 5. Orbital considerations for N₂-splitting into closed-shell terminal nitrides for three-fold symmetry.⁴³

Beyond the electronic configuration, also the ancillary ligands and coordination geometry play an important role for successful N_2 -splitting. The end-on N_2 -bridged dinuclear complex $[\{Mo(N(CH_2CH_2NSitBuMe_2)_3\}_2(\mu-N_2)]$ by Schrock (Figure 7, left) is isoelectronic to the Cummins' system having a π^{10} configuration. Yet, this complex is inert towards N_2 splitting, even though this complex bears σ -donating and π -accepting amide ligands similar to Cummins. Yet, these are linked via an additional amine group that coordinates *trans* to the N_2 -bridge, which weakens the Mo- N_{N_2} bond. The thereof resulting destabilisation of the σ -orbital that is required for nitride formation (see Scheme 5) increases the barrier for splitting substantially. The related three-fold symmetric $[\{MoMes_3\}_2(\mu-N_2)]$ of Floriani is stable towards N_2 -splitting even in refluxing benzene (Figure 7, right). It bears pure σ -donating mesityl ancillary ligands instead of previous described σ - and π -donating amide donors. This likely causes the metal d-orbitals to be lowered in energy, and partially populated, thereby surpassing the favoured π^{10} configuration for N_2 -splitting. Notably, N_2 -splitting was found by means of photochemical activation as method to overcome high barriers.⁴⁸

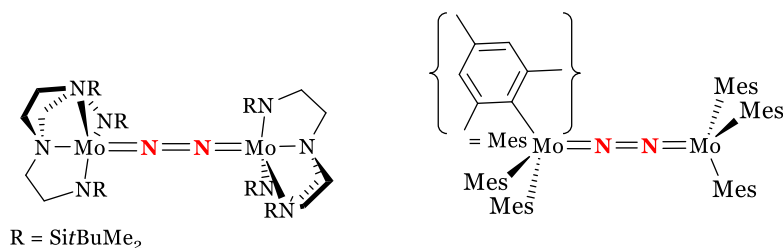
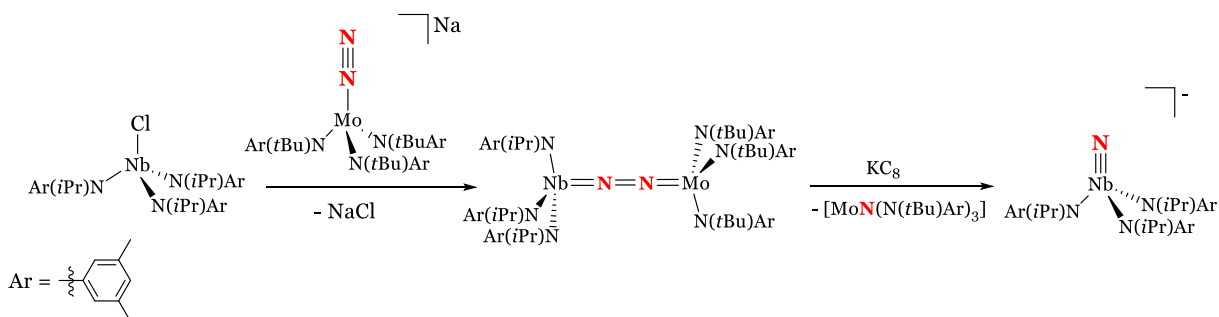


Figure 7. End-on N_2 bridging complexes that are related to the Cummins' system, yet inert to N_2 -splitting to nitrides in a thermal manner.^{48,49}

Several complexes capable of N_2 -splitting into nitrides were discovered since the example by Cummins, covering a wide range of metals and ligands, as extensively reviewed recently.^{1,20} In the following Section, N_2 -splitting for Mo, W, and Re-complexes will be discussed. The Mo complexes are interesting since they continue the seminal work of Cummins, and are mainly inspired by the role of Mo in one of the nitrogenases; W is closely related being in the same group. The Re-complexes will be extensively discussed: the first N_2 -splitting example on Re by our group represents the basis of the research performed within this work. Many of these platforms use pincer ligands, which are stable and easy tuneable regarding their steric and electronic properties.

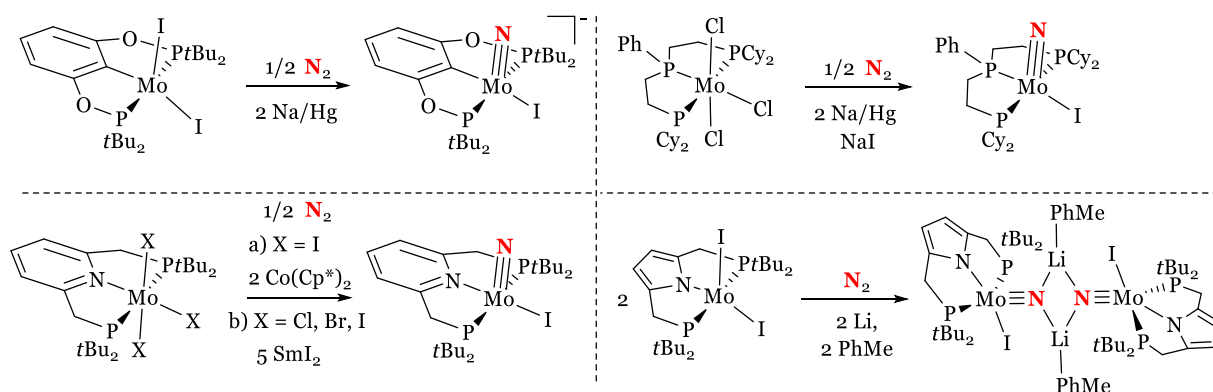
A second example from Cummins represents a bi-metallic Mo/Nb system. The anionic dinitrogen complex $[Mo(N(tBu)Ar)_3(N_2)]^-$ reacts readily with a Nb(IV)-precursor to the end-on N_2 -bridging $[\{Nb(N(iPr)Ar)_3\}\{Mo(N(tBu)Ar)_3\}(\mu-N_2)]$ (Scheme 6). In line with its π^9 -configuration, this compound is stable towards dinitrogen splitting and shows a moderate N_2 -

activation (1.235(10)Å), similar to its heteronuclear analogue [$\{\text{Mo}(\text{NAr}t\text{Bu})_3\}_2(\mu\text{-N}_2)\text{]}^+$. By CV it was shown that this compound can be reduced, and after scanning through this event, the characteristic reduction wave of the molybdenum nitride appears. In line with these observations, reaction with KC_8 yields both the neutral Mo and anionic Nb terminal nitrides.⁵⁰



Scheme 6. Schematic representation of heterobimetallic N₂-cleavage by Cummins.⁵⁰

Several Mo pincer complexes were developed that split N₂ into terminal nitrides as shown in Scheme 7 from the groups of Schrock, Mézailles, and Nishibayashi.^{51–54} All complexes rely on the twofold reduction of a Mo(III)-precursor under a N₂ atmosphere to readily obtain a Mo(IV) nitride, proposedly going via an end-on N₂-bridged intermediate. These formal Mo^I-N₂-Mo^I compounds in an idealised four-fold symmetry follow the same considerations as developed for Cummins' system yet with including the metal-centred δ -orbitals: a $\delta^4\pi^{10}$ configuration allows for splitting into closed shell nitrides. The platform of Schrock yields the anionic nitride $[\text{MoNI}(\text{POCOP})]^-$ (POCOP = C₆H₃-1,3-(OPtBu₂)₂) upon reduction using Na/Hg ($E_p = -2.36$ V vs. Fc⁺⁰)⁵⁵. Upon protonation, they propose the formation of an unusual compound based on its NMR spectroscopic traces and coupling pattern, containing a bridging hydride between one of the Mo-P bonds. Notably, it was attempted to synthesise the chloride and bromide analogues of the precursor. Yet these compounds were always accompanied by mixed halide-iodide impurities, originating from the iodide traces from the ligand.⁵¹ Mézailles and co-workers started from $[\text{MoCl}_3(\text{PPP})]$ (PPP = P(Ph)(CH₂CH₂PCy₂)₂) in presence of an excess NaI, leading to the iodide Mo(IV) nitride. This surprising halide exchange strategy is not extensively discussed, but they propose the end-on N₂-bridging intermediate to already coordinate iodide, and the reaction does not proceed without this additive. Upon using an excess reductant (3 eq. of Na/Hg), the chloride precursor reacts in absence of NaI, to form Mo⁰(N₂)_x-species.⁵⁶ Subsequently, they establish N-Si bond formation and fragment release.⁵⁴



Scheme 7. N₂-splitting into nitrides from Mo pincer complexes by Schrock (top left), Mézailles (top right) and Nishibayashi (bottom).^{51–54,57}

Nishibayashi established N₂-splitting from a PN_{aromatic}P pincer platform, either pyrrole or pyridine based, where the latter represents Millstein's archetypical (de)hydrogenation catalyst.⁵⁸ Starting from [MoI₃(PN_{py}P)] (PN_{py}P = 2,6-(CH₂CH₂PtBu₂)₂NC₅H₃), reduction with 2 eq. of Co(Cp^{*})₂ ($E_{1/2} = -1.84$ V vs. Fc^{+/0} (THF))⁵⁹ under N₂ afforded the nitride and a small amount of over-reduced Mo⁰ end-on N₂-bridged [$\{\text{Mo}(\text{N}_2)_2(\text{PN}_{\text{py}}\text{P})\}_2(\mu\text{-N}_2)$], that does not split in nitrides. Notably, starting from the trichloride analogue precursor in presence of excess Na/Hg, such a Mo⁰ dinuclear species proved the only isolatable compound.⁶⁰ This reflects the high dependency of the reaction outcome on the used reductant and the nature of the ligands. [MoNI(PN_{py}P)] was also accessible in high yields using SmI₂ ($E_p = -1.22$ V vs. Fc^{+/0} (MeCN)) from either the chloride, bromide, or iodide precursor, indicating quick halide exchange.⁵⁷ The pyrrole based [MoI₂(PN_{pyr}P)] (PN_{pyr}P = 2,6-(CH₂PtBu₂)₂NC₄H₂) is reduced with lithium ($E_p = -2.64$ V vs. Fc^{+/0} (NH₃))⁵⁵ under a N₂-atmosphere affording the formal anionic Mo(IV) nitride, that is stabilised as a dinuclear structure with bridging Li linkages.⁵³ Both pyrrole and pyridine nitrides were successfully used for catalytic ammonia formation.^{52,53}

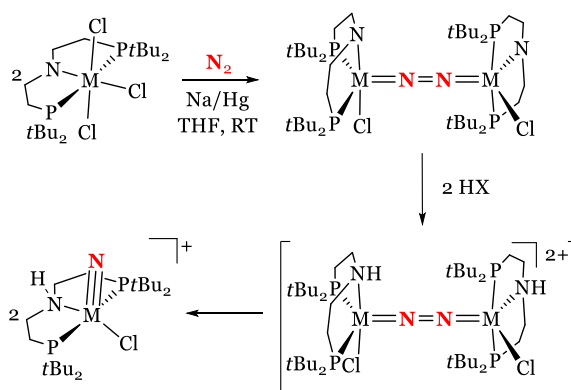
It gets clear from the above-mentioned examples that it is a well-known strategy to exchange the ancillary (halide) ligands on the metal centre and examine the thereof resulting differences. In addition, this strategy is also applied in the N₂-fixation work of Tuzek, Liddle, and Xi using precursors with different halides, yet without an extensive discussion.^{61–63} Since N₂-fixation from a stable precursor is often initiated by an electron transfer, the required redox potentials can have a large influence on the course of the reaction. Changing the ancillary ligands usually changes the redox potentials, as was quantified by Lever, who empirically derived electronic parameters (E_L) for a wide range of ligands originally from a large database of Ru^{III/II} oxidation couples.⁶⁴ The sum of the E_L values combined with a correction factor derived for numerous metals (i.e. Ru, Mo, Re, Fe) and oxidation states generates a decent estimation of the redox

potential for a certain complex.^{64,65} Basically, the E_L of a ligand provides a measurement for the electron donating or accepting properties and some examples are shown in Table 2. For example, the large positive value of dinitrogen ($E_L = +0.68$ V) reflects its π -accepting property and a complex with a coordinated N₂ will be much easier to reduce compared to its analogue without N₂. Strikingly, the halide ligands share virtually the same E_L parameter and their exchange should not affect the redox potentials. Since the above-mentioned examples of N₂-splitting are accompanied by reductively induced halide loss, the distinct different leaving group properties within the halide series ($I^- > Br^- > Cl^-$) might also be a main motivation to apply this halide exchanging strategy. Within the context of this work, the effect of halide exchange for a rhenium N₂-splitting platform is examined and discussed, see Chapter II.2.

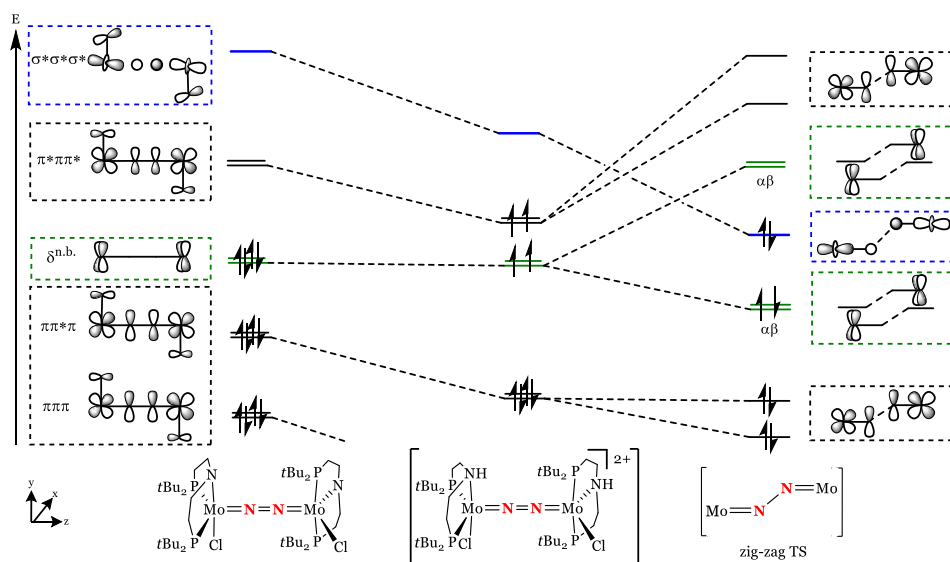
Table 2. Lever electronic parameters (E_L) for selected ligands.⁶⁴

Ligand	N ₂	MeCN	NH ₃	Cl ⁻	I ⁻	Br ⁻	OH ⁻
E_L / V	+0.68	+0.34	+0.07	-0.22	-0.22	-0.24	-0.59

Within our group, N₂-splitting is also established from Mo- and W-pincer. Upon reduction of [MoCl₃(PNP)] (PNP = N(CH₂CH₂PtBu₂)₂⁻) under a N₂-atmosphere, the end-on bridging complex is formed, which is stable towards N₂-splitting as rationalised by its $\delta^4\pi^8$ configuration, see Scheme 8. However, upon two-fold protonation the paramagnetic Mo(V) [MoNCl(HPNP)]⁺ is formed in up to 80 % yield, with the proton on the N_{amide} of the pincer. The same reactivity was found for the tungsten analogue. At low temperatures, a paramagnetic S = 2 intermediate could be spectroscopically characterised, which is assigned to the two-fold protonated compound, that splits first-order into the terminal nitrides.



Scheme 8. Proton coupled N₂-fixation and splitting from [MCl₃(PNP)] (M = Mo, W) by Schneider.^{25,66}

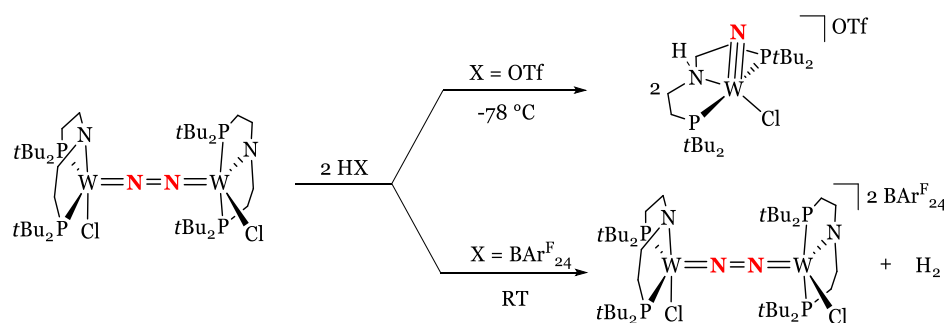


Scheme 9. Singlet to quintet transition upon double protonation of $[\{\text{MoCl}(\text{PNP})\}_2(\mu\text{-N}_2)]$ and the subsequent zig-zag transition state towards N_2 -splitting (where the electron pair in the δ -orbitals in α and β spin polarised).⁶⁶

A rationalisation for this high spin intermediate and the subsequent N_2 -splitting can be based on the MO-scheme consideration, as visualised for the molybdenum case in Scheme 9, showing the $\delta^4\pi^8$ configuration of $[\{\text{MCl}(\text{PNP})\}_2(\mu\text{-N}_2)]$ on the left. The p-orbital of the N_{amide} interacts with the $\{\text{MNNM}\}$ manifold, leading to a destabilisation of the $\{\text{MNNM}\}$ π - and σ -orbitals. Upon protonation of the N_{amide} , this orbital is now engaged in the N-H bond, and the respective $\{\text{MNNM}\}$ -orbitals are stabilised. The δ -orbitals are close in energy to the $\pi^*\pi\pi$ -orbital set, and this (quasi) degeneracy allows a spin crossover to the quintet state, promoting electrons into a for N_2 -splitting desired $\delta^2\pi^{10}$ configuration. Maybe more important, also the σ orbital stabilises upon two-fold protonation, which population and additional stabilisation towards the zig-zag TS is key for successful N_2 -splitting.

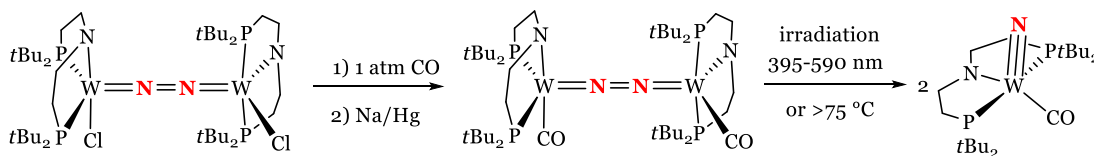
In addition, distinct different reaction outcomes were found upon using different acids with different anions for the tungsten platform: coordinating-anions like OTf^- yielded paramagnetic W(V) nitrides (analogue to the Mo-system), whereas larger non-coordinating anions like $\text{BAR}^{\text{F}}_{24}^-$ yielded the two-fold oxidised end-on N_2 bridging compound and H_2 (Scheme 10). By DOSY NMR spectroscopy, it was found that OTf^- forms a hydrogen bonded complex with the protonated N_{amide} , thereby favouring protonation at this site. From here, a similar mechanism as proposed for Mo leads to N_2 -splitting. This reaction is more favoured at low temperatures to minimise the entropic penalty upon formation of the hydrogen bond. In contrast, larger anions that are not capable of hydrogen bonding induce protonation at the metal centre (which is calculated to be

the most exergonic pathway in absence of hydrogen bonding). From here, the second protonation occurs at the hydride and H₂ is released.



Scheme 10. Anion dependent N₂-splitting or H₂-formation from $[\{WCl(PNP)\}_2(\mu-N_2)]$ by Schneider.²⁵

Ligand exchange on this tungsten dinuclear platform via reaction with CO and subsequent reduction yielded $[\{W(CO)(PNP)\}_2(\mu-N_2)]$, which has a formal $\delta^4\pi^{10}$ configuration, see Scheme 11. These additional electrons are reflected in the substantially shorter N-N bond length upon exchanging the chloride for carbonyl ligands ($\Delta d_{NN} \approx -0.08 \text{ \AA}$), indicating population of the $\pi^*\pi^*$ -orbital. Only at high temperatures, this dimer splits N₂ into $[WN(PNP)(CO)]$, in agreement with a high activation barrier at RT as determined from Eyring analysis ($\Delta G^{\ddagger}_{298K} = 29.4 \text{ kcal mol}^{-1}$). This is the result of the introduction of the π -accepting CO-ligand, which stabilises the $\{MNNM\}$ π -manifold with respect to the σ -orbital. Besides thermal splitting, it was possible to cleave N₂ at RT by means of photochemical activation in high yields.⁶⁷

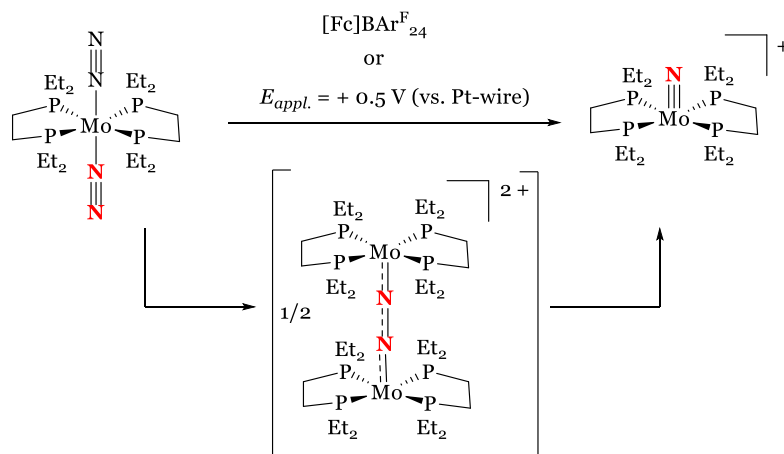


Scheme 11. N₂-splitting from $[\{W(CO)(PNP)\}_2(\mu-N_2)]$ at high temperatures or by photochemistry.⁶⁷

Most above-mentioned examples rely on the use of harsh reductants for N₂-fixation: Na/Hg, KC₈, Li, and Co(Cp^{*})₂. Not only do they generate stoichiometric waste, they have a fixed potential and the therefore usually applied overpotential can introduce unwanted side-reactions. It is therefore an ongoing desire to perform redox-reactions by electrochemical means, ideally using renewable energy sources. Changing from a chemical to electrochemical strategy might not be

so straightforward. Often, the precipitation of salts (i.e. NaX upon reducing a M-X precursor with Na) adds driving force to the reaction. Soluble (homogeneous) reductants such as $\text{Co}(\text{Cp}^*)_2$ will also provide a different concentration profile compared to the heterogeneous nature of the electrode in electrochemical transformations. Yet, the database of examples of N_2 -splitting into terminal nitrides is too small to fully judge the influence of these parameters.

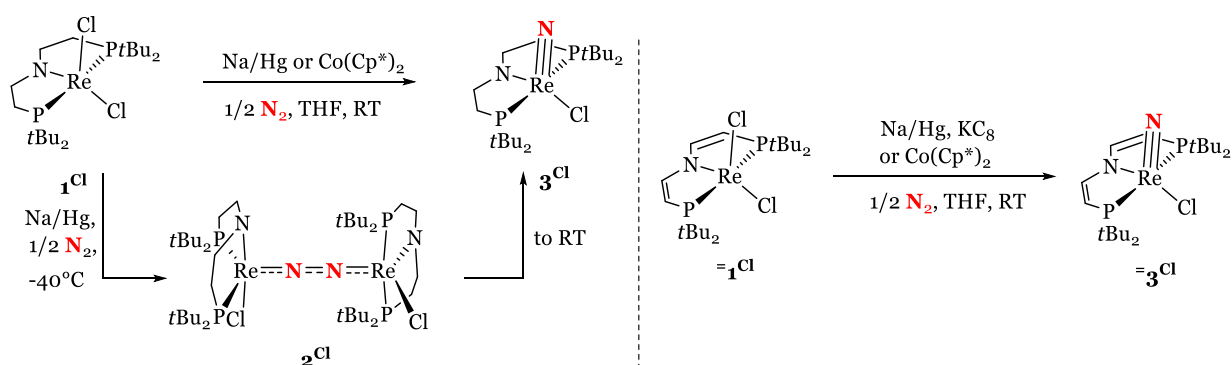
During the course of research executed in this dissertation, Masuda showed electrochemical N_2 -splitting starting from $[\text{Mo}(\text{N}_2)_2(\text{depe})_2]$ (depe = 1,2-(PEt_2) $_2$ - C_2H_4) in 2019, resulting in the terminal cationic Mo(IV)-nitride (Scheme 12). Oxidation using $[\text{Fc}]\text{BAR}^{\text{F}}_{24}$ afforded the nitride in 62 % isolated yield. Alternatively, the transfer of 0.94 electron per Mo in 2 h at $E_{\text{appl.}} = +0.5$ V (vs. the not-well defined Pt-wire) also afforded this nitride, yet no spectroscopic yield is mentioned. Upon oxidation to Mo(I), one dinitrogen ligand de-coordinates and Raman and UV-vis SEC showed the subsequent formation of the end-on N_2 -bound $[\{\text{Mo}(\text{depe})_2\}_2(\mu\text{-N}_2)]$ as intermediate. This formal $\text{Mo}^{\text{I}}(\text{N}_2)^0\text{-Mo}^{\text{I}}$ represents a $\delta^4\pi^{10}$ configuration, required for N_2 -splitting into closed shell nitrides.⁶⁸ Instead of the majority of molecular N_2 -splitting systems that use reductive conditions, this oxidative approach starting from Mo^0 shows how understanding of the N_2 -splitting MO Scheme can lead to successful nitride syntheses.



Scheme 12. (Electro)chemical N_2 -splitting upon oxidation of $[\text{Mo}(\text{N}_2)_2(\text{depe})_2]$ by Masuda.⁶⁸

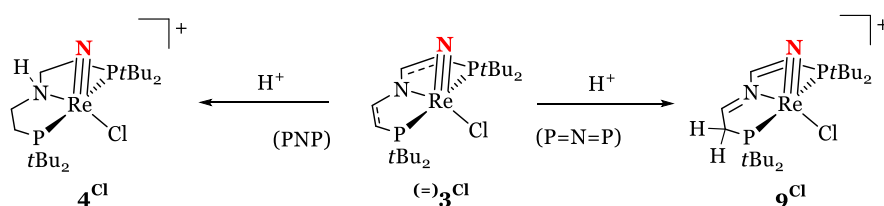
In addition to group 6 metals, N_2 -splitting was also shown for group 7 metals of which the first example was established in our group by Dr. I. Scheibel (née Klopsch) in 2014. Reducing $[\text{ReCl}_2(\text{PNP})]$ ($\mathbf{1}^{\text{Cl}}$) under a N_2 -atmosphere afforded the pale-yellow nitride $[\text{ReNCl}(\text{PNP})]$ ($\mathbf{3}^{\text{Cl}}$) in high yields (85 % using Na/Hg, and 75 % using $\text{Co}(\text{Cp}^*)_2$) (Scheme 13). As intermediate, the end-on N_2 -bridging $[\{\text{ReCl}(\text{PNP})\}_2(\mu\text{-N}_2)]$ ($\mathbf{2}^{\text{Cl}}$) was proposed,⁶⁹ and overall splitting was calculated to be strongly exergonic ($\Delta G^{\circ}_{\text{calc., MO6}} = -40.3$ kcal mol $^{-1}$).⁷⁰ Intrigued by the temporarily red colouration during the reduction reaction, just as the sizeable calculated free

activation energy ($\Delta G^{\ddagger}_{\text{calc., PBE}} = 20.2 \text{ kcal mol}^{-1}$, calcd. from the open shell singlet)⁶⁹, the reduction was carried out at -40°C . This fortunately allowed for the spectroscopic characterisation of **2**^{Cl}. The structure of **2**^{Cl} proved to have both PNP-ligands twisted with respect to each other (Cl-Re-Re-Cl: 112.1°), likely imposed by the bulky *tert*-butyl moieties, and therefore shows a C_2 -symmetry as also shown in solution by NMR spectroscopy. The N-N bond length is $1.202(10) \text{ \AA}$, which is only moderately activated (see Table 1), in line with partial occupation of the $\pi^*\pi\pi^*$ -orbital in a $\delta^4\pi^{10}$ configuration. Upon warming **2**^{Cl} to RT, clean first-order conversion into the nitride was observed. Both the spectroscopic characterisation just as the kinetic analysis of splitting from **2**^{Cl} were not fully complete,⁷¹ which are continued within this work, see Chapter II.1.



Scheme 13. N₂-splitting from [ReCl₂(PNP)] (**1**^{Cl}) (left) and [ReCl₂(P=N=P)] (**=1**^{Cl}) (right) by Schneider.^{69,72}

Inspired by this work, the closely related [ReCl₂(P=N=P)] (P=N=P = N(CHCHPtBu₂)₂⁻) (**=1**^{Cl}) was synthesised bearing the oxidised and thereby unsaturated pincer ligand (Scheme 13). This ligand is well-known within our group, as it provides additional stability against oxidative conditions and was found to stabilise a large range of oxidation states and coordination geometries.^{73–75} Backbone desaturation results in reduced π -donation from the N_{amide} to the metal centre as was confirmed for series of CO or N₂ complexes by IR-spectroscopy.^{76–78} Reduction of **=1**^{Cl} under a N₂ atmosphere using either KC₈, Na/Hg, or Co(Cp^{*})₂ forms the nitride [ReNCl(P=N=P)] **=3**^{Cl}, with a strong dependence between the used reductant and the yield (20 %, 30 %, and 60 %, respectively).⁷⁰ This reductant-dependence behaviour, just as the in general slightly lower nitride yield starting from **=1**^{Cl} compared to **1**^{Cl} are not well understood.⁷¹

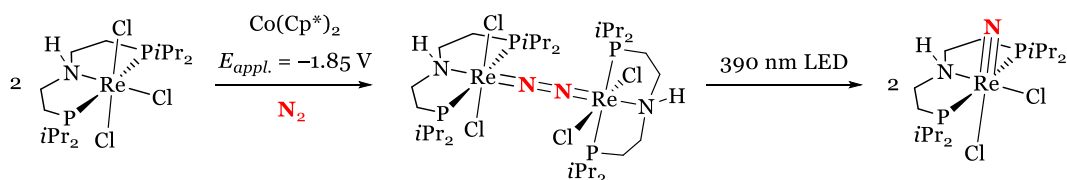


Scheme 14. Protonation of $(=)3\text{Cl}$ nitrides only results in backbone protonation.^{69,72}

The protonation behaviour of both nitrides was examined (towards ammonia formation), yet without imide formation. In the saturated PNP case, protonation occurs on the N_{amide} of the backbone, forming $[\text{ReNCl}(\text{HPNP})]^+$ (4^{Cl}). In contrast, the unsaturated ligand is most basic at a backbone carbon atom, forming $[\text{ReNCl}(\text{N}(\text{CHCHPtBu}_2)(\text{CHCH}_2\text{PtBu}_2))^+]$ (9^{Cl}) (Scheme 14).

Inspired by the good results for N_2 -splitting for 1^{Cl} , it was aimed to expand Re-mediated N_2 -splitting by modifying this platform. One example for modification is here already displayed, namely oxidation of the pincer backbone. Another modification series lies in the steric demand on the phosphorous moiety and its influence on N_2 -splitting. Compared to the *t*Bu moieties, smaller phosphorous substituent would decrease the shielding of the Re-centre substantially. Calculations on a ‘ PMe_2 ’ model compound showed that even though the formation of an end-on N_2 -bridging complex is feasible, subsequent splitting is associated with a large barrier ($\Delta G^{\ddagger}_{\text{calc.}} = 30.2 \text{ kcal mol}^{-1}$). The main reason lies in the different confirmation this hypothetical dinuclear compound adopts: the smaller substituent allows free rotation of the $\{\text{ReCl}(\text{PNP}^{\text{Me}})\}$ -fragment, and the two pincer ligands are oriented with an approx. 180° angle (in contrast to the 90° angle of 2^{Cl} , see Scheme 13). In such an arrangement, the N_{amide} only interacts with one of the orthogonally oriented π -orbitals of the $\{\text{MNNM}\}$ manifold. This lifts the degeneracy, leading to a closed shell singlet ground state that is calculated to have a high barrier for splitting.⁷⁹

Dr. F. Wätjen (né Schendzielorz) explored this strategy using the *iso*-propyl substituted pincer ligand $\text{PNP}^{\text{iPr}} (= \text{N}(\text{CH}_2\text{CH}_2\text{P}^{\text{iPr}})_2^-)$. The five-coordinated complex $[\text{ReCl}_2(\text{PNP}^{\text{iPr}})]$ analogous to 1^{Cl} , is unstable, since it coordinates solvent molecules and generally displays decomposition.⁷¹ Therefore, the trichloride octahedral platform $[\text{ReCl}_3(\text{HPNP}^{\text{iPr}})]$ is used as precursor for N_2 -fixation. Reduction either using $\text{Co}(\text{Cp}^*)_2$ or $E_{\text{appl.}} = -1.85 \text{ V vs. Fc}^{+/0}$ yields the end-on N_2 -bridging $[\{\text{ReCl}_2(\text{HPNP}^{\text{iPr}})\}(\mu\text{-N}_2)]$ (Scheme 15). Despite its isoelectronic structure to 2^{Cl} , this is a stable compound under thermal conditions with respect to N_2 -cleavage. The *trans* arrangement of the PNP^{iPr} ligand towards the $\{\text{MNNM}\}$ -bridge destabilises the σ -orbital set, which needs to be populated for N_2 -splitting. The activation barrier for splitting is calculated to be high ($\Delta G^{\ddagger}_{\text{calc.}} = 41.8 \text{ kcal mol}^{-1}$), and the situation is reminiscent to the dinuclear system by Schrock (see Figure 7), which is also inert to N_2 -cleavage.

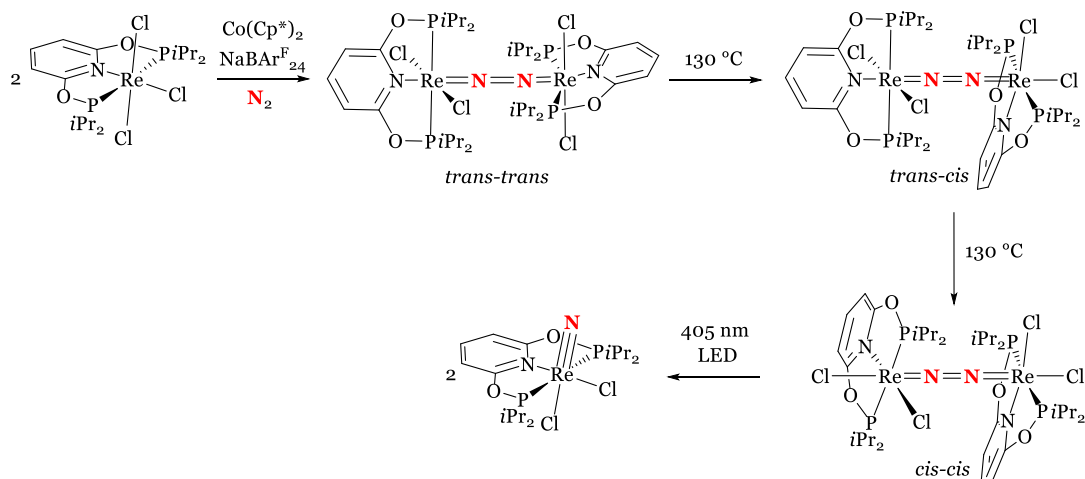


Scheme 15. N₂-fixation and photochemical splitting starting from [ReCl₃(PNP^{iPr})] by Schneider.⁸⁰

To obtain the required metal to ligand electron transfer, it was attempted to activate [$\{\text{ReCl}_2(\text{HPNP}^{\text{iPr}})\}_2(\mu\text{-N}_2)$] by means of photochemistry. Notably, N₂-splitting into terminal nitrides was reported several times in recent years by the groups of Floriani, Cummins, Vogler, Nishibayashi, Sita, Schneider and very recently Miller, of which the latter will be discussed (*vide infra*).^{24,48,67,81–84} Irradiation of [$\{\text{ReCl}_2(\text{HPNP}^{\text{iPr}})\}_2(\mu\text{-N}_2)$] leads to N₂-splitting into [ReNCl₂(HPNP^{iPr})] in 95 % yield. Wavelength selective irradiation showed that the productive electronic transition is around 390 nm, which has $\delta \rightarrow \pi^*\pi^*\pi^*$ metal to ligand charge transfer character. Population of this {MNNM} anti-bonding orbital weakens the NN bond and likely introduces more vibrational flexibility, which promotes the route to the zig-zag TS. The resulting nitride is exclusively found as the *cis*-dichloride isomer, and it could be shown that isomerisation takes place after initial splitting to the *trans*-arrangement, which is destabilised due to the strong *trans* effects of the N_{amide} and N_{nitride}. The nitride's *trans* ligand influence is reflected in the Re-Cl bond lengths: the chloride *trans* to the nitride is elongated >0.2 Å versus the chloride *trans* to N_{amide}.⁸⁰

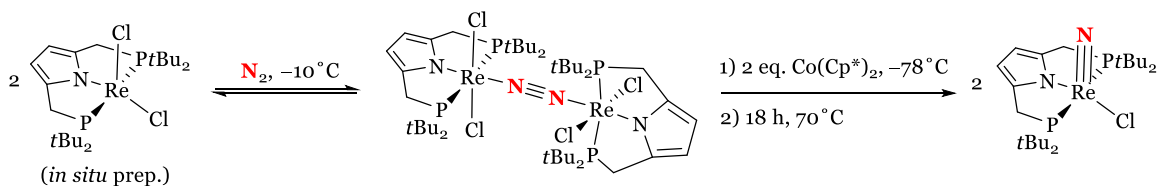
Shortly thereafter, Miller presented the second example of Re-mediated photochemically driven N₂-splitting (Scheme 16). Their starting platform [ReCl₃(PON_{py}OP)] (PON_{py}OP = 2,6-(OPiPr)₂NC₅H₃) bears a pincer ligand that is substantially less electron donating, as reflected by the for N₂-splitting required Re^{III/II} reduction potential at $E_{1/2} = -1.23$ V vs. Fc⁺⁰. This represents a strong anodic shift compared to Re(III) complexes **1**^{Cl} and the closely related [ReCl₃(HPNP^{iPr})] ($E_p = -1.90$ V (see Chapter II.1) and $E_{1/2} = -1.84$ vs. Fc⁺⁰,⁸⁰ respectively). In contrast to these systems, reduction of [ReCl₃(PON_{py}OP)] yields the relatively stable anionic Re^{II} compound without direct chloride loss, which is attributed to the reduced electron donating character of the pincer ligand. Halide abstraction under a N₂-atmosphere results in dinitrogen fixation and the isolation of mainly *trans-trans* [$\{\text{ReCl}_2(\text{PON}_{\text{py}}\text{OP})\}_2(\mu\text{-N}_2)$] with the chlorides on both Re-centres in a *trans* arrangement. This compound was inert to N₂-splitting up to 130 °C yet showed slow isomerisation at these temperatures: initially to the *trans-cis* isomer and finally to the *cis-cis* isomer. All isomers proved inert to N₂-splitting under thermal conditions, rationalised by high computed activation barriers ($\Delta G^\ddagger_{\text{calc.}} = > 50$ kcal mol⁻¹). As shown before, this is attributed to the *trans* arrangement of the ancillary ligands to the {MNNM}-bridge. Yet, photochemical

activation upon irradiation around 400 nm proved successful for splitting into $[\text{ReNCl}_2(\text{PON}_{\text{py}}\text{OP})]$, although all activity originates from the *cis-cis* isomer and the other two isomers remain inert to N_2 -splitting. These remarkable different reaction behaviours are not commented in depth; it is tentatively attributed to the stronger trans ligand $\text{N}_{\text{pyridine}}$ in the *trans-trans* isomer versus a chloride ligand in the *cis-cis* isomer.



Scheme 16. N_2 -fixation to the end-on N_2 -bridging *trans-trans* $[\{\text{ReCl}_2(\text{PON}_{\text{py}}\text{OP})\}_2(\mu\text{-N}_2)]$, its isomerisation and subsequent photochemical activation of the *cis-cis* isomer by Miller.⁸⁴

Very recently, the group of Holland showed N_2 -fixation starting from $[\text{ReCl}_2((\text{PN}_{\text{pyr}}\text{P})]$ ($\text{PN}_{\text{pyr}}\text{P} = 2,6\text{-}(\text{CH}_2\text{PtBu}_2)_2\text{NC}_4\text{H}_2$), see Scheme 17.⁸⁵ In strong contrast to the analogous $\mathbf{1}^{\text{Cl}}$, this compound is not isolatable, and has to be synthesised *in-situ* from the 6-coordinate pyridine coordinating complex. Cooling down a sample under a N_2 -atmosphere yields the formally $\text{Re}(\text{III})$ dinuclear end-on N_2 -bridging $[\{\text{ReCl}_2((\text{PN}_{\text{pyr}}\text{P})\}_2(\mu\text{-N}_2)]$, which is only stable in the solid state. Upon two-fold reduction at low temperatures followed by prolonged heating, N_2 -splitting occurs into the terminal nitride in high yields. Prior to heating, a mixture of unknown products is formed, that must convert into the nitride in high yields.



Scheme 17. N_2 -fixation to the end-on N_2 -bridging $[\{\text{ReCl}_2(\text{PN}_{\text{pyr}}\text{P})\}_2(\mu\text{-N}_2)]$, and subsequent N_2 -splitting via reduction and subsequent heating from Holland.⁸⁵

I.2. Dinitrogen functionalisation

So far, the different binding modes of N₂ with a special focus on end-on N₂-bridging complexes and their subsequent splitting into terminal nitrides were discussed. As another large topic, the functionalisation of N₂ on (mainly) molecular transition metal complexes is addressed. First, formation of ammonia is discussed both with the N-N bond retained and from nitrides resulting from N₂-splitting, away from the industrial and biological pathways (Section I.1.2). Beyond ammonia, N-X bond functionalisation (X = C, Si, and B) is considered a promising alternative. Regarding the research performed within in this work, most attention will be on N-C bond formation starting from terminal nitrides, and the need for introducing electrochemical transformations in this field.

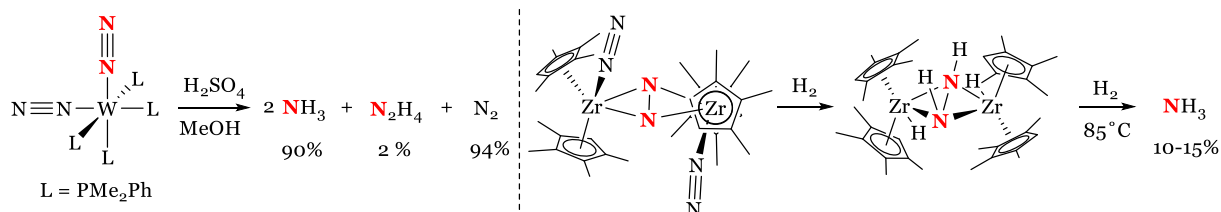
2.1. Ammonia formation

2.1.1. Ammonia formation using chemical reagents

Beyond the Haber Bosch (HB) process, renewed interest in alternative pathways for ammonia formation raised around the 1960's, mainly because of increasing knowledge around nitrogenase. Inorganic compounds capable of N₂-chemistry could function as bio-mimicking models to thrive the understanding of the biological mechanism of dinitrogen activation. Yet, most breakthrough results first came in the current century and an overview of some highlight findings both in the (electro)chemical homogeneous as heterogeneous field are given. An extended overview of all efforts on molecular ammonia formation is recently covered by Peters.⁸⁶

A pioneering example for stoichiometric N-H bond formation comes from Chatt in 1975: protonation of *cis*-[W(N₂)₂(PMe₂Ph)₄] with a strong acid releases ammonium in slightly less than quantitative yields (see Scheme 18). This is accompanied by some hydrazine formation and the release of 1 eq. of N₂, indicating ligand dissociation.^{87,88} It is acknowledged that in absence of external reductant, the metal centre is oxidised and likely W(VI)oxo species are formed. Encouraged by the subsequent isolation of several intermediates, a potential catalytic cycle was formulated for ammonia formation, cycling through Mo^{0/III} states, known as the 'Chatt cycle'. This is also a working hypothesis model for nitrogenase. Compared to the dissociative direct N₂-splitting in the HB process, this mechanism is associative, indicating that the N-N bond is not broken until the first ammonia is released. The functionalisation is proposed to occur via a distal pathway.^{89,90} It is worth mentioning that very recently, a catalytic response was realised for the related *cis*-Mo analogue using the potent SmI₂/ethylene glycol reagent system (*vide infra*).⁹¹

Another iconic example is the hydrogenation of side-on N_2 -bridging $[\{Zr(Cp')_2(N_2)_2\}_2(\mu-\eta^2:\eta^2-N_2)]$ ($Cp' = C_5Me_4H^-$), which splits H_2 to form $[\{Zr(Cp')_2(N_2)_2\}_2(\mu-\eta^2:\eta^2-N_2H_2)]$ complex, see Scheme 18.³⁹ At the time (2004), this was the first characterised example of N_2 hydrogenation to hydrazine on a transition metal. Further hydrogenation at high temperatures releases NH_3 in sub stoichiometric yields. A remarkable aspect of this example is that the closely related yet end-on bridging $[\{Zr(Cp^*)_2(N_2)_2\}_2(\mu-\eta^1:\eta^1-N_2)]$ with per-methylated Cp^* -rings dissociates its N_2 -ligands upon reaction with H_2 . These subtle ligand differences and their implications for its N_2 -reactivity is remarkable. A recent example by Walter also released sub-stoichiometric ammonia from H_2 , but from reaction with N_2 -derived nitrides via a dissociative pathway. Upon reduction of Fe^{II} $[\{FeCp''\}_2(\mu-\eta^2-I)_2]$ ($Cp'' = 1,3,5-(tBu)_3-C_5H_2$) using KC_8 under N_2 , a tri-iron compound is obtained with $(\mu-\eta^3-N)$ nitride linkages. Protonation of this compound releases ammonium in circa 75 % yield. More interestingly, the compound also reacts with (high pressure) H_2 , which was examined both in the solid state and in solution. In the latter, ammonia is formed in low yield (3-7 %), accompanied by the formation of a di-iron nitride species and a bis(imido) species. This latter compound is formed quantitatively from solid-state reactivity with H_2 . One-pot reduction of the starting compound in presence of N_2 and H_2 unfortunately only formed iron-hydrides, hampering catalytic formation of ammonia.⁹²



Scheme 18. Selected examples of stoichiometric ammonia release from N_2 by Chatt and Chirik.^{39,87}

Between the initial work of Chatt and the first example of catalytic ammonia on a well-characterised molecular system, some less-defined examples appeared. Shilov combined $MoCl_5$ -salts, a large excess of Na/Hg and both phosphine and long-chain phosphites ligands, that generates hydrazine and ammonia catalytically. The pre-catalyst is believed to be a Mo(III)phosphine complex, which is not further characterised. In comparison to Chatt, the use of external reducing equivalents was already identified to re-generate a catalytically active species.⁹³ A well-defined molecular system was developed in 2003 by Schrock, using $[Mo((N(HIPT)CH_2CH_2N_3)(N_2))]$ ($HIPT = 3,5-(2,4,6-iPr_3C_6H_2)_2$) as catalyst, Figure 8.⁹⁴ Compared to the earlier N_2 -fixation work (see Figure 7), the instable $N_{amide}-Si$ bonds in the backbone were exchanged for more stable $N_{amide}-C$ bonds with extensive steric bulk to shield the metal centre. Reacting this Mo(III) species in presence of excess luthidinium BAr^F_{24} as acid and

$\text{Cr}(\text{Cp}^*)_2$ ($E_{1/2} = -1.47$ V vs. $\text{Fc}^{+/0}$ (THF))⁵⁹ in benzene unfortunately resulted almost exclusively in hydrogen evolution (HER). HER represents the main competing reaction when ammonia formation is attempted from separate proton and electron sources, since the redox potentials for both reactions are close. This was recently discussed and graphically visualised in a Pourbaix diagram for reactions in MeCN.⁹⁵ To overcome this competing reaction, the solvent was changed to heptane where the acid is only limited soluble, and the reductant was slowly added via a syringe pump. Satisfactory formation of circa 8 equivalents of ammonium per molybdenum was obtained. Labelled ammonia was formed when performing the reaction under $^{15}\text{N}_2$, confirming atmospheric dinitrogen uptake. Several catalytic active intermediates were isolated or separately prepared (i.e. $\text{Mo}-\text{NNH}$, $\text{Mo}-\text{NNH}_2^+$, $\text{Mo}=\text{N}$, and $\text{M}-\text{NH}_3^+$), which allowed to propose a catalytic cycle. In analogy to the ‘Chatt cycle’, this ‘Schrock cycle’ proposes a distal pathway via a Mo nitride, yet cycling through $\text{Mo}^{\text{III/VI}}$ oxidation states.⁹⁴

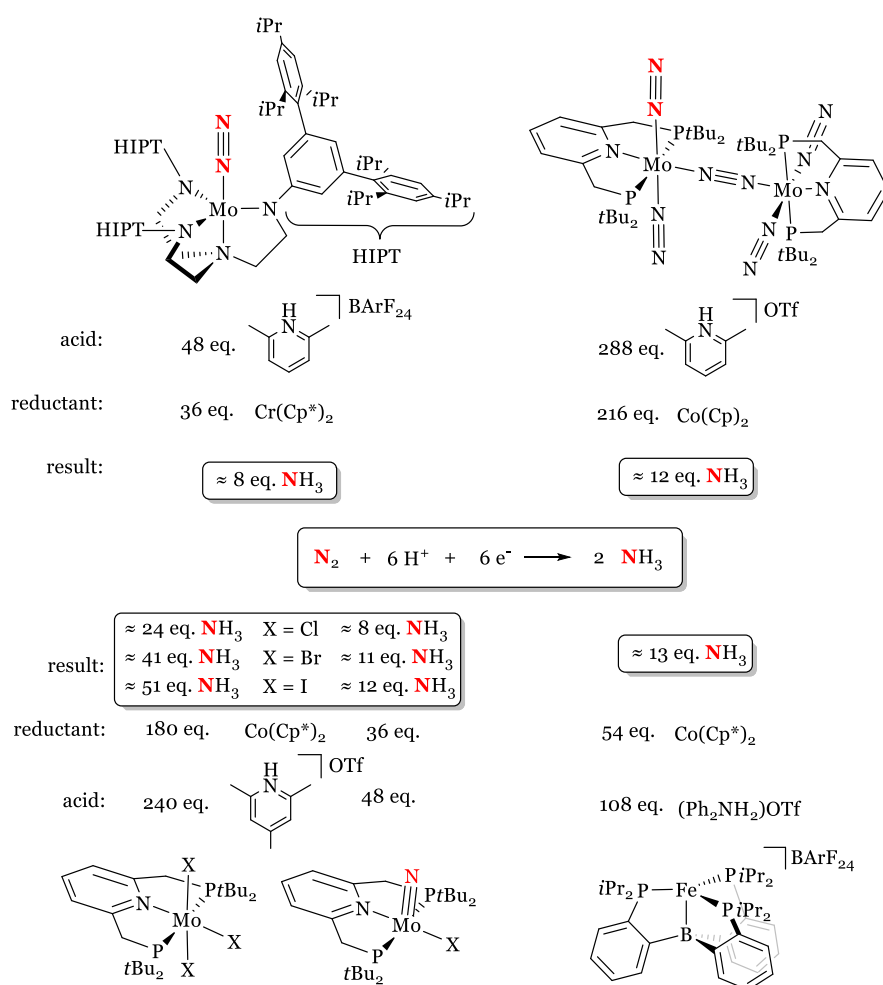
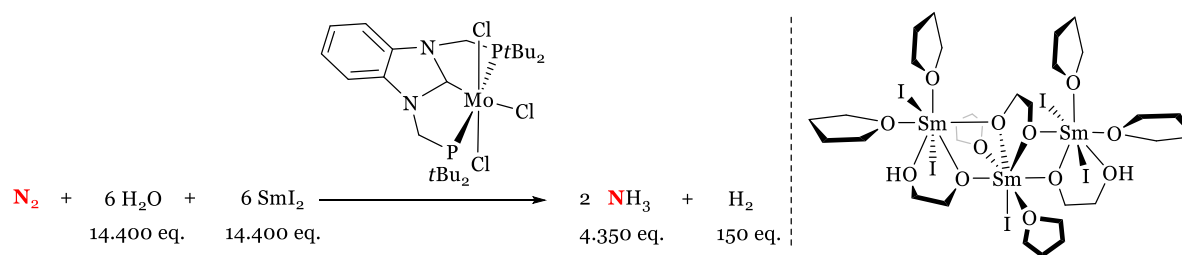


Figure 8. Selected examples of catalytic ammonia generation from molecular complexes using chemical reductants by Schrock, Nishibayashi and Peters. Ammonia eq. are reported normalised per metal centre.^{52,60,94,96}

In 2010, Nishibayashi developed a Mo⁰ system capable of catalytic ammonia formation. Slow addition of Co(Cp)₂ to a solution of dinuclear end-on bridging [$\{\text{Mo}(\text{N}_2)_2(\text{PN}_{\text{Py}}\text{P})\}_2(\mu\text{-N}_2)$] in toluene with luthidinium triflate yields approx. 12 eq. ammonia per Mo-centre (49 % yield), (Figure 8, top right). In addition to ammonia, H₂ is formed in circa 37 % yield.⁶⁰ Initially, an exclusively monomeric mechanism was proposed. Later on, this was re-considered into a distal mechanism where the dinuclear framework is retained for the first ammonia release from the terminal nitrogen. Subsequently a mononuclear nitride complex reacts to form the second equivalent of ammonia, upon which the dinuclear dinitrogen coordination structure is re-formed.⁸²

Catalytic ammonia formation was also established from the same system that shows N₂-splitting into terminal nitrides (Section I.1.4), for both the precursor [$\text{MoX}_3(\text{PN}_{\text{Py}}\text{P})$] as the resulting nitride [$\text{MoNX}(\text{PN}_{\text{Py}}\text{P})$] complexes with X = Cl, Br, and I (Figure 8, bottom right). From this series, a clear preference for catalytic activity moving to the heavier halide congeners was found. The authors claim that this is because the heavier congeners are easier reduced, as apparently the reduction potential of the nitrides follows the same order.⁵²

By now, catalytic ammonia formation is also reported for many transition metals besides Mo. One example using iron is discussed from the group of Peters, using their archetypical tetrapodal triphosphine borane ligand. The complex [$\text{Fe}(\text{P}_3^{\text{B}})]^+$ ($\text{P}_3^{\text{B}} = \text{B}((2\text{-}i\text{Pr}_2)\text{C}_6\text{H}_4)_3$) successfully catalyses dinitrogen to ammonia using KC₈ (circa -2.6 V (NMP))⁹⁷ and HBAR^F₂₄·(Et₂O)₂. Both reagents are strong and to prevent competing HER, the reaction proceeds at low temperatures (-78 °C) in Et₂O.⁹⁶ Yet, better results were obtained by combining Co(Cp*)₂ and (Ph₂PH₂)OTf (Figure 8, bottom right). This is attributed to the formation of protonated [$\text{Co}(\text{Cp}^*)(\eta^4\text{-C}_5\text{Me}_5\text{H})$]⁺OTf that acts as PCET reagent. By calculations, this C-H bond strength is estimated to be approx. 31 kcal mol⁻¹. The resulting diazenido from the first (and most difficult) H-atom transfer to the [Fe-NN] complex is calculated to have a N-H bond strength of 35 kcal mol⁻¹, indicating a feasible initial reaction step. This behaviour is extended by calculations to other Cp-bearing reducing agents, as used in the previous discussed examples. Notably, such a protonated species could be spectroscopically characterised upon reaction between an acid and Co(Cp*)₂ at low temperatures.⁹⁸ The exciting finding of such a potent PCET strategy can of course be used for other transformations beyond N₂-activation.⁹⁹ In general, the many intermediates that were characterised for this system (among which Fe-NNH, Fe-NNH₂, Fe=N⁺, Fe-NH₂NH₂⁺) suggest a hybrid mechanism between a distal and alternating pathway, mainly because of the isolation of the latter intermediate.⁸⁶



Scheme 19. Left: catalytic ammonia formation using $\text{SmI}_2/\text{water}$ by Nishibayashi. Right: A Sm(III) -resting state.⁵⁷

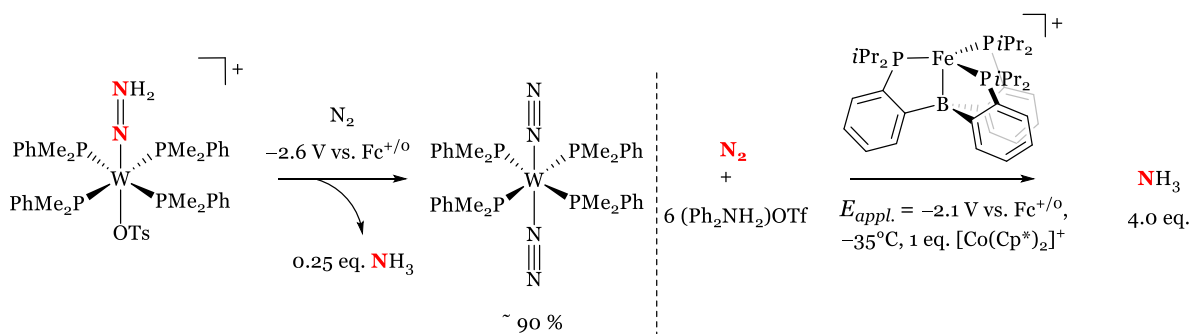
Recently, a very efficient PCET reagent was established for catalytic ammonia formation that represents a substantial improvement within this field. Nishibayashi found that the combination of SmI_2 and alcohols (ethylene glycol) or even water proved an efficient HAT donor for nitrogen reduction on Mo-complexes (Scheme 19). In a large run experiment using $[\text{MoCl}_3(\text{PCP})]$ ($\text{PCP} = 1,3\text{-bis}((\text{di-}t\text{-tert-butylphosphino)methyl)benzamidozole-2\text{-ylidene})$) as catalyst, > 4000 eq. of NH_3 and only 150 eq. of H_2 were found, which correspond to 91 and 2 % yield respectively, see Scheme 19. Also the turn-over frequency is circa 1-2 order of magnitudes larger compared to previous established systems.⁵⁷ The O-H bond strength of a $\text{SmI}_2/\text{H}_2\text{O}$ mixture was recently estimated to be approx. 26 kcal mol⁻¹,¹⁰⁰ which is far below the calculated N-H bond of several diazenido M-NNH species, explaining its efficiency.^{46,101} Notably, catalytic ammonia formation from $[\text{MoX}_3(\text{PN}_{\text{Py}}\text{P})]$ ($\text{X} = \text{Cl}, \text{Br}, \text{I}$) was re-considered using the $\text{SmI}_2/\text{ethylene glycol}$ system where the catalytic activity was found in the order $\text{Cl} \approx \text{Br} > \text{I}$. This is clearly opposite of what was found using $\text{Co}(\text{Cp}^*)_2/\text{collidinium triflate}$ (see Figure 8), yet is not further commented. After catalysis, multinuclear O-linkage Sm(III) compounds were found, see Scheme 19. In a separate study, electrochemical reduction of SmI_3 as model compound was established in high yields, thereby potentially recycling the reducing agent for this reaction.¹⁰² The discovery of this potent reagent in the field of ammonia formation has already inspired established and new systems to explore these promising conditions.^{63,84,91}

2.1.2. Ammonia formation by means of electrochemistry

It is an ongoing effort to replace harsh or energy-consuming reducing agents and perform catalytic ammonia formation by means of electrochemistry. There are roughly two approaches that both try to reconsider the production route or usage of H_2 . As mentioned, the HB process is associated with a large energy consume, mostly because of the fossil-fuel based production of hydrogen. As alternative strategies, either the production of H_2 is envisioned to be electrified via water electrolysis to maintain the conventional HB industry. Alternative, N_2 is directly electrochemically reduced in presence of protons. A benefit of the latter is the possibility to set up this new industry de-centralised close to sources of renewed electricity. The direct reductive

approach could be coupled to e.g. water or hydrogen oxidation. It was recently estimated in detail that without e.g. carbon taxes, both methods are still 2-2.5 times more expensive per ton NH_3 as conventional HB.^{103,104} All the examples discussed herein and in Section I.2.1.2 of electrochemical ammonia formation are far from a commercial application, yet they show the state of the field and general challenges encountered when transforming reactions from chemical reagents towards electrochemistry.

Electrochemical ammonia formation from N_2 mediated by molecular complexes is still very limited.¹⁰⁵ In general, the use of a molecular catalyst is associated with a higher selectivity and therefore this is a highly interesting field. A first well-defined stoichiometric molecular example is from Pickett in 1985, where under reductive conditions at a Hg pool electrode, circa 0.25 eq. of NH_3 was released from hydrazido $[\text{W}(\text{NNH}_2)(\text{OTs})(\text{PMe}_2\text{Ph})_4]^+$ ($\text{OTs} = 4\text{-CH}_3(\text{C}_6\text{H}_4)\text{OS}(\text{O})_2^-$) (Scheme 20). The source of the required protons is intramolecular from the hydrazido compound that reforms a neutral bis (dinitrogen) compound. Likely, no external acid was introduced, as it would exclusively form H_2 under these severe reducing conditions. In subsequent protonation and reduction cycles, 0.75 eq. of ammonia could be collected. Electrocatalysis on molecular complexes was realised only many years later.¹⁰⁶

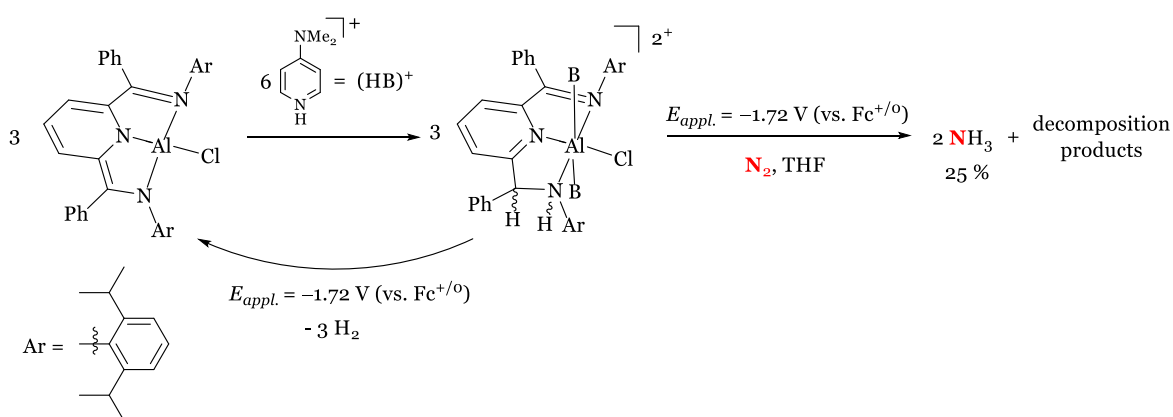


Scheme 20. Examples of electrochemical ammonia release on molecular complexes. Left: first stoichiometric example by Pickett.¹⁰⁶ Right: First electrocatalytic example by Peters.¹⁰⁷

While examining the mechanism of catalytic ammonia formation with Fe-catalyst $[\text{Fe}(\text{P}_3\text{B})]^+$, the group of Peters measured CV of this complex in presence of acid to identify the redox state that initiates catalysis. A current increase of the $\text{Fe}^{1/0}$ reduction upon addition of acid triggered to perform initial electrochemical studies using $\text{HBAr}^{\text{F}_{24}} \cdot (\text{Et}_2\text{O})_2$, that however formed quantitatively 2.0 eq. of NH_3 from coordinated N_2 .¹⁰⁸ In a next attempt using the weaker acid $(\text{Ph}_2\text{PH}_2)\text{OTf}$, they applied the PCET knowledge from the chemical catalysis by adding equivalent(s) of $[\text{Co}(\text{Cp}^*)_2]\text{BAr}^{\text{F}_{24}}$. That proved a promising strategy: electrolysis at $E_{\text{appl.}} = -2.1 \text{ V vs. Fc}^{+/0}$ in Et_2O at -35°C yielded 4.0 equivalents of NH_3 per iron, indicating a catalytic process with a faradaic efficiency (FE) of 28 % (Scheme 20).¹⁰⁷ A glassy carbon working

electrode was applied, which has a large overpotential against competing HER.¹⁰⁹ As counter electrode, a solid sodium rod as sacrificial reductant was used, as Na^+ reduction is stable against electrolysis conditions, and it was made sure that this hypothetical strong reductant is not the origin of ammonia formation.

Although not a catalytic example, Berben applied an NNN-pincer as coordinated to Al for electrochemical NH_3 formation as alternative strategy to transition metals. The starting complex $[\text{Al}(\text{PDI})\text{Cl}]$ ((PDI = 2,6-bis[1-(2,6-diisopropylphenylimino)methyl]pyridine)) can be protonated twice on one of the pincer arms (Scheme 21). This doubly protonated species shows two reductions by CV that increase in current upon titration of 20 eq. of 4-(1,1-dimethylamide)pyridinium. Notably, this behaviour is more prominent under Ar, and it was shown that reductive electrolysis under Ar forms H_2 with regeneration of the starting material. Under N_2 , the HER activity decreases and is accompanied by formation of sub-stoichiometric amounts of NH_3 (circa 25 %).¹¹⁰ A higher yield cannot be obtained, due to catalysts inhibition via ammonia coordination. Likely, a hydride transfer mechanism takes place, without direct interaction between dinitrogen and aluminium.



Scheme 21. Sub stoichiometric NH_3 formation driven by electrochemistry.¹¹⁰

Besides organometallic molecular examples, several examples are known for non-metallic (catalytic) ammonia formation from for instance organic polymers or carbon based nanomaterials.^{111,112} More prominent is the huge body of work on electrochemical ammonia formation for heterogeneous based electrocatalysts. Most of these systems suffer from low selectivity of NH_3 formation over competing HER: faradaic efficiencies for most systems are below or around 10 %.^{113,114} A recent example of relatively high FE ($\approx 20\%$) is given by the group of Zhang. Fe-doped SnO_2 layers catalyses electrochemical ammonia formation in a HCl solution at $E_{\text{appl.}} = -0.3 \text{ V vs. NHE}$ with an overall yield rate of $14 \text{ nmol s}^{-1} \text{ cm}^{-2}$. Although amongst the highest results within the field, it is still far from the formulated goals for commercial interest

($\approx 1 \text{ mmol s}^{-1} \text{ cm}^{-2}$).¹⁰⁴ Interestingly, this material also catalyses ammonia oxidation to nitrates, although the selectivity for this latter reaction is very low.¹¹⁵

Hand in hand with numerous heterogeneous examples appearing in quick pace, critical notes towards the true origin of ammonia come up, as recently addressed by various authors.^{116–118} Many possibilities for (unexpected) background ammonia presence are now identified, i.e. from separator (membrane) material, nitrile gloves, or a non-negligible air concentration. Chorkendorff emphasises the importance of appropriate background studies and presents an extended flow chart that can be followed to ensure that the ammonia originates from N_2 .¹¹⁷ Simonov categorises the established research based on three criteria: 1) if the NH_3 formation is rate sufficiently high, 2) if isotopically labelled ammonia has been formed, and 3) whether the background NO_x impurities in the N_2 feed have been quantified. In their opinion, as none of the reviewed studies accounts for the third criterion, successful electrochemical dinitrogen reduction should be approached carefully.¹¹⁶

2.1.3. Ammonia formation in an electrochemical flow cell

Beyond the question of electrifying the redox steps occurring in ammonia formation (or in a stoichiometric N-C bond formation cycle, *vide infra*), lies the challenge to combine all reactions in such a way that it could turn into a catalytic process. An often-used method is the application of electrochemical flow cells where the reagents and products only have a limited dwell time at the electrode's surface. In recent years, the use of flow cells for CO_2 -reduction chemistry has found increased attention.¹¹⁹ Most of these systems rely on direct electron transfer from the electrode to CO_2 as delivered through gas diffusion electrodes.¹²⁰ Very recently, Machan exemplified CO_2 reduction using the homogeneous mediator $[\text{Ni}(\text{cyclam})]^{2+}$ (cyclam = 1,4,8,11-tetraazacyclotetradecane). At graphite felt electrodes, CO_2 is converted to CO (FE 83 %) at an overpotential of circa 0.6 V in MeCN, mediated by the Ni(II/I) reduction and using NH_4PF_6 as electrolyte and proton donor. As counter reaction, Fc is oxidised. Only minor competing HER is observed (FE 7 %). Interestingly, a flow cell setup was compared to a classical H-cell, indicating a massive drop in activity and CO selectivity (FE 13 %) under otherwise identical conditions, attributed to the apparently beneficial mass transport in the flow cell versus a classical electrochemical set up with stirring bar induced convection. This work exemplifies that a changed electrolysis cell design and mass transport form are not only necessary for upscaling reactions and continuous operation, but reaction outcomes can also be dramatically different.¹²¹

Regarding N_2 -splitting in such a flow cell, the examples are more scarce, and all examples apply, to the best of our knowledge, catalysts with a heterogeneous nature.^{122,123} An impressive study

was published in 2020 by Manthiram,¹²³ where NH_3 is produced in a flow cell, based on the Lithium approach: metallic Li splits N_2 into lithium nitride, which is protonated to release NH_3 . A second cycle is initiated by Li^+ reduction (Figure 9).¹²⁴ Due to the far negative potential required for this latter reaction, it can only occur in organic solvents with a large solvent window (here THF), which in general also have a larger overpotential against competitive HER. Yet, the gas diffusion electrodes are not often applied in organic solvents, and usually, the coupling anodic reaction is basically neglected and consists of solvent oxidation. Manthiram addresses both problems. First, they establish efficient gas transport to the electrode by applying a slight over-pressure. This hinders the organic solvent to ‘wet’ the electrode, which would dissolve the incoming N_2 , and decreasing the activity. Secondly, they couple the cathodic reaction with anodic H_2 oxidation, which allows for continuous operation without unwanted side-products from solvent oxidation. The protons that result from this reaction are shuttled via EtOH as mediator to the catholyte and protonate the nitride to form ammonia. As catalyst for the cathode and anode reaction, simple steel cloths were deposited with Li and Pt, respectively. Using LiBF_4 as electrolyte and a neutral polyporous membrane, NH_3 is formed in high FE (up to 47.5 %) at controlled current electrolysis of 25 mA/cm^2 . As recently emphasised (*vide supra*), atmospheric N_2 uptake was confirmed upon showing similar reactivity regardless of using $^{14}\text{N}_2$ or $^{15}\text{N}_2$. To also address the traditionally very energy consuming H_2 formation, the flow cell is coupled to a H_2O electrolyser, where H_2 is generated by means of electrochemistry, via the overall reaction: $\text{N}_2 + 3 \text{H}_2\text{O} \rightarrow 2 \text{NH}_3 + 1.5 \text{O}_2$. It should be mentioned that the whole set up induces severe ohmic losses (up to 80 %), so that large overpotentials are required. Still, this is a remarkable example of N_2 -splitting at ambient conditions in coupled electrochemical flow cells.

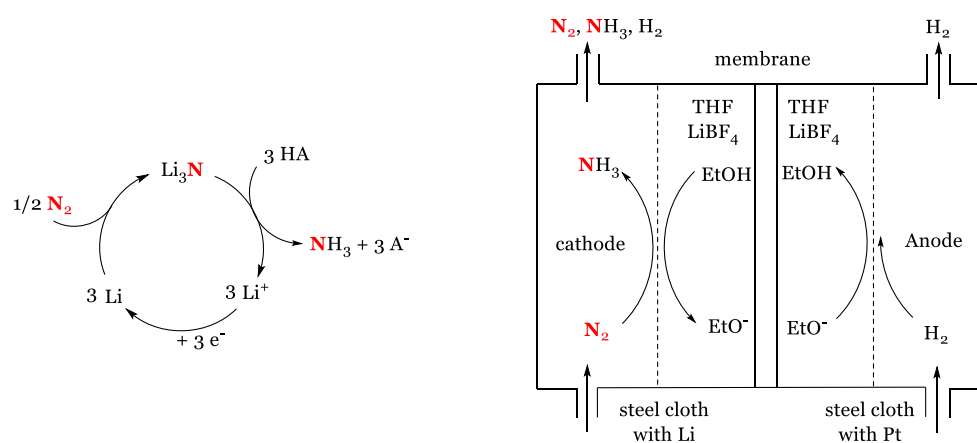


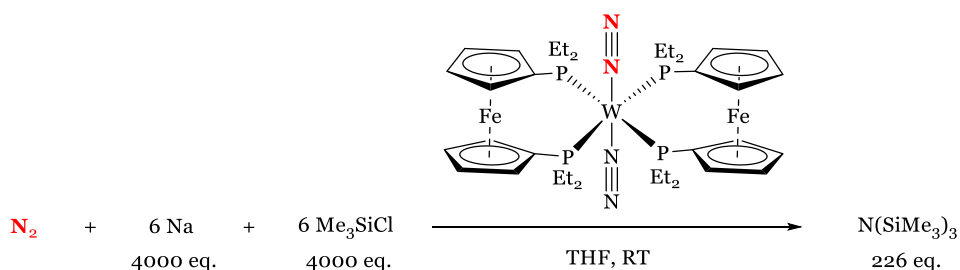
Figure 9. Left: Li-mediated N_2 -splitting and NH_3 formation and release. Right: Coupled N_2 -reduction and H_2 -oxidation in a flow cell set up in THF as combined by Manthiram.¹²³

2.2. N-Element Bond formation

2.2.1. N-X bond formation

Currently, all of the nitrogen-containing chemicals are synthesised from ammonia: roughly 20 % of the overall produced NH_3 is reacted further.¹²⁵ As ammonia production is associated with a very high energy consume, alternative approaches that incorporate N from N_2 avoiding initial synthesis of ammonia are targeted. Besides a large interest in N-C bond formation, N-Si, N-B and even N-P bond formation is reported.^{126,127} N-C bond formation is a main topic within this work, and it is therefore extensively discussed in Section I.2.2.2. Here, only a state-of-the-art or iconic example for N-Si and N-B bond formation is briefly discussed.

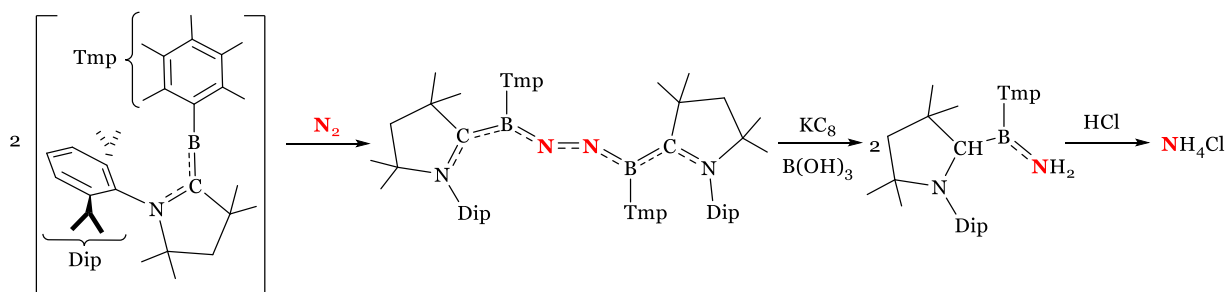
Besides catalytic N-H bond functionalisation, only N-Si bonds are formed catalytically. In general, many complexes that perform catalytic ammonia formation can also be used for catalytic silylation of N_2 to silylamines. Amongst the systems, up to 226 eq. tris(trimethylsilyl)amine were obtained from $[\text{Mo}(\text{N}_2)_2(\text{depf})_2]$ precursor (depf = 1,1-bis(diethylphosphino)ferrocene) using Na and Me_3SiCl , which represents one of the best results obtained so far (Scheme 22).¹²⁸ It should be noted that the silylamine yield with regard to the used equivalents of reductant and silylchloride is 1-2 orders of magnitude below catalytic ammonia formation for molecular complexes known so far.¹²⁷ Although the silylamines can be hydrolysed to ammonia, the atom economy of this reaction is low because of stoichiometric silyl by-products and therefore this reaction is only limitedly useful. Tris(trimethylsilyl)amine itself also has some industrial application, i.e. conversion to dichlorophosphazene and its subsequent polymers.¹²⁹



Scheme 22. Catalytic tris(trimethylsilyl)amine formation by Nishibayashi.¹²⁸

N-B bond formation is established both before and after cleavage of the N-N bond of dinitrogen. Yet, there are no examples for subsequent release of a N-B bond containing fragment and usually the reactivity is limited to the coordination of a BR_3 moiety. A very exceptional recent example

for initial B-N bond formation and subsequent reactivity is given by Braunschweig. In general, it is hard to mimic the partial empty and full d-orbitals of transition metals by p-block elements, which is crucial for N_2 -binding. Yet, Braunschweig found metal-like bonding characteristics between carbonyl and their transient boron compound (TmpB(L)) (L = 1-(2,6-di-*iso*-propylphenyl)-3,3,5,5-tetramethylpyrrolidine-2-ylidene)), which inspired them to extend this system to dinitrogen fixation. Indeed, a N_2 -saturated solution containing this transient boron species (as obtained from reduction of a dibromide analogue) slowly forms a N_2 -bridging dinuclear compound formed (Scheme 23). The N-N bond length indicates moderate activation (1.248(4) Å), and the deviation from linearity is attributed to decreased orbital overlap between B and N, in contrast to transition metals.¹³⁰ Notably, this species can be reduced, and in a follow up study, reduction is combined with protonation. This results in cleavage of the N-N bond and the generation of the corresponding amide. Hydrolysis yields sub-stoichiometric yields of ammonium (up to 27 %), and a mixture of several boron containing compounds.¹³¹ This study and the many intermediates that were characterised will definitely ignite more research towards N_2 -fixation at main group elements.

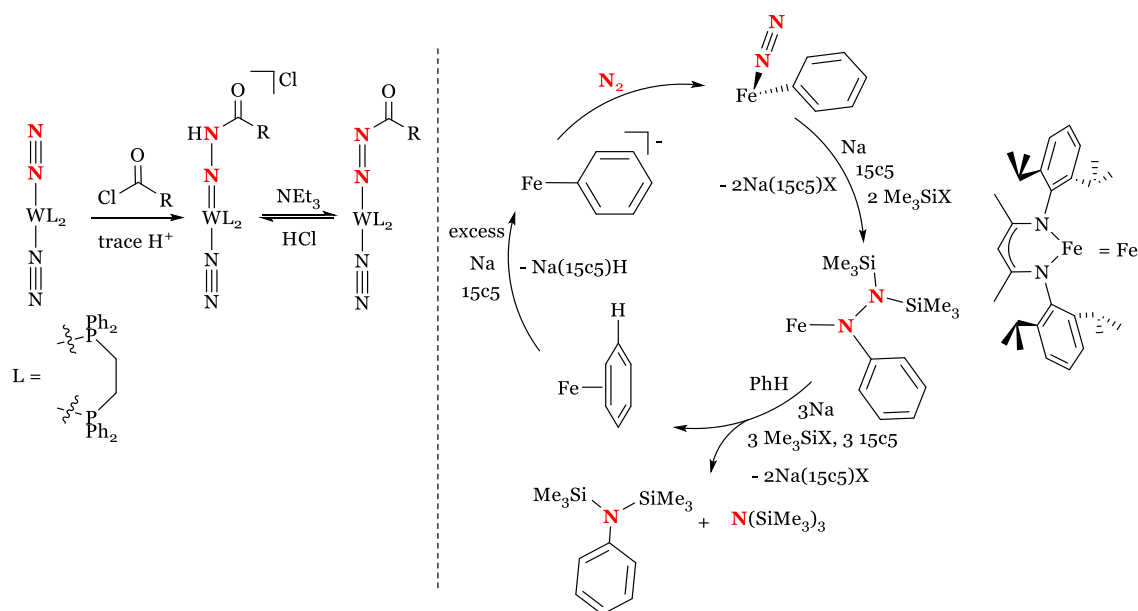


Scheme 23. N_2 -activation on a boron organic compound and subsequent reactions to ammonium by Braunschweig.^{130,131}

2.2.2. N-C bond formation

Within the aim to directly form nitrogen-element bonds from N_2 , N-C bond formation has a lot of attention to generate amines or N-heterocycles. So far, catalytic systems have not been shown but many stoichiometric examples are realised, both with a retained N-N bond or after full cleavage of the triple bond.^{126,127} Within this subchapter, some historical, or promising, or for this work especially relevant examples are discussed.

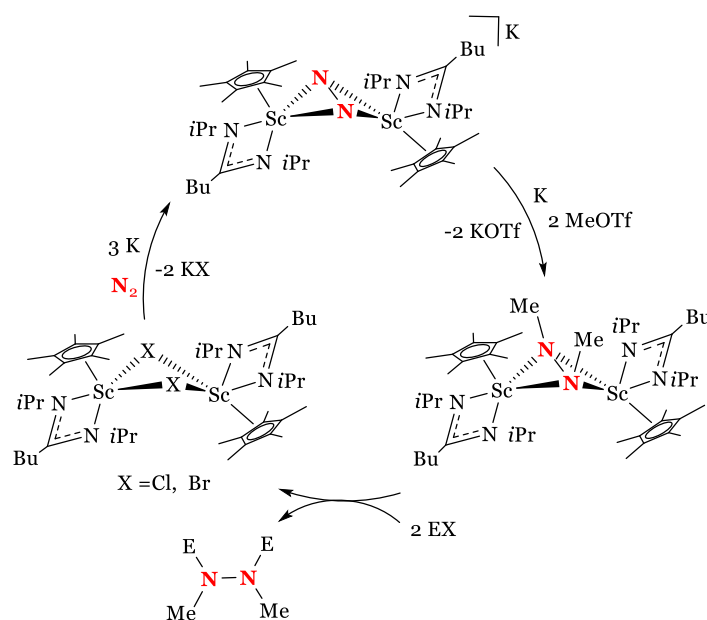
In 1969, Volpin showed N-C bond formation via reacting N_2 with $[TiCl_2(Cp)_2]$ in presence of excess phenyllithium. Besides ammonia, aniline and *ortho*-aminodiphenyl are formed showcasing C-N bond formation. The fate of the Ti-fragment remains unclear and the N-incorporated products are only obtained in low yields.¹³² Directly after, quantitative acylation of coordinated N_2 was shown upon reaction of *trans*- $[W(N_2)_2(dppe)_2]$ (*dppe* = 1,2-bisphenylphosphinoethane) with acetyl- and benzoyl chlorides, Scheme 24. Unexpectedly, the hydrazido complex was formed attributed to traces of water and deprotonation can yield the diazenido compound.¹³³ For related Mo systems, N-fragment release was established as highlighted by means of electrochemistry in Scheme 26 (*vide infra*).



Scheme 24. Left: First example of coordinated N_2 acylation by Chatt.¹³³ Left: Stoichiometric silylated aniline release from N_2 by Holland.¹³⁴

Very recently, an impressive example was reported by Holland for the release of N_2 -derived silylated aniline. Upon reduction of $[Fe(\eta^6-C_6H_6)(HC(CCH_3N(2,6-(iPr)_2C_6H_3)_2))_2]$, using an excess of Na in presence of a crownether, the $Fe-(\eta^1-C_6H_5)$ adduct is formed, see Scheme 24. This occurs via reductive induced oxidative addition of benzene and subsequent hydride abstraction.

This adduct coordinates N_2 when cooling to $-100\text{ }^\circ\text{C}$, and reduction in presence of Me_3SiX ($X = \text{Br, I}$) leads to a surprising structure: besides silylation of the terminal nitrogen (N_β) to form a hydrazido moiety, migration of the aryl group to the N_α occurred. Via control experiments, they propose that these reaction steps follow the same order: first silylation and then migration. Further reduction in presence of silylhalides and benzene provides silylated aniline and amine and the regeneration of the starting complex. This reaction is very impressive, yet unfortunately, no catalysis is realised so far: the C-H activation of the benzene ligand and subsequent hydride loss require at least RT as reaction condition, at which temperature sodium and trimethylsilylhalide are unfortunately incompatible. Larger scale one-pot reactions with repeating temperature cycles and additions of the silyl reagent allowed for formation of aniline up to 85 % yield. Concomitantly, a catalytic yield of silyl amine was found: Fe-degradation products that appear over time apparently catalyse the silylation of N_2 .¹³⁴



Scheme 25. Stoichiometric tetra substituted hydrazido release from N_2 by Xi.⁶²

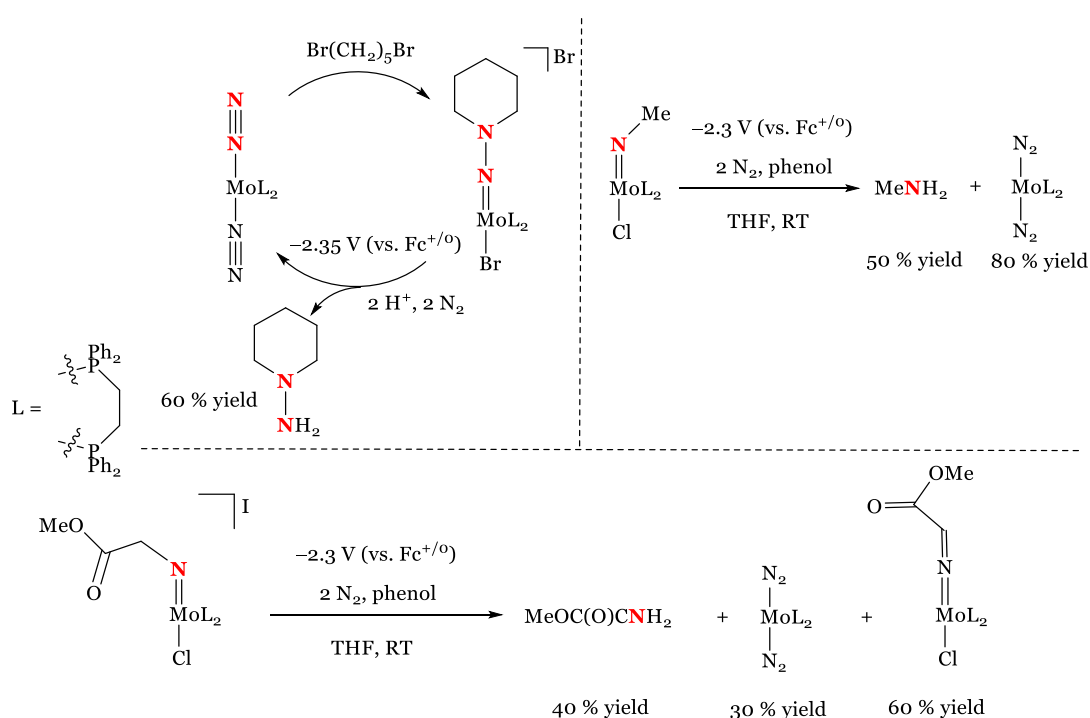
Xi and co-workers recently established N-C bond functionalisation from the side-on N_2 -bridging Sc complex $[\{\text{Sc}(\text{Cp}^*)(\text{C}(\text{Bu})(\text{NiPr})_2)_2(\mu-\eta^2:\eta^2-\text{N}_2)\}]^-$ (Scheme 25). This species was formed upon reduction of a corresponding bridging halide-precursor under a N_2 -atmosphere. Functionalisation using MeOTf forms the doubly methylated hydrazido compound, yet in low yields and accompanied by the oxidised, neutral N_2 -bridged compound. Likely, the Me-reagent gets reduced, reflecting the strong reducing ability of the anionic compound. Subsequent additions of MeOTf and potassium fortunately increases the yield. Starting from this hydrazido species, several transformations are possible, such as protonation, oxidation and further reaction with electrophiles. The latter allowed for regeneration of the starting precursor by

simple addition of electrophilic halides to regenerate [$\{\text{Sc}(\text{Cp}^*)(\text{C}(\text{Bu})(\text{NiPr})_2\}_2(\mu\text{-}\eta^2\text{:}\eta^2\text{-X})_2$] (X = Cl, Br). Via this route, tetra substituted hydrazido compounds were formed and a one-pot reaction with subsequent reduction, methylation and further reaction with benzoyl chloride yielded the product and starting precursor in circa 50 % yield. No catalytic activity is yet possible due to the incompatibility of MeOTf and the strong reductant potassium.⁶²

Both examples by Holland and Xi emphasise a mismatch of redox-potentials between the redox reagent (reductant) to re-generate the metal-N₂ or metal-nitride precursor and the carbon-based reagent for C-N bond functionalisation. Substituting these redox-reagents by means of electrochemistry would at least diminish the over-potential that is now often applied (as only certain redox-potentials are available depending on the chemical reductants).

The examples of electrochemical assisted N-fragment release from defined molecular complexes are limited and this field is dominated by the work of Pickett. A first example is from 1981, starting from *trans*-[Mo(N₂)₂(dppe)₂], Scheme 26. It was shown before that the N_β of a coordinated dinitrogen can be doubly functionalised by alkyl halides, and Br(CH₂)₅Br forms a cyclic piperazine compound.¹³⁵ Reductive CPE of this compound at $E_{\text{appl.}} = -2.35$ V (vs. Fc^{+ / 0}) in THF under a N₂-atmosphere is slow, but reveals the liberation of N-aminopiperidine in 60 % yield accompanied by the transfer of 4 electrons per Mo. No external acid is added to this reaction, and traces of water likely provide the required proton equivalents. The N₂ precursor is re-formed in circa 45 % yield, allowing to formulate a synthetic cycle (see Scheme 26).¹³⁶

From the same group comes the electrochemical release of amines in 1995 and 1997.^{137,138} The nitride [MoN(dppe)₂], which is likely to be derived from N₂ in a complex pathway (*vide infra*), reacts readily with electrophilic alkyl halides, of various chain lengths and functional groups.^{137,139} For instance, an ester functional group containing Mo(IV) imido [Mo(NCH₂C(O)OMe)Cl(dppe)₂]I is formed. Upon reduction at $E_{\text{appl.}} = -2.3$ V vs. Fc^{+ / 0} in THF in presence of phenol and N₂, glycine methyl ester is released. On the Mo-side, both a bis N₂- and an azavinylidene complex are formed, the latter being the result of the starting material acting as sacrificial proton donor, see Scheme 26, bottom. To prevent this and to increase the amide yield, acetic acid was examined as alternative acid. This indeed raises the amide yield up to 80 %, but the acetate coordinates the Mo-centre, which promotes the formation of hydrides and subsequently the formation of H₂. Similar reactivity was also extended to only hydrocarbon substituted imides, as shown by the release of methylamine in Scheme 26, top right.¹³⁸

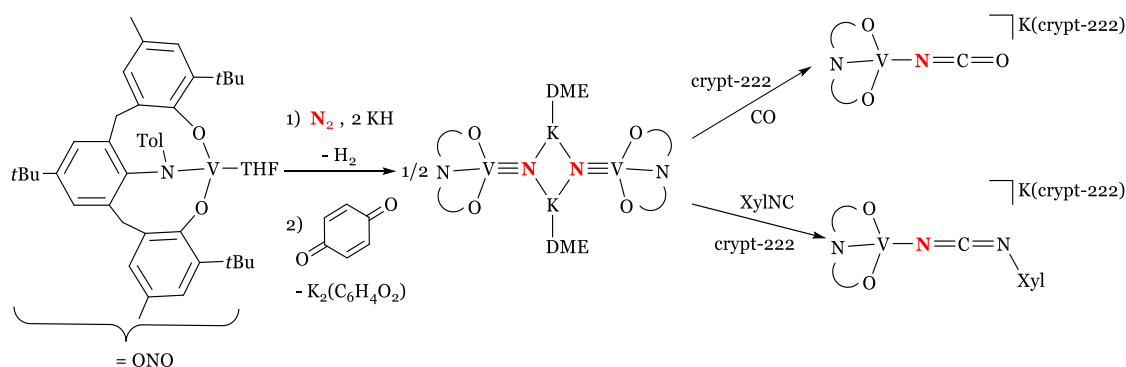


Scheme 26. Electrochemical C-N bond containing fragment release by Pickett. Top left: N-aminopiperidine release from $[\text{Mo}(\text{N}_2)_2(\text{dppe})_2]$.¹³⁶ Top right: methylamine release from $[\text{Mo}(\text{NMe})\text{Cl}(\text{dppe})_2]$ in presence of phenol. Bottom: amine release from $[\text{Mo}(\text{NCH}_2\text{C}(\text{O})\text{OMe})\text{Cl}(\text{dppe})_2]\text{I}$ in presence of phenol.¹³⁷

Regarding N-C bond formation, especially the generation of double or triple bonds in for instance N-heterocycles, heterocummules or nitriles are an appealing target. Focusing on reactions where the N-N bond is retained, Caulton calculated a large series of possible reactions partners for N_2 (i.e. with alkynes) and identified which reactions are exothermic. For instance, the reaction of two equivalents of acetylene with N_2 to pyridazine is strongly exothermic ($\Delta H^\circ = -40.9 \text{ kcal mol}^{-1}$). The double or triple bonds in the products can offset the high energy required for activation of N_2 . Hydrazido products with a single N-N bond can be unfavourable due to electronic repulsion of the nitrogen lone pairs in close proximity.¹⁴⁰ Regarding splitting of N_2 , the full bond energy can be offset for instance by formation of nitriles: the bond energy of $\text{HC}\equiv\text{N}$ ($224 \text{ kcal mol}^{-1}$) is the same of N_2 ($226 \text{ kcal mol}^{-1}$),³ as will be discussed in the next Section. Here, examples of isocyanate and isonitrile are highlighted.

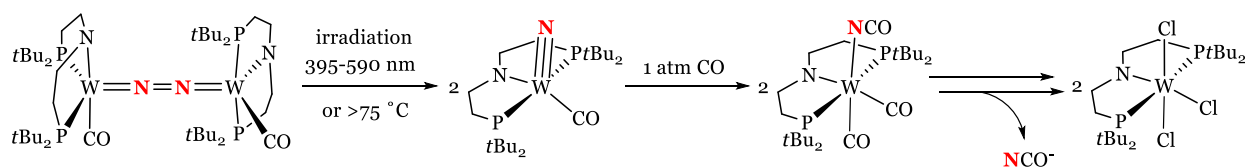
Kawaguchi published the reductive splitting of N_2 starting from $[\text{V}(\text{ONO})(\text{THF})]$ ($\text{ONO} = 2,6$ -(3-*t*Bu-5-Me-2- $\text{OC}_6\text{H}_2\text{CH}_2$)-4-*t*Bu-(*p*-tolyl) NC_6H_4) (Scheme 27). In the initial step, a V(IV) dimeric structure is obtained bridged by nitrides and a potassium moiety has inserted in one of the V-O arms of the ligands. Subsequent oxidation using benzoquinone restores the tridentate ligand coordination and yields terminal nitrides linked via potassium moieties in the solid state.

This nitride reacts both with CO and isonitrile XyNC, upon formation of formal V(III) adducts. Subsequent stoichiometric release of potassium isocyanate in 80 % was established with concomitant reformation of the precursor in a multi-step procedure closing a synthetic cycle. It is not specially mentioned if large-scale one-pot reactions are tried, but it is assumed that the N₂-splitting and the CO coordination reaction step are incompatible, as coordination of the latter would block all available coordination sides for N₂-activation.¹⁴¹



Scheme 27. Isonitrile and isocyanate formation from a vanadium nitride by Kawaguchi.¹⁴¹

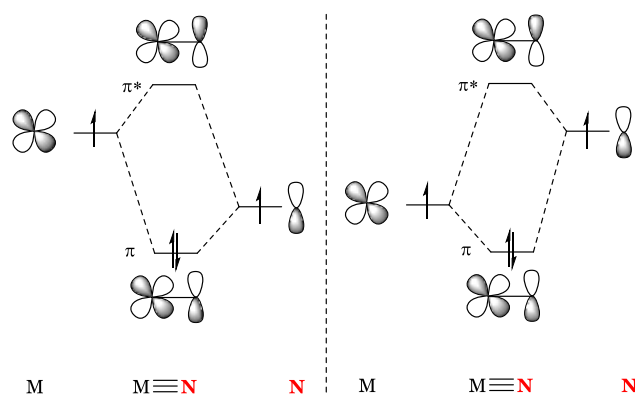
A similar example is from our group by Dr. B. Schluschaß, who reacted the nitride [WN(PNP)(CO)] as established from N₂-splitting (*vide supra*) with CO (Scheme 28). The corresponding isocyanate species is formed via an intramolecular mechanism as was concluded from NMR spectroscopy upon labelling: reaction under ¹³CO leads to the formation of the N¹²CO-analogue. Quantitative release of isocyanate was established upon reaction with TMSCl, and via a two step procedure of oxidation and irradiation, the precursor [WCl₃(PNP)] is formed, which represents the entry for N₂-fixation to close the synthetic cycle.⁶⁷



Scheme 28. Isocyanate formation and release from a tungsten nitride by Schneider.⁶⁷

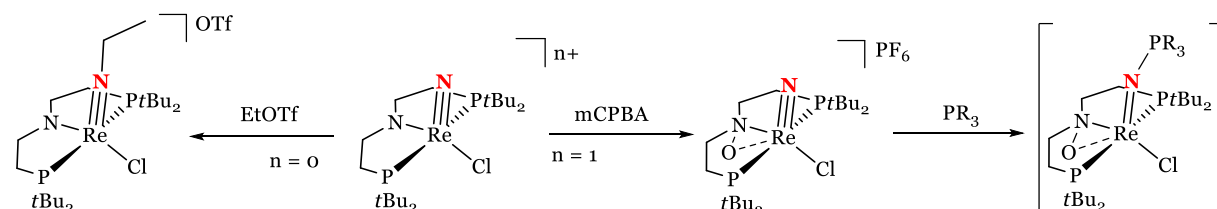
For N-C bond formation (or N-E in general) from terminal nitrides, it is important to know whether the nitride reacts with incoming nucleophiles or electrophiles. This reactivity depends partly on the energy levels of the metal d- and nitrogen p-orbitals that form the (anti)-binding M-N π -bonds. A very schematic representation of two extreme cases is shown in Scheme 29. When the nitrogen orbitals are lower in energy, the π -orbital will be mainly nitrogen-based: the

nitride reacts with incoming electrophiles. In the opposite case, when the metal d-orbitals are lower in energy, the π^* -orbital will be mainly nitrogen based inducing reactivity with incoming nucleophiles. For early transition metals, the d-orbitals are high in energy, resulting in nitrides that react with incoming electrophiles. Moving to the right in the periodic table slowly shows a transition to nitrides that prefer reactivity with incoming nucleophiles,¹⁴² yet nitride reactions with electrophiles is more established in general.



Scheme 29. Schematic MO scheme showing one π orbital set of a metal-nitride fragment to rationalise if the nitride preferentially reacts with an incoming electrophile (left) or nucleophile (right).¹⁴²

The nitride reactivity also depends on the formal metal oxidation state, as is shown for the nitride $[\text{ReNCl}(\text{PNP})]$ (**3^{Cl}**), as obtained from N_2 -splitting (*vide supra*). As Re(V) nitride, it was shown to only react with strong electrophiles such as alkyl triflates. Nucleophiles as MeLi result in halide to methyl exchange on the Re-centre, without nitride involvement. Scheme 30 shows its reaction with EtOTf to $[\text{Re}(\text{NCH}_2\text{CH}_3)\text{Cl}(\text{PNP})]\text{OTf}$, that was further reacted to liberate acetonitrile (*vide infra*).⁷⁹



Scheme 30. Formal metal oxidation state influence on reactivity with incoming electrophiles (left) or incoming nucleophiles (right) on N_2 -derived $[\text{ReNCl}(\text{PNP})]$.^{79,143}

However, oxidation of the nitride leads to different reactivity, as shown by Holland and co-workers. As predicted from its CV, $[\text{ReNCl}(\text{PNP})]$ is readily oxidised at mild potentials to the cationic Re(VI) species. In an attempt to form a $\text{N}_{\text{nitride}}\text{-O}$ bond, its reaction with 3-chlorobenzoic acid (mCPBA) was explored, surprisingly showing $\text{N}_{\text{amide}}\text{-O}$ bond formation to the formal nitroxide Re(VI) compound. The weak O-Re interaction results in some donation of the lone pair

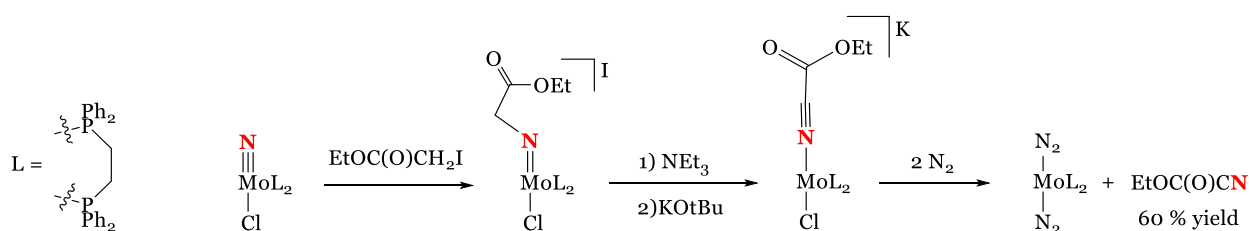
of the oxygen into the Re-N_{nitride} antibonding π -orbital, slightly weakening this bond. Addition of phosphines show reactivity at the N_{nitride}, although the resulting adduct species decompose over time. Phosphines are mainly considered nucleophilic reagents, yet can react ambiguous.¹⁴⁴ Therefore reactions kinetics for P(*p*-F-Ph)₃, PPh₃, and P(*o*-tolyl)₃ were measured in the order of increasing electron density. As the latter phosphine reacts the fastest, their nucleophilic in this reaction is substantiated.¹⁴³ This represents an Umpolung of the reactivity character compared to the neutral Re(V) nitride. This reactivity with a nucleophile is an exemption: in the following Section N₂ to nitrile transformation is discussed, for which C-N bond formation is almost exclusively based on nitrides reacting with electrophiles.

2.2.3. Nitrile generation from N₂

Within the context of this work, most attention is given to the synthesis of nitriles from N₂, which in industry relies on building blocks starting from ammonia. Nitriles are important chemical compounds for instance in adhesive chemistry and polymer industry for either rubber or synthetic polymers. For this latter, especially acrylonitrile and adiponitrile are important. Acrylonitrile is commercially synthesised since the 1960's, initially both via ammoxidation of propylene, and the catalytic addition of HCN to acetylene. Because of safety and high costs, this latter process was discontinued, and circa 5 million tons are now produced per year via ammoxidation.¹⁴⁵ As side product, acetonitrile is generated, that mostly finds use as organic solvent. Reduction of acrylonitrile in presence of protons leads to coupling to form adiponitrile, which is a building block for nylon. This is done by means of electrochemistry, which represents one of the most developed electrochemical organic transformations by industry today.¹⁴⁶

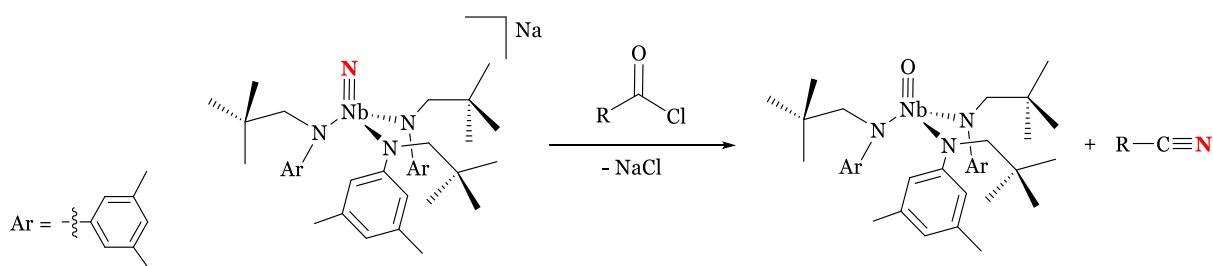
By now, there are a handful of examples of stoichiometric nitrile syntheses directly from N₂ on molecular compounds. A pioneering example for nitrile release is the somewhat in literature hidden example by Pickett in 1995 starting from the terminal nitride [MoNCl(dppe)₂], which is functionalised to Mo(IV) imido [Mo(NCH₂C(O)OEt)Cl(dppe)₂]I (Scheme 31). Upon deprotonation, a neutral azavinyl Mo(II) intermediate is formed, that is deprotonated a second time (yet with a stronger base) to the anionic [Mo(NCC(O)OEt)Cl(dppe)₂]⁻. It is assumed that the electron withdrawing ester group allows for this twofold deprotonation. The formation of a nitrile functional group from a N-C single bond requires an overall four-fold oxidation and two-fold deprotonation. Here, the deprotonation is inter-, and the oxidation is intra-molecular: the Mo(IV) is parallelly reduced to Mo(0). The nitrile is readily released in good yields upon introducing an additional ligand, i.e. either 1 atm of CO or N₂, yielding the bis CO- or N₂-complex.¹³⁷ The latter Mo(0) complex can split N₂ into a terminal nitride complex in a complex, multistep procedure. First, twofold addition of an alkylbromide yields the hydrazido complex

$[\text{MoBr}(\text{N}_2\text{R}_2)(\text{dppe})_2]\text{Br}$. Subsequent double reduction (both chemical and electrochemical pathways are established)¹³⁶ to $[\text{Mo}(\text{N}_2\text{R}_2)(\text{dppe})_2]$ and protonation using HBr, splits the N-N bond into R_2NH and parent imido $[\text{Mo}(\text{NH})\text{Br}(\text{dppe})_2]$.¹⁴⁷ The latter is readily deprotonated to the terminal nitride. The chloride congener was explored for the nitrile release in Scheme 31, and to the best of our knowledge, the N_2 -splitting was not examined with chloride. Although a similar N_2 -splitting reactivity is to be expected with chloride, halogen exchange can occur at the imido level. The CV of $[\text{Mo}(\text{NR})\text{X}(\text{dppe})_2]\text{X}$ shows an irreversible, two-electron reduction, upon which $[\text{Mo}(\text{NR})(\text{dppe})_2]$ is formed that can be oxidised and re-coordinates a halide ligand.¹³⁸ Here a Br to Cl exchange can be envisioned, to re-obtain the imido species that closes the synthetic cycle. The recent work by Masuda, see Scheme 12, showcasing electro-oxidative N_2 -splitting on the very related depe ligand system, yields the nitride compound and is assumed to also provide a N_2 -derived nitride for this ligand system.



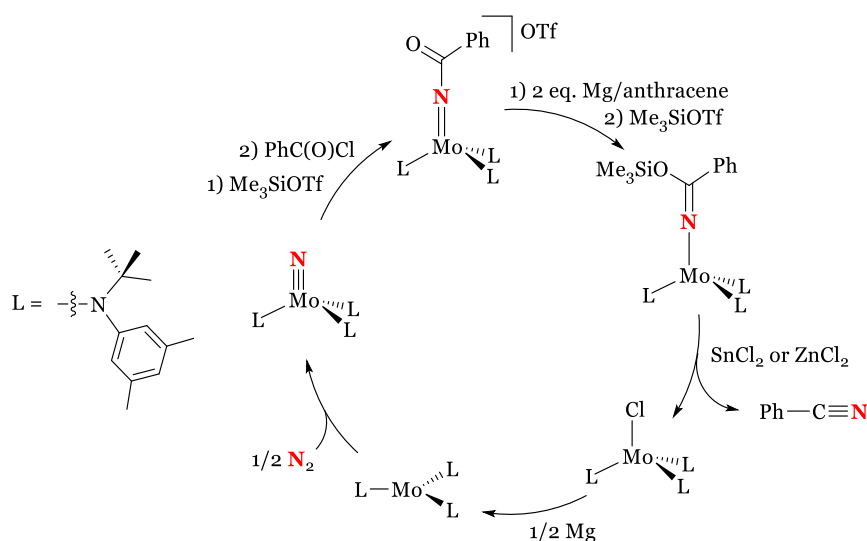
Scheme 31. Nitrile release from $[\text{MoNCl}(\text{dppe})_2]$ upon reaction with an alkyl iodide and twofold deprotonation.¹³⁷

Cummins developed two examples of nitrile formation. First in 2004, from the N_2 -derived nitride of a heterobimetallic Mo-Nb system, see Scheme 32.⁵⁰ A neopentyl (Np) substituted amide ligand was used here instead of the originally examined *iso*-propyl or *tert*-butyl substituted amide ligands for the Nb and Mo precursor, respectively (Scheme 4 and 6). Easier synthetic access to $\text{Na}[\text{Mo}(\text{N}(\text{Np})(2,4\text{-dimethylbenzene}))_3(\text{N}_2)]$ is found upon introducing this extra CH_2 -group. Reacting this anionic compound with $[\text{Nb}(\text{OTf})(\text{N}(\text{Np})(2,4\text{-dimethylbenzene}))_3]$ and subsequent reduction splits into the molybdenum and niobate nitride complexes. The latter reacts readily with several acid chlorides to release the corresponding nitriles in excellent yields. The extra CH_2 group in the ligand backbone proved instrumental for reactivity at room temperature. For the *tert*-butyl substituted amide nitride, the imide is an isolatable species and subsequent nitrile formation is only observed after heating. This is attributed to the increased steric demand of *tert*-butyl. The Nb oxo species is transformed into the for N_2 -splitting relevant triflate species via a two-step procedure. In this manner, a full synthetic cycle is developed, yet with a stoichiometric formation of an unused Mo nitride.¹⁴⁸



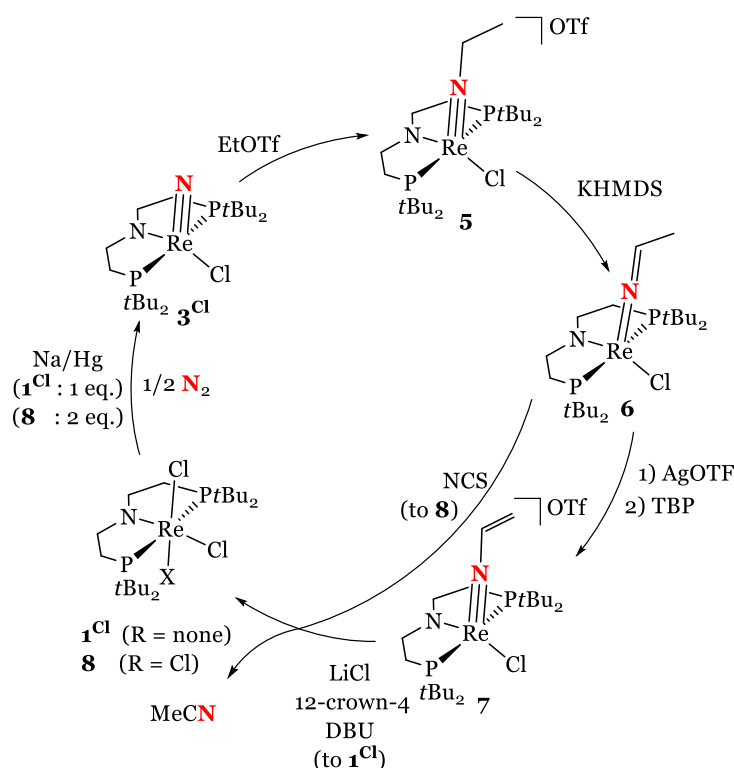
Scheme 32. Key acylation step of $[\text{NbN}(\text{N}(\text{Np})(2,4\text{-}(\text{CH}_3)_2\text{C}_6\text{H}_4))_3]$ with several acid chlorides to form the corresponding nitriles and the Nb oxo complex.¹⁴⁸

Cummins already reported the direct C-N bond formation for their pioneering nitride $[\text{MoN}(\text{N}(t\text{Bu})(2,4\text{-}(\text{CH}_3)_2\text{C}_6\text{H}_3))_3]$ with the strong electrophile $\text{PhC}(\text{O})\text{OTf}$, forming the corresponding imido.¹⁴⁹ A direct reaction with weaker electrophiles was not observed. In a desire to use acid chlorides as electrophiles, the nitride was first activated by Me_3SiOTf and then reacted with $\text{PhC}(\text{O})\text{Cl}$ (Scheme 33). The now resulting Mo(VI) imido can be reduced twice in presence of an additional equivalent of Me_3SiOTf to generate the isolatable Mo(IV) ketimido species. Subsequently, the addition of Lewis acids SnCl_2 or ZnCl_2 releases benzonitrile in high yields (> 90 %), where the Lewis acid cleaves off the trimethylsiloxy-group and leaves a Mo(IV) chloride. This is reduced once to re-generate the N_2 -splitting Mo(III) complex $[\text{MoN}(t\text{Bu})(2,4\text{-}(\text{CH}_3)_2\text{C}_6\text{H}_3)_3]$. Via the same principles, the formation of acetonitrile and pivalonitrile ($t\text{BuNC}$) was achieved. Reduction of the resulting Mo^{IV} compound initiates a second stoichiometric N_2 -splitting cycle.¹⁵⁰



Scheme 33. Stoichiometric cycle for N_2 -splitting, benzoylchloride reactivity and Lewis acid assisted benzonitrile release from $[\text{MoN}(\text{N}(t\text{Bu})(2,4\text{-}(\text{CH}_3)_2\text{C}_6\text{H}_3))_3]$ developed by Cummins.¹⁵⁰

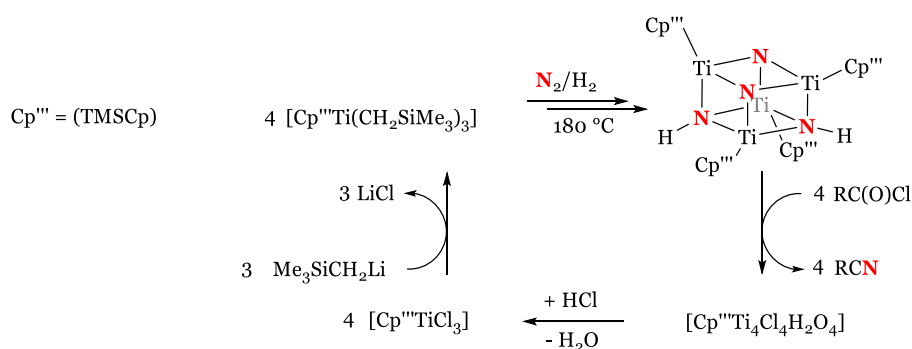
Dr. I. Scheibel functionalised the nitride product **3^{Cl}** of N₂-splitting as described in Section I.1.4, upon reaction with an electrophilic reagent. Unfortunately, **3^{Cl}** only reacts with strong reagents (alkyl triflates), and Me-, Et-, and *in situ* formed benzyl-OTf showed C-N bond formation of the nitride. This is exemplified in Scheme 34 for the reaction of **3^{Cl}** with EtOTf to form [Re(NEt)Cl(PNP)]OTf (**5**). From this complex, MeCN was formed and released.¹⁵¹ This was first approached via the strategy of deprotonation and intramolecular reduction of the Re(V) imido **5** to ultimately form Re(I), analogous to the example of Pickett (*vide supra*). Reaction of **5** with strong base KHMDS results in clean deprotonation of the C_α of the ethyl-group into formal azavinylidene Re(III) [Re(NCHCH₃)Cl(PNP)] (**6**). The second deprotonation step proved more difficult, as the resulting Re(I) is only isolated upon stabilisation with additional π-accepting ligands. MeCN is almost quantitatively released when **6** is reacted with KHMDS in presence of *tert*-butylisocyanide to form [Re(PNP)(CN*t*Bu)₂]. Unfortunately, it was not yet possible to transform this Re(I) species to a for N₂-splitting suitable starting platform. Therefore, instead of the Re-centre as intramolecular oxidant, the use of external oxidants was examined to circumvent the Re(I) oxidation state.



Scheme 34. Stoichiometric N₂-splitting and functionalisation cycle to release MeCN from the PNP-pincer platform [ReCl₂R(PNP)] (**1^{Cl}** (R = none) or **8** (R = Cl)) by Schneider.¹⁵¹

To do so, the second deprotonation was accompanied by a two-fold oxidation upon reacting **6** with AgOTf and subsequently 2,4,6-tri-*tert*-butylphenoxy (TBP) as PCET reagent. The resulting complex is described either as an acetonitrile Re^{III} or vinyl imido Re^V tautomer:

[Re(NCCH₃)Cl(PNP)]OTf or [Re(NCHCH₂)Cl(PNP)]OTf (**7**), respectively. By NMR spectroscopy, the latter description was found to be more suitable. From **7**, MeCN is readily released in presence of sub stoichiometric amounts of DBU (to facilitate the tautomerisation), LiCl (to offer chloride ligands for the Re-centre to form **1^{Cl}**) and crown ether 12-crown-4. Yet, the yield in both MeCN and a Re-product was rather low (around 30 %). Alternatively, **6** is reacted with 2 eq. of N-chlorosuccinimide (NCS), that can act as a one or two electron oxidation, a base and a chloride donor; the three requirements for this transformation. MeCN and the Re(IV) compound [ReCl₃(PNP)] (**8**) are obtained in high yields (80 % and 93 %, respectively). Successful N₂-splitting was extended to this Re(IV)-platform upon reduction using 2 eq. of Na/Hg to **3^{Cl}** in good yields. Hereby, a synthetic cycle is closed incorporating N₂-splitting, electrophilic C-N bond formation and subsequent MeCN release. Noteworthy, the same procedure was used for the successful release of benzonitrile starting from **3^{Cl}** and freshly prepared PhCH₂OTf.¹⁵² The release of nitriles from this system relies on the use of the strong electrophile EtOTf and the harsh oxidant NCS. The incompatibility of these reagents and the reducing agent as required for N₂-splitting will hinder this cycle to go beyond being stoichiometric. As outlined in Section I.2.4, an objective of this work is to achieve nitrile release electrochemically and thereby circumventing the use of NCS.

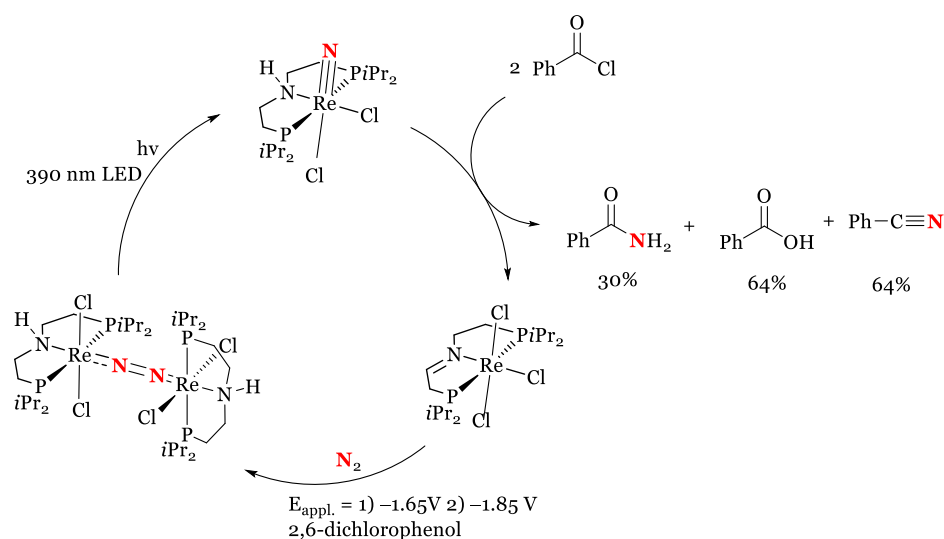


Scheme 35. Nitrile formation from the cubane complex [$\{\text{TiCp}'''\}_4(\mu_3\text{-NH})_2(\mu_3\text{-N})_2$] (Cp''' = C₅Me₄SiMe₃) obtained after N₂-splitting and subsequent regeneration of the starting complex by Hou.¹⁵³

Parallel, the group of Hou and co-workers released nitriles from their mixed diimide dinitride titanium complex [$\{\text{TiCp}'''\}_4(\mu_3\text{-NH})_2(\mu_3\text{-N})_2$] (Cp''' = C₅Me₄SiMe₃) obtained from N₂-splitting.¹⁵⁴ Reaction of this latter compound with 4 eq. of an acid chloride at slightly elevated temperatures (60 °C), cleanly afforded the corresponding nitriles and the generation of a mixture of (less-defined) titanium complexes. However, it proved possible to obtain a selective species again upon protonation that is transformed into the precursor for N₂-splitting by using an organolithium reagent. Notably, several acid chlorides with various functional groups were

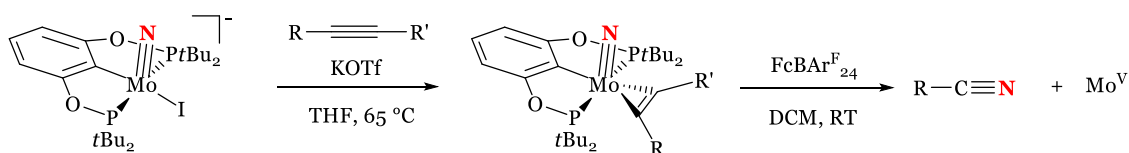
tested that all show high yields. Even alkyl acid chlorides function well, although the reaction temperature has to be raised.¹⁵³

The nitride $[\text{ReNCl}_2(\text{HPNP}^{\text{iPr}})]$ of Dr. F. Wätjen as introduced in Section I.1.4 was also used for subsequent nitrile release (Scheme 36). It was found to exhibit sufficient nucleophilic character to react with PhC(O)Cl at $80\text{ }^\circ\text{C}$ overnight. This electrophile is to the best of our knowledge not examined for the related nitride $\mathbf{3}^{\text{Cl}}$. Still, a comparison between the related systems is possible, as both $\mathbf{3}^{\text{Cl}}$ and $[\text{ReNCl}_2(\text{HPNP}^{\text{iPr}})]$ were reacted with acetyl chloride, and only for the latter conversion was observed.⁷⁹ Therefore, the six-coordinate nitride bearing the $(\text{HPNP}^{\text{iPr}})$ is believed to be a better nucleophile. Upon reaction with benzoyl chloride, a mixture of organic products was obtained that was identified as benzamide, benzonitrile, and benzoic acid in good yield, the latter being the product of the reaction between benzoyl chloride and benzamide. The required $2e^-/2\text{H}^+$ for this reaction originate from the pincer backbone and the imine compound $[\text{ReCl}_3(\text{N}(\text{CHCH}_2\text{P}^{\text{iPr}_2})(\text{CH}_2\text{CH}_2\text{P}^{\text{iPr}_2}))]$ was isolated, indicating metal-ligand cooperativity. Regeneration of the ligand backbone is achieved by consecutive reaction with a hydride to $[\text{ReCl}_3(\text{PNP}^{\text{iPr}})]$ and proton donor to $[\text{ReCl}_3(\text{HPNP}^{\text{iPr}})]$, and even more elegantly by electrochemical reduction in presence of protons. Continuing electrochemical reduction at slightly more negative potential in presence of N_2 forms the dinuclear end-on N_2 -bridging compound. This now stoichiometric cycle looks very promising towards a catalytic future. Yet it still has challenges: the high temperature required for reaction with benzoyl chloride, and the electrochemical formation of the dinuclear compound and its subsequent photochemical splitting show low compatibility.⁸⁰



Scheme 36. Benzoyl chloride reaction cycle and subsequent electrochemical ligand re-reduction, N_2 -activation and photochemical splitting by Schneider.

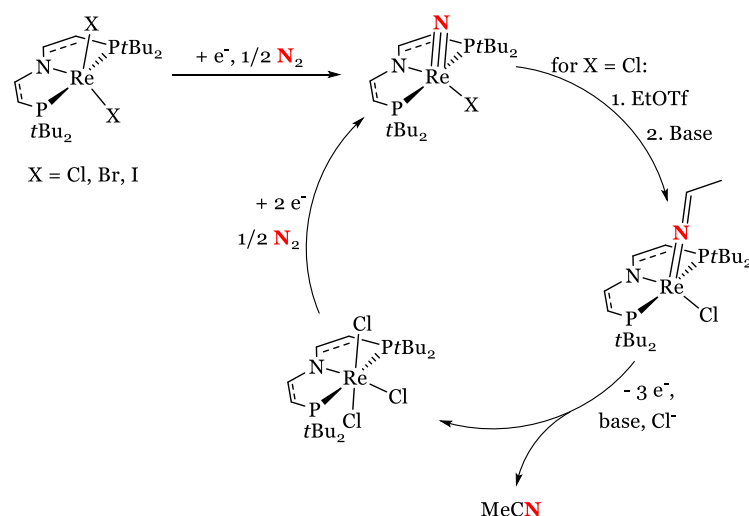
Very recently, Mézailles and co-workers continued on the N₂-derived nitride by Schrock in a refreshing approach to generate nitriles. Starting from [MoNI(POCOP)]⁻ (POCOP = C₆H₃-1,3-(OPtBu₂)₂), alkyne addition in presence of an iodide-abstracting salt resulted in alkyne-coordinated neutral Mo(IV) nitrides, initially inert to further N-C bond insertion (Scheme 37). Fortunately, direct RT metathesis is observed upon oxidation, generating nitriles in high yields, and a Mo^V species that is ascribed to an alkyne nitride complex. The striking different reactivity upon the one-electron withdrawal was rationalised by DFT. Comparing pathways between Mo^V and Mo^{IV} starting platforms reveal that substantial higher barriers are to overcome in case of the latter. This is especially highlighted in the first reaction: rotation of the coordinated alkyne to become co-planer with the nitride is a pre-requisite for metathesis, and it is substantially easier starting from Mo(V). Additionally, the process is overall endergonic for Mo^{IV}, in contrast to a strong exergonic pathway for the Mo^V stage, which is partly attributed to the increased electron density of the lower oxidation state.¹⁵⁵



Scheme 37. Nitrile formation via metathesis starting from a N₂-derived Mo^{IV} nitride.¹⁵⁵

I.3. Research scope

This project continues the Re-mediated N₂-splitting and functionalisation as started by Schneider in 2014. As shown in the previous Sections, the N₂-splitting from [ReCl₂(PNP)] (**1**^{Cl}) relies on harsh reductants and with the reagents used for subsequent C-N bond functionalisation and oxidative fragment release, it represents an incompatible mixture. To move this synthetic cycle into the direction of a catalytic future, a next step is the replacement of the harsh chemical redox agents by means of electrochemistry, which is pursued within this work. Furthermore, the examples for Re-mediated N₂-splitting are still limited, and a larger database is desired for more understanding of this process. These various goals, as visualised in Scheme 38, are addressed in Section II *Results and Discussion*.



Scheme 38. Aimed electrification and platform modification of the Re-mediated N₂-splitting and functionalisation to MeCN.

In *Chapter II.1*, the electrification of N₂-splitting from **1**^{Cl} is examined in detail. Encouraged by successful electrosynthesis of **3**^{Cl}, we used CV to examine the mechanism of this reaction that follows the same pathway for both electrochemical and chemical reduction. The final elemental step of this pathway prior to splitting is the assembly of intermediate **2**^{Cl}, which characterisation is continued, and we examine its splitting into the nitride **3**^{Cl}.

To extend the database of platforms for Re-mediated (electro)chemical N₂-splitting, we used two of the modification possibilities this platform offers. First, we exchange the chloride ligands for bromide and iodide ligands as described in *Chapter II.2*. We examine the influence of the hereby-modified electronic and steric properties on the N₂-splitting ability and its mechanism. In addition, we characterise the dinuclear intermediates **2**^{Br} and **2**^I spectroscopically. As second

modification possibility, we examine the oxidised P=N=P-backbone starting platform for electrochemical N₂-splitting in *Chapter II.3*. The influence of the decreased electron donating properties of this ligand are assessed for the chloride and iodide platform.

In *Chapter II.4*, we focus on N₂-functionalisation, by aiming for MeCN formation and release by means of electrochemistry. Although this turned out to be possible for the originally established PNP-compounds, we found unselective formation of several compounds on the Re-side. Therefore, we extend this C-N bond functionalisation and (electro)chemical MeCN release to the P=N=P-platform, which is more stable under oxidative conditions.

With the established electrochemical N₂-splitting and MeCN release in hand, a next directive is to perform these reactions in a flow cell set up with electrochemical equipment. As initial research, a commercially obtained flow cell was modified to fit with our experimental procedures and initial N₂-splitting studies on **1^{Cl}** were performed as described in *Chapter II.5*.

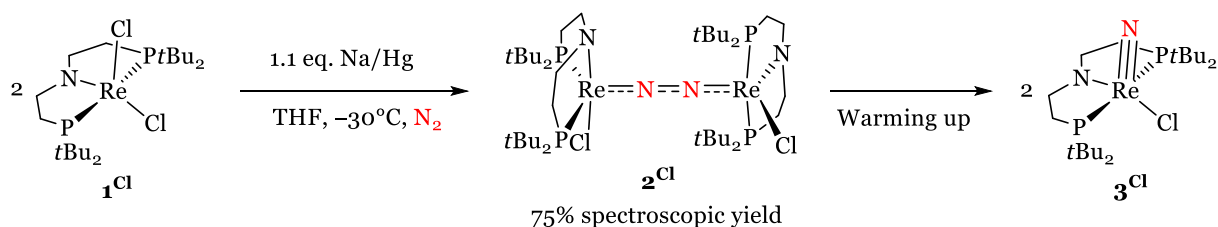
II Results and Discussion

II.1: Mechanism of (electro)chemical N₂-splitting from [ReCl₂(PNP)]

Parts of this Chapter were published in the *Journal of the American Chemical Society* under the title: 'Mechanism of Chemical and Electrochemical N₂ Splitting by a Rhenium Pincer Complex' in **2018**.⁷⁰

1.1. Dinuclear N₂-bridged intermediate and its splitting into nitrides

Chemical N₂-splitting starting from a molecular Re-complex was established in our group using the platform [ReCl₂(PNP)] (**1**^{Cl}) forming the terminal nitride [ReNCl(PNP)] (**3**^{Cl}) in yields up to 85 % ((PNP) = N(CH₂CH₂PtBu₂)₂⁻), as elaborated in Section I.1.4. This directly raised the question for the existence of a possible N₂-bridged intermediate, as initiated experimentally by Dr. F. Wätjen (né Schendzielorz); chemical reduction of **1**^{Cl} at low temperatures (-40 °C) forms C₂-symmetric [{ReCl(PNP)}₂(μ-N₂)] (**2**^{Cl}), showing coupling doublets by ³¹P{¹H} NMR spectroscopy (Scheme 39). Upon warming, this species converts to **3**^{Cl}, proving its role as intermediate in N₂-splitting. ¹H NMR spectroscopy showed paramagnetically shifted, yet sharp signals in the range of +12 to -17 ppm, among which by ¹H COSY NMR spectroscopy eight signals for the PNP-pincer backbone proton are identified. The allocation of the four *tert*-butyl groups remained unclear, due to their broadness at low temperatures. **2**^{Cl} could not be isolated, yet crystals suitable for XRD spectroscopy were obtained, that confirm its structure.⁷¹ From this already elaborate starting point, the properties of **2**^{Cl} and its role in N₂-splitting are examined further within this work.



Scheme 39. Reduction of **1**^{Cl} at -30 °C with Na/Hg affords **2**^{Cl} in 75 % spectroscopic yield, which splits into **3**^{Cl} upon warming up in a first order manner.

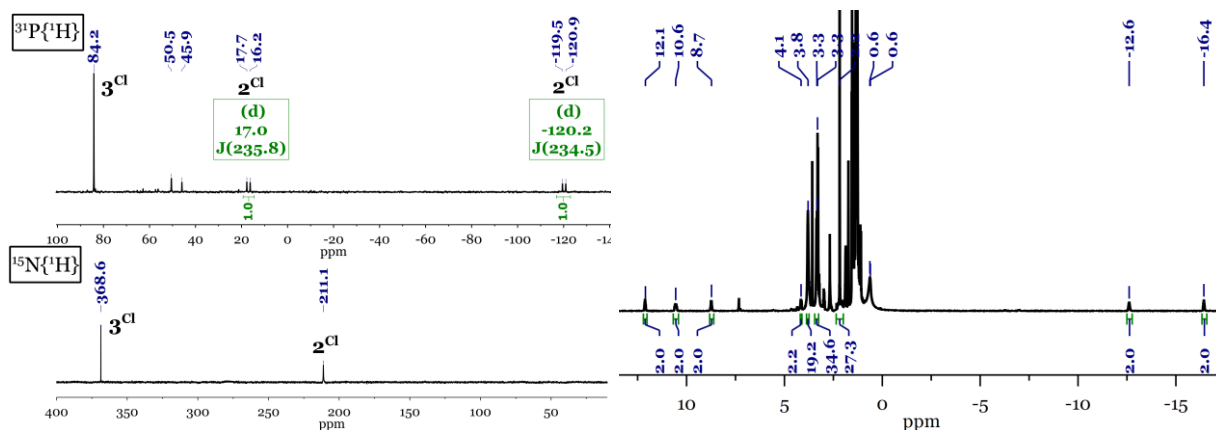


Figure 10. Left: NMR spectroscopy of a mixture of **2**^{Cl} and **3**^{Cl} at -30 °C, $^{31}\text{P}\{^1\text{H}\}$ NMR spectrum (top) and $^{15}\text{N}\{^1\text{H}\}$ NMR spectrum (bottom). Right: ^1H NMR spectrum of **2**^{Cl} in *d*₈-THF at -15 °C with addition of hexamethylbenzene as internal standard to quantify **2**^{Cl}.

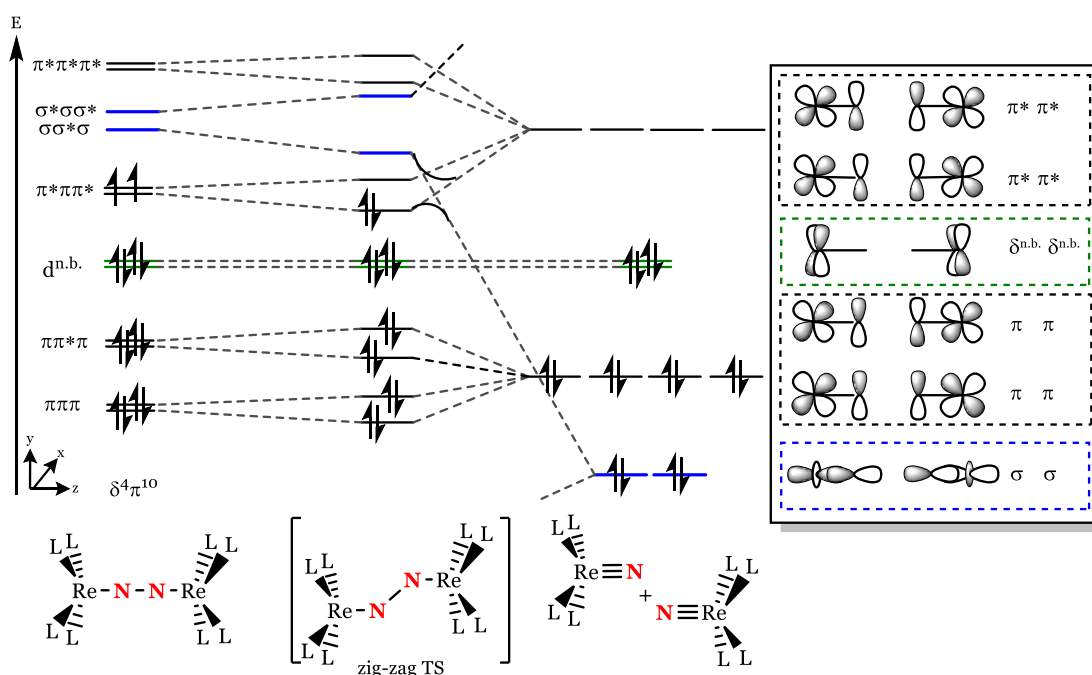
First, the intense red colour of a solution of **2**^{Cl} was examined by UV-vis spectroscopy showing two absorption maxima at 533 and 375 nm. Resonance Raman with excitation wavelengths at 467 and 633 nm did unfortunately not reveal a N₂-stretching frequency that could complement the N-N bond length for insight into the degree of N₂-activation. Furthermore, the NMR characterisation of **2**^{Cl} was completed. Upon measuring NMR spectroscopy at higher temperatures ($-15/-10$ °C), the *t*Bu-groups sharpen, and we were able to identify four moieties via coupling by ^1H COSY NMR spectroscopy. As already stated, **2**^{Cl} is not isolatable, and its yield was therefore determined spectroscopically to be circa 75 %. Since **3**^{Cl} is formed in 85 % yield via reduction at RT, our spectroscopic yield of **2**^{Cl} indicates formation of some additional side products upon performing the reduction at low temperatures (which are observed around 50 ppm, see Figure 10). Rarely, another set of coupling doublets was visible by NMR spectroscopy in low amounts ($\delta^{31}\text{P}\{^1\text{H}\}$ [ppm] = 64.8 (d, $^2J_{\text{PP}} = 225$ Hz), -10.8 (d, $^2J_{\text{PP}} = 225$ Hz)). It will not be discussed here, yet it is briefly addressed in Section II.2.4, where a similar and more persistent compound is found when reducing the bromide analogue. Reduction of **1**^{Cl} under a $^{15}\text{N}_2$ -atmosphere revealed a $^{15}\text{N}\{^1\text{H}\}$ singlet at 211 ppm, alongside the signal of **3**^{Cl} at 369 ppm, which is consistent with a symmetrically bound N₂ (in contrast to a terminal N₂ ligand) (Figure 10). Although this value lies in the typical range for coordinated N₂,¹⁵⁶ it notably differs for the isostructural $[\{\text{MCl}(\text{PNP})\}_2(\mu\text{-N}_2)]$ ($\delta^{15}\text{N} = 69$ ppm (M = Mo), and $\delta^{15}\text{N} = 30$ ppm (M = W)).^{25,66}

The unusual strongly shifted, yet narrow NMR lines as found for **2**^{Cl} are tentatively attributed to an expression of temperature independent paramagnetism (TIP). This arises from mixing of excited states via spin-orbit coupling into a thermally well separated ($\gg k_{\text{B}}T$) ground state. This

phenomenon is well-known for d^4 Re(III) phosphine complexes, i.e. $[\text{ReCl}_3(\text{PMe}_2\text{Ph})_3]$, $[\text{ReCl}_3(\text{PEt}_2\text{Ph})_3]$ ¹⁵⁷ and $[\text{ReCl}_3(\text{HN}(\text{CH}_2\text{CH}_2\text{P}i\text{Pr}_2)_2)]$ or $[\{\text{ReCl}_2(\text{HN}(\text{CH}_2\text{CH}_2\text{P}i\text{Pr}_2)_2)(\mu\text{-N}_2)\}]^{\text{80}}$ of which the latter is isoelectronic to $\mathbf{2}^{\text{Cl}}$. Variable-Temperature (VT-) NMR spectra of $\mathbf{2}^{\text{Cl}}$ between -55 and -5 °C show that most signals are basically temperature independent, supporting the TIP assignment, see Figure A1. Only the ^{31}P NMR resonance at -120 ppm and three ^1H NMR signals of the PNP-ligand backbone shift temperature-dependently ($\Delta\delta > 1.0$ ppm), yet show a linear behaviour when plotted vs. T^{-1} (Curie Plots, Figure A1). The *tert*-butyl signals exhibit significant broadening at lower temperatures, suggesting that additional dynamic processes might be responsible for the temperature dependence of these signals, such as freezing out of bond rotations. It must be stated that the temperature window for this VT-NMR analysis was chosen rather small ($\Delta T = 50$ °C). Unfortunately, its electronic structure cannot be further analysed by SQUID magnetometry due to its limited stability at RT and only 75 % spectroscopic purity.

Due to these spin-orbit coupling effects, DFT is unable to describe $\mathbf{2}^{\text{Cl}}$ properly. Yet, the DFT calculations as performed by Dr. M. Finger could fully reproduce the molecular geometry as found by Dr. F. Wätjen. Within a localised description of the core, the rhenium-centred spin density agrees with a $\text{Re}^{\text{II}}(\text{N}_2)\text{-Re}^{\text{II}}$, or alternative a $\text{Re}^{\text{III}}(\text{N}_2)^{2-}\text{-Re}^{\text{III}}$ formulation. However, oxidation states can be meaningless in case of high covalent metal-ligand multiple bonding, as was addressed in literature for nitrosyl and nitride complexes.¹⁵⁸ A more covalent binding picture of such a $\{\text{MNNM}\}$ -fragment was presented in Section I.1.3. The 14 valence electrons that such a $\{\text{Re}^{\text{III}}(\text{N}_2)\text{-Re}^{\text{III}}\}^{2-}$ fragment offer are distributed over the Re-N-N-Re manifold and non-bonding δ -orbitals, see Scheme 40. The thereof resulting $\delta^4\pi^{10}$ configuration was substantiated by computations.

Such a π^{10} -configuration is associated with the formation of stable, closed-shell nitrides, as discussed in Section I.1.4. From $\mathbf{2}^{\text{Cl}}$, it was calculated that the transition state for splitting into nitrides exhibits a Re-N-N-Re in-plane zig-zag structure. Upon approaching this transition state, the high lying $\sigma\text{ReN}\text{-}\sigma^*\text{NN}\text{-}\sigma\text{ReN}$ gains considerable σReN and $\sigma^*\text{NN}$ character and is gradually stabilised with respect to the π -manifold. Population of this molecular orbital from the $\pi^*\text{ReN}\text{-}\pi\text{NN}\text{-}\pi^*\text{ReN}$ level leads to N-N bond weakening and simultaneous Re-N strengthening, and ultimately N-N cleavage.



Scheme 40. Qualitative MO-scheme representing the $\delta^4\pi^{10}$ configuration of $L_4Re^{II}(N_2)Re^{II}L_4$ (representing **2^{Cl}**), and subsequent N₂-splitting into terminal nitrides. The MO's of the nitride are depicted on the right.

The activation parameters for this process can be obtained via NMR spectroscopic analysis of splitting from **2^{Cl}** into **3^{Cl}**, justified by the observation of **2^{Cl}** in high spectroscopic yields at low temperatures and its selective splitting into **3^{Cl}**. Therefore, we monitored decay of **2^{Cl}** by ¹H NMR spectroscopy at temperatures ranging from -15 to $+7.5$ °C. Plotting this conversion agreed with first-order kinetics over two half-lives; exemplarily conversion traces for each temperature are shown in Figure 11. An Eyring analysis over this temperature range provides activation parameters for N₂-splitting: $\Delta H^\ddagger = 24 \pm 1$ kcal mol⁻¹ and $\Delta S^\ddagger = 14 \pm 3$ cal mol⁻¹ K⁻¹, in agreement with a short lived intermediate at RT. In the context of this in-depth study, Dr. M. Finger performed calculations that reflect the full N₂-splitting mechanism of **1^{Cl}** (*vide infra*).⁷⁰ The computed free energy of activation is higher than the experimental value ($\Delta G^\ddagger_{298K, Cacl.} = +26.9$ kcal mol⁻¹, $\Delta G^\ddagger_{298K, Exp.} = +19.8$ kcal mol⁻¹), but the calculated enthalpy of activation is in excellent agreement with the experiment ($\Delta H^\ddagger_{298K, Cacl.} = +26.2$ kcal mol⁻¹) and only the activation entropy is deviating from the calculated value ($\Delta S^\ddagger_{Cacl.} = -3$ cal mol⁻¹ K⁻¹). The experimental value suggests that formation of the proposed zig-zag transition state is accompanied by an increase in entropy. In contrast, the calculated value describes an entropically neutral process upon splitting via this transition state. These computations are supported by comparison to the activation entropy for N₂-splitting of related compounds [$\{Mo(HPNP)Cl\}_2(\mu-N_2)$], [$\{W(CO)(PNP)\}_2(\mu-N_2)$] by Schneider, or the pioneering example of [$\{Mo(N(CD_3)CH_3)(3,5-C_6H_3(CH_3)_2)\}_3(\mu-N_2)$] by Cummins (ΔS^\ddagger_{exp} [cal mol⁻¹ K⁻¹] = $-5.7, +2.3,$ or $+2.9$, respectively).^{43,66,67} The activation entropy is very sensitive towards the fit of the data,

since it is calculated from the y-intercept. Due to the small temperature range that was examined ($\Delta T = 22.5\text{ }^{\circ}\text{C}$) the experimental value as derived herein should be handled with care.

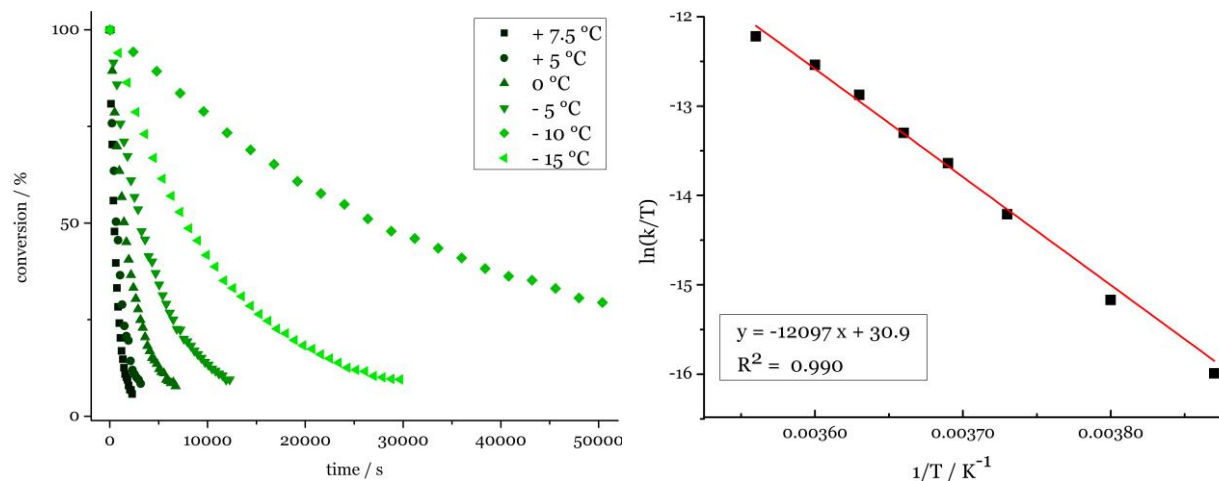


Figure 11. Left: Exemplary conversion plots vs. time. Right: Eyring plot for the conversion of 2^{Cl} to 3^{Cl} in the temperature range from -15 to $+7.5\text{ }^{\circ}\text{C}$.

With 2^{Cl} identified as the intermediate that splits N_2 towards nitride 3^{Cl} , reactions potentially relevant to its assembly were examined, i.e. dinitrogen coordination to 1^{Cl} . Collaboration partners^a examined possible N_2 -coordination by IR spectroscopy. A solution of 1^{Cl} in THF under 1 atm N_2 gave no indication of end-on binding of dinitrogen. In addition, UV-vis spectra under Ar or N_2 are identical, even upon cooling from RT to $-78\text{ }^{\circ}\text{C}$.⁷⁰ In the context of this work, 1^{Cl} was examined by NMR spectroscopy as recorded under Ar or N_2 (4 atm), showing no difference even upon cooling to $-95\text{ }^{\circ}\text{C}$ (see Figures A2). From $-40\text{ }^{\circ}\text{C}$ and lower, broadening, disappearance and splitting of the *t*Bu-moieties is observed, indicating freezing out of the P-C bond rotation and the appearance of the individual methyl resonances. These experiments speak against a pre-equilibrium to form $[\text{ReCl}_2(\text{N}_2)(\text{PNP})]$ and by NMR spectroscopy an upper limit for this N_2 pre-equilibrium to 1^{Cl} can be estimated ($K_{\text{eq}} < 1\text{ M}^{-1}$, see experimental Section IV.6.1). Additionally, potential reactivity of 1^{Cl} with chloride anions is assessed, as it is released during the N_2 -splitting reaction. NMR spectroscopic monitoring of a solution of 1^{Cl} under N_2 in presence of 5 eq. of $(n\text{Bu}_4\text{N})\text{Cl}$ indicate no chloride association over more than 48 h (Figure A3). These coordination studies demonstrate that the initial step most likely consists of reduction of rhenium(III). Therefore, the formation pathway of 2^{Cl} was examined via electrochemical methods.

^a IR and UV-vis spectroscopy performed by Dr. B.M. Lindley, under supervision of Prof. Dr. A.J.M. Miller, University of North Carolina at Chapel Hill.

1.2. Electrochemical N₂-splitting from [ReCl₂(PNP)]

To probe whether N₂-splitting can be driven electrochemically, controlled potential electrolysis (CPE) of **1**^{Cl} was explored in THF at $E_{\text{appl.}} = -1.90$ V vs. Fc^{+ / 0} under 1 atm N₂, based on the CV data for **1**^{Cl} (*vide infra*).^b During CPE for circa 1.5 h, the colour of the solution changed from purple to yellow and 1.2 electrons were transferred per rhenium. Concomitantly, a main oxidative feature is formed at $E_p = 0.00$ V at scan rate (v) = 0.1 Vs⁻¹, which is in proximity to the Re(VI/V) oxidation of **3**^{Cl} at $E_{1/2} = -0.09$ V, see Figure 12.^c Addition of some **3**^{Cl} to this experiment shows an increase of this feature, underlining the formation of nitride via electrochemical reduction (Figure 12). It is noted that in initial electrochemical N₂-splitting attempts no clear evidence for **3**^{Cl} by CV was found. This might be the result of using Pt as CPE working electrode (WE), or only using low Re-complex concentrations. The oxidation of **3**^{Cl} appears irreversible in the CPE set up even when reversing the scan directly after this feature. This is in contrast to the isolated species, which appears reversible. In a control experiment as presented in Figure A4, we mimicked CPE conditions by measuring **3**^{Cl} in presence of chloride ions. Indeed, the Re(VI/V)-reversibility is directly lost upon addition of only 1 eq. of (*n*He₄N)Cl, presumably upon formation of 6-coordinate [ReNCl₂(PNP)]. Further anodic appearing oxidative features are attributed to PNP-ligand oxidation, as especially favoured in presence of a base.

Analysis of the CPE product mixture by ³¹P{¹H} NMR spectroscopy showed formation of **3**^{Cl} in circa 60 % yield, which was reproduced at least three times. Since 1.2 electrons per Re are needed, this corresponds to a faradaic yield of circa 50 %. Analogous reductive CPE of **1**^{Cl} under 1 atm Ar gave an intractable mixture of unidentified products. At the time this work was published (2018), the conversion of **1**^{Cl} to **3**^{Cl} represented the first electrochemical synthesis of a terminal nitride from N₂. The established yield of **3**^{Cl} from CPE is slightly below the yield as found for chemical reduction using Na/Hg (85 %) or Co(Cp*)₂ (75 %). A productive role for chloride abstraction by the chemical reductant (via precipitation of NaCl or [Co(Cp*)₂]Cl in THF) can be envisioned (since it is an elemental reaction step via *K*₄, *vide infra*). This functionality is absent in the case of electrochemical reduction, maybe leading to lower yields. Besides **3**^{Cl}, several diamagnetic compounds are present in low intensity that were not further investigated.

^b All potentials within this work are given versus the Fc^{+ / 0} couple, unless stated otherwise.

^c In the context of this study, the redox potential of **3**^{Cl} was reconsidered in THF using iR-compensation, instead of in DCM as was published ($E_{1/2, \text{publ.}} = -0.13$ V). The reversible oxidation of **3**^{Cl} was found at $E_{1/2} = -0.09$ V.

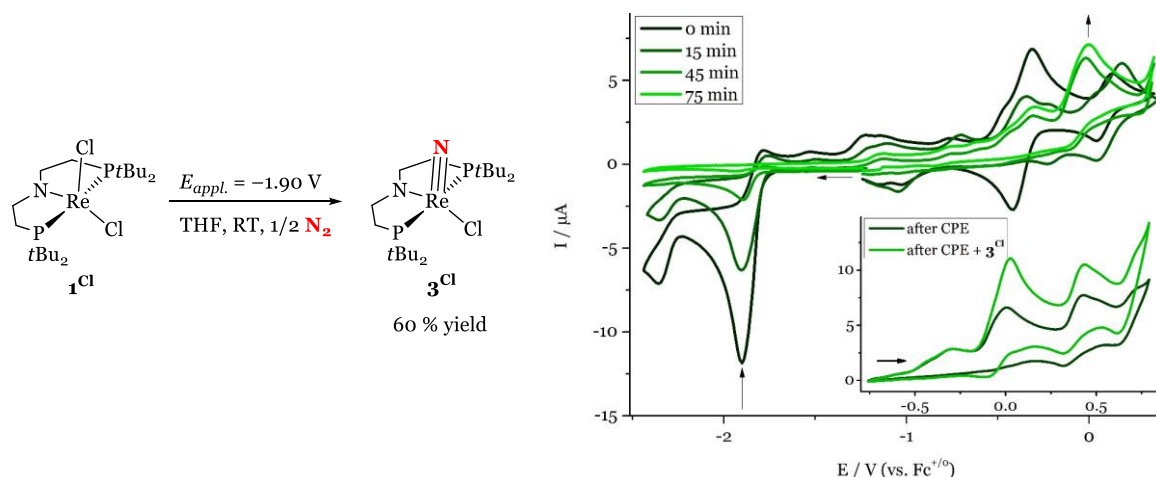


Figure 12. Left: electrochemical N_2 -splitting from **1^{Cl}** into **3^{Cl}** via CPE at $E_{\text{appl.}} = -1.90 \text{ V}$. Right: CVs corresponding to the CPE. Inset: zoom of the oxidative area after CPE and after subsequent addition of **3^{Cl}**.

To probe the build-up of intermediates during electrolysis, N_2 -splitting of **1^{Cl}** was examined by UV-vis spectroelectrochemistry (SEC).^d Electrolysis resulted in conversion of **1^{Cl}** ($\lambda_{\text{max.}} = 530 \text{ nm}$) to a new species with strong absorbance at 384 and 537 nm within 60 seconds, that is not formed when the same experiment is conducted under Ar. This intermediate is assigned as the N_2 -bridged dinuclear **2^{Cl}**, based on the close agreement of the spectral features as experimentally determined via chemical reduction at $-30 \text{ }^\circ\text{C}$ (see Chapter II.1.1) or the TD-DFT computed UV-vis spectrum for **2^{Cl}** (Figure A21, Section II.2.4). The intermediate converts to product **3^{Cl}** ($\lambda_{\text{max.}} = 393 \text{ nm}$). Kinetic data for the N_2 -splitting reaction was obtained by monitoring the decay of **2^{Cl}** in the time period after a minimum in electrolytic current was reached (after approx. 100 s) to avoid significant impact by diffusion and additional formation of **2^{Cl}**. The half-life obtained under these conditions for the conversion of **2^{Cl}** into **3^{Cl}**, $\tau_{1/2} = 28 \text{ s}$ at 298 K, is in close agreement with the rate constant derived from the Eyring analysis of chemical N_2 -splitting of the same reaction ($k_{298\text{K}} = 0.018 \text{ s}^{-1}$, $\tau_{1/2} = 38 \text{ s}$).

This experiment indicates that the same N_2 -bridged intermediate is formed in both chemical and electrochemical reductions and it is the only intermediate that is observed. Its formation must be fast compared to the time scale of UV-vis and NMR spectroscopy. This mechanistic connection and the relatively high Faradaic yield found for **1^{Cl}** offer the possibility of

^d UV-vis SEC was performed by Dr. B.M. Lindley, under supervision of Prof. Dr. A.J.M. Miller. In the context of this work, the here described experiment and kinetics were reproduced to verify our UV-vis SEC set up and discussed in Section II.2.4. The results of the cooperation partners are discussed here, since they are a key rationale for the mechanistic study within this Chapter.

electrochemical examination of a full N₂-splitting sequence. We therefore examined the electrochemistry of **1**^{Cl} by CV in detail in the next Sections.

1.3. CV study of [ReCl₂(PNP)] under Ar

On the pathway from **1**^{Cl} to N₂-bridged **2**^{Cl}, several elementary steps must be involved, i.e. reduction, chloride loss, N₂-coordination, and a reaction forming a dinuclear compound. We therefore turned to CV to gain a deeper understanding of the initial steps of reductive N₂-cleavage. The CV of **1**^{Cl} under Ar was examined first in order to rationalise the redox behaviour of the rhenium platform in absence of N₂.

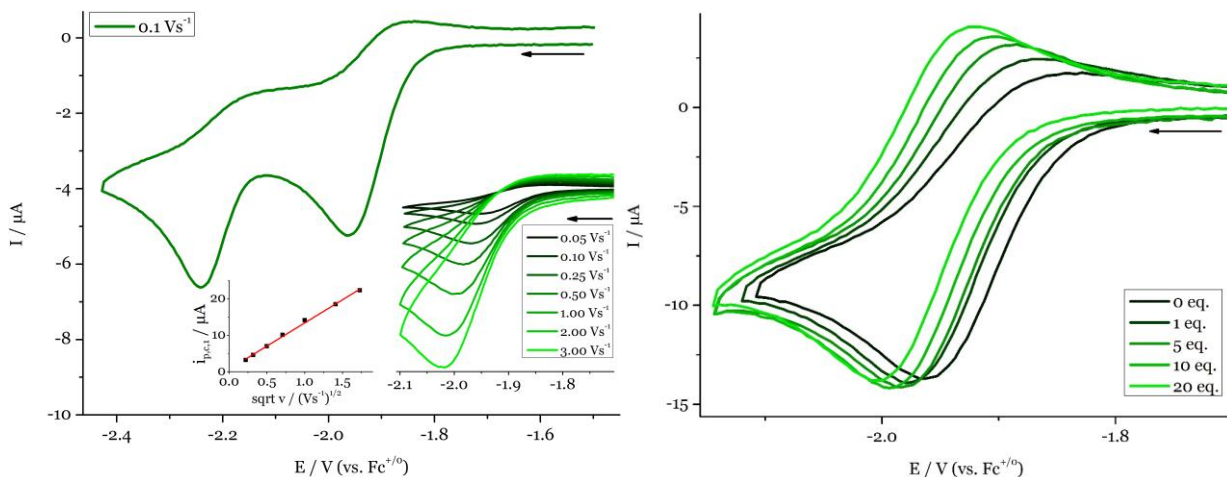
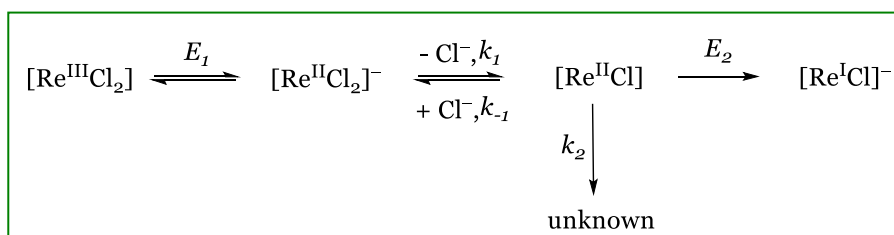


Figure 13. Left: CV of the reductive area of 1.0 mM **1**^{Cl} in THF with 0.2 M (nBu₄N)PF₆, $\nu = 0.1 \text{ Vs}^{-1}$ under Ar. Inset bottom right: ν -dependence of the first reduction. Inset bottom left, plot of $i_{p,c,1}$ vs. $\nu^{1/2}$. Right: CV of the first reduction of 0.8 mM **1**^{Cl} in THF with 0.2 M (nBu₄N)PF₆ in presence of 0-20 eq. of (nBu₄N)Cl under Ar, $\nu = 0.1 \text{ Vs}^{-1}$ (measurement performed on a WE with $A = 0.071 \text{ cm}^2$ instead of the commonly used $A = 0.020 \text{ cm}^2$).

The oxidative features of **1**^{Cl} are discussed in Chapter II.3. The reductive area of **1**^{Cl} under Ar shows two reduction processes at $E_p = -1.96$ and -2.24 V at $\nu = 0.1 \text{ Vs}^{-1}$. A linear relationship between the peak current ($i_{p,c,1}$) vs. $\nu^{1/2}$ indicates that the species that is reduced is freely diffusing in solution, see Figure 13. The first reduction is irreversible, even when scanning to high ν , which is accompanied by a cathodic peak potential shift ($\Delta E_p = 0.04 \text{ V}$ from $\nu = 0.1$ to 3.0 Vs^{-1}). This suggests that the first reduction is coupled to a chemical reaction. Since chloride dissociation is considered a plausible reduction-triggered chemical step, the influence of chloride on the first reduction process was examined. Upon addition of 20 eq. of (nBu₄N)Cl, the first reduction shifts cathodically by circa 0.04 V, accompanied by increased reversibility ($i_{p,c,1}/i_{p,a,1} = 1.8$ at 20 eq. Cl⁻,

$v = 0.1 \text{ Vs}^{-1}$), Figure 13. The second reduction process remains irreversible at all examined scan rates and is essentially unaffected by chloride addition (Figure A6). Varying the concentration of $\mathbf{1}^{\text{Cl}}$ from 0.5 to 4 mM has barely any effect on the overall features of the CV and the peak current ratio remains the same ($i_{p,c,1}/i_{p,c,2} \approx 0.8\text{-}0.9$) (Figure A6). The reversibility of the first peak initially seems to increase, but the peak ratio does not change ($i_{p,c,1}/i_{p,a,1} = 3.1$ ($c_{\text{Cl}^-} = 1.0 \text{ mM}$) and 3.2 ($c_{\text{Cl}^-} = 4.0 \text{ mM}$)).

These observations agree with an *electrochemical-chemical-electrochemical (ECE)* mechanism; initial reduction of $\mathbf{1}^{\text{Cl}}$ forms $[\text{ReCl}_2(\text{PNP})]^-$, which undergoes reversible chloride ligand dissociation forming $[\text{ReCl}(\text{PNP})]$. This species is subsequently reduced at the second reduction feature. The proposed *ECE*-mechanism model was probed by digital simulation of the electrochemical data, which is performed by prof. Dr. I. Siewert. To satisfactory model the peak current of the second-, and the reversibility of the first reduction, unimolecular decay (k_2) of $[\text{ReCl}(\text{PNP})]$ has to be included besides reduction of $[\text{ReCl}_2(\text{PNP})]$ (E_1) and $[\text{ReCl}(\text{PNP})]$ (E_2). Both reductions are connected by reversible chloride dissociation (K_1, k_1) (Scheme 41). The simulation parameters of the best fit are given in Table 3, and overlays of the experimental and simulated CV data can be found as published.⁷⁰



Scheme 41. Minimal mechanistic model of reduction of $\mathbf{1}^{\text{Cl}}$ under Ar. The PNP-pincer ligand is omitted for all species for clarity.

Table 3. Thermodynamic and kinetic parameters of $\mathbf{1}^{\text{Cl}}$ as obtained via simulation of CV data under Ar.^e

$\mathbf{1}^{\text{Cl}} / \text{Ar}$	K_1 / M	k_1 / s ⁻¹	k_2 / s ⁻¹	E_1 / V	E_2 / V
	0.05	$1 \cdot 10^3$	0.11	-2.00	-2.29
				$\alpha_1 = 0.5$	$\alpha_2 = 0.8$
				$k_{s,1} = 0.05 \text{ cm}^2/\text{s}$	$k_{s,2} = 0.05 \text{ cm}^2/\text{s}$

^e Digital Simulation of the CV data was performed by Prof. Dr. I. Siewert.

A sensitivity analysis of these results showed that doubling/halving the rate and equilibrium constants of chloride loss (k_1 and K_1) as extracted from the chloride titration experiments, lead to considerably worse fits. Doubling/halving of k_2 leads to a substantially worse fit for the second reduction peak, which cannot be compensated satisfactorily by changing k_1 .

1.4. CV study of [ReCl₂(PNP)] under N₂ towards a N₂-splitting mechanism

The CV of **1**^{Cl} under 1 atm of N₂ is dramatically different than under Ar, as shown in Figure 14. The first reduction becomes narrow, shifts its peak potential anodically by circa 60 mV to $E_p = -1.90$ V at $\nu = 0.1$ Vs⁻¹, and increases substantially in current, indicative of a multi-electron reduction. The feature that is assigned to the reduction of [ReCl(PNP)] near $E_p = -2.2$ V under Ar is absent under N₂, indicating that N₂-coordination is involved prior to this potential. A new, minor, and irreversible feature is observed at $E_p = -2.36$ V at $\nu = 0.1$ Vs⁻¹.

First, the reduction that is relevant for (electro)chemical N₂-splitting at $E_p = -1.90$ V is examined in depth. Upon increasing the scan rate, the peak potential of this reduction process shifts cathodically, which indicates that coupled chemical reactions follow initial reduction, see Figure 15. This reactivity must involve N₂-coordination. The characteristic reversible Re(VI/V) oxidation of nitride **3**^{Cl} ($E_{1/2} = -0.09$ V) is not observed among the several oxidation features when returning the sweep after this initial reduction, indicating that the nitride is not produced at the electrode in significant quantities within the timescale of CV as measured within this study (Figure 14). This is in line with the relatively slow N₂-splitting constant as derived for **2**^{Cl} in Section II.1. Furthermore, the onset of a reverse wave is visible from $\nu = 0.25$ Vs⁻¹ and onwards, leading to an $i_{p,c,1}/i_{p,a,1} = 2.6$ at $\nu = 1.5$ Vs⁻¹ (Figure 15). This reversibility onset is in contrast to the data under Ar, where the [ReCl₂(PNP)]^{0/-} reduction coupled to chloride loss showed no reversibility. Either this reduction is coupled to reversible chemical reactions when measuring under N₂, or the subsequent electron transfers that occur within this multi-electron feature display some reversibility.

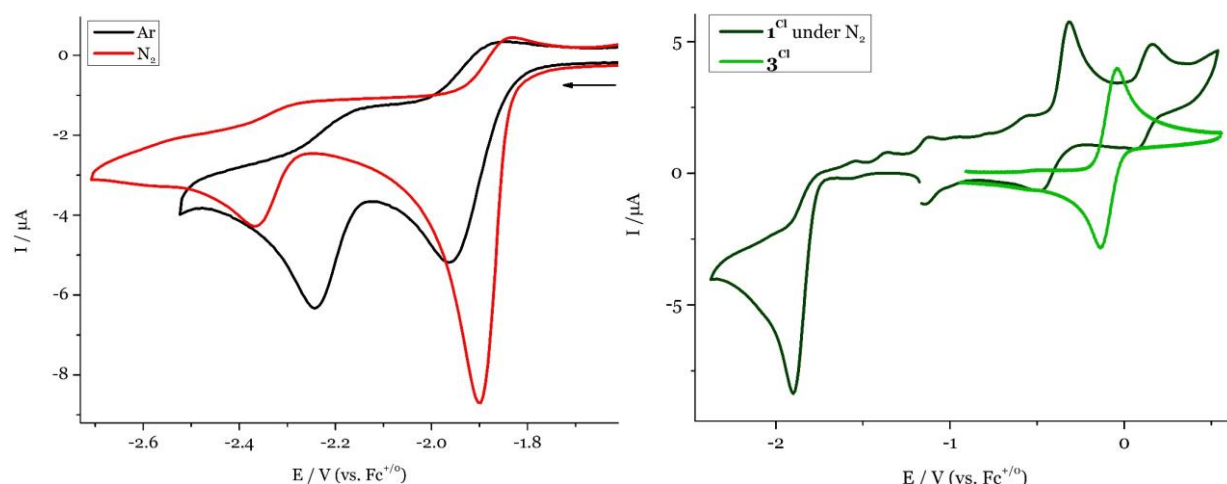


Figure 14. Left: CV data of 1.0 mM $\mathbf{1}^{\text{Cl}}$ in THF with 0.2 M $(n\text{Bu}_4\text{N})\text{PF}_6$ under 1 atm N_2 (red), and Ar (black), $\nu = 0.1 \text{ Vs}^{-1}$. Right: comparison of the whole spectrum of 1.0 mM of $\mathbf{1}^{\text{Cl}}$ with 1.0 mM of $\mathbf{3}^{\text{Cl}}$, both in THF with 0.2 M $(n\text{Bu}_4\text{N})\text{PF}_6$ at $\nu = 0.1 \text{ Vs}^{-1}$.

Titration of $\mathbf{1}^{\text{Cl}}$ with chloride ions leads to a cathodic shift of the peak potential of the initial reduction of $\mathbf{1}^{\text{Cl}}$, which is circa 0.04 V upon addition of 20 eq. of $(n\text{Bu}_4\text{N})\text{Cl}$, similar to the CV under Ar. The ratio of cathodic and anodic peak currents increases and is 2.8 at $\nu = 0.1 \text{ Vs}^{-1}$. To probe for coupled reactivity with N_2 , electrochemistry of $\mathbf{1}^{\text{Cl}}$ was measured in an autoclave with electrochemical feedthroughs (see Experimental Section IV.4.1 for details). The N_2 -pressure, and thereby the N_2 -concentration (according Henry's Law), was increased from atmospheric pressure to 11 bars in intervals of 2 bars, which has minimal changes on the first reduction feature. The peak potential is constant (within an experimental error of 0.01 V), and the current increases by circa 10% and plateaus after 7 bars and upwards. Note that the absolute potential is off by 0.03 V ($E_{p,\text{autoclave}} = -1.93 \text{ V}$, $\nu = 0.1 \text{ Vs}^{-1}$). This was also found in control experiments with both Fc and Fc^* : the difference in their potential is larger than the literature value ($\Delta E_{\text{Fc}-\text{Fc}^*,\text{autoclave}} = 0.455$, $\Delta E_{\text{Fc}-\text{Fc}^*,\text{lit}} = 0.427 \text{ V}$), and we emphasise the trends more than the absolute potential values. Depressurising the system reverses the current increase to most extend, see Figure A7. Upon increasing the Re-concentration from 0.5 to 4.0 mM of $\mathbf{1}^{\text{Cl}}$, no peak potential changes are observed.

The current of the smaller reduction feature at $E_p = -2.36 \text{ V}$ decreases upon increasing the scan rate and then disappears altogether from $\nu = 1.5 \text{ Vs}^{-1}$ onwards. Upon increasing the N_2 -pressure, this feature gets less prominent. Both observations could indicate that this cathodic wave belongs to the reduction of $\mathbf{2}^{\text{Cl}}$: The ν -dependency indicates that this species is more prominent at lower scan rates, allowing time for a dimerization reaction. The N_2 -pressure dependency could be explained by the coordination of several N_2 -ligands to a reduced monomer blocking all

coordination sites and thereby preventing dimerization. A more extended discussion following this hypothesis for **2^X** (X = Cl, Br, and I) is in Section II.2.8.

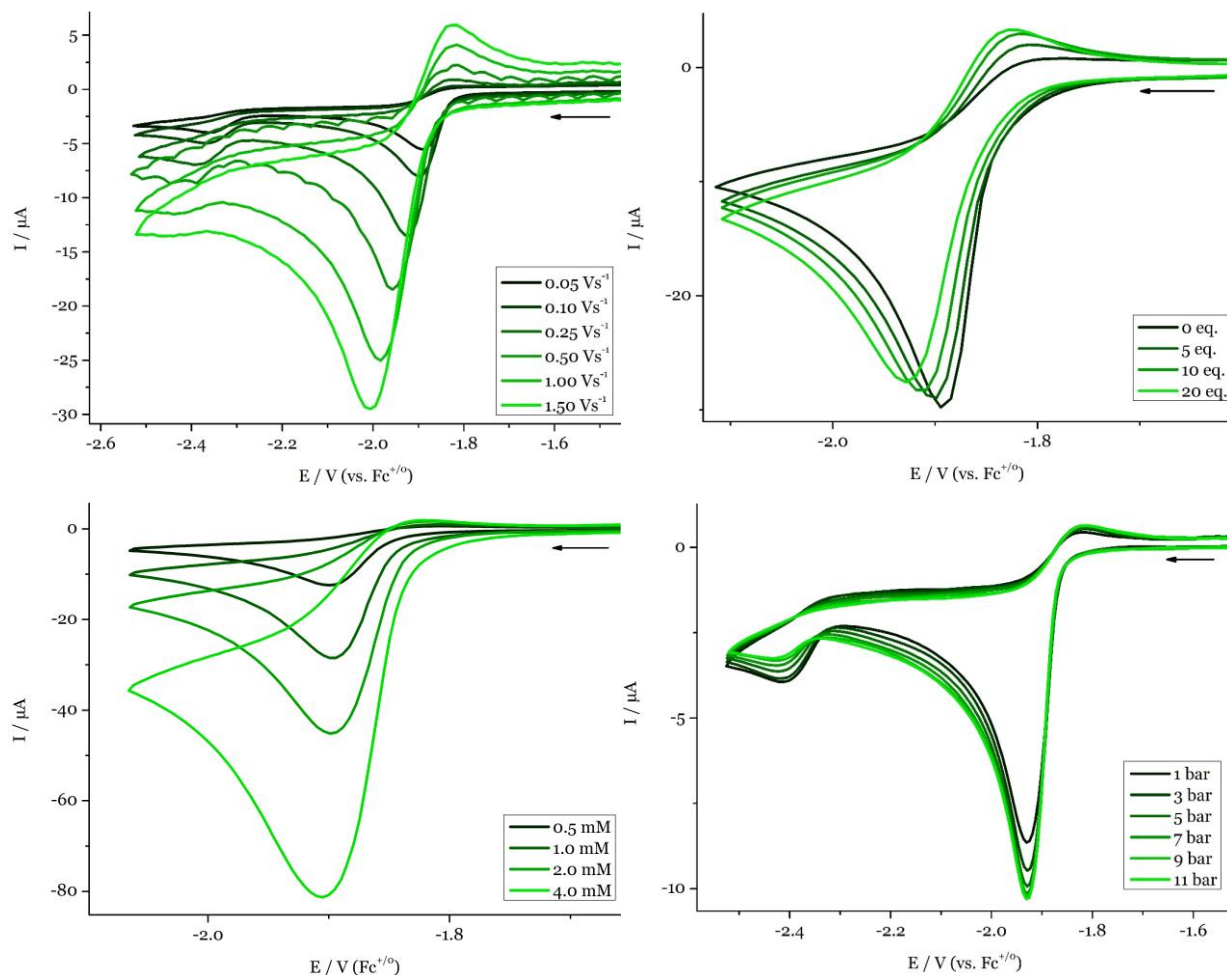
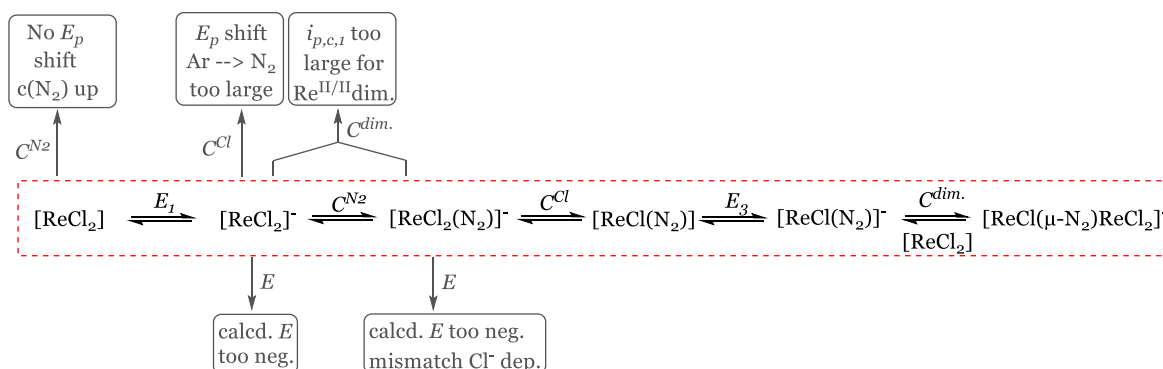


Figure 15. CV of **1^{Cl}** in THF with 0.2 M (*n*Bu₄N)PF₆ under N₂. Top left: v -dep on a 1 mM solution of **1^{Cl}**. Top right: Cl⁻ dependence of a 1.0 mM solution of **1^{Cl}**, $v = 0.1$ Vs⁻¹, from 0-20 eq. (measurement performed on a WE with $A = 0.071$ cm² instead of the commonly used $A = 0.020$ cm²). Bottom left: concentration dependence of the first reduction feature of **1^{Cl}**, $v = 0.1$ Vs⁻¹, from 0.5 to 4.0 mM. Bottom right: N₂-pressure dependence of a 1.0 mM solution of **1^{Cl}**, $v = 0.1$ Vs⁻¹, from 1-11 bars.

In order to construct a mechanism from **1^{Cl}** into **3^{Cl}**, we first consider the elemental steps that have to occur during this reaction, which include reduction (E), chloride loss (C^{Cl}), N₂-coordination (C^{N_2}), and dimerization ($C^{dim.}$). From the experiments, we can summarise the following trends that provide the guidelines for the digital simulation of the CVs. When measuring CV of **1^{Cl}** under N₂, the initial, for electrochemical N₂-splitting relevant reduction of **1^{Cl}** has a multi-electron character and is clearly coupled to both N₂ coordination and chloride loss. No clear hint for the dimerization reaction is observed, besides that any influence of a

bimolecular reaction is minimal on the first reduction. Based on these trends and the basic *ECE*-mechanism for reduction of $\mathbf{1}^{\text{Cl}}$ under Ar, we considered several pathways to form $\mathbf{2}^{\text{Cl}}$ from $\mathbf{1}^{\text{Cl}}$. Their plausibility is mainly judged by digital simulation as performed by Prof. Dr. I. Siewert. A main goal was to minimise the fitting parameters to prevent over-parametrisation. The multielectron character of this first reduction wave is explained by one Re-fragment which is rapidly reduced twice to a Re(I) species, prior to formation of a dinuclear compound with a parent $\mathbf{1}^{\text{Cl}}$. Alternative pathways involving $\text{Re}^{\text{II}}/\text{Re}^{\text{II-}}$ or mixed-valent $\text{Re}^{\text{II}}/\text{Re}^{\text{III}}$ dimerization would give rise to lower current of this first wave, as was found by digital simulation. Therefore, $C^{\text{dim.}}$ is taken to be the last step of the reaction sequence, see Scheme 42. Several pathways could be envisioned that start with C^{N_2} prior to reduction. These pathways are unlikely due to the lack of NMR, UV-vis and IR spectroscopic evidence for a pre-equilibrium with N_2 (see Section II.1.1), and could be excluded by the simulations using the experimentally estimated upper limit of a pre-coordination equilibrium ($K_{\text{eq}} < 1 \text{ M}^{-1}$). The most important criterion for excluding these possible pathways was the experimentally found absence of a peak potential shift upon increasing the N_2 -pressure; any mechanism starting with C^{N_2} is simulated to have a dramatic shift of the peak potential with increasing N_2 -pressure.



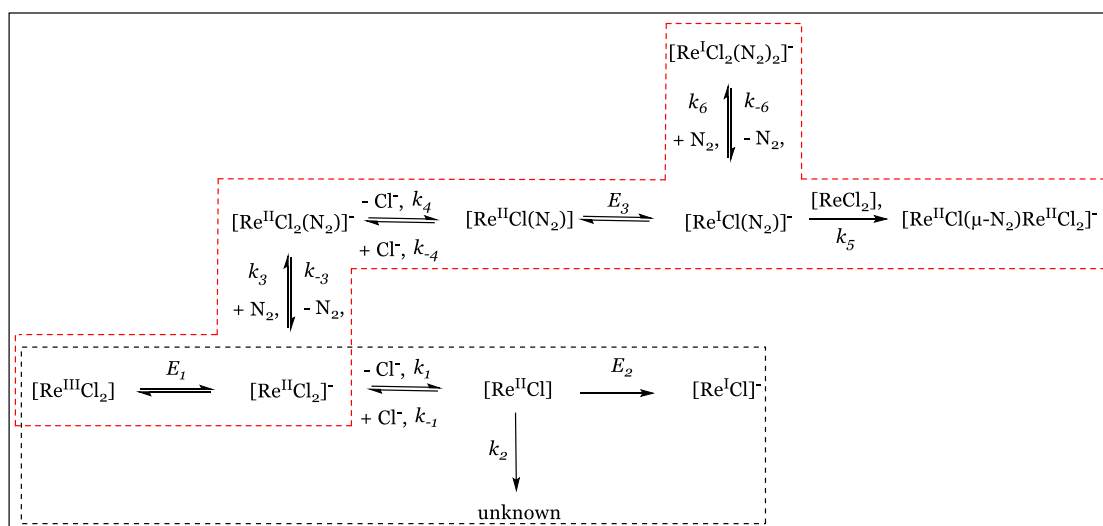
Scheme 42. Flowchart for the determination of the minimally occurring N_2 -splitting mechanism including a brief description of the experimentally found or calculated criteria based on which alternative pathways (in grey) were discarded.

Subsequently considered pathways all involve reduction of $\mathbf{1}^{\text{Cl}}$ as initial reaction step (E_1), followed by various sequences of C^{N_2} , C^{Cl} and the required second reduction E . The possibility that the second reduction directly follows E_1 is immediately discarded based on the Ar data and the calculated reduction potential of $[\text{ReCl}_2(\text{PNP})]^-$, which is way too negative ($E_{1/2} = -4.0 \text{ V}$).⁷⁰ Any mechanism including C^{Cl} after initial reduction following an $EC^{\text{Cl}} \cdots$ -pathway would follow the reduction and kinetic of chloride loss just as observed under argon. Yet, the large anodic peak potential shift when measuring under N_2 instead of Ar seem unrealistic when the initial two elemental steps are identical. Indeed, even with diffusion-controlled N_2 -binding, the simulation

could not account for the peak potential shift observed under N₂. For the remaining scenario, where initial reduction is coupled to C^{N₂}, either EC^{N₂}EC^{Cl}EC^{dim.} or EC^{N₂}C^{Cl}EC^{dim.} is possible. The first scenario features the reduction of the product of reduction of **1**^{Cl} followed by N₂-binding: [ReCl₂(N₂)(PNP)]⁻. Not only is this reduction potential calculated to be more negative ($E_{1/2} = -3.3$ V),⁷⁰ the chloride dependency of the current could not adequately be simulated via this pathway. This brings us to an EC^{N₂}C^{Cl}EC^{dim.}-pathway to form **2**^{Cl} from **1**^{Cl}, which allowed to simulate all CV trends in a satisfactory manner. This pathway will be discussed extensively in the next Section.

1.5. Discussion of the N₂-splitting mechanism

The minimal scenario that could adequately simulate the CV data is the EC^{N₂}C^{Cl}EC^{dim.}-pathway, as presented in Scheme 43. Reduction of **1**^{Cl} is followed by N₂-binding to form [ReCl₂(N₂)(PNP)]⁻. This Re(II) species undergoes chloride loss to neutral [ReCl(N₂)(PNP)], which is reduced once more and ultimately comproportionates with parent **1**^{Cl}. Subsequent or simultaneous chloride loss would form the N₂-bridged **2**^{Cl}, but for simplicity, this process was not included in the simulations. All steps will be discussed extensively in this Section. The only trend that is not accounted for within this model is the rising current of the first reduction of **1**^{Cl} upon increasing the N₂-pressure. The conversion of [Re^ICl(N₂)(PNP)]⁻ to bis-dinitrogen complex [Re^ICl(N₂)₂(PNP)]⁻ through an additional N₂-binding equilibrium can account for this observation, as indicated with K_6 and k_6 in Scheme 43. Formation of such a Re(I) might inhibit dimerization to **2**^{Cl}, thereby preventing the depletion of **1**^{Cl} in the diffusion layer, which results in higher currents at higher N₂-pressure. This additional step can be included in the model leaving the simulations for ambient pressures virtually unchanged.



Scheme 43. Minimal mechanistic model for the simulation of the CV data of 1^{Cl} under Argon (black box), or N_2 (red box). The PNP-ligand is omitted for clarity.

The simulation parameters were chosen to maintain the parameters from the Ar data (K_1 , k_2 , E_1 , E_2), and to minimise the number of variables in the simulations. The numerical ranges of the fit parameters under N_2 (E_3 , k_3 , K_3 , k_4 , K_4 , k_5 , k_6 , K_6) are presented in Table 4. The simulated and experimental CV data are in good agreement over a wide scan rate and chloride ion concentration range. In addition, this pathway (and its alternatives) was calculated by DFT, showing a reasonable agreement. In general, the values are less well defined compared to the EC^ClE -mechanism under Ar, and are therefore mostly given as range or lower limits in Table 4. The N_2 -coordination equilibrium (K_3) and subsequent chloride loss (k_4) interdepend to a certain extent; a lower k_4 is partially compensated by a larger K_3 . The potential value E_3 is less well defined by the simulation, since changes of ± 0.02 V do not change the simulation quality significantly.

Table 4. Thermodynamic and kinetic parameter ranges for the reduction of 1^{Cl} presented in Scheme 43 as obtained via simulation of CV data under N_2 . Values in parentheses are used for the simulation as depicted in Figure 16.^f

$1^{Cl} / N_2$	K_3 / M^{-1}	k_3 / $M^{-1}s^{-1}$	K_4 / M	k_4 / s^{-1}	k_5 / $M^{-1}s^{-1}$	K_6 / M^{-1}	k_6 / $M^{-1}s^{-1}$	E_3 / V
	$5 \cdot 10^3 - 1 \cdot 10^4$	$> 5 \cdot 10^7$	$2 \cdot 10^{-2} - 2 \cdot 10^{-3}$	$> 5 \cdot 10^2$	$4 \cdot 10^3 - 1 \cdot 10^4$	$1 \cdot 10^3$	$5 \cdot 10^1$	$-1.84 - -1.88$
	($1 \cdot 10^4$)	($5 \cdot 10^9$)	($5 \cdot 10^{-3}$)	($1 \cdot 10^5$)	($7 \cdot 10^3$)			(-1.86) ($\alpha_3 = 0.3$) ($k_{s,3} = 0.01$ cm ² /s)

^f Digital Simulation of the CV data was performed by Prof. Dr. I. Siewert.

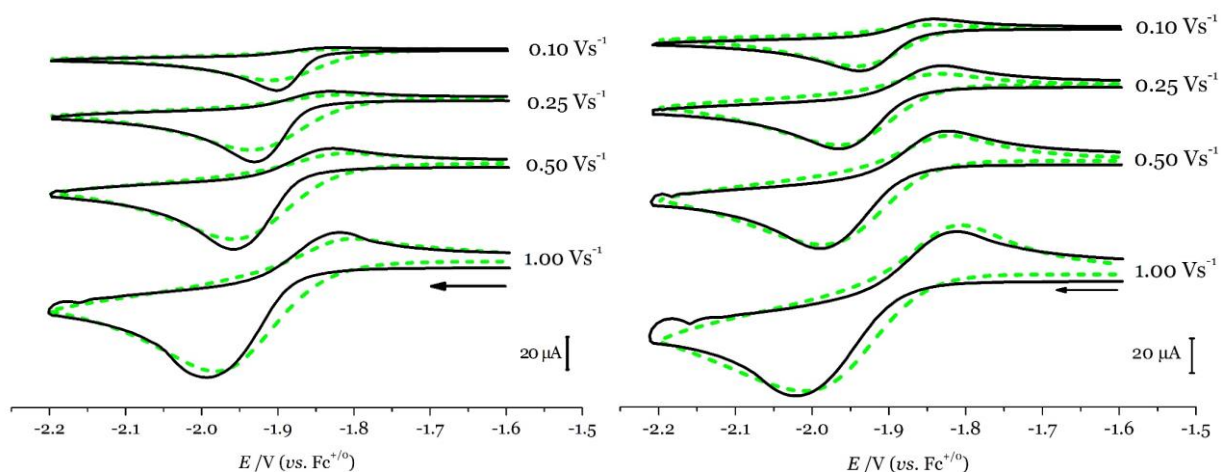


Figure 16. Overlay of experimental (black solid lines) and simulated (green dashed lines) CV data for **1**^{Cl} under N₂ in THF with 0.2 M (nBu₄N)PF₆. Simulation according to Scheme 43 (without K₆), with the thermodynamic and kinetic parameters given in Table 4. Left: 1.0 mM **1**^{Cl}. Right: **1**^{Cl} in presence of 20 eq. of (nBu₄N)Cl.

The initial reaction is reduction of **1**^{Cl} at E_1 , as also present under Ar. By DFT computations, only small structural changes are found within the [ReCl₂(PNP)]^{0/-} couple, which is in line with an electrochemical reversible electron transfer. Upon reduction, this anionic platform is now capable of N₂-coordination, which is both thermodynamically favourable ($K_3 \approx 10^4 \text{ M}^{-1}$) as kinetically very rapid ($k_3 > 5 \cdot 10^7 \text{ M}^{-1}\text{s}^{-1}$). This is in sharp contrast to the unobserved binding of dinitrogen to the Re(III) starting platform ($K_{eq} < 1.0 \text{ M}^{-1}$). This increased affinity for the π -accepting ligand N₂ is anticipated for the more electron rich, anionic Re(II) complex. Similar trends are well known and were quantified by Peters and Mock (Figure 17). Peters found an increase in N₂-binding affinity by six orders of magnitude upon reduction of a low-valent bimetallic iron complex.¹⁵⁹ Their rate of N₂-binding ($k_{N_2} = 3 \cdot 10^6 \text{ M}^{-1}\text{s}^{-1}$) is in the similar range as found for [ReCl₂(PNP)]⁻. In addition, the group of Mock established a N₂-coordination series including three oxidation states, where the equilibrium constant is improved by the order of 27 upon reduction of Fe^{II} to Fe⁰.¹⁶⁰

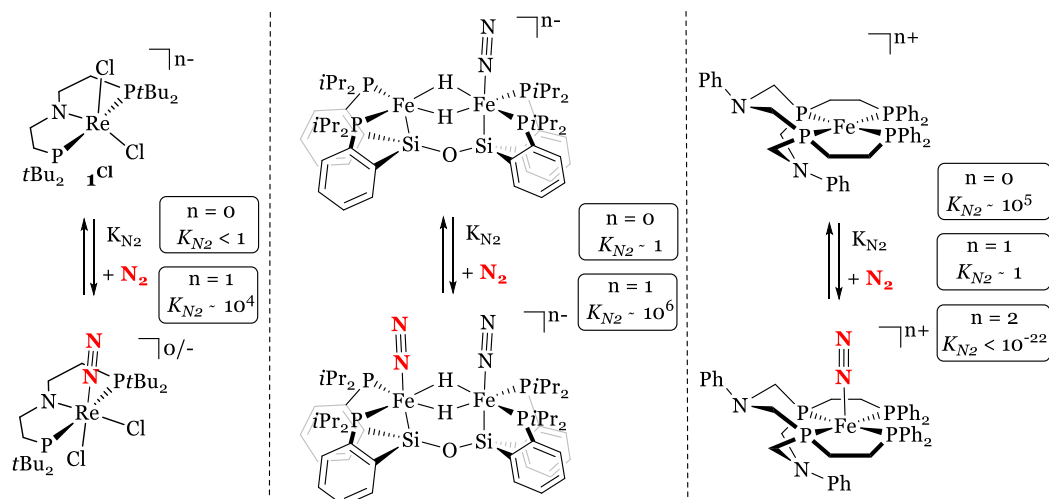


Figure 17. Increasing N_2 -affinity upon reduction as shown within this work on $\mathbf{1}^{Cl}$ (left), and examples on Fe from the group of Peters (middle) and Mock (right).^{159,160} All equilibrium constants are in M^{-1} .

This model reveals two key findings about N_2 -coordination: it occurs on the *formal Re(II) oxidation state*, and *before chloride dissociation*. Rapid N_2 -binding to Re(II) is a prerequisite to avoid the unimolecular decay after chloride loss as described by k_2 . Our bulky pincer ligand, which enforces a five-coordinate geometry of $\mathbf{1}^{Cl}$, might be instrumental here for productive N_2 -activation: no ligand has to detach before N_2 -coordination can occur at a generally unstable Re(II) oxidation state.

Subsequently, the six-coordinate anionic species $[ReCl_2(N_2)(PNP)]^-$ undergoes chloride loss, which is thermodynamically not favoured ($K_4 \approx 10^{-2} M$), but rapid ($k_4 > 5 \cdot 10^2 s^{-1}$). The rate is comparable or larger to chloride dissociation from $[ReCl_2(PNP)]^-$ under Ar ($k_1 = 1 \cdot 10^3 s^{-1}$), and considerably faster than chloride loss from $[ReCl_3(PMe_2Ph)_3]^-$, as reported with $k = 0.9 s^{-1}$, or from $[ReCl_3(dppe)(PPh_3)]^-$, as reported with $k \approx 1 s^{-1}$.^{161,162} Chloride dissociation for our complexes is likely facilitated by the bulky *tert*-butyl moieties and the strong amide π -donating ability of the PNP-ligand. Especially the influence of the latter should not be underestimated. For instance, the $Re^{III/II}$ reductions of $[ReCl_3(HPNP^{iPr})]$ and $[ReCl_3(PON_{py}OP)]$ ($PON_{py}OP = 2,6-(OPiPr)_2NC_5H_3$) with dramatically decreased N_{pincer} to Re electron-donation, appear reversible.^{80,84} Chemical reduction of the latter even afforded the stable rhenate $[ReCl_3(PON_{py}OP)]^-$ complex, showcasing the decreased preference for chloride loss.⁸⁴ The result of these two reaction steps is an associative substitution to form the five-coordinate $[ReCl(N_2)(PNP)]$.

Due to this overall associative ligand-exchange from a π -donating chloride- to a π -accepting dinitrogen ligand, the resulting complex can be reduced once more at a slightly milder potential compared to $\mathbf{1}^{\text{Cl}}$ ($E_3 = -1.86$ V). This *potential inversion* leads to the characteristic narrow, multi-electron reduction wave for $\mathbf{1}^{\text{Cl}}$ under N₂ and could also be backed up by the respective calculated potentials ($E_{1,\text{calc.}} = -2.08$ V, $E_{3,\text{calc.}} = -2.02$ V).⁷⁰ This subsequent reduction to the more stable Re(I) state, likely prevents decomposition at the Re(II) state (as also found within this work as expressed with k_2). An even larger *potential inversion* was found for [ReCl₂(dppe)₂]⁺, which is reduced in DMF at $E_{1/2} = -0.70$ V.¹⁶³ The dinitrogen bound species [ReCl(N₂)(dppe)₂] is reversible oxidised at $E_{1/2} = -0.29$ V in THF, corresponding to the Re^{II/I} reduction.¹⁶⁴ Despite the formal lower oxidation state of the latter, it is reduced at substantially more positive potential. The onset of reversibility that is found for the first reduction feature of $\mathbf{1}^{\text{Cl}}$ under N₂ upon increasing ν is assigned to this [ReCl(N₂)(PNP)]^{o/-} couple, since the initial reduction within this wave ([ReCl₂(PNP)]^{o/-}) coupled to chloride loss remains irreversible as was shown when measuring the ν -dependency under Ar.

Formation of $\mathbf{2}^{\text{Cl}}$ requires a bimolecular reaction step. Since the overall transformation from $\mathbf{1}^{\text{Cl}}$ into $\mathbf{2}^{\text{Cl}}$ required one electron per rhenium, and Re(II) is easily reduced to Re(I), the proposal involves comproportionation of Re(III) and Re(I) by reaction of $\mathbf{1}^{\text{Cl}}$ with [ReCl(N₂)(PNP)]⁻. These two species can react as the anionic Re(I) complex diffuses away from the electrode and $\mathbf{1}^{\text{Cl}}$ (which concentration is at that point depleted at the electrode surface) diffuses towards the electrode, and is simulated as an irreversible reaction with $k_5 \approx 7 \cdot 10^3$ M⁻¹ s⁻¹. At this point, it should be stated that during CPE the solution is stirred in contrast to unstirred CV measurements. In such a situation, the mechanic force dominates the mass transport, analogous to i.e. applying a rotating disc electrode. Indeed, the stirred CV using the stirrers as used for CPE shows a plateau current, indicating a concentration profile that reaches a steady state. Still, the existence of a diffusion layer justifies the described reactivity. The result of this coupling reaction is [{ReCl(PNP)}{ReCl₂(PNP)}(μ -N₂)]⁻, which is the chloride adduct of $\mathbf{2}^{\text{Cl}}$. To prevent over-parameterisation, the required chloride loss was not accompanied in the simulations, since no information about this reaction is obtained via CV. DFT calculations suggest that the combined dimerization and chloride dissociation is strongly exergonic ($\Delta G^\circ_{\text{calc.}} = -12.0$ kcal mol⁻¹).

Accordingly, at least five steps occur during the sweep of a CV to form N₂-bridged intermediate $\mathbf{2}^{\text{Cl}}$ from molecular N₂. After establishing this pathway, we can discuss the by DFT calculated

degree of N₂-activation along the pathway, see Table 1 for reference values.[§] N₂-coordination to form [ReCl₂(N₂)(PNP)]⁻ is accompanied by moderate N-N bond activation as reflected in a calculated stretching frequency of 1975 cm⁻¹. The hypothetical Re(III) congener of this species is calculated at 2105 cm⁻¹. Subsequent chloride loss and reduction to [ReCl(N₂)(PNP)]⁻ is accompanied by a slight bathochromic shift to 1935 cm⁻¹ and some electron density accumulation on the terminal nitrogen atom. However, due this moderate degree of activation, this species is still best described as Re^I-(N₂) as opposed to a Re^{III}-(N₂)²⁻ diazenido complex. Upon dimerization into **2^{Cl}** the N-N bond distance (1.20 Å (DFT), and 1.202(10) Å (XRD)) and the calculated stretching frequency (1771 cm⁻¹) range between typical values for a moderately activated N₂-ligand and a diazenido (N₂)²⁻-bridge.¹⁶ Considerable N₂-activation is first obtained upon dimerization to **2^{Cl}**, thereby avoiding unfavourable one-electron reduction of N₂.¹⁶⁵

[§] DFT calculations performed by Dr. M. Finger

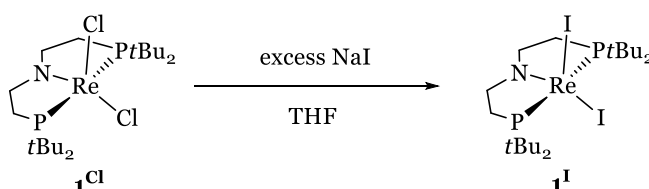
II.2: Influence of halide substitution on N₂-splitting

Parts of this Chapter are published in: '(Elektro-)chemische N₂-spaltung an einem Rhenium-PNP-Pinzetten-Komplex', P.A. Wieser, **2018**, Bachelorthesis, Georg-August-Universität Göttingen.

2.1. Synthesis of the bromide and iodide starting platforms

In Chapter II.1, we activated N₂ by means of electrochemistry starting from [ReCl₂(PNP)] (**1**^{Cl}) and performed an extensive mechanistic study accounting for all minimal occurring reaction steps to form [ReNCl(PNP)] (**3**^{Cl}). In this Chapter, the platform is extended by changing the halide ligands to bromide and iodide to examine if and how their different properties influence the (electro)chemical N₂-splitting performance and to substantiate or expand our understanding of the corresponding mechanism.

Access to the iodide-substituted analogue of **1**^{Cl} was established in our group via salt metathesis, which is a well-known strategy to exchange halogen substituents. Fergusson and Hevelt for instance showed the exchange of chloride to bromide or iodide in [ReOCl₃(Et₃P)₂], by reacting it with LiBr or NaI, respectively.¹⁶⁶ Analogous, Dr. J. Abbenseth reacted **1**^{Cl} with an excess of NaI, upon which halogen-substitution readily occurs, see Scheme 14. Repetitive extractions with benzene afford [ReI₂(PNP)] (**1**^I) in 90 % yield.¹⁶⁷ In a slightly modified procedure used herein, the second benzene extraction is performed over Celite, yielding **1**^I in circa 85 %.



Scheme 14. Synthesis of **1**^I via salt-metathesis starting from **1**^{Cl}.¹⁶⁸

The bromide congener [ReBr₂(PNP)] (**1**^{Br}) was not reported before, and its synthesis was attempted by the same halogen exchange strategy. No reactivity was however observed upon reacting **1**^{Cl} with NaBr. Changing to more soluble LiBr resulted in full conversion, with concomitant formation of two species according to two new singlets in ³¹P{¹H} NMR spectroscopy at –81 ppm and –110 ppm (**1**^{BrCl} and **1**^{Br} respectively, *vide infra*).

Unfortunately, independent of the equivalents of added LiBr, no product was formed selectively. Therefore, halogen exchange to access $\mathbf{1}^{\text{Br}}$ was discarded, and we attempted a synthesis pathway similar to synthesis of $\mathbf{1}^{\text{Cl}}$.

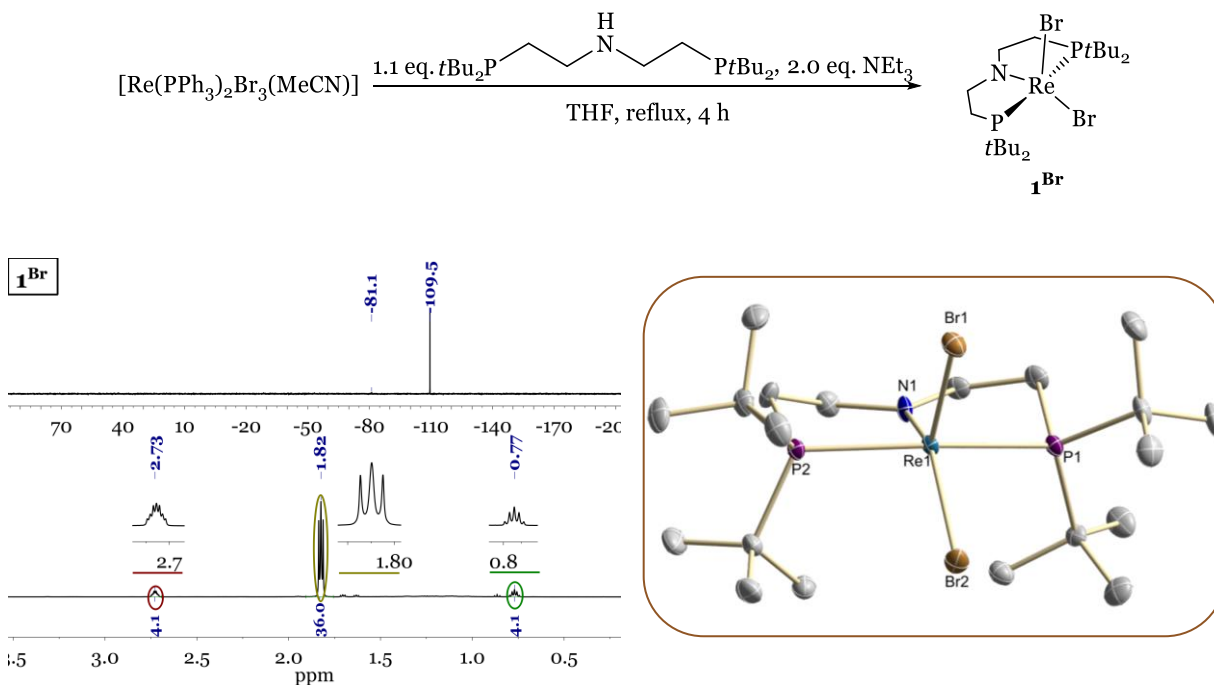


Figure 18. Top: Synthesis of $\mathbf{1}^{\text{Br}}$. Bottom left: NMR spectroscopy of $\mathbf{1}^{\text{Br}}$: $^{31}\text{P}\{^1\text{H}\}$ NMR spectrum (top), and ^1H NMR spectrum (bottom). Bottom right: Molecular structure of $\mathbf{1}^{\text{Br}}$: ORTEP plot with anisotropic displacement parameters drawn at the 50% probability level. Hydrogen atoms omitted for clarity. Selected bond lengths (Å) and angles (deg.): Re-Br1: 2.4635(5), Re-Br2: 2.5123(5), Re-N1: 1.917(4), Re-P1: 2.4109(11), Re-P2: 2.4111(12), P2-Re-P1: 162.30(4), Br1-Re-Br2: 102.301(17), N1-Re-Br2: 144.04(12).

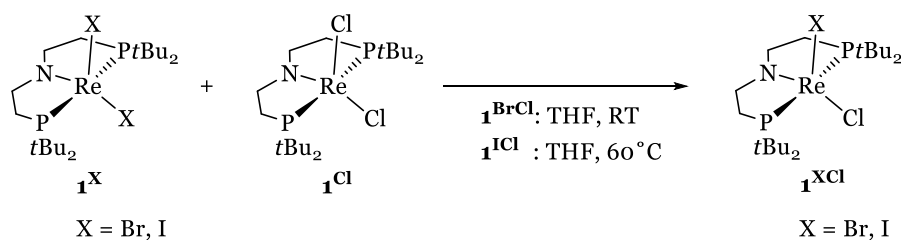
The rhenium(III)-precursor $[\text{Re}(\text{PPh}_3)_2\text{Br}_3(\text{MeCN})]$ ^{169,170} reacts with the PNP-ligand in presence of base, resulting in a colour change from orange to dark brown (Figure 18). The corresponding $^{31}\text{P}\{^1\text{H}\}$ NMR spectrum shows a main feature at -110 ppm and three signals by ^1H NMR spectroscopy that integrate 36:4:4, indicating a C_{2v} -symmetric species. After work up, a brown solid is obtained and LIFDI mass spectroscopic analysis confirms successful synthesis of $\mathbf{1}^{\text{Br}}$. By layering a benzene solution with pentane, single crystals suitable for X-ray spectroscopy of $\mathbf{1}^{\text{Br}}$ were obtained (Figure 18). $\mathbf{1}^{\text{Br}}$ has a short PNP $\text{N}_{\text{amide}}\text{-Re}$ distance of 1.917(4) Å and a pyramidalised N_{amide} ($\sum_{\text{bond angles}} = 359.8^\circ$), indicating strong $\text{N} \rightarrow \text{Re}$ π -donation, analogous to its chloride and iodide congeners (N-Re [Å] = 1.923(7) ($\mathbf{1}^{\text{Cl}}$), 1.926(2) ($\mathbf{1}^{\text{I}}$)).^{69,167} A τ_5 -value of 0.30 indicates distortion from both trigonal bipyramidal and square pyramidal geometry.¹⁷¹ Comparing the molecular structures of $\mathbf{1}^{\text{X}}$ (X = Cl, Br, or I), we observe a trend towards a square pyramidal geometry being a better description going to the heavier halide homologues based on the τ_5 -values ($\tau_5 = 0.37$ ($\mathbf{1}^{\text{Cl}}$), 0.18 ($\mathbf{1}^{\text{I}}$)). This is tentatively attributed to the increased atomic

radius down the halogen group: in a square pyramidal geometry, steric hindrance is minimised by increasing the distance between the *t*Bu-groups and the halogen atoms.

Both $^{31}\text{P}\{\text{H}\}$ and ^1H NMR shifts are unusual for a diamagnetic complex, and this observation is attributed to TIP, as proposed for several Re(III)-species (Section II.1.1). SQUID magnetometry was performed on $\mathbf{1}^{\text{Cl}}$ and $\mathbf{1}^{\text{I}}$, revealing TIP with molar susceptibilities of $282.6 \cdot 10^{-6} \text{ cm}^3 \text{ mol}^{-1}$ ($\mathbf{1}^{\text{Cl}}$) and $248.4 \cdot 10^{-6} \text{ cm}^3 \text{ mol}^{-1}$ ($\mathbf{1}^{\text{I}}$).¹⁶⁸ Although no SQUID magnetometry was measured for $\mathbf{1}^{\text{Br}}$, it is expected to possess similar values.

Although $\mathbf{1}^{\text{Br}}$ is synthesised analytically pure according to combustion analysis, we observe a C_s -symmetric impurity at $\delta_{^{31}\text{P}\{\text{H}\}} = -81 \text{ ppm}$ in about 2-5 %. Strikingly, its NMR features are precisely in between $\mathbf{1}^{\text{Br}}$ and $\mathbf{1}^{\text{Cl}}$ ($\delta_{^{31}\text{P}\{\text{H}\}} = -110 \text{ ppm}$ ($\mathbf{1}^{\text{Br}}$), -51 ppm ($\mathbf{1}^{\text{Cl}}$)), pointing in the direction of partial halide exchange. Indeed, when in a separate experiment $\mathbf{1}^{\text{Br}}$ and $\mathbf{1}^{\text{Cl}}$ are mixed in equimolar amounts, we see formation of the same species with a LIFDI mass of 661.2 m/z, matching to $[\text{ReBrCl}(\text{PNP})]$ ($\mathbf{1}^{\text{BrCl}}$) (see Scheme 45). The exchange reaction does not go to completion, and due to the same solubility properties, $\mathbf{1}^{\text{BrCl}}$ cannot be isolated. Similar behaviour is observed when $\mathbf{1}^{\text{Cl}}$ and $\mathbf{1}^{\text{I}}$ were mixed, yet upon heating (60 °C): formation of a C_s -symmetric species with a LIFDI mass of 709.1 m/z, corresponding to $[\text{ReClI}(\text{PNP})]$ ($\mathbf{1}^{\text{ClI}}$). The chloride that needs to be present to form $\mathbf{1}^{\text{BrCl}}$ in the synthesis of $\mathbf{1}^{\text{Br}}$ most likely originates from traces of chlorinated solvents or agents in the glovebox atmosphere. Performing the work up or storage of $\mathbf{1}^{\text{Br}}$ in a chlorinating-agents free glovebox decreases the presence of $\mathbf{1}^{\text{BrCl}}$, yet it never fully disappears. A comparable problem is described by Schrock, where a persistent chloride impurity prohibits full purification of $[\text{ReBr}(\text{N}(\text{CH}_2\text{CH}_2\text{NC}_6\text{F}_5)_3)]$.¹⁷² Upon characterisation via XRD, the electron density of the axial halide can only be fitted when a ratio between bromide and chloride is considered. Although their synthetic approach is a template synthesis from a related chloride oxo complex, they attribute the chloride presence to residual DCM. For the parallel developed six-coordinate $[\text{ReX}_3(\text{PNP}^{\text{Pr}})]$ platforms within our group ($X = \text{Cl}, \text{Br}, \text{I}$), these problems were not encountered,^h hinting towards an associative mechanism for formation of $\mathbf{1}^{\text{XCl}}$.

^h Unpublished results of M. Fritz, M.Sc.

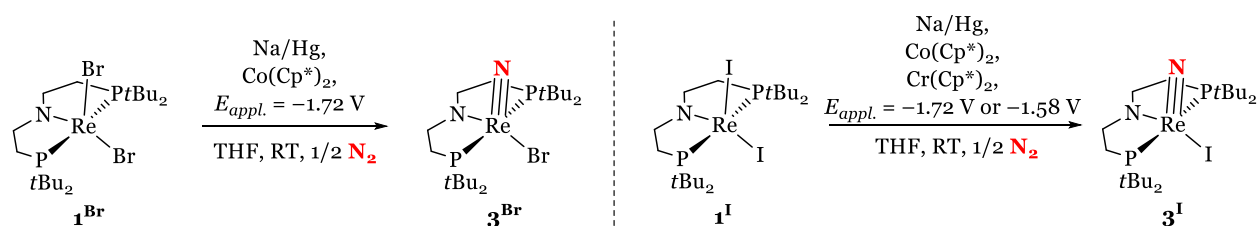


Scheme 45. Reacting $\mathbf{1}^{\text{Br}}$ or $\mathbf{1}^{\text{I}}$ with $\mathbf{1}^{\text{Cl}}$ results in formation of $\mathbf{1}^{\text{BrCl}}$ or $\mathbf{1}^{\text{ICl}}$ as evidenced spectroscopically.

2.2. (Electro)chemical N₂-splitting of $\mathbf{1}^{\text{Br}}$ and $\mathbf{1}^{\text{I}}$

Upon establishing synthetic access to $\mathbf{1}^{\text{Br}}$ and $\mathbf{1}^{\text{I}}$, we explored their N₂-splitting ability. Chemically, $\mathbf{1}^{\text{Br}}$ and $\mathbf{1}^{\text{I}}$ are readily reduced under 1 atm N₂ using equimolar amounts of Na/Hg (-2.36 V)⁵⁵ or Co(Cp*)₂ ($E_{1/2} = -1.84$ V in THF).⁵⁹ In addition, Cr(Cp*)₂ ($E_{1/2} = -1.47$ V in THF)⁵⁹ also reduces $\mathbf{1}^{\text{I}}$. In all cases, reduction is accompanied by a colour change via red to light brown and the formation of [ReNBr(PNP)] ($\mathbf{3}^{\text{Br}}$) or [ReNI(PNP)] ($\mathbf{3}^{\text{I}}$) as confirmed via NMR spectroscopy and comparison to independently synthesised nitrides, as extensively described in Section II.2.3. Atmospheric N₂-uptake is confirmed by reduction of $\mathbf{1}^{\text{Br}}$ and $\mathbf{1}^{\text{I}}$ under a ¹⁵N₂-atmosphere, resulting in a singlet resonance in the ¹⁵N NMR spectrum that compares well with the chemical shift as found for the chloride congener ($\delta^{15}\text{N}\{\text{H}\} = 375$ ppm ($\mathbf{3}^{\text{Br}}$), 381 ppm ($\mathbf{3}^{\text{I}}$), 371 ppm ($\mathbf{3}^{\text{Cl}}$)⁶⁹). In the bromide case, where minor $\mathbf{1}^{\text{BrCl}}$ is present, we see formation of some $\mathbf{3}^{\text{Cl}}$ ($\approx 2\%$ yield), (Figure A8), indicating bromide as leaving group during N₂-splitting.

By addition of a ³¹P- and/or a ¹H-NMR standard the N₂-splitting yields for $\mathbf{3}^{\text{Br}}$ and $\mathbf{3}^{\text{I}}$ were determined. Yield determination via ¹H NMR spectroscopy was not possible for every reaction, e.g. reduction of $\mathbf{1}^{\text{I}}$ with Na/Hg, because of overlapping side-product peaks. In other cases, yield determination via both ³¹P- and ¹H-NMR spectroscopy was accessible, e.g. for reduction of $\mathbf{1}^{\text{I}}$ with Cr(Cp*)₂, giving matching results. In general, $\mathbf{3}^{\text{Br}}$ and $\mathbf{3}^{\text{I}}$ can be obtained in moderate to high yields via chemical N₂-splitting (80% for $\mathbf{3}^{\text{Br}}$ (Na/Hg), and 60% for $\mathbf{3}^{\text{I}}$ (Cr(Cp*)₂ or Co(Cp*)₂). Decreased spectroscopic yield is found when using Na/Hg for synthesis of $\mathbf{3}^{\text{I}}$ (30%), or Co(Cp*)₂ for $\mathbf{3}^{\text{Br}}$ (45%). These yields are at least reproduced once and spread between the individual runs around 10% (i.e. 76% and 85% for synthesis of $\mathbf{3}^{\text{Br}}$ using Na/Hg as reductant, further exact numbers are given in the Experiment Section IV.5).



Scheme 46. Left: (Electro)chemical N_2 -splitting from $\mathbf{1}^{\text{Br}}$ into $\mathbf{3}^{\text{Br}}$ using Na/Hg, $\text{Co}(\text{Cp}^*)_2$, or via CPE with an applied potential of $E_{\text{appl.}} = -1.72$ V. Right: (Electro)chemical N_2 -splitting from $\mathbf{1}^{\text{I}}$ into $\mathbf{3}^{\text{I}}$ using Na/Hg, $\text{Co}(\text{Cp}^*)_2$, $\text{Cr}(\text{Cp}^*)_2$ or via CPE with an applied potential of $E_{\text{appl.}} = -1.72$ V or -1.58 V.

Electrochemical synthesis of $\mathbf{3}^{\text{Br}}$ and $\mathbf{3}^{\text{I}}$ was explored by CPE in a N_2 -atmosphere containing MBraun Glovebox at the potential of the first reduction as obtained via CV analysis (see Section II.2.5). CPE for $\mathbf{1}^{\text{Br}}$ at $E_{\text{appl.}} = -1.72$ V results in a colour change from purple to yellow and the transfer of circa 1.2 electrons per Re. Concomitantly, *in situ* CV shows a new, prominent, and irreversible peak in the oxidative region with $E_p = -0.02$ V (Figure 19), close to the Re(VI/V) oxidation of $\mathbf{3}^{\text{Br}}$ ($E_{1/2} = -0.05$ V). Although these potentials are slightly apart, no iR-compensation is applied when measuring CV in a CPE set up. Upon addition of separately synthesised $\mathbf{3}^{\text{Br}}$ following CPE, the current of this new wave increases confirming nitride formation (Figure A11). The irreversibility of this feature is not clear at this point. In a control experiment, $\mathbf{3}^{\text{Br}}$ was examined in presence of $(n\text{He}_4\text{N})\text{Br}$ to mimic bromide release as under CPE conditions (Figure 19). However, the Re(VI/V) oxidation couple maintains reversible (at higher bromide concentrations (i.e. 5 eq.) the oxidations of $\mathbf{3}^{\text{Br}}$ and Br^- are overlapping). This is in contrast to titration of $\mathbf{3}^{\text{Cl}}$ with Cl^- , which indicates chloride coordination upon oxidation. An explanation might be the increased halide radius in case of bromide. To test this hypothesis, it would be interesting to add a smaller ligand and explore if the $\text{Re}^{\text{VI/V}}$ reversibility is lost in that case. We tentatively attribute the irreversible oxidation of $\mathbf{3}^{\text{Br}}$ under CPE conditions to coupled chemistry with unknown side products. $^{31}\text{P}\{^1\text{H}\}$ -NMR confirmed the formation of $\mathbf{3}^{\text{Br}}$ in 55 % spectroscopic yield, which represents a FE of circa 45 %.

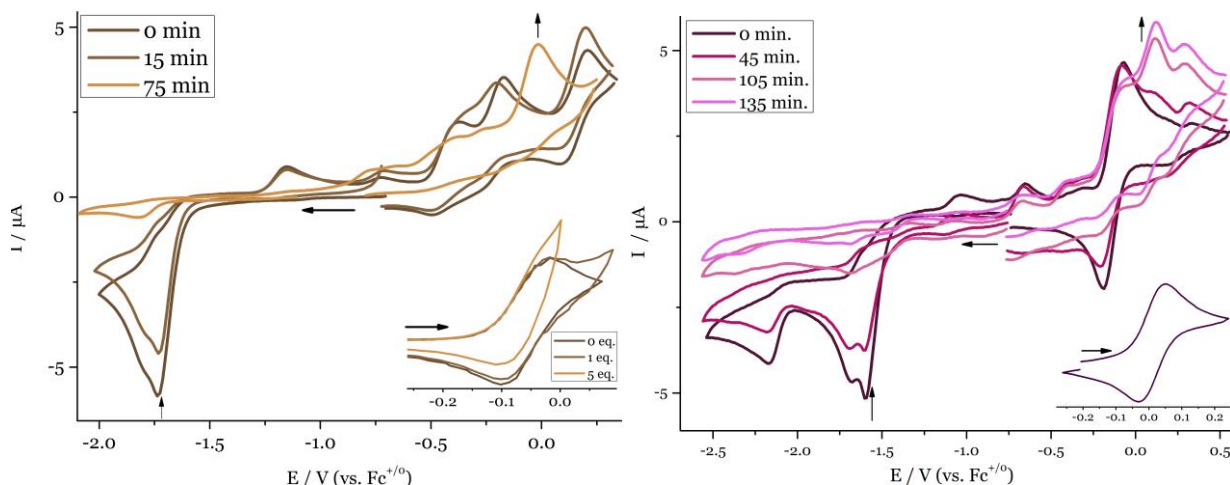


Figure 19. Left: CPE of **1**^{Br} at $E_{\text{appl.}} = -1.72$ V as monitored by CV. Inset: CV of the Re(VI/V)-oxidation of isolated **3**^{Br} in THF with 0.2 M (*n*Bu₄N)PF₆ in presence of 1 and 5 eq. of (*n*He₄N)Br, $\nu = 0.1$ V s⁻¹. Right: CPE of **1**^I at $E_{\text{appl.}} = -1.58$ V as monitored by CV. Inset: CV of the Re(VI/V)-oxidation of isolated **3**^I in THF with 0.2 M (*n*Bu₄N)PF₆.

CPE of **1**^I was performed at $E_{\text{appl.}} = -1.58$ V, which is accompanied by a colour change from green to brown and a transfer of 1.07 electrons per Re. In the CV traces in Figure 19, we see various oxidative waves appearing of which the wave of +0.06 V is close to the Re(VI/V) oxidation of **3**^I ($E_{1/2} = 0.01$ V) (see Section II.2.3). Upon addition of some separately synthesised **3**^I after a CPE experiment, this feature also clearly increases in intensity (Figure A11), confirming nitride synthesis. The nitride was spectroscopically quantified in about 50 % yield by ³¹P{¹H} NMR spectroscopy, which corresponds to 47 % FE. Notably, CPE at more negative potential ($E_{\text{appl.}} = -1.72$ V) yields more **3**^I (65 %), which corresponds to a FE of 60 %. For both the bromide- and the iodide-case, CPE under argon only resulted in trace amounts of the corresponding nitrides.

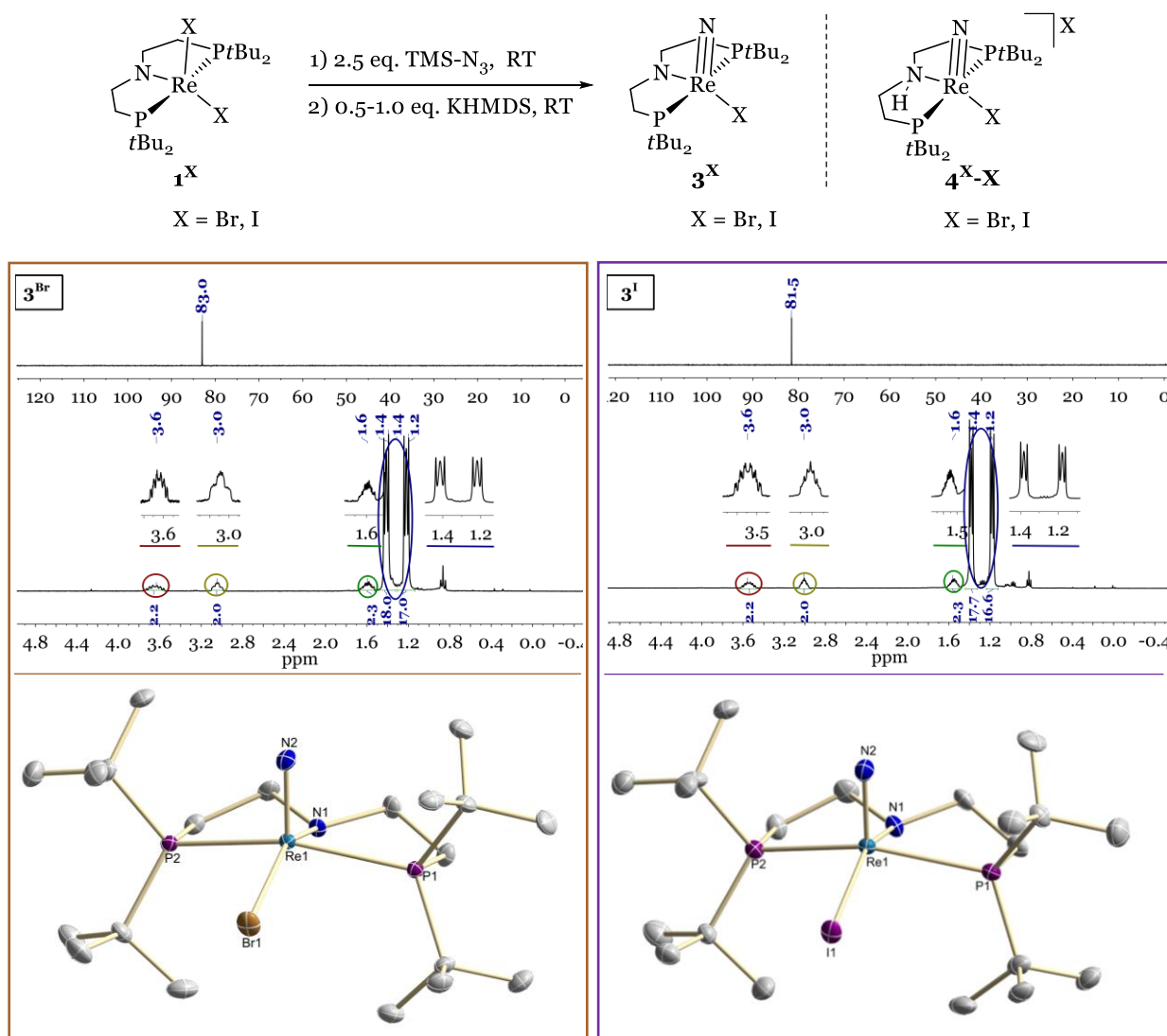
Having established an electrochemical yield of **3**^{Br} and **3**^I of about 60 %, the question rises which other products are formed. The CV traces show the presence of multiple peaks in the oxidative region. Unfortunately, only crude spectroscopic information is obtained as it was found very hard to separate the nitrides from the electrolyte: the nitrides are barely soluble in pentane and column chromatography resulted in partial decomposition. Mass spectroscopic analysis is hampered by the presence of the (*n*Bu₄N)-cation, since this obstructs the tubing. The ³¹P{¹H} NMR spectra for quantification are low in intensity (see Figures A8 and A9), and only reveal a few side products present in low amounts. Likely, additional compounds remain in the noisy baseline or are paramagnetic (¹H NMR spectroscopy was not measured after electrolysis). Although no side-product could be identified, we showed electrochemical N₂-splitting also for the **1**^{Br} and **1**^I platform in quite good yields.

In Chapter II.1, we presented a pathway as minimal mechanistic model for (electro)chemical N₂-splitting for **1^{Cl}**. To answer if the bromide and iodide congeners split N₂ via a similar model, we need to collect spectroscopic evidence if an analogous N₂-bound dimer as **2^{Cl}** is found as intermediate, which is discussed in Section II.2.4.

2.3. Synthesis of nitride reference species

To interpret the outcome of (electro)chemical N₂-splitting, we synthesised the expected nitride products independently. First, we examined halogen-exchange at the nitride level, by reacting **3^{Cl}** with excess NaI to form **3^I**. A new peak in the ³¹P{¹H}-NMR at 81.5 ppm is attributed to the desired product, due to the similarity with the chloride congener ($\delta^{31\text{P}\{^1\text{H}\}} = 84.2$ ppm (**3^{Cl}**)).⁶⁹ However, **3^{Cl}** was still present after heating for 48 h, indicating a very slow reaction. Therefore, nitride synthesis was examined using azide reagents. First, we reacted **1^{Br}** and **1^I** with PPN-N₃ resulting in a colour change towards yellow. ³¹P{¹H} NMR spectroscopy indicated partial conversion after several hours to a reaction mixture amongst which species are identified at 83.0 ppm and 81.5 ppm, respectively. Corresponding LIFDI mass spectra showed peaks at 640.1 m/z (calcd. for **3^{Br}**: 640.1 m/z) and 688.1 m/z (calcd. for **3^I**: 688.2 m/z), confirming successful synthesis of both nitride compounds.

In contrast to PPN-N₃, addition of TMS-N₃ to **1^{Br}** and **1^I** showed full conversion already after minutes and was therefore chosen as reagent to optimise the synthesis procedure. In both bromide and iodide case, a pentane insoluble C_s-symmetric species was obtained in about 30 % yield. In case of iodide, this species was examined in more detail, and reversing the addition order of the reagents (**1^I** to TMS-N₃ instead of *vice versa*) and using a large excess of azide-source, this unknown species was almost selectively synthesised ($\delta^{31\text{P}\{^1\text{H}\}} = 69$ ppm). A ¹H NMR spectroscopic feature is found at 7.3 ppm integrating to one proton, indicating PNP-backbone protonation. X-ray analysis of single crystals confirmed partial hydrolysis of **3^I** to form [Re(N)I(HPNP)]I (**4^{I-I}**), attributed to traces of trimethylsilanol in the azide-source, since no better reaction outcomes were obtained with freshly distilled TMS-N₃ and the silanol cannot be removed via distillation.



In the bromide case, similar behaviour is observed: an additional singlet in the ³¹P{¹H}-NMR spectrum at 70 ppm combined with a mass spectroscopic signal corresponding to a [ReNBr(HPNP)]⁺ fragment indicates analogous formation of **4^{Br-Br}**. Both molecules show that for **3^{Br}** and **3^I** the preferred protonation site is the PNP-backbone amide moiety, as in the case of **3^{Cl}**. To still obtain high nitride yields, we applied a base (KHMDS) to the reaction mixture in (sub)stoichiometric equivalents (NEt₃ showed no reaction), resulting in clean nitride synthesis in high yields (89% for **3^{Br}** and 87 % for **3^I**).

X-ray analysis of **3^{Br}** and **3^I** show 5-coordinate compounds with the nitride in apical positions and Re-N_{nitride} distances similar to their chloride congener (1.652(3) Å (**3^{Br}**), 1.651(4) Å (**3^I**), vs. 1.643(6) Å (**3^{Cl}**))¹⁷³. The Re-N_{amide} bonds (**3^{Br}**: 2.017(3) Å and **3^I**: 2.020(4) Å) are slightly elongated compared to the corresponding dihalide species, reflecting the decreased N_{amide} → Re π bonding due to the absence of vacant, appropriate d-orbitals (d_{xz} and d_{yz}) at the metal centre. Both nitrides show a slightly distorted square pyramidal geometry based on their τ₅-values. A similar trend is observed here as in the dihalide compounds **1^X**: the τ₅-value decreases for the heavier homologues (τ₅ = 0.14 (**3^{Cl}**)¹⁷³, 0.06 (**3^{Br}**), 0.02 (**3^I**)).

3^{Br} and **3^I** were characterised electrochemically in THF, revealing for each two oxidation events. The Re(VI/V) oxidations are reversible (see Figure 19 and A12), and a slight anodic shift is observed when comparing the nitride series ($E_{1/2} = -0.09$ V (**3^{Cl}**), -0.05 V (**3^{Br}**), 0.01 V (**3^I**)). A second oxidation occurs at more anodic potential $E_p = 0.86$ V (**3^{Br}**), 0.85 V (**3^I**) which likely has a multi-electron character based on the high forward peak current, and shows a large ΔE_p (0.151 V for **3^I** and 0.317 V for **3^{Br}**). Within this work, we compared the chloride nitride **3^{Cl}** with its unsaturated congener [ReNCl(N(CHCHPtBu₂)₂)] (= **3^{Cl}**) (Figure A4). Similar to the bromide and iodide platform, **3^{Cl}** reveals an irreversible oxidation at $E_p = 0.84$ V that disappears in the CV of the unsaturated analogue. Based on this observation, the striking peak potential similarities, and the multi-electron character of the forward peak, this oxidation is attributed to partial PNP-backbone oxidation. **3^I** reveals an irreversible reduction event ($E_{p,c} = -3.05$ V, $\nu = 0.1$ Vs⁻¹). Although still very negative, it is the most electropositive potential amongst this nitrides series **3^X** that can be reduced within the electrochemical window of THF (up to -3.5 V).¹⁷⁴

2.4. Characterisation of dinuclear N₂-bound intermediate

In case of **1^{Cl}**, we were able to characterise end-on N₂-bridged dinuclear complex **2^{Cl}** as intermediate for N₂-splitting via both UV-vis SEC and NMR spectroscopy. Aiming to either confirm or expand the N₂-splitting model discussed in Chapter II.1, we searched for intermediates first by means of UV-vis SEC. Upon performing CPE at the onset of the reduction wave of **1^{Br}** or **1^I**, two absorption bands increase in intensity with a maximum around 400 and 550 nm within 2-3 minutes, see Figure 22. These bands then decay and a weakly coloured reaction mixture without strong absorption bands in the vis-region is obtained after circa 5-10 minutes.

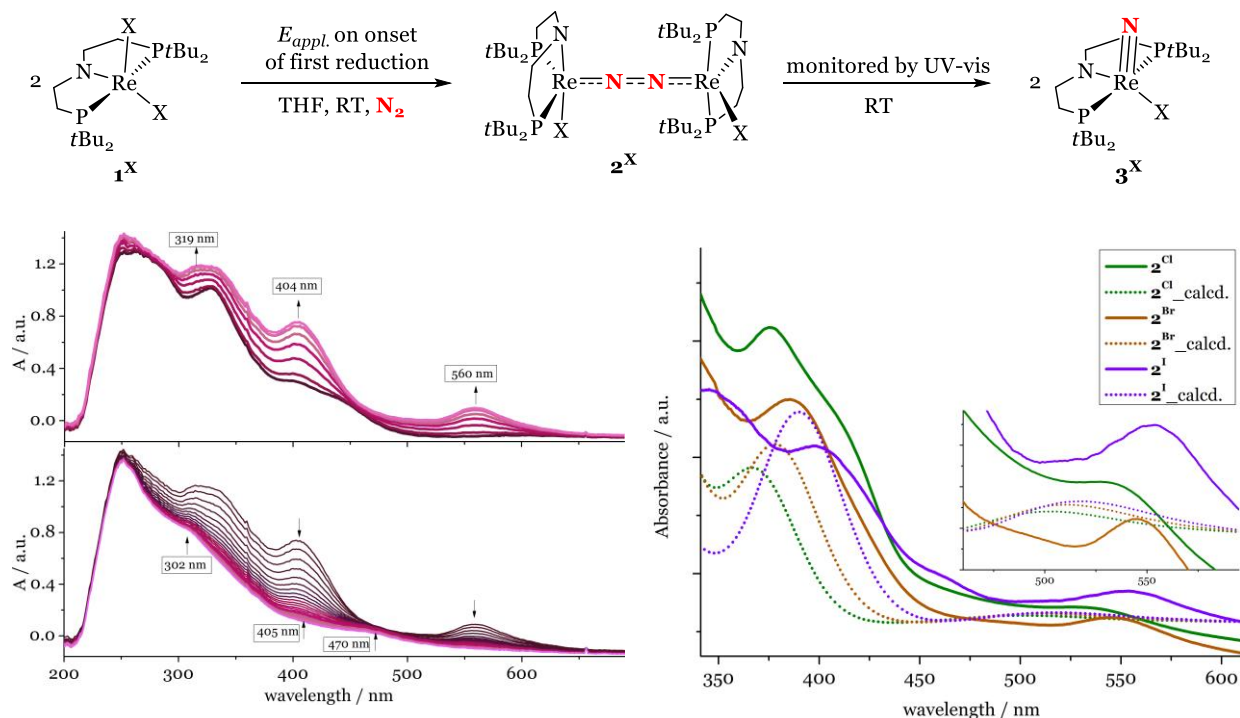


Figure 21. Top: Reductive CPE on **1^X** to form **2^X** which converts into **3^X**. Bottom left: Exemplary UV-vis SEC traces following CPE of **1^I** to form **2^I** (top) and subsequent conversion into **3^I** (bottom). Each line represents circa 15 seconds of reaction time. Right: UV-vis of **2^X** formed via chemical reduction (solid line) and the TD-DFT calculated spectra (dotted line).

These observations are basically identical to the chloride case and can therefore be interpreted as the reductively induced formation of dinuclear end-on N₂-bridging [$\{\text{ReX}(\text{PNP})\}_2(\mu\text{-N}_2)$] complexes, with X = Br for **2^{Br}** and X = I for **2^I**, and their subsequent splitting into pale nitrides. The UV-vis traces during reduction of **1^I** that show formation of **2^I** and its conversion are presented as example (Figure 21, left). During chemical reduction of **1^{Br}** and **1^I**, the reaction mixtures show a temporary red colour with UV-vis absorption maxima that are in good agreement (± 10 nm) with the maxima as obtained by CPE (Figure 21). As in the chloride case, this observation underlines that the same dinuclear N₂-bound intermediate **2^{Br}** and **2^I** is formed via electrochemical and chemical reduction. The absorption maxima within this series **2^X** show a small red shift going down the halogen group, but are basically independent of the halide, indicating that the transitions must be within the $\{\text{ReNNRe}\}$ -fragment. This is complemented by comparison to end-on dinuclear N₂-bridging complexes that also have a $(\delta^4)\pi^{10}$ configuration, i.e. [$\{\text{MoCO}(\text{PNP})\}_2(\mu\text{-N}_2)$], [$\{\text{Mo}(\text{N}(\text{tBu})(3,5\text{-C}_6\text{H}_3(\text{CH}_3)_2)_3\}_2(\mu\text{-N}_2)$], [$\{\text{ReCl}_2(\text{PNP}^{\text{iPr}})\}_2(\mu\text{-N}_2)$] and [$\{\text{MoCp}^*(\text{depf})\}_2(\mu\text{-N}_2)$] (depf = 1,1'-bis(diethylphosphino)ferrocene).^{67,71,82,175} Just as **2^X**, these complexes share a low-energy absorption that represents an excitation within the $\{\text{MNNM}\}$ -manifold. The TD-DFT calculated absorption maxima for the series **2^X** also move to lower energies for the higher homologues, although all absolute values are slightly blue-shifted

compared to the experiment (Figure 21). In the case of **2^I**, a UV absorption maximum at 319 nm is observed, that was not elucidated for **2^{Cl}** or **2^{Br}** due to noisy and overlapping data in that region.

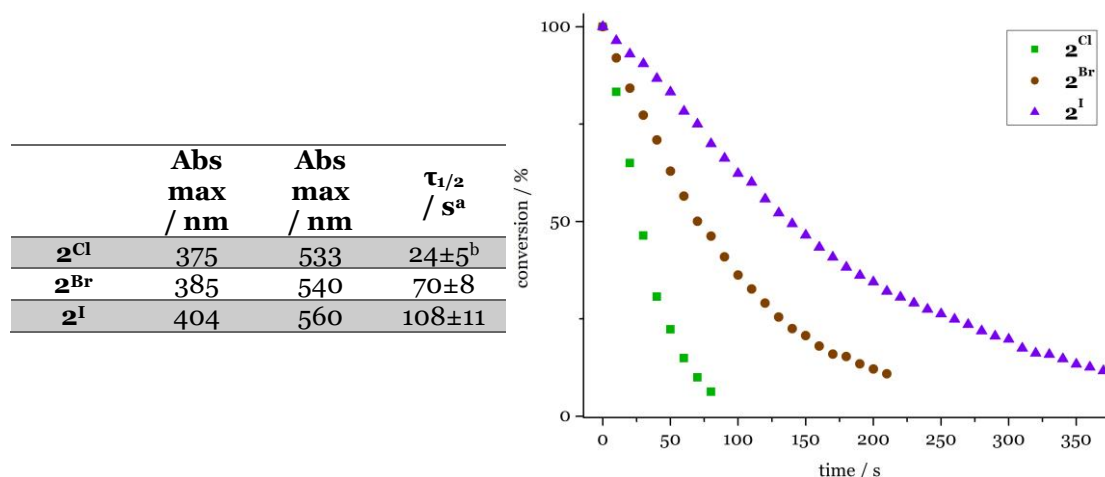


Figure 22. Left: Table with absorption maxima and half-life values of dinuclear **2^X** compounds as derived from UV-vis SEC. ^a The half-life times represent the average of 3 runs. ^b $-\tau_{1/2}$ for **1^{Cl}** was described in Chapter II.1 to be 28 s as determined by cooperation partners. Right: Exemplary conversion traces of **2^X** as derived via UV-vis SEC.

We can follow the decay of the absorption bands of **2^{Br}** and **2^I** to get their half-lives as discussed in Section II.1.2 for **2^{Cl}**. Those data were measured by cooperation partners in a different set up; the determination of the half-life for **2^{Cl}** was repeated here to allow a correct comparison within the **2^X**-series. As slight improvement to the previous measurement, we secured that kinetic analysis started *after* the CPE was finished, preventing that more of **2^X** is formed. Furthermore, in lack of temperature control, all measurements were performed at the same day aiming for a comparable glovebox temperature. Under these conditions, we measured conversion of **2^X** over three half-lives (Figure 22 and Figure A15). The half-life time of 24±5 s for **2^{Cl}** is in perfect agreement with the reported value (28 s).⁷⁰ When going down the halogen group, the half-life time increases moderately from 70±8 s for **2^{Br}** to 108±11 s for **2^I**. Relating these values to the half-life time of the chloride congener via the Arrhenius equation, slightly increased barriers for N₂-splitting are found by circa 0.6 and 0.9 kcal mol⁻¹. This might be attributed to the increased radii, which will hinder formation of the proposed zig-zag transition state as proposed for N₂-splitting from **2^X**.

To extend the characterisation of **2^{Br}** and **2^I**, the corresponding dihalide complexes were chemically reduced in *d*₈-THF at -30 °C, and the resulting red solution was analysed by NMR spectroscopy. In the bromide case, two strongly separated doublets in the $^{31}\text{P}\{^1\text{H}\}$ NMR spectrum were found ($\delta^{31}\text{P}\{^1\text{H}\}$: -159.4 , -12.3 ppm (-30 °C)) that couple in the ^{31}P COSY spectrum (Figure 23 and A13). The large coupling constant ($^2J_{\text{PP}} = 227$ Hz) indicates a *trans* arrangement of the phosphorous moieties. Based on the analogies to **2^{Cl}**, we assign these features to **2^{Br}**.

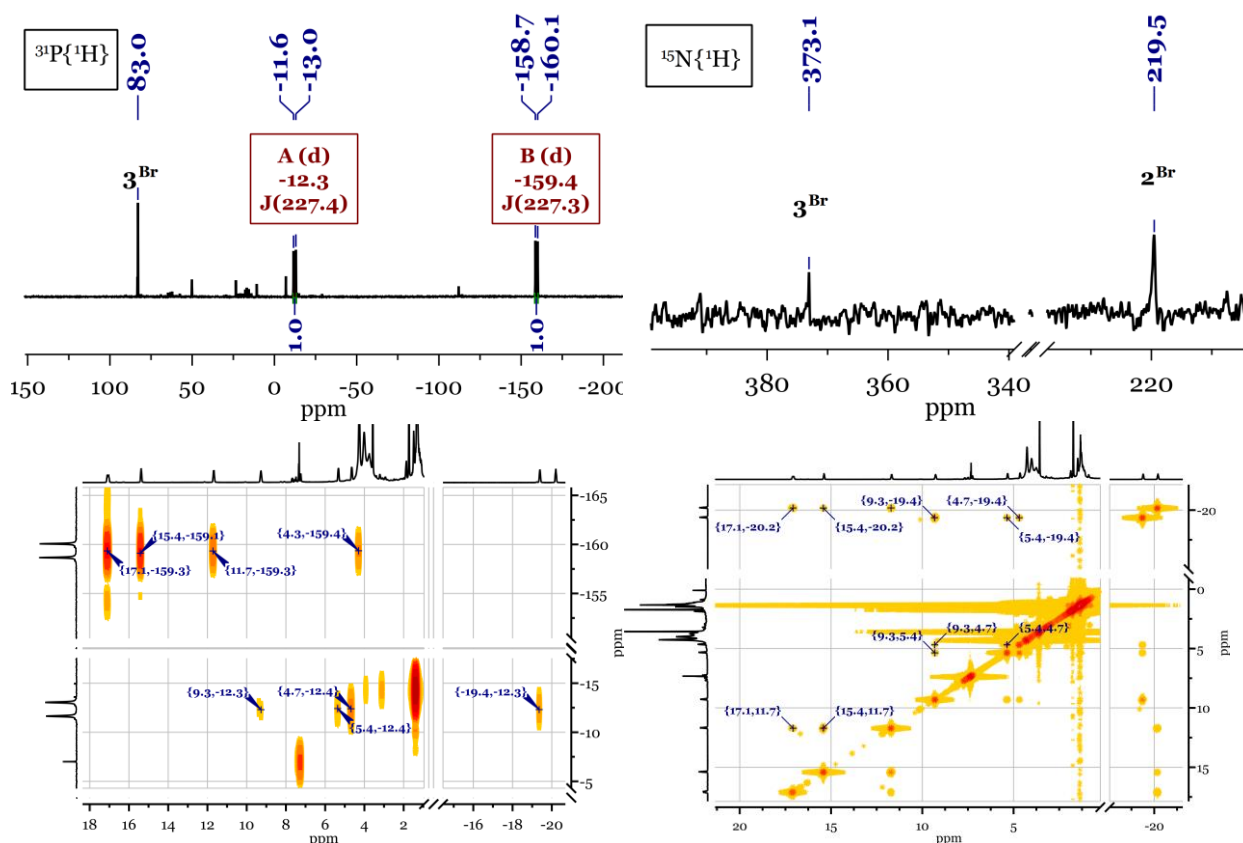


Figure 23. **2^{Br}** in *d*₈-THF at -30 °C. Top left: $^{31}\text{P}\{^1\text{H}\}$ NMR spectrum. Top right: $^{15}\text{N}\{^1\text{H}\}$ NMR spectrum. Bottom left: ^1H - ^{31}P HMBC NMR spectrum. Bottom right: ^1H COSY NMR spectrum at -75 °C.

The $^{31}\text{P}\{^1\text{H}\}$ NMR features of **2^{Br}** couple in a ^{31}P - ^1H HMBC NMR spectrum to several (paramagnetically shifted) signals in the ^1H NMR spectrum. These proton signals couple to each other as revealed by ^1H COSY NMR, allowing us to identify 8 equally integrating signals that we assign to backbone CH_2 -groups of a C_2 -symmetric **2^{Br}** molecule (Figure A23). The 4 expected *tert*-butyl signals are less straight forward to allocate. When lowering the temperature measuring variable temperature (VT-) NMR (Figure A16), we can however clearly distinguish the slightly shifting and broadening *tert*-butyl groups of **2^{Br}** from the diamagnetic compounds (**1^{Br}** and **3^{Br}**) and smaller side products: 3 features around 4 ppm and 1 broad signal at -0.7 ppm

(-30°C). Upon reducing $\mathbf{1}^{\text{Br}}$ under a $^{15}\text{N}_2$ atmosphere, we assign a broad singlet at 219.5 ppm to the dinuclear $^{15}\text{N}_2$ -bound complex, based on the similarity to the chloride platform ($\delta^{15}\text{N}\{\text{H}\}$ ($\mathbf{2}^{\text{Cl}}$) = 211.1 ppm), and its disappearance when the sample is warmed to RT (Figure 23). The low intensity of this measurement adds some uncertainty to this assignment.

In the ^{31}P COSY spectrum, another set of coupling doublets was found ($\delta^{31}\text{P}\{\text{H}\} = -14.3$ and $+63.9$ ppm), corresponding to a side-product present in circa 5-10 %. Similar features were found in case of reduction from $\mathbf{1}^{\text{Cl}}$ (see Section II.1.1). Formation of this side-product could not be prevented, and *in situ* characterisation of $\mathbf{2}^{\text{Br}}$ was performed in its presence. It is not formed in absence of dinitrogen and therefore, it might be another dinuclear structure coordinating N_2 . The features disappear upon increasing the temperature, indicating a transient nature, and the phosphorous atoms are in a *trans* arrangement ($^2J_{\text{PP}} = 220$ Hz). The $^{31}\text{P}\{\text{H}\}$ features couple to proton signals mainly in the diamagnetic region ($\delta^{\text{H}} = 3.92, 3.66, 3.09,$ and 2.63 ppm (pincer backbone protons), $1.36, 1.23$ ppm (*t*Bu-groups)), and to a multiplet at -7.55 ppm. The latter couples via ^1H COSY NMR to a backbone feature. Unfortunately, no information about its integral is obtained as the other signals are obscured. Due to the typical diamagnetic resonances of the ^1H NMR features, and the absence of a significant shift when measuring VT-NMR (maximal shift: $\Delta\delta^{\text{H}} = 0.05$ ppm, $\Delta\delta^{31}\text{P}\{\text{H}\} = 1.0$ ppm, see Figure A16), we consider this a diamagnetic species, and assign the feature at -7.55 ppm to a hydride. The formation of a dimeric species seems unlikely, based on its few ^1H NMR spectroscopic resonances. Formation of a hydride species combined with a low symmetry species can be strong indications for cyclometallation, where a C-H bond of a *tert*-butyl moiety is activated on the metal centre. Yet, the peak separation in $^{31}\text{P}\{\text{H}\}$ NMR ($\Delta\delta^{31}\text{P}\{\text{H}\} \approx 80$ ppm) is way larger than experimentally observed for comparable complexes, and also more ^1H NMR spectroscopic features would be expected.^{168,176,177} The nature of this species remains therefore unknown. We also performed this reduction of $\mathbf{1}^{\text{Br}}$ in presence of $(n\text{He}_4\text{N})\text{Br}$. Formation of $\mathbf{2}^{\text{Br}}$ is unaffected as proven by identical NMR features with or without additive. The above-mentioned side-product is not formed, but a new set of coupling doublets are observed ($\delta^{31}\text{P}\{\text{H}\} = 30.0$ and 81.8 ppm, $^2J_{\text{PP}} = 213$ Hz). The $(n\text{He}_4\text{N})$ -cation unfortunately obscures most of the ^1H NMR spectrum, yet the new species shows a hydride signal appearing as a doublet at -6.5 ppm. Both observations also fit to a cyclometallation reaction (the lower $\Delta\delta^{31}\text{P}$ is now strongly indicative for cyclometallation). The ratio between this new species and $\mathbf{2}^{\text{Br}}$ increases when more bromide anions are added (10 or 20 eq. vs. $\mathbf{1}^{\text{Br}}$). Furthermore, a new singlet at 84.5 ppm arises, indicative of a Re(V)-compound, that remains after warming to RT but unfortunately decomposes during work-up. In future

research, *in situ* ESI-MS should be performed to identify either of these triggering asymmetric side-products both with and without bromide addition.

With successful characterisation of **2^{Br}** in hand, we turned to the iodide platform. In case of **1^I**, reduction was performed with Co(Cp*)₂, and the obtained red mixture was analysed by NMR spectroscopy at -30 °C. However, no signals were found in the ³¹P{¹H} NMR spectrum over a wide range (-2000 to +1000 ppm) that resemble a dinuclear compound (coupling doublets). Nevertheless, a defined set of paramagnetic shifted (-25 to +21 ppm), but sharp signals is found in the ¹H NMR spectrum, that is closely similar to **2^{Cl}** and **2^{Br}** (Figure 24 and A17). Amongst these, we can identify eight signals with an equal integral of which most couple via ¹H COSY NMR spectroscopy (Figure 24), assigned to CH₂-backbone signals of **2^I**. As for **2^{Br}**, the broadened *tert*-butyl signals at lower temperatures hinder their direct allocation and only by VT-NMR, the signal can be identified (3 features around 4 ppm and 1 broad signal at -1.1 ppm (-30°C)). No ¹⁵N{¹H} signal was found for **2^I** when performing its synthesis under a ¹⁵N₂-atmosphere. A similar situation is found for the related δ⁴π¹⁰ N₂-bridging dinuclear [W(CO)(PNP)]₂(μ-N₂), which also lacks heteronuclear NMR resonances and shows broadly shifted ¹H NMR spectroscopic features over 30 ppm. Its open-shell character was confirmed by SQUID magnetometry that was fitted as a S = 1, g_{av} = 1.74 system with large zero-field splitting of 407 cm⁻¹.⁶⁷

In all synthesis attempts for this dinuclear N₂-bound iodide analogue, **1^I** was always still present in large amounts. In addition, significant quantities of a diamagnetic side-product are formed (δ³¹P{¹H} = 15.3) that likely contains a hydride group, as a signal at -7.8 ppm is found in the ¹H NMR spectrum. It is not unknown that Co(Cp*)₂ can act as PCET reagent upon forming hydride species and [Co(Cp*)(CpMe₄CH₂)],¹⁷⁸ as was shown for the chloride platform. Reduction of **1^{Cl}** using 2 eq. of this reductant leads to exclusive formation of [ReCl(H)(PNP)] with similar NMR traces (δ³¹P{¹H} = 29.8 ppm, δ¹H = -9.3 ppm).⁷¹ Analogous formation of [Re(H)I(PNP)] consuming 2 eq. of [Co(Cp*)₂], would explain why **1^I** is still present.

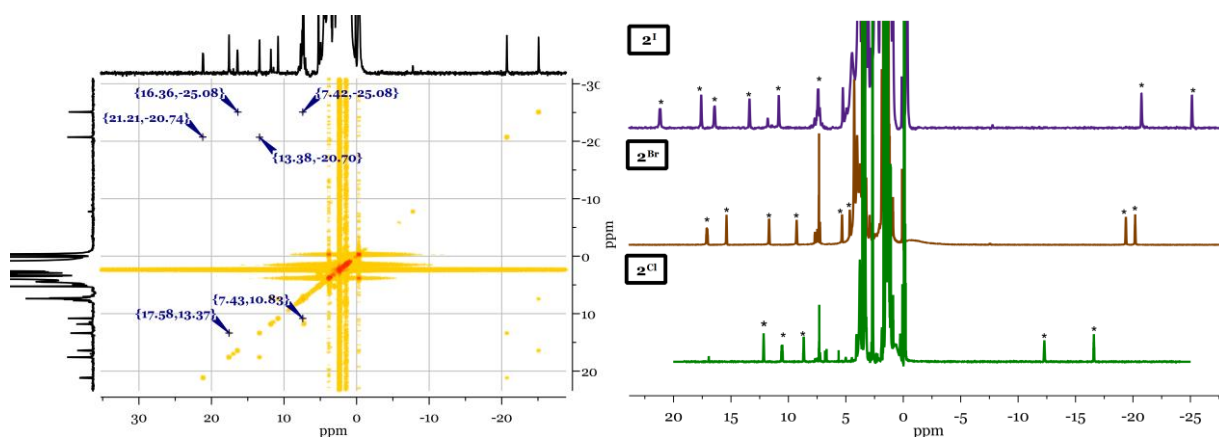


Figure 24. Left: ^1H - ^1H COSY NMR spectrum of **2^I** in d_8 -THF at -30°C . Right: Comparison of the ^1H NMR spectra of **2^{Cl}**, **2^{Br}**, and **2^I** in d_8 -THF at -30°C . Backbone signals marked with an asterisk.

In direct comparison of the ^1H NMR spectra of **2^X** (Figure 24), it becomes clear that going to heavier homologues, the peaks are more shifted in the paramagnetic regime. The peaks are not broader: the line-width at half-height (LW_{HH}) remains around 30 Hz within the series. Yet, the visibility of the coupling decreases: whereas the J-coupling of the backbone features is resolved for **2^{Cl}**, **2^I** only possesses singlets. The paramagnetic contribution increases when going down the group as a result of more spin orbit coupling involved for the heavier elements,¹⁷⁹ as also reflected by the missing heteronuclear NMR spectroscopic features of **2^I**. Unfortunately, despite having longer lifetimes than the chloride analogue, the RT stability of both **2^{Br}** and **2^I** is still too low to perform SQUID magnetometry. Strikingly, all three **2^X** show an identical pattern within the *tert*-butyl moieties: three comparably sharp resonances close to 4 ppm and one very broad upfield shifted signal ($\delta_{\text{H}} = 0.7$ ppm (**2^{Cl}**), -0.7 ppm (**2^{Br}**) and -1.1 ppm (**2^I**)), indicating different dynamics for this group.

To get a first indication of the electronic ground state of **2^{Br}** and **2^I**, VT-NMR was performed over a temperature range of 100 °C, as presented in Figures 25 and A16. Clearly, we see some temperature dependence on the NMR shifts. By ^1H NMR spectroscopy, we observe that the backbone peaks with the most paramagnetic shifted resonance, shift towards the diamagnetic region when warming up (up to 3 ppm for **2^{Br}** and up to 5 ppm for **2^I**). Upon cooling, we see the broadening of the *tert*-butyl peaks, which indicates freezing of the C-C bond rotation that originally renders the methyl groups equivalent. Notably, the broad signal at -0.7 ppm (**2^{Br}**) and -1.1 ppm (**2^I**), fully disappears and sharp features appear $<-50^\circ\text{C}$ assigned to the now inequivalent methyl groups.

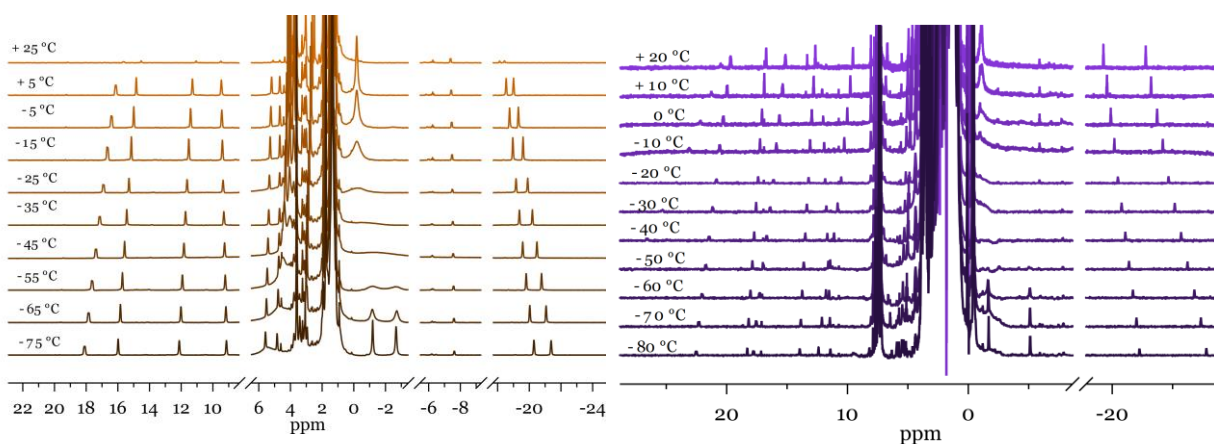


Figure 25. ^1H VT-NMR spectroscopy of $\mathbf{2}^{\text{Br}}$ (left) and $\mathbf{2}^{\text{I}}$ (right) in *ds*-THF over a temperature range of 100 °C.

Plotting the change in the chemical shift versus T^{-1} (Figure A16 and A17) reveals non-negligible bending for those signals that shift significantly. This is in contrast to what was published for $\mathbf{2}^{\text{Cl}}$.⁷⁰ However, in that case, VT-NMR was explored for a smaller temperature range (55 °C) and its linear behaviour between $\Delta\delta$ vs. T^{-1} should be handled with care. The order of temperature dependence can be traced back to the different contributions to the chemical shift for open-shell compounds. In addition to a diamagnetic shielding factor, it is build up by a *Fermi-contact* term and a *pseudo-contact* term. The first reflects the ‘through bond’ interaction between the metal centre and the measured nucleus and scales with the partial electron density of the latter; it is thereby a measurement for covalency. The latter reflects ‘through space’ contributions via dipole interactions and scales with the distance between the metal centre and the measured nucleus ($1/r^3$, with r being the distance between the unpaired electron and the NMR active nucleus). In early, simplified models, it is proposed that the *contact term* scales with T^{-1} and the *pseudo-contact* term with T^{-2} .^{180,181} Sometimes, clearly one of the terms contribute more, e.g. the *pseudo-contact* term for lanthanide complexes that usually form weakly covalent bonds.¹⁸² In recent literature, it is acknowledged that this picture from early work is too simplified, especially if second order spin orbit coupling introduces anisotropy in form of either zero field splitting or an anisotropic electron g -factor. Indeed, if for instance the latter is minimal, the above mentioned early relationship can be found for certain spin states, as extensively calculated by Autschbach.^{180,181} For $\mathbf{2}^{\text{Br}}$ and $\mathbf{2}^{\text{I}}$, no clear scaling with T^{-1} or T^{-2} was found and linearity is observed when plotting $\Delta\delta$ vs. T (Figure 26). This clearly indicates that a distinct separation between the two terms is not possible, which we attribute to a large anisotropy of the g -factor (Δg) for both $\mathbf{2}^{\text{Br}}$ and $\mathbf{2}^{\text{I}}$, originating from second order spin orbit coupling effects. This phenomenon might be linked to the striking, and so far unexplained large chemical shift difference between the phosphorous moieties ($\Delta\delta^{31\text{P}^{\text{I}}\text{H}}$ NMR \approx 130 ppm ($\mathbf{2}^{\text{Cl}}$), 145 ppm ($\mathbf{2}^{\text{Br}}$)),

which also indicates anisotropy within the molecules. In lieu of SQUID measurements, no deeper insight is obtained at this point.

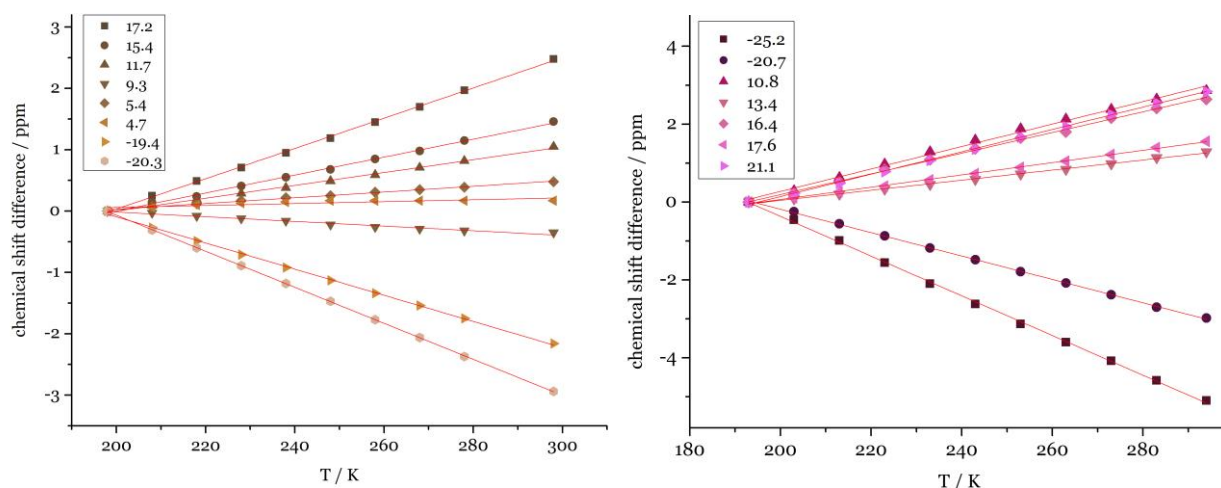


Figure 26. $\Delta\delta$ vs. T curves for the eight CH_2 -backbone features of $\mathbf{2}^{\text{Br}}$ (left) and $\mathbf{2}^{\text{I}}$ (right). The graph legend refers to the chemical shift of the peaks at -30 °C.

To gain more information from NMR spectroscopy about the solution structure of these complexes, we attempted to use the quadrupole active nucleus ^{14}N that the N_2 -bridge offers. Because of magnetic anisotropy, an additional quadrupole splitting might be observable by NMR spectroscopy, which could provide information about the magnetic susceptibility tensor. Knowing the susceptibility tensor would allow for discrimination between *contact* and *pseudo-contact* contributions to the chemical shift, thereby gaining structural information about $\mathbf{2}^{\text{X}}$ in solution. This might provide an rationale for the anisotropy in the molecule as reflected in the large separation between the ^{31}P NMR spectroscopic signals for $\mathbf{2}^{\text{Cl}}$ and $\mathbf{2}^{\text{Br}}$ (*vide supra*). This experiment is well known for compounds containing ^2H -nuclei.^{183–186} As first attempt, we scrutinised if one could see a ^{14}N NMR resonance and if such a quadrupole splitting is observed. This experiment was performed using $\mathbf{2}^{\text{Cl}}$, since it is *in situ* accessible in high yields. Upon measuring $\mathbf{2}^{\text{Cl}}$ as synthesised under a $^{14}\text{N}_2$ -atmosphere at -30 °C, we see a ^{14}N NMR signal at 210 ppm, in alignment with the ^{15}N NMR signal (see Figure A18). Yet, the peak is so broadened (LWHH \approx 700 Hz), that no splitting pattern is recognisable. The linewidth is proportional to Q^2 , which might explain why such experiments are only reported for ^2H ($Q = 0.0029$ b (^2H)) and 0.0193 b (^{14}N)).¹⁸⁷

En route in the characterisation of $\mathbf{2}^{\text{Br}}$ and $\mathbf{2}^{\text{I}}$, resonance Raman spectroscopy was attempted to get insight in the NN stretching frequency. Yet, no signal for the N_2 -bridge could be found, and likely, the excitation wavelengths (457 nm and 633 nm) are too far apart from the absorption

maxima of the dinuclear compounds (Figure 22). Despite several attempts, single crystals suitable for X-ray analysis of either $\mathbf{2}^{\text{Br}}$ or $\mathbf{2}^{\text{I}}$ could not be obtained.

2.5. Initial electrochemical analysis of the $\mathbf{1}^{\text{x}}$ platforms

With successful (electro)chemical N_2 -splitting for $\mathbf{1}^{\text{Br}}$ and $\mathbf{1}^{\text{I}}$ in hand, we can make some initial comments on a potential N_2 -splitting mechanism. Figure 27 shows a CV-overlay of the reductive area of a 1 mM solution of $\mathbf{1}^{\text{Cl}}$, $\mathbf{1}^{\text{Br}}$, and $\mathbf{1}^{\text{I}}$ under a N_2 -atmosphere in THF. Comparing the CV's reveal interesting differences that are briefly commented here.

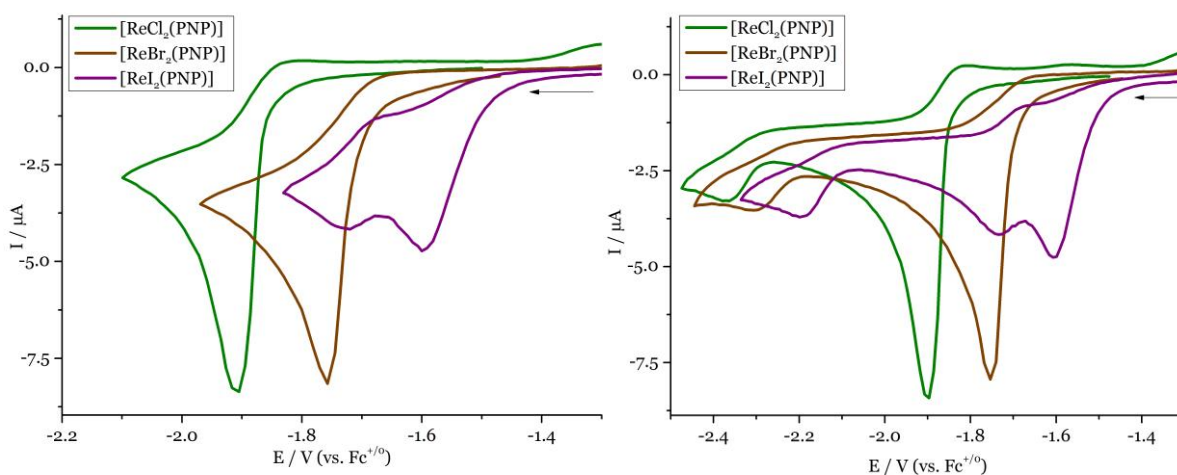


Figure 27. CV overlay of 1 mM of $\mathbf{1}^{\text{Cl}}$, $\mathbf{1}^{\text{Br}}$, and $\mathbf{1}^{\text{I}}$ under N_2 in THF with 0.2 M $(n\text{Bu}_4\text{N})\text{PF}_6$ at $\nu = 0.1 \text{ Vs}^{-1}$. Left: only first reduction area. Right: extended reduction area.

Most striking is the strong anodic shift of the first reduction event upon substituting chloride to bromide and iodide ($E_{p,c,1} = -1.90 \text{ V}$ ($\mathbf{1}^{\text{Cl}}$), -1.76 V ($\mathbf{1}^{\text{Br}}$), -1.60 V ($\mathbf{1}^{\text{I}}$), $\nu = 0.1 \text{ Vs}^{-1}$), allowing for much milder CPE potentials or reductants for N_2 -splitting in case of the heavier halides. This potential shift is well beyond the *Lever* E_L parameters, as discussed in Section I.1.4. Secondly, we see that the CV trace of $\mathbf{1}^{\text{Br}}$ resembles more or less the trace of $\mathbf{1}^{\text{Cl}}$: one basically irreversible and sharp reduction event with an $i_{p,c}$ of circa $8 \mu\text{A}$ at a 1.0 mM Re-concentration. In contrast, the CV of $\mathbf{1}^{\text{I}}$ is dramatically different having two reductions in close proximity. An irreversible reduction is followed by a quasi-reversible second reduction. Both are lower in current compared to the features observed for $\mathbf{1}^{\text{Cl}}$ and $\mathbf{1}^{\text{Br}}$. Upon scanning more negative all three platforms reveal a small, irreversible reduction feature at lower potentials ($E_{p,c} = -2.36 \text{ V}$ ($\mathbf{1}^{\text{Cl}}$), -2.31 V ($\mathbf{1}^{\text{Br}}$), -2.20 V ($\mathbf{1}^{\text{I}}$), $\nu = 0.1 \text{ Vs}^{-1}$).

In Chapter II.1, we established for the chloride platform that dinuclear $\mathbf{2}^{\text{Cl}}$ is formed via a $EC^{N_2}C^{\text{Cl}}EC^{\text{dim.}}$ -mechanism. Based on the similar CV traces under N_2 , we hypothesise that $\mathbf{1}^{\text{Br}}$ follows a similar pathway: two *potential inversed* reductions with coupled chemistry result in a multi-electron, sharp, irreversible CV trace. In strong contrast is the CV of $\mathbf{1}^{\text{I}}$. If N_2 -splitting on $\mathbf{1}^{\text{I}}$ follows the same $EC^{N_2}C^{\text{X}}EC^{\text{dim.}}$ -mechanism (C^{X} stands for halide loss), these reductions could represent both electron transfers of the established mechanism ($[\text{ReI}_2(\text{PNP})]^{0/-}$ and $[\text{ReI}(\text{N}_2)(\text{PNP})]^{0/-}$), without a *potential inversion*. To explore this hypothesis, an extended electrochemical analysis for $\mathbf{1}^{\text{I}}$ is presented in Section II.2.7. The electrochemistry of $\mathbf{1}^{\text{Br}}$ is discussed in Section II.2.6.

2.6. CV Study of $[\text{ReBr}_2(\text{PNP})]$ under Ar and N_2

The CV of $\mathbf{1}^{\text{Br}}$ under Ar reveals two oxidations and two reductions. Both oxidations appear quasi-reversible (Figure A19). The first oxidation ($E_{p,a,1} = -0.25 \text{ V}$, $\nu = 0.1 \text{ Vs}^{-1}$) remains quasi-reversible up to $\nu = 5.0 \text{ Vs}^{-1}$ ($i_{\text{pf}}/i_{\text{pr}} \approx 1.8$), whereas the second oxidation is reversible at $\nu = 2.0 \text{ Vs}^{-1}$ ($E_{1/2} = +0.08 \text{ V}$, $i_{\text{pf}}/i_{\text{pr}} \approx 1$). Upon increasing ν , the ratio between both oxidations increases ($i_{p,a,1}/i_{p,a,2} = 1.4$ ($\nu = 0.1 \text{ Vs}^{-1}$), 3.0 ($\nu = 2.0 \text{ Vs}^{-1}$)), indicating that the second event corresponds to the product of initial oxidation and a coupled chemical reaction of $\mathbf{1}^{\text{Br}}$. The two reductions belong to freely in solution diffusing species, and appear irreversible up to $\nu = 2.0 \text{ Vs}^{-1}$ ($E_{p,c,1} = -1.78 \text{ V}$, $E_{p,c,2} = -2.21 \text{ V}$, $\nu = 0.1 \text{ Vs}^{-1}$), even when only scanning the first reduction (Figure 28 and A19).

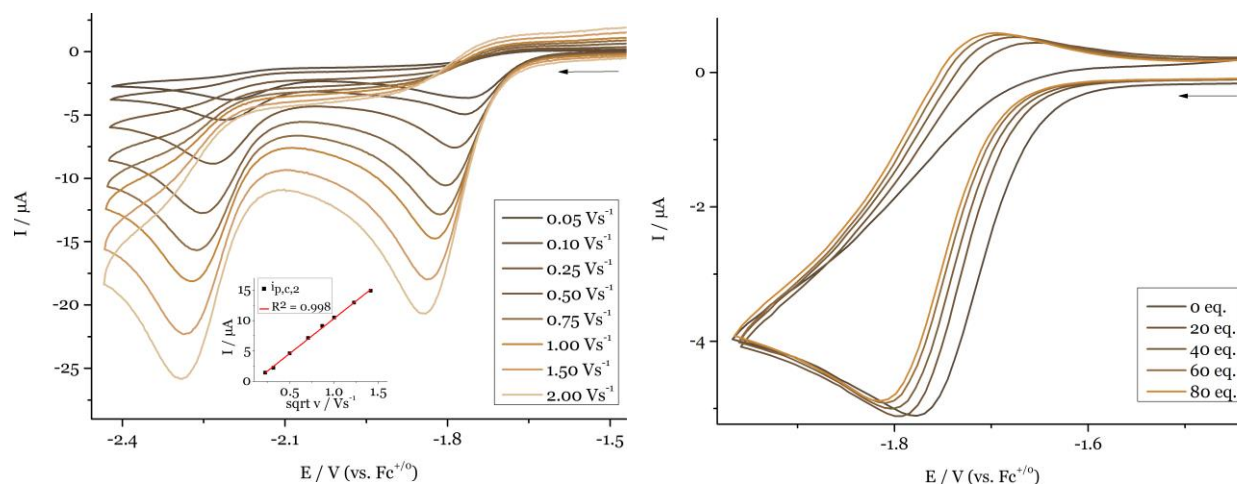


Figure 28. CV data of 1.0 mM solutions of $\mathbf{1}^{\text{Br}}$ in THF with 0.2 M $(n\text{Bu}_4\text{N})\text{PF}_6$ under Ar. Left: ν -dependence of the reductive area. Inset: plot of $i_{p,c,2}$ vs. $\nu^{1/2}$. The plot of $i_{p,c,2}$ vs. $\nu^{1/2}$ is presented in Figure A19. Right: first reductive wave with addition of 0-80 eq. of $(n\text{He}_4\text{N})\text{Br}$, $\nu = 0.1 \text{ Vs}^{-1}$.

Both reductions are coupled to a chemical reaction as shown by a cathodic shift when increasing ν , in line with their irreversibility. Parallel to this shift, the ratio between both reductions decreases upon increasing ν ($i_{p,c,1}/i_{p,c,2} = 1.9$ ($\nu = 0.05 \text{ Vs}^{-1}$), 1.1 ($\nu = 2.0 \text{ Vs}^{-1}$)). This indicates that after initial reduction, competing chemical reactions occur: a chemical reaction results in formation of the species reduced at the second reduction wave in an *ECE*-mechanism, and a reaction not forming that species (as less of the second wave is present at low ν).

Based on the similarities with **1**^{Cl} so far, we probed the possibility of halogen loss as chemical reaction coupled to the first reduction. In initial attempts, 0-20 eq. of (*n*He₄N)Br are titrated in a solution of **1**^{Br}, as these conditions proved sufficient to examine chloride loss from [**1**^{Cl}]⁻. Yet, the CV appearance changes only minimally, clearly reflecting the better leaving group properties of bromide. Titration of 0-80 eq. of bromide-ions shifts the first reduction cathodically by circa 0.035 V accompanied by the appearance of a small reverse wave. Although this reverse wave seems to plateau at lower scan rate, a continuous increase is observed at for instance $\nu = 2.0 \text{ Vs}^{-1}$ (Figure A19). These observations indicate that **1**^{Br} loses bromide after its initial reduction, forming [ReBr(PNP)], which is proposed to be reduced at the second reduction. This *EC^{Br}E*-mechanism is analogous to **1**^{Cl} as measured under Ar. Based on the bromide titration experiment, the coupled bromide loss after initial reduction will likely be more favoured and/or faster compared to chloride loss from [ReCl₂(PNP)]⁻. Furthermore, the difference in potential between [ReX₂(PNP)]^{0/-} and [ReX(PNP)]^{0/-} (X = Cl, Br) is larger for **1**^{Br} than for **1**^{Cl} ($\Delta E = 0.43 \text{ V}$, 0.30 V, respectively), although the latter value is based on simulated potentials and the former only on peak potentials.

In Figure 29, a comparison of the reductive area of **1**^{Br} measured under Ar and N₂ is shown. Similar to **1**^{Cl}, the first reductive event under N₂ changes into a sharp, multi-electron wave, and shifts anodically by circa 0.035 V. This shift was reproduced several times and represents an averaged result (Table A9). Furthermore, we see that the proposed [ReBr(PNP)]^{0/-} wave as found under Ar disappears when measuring under N₂ and instead a lower current reduction is observed ($E_p = -2.31 \text{ V}$, $\nu = 0.1 \text{ Vs}^{-1}$). Both observations (the anodic shift and the disappearing reduction) indicate the coupling of N₂-coordination within the first reduction wave. These similarities between the chloride and bromide platform lets us firmly hypothesise that the current increase and potential shift are attributed to the same N₂-splitting mechanism: reduction of [ReBr₂(PNP)] coupled to N₂-coordination and halogen loss, subsequent reduction of [ReBr(N₂)(PNP)] and dimerization to form **2**^{Br}. Both reductions are *potential inversed* and appear therefore as a sharp multi-electron wave. To get more insights in N₂-fixation on **1**^{Br}, ν -, concentration-, and N₂-pressure dependent CV data under N₂ were measured.

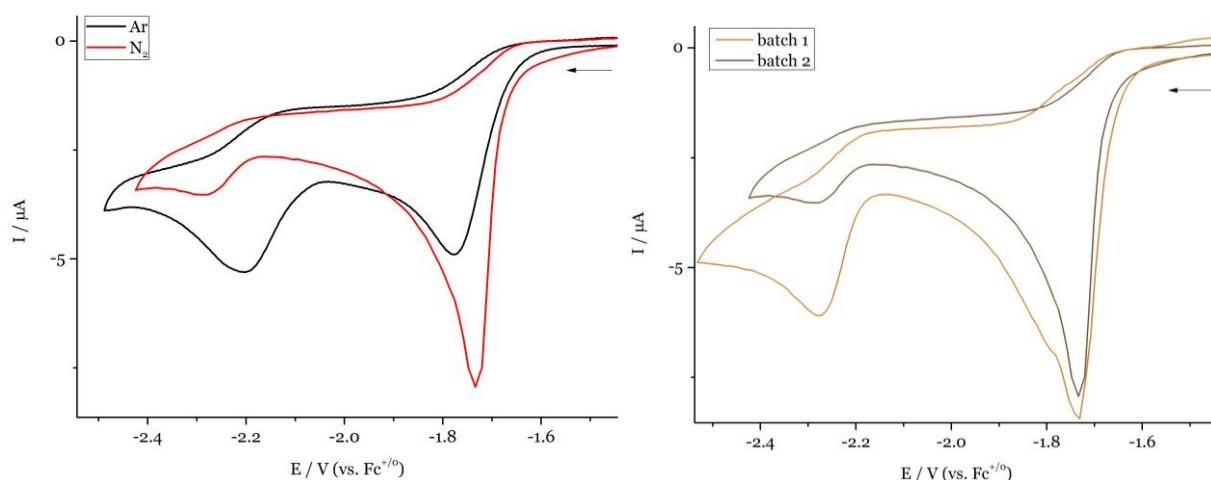


Figure 29. Left: CV comparison of a 1 mM $\mathbf{1}^{\text{Br}}$ solution with 0.2 M $(n\text{Bu}_4\text{N})\text{PF}_6$ in THF, measured under argon (black) and under dinitrogen (red), $\nu = 0.1 \text{ Vs}^{-1}$. Right: CV under N_2 of a 1.0 mM solution of $\mathbf{1}^{\text{Br}}$ of two different batches, $\nu = 0.1 \text{ Vs}^{-1}$.

However, when repeatedly measuring $\mathbf{1}^{\text{Br}}$ under N_2 , we noticed that every batch of $\mathbf{1}^{\text{Br}}$ showed slightly different reductive traces. An extreme example thereof is given in Figure 29, where the CV of two batches of $\mathbf{1}^{\text{Br}}$ are compared under otherwise identical conditions. In a batch (labelled batch 1 in Figure 29), we see a small, yet clearly visible feature right after the first reduction with $E_p = -1.8 \text{ V}$ and the second reduction wave ($E_p = -2.3 \text{ V}$) is much more prominent compared to a second batch. Comparing the $^3\text{P}\{^1\text{H}\}$ NMR spectra of both CV batches, we see that $\mathbf{1}^{\text{BrCl}}$ is present in different quantities (circa 8 % in the one batch, and 3 % in the second batch, based on both ^1H and $^3\text{P}\{^1\text{H}\}$ NMR integration). It is assumable that $\mathbf{1}^{\text{BrCl}}$ is reduced at a potential in between $\mathbf{1}^{\text{Br}}$ and $\mathbf{1}^{\text{Cl}}$ and is therefore loosely attributed to the reduction at $E_p = -1.8 \text{ V}$. In a future experiment, the addition of small quantities of chloride ions could qualitatively confirm this hypothesis, as $\mathbf{1}^{\text{BrCl}}$ is formed under those conditions. The increased current of the second reduction wave is not understood. The amount of impurities in batch 1 represent the most extreme case as observed within this work, but in general, the presence of varying amounts of impurities complicate the electrochemical analysis.

When measuring the reductive area of $\mathbf{1}^{\text{Br}}$ with increasing ν under N_2 , we observe that the first reduction strongly shifts cathodically, indicating coupled chemistry (Figure 30). From $\nu = 1.0 \text{ Vs}^{-1}$ and onwards, a small reverse feature is observed. Based on the results from $\mathbf{1}^{\text{I}}$ (*vide infra*), we attribute this onset of reversibility to the $[\text{ReBr}(\text{N}_2)(\text{PNP})]^{0/-}$ couple present within this wave. Titration of $(n\text{He}_4\text{N})\text{Br}$ into a solution of $\mathbf{1}^{\text{Br}}$, results in an increased reversibility at higher ν (Figure 30), and a cathodic shift at lower ν (about 0.02 V at $\nu = 0.1 \text{ Vs}^{-1}$, see Figure A20). This identifies bromide loss as a coupled chemical reaction after initial reduction of $\mathbf{1}^{\text{Br}}$ under N_2 . Increasing the concentration of $\mathbf{1}^{\text{Br}}$ and measuring CV of the reductive area shows that the

ratio decreases between the first and far cathodic waves ($i_{p,c,1}/i_{p,c,2} = 3.1$ at 0.5 mM and 1.7 at 4.0 mM, see Figure 30). This means that the species being reduced at the second wave likely is the product of reduction and a bimolecular reaction of **1**^{Br}. The thereby expected slight anodic shift on the first wave is not observed. In this measurement however, the before mentioned impurity is clearly visible and the data should be handled with care.

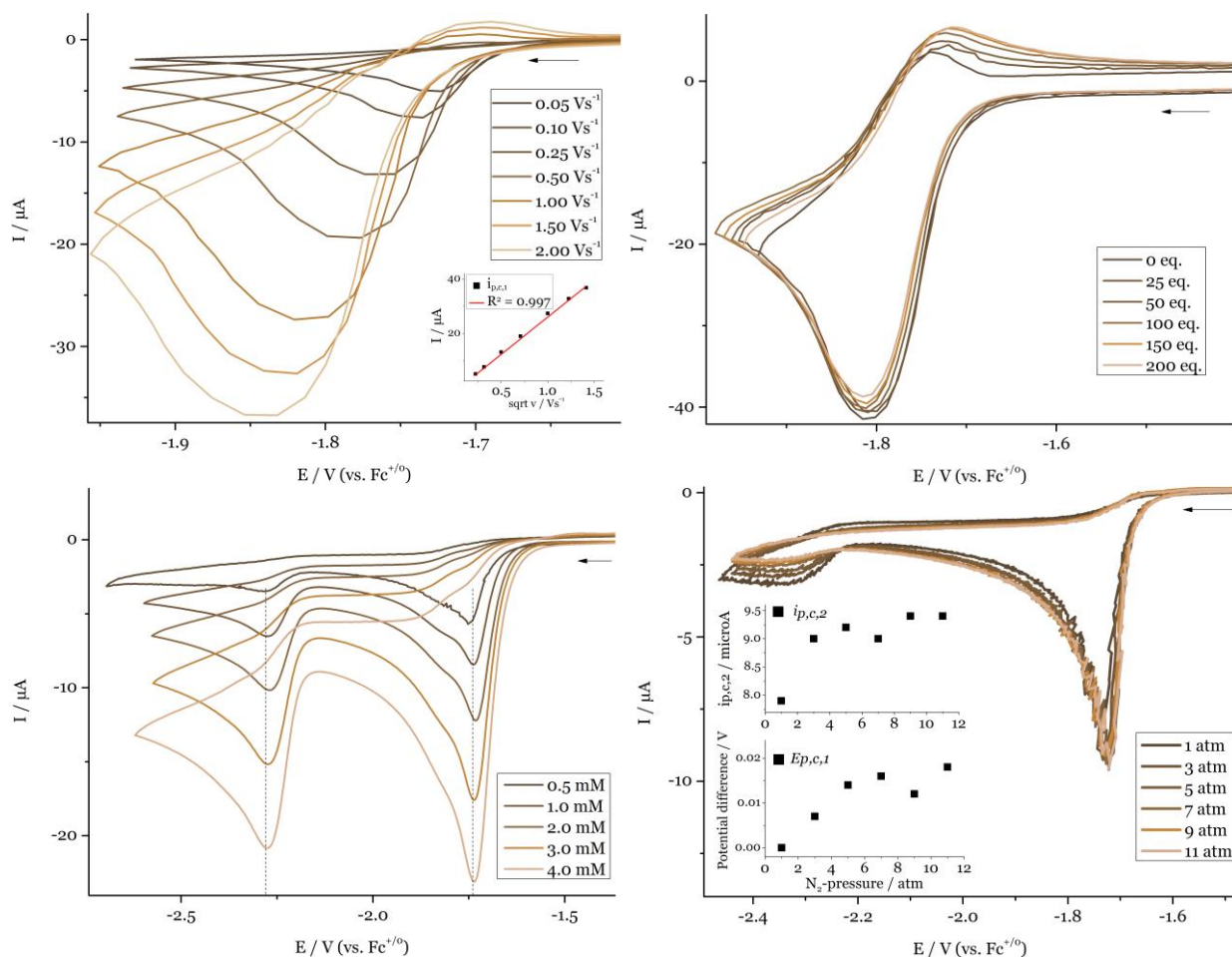
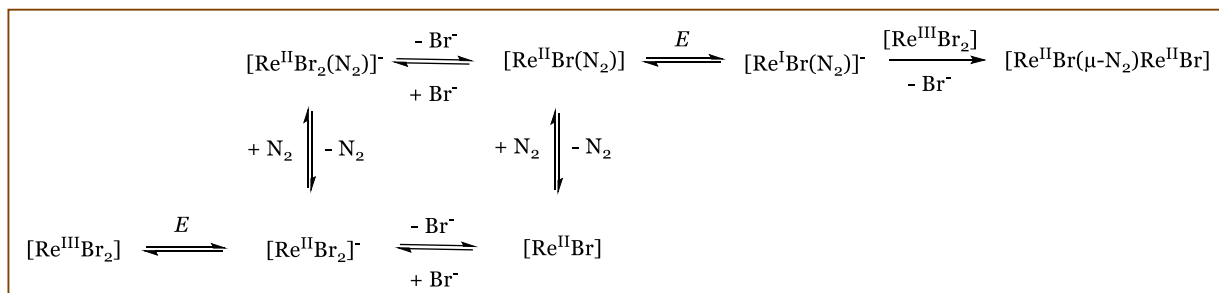


Figure 30. CV data of 1.0 mM solutions of **1**^{Br} in THF with 0.2 M (*n*Bu₄N)PF₆ under a N₂ atmosphere. Top left: scan rate dependence of the first reduction. Inset: plot of $i_{p,c,1}$ vs. $v^{1/2}$. Top right: first reductive wave with addition of 0-200 eq. of (*n*He₄N)Br, $v = 2.0$ Vs⁻¹. Bottom left: concentration dependence of both reductions, $v = 0.1$ Vs⁻¹. Bottom right: N₂-pressure dependence of a 1.0 mM solution, $v = 0.1$ Vs⁻¹. Inset top: plot of $i_{p,c,2}$ vs. N₂-pressure. Inset bottom: plot of peak potential difference of $E_{p,c,1}$ vs. N₂-pressure (compared to 1 atm).

Upon increasing the N₂-pressure, we see a small increase of current on the first reduction wave and a slight anodic shift of about 0.015 V (Figure 30). This shift could indicate that the N₂-coordination reaction on **1**^{Br} is influenced by increasing the N₂-concentration, and can therefore only be moderately fast or having an equilibrium constant closer to unity (in contrast to the situation of **1**^{Cl}: $K_3 \approx 1 \cdot 10^4$ M⁻¹, $k_3 > 1 \cdot 10^7$ M⁻¹ s⁻¹). However, the data are too noisy to interpret firmly. Clearer is the gradual current decrease of the second reduction, likely indicating that

formation of the corresponding species is in competing with a N₂-binding reaction after the first reduction wave.



Scheme 47. Proposed mechanistic model based on the CV data of **1^{Br}** for N₂-splitting. The PNP-ligand is omitted for clarity.

To summarise the CV of **1^{Br}** under N₂, we propose that initial reduction of [ReBr₂(PNP)] is coupled to both bromide loss and N₂-coordination, followed by a second reduction assigned to the [ReBr(N₂)(PNP)]^{0/-} couple, similar to **1^{Cl}** (Scheme 47). Based on this analogy, we propose that after the second reduction, dimerization and subsequent bromide loss take place to form **2^{Br}**. We hypothesise that N₂-coordination on **1^{Br}** is slower and more in equilibrium compared to **1^{Cl}**. Therefore, the order of bromide loss and N₂-coordination after initial reduction cannot be specified, see Scheme 47. All further in-depth analyses by digital simulation to confirm this N₂-activation model are hampered by the small impurity present in the starting material and the inability to get reproducible data. We leave the bromide platform at this qualitative level.

2.7. CV Study of [ReI₂(PNP)] under Ar and N₂

Since the electrochemical features of **1^I** are strikingly different compared to its chloride and bromide congeners, this platform has a high potential to expand our mechanistic understanding for N₂-splitting and herein an extended electrochemical analysis of **1^I** is presented.

The oxidative area of **1^I** reveals a diffusion-controlled but quasi-reversible oxidation that becomes fully reversible from 1.0 Vs⁻¹ onwards ($E_{1/2} = -0.23$ V), see Figure A21. Two small waves are observed afterwards ($E_{p,a,2} = +0.20$ V, $E_{p,a,3} = +0.50$ V), that disappear at higher ν . They are therefore attributed to products formed by oxidation and partially occurring coupled chemical reaction(s) of **1^I**. Comparable behaviour was observed for the bromide and chloride congener (see above and Chapter II.3, respectively). More anodically, a second irreversible oxidation appears ($E_{p,a,3} = +0.65$ V, $\nu = 0.1$ Vs⁻¹).

Analogous to **1^{Cl}** and **1^{Br}**, **1^I** also shows two reductions in its CV measured under Ar. The first reduction ($E_{p,c,1} = -1.61$ V, $\nu = 0.1$ Vs⁻¹, see Figure 31) appears irreversible over a wide scan rate range (from 0.05 Vs⁻¹ up to 3.0 Vs⁻¹) and couples to a chemical reaction due to its strong cathodic shift upon increasing ν . The second reduction appears 0.6 V more cathodic, which shows the onset of a reverse wave from 0.5 Vs⁻¹ ($E_p = -2.23$ V, $\nu = 2.0$ Vs⁻¹, see Figure A21) and shifts moderately cathodic when scanning at higher ν . Both reductions belong to freely diffusing species in solution. Increasing the Re-concentration from 0.5 to 3.5 mM leaves the first reduction wave barely untouched, whereas the second reduction feature shifts cathodically by about 0.035 V, see Figure A21. The ratio between both reduction waves is unaffected ($i_{p,c,1}/i_{p,c,2} \approx 2.3$ for 0.5 mM and ≈ 2.5 for 3.5 mM). On the contrary, scan rate dependent data show an increased ratio at higher ν ($i_{p,c,1}/i_{p,c,2} \approx 2$ for 0.1 Vs⁻¹ and ≈ 1 for 2.0 Vs⁻¹), see Figure 31. This behaviour indicates that a chemical reaction is coupled to the initial reduction of **1^I**, which prevents formation of the species reduced at the second reduction wave, i.e. a decomposition pathway. In general, the current of **1^I** for a one-electron transfer at 1.0 mM (circa 4.5 μ A) is below that for **1^{Cl}** (circa 5 μ A). This is traced back to their different diffusion constants via the Randles-Ševčík equation (see eq. 10 in Section IV.6.4): D for **1^{Cl}** is about $9.1 \cdot 10^{-6}$ cm²s⁻¹, whereas **1^I** displays a D of $8.2 \cdot 10^{-6}$ cm²s⁻¹ as determined by ¹H DOSY NMR, attributed to its increased size.

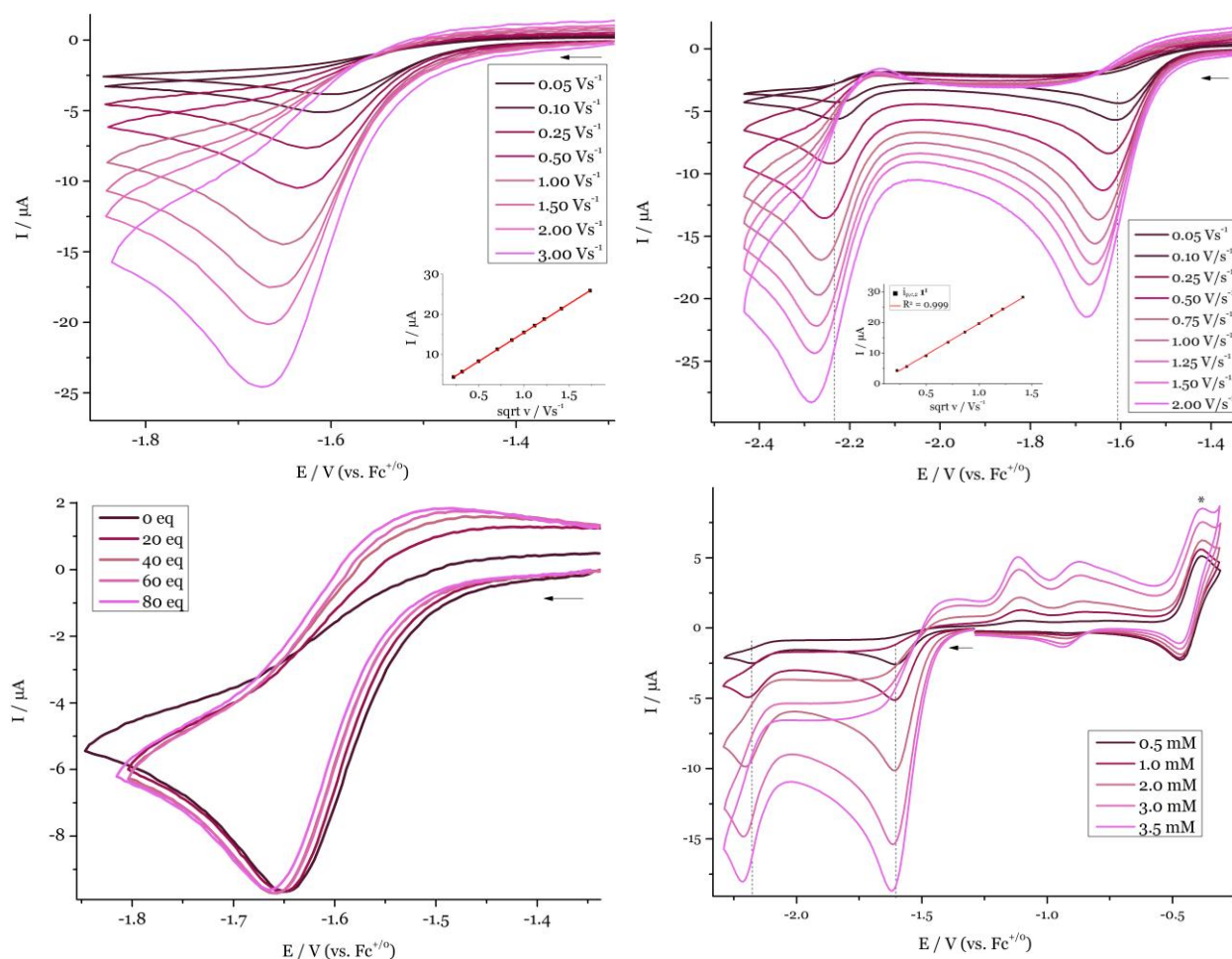


Figure 31. CV data of **1I** in THF with 0.2 M $(n\text{Bu}_4\text{N})\text{PF}_6$ measured under Ar. Top left: scan rate dependence of the first reductive wave for a 1 mM solution. Inset: plot of $i_{p,c,1}$ vs. $v^{1/2}$. Top right: scan rate dependence of the two reductive waves for a 1.2 mM solution. Inset: plot of $i_{p,c,2}$ vs. $v^{1/2}$. Bottom left: first reductive wave with addition of 0-80 eq. of $(n\text{He}_4\text{N})\text{I}$, $v = 1.0 \text{ Vs}^{-1}$ for a 0.8 mM solution. Bottom right: concentration dependence of the two reductive waves at $v = 0.1 \text{ Vs}^{-1}$

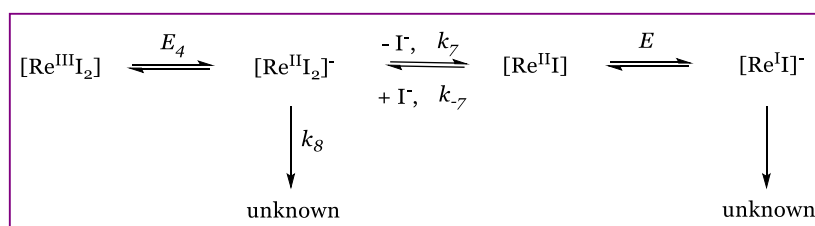
It is expected that reduction of **1I** is coupled to halide loss similar to **1Br** and **1Cl**, which connects both reductions. When setting up the experiment to titrate different equivalents of $(n\text{He}_4\text{N})\text{I}$ to **1I**, we faced problems with referencing the measurements: the oxidation of the commonly used $[\text{Fc}^*]^{+/0}$ oxidation couple ($E_{1/2} -0.427 \text{ V}$ in THF) is overlapping with iodide oxidation ($E_p = -0.4 \text{ V}$, Figure A21), which made referencing impossible at higher iodide concentrations. Therefore, various coordination complexes, and a $\text{Ag}^{+/0}$ - or $[\text{Fc}]^{+/0}$ -electrode were explored as (pseudo-) reference possibility, each with its own challenges, as described in Appendix A4.1. A sound method was found in using $[\text{Co}(\text{Cp}^*)_2]\text{PF}_6$ as reference compound, which is reduced more negative than **1I**. We reproduced the iodide titration five times and repeated it without the presence of a reference to get analysable data. Upon increasing addition of $(n\text{He}_4\text{N})\text{I}$, we observe a cathodic shift (up to 0.026 V at 0.1 Vs^{-1} from 0-80 eq.) and the onset of a reverse wave, indicating iodide loss as coupled reaction. Just as for **1Br**, we need substantial (and even more)

equivalents of halide to induce these changes. In a separate experiment, the stability of **1**^I against these high iodide concentrations was confirmed (Figure A25).

Based on these observations, we can formulate an *EC^IE*-type mechanism for **1**^I, where *C^I* represents iodide loss, to understand the CV data under Ar (see Scheme 48): after reduction of [ReI₂(PNP)]⁻, and iodide loss to [ReI(PNP)]⁻, this species is reduced once more. A decomposition pathway must be present on the Re(II) stage, either prior or after iodide loss, to account for the *v*-dependent ratio between [ReI₂(PNP)]⁻ and [ReI(PNP)]⁻, and the only limited reversibility upon titration of iodide.

The nature of the electron transfer of [ReI(PNP)]⁻, the formed species after the *EC^IE*-pathway, and its coupled chemical reaction(s) are not elucidated. In case of **1**^{Cl}, an irreversible electron transfer was included in the model to account for its irreversible appearance. In the iodide case, we observe the onset of a reverse wave at higher *v*, which makes the electron transfer of this reduction at least quasi-reversible and [ReI(PNP)]⁻ must undergo coupled chemistry. This reduction wave is not influenced by iodide titration (see Figure A21), ruling out the already unlikely iodide loss from this four-coordinate anionic species. A bimolecular reaction could be reasonable due to coordinatively unsaturated nature of this species; it is however in contrast to the cathodic peak potential shift upon increasing concentration. The nature of this chemical reaction remains unknown.

We turned to digital simulation to substantiate the *EC^IE*-proposal, as performed by Prof. Dr. I. Siewert, containing initial reduction of **1**^I (*E_d*), and reversible iodide loss (*K₇*, *k₇*) from [ReI₂(PNP)]⁻. As already analysed from the experiments, a unimolecular decomposition pathway (*k₈*) had to be included, also to account for the limited reversibility upon iodide addition to **1**^I (Scheme 48). The simulation parameters for the best fit are given in Table 5. Iodide loss after reduction is fast and the equilibrium constant represents a close to thermoneutral process. At this stage, halide loss between [ReCl₂(PNP)]⁻ (*k₁* = 1·10³ s⁻¹, *K₁* = 0.05 M) and [ReI₂(PNP)]⁻ (*k₇*, *K₇*, see Table 5) can be compared. These values clearly reflect the better leaving group character of iodide. From *trans*-[MoX(NEt)(dppe)₂] (X = Cl or I), a similar increase in halide loss was found when going from chloride to iodide (*k_{Cl loss}* ≈ 15 s⁻¹, *k_{I loss}* ≈ 50 s⁻¹).¹³⁸ The second reduction was not encountered in the simulation, as it is way beyond the potential required for N₂-splitting. In Scheme 48, it is depicted as a reversible electron transfer coupled to a not further specified chemical reaction (see above).



Scheme 48. Model for electrochemical reduction of **1^I** under Ar. The PNP-ligand is omitted for clarity.

Table 5. Thermodynamic and kinetic parameters obtained from digital simulations of **1^I** under Ar.ⁱ

1^I / Ar	E_4 / V	K_7 / M	k_7 / s ⁻¹	k_8 / s ⁻¹
	-1.665 $\alpha_4 = 0.5$ $k_{s,4} = 0.04 \text{ cm}^2/\text{s}$	3	$3 \cdot 10^4$	$1 \cdot 10^2$

A sensitivity analysis shows that the value for K_7 is quite solid: increasing its value would not lead to a peak potential shift upon addition of iodide and decreasing its value should induce a current increase upon iodide addition, both in contrast to the experiment. The values for k_7 and k_8 are interdependent and therefore less well defined. Yet, they need to be within the order of magnitude as stated in Table 5 to still describe the measurements well.

Comparing the CV data of **1^I** under Ar vs. N₂, we see that at low scan rates ($\nu = 0.1 \text{ Vs}^{-1}$) two reductions appear under N₂ at the potential of the first reduction under Ar. The new appearing reduction must therefore be a product of N₂-coordination (see Figure 32). When scanning more cathodic, the quasi-reversible cathodic feature assigned to the [ReI(PNP)]^{0/-} reduction under Ar ($E_{p,c} = -2.24 \text{ V}$, $\nu = 0.1 \text{ Vs}^{-1}$) disappears, and instead a lower current third reduction feature is visible ($E_{p,c} = -2.20 \text{ V}$, $\nu = 0.1 \text{ Vs}^{-1}$), that decreases upon increasing ν (see Figure 32 and A22). These observations are analogous to **1^{Br}** and **1^{Cl}**. To begin with, we focus on the first reductive area, as it is the relevant potential region for N₂-splitting.

Initial comparison between Ar and N₂ data of 1 mM solutions at low scan rates shows unchanged peak potentials and currents from Ar to N₂. We repeated referencing experiments on a 1 mM solution several times to substantiate this observation, see Table A15. The first reduction peak when going from Ar to N₂ only experiences a small anodic shift of 0.013 V at $\nu = 0.1 \text{ Vs}^{-1}$, yet with a standard deviation of circa 0.015 V, and an unchanged peak current at this scan rate. When measuring the ν -dependency of this region, the two reductions merge into each other. This

ⁱ Digital simulation performed by Prof. Dr. I. Siewert.

results in an overall current increase, shown by comparing the Ar with the N₂ data at higher scan rates ($\nu = 1.0 \text{ Vs}^{-1}$ in Figure 32). This phenomenon occurs as the first reduction feature shifts cathodic by 0.055 V from $\nu = 0.1 \text{ Vs}^{-1}$ to 2.0 Vs^{-1} , whereas the second reduction feature barely shifts over this range. Furthermore, the first reduction remains irreversible up to high ν , whereas the second features appears (quasi-)reversible already at low ν . The reversibility criterion i_{pf}/i_{pr} cannot be evaluated for this second reduction feature due to the proximity of both peaks, but its E_{pf} is constant with increasing ν . Strikingly, its peak-to-peak separation on this second feature is very close to its maximum value of 0.06 V at RT as described by the *Nernst* equation for a one-electron transfer. The current ratio $i_{p,c,1}/i_{p,c,2}$ (although not easily determined due to the close proximity of both peaks) increases with increasing ν under N₂, which is also clearly visualised in the ν -normalised CV (see Figure 32).

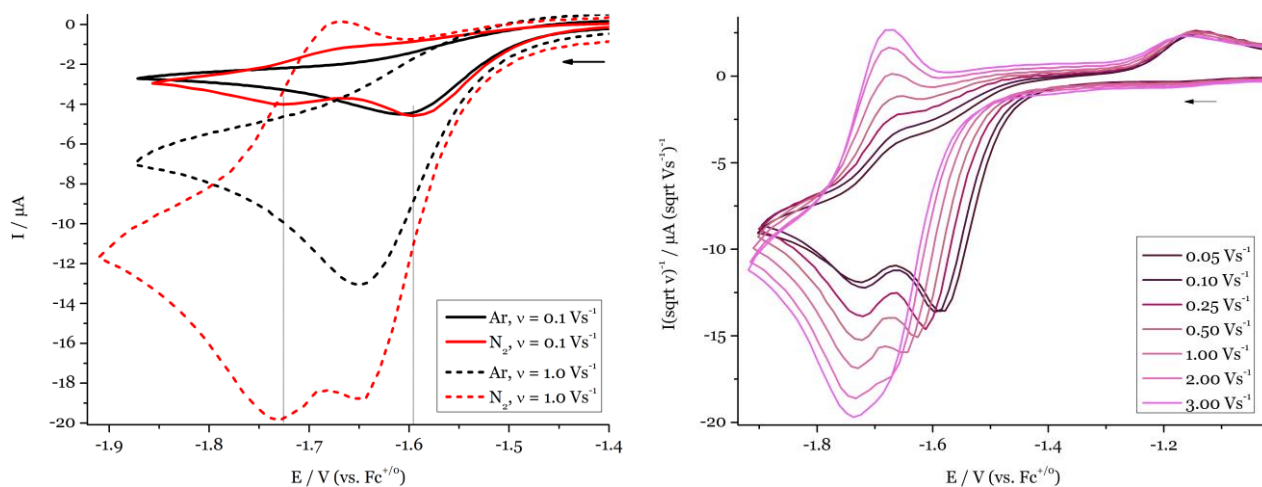


Figure 32. Left: CV comparison of a 1 mM **1**^I solution with 0.2 M (*n*Bu₄N)PF₆ in THF, $\nu = 0.1 \text{ Vs}^{-1}$ (solid line) $\nu = 1.0 \text{ Vs}^{-1}$ (dashed line), measured under Ar (black) and under N₂ (red). Right: scan rate normalised data of the first two reductive waves of a 1 mM **1**^I solution in THF with 0.2 M (*n*Bu₄N)PF₆ under an N₂ atmosphere.

Combining these three observations made so far about the first two reductions (the irreversibility on the first feature, its strong cathodic shift, and the changing current ratio between these waves upon increasing ν), we conclude that these are described best by an *ECE*-mechanism where coupled chemistry after initial reduction forms a species, which is reduced at the second reduction wave. These trends and especially the scan rate dependency of the overall current cannot simply be explained by the minimum model that we proposed for formation of **2**^{Cl}: stepwise Re(III/II) and Re(II/I) reductions connected by N₂-coordination and halide loss, yet in this iodide case without *potential inversion*. As described in Chapter II.1, the high (and ν -independent) current for **1**^{Cl} results from the two electron Re(III) reduction and subsequent comproportionation mechanism (labelled from here *2e/comp*). Alternatively, formation of **2**^X

by a one electron Re(III) reduction and Re(II)/Re(II) dimerization ($1e/dim$) should lead to lower currents. Based on the v -dependence of the overall current and the longer life-time of species with the formal Re^{II} oxidation state, we propose the existence of two competing pathways for the formation of **2I**: a $2e/comp$ pathway that is dominant at high scan rates in analogy to **2Cl** and a $1e/dim$ mechanism that governs at low scan rates, due to rapid Re(II)/Re(II) dimerization.

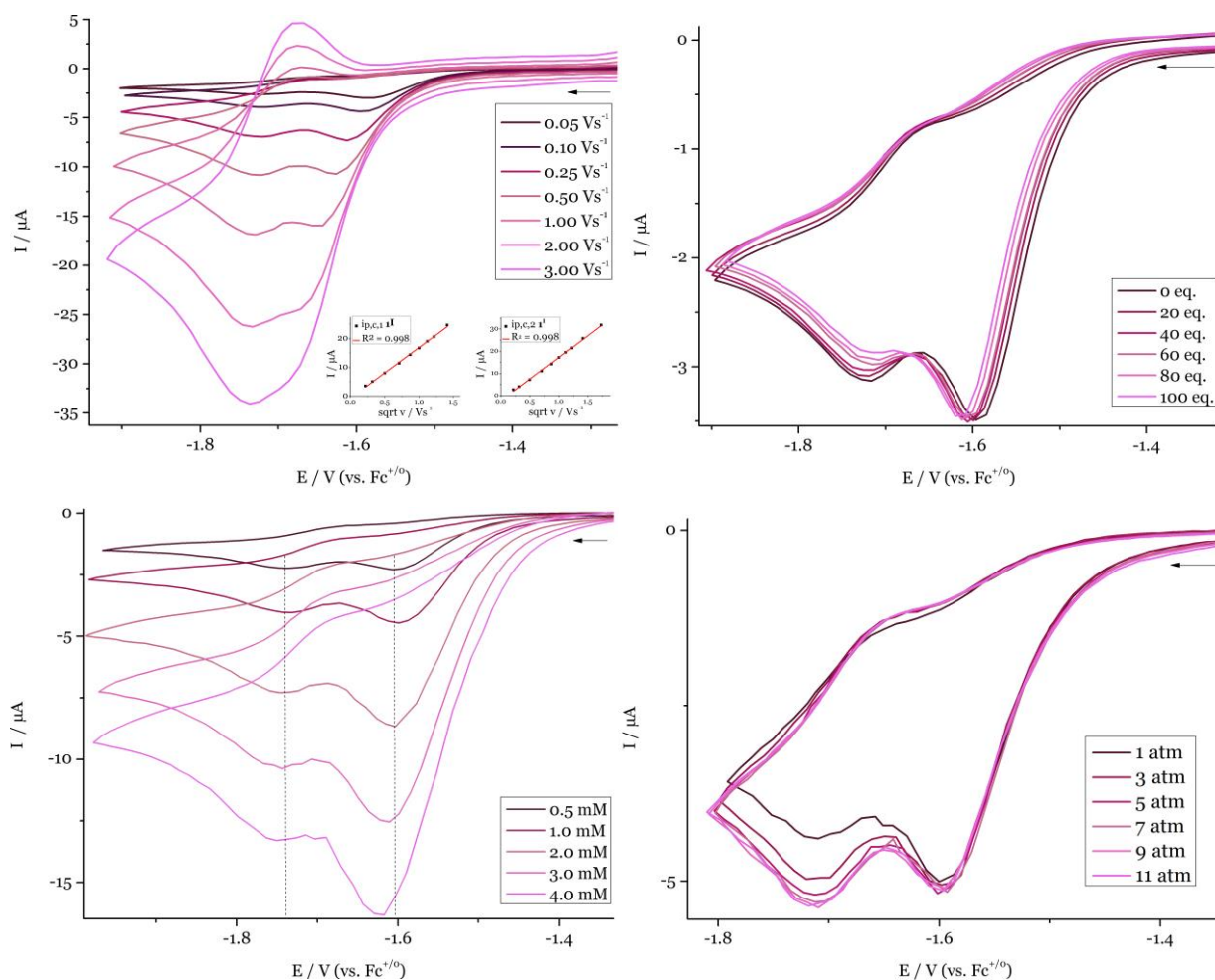


Figure 33. CVs of the first two reductions of **1I** under N₂ with 0.2 M (nBu₄N)PF₆ in THF. Top left: v -dependency of a 1 mM solution. Insets: plot of $i_{p,c,1}$ (left), or $i_{p,c,2}$ (right) vs. $v^{1/2}$ (for $i_{p,c,2}$ the same baseline as for $i_{p,c,1}$ was used). Top right: 0.8 mM solution with addition of (nHe₄N)I, $v = 0.1$ Vs⁻¹. Bottom left: conc. dependent data, $v = 0.1$ Vs⁻¹. Bottom right: N₂-pressure data of a 1 mM solution, $v = 0.1$ Vs⁻¹.

To examine this proposal in detail and the coupled chemistry on the first reduction, we measured CV in the presence of different equivalents of (nHe₄N)I, as referenced using [Co(Cp*)₂]PF₆ (see Section A4.1). Just as for reductively induced iodide loss under Ar, addition of substantial iodide source (0-100 eq.) is required, which shifts the first feature cathodically by 0.02 V at $v = 0.1$ Vs⁻¹ (Figure 33). This is accompanied by a decrease of the second feature, which is even more prominent when measuring a higher v (Figure A22). The species at the second reduction

wave is formed after iodide loss, which would agree with the proposal of it being the [ReI(N₂)(PNP)]^{0/-} couple.

When increasing the Re-concentration, a striking observation is the increasing ratio between both reduction features: the ratio between $i_{p,c,1}/i_{p,c,2}$ changes from ≈ 2.8 at 0.5 mM to ≈ 4.8 at 4.0 mM (Figure 33). Due to the proximity of both reductions, the trend is emphasised instead of the absolute numbers, as also reflected in the concentration-normalised data (Figure A22). Because of this tendency, the iodide titration under N₂ was performed at 0.8 mM concentration when the second feature is more present. We conclude that a bimolecular reaction coupled to initial reduction prevents formation of the species accountable for the second reduction feature. Due to this bimolecular reaction, a slight anodic shift is expected on the first wave with increasing concentration, which we barely observe (considering the 4 mM as outlier). Nevertheless, this behaviour supports the hypothesis that initially formed Re(II)-species can be directly consumed in a bimolecular pathway (*1e/dim*) prior to further reduction to Re(I).

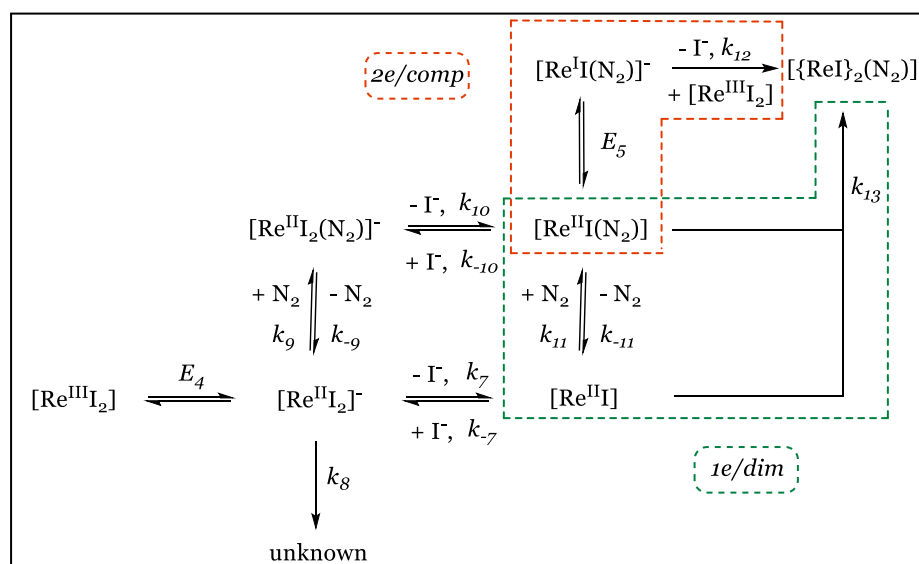
More cathodically, the reduction feature at $E_{p,c} = -2.20$ V, $\nu = 0.1$ Vs⁻¹ gains more prominence at increasing concentration: $i_{p,c,1}/i_{p,c,3}$ changes from 4.3 at 0.5 mM to 2.1 at 4.0 mM. Either the species belonging to this third reduction is formed when more of **1^I** is present, or when less of the second reduction takes place. Because of this latter possibility, it is initially tempting to assign this feature to the reduction of [ReI(PNP)]^{0/-} as observed under Ar, since its reduction potential is in a similar range. Yet, the decreasing current ratio indicates that this feature must be the product of a bimolecular reaction initiated by reduction of **1^I**. Secondly, no reversibility is shown for this feature at high ν at 4.0 mM (which is found for [ReI(PNP)]^{0/-}), therefore we can exclude this possibility.

The CV trace of **1^I** was also evaluated under increasing N₂-pressure, where we observe that the first reduction wave is invariant both in peak current and potential with respect to N₂-pressure (1-11 atm, see Figure 33), although the data are a bit noisy. The second reduction feature shows an initial increase to about 5-7 bars, after which additional N₂-pressures seems to not influence the peak current any further. These observations support the assumption that the second reduction to wave is [ReI(N₂)(PNP)]^{0/-}. Furthermore, a N₂-binding pre-equilibrium prior to the first reduction could be excluded based on high-pressure NMR spectroscopy ($K_{pre-equilibrium} < 1.0$ M⁻¹, see Section IV.6.2). The N₂-coordination reaction likely proceeds in a comparable time scale as iodide loss, due to a missing pronounced anodic shift of the initial reduction when going from Ar to N₂. It has yet to be slow enough to within the CV time scale regime, since the second reduction becomes more prominent with increasing ν and N₂-pressure

(indicating that on the CV time scale, it is still possible to influence this reaction). When measuring the extended reductive area, we see that the far cathodic reductive feature diminishes upon increasing N_2 -pressure (Figure A22), as observed for the bromide and chloride congeners.

Summarised, the above-discussed data show that under N_2 , $\mathbf{1}^I$ is reduced and subsequently coupled to iodide loss and N_2 -fixation (in unknown order), and a competing bimolecular reaction. The first two reactions form a species that is reduced at a slightly more electronegative potential compared to $\mathbf{1}^I$, hereby assigned to $[ReI(N_2)(PNP)]^{0/-}$. The observations are in line with the co-existence of both *2e/comp* and *1e/dim* pathways dependent on v - and Re -concentration to ultimately form dinuclear $\mathbf{2}^I$. With these guidelines from the experimental data in hand and the already substantiated Ar model, we turned to digital simulation of the CV-traces under N_2 .

A minimal mechanistic model could be derived by digital simulation performed by Prof. Dr. I. Siewert, as presented in Scheme 49. The simulation parameters for the best fit are given in Table 6. The parallel existence of both *2e/comp* and *1e/dim* pathways is needed to model the CV data satisfactory. In the following, all steps of these paths are discussed in more detail.



Scheme 49. Minimal mechanistic model for electrochemical reduction of $\mathbf{1}^I$ under N_2 to form $\mathbf{2}^I$. For each pathway (*1e/dim* or *2e/comp*), the defining reaction is highlighted. The PNP-ligand is omitted for clarity.

Table 6. Thermodynamic and kinetic parameters obtained from digital simulations of **1^I** under N₂.^j

1^I / N₂	K_9 / M ⁻¹	k_9 / M ⁻¹ s ⁻¹	K_{I0} / M	k_{I0} / s ⁻¹
	6·10 ⁵	1·10 ³	5·10 ⁻³	5
K_{II} / M ⁻¹	k_{II} / M ⁻¹ s ⁻¹	E_5 / V	k_{I2} / M ⁻¹ s ⁻¹	k_{I3} / M ⁻¹ s ⁻¹
1·10 ³	3·10 ⁴	-1.715 $\alpha_9 = 0.5$ $k_{s,9} = 0.5 \text{ cm}^2/\text{s}$	3·10 ⁴	1·10 ⁵

Starting from initial reduction of **1^I**, a reasonable fitting of the data is only possible if both reaction orders between N₂-coordination and iodide loss to ultimately form [ReI(N₂)(PNP)] are considered. [ReI₂(PNP)]⁻ either reacts with N₂ as described by K_9 and k_9 or loses iodide as present under Ar via K_7 (3 M) and k_7 (3·10⁴ s⁻¹). These reactions are in direct competition and although the N₂-coordination is thermodynamically more favoured, iodide loss is one order of magnitude faster. The subsequent reaction has the reversed nature: either iodide loss via K_{I0} and k_{I0} or N₂-coordination via K_{II} and k_{II} . Both N₂-coordination reactions underline our finding from Chapter II.1 that Re(II) is the oxidation state to coordinate N₂. The four equilibrium constants of these reactions interdepend, and a fixed point was found in K_7 as obtained from the measurements under Ar. In case N₂-coordination is the initial reaction to form octahedral [ReI₂(N₂)(PNP)]⁻, the increased N₂-affinity upon reduction from Re^{III} to Re^{II} ($K_{pre-equilibrium} < 1.0 \text{ M}^{-1}$ vs. $K_9 = 6 \cdot 10^5 \text{ M}^{-1}$) is even a little more expressed in this iodide case as compared to chloride (where $\approx 10^4$ increased affinity was found (Section II.1.5)). The subsequent iodide loss from the octahedral species is uphill ($K_{I0} = 5 \cdot 10^{-3} \text{ M}$) and rather slow ($k_{I0} = 5 \text{ s}^{-1}$), therefore only relevant at low scan rates. Compared to iodide loss from the five-coordinate reduction product [ReI₂(PNP)]⁻ ($K_7 = 3 \text{ M}$, $k_7 = 3 \cdot 10^4 \text{ s}^{-1}$), this is both substantially less favoured and slower. This finding is in contrast to the chloride situation: a comparable or even faster halide loss was found from the octahedral species compared to the five-coordinate ($k_{I,Cl, 5\text{-coordinate}} = 1 \cdot 10^3 \text{ s}^{-1}$, $k_{I,Cl, 6\text{-coordinate}} > 5 \cdot 10^2 \text{ s}^{-1}$). This behaviour in the case of chloride was attributed to the PNP-ligand properties (bulky *tert*-butyl moieties and a strong PNP_{amide} π -donor that facilitates halide loss). If steric factors would play a large role, dissociation of bulkier iodide from the octahedral species [ReI₂(N₂)(PNP)]⁻ is expected to occur easier (both in comparison to the five-coordinate [ReI₂(PNP)]⁻, and the chloride octahedral congener). In light of the contradicting findings herein, halide loss might be governed by electronic factors. From the 5-

^j Digital simulation performed by Prof. Dr. I. Siewert.

([ReX₂(PNP)]⁻) to the 6- ([ReX₂(N₂)(PNP)]⁻) coordinate complex, the negative charge is partially compensated by coordination of the π -accepting N₂-ligand. Combined with the decreased donor properties of iodide vs. chloride (*vide infra*), this can rationalise the different halide loss patterns.

From [ReI(N₂)(PNP)], the *2e/comp* pathway considers reduction of [ReI(N₂)(PNP)] (E_5) at a potential slightly negative compared to initial reduction of **1^I**, thereby showing no potential inversion, which is discussed in Section II.2.8. This reduction is followed by a comproportionation with [ReI₂(PNP)] and iodide loss towards **2^I** (k_{12}). This reaction is in the same order of magnitude compared to the chloride case ($k_5 \approx 7 \cdot 10^3 \text{ M}^{-1} \text{ s}^{-1}$). For the *1e/dim* pathway, including dimerization of two Re(II)-species, reasonable agreement between experiment and simulation is obtained by considering a bimolecular reaction between [ReI(PNP)] and [ReI(N₂)(PNP)] to form **2^I** (k_{13}). These interpretations are supported by the basic comparison between the CVs of **1^X** (X = Cl, Br, I): the absence of the potential inversion increases the lifetime of Re(II)-species, enabling their direct dimerization. At high scan rates, **2^I** is mainly formed via the comproportionation reaction, since the reduction potential for [ReI(N₂)(PNP)] is reached much faster. This potential is not reached when the CV is scanned at slow scan rates and the bimolecular pathway becomes the dominant pathway, just as for higher Re-concentrations.

2.8. Halide Comparisons and trends

(Electro)chemical N₂-splitting and (electro)chemical mechanistic investigations are now performed on three starting platforms that only vary their halide ligand, which allows us to comment on results or trends that we found during this study.

Trends in N₂-splitting abilities

The determined yields of **3^{Br}** and **3^I** are listed in Table 7, with yields for **3^{Cl}** added for comparison. In general, **3^{Br}** and **3^I** can be obtained in moderate to high yields via chemical N₂-splitting.

Table 7. Spectroscopic yields of **3^{Cl}**, **3^{Br}**, and **3^I** via (electro)chemical N₂-splitting.^a

Chemical		3^{Cl}	3^{Br} , ^c	3^I , ^c
	Na/Hg	85 % ^b	80 %	30 %
	Co(Cp*) ₂	75 % ^b	45 %	60 %
	Cr(Cp*) ₂	-	-	58 %
Electrochemical	<i>E</i> _{appl.} /V			
	-1.90	60 %	-	-
	-1.72	-	55 %-	65 %
	-1.58	-	-	50 %

^a Average yield over at least two runs, individual yields listed in the Experimental Section IV.5. - indicates the experiment was not performed. ^b yields determined via integration of all ³¹P{¹H}NMR peaks. ^c Yields determined via addition of an internal standard either via ³¹P{¹H} NMR or ¹H NMR spectroscopy.

The reduction potential of Cr(Cp*)₂ (-1.47 V)⁵⁹ should regarding the reduction potential of **1^I** not be sufficient to reduce this compound; (partial) precipitation of [Cr(Cp*)₂]I likely adds the required driving force. The best yields for **3^{Cl}** and **3^{Br}** were obtained using Na/Hg, yet **3^I** is only formed in low yields. The large overpotential when using Na/Hg to reduce **1^I** (circa 0.7 V) likely leads to unproductive over-reductions. Homogeneous reductant Co(Cp*)₂ is performing slightly worse for synthesis of **3^{Cl}** and **3^{Br}** (vs. Na/Hg), which can be the effect of very efficient halide removal by precipitation of NaCl or NaBr, respectively.

It was imagined that exchanging the halide ligands from chloride to bromide and iodide would influence the efficiency of N₂-splitting, based on their different leaving group- and steric properties. However, it is concluded that for both electro- and chemical N₂-activation, the nitride yields are basically independent of the halide of the starting platform. The differences within chemical N₂-splitting (85 % **3^{Cl}** and 80 % **3^{Br}** using Na/Hg vs. 60 % **3^I** for Co(Cp*)₂), are comparably small and might be the result of the different nature of the reductant (heterogeneous vs. homogeneous). A heterogeneous reductant without a large overpotential might be more beneficial due to higher local concentrations and therefore allows less decomposition on the Re(II)-level. In future research, it would be interesting to examine a heterogeneous reductant in the potential range required for **1^I** to examine this hypothesis.

For electrochemical N₂-splitting, the yield for all three platforms is around 60 % and FE efficiency is around 50 %. In case of **1^I**, a slightly better reaction outcome is observed when electrolyzing at the peak potential of the second reduction. This CPE potential clearly triggers the *2e/comp* over the *1e/dim* pathway. The higher nitride yield might indicate that this first

pathway is more efficient, although in general a more negative CPE potential will speed up reactions,¹⁸⁸ and therefore maybe afford higher nitride yields.

Without observing a preferred halide concerning nitride yields, the iodide platform clearly overrules bromide and chloride. Moving to the heavier homologues in the halogen group, a 0.15 V less electronegative reducing agent or applied potential is required for N₂-splitting. Moving to these more benign conditions upon halide exchange is an important finding for future research.

Trends in redox potentials

During analysis of the three halide-substituted platforms, we encountered three sets of redox potentials. The redox potentials of fully reversible Re(VI/V) oxidation of **3^X** (X = Cl, Br, and I), the Re(II/I) reduction of [ReCl(N₂)(PNP)] and [ReI(N₂)(PNP)], and the Re(III/II) reduction of **1^X**. In the latter case, we experimentally only have access to a peak potential for **1^{Br}**, but for **1^{Cl}** and **1^I**, the redox potential was obtained via digital simulation. Comparing these, we clearly see a less electron rich metal centre going down the halide group.

Table 8. Redox potentials of **1^X**, [ReX(N₂)(PNP)], and **3^X**.

	Re(III/II) 1^X		[ReX(N ₂)(PNP)]	Re(IV/V) 3^X
	E_p / V	E_o (sim.) / V	E_o (sim.) / V	$E_{1/2}$ / V
Cl	-1.96	-2.00	-1.84 - -1.88	-0.09
Br	-1.78	- ^a	- ^a	-0.05
I	-1.61	-1.67	-1.72	+0.01

^a – simulation not performed for the bromide platform

As elaborated in Section I.1.4, chloride, bromide, and iodide have basically the same *Lever Parameter* (E_L Cl/I: -0.24 V, E_L Br: -0.22 V), which implies halogen-substitution should barely shift the redox potential.⁶⁴ This is in contrast to the here shown results. However, the Re(VI/V) couple was not assessed by Lever, and the Re(III/II) couple is only examined on a limited database. Within this already limited database, it is basically impossible to examine for trends amongst the halide ligands (16, 3, and o complexes are examined containing Cl, Br, and I, respectively).⁶⁵ Therefore, we do not rely on the *Lever Parameters* to interpret these Re-trends.

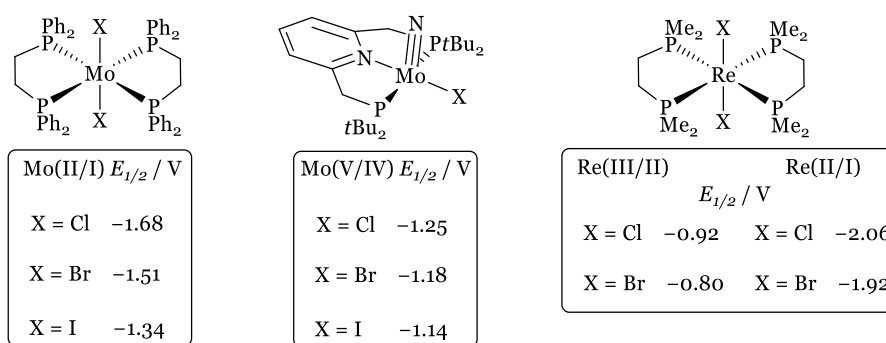


Figure 34. Comparison to other compound series that show different redox potentials upon halide exchange by the groups of Pickett, Nishibayashi, and Deutsch.^{52,163,189}

Beyond the *Lever Parameters*, there seems to be literature precedent that the donor properties decrease going from Cl to I. For instance, the group of Pickett examined the redox characteristics of $[\text{MoX}_2(\text{dppe})_2]$ (dppe = 1,2-bis(diphenylphosphino)ethane), and find an increasingly milder reduction potential going down the group ($E_{1/2} = -1.68$ V (X = Cl), -1.51 V (X = Br), -1.34 V (X = I) vs. the saturated calomel electrode (SCE)), see Figure 34. These values should be handled with some care: although all reductions show a reverse peak, at lower scan rates they couple to halide loss and it is not specified at which scan rate these potentials are read off.¹⁸⁹ Another example is given by Nishibayashi, who established the five-coordinate Mo nitrides $[\text{MoNX}(\text{PN}_{\text{pyr}}\text{P})]$ ($\text{PN}_{\text{pyr}}\text{P} = 2,6\text{-bis}(\text{di-}t\text{-tert-butyl-phosphinomethyl})\text{pyridine}$) with X = Cl, Br, I. They share a very mild, reversible Mo(V/IV) oxidation revealing an anodic shift when going from Cl to I ($E_{1/2} = -1.25$ V (X = Cl), -1.18 V (Br), -1.14 V (I)). These shifts are strikingly similar to our $\mathbf{3}^{\text{X}}$ series. It is also reported that these nitrides can be reduced, yet these waves appear irreversible and are substantially decreased in current compared to the one electron oxidations, and are therefore not over-interpreted.⁵² Deutsch and co-workers isolated Re(III) $[\text{ReX}_2(\text{dmpe})_2]^+$ (dmpe = 1,2-bis(dimethylphosphino)ethane) with X = Cl and Br, and both show two subsequent and reversible reductions with an anodic shift when going from Cl to Br ($E_{1/2} = -0.92$ V for $\text{Re}^{\text{III/III}}$ and -2.06 V for $\text{Re}^{\text{II/I}}$ (X = Cl), $E_{1/2} = -0.80$ V for $\text{Re}^{\text{III/II}}$ and -1.92 V for $\text{Re}^{\text{II/I}}$ (X = Br)). These reductions were actually used to derive the *Lever Parameters*, partially covering for the different reduction potentials, yet not to its full extent.

An explanation for this decreased electron donating property when going down the halide group is summarised by Lautens and Fagnou, focusing on the interaction between the halide ligands and the metal.¹⁹⁰ This interaction consists of a ligand to metal σ -donation, which increases down the halide group based on decreasing electronegativity. This is accompanied by a π -donation from the ligand into empty metal d-orbitals, which decreases going down the halide group (Figure 35). When this latter interaction dominates (when a d-orbital of appropriate symmetry

is vacant), iodide is the least donating ligand within the halide series as here examined. In both Re(III) $\mathbf{1}^X$ and Re(V) $\mathbf{3}^X$, the d-electron count could allow an appropriate d-orbital to accept π -donation. To substantiate this rather qualitative picture, Odom developed the *Ligand Donor Parameters* (LDP) for a series of monoanionic ligands, as quantified via the rotational barrier of the amide groups in $[\text{CrN}(\text{NiPr}_2)_2\text{X}]$ as determined via Spin Saturation Transfer NMR spectroscopy. The stronger the ligand X donates, the lower the rotational barrier for the amide is, leading to LDP's in the unit of energy per mole. For the here examined halides, they find decreasing donating properties in the order $\text{Cl} > \text{Br} > \text{I}$ (LDP in $\text{kcal mol}^{-1} = 15.05 \pm 0.29$ (Cl), 15.45 ± 0.30 (Br), 15.80 ± 0.30 (I)).¹⁹¹ This could provide an explanation for the lower electron donating properties going to the heavier halide homologies. It should be noted that this system represents a high valent complex, which in our case would be only valid for the trend for $\mathbf{3}^X$. Nevertheless, this explanation line matches with our results as obtained herein.

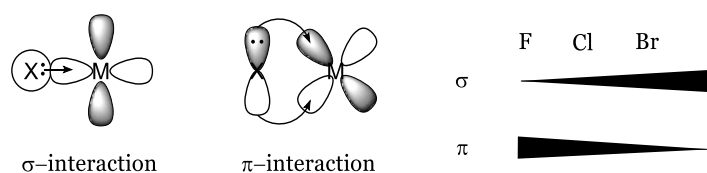


Figure 35. Metal-halide σ - and π -interactions.

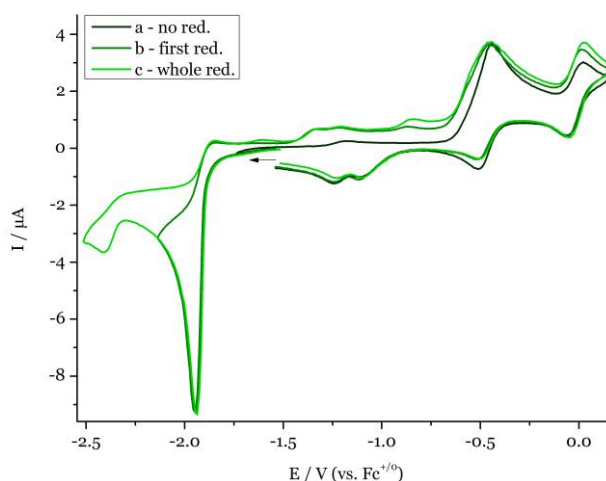
Another trend in the redox-potentials is shown in the N_2 -splitting mechanistic model, where two reductions are proposed, $[\text{ReX}_2(\text{PNP})]^{0/-}$ and $[\text{ReX}(\text{N}_2)(\text{PNP})]^{0/-}$. For $\mathbf{1}^{\text{Cl}}$ and $\mathbf{1}^{\text{I}}$, the reduction potentials could be obtained via digital simulation of the CV traces, and were additionally calculated by DFT (Table 9). The chemical difference between both reductions is a) different formal oxidation state: Re(III) for the first and Re(II) for the latter reduction, and b) the exchange of a donating halide ligand with a π -accepting N_2 -ligand. The balance between both phenomena cause for a *potential inversion* in case of bromide and chloride, and a peak deconvolution in case of iodide. This underlines the statement about the different donation properties of the halides: since chloride and bromide are more electron donating, the influence on exchanging one for a N_2 -ligand has a larger influence than the different formal oxidation state. The opposite must be the case for iodide, the decreased donor properties are less of an influence than the formal changed oxidation state.

Table 9. Simulated and calculated redox potentials of $[\text{ReX}_2(\text{PNP})]^{0/-}$ and $[\text{ReX}(\text{N}_2)(\text{PNP})]^{0/-}$.

	$[\text{ReX}_2(\text{PNP})]^{0/-}$		$[\text{ReX}(\text{N}_2)(\text{PNP})]^{0/-}$	
	$E_o(\text{sim}) / \text{V}$	$E_o(\text{calc.}) / \text{V}^{\text{k}}$	$E_o(\text{sim}) / \text{V}$	$E_o(\text{calc.}) / \text{V}$
Cl	-2.00	-1.98	-1.84 to -1.88	-1.94
I	-1.67	-1.58	-1.72	-1.69

Visibility of dinuclear N_2 -bound $\mathbf{2}^{\text{X}}$ in CV

The product of the proposed N_2 -binding, halogen loss and dimerization reactions is dinuclear $\mathbf{2}^{\text{X}}$ and we probed for its presence in CV. There is precedent in literature that N_2 -bridging complexes with a $(\delta^4)\pi^{10}$ configurations can be oxidised twice to the $\delta^4\pi^9$ ($[\mathbf{2}^{\text{X}}]^+$) and $\delta^4\pi^8$ ($[\mathbf{2}^{\text{X}}]^{2+}$) state. The corresponding potentials are (rather) mild, as was found for Cummins π^{10} system $[\{\text{Mo}(\text{N}(t\text{Bu})(3,5\text{-C}_6\text{H}_3(\text{CH}_3)_2)_3\}_2(\mu\text{-N}_2)]$ ($E_{1/2} = -1.46 \text{ V}$ and -0.32 V (THF))²⁴, the $\delta^4\pi^{10}$ system $[\{\text{ReCl}_2(\text{PNP}^{\text{IPr}})\}_2(\mu\text{-N}_2)]$ as found by Dr. F. Wätjen (né Schendzielorz) ($E_{1/2} = -1.03$ and -0.37 V (THF))⁷¹, and the tungsten π^{10} dimer $[\{\text{W}(\text{N}(\text{CH}_2\text{CH}_2\text{N}(4\text{-}t\text{BuC}_6\text{H}_4)_3)_2(\mu\text{-N}_2)]$ by Schrock ($E_{1/2} = -1.63$ and -0.37 V (THF)).¹⁹²

**Figure 36.** Exemplary CV traces of a 1.0 mM solution of $\mathbf{1}^{\text{Cl}}$ in THF with 0.2 M $(n\text{Bu}_4\text{N})\text{PF}_6$ under an N_2 atmosphere. Measured three ranges, scanning through: a) only the oxidative area, b) the first reductive area, then the oxidative area, c) the whole reductive area, then the oxidative area.

Upon measuring CV of $\mathbf{1}^{\text{X}}$, we scanned a) in oxidative direction only, b) through the first reduction wave(s) which are proposed to productively form $\mathbf{2}^{\text{X}}$ and subsequently the oxidative area, and c) through the whole reductive area and subsequently the oxidative area (see Figure 36 for the CVs of $\mathbf{1}^{\text{Cl}}$ and A26 for the CVs of $\mathbf{1}^{\text{Br}}$ and $\mathbf{1}^{\text{I}}$). This comparison allows us to identify if

^k Calculations performed by Dr. M. Finger using: Mo6/def2-TZVP (SMD: THF) // D3(BJ)-PBEo/def2-TZVP, def2-SVP(C,H)

oxidative features of $\mathbf{2}^{\mathbf{X}}$ are present after scanning condition b. Unfortunately, no oxidative features are present that resemble two successive (reversible) oxidations. All new features up to a potential of 0 V are present in the CV following conditions of b and c, which indicates that the proposed oxidations of $\mathbf{2}^{\mathbf{X}}$ are not visible in the CV. Likely, the formation of $\mathbf{2}^{\mathbf{X}}$ is too slow to be observed in the CV in substantial quantities.

Another observation that triggered the search for $\mathbf{2}^{\mathbf{X}}$ in the CV data, is the appearance of an irreversible, small reduction under N_2 at $E_p = -2.4$ V for $\mathbf{1}^{\text{Cl}}$, -2.3 V for $\mathbf{1}^{\text{Br}}$, and -2.2 V for $\mathbf{1}^{\text{I}}$ ($\nu = 0.1 \text{ Vs}^{-1}$). This feature grasps attention in the ν -, N_2 - and concentration-dependent data that could hint its belonging to $\mathbf{2}^{\mathbf{X}}$. In both before mentioned $(\delta^4)\pi^{10}$ systems by Cummins and Wätjen, an irreversible reduction is observed at $E_p = -2.4$ V ($\nu = 0.1 \text{ Vs}^{-1}$)^{71,193}. The calculated reduction potentials of $\mathbf{2}^{\mathbf{X}}$ are in the same range ($E_{p,\text{calcd.}} = -2.61$ V ($\mathbf{2}^{\text{Cl}}$), -2.58 V ($\mathbf{2}^{\text{Br}}$) and -2.39 V ($\mathbf{2}^{\text{I}}$))^k. When measuring $\mathbf{1}^{\mathbf{X}}$ ν -dependent under N_2 , this feature diminishes with increasing scan rate, strongly indicating that the corresponding species is a follow up product of a relatively slow chemical reaction following the first reduction(s). Secondly, upon increasing the N_2 -pressure, this reduction also decreases, indicating that its formation is in competition with a N_2 -binding reaction. Coordination of additional N_2 -ligands to e.g. $[\text{ReX}(\text{N}_2)(\text{PNP})]$ or $[\text{ReX}(\text{N}_2)(\text{PNP})]^-$ could block the free coordination site and prevent formation of $\mathbf{2}^{\mathbf{X}}$. An explanation in this direction was successfully introduced in case of $\mathbf{1}^{\text{Cl}}$ in Chapter II.1 to account for the N_2 -pressure data. The concentration dependent data of $\mathbf{1}^{\text{I}}$ and $\mathbf{1}^{\text{Br}}$ showed an increase of this far cathodic wave upon increasing concentrations, indicating the species forms via a bimolecular reaction. So far, this is in line with this reduction wave belonging to $\mathbf{2}^{\mathbf{X}}$. In addition, due to the deconvolution of $[\text{ReI}_2(\text{PNP})]^{0/-}$ and $[\text{ReI}(\text{N}_2)(\text{PNP})]^{0/-}$ in case of $\mathbf{1}^{\text{I}}$, it is observed that the $[\text{ReI}(\text{N}_2)(\text{PNP})]^{0/-}$ reduction wave disappears parallel with the increase of this far cathodic wave. At high concentrations, the $1e/\text{dim}$ is more favoured over the $2e/\text{comp}$ pathway, and it might be that more of the dinuclear species is formed. Yet, the relatively high concentrations of $\mathbf{2}^{\mathbf{X}}$ that would lead to these substantial peak currents of this far cathodic wave are in contrast to the here above described experiment, where no onset for the oxidative features of $\mathbf{2}^{\mathbf{X}}$ was observed. This remains therefore an unsolved question and in future research, either low temperature CV should be examined or chemical access to $[\mathbf{2}^{\mathbf{X}}]^+$ and $[\mathbf{2}^{\mathbf{X}}]^{2+}$ should be pursued.

II.3: The influence of ligand oxidation on N₂-splitting

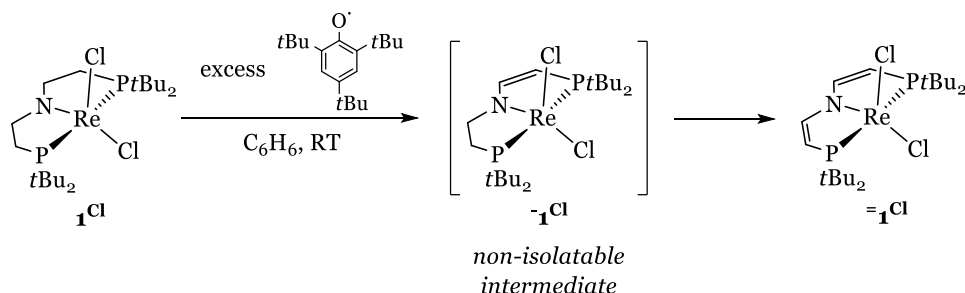
Parts of this Chapter are published in the *European Journal of Inorganic Chemistry* under the title: '(Electro)chemical Splitting of Dinitrogen with a Rhenium Pincer Complex' in **2020**.⁷²

Parts of this Chapter are published in: *Implementierung einer Flow-Zelle in die elektrochemische Stickstoffspaltung*, C.M.G.K. von Petersdorff-Campen **2020**, Bachelorthesis, Georg-August-Universität Göttingen.

3.1. Synthesis attempts towards the partially unsaturated chloride platform

To expand our Re-mediated N₂-splitting platform **1**^{Cl}, we examined the influence of halide exchange in Chapter II.2. Another variation strategy lies at the PNP-ligand, since it can be oxidised and deprotonated to for instance the half saturated vinyl ligand (N(CHCHPtBu₂)(PCH₂CH₂PtBu₂))⁻ (P=NP) or the fully saturated divinyl ligand (N(CHCHPtBu₂)₂)⁻ (P=N=P) in 2e⁻/2H⁺ transformations each. Upon desaturation, decreased N_{amide} to metal donation results in reduced electron density at the metal centre. Chemical N₂-splitting was established from the unsaturated Re-platform [ReCl₂(P=N=P)], as elaborated in Section I.1.4. Yet, a strong dependence of the reductant on the nitride yield was found for this starting complex, which was not well understood. Likely, the decreased donor properties of the oxidised ligand alter the redox-properties of the involved N₂-splitting compounds, which is examined within this Chapter.

Ligand desaturation is performed via template synthesis, i.e. starting from the already complexed ligand. Dr. Isabel Scheibel (née Klopsch) and Dr. Florian Wätjen (né Schendzielorz) developed the synthesis pathway to the chloride platform with the desaturated ligand [ReCl₂(P=N=P)] (=1^{Cl}): **1**^{Cl} is reacted with an excess of 1,3,5-tris(*tert*-butyl)phenoxy-radical (TBP) as PCET reagent, see Scheme 50. During this synthesis, a C₁-symmetric product was observed by NMR spectroscopy with a chemical shift in between **1**^{Cl} and =1^{Cl}, assigned to the complex bearing the half-saturated P=NP ligand [ReCl₂(P=NP)] (-1^{Cl}).^{71,79} Upon reacting **1**^{Cl} with only two equivalents of TBP, a mixture between all three compounds was observed.⁷⁹ If this species could be synthesised selectively, another series of three starting platforms would be established, namely [ReCl₂(PNP)] (1^{Cl}), [ReCl₂(P=NP)] (-1^{Cl}), and [ReCl₂(P=N=P)] (=1^{Cl}). Within the context of this work, we *briefly* examined a different reaction pathway to aim for selective access to -1^{Cl}, by separate deprotonation and (electro)chemical oxidation instead of using the PCET reagent TBP.



Scheme 50. Established synthesis of $=\mathbf{1}^{\text{Cl}}$ using TBP via the half-saturated $\mathbf{-1}^{\text{Cl}}$ that could not be isolated.^{71,79}

By CV, we found that $\mathbf{1}^{\text{Cl}}$ shows two quasi-reversible oxidations, at $E_{1/2} = -0.48$ V and -0.02 V (Figure 37 and A6) that belong to freely diffusion species in solution as judged from a linear relationship between $i_{p,a}$ vs. $v^{1/2}$. The current ratio between both oxidations is quite high and slightly increases when going to higher v ($i_{p,a,1}/i_{p,a,2} = 3.9$ ($v = 0.1$ Vs⁻¹), and 5.0 (1.0 Vs⁻¹)), suggesting that the two oxidations are coupled via a chemical reaction. However, this area was not examined in detail (i.e. towards higher v to induce more dramatic changes). These oxidations are assumed to be metal-based, as ligand oxidation is usually found at higher potentials: within this work, we found clear indications for ligand oxidation potentials in the range of 0.6 to 0.9 V, as recognised by their multi-electron character wave, and its disappearance when measuring the same compound bearing the P=N=P-ligand. Ligand oxidation is for instance proposed around 0.85 V for $\mathbf{3}^{\text{X}}$ (X = Cl, Br, I) or around 0.6 V for [Re(NCHCH₃)Cl(PNP)] (**6**) (see Section II.2.3 and II.4.1, respectively). Yet, in presence of a base, we introduce deprotonation reactions coupled to the oxidation, which will shift the potential to substantial milder potentials. Therefore, we measured the oxidative area of $\mathbf{1}^{\text{Cl}}$ in presence of base. Upon addition of DBU multiple new waves are observed indicating that DBU reacts with $\mathbf{1}^{\text{Cl}}$ prior to oxidation in a non-selective manner; it is therefore discarded as reagent. A possible reaction might be the coordination of DBU via either one of the amine functional groups. Earlier, it was found by Dr. I. Scheibel that upon deprotonation of [ReCl₃(HN(CH₂CH₂PiPr₂)₂)] with a structurally similar base as DBU, the main reaction outcome was a species coordinating the base.⁷⁹

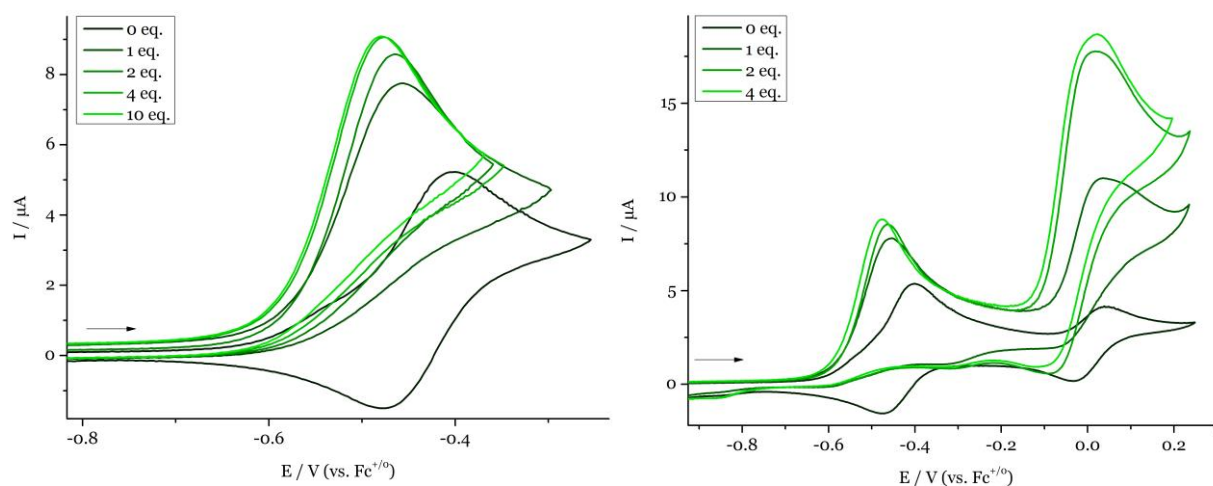
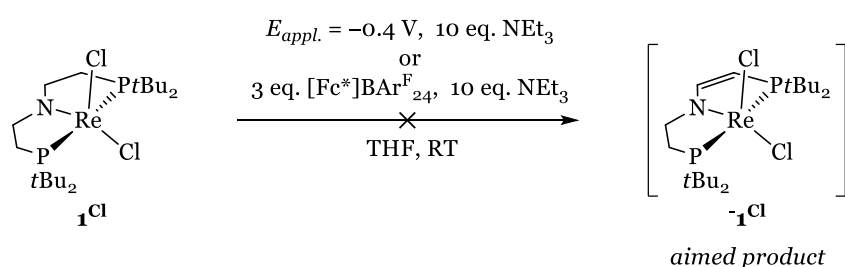


Figure 37. CV of a 1.0 mM solution of $\mathbf{1}^{\text{Cl}}$ in THF with 0.2 M $(n\text{Bu}_4\text{N})\text{PF}_6$ and 0-10 eq. of NEt_3 . Left: first oxidation wave. Right: both oxidation waves, only 0-4 eq. NEt_3 .

NEt_3 proved more promising: the otherwise quasi-reversible first oxidation of $\mathbf{1}^{\text{Cl}}$ directly appears irreversible after addition of only 1 eq. (Figure 37). Concomitantly, the peak potential shifts anodically and its current increases. Both phenomena seem to reach a maximum effect after the addition of 4 eq. All changes in the CV point towards the ability of NEt_3 to deprotonate $[\mathbf{1}^{\text{Cl}}]^+$, and the generation of a species that is oxidised in the same potential range as $\mathbf{1}^{\text{Cl}}$ or easier via a *potential inversion*, explaining the current increase. We hypothesise that after the first oxidation, deprotonation forms a complex bearing the neutral imine ligand $(\text{N}(\text{CHCH}_2\text{PtBu}_2)(\text{PCH}_2\text{CH}_2\text{PtBu}_2))$. It was shown before on for instance Pd- and Ir-complexes that the protons next to the amide moiety are the most acidic after oxidation.¹⁹⁴ Since this imine species contains a formal Re(II) centre, it is reasonable that its oxidation is either similar or easier compared to $\mathbf{1}^{\text{Cl}}$. Subsequent oxidation and deprotonation would form $\mathbf{1}^{\text{Cl}}$ via an overall *ECEC*-pathway. Combining the oxidation potential and the indications by CV that NEt_3 can deprotonate $[\mathbf{1}^{\text{Cl}}]^+$ roughly gives an upper limit $\text{BDFE}_{(\text{C-H})}$ of $\leq 68 \text{ kcal mol}^{-1}$.¹⁹⁵ This is in well agreement with the TBP radical ($\text{BDFE}_{\text{TBP}}(\text{THF}) = 74.4 \text{ kcal mol}^{-1}$) be sufficient for HAT reactivity.¹⁹⁵ More anodically a second, broader, and irreversible wave is found ($E_p = 0.0 \text{ V}$, $\nu = 0.1 \text{ Vs}^{-1}$) which resembles two oxidations in close proximity. This event is still well separated from oxidation of NEt_3 ($E_p = 0.5 \text{ V}$, $\nu = 0.1 \text{ Vs}^{-1}$, see Appendix A2) and most likely represents the further saturation of the backbone towards $\mathbf{1}^{\text{Cl}}$.

Based on these CV data, we first explored the electrochemical synthesis of $\mathbf{1}^{\text{Cl}}$, by performing CPE at $E_{\text{appl.}} = -0.4 \text{ V}$ (Scheme 51) in presence of 10 eq. of NEt_3 . However, full conversion of this first wave only resulted in the transfer of one electron per rhenium atom, whereas (at least) two electrons were expected based on its CV trace. Both $^3\text{P}\{^1\text{H}\}$ and ^1H NMR spectra in d_8 -THF after CPE are basically featureless, besides electrolyte and HNEt_3^+ . This either indicates that all

compound is severely decomposed, or a paramagnetic product is formed that overlaps with the electrolyte or shows especially broad peaks. Formation of a Re(IV) species is not impossible, as the applied CPE potential is close towards the envisioned oxidation potential of -1^{Cl} . We assume it is between the potentials of 1^{Cl} and =1^{Cl} ($E_{1/2} = -0.48 \text{ V}$ and $E_p = -0.05 \text{ V}$, $\nu = 0.1 \text{ Vs}^{-1}$, respectively). However, when -1^{Cl} is formed and subsequently oxidised, three electrons should be transferred during CPE, in contrast to the experiment. An explanation of this odd one electron transfer could be a comproportionation, where the product of a two-electron oxidation reacts with a non-oxidised species. However, the resulting Re(IV) species should be redox-inactive within this potential range (as we see no peak appearing), which is rather unrealistic. No species could be extracted by non-polar solvents, inhibiting mass spectroscopic analysis due to the presence of the ($n\text{Bu}_4\text{N}$)-cation. In future research, the presence of paramagnetic species should be probed by EPR-spectroscopy. The outcome of this reaction is within this work not elucidated.



Scheme 51. CPE of 1^{Cl} in presence of 10 eq. NEt_3 in THF aiming for $[\text{-1}^{\text{Cl}}]^+$.

In a first attempt, we also examined chemical oxidation of 1^{Cl} in presence of NEt_3 and 3 eq. of $[\text{Fc}^*]\text{BAR}^{\text{F}}_{24}$, to account for a possible oxidation of -1^{Cl} to $[\text{-1}^{\text{Cl}}]^+$. The colour of the reaction mixture quickly changes to green and both Fc^* and protonated HNEt_3^+ are observed, besides unreacted $[\text{Fc}^*]\text{BAR}^{\text{F}}_{24}$. Quite selectively, a diamagnetic C_s -symmetric species is formed with a $^{31}\text{P}\{\text{1H}\}$ NMR feature at 99.6 ppm, indicating no subsequent oxidation to the Re(IV)-stage. This species can however not bear the neutral imine ligand $\text{N}((\text{CHCH}_2\text{PtBu}_2)(\text{PCH}_2\text{CH}_2\text{PtBu}_2))$, since it is C_1 -symmetric. No further product identification was performed at this stage, which should be repeated in future research.

In the initial attempts as discussed here, it was not possible to synthesise -1^{Cl} , although both the electro- and chemical oxidation were not sufficiently reproduced, nor fully analysed and should therefore not be over-interpreted. In future research, both goals of getting access to the half-saturated system or to perform the desaturation electrochemically, are better explored starting from the octahedral $[\text{ReCl}_3(\text{PNP})]$ (**8**) platform. Having a coordinatively saturated complex will likely prevent certain decomposition pathways. The oxidation potential of **8** ($E_{1/2} = 0.05 \text{ V}$) is

still far enough separated from the oxidation potential of NEt_3 (Appendix A2), allowing it to be the base of choice for initial attempts for this reaction in future research.

3.2. Electrochemical N_2 -splitting from the unsaturated chloride platform

Chemical N_2 -splitting from $=\mathbf{1}^{\text{Cl}}$ was explored by Dr. Florian Wätjen, showing a strong dependence of the nitride yield and the used reductant: $\text{Co}(\text{Cp}^*)_2$ yields $[\text{ReNCl}(\text{P}=\text{N}=\text{P})]$ ($=\mathbf{3}^{\text{Cl}}$) in 60 % yield, whereas only 30 % and 20 % with Na/Hg or KC_8 were obtained, respectively. For electrochemical N_2 -splitting, CPE of a 1.0 mM solution of $=\mathbf{1}^{\text{Cl}}$ was carried out at $E_{\text{appl.}} = -1.67$ V based on the peak potential of the first reduction wave in the CV under N_2 in THF (Section II.3.3). Transfer of approximately 1.2 electrons per rhenium over the course of 2 h was accompanied by a gradual colour change of brown towards green. Concomitantly, amongst several small oxidative waves, one reversible feature is formed in the CV with a $E_{1/2} = 0.23$ V and by $^3\text{P}\{^1\text{H}\}$ NMR spectroscopy, a single species was observed ($\delta^{31\text{P}\{^1\text{H}\}} = 71.8$ ppm). Both indicate successful formation of $=\mathbf{3}^{\text{Cl}}$ by comparison to the independently synthesised nitride ($E_{1/2} = 0.21$ V).⁷² It was shown in a separate experiment, that the $\text{Re}(\text{VI}/\text{V})$ -oxidation remains reversible even in the presence of 1 eq. of Cl^- , as is at least the case in electrochemical conditions (Figure 38). Its yield proved however only to be around 15 % based on $^3\text{P}\{^1\text{H}\}$ NMR integration. This is in stark contrast to the yield using $\text{Co}(\text{Cp}^*)_2$, and closer to the heterogeneous reductants (Na/Hg , KC_8). Furthermore, it is significantly lower than the electrolysis yield of $\mathbf{3}^{\text{Cl}}$ (60 %).

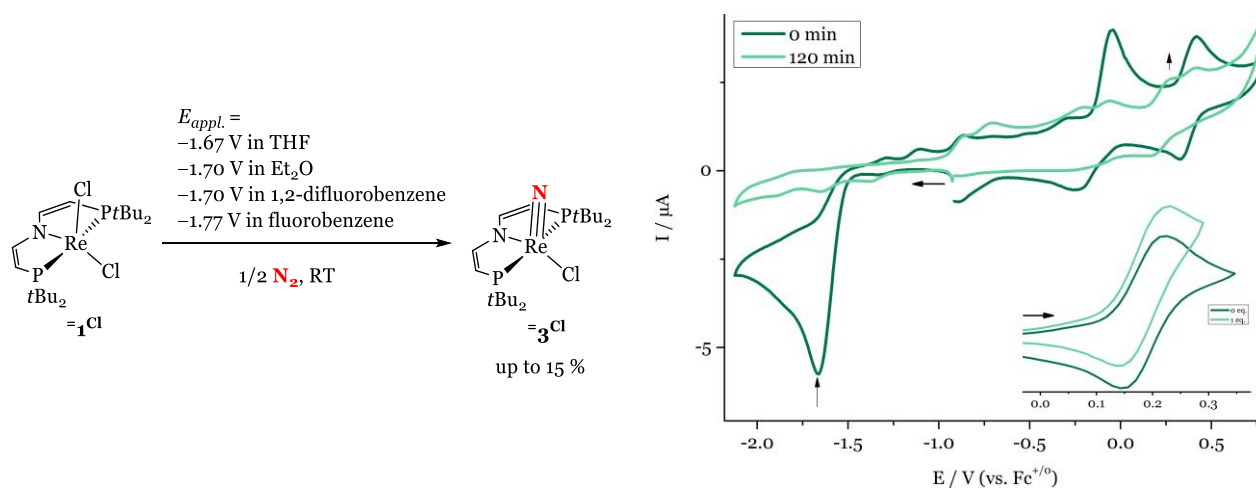


Figure 38. Left: Electrochemical N_2 -splitting from $=\mathbf{1}^{\text{Cl}}$ into $=\mathbf{3}^{\text{Cl}}$ via CPE in different solvents. Right: CPE of a 1.0 mM solution of $=\mathbf{1}^{\text{Cl}}$ at $E_{\text{appl.}} = -1.67$ V in THF as monitored by CV. The arrow in the anodic region indicates the rise of an oxidation assigned to $=\mathbf{3}^{\text{Cl}}$. Inset: reversible oxidation of isolated $=\mathbf{3}^{\text{Cl}}$ and in presence of 1 eq. of $(n\text{He}_4\text{N})\text{Cl}$. The current rise is attributed to a new oxidation appearing in presence of Cl^- appearing directly after the $\text{Re}(\text{VI}/\text{V})$ wave.

All electrochemical N₂-splitting in Chapter II.1 and 2 so far is performed in THF as solvent. It was originally the solvent of choice because of its polarity leading to good solubility of all Re-complexes and N₂ (6.4 mM)¹⁹⁶. It has a relatively low tendency to coordinate the metal centre, in contrast to MeCN which coordinates **1**^{Cl}.⁷⁹ In addition, THF is readily and thoroughly dried using Na/K, which is necessary for the strongly reductive conditions. For this platform, we also explored other solvents, which is mainly motivated by considering the nitride functionalisation for this platform, which is only done by strong electrophiles, i.e. EtOTf (see Section I.2.3). Such electrophilic triflates are incompatible with THF towards ring-opening polymerisation, and therefore an alternative solvent is required. In electrochemical C-N fragment release as described in Chapter II.4, better results were obtained using the unsaturated ligand platform, explaining the rationale behind screening different solvents from this unsaturated platform =**1**^{Cl}. Notably, it was reported for instance that halide loss kinetics can be substantially different upon changing the solvent, and this might lead to different reaction outcomes, i.e. higher nitride yields.¹⁸⁹

Table 10. Selected properties and results of the herein examined solvents for electrochemical N₂-splitting for 2.0 mM solutions of =**1**^{Cl} with (*n*Bu₄N)PF₆ electrolyte for THF, fluoro- and 1,2-difluorobenzene and (*n*Bu₄N)BAR^F₂₄ electrolyte for Et₂O.

	Dielectric constant ¹⁹⁷	Dipole moment ¹⁹⁷ d / D	N ₂ -solubility ¹⁹⁸ / mM	Water content / mM ^b	= 3 ^{Cl} yield
1,2-difluorobenzene	14.3	2.53	n.d. ^a	0.1	4/ 15 ^c
THF	7.6	1.69	6.4	0.3	11
Fluorobenzene	5.4	1.66	n.d. ^a	0.1	8
Et ₂ O	4.3	1.30	8.8	0.1	4

^a The closest related molecule that was examined is hexafluorobenzene with a N₂-solubility of 15.6 mM. ^b As determined via a Karl-Fischer Titration, leading to mass H₂O/mass solvent values (1,2-difluorobenzene: 2.1 ppm, THF: 5.7 ppm, Fluorobenzene: 2.0 ppm, Et₂O: 1.8 ppm) which were re-calculated to concentrations. ^c Using a starting concentration of circa 6 mM =**1**^{Cl} (corresponding to a 10 mg scale).

We expanded electrochemical N₂-splitting to fluorobenzene, 1,2-difluorobenzene and Et₂O, which all show compatibility with EtOTf over at least 48 h. To judge the polarity of these solvents, we considered the dielectric constant and dipole moment (Table 10). Whereas fluorobenzene is in the polarity range of THF, 1,2-difluorobenzene is more, and Et₂O is less polar compared to THF. No values regarding N₂-solubility in fluorobenzene or 1,2-difluorobenzene are available, but the concentration for the related hexafluorobenzene (15.8 mM) is clearly higher than THF, just as is the case for Et₂O (8.8 mM). The water content for the examined solvents was determined to be between 0.1-0.3 mM, which was still unpleasantly high taking into account that it was freshly dried over either Na/K (Et₂O/THF) or CaH₂ (fluorinated

benzenes). The scale of electrolysis was therefore considerably higher than this water content (approx. 3.0 mM) to prevent substantial decomposition.

CPE was performed in these solvents at the peak potential of the first reduction wave as found by CV (*vide infra* for a short description of the CVs in Figure 41). In all cases, full conversion was accompanied by the transfer of approx. 1 electron per Re and the formation of $=\mathbf{3}^{\text{Cl}}$ as judged by NMR spectroscopy. Yet, the nitride yields are poor ($\approx 5\text{-}10\%$), and clearly not an improvement compared to THF. For 1,2-difluorobenzene, an additional experiment with larger Re-concentration ($\approx 6.0\text{ mM}$) offered a nitride yield of 15 %, which is at least in the range of the THF performance.

After establishing electrochemical synthetic access to $=\mathbf{3}^{\text{Cl}}$ in poor yields, it was questioned which other species are formed. Even though the nitride is formally Re(V), and is considered a stable species, its stability under CPE conditions was examined. Therefore, we electrolysed $=\mathbf{3}^{\text{Cl}}$ in presence of 1 eq. of $(n\text{He}_4\text{N})\text{Cl}$ at the N_2 -splitting potential ($E_{\text{appl.}} \approx -1.7\text{ V}$) for 100 min (Figure A27). No decomposition of the nitride was observed, neither in the CVs, nor via NMR spectroscopy upon extraction with pentane after CPE. Thus, off-pathway reactions must occur before or during N_2 -splitting which decrease the yield. In experiments with a low starting concentration of $=\mathbf{1}^{\text{Cl}}$ (1.0 mM) in THF, no other ${}^3\text{P}\{^1\text{H}\}$ NMR features are visible due to low intense spectra. At higher concentrations whilst examining the different solvents, a rather broadened feature ($\delta_{{}^3\text{P}\{^1\text{H}\}} = 42.0\text{ ppm}$) was observed in all cases. Since the NMR samples were prepared under a N_2 -atmosphere, a possible N_2 -coordination equilibrium was considered that would cause broadening of the signal. However, changing the atmosphere to Ar has no effect on its position nor linewidth. In order to separate this species (or any species) from the electrolyte, extractions with Et_2O or pentane were performed. Yet, neither in the non-polar, nor in the electrolyte containing fraction, a species at $\delta_{{}^3\text{P}\{^1\text{H}\}} = 42.0\text{ ppm}$ was re-found, which might indicate its decomposition during work up. ${}^1\text{H}$ NMR spectroscopy was measured for the non-polar fractions without electrolyte. No indications for paramagnetic species are observed, which is corroborated by the absence of an EPR signal (RT, benchtop EPR spectrometer) as tested after CPE in 1,2-difluorobenzene. For all solvents, the ${}^1\text{H}$ NMR spectrum shows the presence of a species with one or multiple *t*Bu signal(s) at +1.34 ppm (identified since it appears as an archetypical *t*Bu pseudo triplet in the ${}^1\text{H}$ - and a singlet in ${}^1\text{H}\{{}^3\text{P}\}$ NMR spectrum), that via a ${}^1\text{H}$ COSY NMR spectrum correlates to a rather broad feature at 2.9 ppm. Besides, in the case of 1,2-difluorobenzene, a C_s -symmetric species is observed that has its signals in striking close proximity to the nitride $=\mathbf{3}^{\text{Cl}}$ (δ_{H} backbone protons: 4.2 and 6.6 ppm vs. 7.0 and 4.3 ppm of $=\mathbf{3}^{\text{Cl}}$), present in circa 5%. Due to this similarity, it is likely also a Re(V)-species, and an oxo-species is

the most likely candidate. Mass spectroscopic analysis of this species showed oxygen-containing peaks (at 594.3 m/z for a [ReOCl(P=N=P)]⁺-fragment or at 575.4 m/z for a [ReO₂(P=N=P)]⁺-fragment). The appearance of any oxygen containing species is attributed to residual water. In future research, the deliberate synthesis of an oxo-species as reference compound should be intended by reacting =**1**^{Cl} with Me₃NO in presence of e.g. a sodium salt, as was used for successful synthesis of [ReOCl(PNP)]BF₄ from **1**^{Cl}.⁷¹

In order to examine the possibility of decomposition before N₂-splitting, the stability of =**1**^{Cl} in THF in the presence of N₂ and chloride ions was assessed. NMR spectroscopic monitoring under 1 atm N₂ reveals partial conversion to several unidentified new species in the spectral range $\delta^{31\text{P}\{^1\text{H}\}} = 20\text{-}60$ ppm over the course of 48 h. Since =**1**^{Cl} proved stable under Ar in an otherwise identical experiment, this suggests chemical instability under a N₂ pressure. CV characterisation at higher N₂-pressure initially shows a slight rise in current of the reduction feature by approx. 5 % upon increasing pressure from 1 to 11 bars. However, keeping the sample under these conditions over the course of 45 min leads to a current drop by about 20 % (Figure A28). ³¹P{¹H} NMR spectroscopic analysis after this experiment shows complete conversion into an intractable reaction mixture (Figure A28). Even more rapid decay was found upon addition of a chloride source: a mixture of =**1**^{Cl} and (nBu₄N)Cl under 1 atm N₂ gradually changes colour from light brown to green over the course of only a couple of hours, with concomitant formation of a mixture of diamagnetic and paramagnetic species (Figure 39).

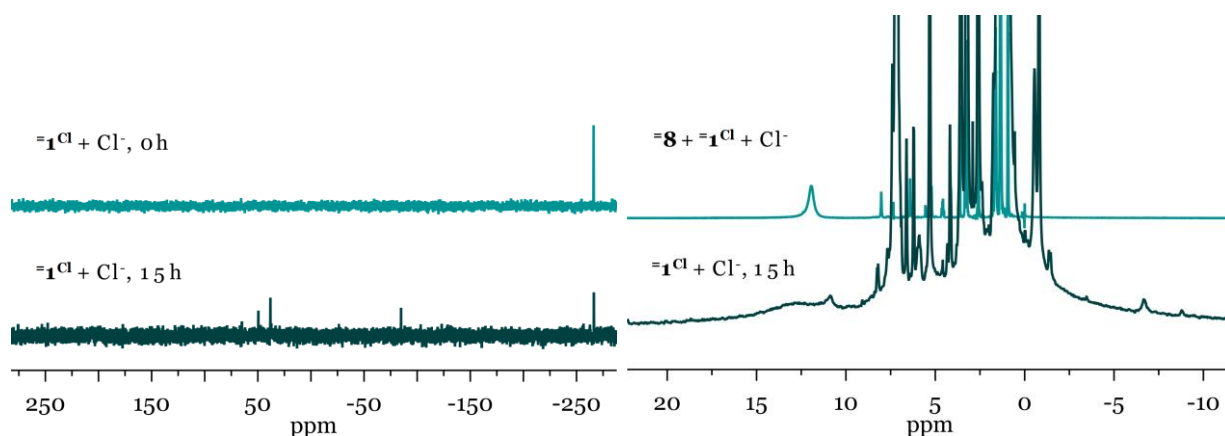
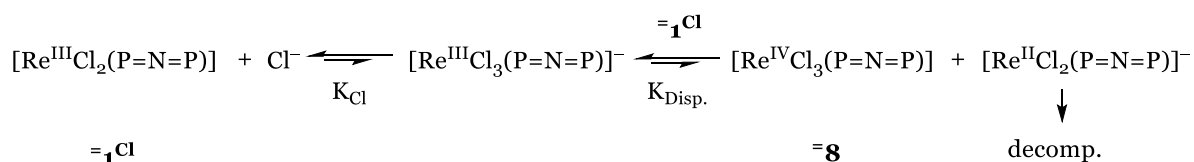


Figure 39. Left: ³¹P{¹H} NMR of =**1**^{Cl} with 5 eq. of (nBu₄N)Cl in THF at 0 h and after 15 h. Right: ¹H NMR spectrum comparison of =**1**^{Cl} with 5 eq. of (nBu₄N)Cl in C₆D₆ (bottom) and an equimolar mixture of =**8**, =**1**^{Cl} and (nBu₄N)Cl in d₈-THF.

To examine whether any of this paramagnetic compounds is a Re(IV)-species, we mixed equimolar amounts of =**1**^{Cl}, (nBu₄N)Cl and [ReCl₃(P=N=P)] (= **8**). The otherwise sharp NMR signals of this latter species (see Section II.4.5) broaden, shift, and loose intensity, leaving a

broad signal at $\delta^1_H = +12$ ppm. Interestingly, a signal at a very similar chemical shift is present when allowing a mixture of $=\mathbf{1}^{Cl}$ and a chloride source to stand over a period of time (see Figure 39) (the slight deviation is attributed to the different solvents in which these spectra are measured). This could indicate that some $=\mathbf{8}$ is formed when $=\mathbf{1}^{Cl}$ and chloride slowly react over hours (along with other unidentified products based on 1H NMR signals at -6 and -9 ppm for instance). To account for this observation, we propose that initial chloride association forming $[ReCl_3(P=N=P)]^-$ initiates a disproportionation reaction from which $=\mathbf{8}$ must be formed. Reactivity between $[ReCl_3(P=N=P)]^-$ and $=\mathbf{1}^{Cl}$ would explain the appearance of a Re(IV)-species (Scheme 52). The simultaneously formed Re(II)-species $[ReCl_2(P=N=P)]^-$ most likely decomposes due to its reactive nature. The NMR signals of $=\mathbf{8}$ only change in presence of both $=\mathbf{1}^{Cl}$ and chloride source (mixing $=\mathbf{8}$ and $=\mathbf{1}^{Cl}$ has no influence on the NMR features), which is explained by a redox equilibrium between $[ReCl_3(P=N=P)]^-$ and $=\mathbf{8}$.



Scheme 52. Proposed chloride induced disproportionation reaction of $=\mathbf{1}^{Cl}$.

To evaluate the likeliness of such a decomposition pathway, both chloride association to $=\mathbf{1}^{Cl}$ to form $[ReCl_3(P=N=P)]^-$ and its subsequent disproportionation are considered, described with K_{Cl} and $K_{Disp.}$ in Scheme 52, respectively. The *directly* measured $^3P\{^1H\}$ NMR spectrum of $=\mathbf{1}^{Cl}$ is unchanged in the presence of circa 5 eq. of $(nBu_4N)Cl$, and no signals are present that could be assigned to $[ReCl_3(P=N=P)]^-$ (Figure 39). This allows for the estimation of an upper limit for K_{Cl} , assuming slow chloride exchange. Considering a signal to noise ratio of 3:1, an upper detection limit for $[ReCl_3(P=N=P)]^-$ is derived to be approximately 3 mM. Via equation (1) and the following concentrations: $c(=\mathbf{1}^{Cl})_{starting} = 8.3$ mM, $c(Cl^-)_{starting} = 39.1$ mM, $c([ReCl_3(P=N=P)]^-)_{upper\ limit} \approx 3$ mM, $c(=\mathbf{1}^{Cl})_{limit} \approx 5.3$ mM, $c(Cl^-)_{limit} \approx 36.1$ mM, we can estimate the association equilibrium constant to be $K_{Cl} \leq 0.015$, indicating an uphill equilibrium by circa $\Delta G^o_{Cl} \geq 2.5$ kcal mol $^{-1}$.

$$K_{Cl} = \frac{c([ReCl_3(P=N=P)]^-)}{c(=\mathbf{1}^{Cl}) * c(Cl^-)} \quad (1)$$

$$K_{Disp.} = e^{\frac{n_1 n_2 F (E^o_{=1Cl} - E^o_{=8})}{RT}} \quad (2)$$

The subsequent disproportionation is evaluated based on the reduction potential of $=\mathbf{1}^{\text{Cl}}$ which forms $[\text{ReCl}_2(\text{P}=\text{N}=\text{P})]^-$ and the reduction potential of $=\mathbf{8}$, which corresponds to the oxidation of $[\text{ReCl}_3(\text{P}=\text{N}=\text{P})]^-$, via equation (2). The first potential is derived from digital simulation as presented in Section II.3.3 ($E_6, =\mathbf{1}^{\text{Cl}} = -1.75 \text{ V}$), and the latter reduction potential is derived from CV at the most reversible conditions measured ($E_{1/2, =\mathbf{8}} \approx -0.9 \text{ V}$, $i_{\text{pf}}/i_{\text{pr}} = 1.8$, $v = 20 \text{ Vs}^{-1}$, Section II.4.5). This leads to a $K_{\text{Disp.}}$ of circa $4 \cdot 10^{-15}$,¹⁷⁴ and a subsequent uphill equilibrium by about 20 kcal mol⁻¹. Overall, the disproportionation triggered by chloride association is uphill by $\Delta G \geq 22.5 \text{ kcal mol}^{-1}$ and a likely higher activation barrier. Even though the decomposition of the resulting Re(II)-species $[\text{ReCl}_2(\text{P}=\text{N}=\text{P})]^-$ will add driving force for the reaction to occur, it represents a rather slow process. However, electrochemical reduction occurs on a longer time scale (2 h) compared to chemical N₂-splitting (5 min), indicating that this decomposition pathway could play a role since chloride ions accumulate during electrolysis. In general, the instability to chloride and in a lower degree to N₂, and the longer exposure of $=\mathbf{1}^{\text{Cl}}$ towards both in electrochemical N₂-splitting will have a detrimental effect on the nitride yields.

In sharp contrast, parent $\mathbf{1}^{\text{Cl}}$ proved stable under these conditions over an extended period of time (see Chapter II.1.1). Structural comparison is not possible between $=\mathbf{1}^{\text{Cl}}$ and $\mathbf{1}^{\text{Cl}}$ directly, because of the lacking XRD analysis of $=\mathbf{1}^{\text{Cl}}$. Fortunately, both nitrides $\mathbf{3}^{\text{Cl}}$ and $=\mathbf{3}^{\text{Cl}}$ were analysed by XRD, which show only minor differences: the steric shielding of the Re-centre as expressed by the pincer P-Re-P bite angle is basically unchanged (P-Re-P: 156.16(7)° ($\mathbf{3}^{\text{Cl}}$)¹⁷³ and 155.11(13)° ($=\mathbf{3}^{\text{Cl}}$)). For the $\mathbf{1}^{\text{I}}$ and $=\mathbf{1}^{\text{I}}$ couple, only a slightly decreased bite angle was found (P-Re-P: 161.62(3)° ($\mathbf{1}^{\text{I}}$) and 158.12(4)° ($=\mathbf{1}^{\text{I}}$)), as a result of the more rigid P=N=P-ligand.¹⁶⁸ We therefore tentatively associate the reduced stability of $=\mathbf{1}^{\text{Cl}}$ to electronic reasons. Backbone unsaturation diminished the donor properties and increases the metal Lewis acidity. Regardless, the estimated decay rate of the chloride-induced disproportionation type reaction suggest that further processes contribute to the low nitride electrolysis yields. Therefore, the reduction of $=\mathbf{1}^{\text{Cl}}$ was examined in depth by CV, as presented in the next Section.

3.3. CV Study of [ReCl₂(P=N=P)]

The oxidative electrochemistry of =1^{Cl} was already discussed by Dr. F. Wätjen, and will not be discussed herein.⁷¹ In the reductive area of =1^{Cl} under Ar, (Figure 40) two irreversible reductive features are shown at $E_{p,c,1} = -1.75$ V and $E_{p,c,2} = -1.95$ V (both $\nu = 0.1$ Vs⁻¹). The peak currents $i_{p,c,1}$ and $i_{p,c,2}$ scale linearly with $\nu^{1/2}$. Both reductions distinctively shift cathodic upon increasing scan rates, accompanied with decreasing current ratio ($i_{p,c,1}/i_{p,c,2} \approx 7$ ($\nu = 0.05$ Vs⁻¹) ≈ 3 ($\nu = 1.0$ Vs⁻¹)). These characteristics suggest the presence of competing chemical reaction pathways after initial reduction of =1^{Cl} , and must include decay to a species that is redox-inactive in the examined potential range.

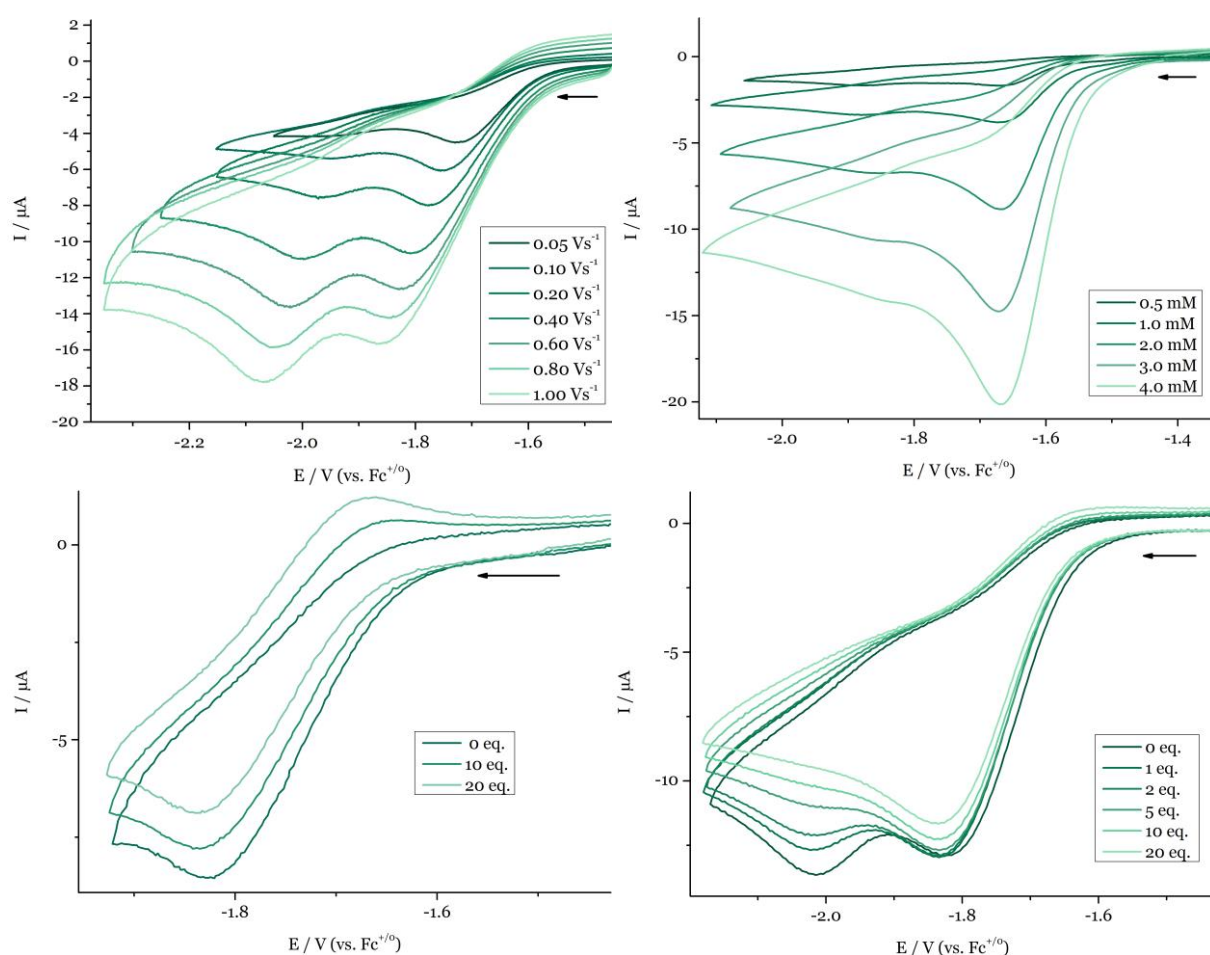


Figure 40. CVs of the reductive area of =1^{Cl} in THF with 0.2 M ($n\text{Bu}_4\text{N}$)PF₆ under Ar. Top left: Scan rate dependence a 1.0 mM solution. Top right: Concentration dependence, $\nu = 0.1$ Vs⁻¹. Bottom left: First reduction in presence of varying amounts of ($n\text{Bu}_4\text{N}$)Cl ($\nu = 0.5$ Vs⁻¹). Bottom right: Whole reductive area in presence of varying amounts of ($n\text{Bu}_4\text{N}$)Cl ($\nu = 0.5$ Vs⁻¹).

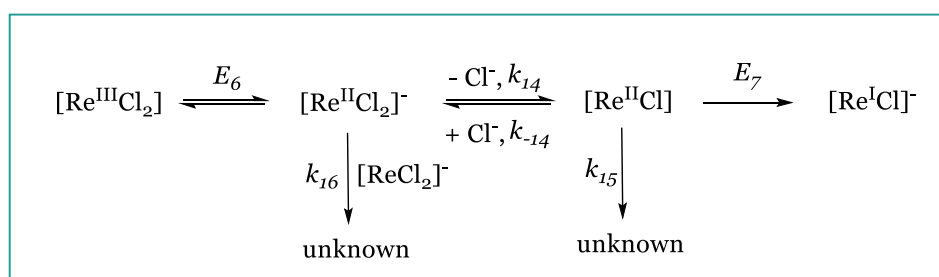
The reductive area of 1^{Cl} shows a comparable pattern, yet without the changing current ratio upon varying ν . It is noted here that the potential difference between these two reductions is

significantly decreased compared to the saturated platform ($\Delta E_{p,c,2-p,c,1} = 0.30$ V (**1**^{Cl}), 0.16 V (**=1**^{Cl})). In general, initial reduction of **=1**^{Cl} is anodically shifted by approx. 0.23 V with respect to **1**^{Cl}, as was found for the Re(VI/V) oxidation for the corresponding nitrides ($E_{1/2,3}^{\text{Cl}} = -0.09$ V, $E_{1/2,3}^{\text{Cl}} = 0.21$ V).⁷² This shift is associated with weaker π -donation from the P=N=P-pincer ligand.

Further insight in the coupled chemistry was obtained by electrochemical evaluation at varying conditions (see Figure 40). To probe for coupled chloride loss, varying amounts of (*n*Bu₄N)Cl were added to a solution of **=1**^{Cl}. This experiment proved difficult, since current drops were observed with increasing chloride concentration. We already established the instability of **=1**^{Cl} against addition of chloride by NMR spectroscopy (*vide supra*), yet at a slower timescale; this rapid current drop is therefore not understood to its full extent. The dryness of the chloride source was confirmed by the absence of an O-H stretch by IR spectroscopy. The experiment was performed quickly, which allows us to identify the key trends, namely a modest increased reversibility and a slight cathodic shift obtained for the first reductive event (circa 0.01 V from 0-20 eq. Cl⁻, $\nu = 0.5$ Vs⁻¹). This is in line with coupled, fast, and reversible chloride dissociation (**C**^{Cl}) after initial reduction of **=1**^{Cl}. The second reduction feature is also influenced by increasing chloride concentration: it shifts cathodically and decreases in current (more than accounting for **=1**^{Cl} decomposition). The concentration dependent data of **=1**^{Cl} shows increasing current ratio between the two reductive waves at higher rhenium concentration ($i_{p,c,1}/i_{p,c,2} \approx 5$ (1.0 mM), ≈ 18 (4.0 mM)). Within the experimental error, no peak potential shift is observed. In a simplified explanation, the current ratio trend indicates that the decay pathway between the two reductions, is bimolecular in nature.

Our previous electrochemical study for the reduction of **1**^{Cl} allowed for rationalisation of the CV data under Ar by an **EC**^{Cl}**E**-mechanism, extended by unimolecular decay at the Re(II) stage after chloride loss. As summarised for **=1**^{Cl}, the CV data indicates at least two coupled chemical reactions after initial reduction event: chloride dissociation to form [ReCl(P=N=P)] in competition with a bimolecular decay of [ReCl₂(P=N=P)]⁻. Via digital simulation, Prof. Dr. I. Siewert could simulate all CV data of **=1**^{Cl} under Ar as presented in Scheme 53, with simulation parameters in Table 11. The overlays between the experimental and simulated CVs are published elsewhere.⁷² Within the proposed pathway, reduction of **=1**^{Cl} (E_6) is followed by reversible chloride dissociation (K_{14}) and Re(II/I) reduction (E_7). Compared to **1**^{Cl} ($K_I = 0.05$ M, $k_I = 1 \cdot 10^3$ s⁻¹), the chloride dissociation is in similar range, only modestly slower. Importantly, satisfactory modelling requires two decay routes: unimolecular decay of [ReCl(P=N=P)] (k_{15}) after chloride loss, as proposed and slightly larger than for **1**^{Cl} ($k_{decay,2} = 0.11$ s⁻¹), and bimolecular

decay of $[\text{ReCl}_2(\text{P}=\text{N}=\text{P})]^-$ (k_{16}) to account for the higher current ratio $i_{p,c,1}/i_{p,c,2}$ upon Re-concentration increase. The nature of this bimolecular pathway is not known, but simple disproportionation of $[\text{ReCl}_2(\text{PNP})]^-$ to a Re(I)-species and $=\mathbf{1}^{\text{Cl}}$ can be excluded, since simulations of such a pathway predict a higher current ($i_{p,c,1}$) in contrast to the experimental data. Speculatively, it might be the formation of a chloride bridging dinuclear species. The altered backbone must however induce this reaction, since this pathway plays no significant role in reduction of $\mathbf{1}^{\text{Cl}}$. Most likely, this is due to the changed electronics as the steric differences are small, rendering the Re-centre a stronger Lewis acid. A sensitivity analysis reveals that the fitted parameters are quite sensitive with respect to doubling or halving the decay constants k_{15} or k_{16} . However, the two parameters are correlated: a higher bimolecular rate constant k_{16} can be partially compensated by lowering k_{15} (and *vice versa*).



Scheme 53. Minimal mechanistic model of reduction of $=\mathbf{1}^{\text{Cl}}$ under Ar. The P=N=P-pincer ligand is omitted for all species for clarity.

Table 11. Thermodynamic and kinetic parameters of $=\mathbf{1}^{\text{Cl}}$ as obtained via simulation of CV data under Ar.¹

$=\mathbf{1}^{\text{Cl}} / \text{Ar}$	K_{14} / M	k_{14} / s^{-1}	k_{15} / s^{-1}	k_{16} / $\text{M}^{-1}\text{s}^{-1}$	E_6 / V	E_7 / V
	0.01	$1 \cdot 10^2$	2	$2.5 \cdot 10^4$	-1.75	-1.92
					$\alpha_6 = 0.5$	$\alpha_7 = 0.5$
					$k_{s,6} = 0.01 \text{ cm}^2/\text{s}$	$k_{s,7} = 0.005 \text{ cm}^2/\text{s}$

Measuring under N_2 instead of Ar, we see an anodic peak potential shift of the first reduction of $=\mathbf{1}^{\text{Cl}}$ by circa 0.085 V to $E_{p,c,1} = -1.67 \text{ V}$, $\nu = 0.1 \text{ Vs}^{-1}$, accompanied by a small current increase (5 %) (Figure 41). The second reduction feature as present under Ar (E_7), is vanished without the appearance of new reductive events. Both anodic potential shift and the disappearance of the Re(II/I) reduction are in agreement with dinitrogen coordination at the Re(II) stage, as established in Chapter II.1 and 2. We leave the interpretation of the CV under N_2 at this level, because of the low faradaic yield for electrochemical N_2 -splitting for this unsaturated platform.

¹ Digital Simulation of the CV data were performed by Prof. Dr. I. Siewert.

It should be noted at this point that N₂-splitting from =**1**^{Cl} is imagined to also occur via a dinuclear N₂-bridged compound, analogue to **2**^X. NMR spectroscopic studies to this hypothetical intermediate were performed by Dr. F. Wätjen, without direct success, which was also not continued within the course of this work.

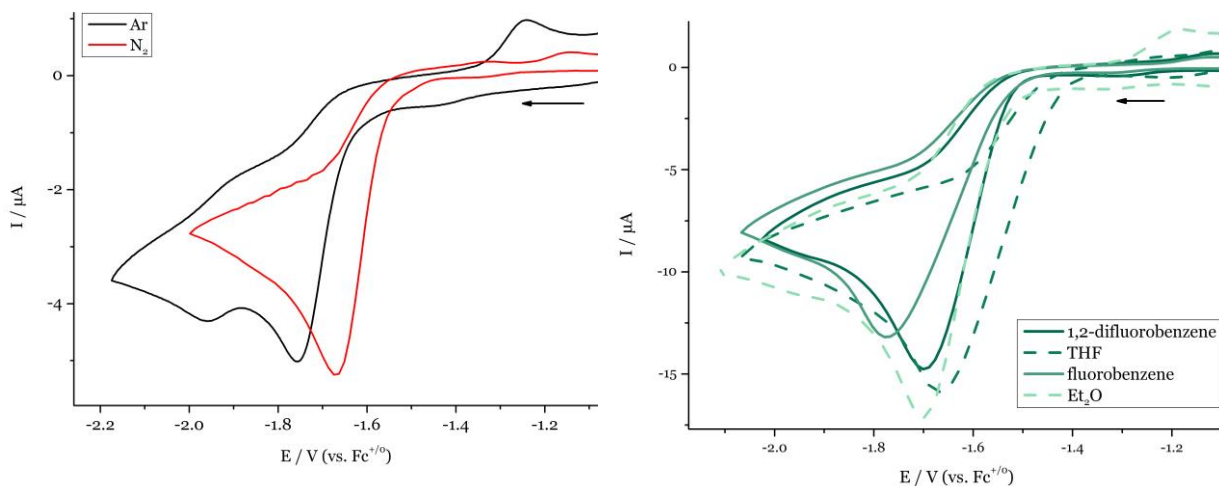


Figure 41. Left: CV of a 1.0 mM solution of =**1**^{Cl} in THF with 0.2 M (*n*Bu₄N)PF₆ under Ar (black), and N₂ (red), $\nu = 0.1$ Vs⁻¹. Right: CV Comparison of the reductive area of a approx. 3.0 mM solution of =**1**^{Cl} in THF, fluorobenzene, 1,2-difluorobenzene with (*n*Bu₄N)PF₆ and Et₂O with (*n*Bu₄N)BARF₂₄, $\nu = 0.1$ Vs⁻¹. The dashed lines are only to ease the eye in distinguishing the CV traces.

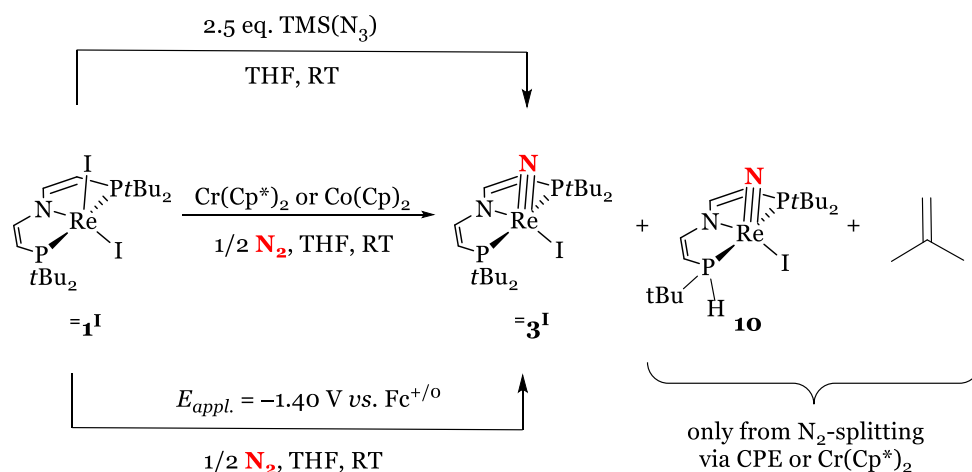
For this platform, electrochemical N₂-splitting was also examined in different solvents, as presented in Section II.3.2. The corresponding CVs, as presented in Figure 41, were measured only twice; therefore the peak currents and potentials should be handled with care. It is apparent that the peak potential is only slightly deviating between the solvents ($E_p = -1.67$ V (THF), -1.70 V (1,2-difluorobenzene and Et₂O), -1.77 V (fluorobenzene), $\nu = 0.1$ Vs⁻¹). The more cathodic peak potential of fluorobenzene is attributed to its low overall conductivity. Although a 0.3 M electrolyte concentration was used to minimise the negative effects associated with high resistance (i.e. smeared out waves that are less well interpretable), a large uncompensated resistance value remained. The peak current $i_{p,c}$ is within 10-15 % for THF, 1,2-difluorobenzene and Et₂O, which is similar enough to state that there is no substantial peak current influence of the solvent. A stronger deviation is observed for fluorobenzene, attributed to the before-mentioned resistance complications.

3.4. (Electro)chemical N₂-splitting from [ReI₂(P=N=P)]

In addition to the unsaturated chloride platform, Dr. J. Abbenseth developed the unsaturated iodide analogue [ReI₂(P=N=P)] (**=1^I**), that was not yet explored for N₂-fixation. Since electrochemical nitride yields starting from **=1^{Cl}** are low (15%), and the unsaturated platform is the best performing in electrochemical N-fragment release (see Chapter II.4), the search for a well-performing unsaturated platform for electrochemical N₂-splitting is ongoing. The iodide analogue might be promising, since its reduction potential will be mild (due to the weaker electron donating properties of iodide vs. chloride, see Chapter II.2). We synthesised **=1^I** by reacting its saturated analogue with an excess of TBP, and extraction with pentane, as described by Dr. J. Abbenseth.¹⁶⁸ By CV, the first, irreversible reductive event is at $E_{p,c,1} = -1.40$ V, $\nu = 0.1$ Vs⁻¹. Amongst the platforms studied in this work, this reduction potential associated with N₂-splitting (*vide infra*) represents the mildest encountered.

Based on this reduction potential, we tested N₂-activation using Co(Cp)₂, Cr(Cp*)₂, and via CPE at $E_{appl.} = -1.40$ V (Scheme 54). The potential of this first reductant Co(Cp)₂ ($E_{1/2} = -1.32$ V in THF) should not be sufficient, and initial attempts with stoichiometric amounts indeed barely showed any conversion. However, when taking a slight excess of 2.5 eq. a colour change from dark to lighter brown occurred and no starting material was found by ³¹P{¹H} NMR spectroscopy. Successful reduction of **=1^{Cl}** despite the potential mismatch is likely driven by partial precipitation of [Co(Cp)₂]I. One main feature in ³¹P{¹H} NMR spectroscopy at 70 ppm is found, that corresponds to a C_s-symmetric species in the ¹H NMR spectrum. The chemical shifts are very similar to **=3^{Cl}**, and formation of [ReNI(P=N=P)] (**=3^I**) could be confirmed by its independent synthesis via reaction of **1^I** and TMSN₃ (Figure 42, right). The nitride was however only formed in circa 20 %. Since this run represents a single result, its value should be handled with care. A long ³¹P{¹H} NMR spectrum revealed the presence of numerous species (i.e. a broad feature at $\delta^{31P\{^1H\}} = 41.8$ ppm), in agreement with a low nitride yield. A species with such a resonance is strikingly similar as found in the case after CPE of **=1^{Cl}** ($\delta^{31P\{^1H\}} = 42.0$ ppm). Its nature was in this situation starting from **=1^I** not further examined. More successful was the reduction using Cr(Cp*)₂ ($E_{1/2} = -1.47$ V in THF),⁵⁹ yielding **=3^I** in 43 % yield. Besides the nitride, another species with two coupling doublets in the ³¹P{¹H} NMR spectrum is observed. When performing the same reaction under a ¹⁵N₂ atmosphere, two singlets appear in the typical nitride region (between 350 and 450 ppm as found for Re(V) nitrides herein and in other work^{69,80,84}). The nature of this apparently N-incorporated side-product will be discussed below. When the same reduction is performed under Ar, NMR spectroscopy revealed no Re-complex features

neither in the ³¹P{¹H} NMR in a broad range (−1000 to +1000 ppm), nor in the ¹H NMR spectrum. In the latter, formation of isobutene was observed. Possible formation of a stable Re(II) compound in absence of N₂ was examined by measuring EPR, which showed no signals. It could be that the conditions (RT and benchtop EPR spectrometer) are not sufficient to detect such a Re(II)-species, although a related Re(II)-compound [ReCl₃(PON_{py}OP)][−] (PONOP = 2,6-bis(diisopropylphosphinito)pyridine) gave an EPR signal at RT (yet measured in the solid state).⁸⁴ Most important however is the absence of nitride when reducing under Ar, which together with the experiment under ¹⁵N₂, confirms atmospheric uptake of N₂.



Scheme 54. (Electro)chemical N₂-splitting from =**1**^I into =**3**^I and the independent synthesis of the latter by using TMS-N₃. Upon N₂-splitting via CPE or Cr(Cp^{*})₂, **10** and isobutene (as characterised in case of Cr(Cp^{*})₂) are formed.

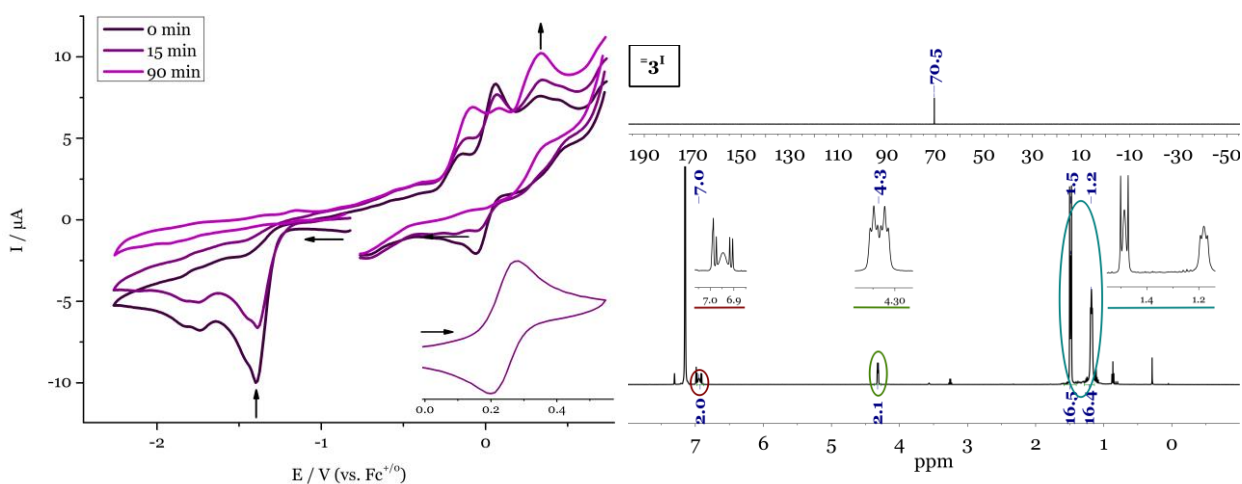


Figure 42. Left: CPE of =**1**^I at $E_{\text{appl.}} = -1.40 \text{ V}$ in THF as monitored by CV. The arrows indicate in the cathodic region the CPE potential and in the anodic region the rise of an oxidation assigned to =**3**^I. The inset is the Re(VI/V) oxidation of isolated =**3**^I. Right: NMR spectroscopy of =**3**^I in C₆D₆: ³¹P{¹H} NMR spectrum (top) and ¹H NMR spectrum (bottom).

To activate N₂ by electrochemical means, CPE was performed on =**1**^I in THF at $E_{\text{appl.}} = -1.40 \text{ V}$. The conversion of =**1**^I is accompanied by a colour change from dark brown to dark green, and the

transfer of 1.2 electrons per rhenium over the course of 1.5-2 h. By CV, a quasi-reversible oxidation wave appears with $E_{1/2} = 0.25$ V, which is exactly at the potential of the Re(VI/V) oxidation of $=\mathbf{3}^{\text{I}}$ as measured from an isolated sample ($E_{1/2} = 0.24$ V) (see Figure 42 and A30). By ^1H NMR spectroscopy, formation of the nitride was confirmed, yet quantified only in about 12 % yield, as averaged over three runs.

Besides $=\mathbf{3}^{\text{I}}$, the $^{31}\text{P}\{^1\text{H}\}$ NMR spectrum after CPE also showed doublets at 73 and 46 ppm, as was found for reduction using $\text{Cr}(\text{Cp}^*)_2$ (and in trace amounts using $\text{Co}(\text{Cp})_2$). These doublets integrate 1:1, couple to each other via a ^{31}P COSY NMR spectroscopy, and show a *trans*-coupling constant ($^2J_{\text{PP}} = 152$ Hz). An initial proposal for a C_1 -symmetric species when working with the (P=N=P)-ligand would be the resulting species after a protonation reaction. Complexes bearing this ligand have the most basic reaction site at the backbone, as was shown for protonation of $=\mathbf{3}^{\text{Cl}}$ and $[\text{NiBr}(\text{P}=\text{N}=\text{P})]$.^{72,199} Treatment of $=\mathbf{3}^{\text{I}}$ with HOTf results directly in formation of a dark red species showing coupling doublets by $^{31}\text{P}\{^1\text{H}\}$ NMR spectroscopy ($\delta_{^{31}\text{P}\{^1\text{H}\}} = 72.5$ and 70.2 ppm) (Figure 43). The corresponding ^1H NMR spectrum shows 4 inequivalent *tert*-butyl groups and 5 equally integrating backbone signals. Unequivocal prove for backbone protonation to $[\text{ReNI}(\text{N}(\text{CHCH}_2\text{PtBu}_2)(\text{CHCHPtBu}_2)]\text{OTf}$ ($\mathbf{9}^{\text{I}}\text{-OTf}$) comes from the ^1H - ^{13}C HSQC NMR, showing a cross peak between an upfield shifted carbon at 40.6 ppm and two backbone proton peaks at 4.3 and 3.4 ppm. These NMR resonances do not resemble our C_1 -symmetric side-product and discard that protonation causes its formation upon N_2 -splitting.

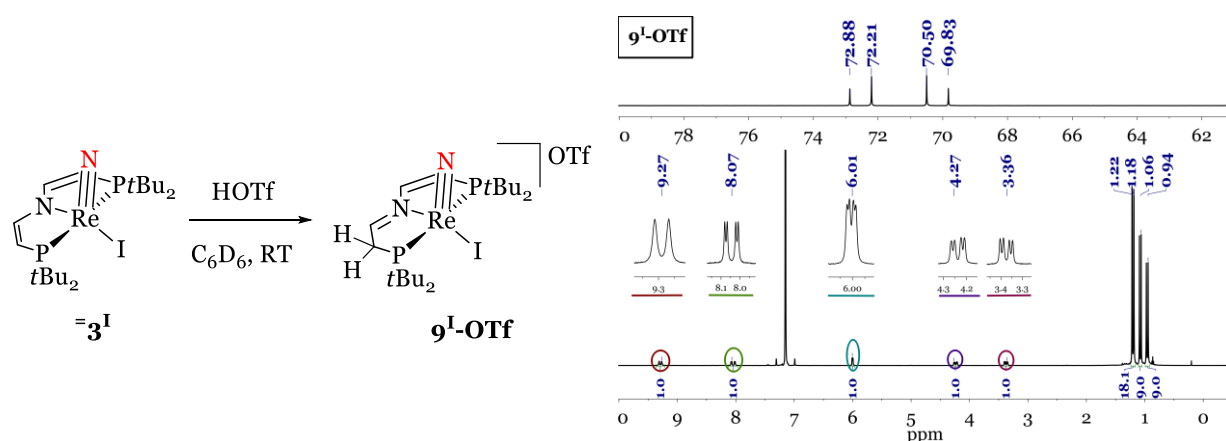


Figure 43. Left: protonation of $=\mathbf{3}^{\text{I}}$ with HOTf yields $\mathbf{9}^{\text{I}}\text{-OTf}$. Right: NMR spectroscopy of $\mathbf{9}^{\text{I}}\text{-OTf}$ in C_6D_6 . Bottom: ^1H NMR, Top: $^{31}\text{P}\{^1\text{H}\}$ NMR.

The chemical shift difference of this side-product between the doublets in $^{31}\text{P}\{^1\text{H}\}$ NMR spectroscopy ($\delta_{^{31}\text{P}\{^1\text{H}\}} = 73$ and 46 ppm, $\Delta\delta = 30$ ppm), is reminiscent of cyclometallation via formal C-H activation of a *tert*-butyl moiety of the metal. Several examples of cyclometallation

are known in *tert*-butyl carrying phosphorous based pincer chemistry, i.e. from the group of Mayer,¹⁷⁶ and within our group starting from an Osmium nitride bearing the P=N=P-ligand.¹⁶⁸ The upfield shift in a cyclometallated product is due to ring strain that the phosphorous atom in the four-membered ring experiences.²⁰⁰ The ¹H NMR spectroscopic analysis of the side-product was initially hindered by the presence of a C_{2v}-symmetric unknown compound and =**3I**, both with comparable shifts and similar solubility properties in pentane. Via extraction with hexamethyldisiloxane (HMDSO), we could increase the ratio between the C₁-symmetric side-product and the other Re-species, which facilitates a more in-depth look. By ¹H{³¹P} NMR spectroscopy, five equally integrating resonances are observed in the typical backbone range for the P=N=P-ligand (from 4-8 ppm), and three *tert*-butyl moieties. Notably, measuring a ¹H NMR spectrum shows that one of the smaller features at 5.7 ppm splits into two doublets, with a large coupling constant (¹J_{HP} = 356 Hz), as reminiscent of a direct P-H bond.^{200,201} In the reverse experiment, we found the same coupling constant in the ³¹P NMR spectrum, as the doublet around 46 ppm splits into a doublet of doublets (Figure 44). Combining these observations with the appearance of two singlets in the ¹⁵N{¹H} NMR spectrum, we propose formation of nitride species [ReNI{N(CHCHPh*t*Bu)(CHCHPh*t*Bu₂)}] (**10**) where one *tert*-butyl moiety has decomposed and isobutene is released. Isobutene was actually found in the ¹H NMR spectrum after chemical reduction using Cr(Cp*)₂ at 1.73 and 4.65 ppm. Due to overlapping signals, the amount cannot be quantified. When splitting N₂ on =**1I** by means of electrochemistry, vacuum is applied to the sample before NMR spectroscopic analysis, hindering the detection of this decomposition product. By loosely comparing the integration between the ³¹P{¹H} NMR spectrum corresponding to the ¹⁵N{¹H} NMR spectrum in Figure 44, =**3I** and **10** are assigned to the peak at 370.2 ppm and 364.3 ppm, respectively. This mixture was further examined by LIFDI mass spectroscopy, confirming formation of **10** at 628.1 m/z (calcd. for C₃₆H₃₂N₂P₂ReI: 628.1 m/z). The stretching frequency of the P-H bond is not easily assigned as attempted via ATR IR spectroscopy. Three possible, very weak frequencies are found at 1833, 2304, and 2447 cm⁻¹ (Figure A31). The first one is too low for a P-H stretching frequency,^{202,203} and the middle one is more likely an overtone of a strong vibration at 1152 cm⁻¹. The peak at 2447 cm⁻¹ could therefore be the P-H stretching of **10**, but the peaks are very low in intensity. In future research, when larger amounts of this mixture are obtained, full separation of =**3I** and **10** could be realised by subsequent extractions with HMDSO or with cold HMDSO, that eases its full characterisation. Despite several attempts, no crystals suitable for XRD spectroscopy could be obtained.

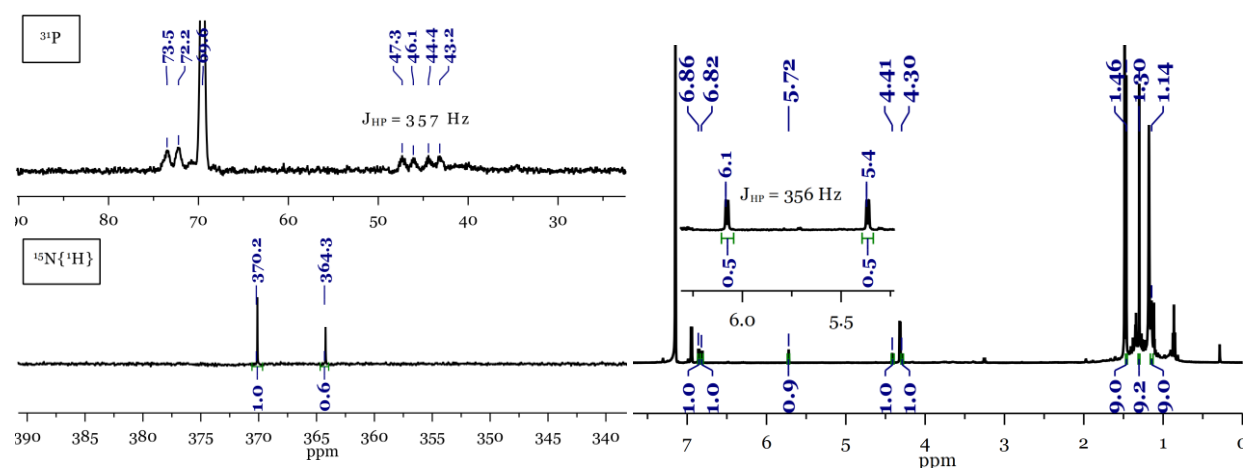


Figure 44. NMR spectroscopy of a mixture of **3I** and **10**. Left: ^{31}P NMR spectrum (top), $^{15}\text{N}\{^1\text{H}\}$ NMR (bottom). Right: $^1\text{H}\{^{31}\text{P}\}$ NMR spectrum, where only the peaks belonging to **10** are integrated and assigned. Inset: ^1H NMR spectrum of the region between 5.2 and 6.3 ppm.

Identifying **10** as unexpected side-product, it raises the question how and why it is formed. An isolated sample of **3I** proves stable in solution over a prolonged time, indicating that formation of **10** requires the reagents and/or intermediates present during N_2 -splitting. In general, this type of reactivity is not unprecedented in our group. Dr. M. van Alten (né Kinauer) studied the reactivity of imido complex $[\text{Ir}(\text{N}t\text{Bu})(\text{P}=\text{N}=\text{P})]$ with nucleophiles. This was hindered by the complex' instability at higher temperature, yielding 1 eq. of isobutene and the C_1 -symmetric $[\text{Ir}(\text{NH}t\text{Bu})\{\text{N}(\text{CHCHPtBu}_2)(\text{CHCHPtBu})\}]$. One *tert*-butyl moiety here decomposed into isobutene and a hydrogen atom, which is accepted by the imido moiety, transforming it into an amido ligand.¹⁷⁷ The analogy with the work as described herein is evident, where for **10** the phosphorous moiety serves as H-atom acceptor. Noteworthy, Dr. I. Scheibel describes formation of a C_1 -symmetric product upon initial attempts of reducing **3Cl** using a strong reductant (KC_8 ($E_p \approx -2.6$ V (*N*-methylpyrrolidone))⁹⁷), which also has only three *tert*-butyl moieties and is accompanied by isobutene formation.⁷⁹ The fate of the H-atom was not clarified. It is assumed that this kind of reactivity is induced by reducing conditions or an electron rich metal, promoting the most likely first step of oxidative addition of a *tert*-butyl C-H bond. In the Ir-case no external reagents are required for decomposition, but the complex itself is quite reducing as reflected by its mild oxidation potential of $E_{1/2} = -0.9$ V.¹⁷⁷ Comparing the strong reductant used in case of **3Cl** and the mild conditions as applied here or in the Ir-case to induce a comparable reactivity, we tentatively ascribe the introduction of the unsaturated $\text{P}=\text{N}=\text{P}$ -ligand to favour such a pathway. The chloride analogue of **10** was never observed, yet cannot be ruled out (lower nitride yields are observed for this system anyway). It might well be that **10** is only a stable compound because of the sterically demanding iodide or in absence of chloride, being a stronger base as iodide.

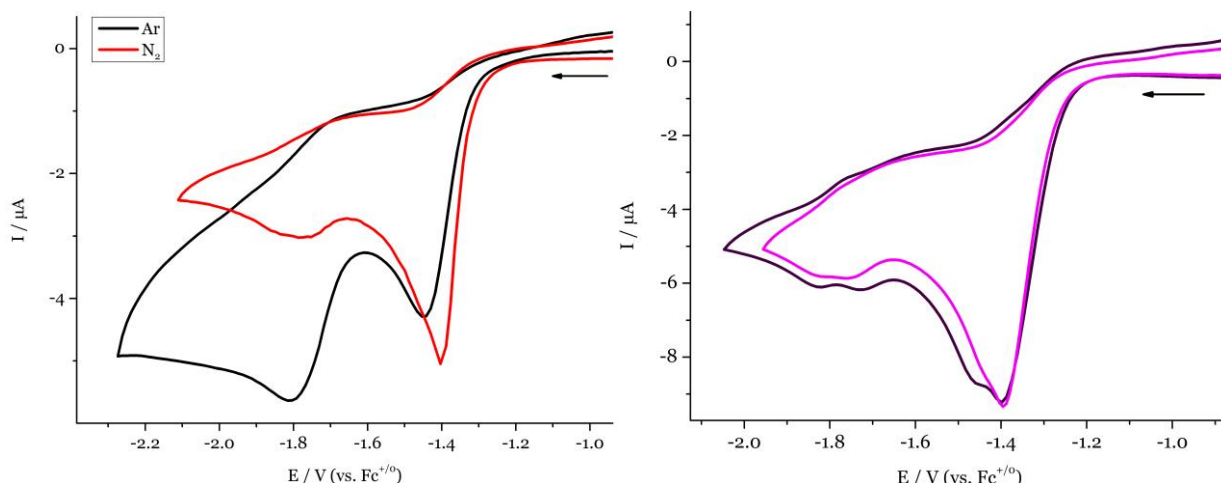


Figure 45. Left: a preliminary comparison of circa 1 mM $\text{=}\mathbf{1}^{\mathbf{I}}$ under N₂ (red) and Ar (black) in THF with 0.2 M (*n*Bu₄N)PF₆, $\nu = 0.1 \text{ Vs}^{-1}$. Right: A comparison of circa 2 mM $\text{=}\mathbf{1}^{\mathbf{I}}$ in THF with 0.1 M (*n*Bu₄N)PF₆, $\nu = 0.1 \text{ Vs}^{-1}$, two different experiments from the same batch.

The potential for (electro)chemical N₂-splitting was obtained via CV of $\text{=}\mathbf{1}^{\mathbf{I}}$, which will be shortly discussed. Since these CVs are not sufficiently reproduced (and show differences between measurements from the same batch when measuring under N₂, *vide infra*), the data should be handled with care. CV of $\text{=}\mathbf{1}^{\mathbf{I}}$ under Ar shows two reductions at $E_{p,c,1} = -1.44 \text{ V}$ and $E_{p,c,2} = -1.81 \text{ V}$ at $\nu = 0.1 \text{ Vs}^{-1}$, that appear irreversible even when only the first event is scanned (Figure 54 and A32). The first peak is substantially shifted to milder potentials compared both to its saturated analogue $\mathbf{1}^{\mathbf{I}}$ ($E_p = -1.61 \text{ V}$) or its chloride analogue $\text{=}\mathbf{1}^{\mathbf{Cl}}$ ($E_p = -1.75 \text{ V}$). The first effect is attributed to reduced π -donation from the backbone upon desaturation and the second effect to reduced donor properties of iodide vs. chloride. In strong analogy to $\mathbf{1}^{\mathbf{I}}$ or $\text{=}\mathbf{1}^{\mathbf{Cl}}$, the two reductions under Ar are likely coupled by reversible halide loss in between and are assigned to the [ReI₂(P=N=P)]^{0/-} and [ReI(P=N=P)]^{0/-} couples. For the chloride species $\text{=}\mathbf{1}^{\mathbf{Cl}}$, it was found that the difference between the reductions is decreased when the ligand is unsaturated ($\Delta E_{p,c,2} - \Delta E_{p,c,1} = 0.30 \text{ V}$ for $\mathbf{1}^{\mathbf{Cl}}$ and 0.16 V for $\text{=}\mathbf{1}^{\mathbf{Cl}}$). Here, the same trend is observed ($\Delta E_{p,c,2} - \Delta E_{p,c,1} = 0.60 \text{ V}$ for $\mathbf{1}^{\mathbf{I}}$ and 0.37 V for $\text{=}\mathbf{1}^{\mathbf{I}}$). It might indicate that the second reduction is partially ligand based, which would then be favoured for the conjugated P=N=P-ligand. Notably, the (P=N=P)-ligand is potentially non-innocent and can undergo versatile proton/electron transfer at the vinyl-groups.¹⁹⁹ The oxidative area of $\text{=}\mathbf{1}^{\mathbf{I}}$ shows a quasi-reversible oxidation ($E_{1/2} = -0.01 \text{ V}$ at $\nu = 2.0 \text{ Vs}^{-1}$), which is shifted anodically by 0.21 V compared to $\mathbf{1}^{\mathbf{I}}$, and assigned to the Re(IV/III)-oxidation (Figure A32).

When measuring $\text{=}\mathbf{1}^{\mathbf{I}}$ under a N₂-atmosphere, the first reduction at $E_{p,c,1} = -1.40 \text{ V}$ ($\nu = 0.1 \text{ Vs}^{-1}$) appears irreversible and shifts cathodically when measuring up to $\nu = 5.0 \text{ Vs}^{-1}$. Compared to Ar, this feature is found 0.04 V more anodically and displays a current increase of circa 15 %. Since

these CVs are not repeated multiple times, the emphasis is here on both trends (slight anodic shift and current increase). Actually, within the same batch and upon usage of the same electrodes, electrolyte-, and solvent batches, this first reduction feature is sometimes found with a small shoulder on its cathodic side (Figure 45, right). This might be because of fouling of the working electrode and in future research, this should be examined by repeatedly polishing the disk electrode when this double peak feature is observed. Nevertheless, the observed changes on the first feature when measuring under N₂ are accompanied by a different appearance of the reduction assigned to [ReI(P=N=P)]^{0/-} under Ar; this feature is either decreased in intensity or vanished completely and a new feature with the same potential is observed. At this point, we cannot distinguish between both possibilities. In all cases, it is in line with N₂-coordination at the Re(II)-stage.

3.5. Initial attempts to form ammonia from the iodide platform

Regarding N₂-functionalisation, this work mostly relates to C-N bond formation and subsequent fragment release as was established from **3^{Cl}** and extended to **=3^{Cl}** in Chapter II.4. However, the electrochemistry of the iodide nitrides **3^I** and **=3^I** revealed a distinct reduction feature. Although these features are at very negative potentials ($E_p = -3.04$ V (**3^I**), and -2.97 V (**=3^I**), $\nu = 0.1$ Vs⁻¹), it inspired us to consider formation of NH₃ from these platforms. During the time period this research was executed, a very potent and promising PCET reagent, a combination of SmI₂ and H₂O, was reported for NH₃ ammonia by Nishibiyashi, as highlighted in Section I.2.1. Inspired by their results, we dissolved **3^I** and **=3^I** in THF with 10 eq. of SmI₂, and added 100 eq. H₂O, analogous to a procedure by Miller, who generate NH₃ in circa 75 % from [ReCl₃(PONOP)] (PONOP = 2,6-bis(diisopropylphosphinito)pyridine).

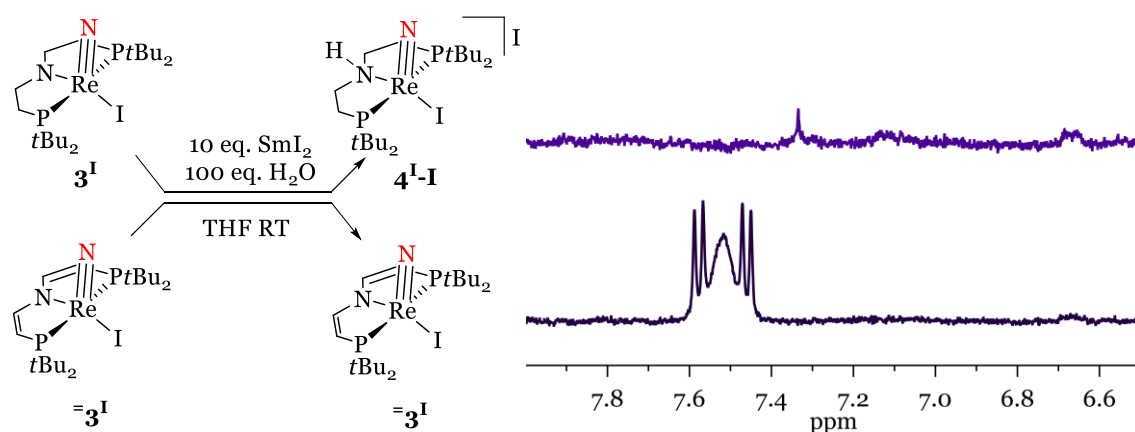


Figure 46. Left: Reaction scheme for the attempt to form NH_3 separately from $\mathbf{3}^{\text{I}}$ and $=\mathbf{3}^{\text{I}}$ using $\text{SmI}_2/\text{H}_2\text{O}$, upon which exclusively $\mathbf{4}^{\text{I-I}}$ and $=\mathbf{3}^{\text{I}}$ are found, respectively. Right: Zoom of region between 6.5 and 8.0 ppm of the ^1H NMR in d_8 -THF after the reaction to check for NH_3 formation, starting from $\mathbf{3}^{\text{I}}$ (top), and $=\mathbf{3}^{\text{I}}$ (bottom).

After combining all reagents, a temporally red colouration indicated formation of the $\text{SmI}_2/\text{H}_2\text{O}$ complex, and strong gas release is attributed to H_2 -formation, similarly to the literature procedures. After evaporation *in vacuo*, the reaction mixtures were examined by NMR spectroscopy, showing the quantitative formation of $\mathbf{4}^{\text{I-I}}$ when starting from the PNP-platform or the retain of $=\mathbf{3}^{\text{I}}$ in the other case. This reflects the higher basicity of $\mathbf{3}^{\text{I}}$ bearing the strong π -amide donor in the backbone compared to its unsaturated analogue. Besides, no traces of NH_4^+ -formation are found, as judged by the blank ^1H NMR spectrum in the region around 7.2 ppm, where NH_4^+ appears as broad triplet under these conditions.⁸⁴ Even if protonation of NH_3 would not be its full extent (which speaks against the procedures of Nishibayashi and Miller),^{57,84} its formation is highly unlikely as not even traces of ammonium are found in these NMR spectra and the rhenium complexes maintain their ligand environment (besides protonation of $\mathbf{3}^{\text{I}}$). This indicates that for these nitrides, the barrier for PCET reactions at the nitride from the $\text{SmI}_2/\text{H}_2\text{O}$ complex is too high and if this goal is continued in future research, a stronger acid/reductant combination should be examined.

3.6. Discussion of the (electro)chemical N₂-splitting yields

Upon establishing (electro)chemical N₂-splitting for the unsaturated chloride and iodide platforms, and an in depth electrochemical study to =1^{Cl} , their performance regarding nitride yields can be discussed. In case of =3^{I} , the identification of **10** as a product of N₂-splitting, allows us to add its yield to the overall N-containing product balance, see Table 12. Regarding nitride synthesis using chemical reductants, the results obtained from the =1^{I} platform are from this work and are compared with the results starting from =1^{Cl} as executed by Dr. F. Wätjen.⁷² Taking all known N-containing species in account, these systems behave similar, and nitride is obtained in yields up to 60-65 %. In case of =1^{Cl} , the extended electrochemical study under Ar revealed that the Re(II/I) reduction feature is more anodically shifted compared to 1^{Cl} , and strong reductants as Na/Hg and KC₈ likely lead to over-reduction and decomposition. Even though this reduction disappears when measuring under N₂, such a heterogeneous reductant is accompanied with strong concentration gradients where maybe local N₂-concentrations are depleted. For =1^{I} , very negative or heterogeneous based chemical reductants were not yet examined and could be considered in future research to complete the picture. Striking is the low yield of =3^{I} as obtained using cobaltocene, which might have to do with the reduction potential mismatch.

Table 12. (Electro)chemical N₂-splitting from the =1^{X} platforms (X = Cl, I) in THF. ^a

Chemical	=3^{Cl}	=3^{I}	10
Na/Hg	30 % ⁷²	-	-
Co(Cp*) ₂	60 % ⁷²	-	-
Cr(Cp*) ₂	-	43 %	21 %
Co(Cp) ₂	-	20 %	traces
<hr/>			
Electrochemical	E_{appl}/V		
	-1.67	15 %	-
	-1.41	-	10 %
			5 %

^a - indicates the experiment is not performed.

By means of electrochemistry, overall nitride yield(s) are low for both platforms (circa 15 %), which markedly differs from parent 1^{Cl} and 1^{I} (circa 60 % yield). For both parent platforms, we could demonstrate rapid N₂-activation ($k_3 > 5 \cdot 10^7 \text{ M}^{-1} \text{ s}^{-1}(\text{1}^{\text{Cl}})$, $k_9 = 3 \cdot 10^4 \text{ M}^{-1} \text{ s}^{-1}$ or $k_{11} = 1 \cdot 10^3 \text{ M}^{-1} \text{ s}^{-1}(\text{1}^{\text{I}})$) by species at the formal Re(II) oxidation state. Therefore, the lifetime of this state influences the N₂-fixation efficiency. For =1^{Cl} , the unimolecular decay pathway (k_{15}) is slightly more prominent than for 1^{Cl} . More importantly, a bimolecular pathway (k_{16}) from $[\text{ReCl}_2(\text{PNP})]^-$ may significantly reduce the lifetime of Re(II) species. Besides lowering the

electrosynthetic yield, this pathway might also be detrimental for other heterogeneous reductants (i.e. Na/Hg or KC₈), due to the aforementioned high local concentrations of reduced Re-species. With this reaction in mind, it should be noted that CPE for **1**^{Cl} was performed in a lower and higher concentration range (1 or circa 3 mM), both giving circa 15 % yield. At low concentrations, the effect of the water content of THF should not be underestimated (see Section II.3.2), whereas at higher concentrations this bimolecular decomposition pathway can come in play. For **1**^{Cl}, no improvement was observed when performing the reaction in different solvents. This is in line with none of the here mentioned considerations for the decreased yield to be specifically solvent dependent.

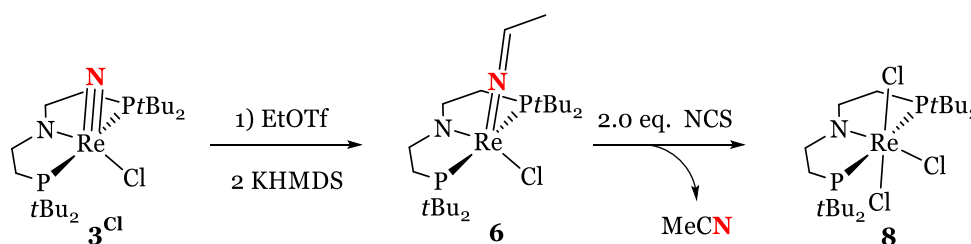
For **1**^{Cl}, we proposed a chloride induced disproportionation type reaction that might play a role in decreased nitride yields upon electrochemical N₂-activation, initiated by an uphill chloride coordination ($K_{Cl} \leq 0.015$). Notably, **1** proves stable in presence of (*n*He₄N)I over the course of at least 120 hours, in sharp contrast to its chloride analogue (Figure A34). It is not surprising that a similar reaction for iodide is significantly more uphill, due to the higher steric demand of iodide. Since both platforms are behaving similarly mediocre, this sheds a milder light on the importance of this reaction as explanation for reduced nitride yields by electrochemical N₂-splitting.

II.4: Electrochemical MeCN release

A part of this Chapter is published in: ‚Elektrochemische Freisetzung von Acetonitril aus einem Rhenium PNP-Pinzetten Komplex‘, C.I. Kiene, **2019**, Bachelorthesis, Georg-August-Universität Göttingen.

4.1. Electrochemical MeCN release from [Re(NCHCH₃)Cl(PNP)]

The N₂-derived nitride [ReNCl(PNP)] (**3^{Cl}**) was functionalised via C-N bond formation by EtOTf, as elaborated in Section I.2.2.3. Subsequent deprotonation with the strong base KHMDS yields azavinylidene [Re(NCHCH₃)Cl(PNP)] (**6**), from which MeCN was released by oxidation and deprotonation in presence of chloride ions to regenerate [ReCl₃(PNP)] (**8**). In the established method, all three required reagents (oxidant, base, and chloride source) are provided by the multifunctional reagent NCS, see Scheme 55.¹⁵¹ The mechanism of this oxidation is not well understood: two equivalents of *H*-succinimide are formed although only one proton originates from **6** to release MeCN. As alternative to a chemical reagent, the required oxidation equivalents can originate from electrochemistry, where the potential can be chosen selectively. To probe for promising conditions to transfer this MeCN release step towards electrochemical conditions, the electrochemistry of **6** was examined in presence of a base and a chloride source.



Scheme 55. The previously established N-C bond functionalisation and MeCN release from **3^{Cl}**.¹⁵¹

The CV of **6** in THF shows 4 oxidative events, see Figure 47. The first event at $E_{1/2} = -0.49$ V is fully reversible, diffusion controlled and assigned to a metal-centred Re(IV/III) oxidation (Figure A36). Its one-electron character was confirmed in a separate coulometric experiment. The subsequent three oxidations are at $E_p = 0.50$ V, 0.61 V, and 0.95 V at $\nu = 0.1$ Vs⁻¹. After scanning through the latter two events, the Re(IV/III) oxidation loses its reversibility, indicating that these are coupled to irreversible chemical reactions. They are therefore assigned to ligand backbone oxidation, as corroborated by their absence in the CV comparison between **6** and unsaturated [Re(NCHCH₂)Cl(P=N=P)] (**6**) (Figure 47, *vide infra* for its synthesis). In addition, **6** shows an irreversible, far negative reduction at $E_p = -3.14$ V at $\nu = 0.1$ Vs⁻¹ (Figure A36).

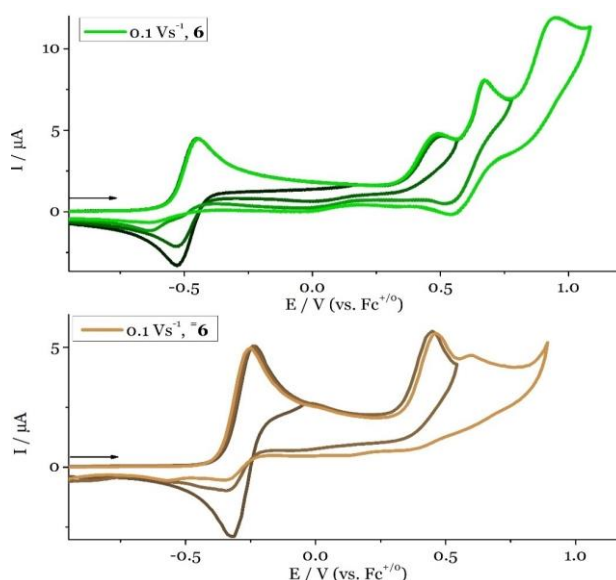


Figure 47. CV of the oxidative region of **6** (top) and **6** (bottom) in THF with 0.2M (*n*Bu₄N)PF₆, $\nu = 0.1 \text{ Vs}^{-1}$.

To enable electrochemical MeCN generation and release, the CV of **6** was examined in presence of base and chloride source (*n*He₄N)Cl. The electrochemistry of the explored additives was tested to secure redox-inertness in our region of interest, as presented in Appendix A2. A successful base for this reaction would be capable of deprotonating [**6**]⁺, of which the product can be oxidised again to formally form the [ReCl(NCCH₃)(PNP)]⁺-adduct via an *ECE*-mechanism. This is indicated in the CV by the loss of reversibility of the Re(IV/III) oxidation of **6** and the appearance of an additional oxidation wave. The addition of 4 eq. of NEt₃ has only little effect on the first oxidation of **6**, see Figure 48. A slight current increase is observed at $\nu = 0.1 \text{ Vs}^{-1}$, and the reversibility slightly decreases ($i_{p,a}/i_{p,c}$ changes from 1.0 to 1.25 at $\nu = 0.1 \text{ Vs}^{-1}$ upon addition of 4 eq. of NEt₃). At $\nu = 1.0 \text{ Vs}^{-1}$ no influence is observed, indicating that NEt₃ is most likely close to the pK_a of [**6**]⁺ (pK_a NEt₃ (THF) = 14.0)²⁰⁴, and the reaction is in equilibrium. More eq. of NEt₃ should have been added to examine this hypothesis, which was not tested in the context of this work. Subsequent addition of Cl⁻ ions results in an anodic peak potential shift of the Re(IV/III) oxidation, and the appearance of an additional, irreversible oxidative wave. Notably, the same behaviour was observed when no base was present. These observations strongly indicate that chloride association can be coupled to the Re(IV/III) oxidation of **6**, yielding [ReCl₂(NCHCH₃)(PNP)], which is subsequently irreversibly oxidised at $E_p = -0.32 \text{ V}$ ($\nu = 1.0 \text{ Vs}^{-1}$). This Re(V/IV) oxidation appears at only a slightly more positive potential compared to the Re(IV/III) oxidation of **6**, attributed to the newly coordinated, electron-donating chloride ligand. This species and the origin of its irreversible oxidation were not investigated further.

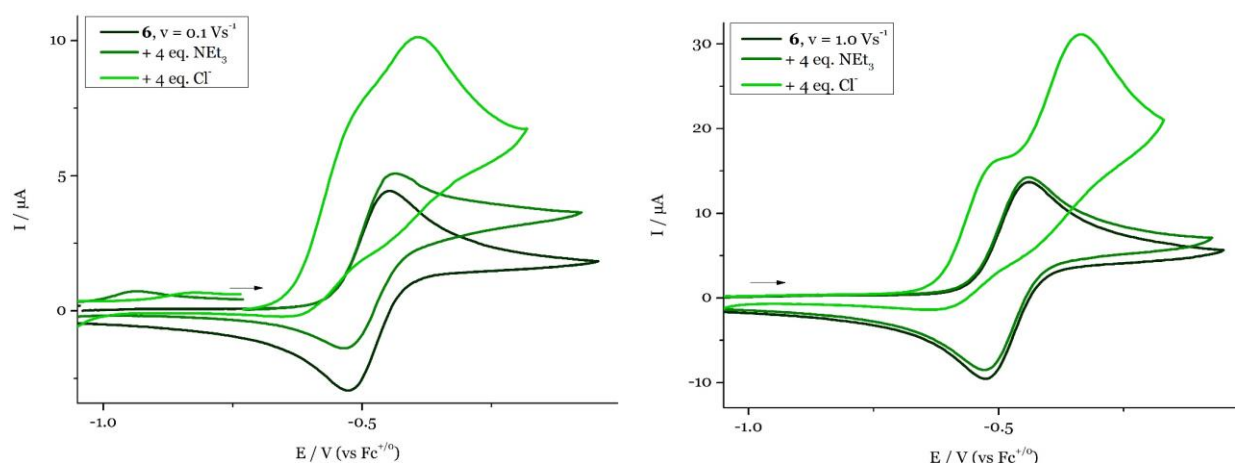


Figure 48. CV of the oxidation of **6** in presence of 4 eq. NEt_3 and subsequently 4 eq. $(n\text{He}_4\text{N})\text{Cl}$ $v = 0.1 \text{ Vs}^{-1}$ (left) $v = 1.0 \text{ Vs}^{-1}$ (right) in THF with $0.2 \text{ M } (n\text{Bu}_4\text{N})\text{PF}_6$.

Since NEt_3 proved too weak to induce significant changes in the CV, stronger bases were explored. Addition of 10 eq. of DBU ($\text{pK}_a = 18.1$ (THF))²⁰⁴ to **6** and measuring the Re(IV/III) oxidation shows an anodic shift of circa 0.03 V , a complete loss of reversibility and a strong ($>$ twofold) current increase (Figure 49). All observations indicate the coupling of the Re(IV/III) oxidation to deprotonation and the subsequent oxidation of the product. Notably, 4 eq. of DBU already showed this behaviour. Subsequent addition of chloride causes the first redox event to shift even more anodically and a second oxidation is shown in proximity. Although this initially looks similar to the CV of **6** and $(n\text{He}_4\text{N})\text{Cl}$ alone (or additional presence of NEt_3 as shown in Figure 48, left), the current on the second oxidation is substantially higher and increases further thereafter when DBU is present, reflecting the influence of the base. Similar results were obtained by using the slightly weaker tetramethylguanidine (TMG) as base ($\text{pK}_a = 17.0$ (THF))²⁰⁴. However, the CV appearance changed over time and this reagent was therefore not examined further.

With DBU as base of choice, scanning through this oxidative wave hopefully generates MeCN and leaves a Re complex-fragment that is trapped by the Cl^- anions to form $[\text{ReCl}_3(\text{PNP})]$ (**8**). This might be visible in the cathodic reverse trace in the CV. The irreversible Re(IV/III) reduction of **8** is found at $E_p = -1.10 \text{ V}$ at $v = 0.1 \text{ Vs}^{-1}$, which shifts cathodically in presence of Cl^- (*vide infra*, Section II.4.5). In this region, only a very small wave at $E_p = -1.12 \text{ V}$ is found in the cathodic reverse trace of the CV of **6** in presence of DBU and Cl^- (Figure 49). We therefore state that at least no significant amount of **8** is formed on the CV timescale.

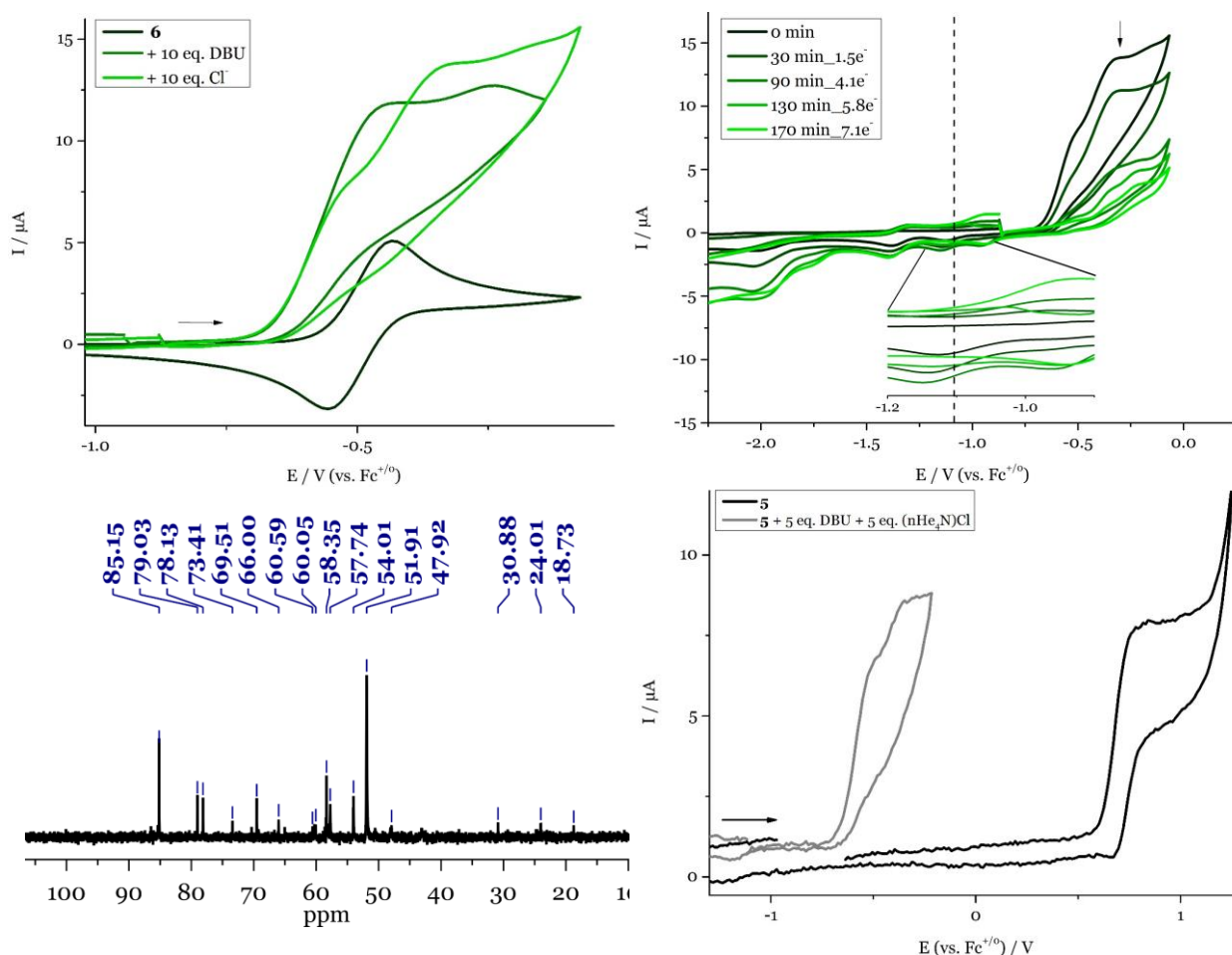
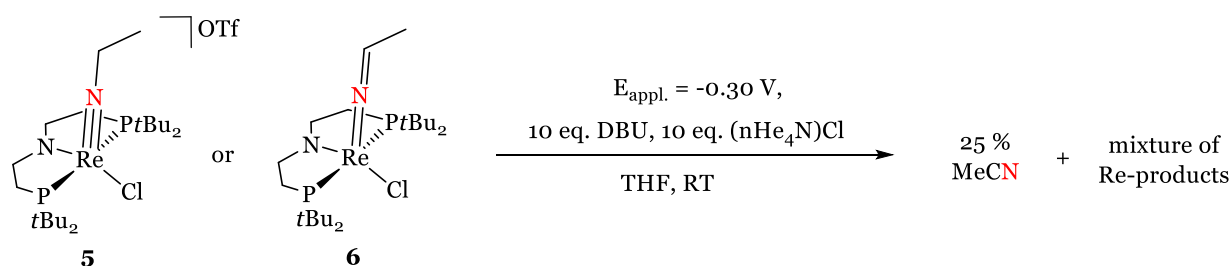


Figure 49. Top left: CV of the Re(IV/III)-oxidation of **6** at $\nu = 0.1 \text{ Vs}^{-1}$ in presence of 10 eq. DBU and subsequently 10 eq. $(n\text{He}_4\text{N})\text{Cl}$ in THF with $0.2 \text{ M } (n\text{Bu}_4\text{N})\text{PF}_6$. Top right: CPE of the previous mixture at $E_{\text{appl.}} = -0.30 \text{ V}$ with a zoom of the region between -0.9 V and -1.2 V . The dashed line represents the potential of the reduction of **8**. Bottom left: $^3\text{P}\{^1\text{H}\}$ NMR spectrum of the crude inorganic fraction of the CPE in normal THF. Bottom right: CV of the oxidative region of **5** at $\nu = 0.1 \text{ Vs}^{-1}$ in presence of 5 eq. DBU and 5 eq. $(n\text{He}_4\text{N})\text{Cl}$ (left) in THF with $0.2 \text{ M } (n\text{Bu}_4\text{N})\text{PF}_6$.

Performing a CPE of this mixture at the peak potential of the second oxidation wave at $E_{\text{appl.}} = -0.30 \text{ V}$ results in a colour change from brown to orange and a transfer of circa 7 electrons per rhenium metal (as averaged over three experiments) (Scheme 56). During electrolysis, no significant wave appears close to the Re(IV/III) reduction of **8**. The before mentioned small feature at $E_p = -1.12 \text{ V}$ remains around circa $0.5 \mu\text{A}$ peak current until 90 min. of CPE time after which it decreases. A small wave at $E_p = -0.96 \text{ V}$ appears, which is too electropositive to correspond to the reduction of **8**. After electrolysis, the volatiles are vacuum transferred to a separate container and checked for the presence of MeCN by GC chromatography. Although obtaining a calibration curve for quantifying MeCN in THF proved challenging (see Section IV.3 for details), a reproducible release of circa 25% MeCN is established (based on two runs of 20 % and 32 % yield). This yield is only low and it is considered

if MeCN acts as a ligand to coordinatively unsaturated species. Therefore, we added in a separate experiment 5 eq. of a strong ligand (*t*BuCN) to the crude inorganic fraction, which could release MeCN as hypothetical ligand. Yet, no additional acetonitrile was obtained. On the inorganic side, the crude fraction was measured by NMR spectroscopy, and unfortunately, no **8** was found in the ¹H NMR spectrum. Even though a large excess of electrolyte is present, **8** should be easily identified due to its paramagnetic nature. This is in agreement with the absence of any peak in the right potential range for **8** in the CVs of the CPE. Furthermore, no broad paramagnetic peaks are observed. Instead, the ³¹P{¹H} NMR spectrum shows various compounds (Figure 49). No possible doublet pairs with the same coupling constant could be identified, indicating it to be at least >10 individual species. Extraction attempts with Et₂O proved that most of these species were rather polar and not separable from the electrolyte, which inhibits mass spectroscopic analysis. To check if too little chloride source was present during standard CPE conditions (10 eq. of (*n*He₄N)Cl) to form **8**, the reaction was repeated with 60 eq., yet with the same results.



Scheme 56. Electrochemical oxidation of **6** (either isolated or *in situ* formed from deprotonation of **5**) in presence of DBU and (*n*He₄N)Cl to release acetonitrile and a mixture of unknown Re-complexes.

In the course of this work, the deprotonation of the imido species [Re(NCH₂CH₃)Cl(PNP)]OTf (**5**) towards **6** was reconsidered, since the published route¹⁵¹ relies on the strong base KHMDS (pKa HMDS (THF) \approx 26).²⁰⁵ Ideally and more economically, the same base would be used for electrochemical MeCN release and deprotonation of **5**. To our positive surprise does DBU readily deprotonate **5** to quantitatively form **6** as characterised by NMR spectroscopy. The same is displayed by electrochemistry: **5** is irreversibly oxidised at a far anodic potential ($E_p = 0.81$ V, $\nu = 0.1$ Vs⁻¹). Upon addition of 5 eq. DBU, the colour changes from green to brown and the first oxidation is found at $E_p = -0.47$ V, indicating *in situ* formation of **6**. Subsequent addition of 5 eq. of (*n*He₄N)Cl leads to the same oxidative feature as starting from isolated **6** (Figure 49), and oxidative CPE on this mixture gives the same results. Although the electrolysis results do not invite to think towards catalytic N₂-splitting and functionalisation on this platform, modifying this deprotonation towards a milder reagent is noteworthy.

After establishing electrochemical MeCN release from **6**, initial considerations about the mechanism can be made. The transformation of the azavinylidene **6** to MeCN is accompanied by a deprotonation (*C*) and two oxidation steps (*2xE*). Isolated **6** is not deprotonated by DBU and based on the current increase in the CV upon addition of base, these fundamental steps can be arranged in an *ECE* mechanism: oxidation to [**6**]⁺, deprotonation and subsequent oxidation. The overall outcome of these steps is generation of [Re(NCH₂CH₂)Cl(PNP)]OTf (**7**), see Figure 50. The synthesis of **7** is already established via chemical oxidation and subsequent PCET reactivity (Figure 50), and by its NMR characteristics found to be best described as the Re(V) vinylimido tautomer. In the proposed *ECE*-mechanism, the potential of the second oxidation should correspond to the Re(V/IV) reduction potential of **7**. Since no CV of this compound was measured, its synthesis using AgOTf and TBP was repeated. Unfortunately, **7** was not synthesised as clean as in the published procedure but could only be isolated in circa 90% purity based on ³¹P{¹H}NMR spectroscopy (Figure A37). Still, CV was measured of this batch, to get an estimation of the Re(V/VI) reduction potential and its relevance in the CV of **6** upon addition of base. **7** shows one irreversible reduction at $E_p = -1.38$ V at $\nu = 0.1$ Vs⁻¹ (Figure 50). Although this value seems quite negative for a cationic Re(V) compound, it is not unprecedented: cationic Re(V) imido compounds **5** and =**5** are reduced in the same potential region ($E_p = -1.84$ V at $\nu = 0.1$ Vs⁻¹ (**5**), $E_{1/2} = -1.33$ V (= **5**)) (Figure A35). Besides, **7** displays an irreversible oxidation with multi-electron character at $E_p = 0.83$ V at $\nu = 0.1$ Vs⁻¹, attributed to PNP-ligand backbone oxidation. Considering the basic *ECE*-oxidative mechanism, this indicates a remarkable *potential inversion*: the first *E* (oxidation of **6**) is at $E_{1/2} = -0.49$ V, compared to the second *E* (analogue to the reduction of **7**) at $E_p = -1.38$ V. To probe if this second *E* can be the oxidation envisioned to form **7**, we briefly turned to digital simulation. As presented in Appendix Figure A37, the Re(IV/III) oxidation of **6** is simulated in agreement with the experimentally observed $E_{1/2} = -0.49$ V. In a next step, this oxidation of **6** is coupled to deprotonation and subsequent oxidation at $E_{1/2} = -1.38$ V to mimic the [**7**]^{0/-} oxidation in this process, see Figure 50. This reveals a current increase and anodic shift in such a manner that it is considered realistically that such a strong *potential inversion* appears. From the simulations, it becomes clear that a current increase of a two-electron process is too small to account for the experimental observed increase after addition of base. This strongly suggest that additional electron transfers occur within this oxidation process.

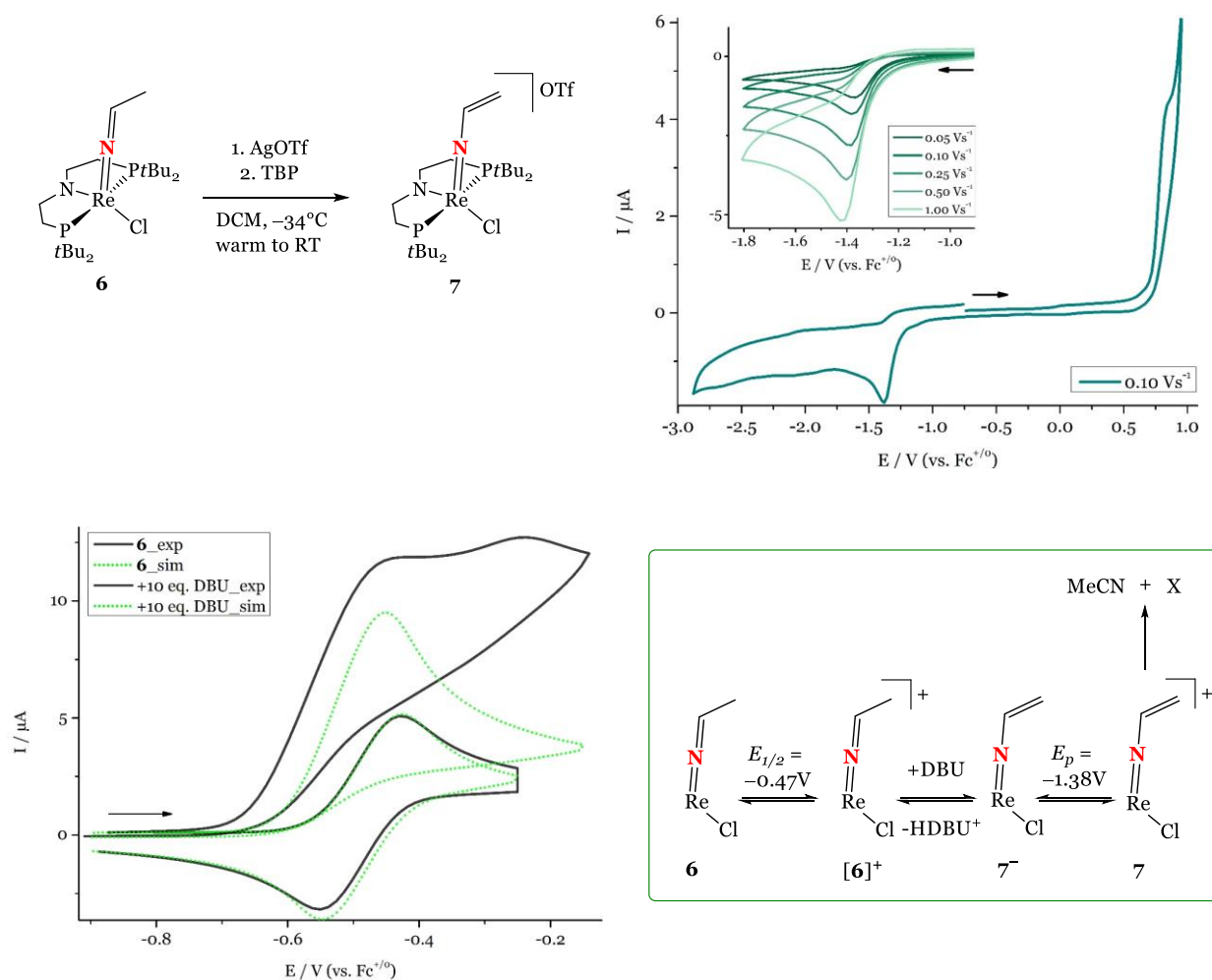


Figure 50. Top left: Synthesis of **7** as published by Schneider.¹⁵¹ Top right: CV of **7** in THF with 0.2 M $(n\text{Bu}_4\text{N})\text{PF}_6$ at $v = 0.1 \text{ Vs}^{-1}$. Inset: scan rate dependence of the first reduction. Bottom left: Simulation attempt of the Re(IV/III) oxidation of **6** before and after addition of 10 eq. of DBU. The electron transfers were simulated with $E_{1/2} = -0.49 \text{ V}$, and -1.38 V respectively, where the latter represents the reduction of **7** as found by CV. The parameters for the chemical reactions used for this simulation are: $K_{\text{deprotonation}} = 10$, $k_{\text{deprotonation}} = 1 \cdot 10^4 \text{ M}^{-1} \text{ s}^{-1}$, $K_{\text{MeCN release}} = 1 \text{ M}$, $k_{\text{MeCN release}} = 1 \cdot 10^4 \text{ s}^{-1}$. For more simulation parameters, see Figure A37. Bottom right: the simulated pathway: proposed ECE-mechanism from **6** to form **7** and subsequent MeCN release to a redox-inactive species X. The PNP-ligand is omitted for clarity.

To recapitulate the findings so far: oxidative CPE of **6** (either added as isolated material or formed *in situ* by deprotonation of **5**) in presence of DBU and $(n\text{He}_4\text{N})\text{Cl}$ affords 25 % of MeCN and a mixture of Re-compounds, yet no **8**. Importantly, circa seven electrons per rhenium are needed to fully convert the starting material by CV, whereas only three are necessary to successfully release MeCN and form **8**. These findings are in sharp contrast to chemical MeCN release, where **8** is found in circa 90% yield. One possibility for not generating **8** during CPE is an over-oxidation to the Re(V) stage, since an unlimited (and maybe drifting) oxidative potential can be present under CPE conditions. This would explain the need of more than three electrons. Yet, the quasi-reversible Re(V/IV) oxidation of **8** comes at $E_{1/2} = +0.05 \text{ V}$, thus the $>0.3 \text{ V}$ less oxidising CPE potential most likely prevents further oxidation. The origin of the over-oxidation

is therefore attributed to reaction of the PNP-ligand backbone. Especially in presence of excess base, the oxidation can be coupled to follow-up chemistry (deprotonation) via PCET, shifting it to milder potentials (as shown for **1^{Cl}** in Chapter II.3.1). Such further oxidations would also support the higher current deviating from a two-electron process observed after addition of base to **6** in Figure 50. Backbone based reactivity was also suspected by Dr. I. Scheibel (née Klopsch), who examined the oxidation of **7** with CuCl₂ upon which a C₁-symmetric species was generated by ³¹P{¹H} NMR spectroscopy.⁷⁹ Although we have no clear indication for the presence of C₁-symmetric species under CPE conditions, multiple (redox-active) follow-up reactions must occur to account for the mixture of various Re-compounds and the high amount of transferred electrons. Since the regeneration of a Re-species capable of reductive N₂-fixation is a prerequisite towards a (pseudo-)catalytic approach, the same (electro)chemical MeCN release was explored with the unsaturated (P=N=P)-ligand, as described in the next Sections.

4.2. Platform modifications to the unsaturated ligand

To explore (electro)chemical release of MeCN from unsaturated [Re(NCHCH₂)Cl(P=N=P)] (=6), its synthesis needs to be developed. First, the PCET route was examined by addition of excess TBP to either **5** or **6** at reaction temperatures RT and 50 °C. However, no conversion was observed at any condition. This implies that the (P=N=P)-ligand backbone protons have a higher BDFE_(C_{PNP}-H) compared to the O-H of the TBP (BDFE_{TBP} (THF) = 74.4 kcal mol⁻¹).¹⁹⁵ Subsequently, the electrophilic functionalisation was started from nitride [ReNCl(P=N=P)] (=3^{Cl}) with EtOTf. Notably, such reactivity was already established for the similar reaction with MeOTf. Several conditions were explored to obtain full conversion of which 10 eq. of EtOTf at 80°C represents the fastest route; no starting material remains after 90 minutes. Towards a (pseudo-)catalytic application, functionalisation at RT is elegant, and this could be achieved, yet with more severe reaction conditions (20 eq. of EtOTf and 48 h reaction time). The ethylation conditions for =3^{Cl} are more harsh compared to ethylation of 3^{Cl}, for which at RT only 1.2 eq. of EtOTf are required for full conversion after 24 h. This is attributed to the reduced nucleophilic character of =3^{Cl} because of backbone desaturation. In the crude ³¹P {¹H} NMR spectrum after reaction with EtOTf, two species are observed of which the major feature comes at 87.0 ppm, which resembles the saturated imido analogue ($\delta^{31P} \{^1H\}$ **5** = 90.1 ppm). This species can be isolated via crystallisation from THF/Et₂O in 55 % yield, and LIFDI mass spectroscopy confirms the formation of [Re(NCH₂CH₃)Cl(PNP)]OTf (=5). By ¹H NMR spectroscopy, the incorporated

ethyl fragment is clearly assigned to the nitride-*N*, since no 2D NMR coupling between the protons of the (P=N=P)-backbone and the ethyl moiety is observed. XRD of single crystals provides the molecular structure of **5**, where the Re coordinates in a distorted square pyramidal geometry ($\tau_5 = 0.14$), see Figure 51.^{m,171} Compared to the parent nitride, the Re-N_{imido} bond is basically untouched (Re-N2 = 1.647(18) Å (**3**^{Cl})⁷² and 1.680(5) Å (**5**)).

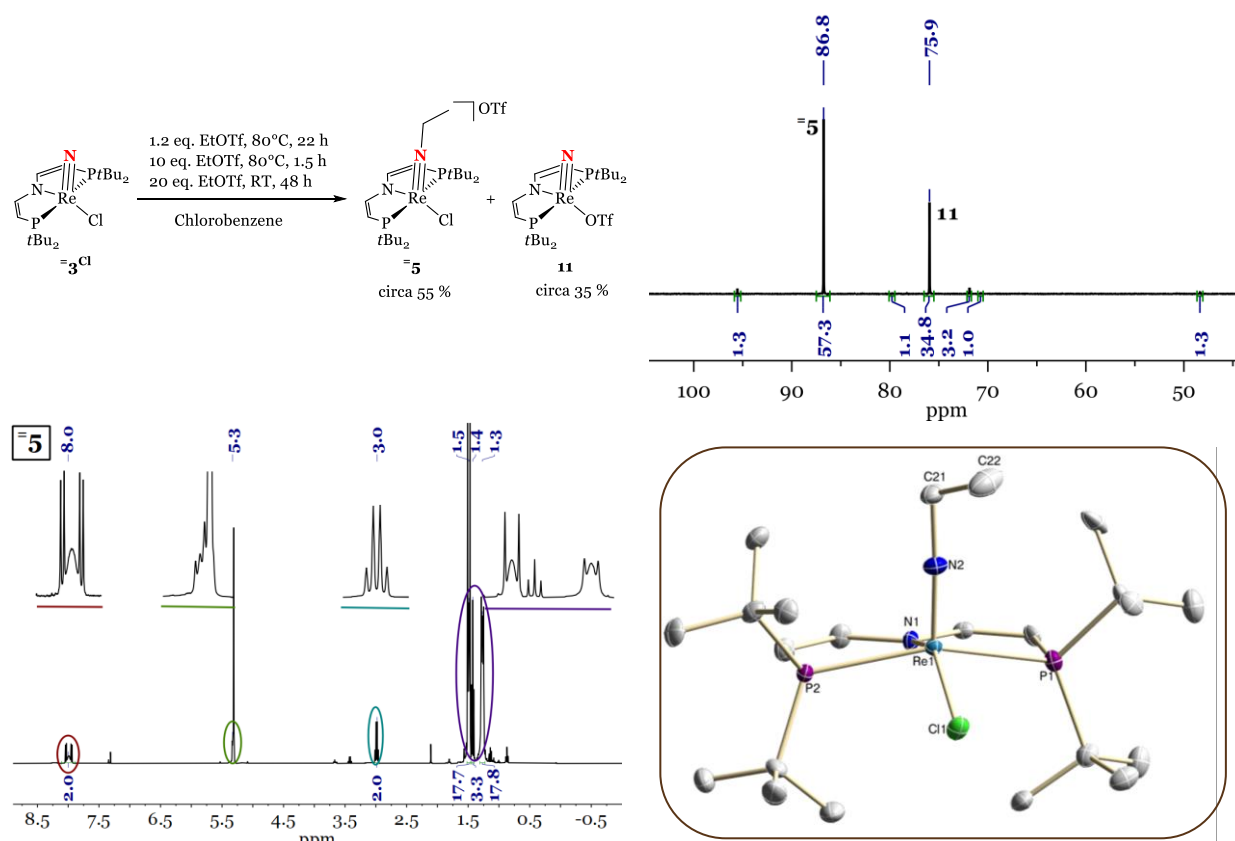
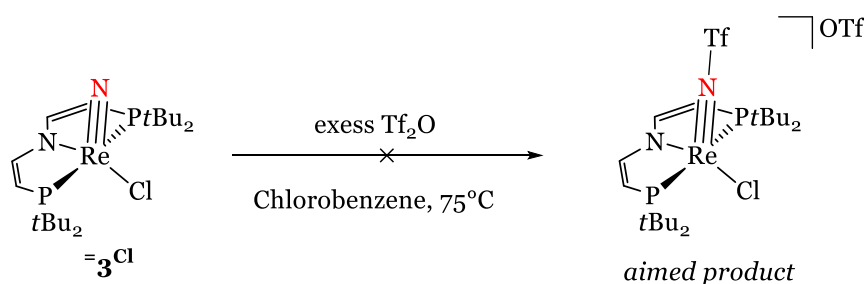


Figure 51. Top left: Synthesis of **5** from **3**^{Cl} with different eq. of EtOTf in chlorobenzene with **11** as side-product. Top right: crude ³¹P{¹H} NMR spectrum after reaction of **3**^{Cl} with EtOTf. Bottom left: ¹H NMR spectrum of **5** in CD₂Cl₂. Bottom right: ORTEP plot of **5** with anisotropic displacement parameters drawn at the 50% probability level. Hydrogen atoms and the anion are omitted for clarity. Selected bond lengths (Å) and angles (deg.): Re-Cl1: 2.3608(14), Re-N2: 1.680(5), Re-N1: 2.005(4), Re-P1: 2.4832(15), Re-P2: 2.4695(15), N2-C21: 1.449(7), P2-Re-P1: 151.54(5), N1-Re-N2: 110.4(2), N1-Re-Cl1: 143.11(13).

Besides **5**, a second species ($\delta^{31P\{^1H\}} = 75.8$ ppm) is always present in the crude reaction mixtures in circa 35 %, independent of the applied synthesis route (Figure 51). Additionally, its formation is also solvent independent, as an identical ratio between **5** and this species was observed in C₆D₆, chlorobenzene and THF (quickly measured before THF polymerisation occurred). It is

^m XRD performed by Dr. J. Abbenseth

Et₂O-soluble, which is distinctively different than imido **5**, and a relatively purified batch shows C_s-symmetry on the NMR time scale, see Figure 52. Initially, the presence of a signal in the ¹⁹F NMR spectrum triggered us to suspect triflation of the nitride-N. Especially because in case of the saturated nitride, such reactivity was observed upon reaction of **3**^{Cl} with Tf₂O to form [Re(NSO₂CF₃)Cl(PNP)]OTf. To probe this hypothesis, **3**^{Cl} was reacted with 1 eq. Tf₂O in chlorobenzene (Scheme 57).



Scheme 57. Attempted synthesis of [ReCl(NSO₂CF₃)(P=N=P)]OTf to test the hypothesis of its formation during synthesis of **5**.

However, no initial conversion was observed and only after substantial heating (75 °C) and the addition of a large excess of Tf₂O (circa 100 eq.), full conversion was achieved into a species with a ³¹P{¹H} NMR resonance at 75.8 ppm, precisely similar to the unknown side-product. This is in sharp contrast to the straightforward reactivity of **3**^{Cl} with Tf₂O. Although this could indicate that the side-product is [ReCl(NSO₂CF₃)(P=N=P)]OTf, two signals are to be expected in the ¹⁹F NMR and a cationic species is not in agreement with Et₂O-solubility. Furthermore, in the reaction of **3**^{Cl} with EtOTf, the side product is readily formed by only using 1 eq., in contrast to the many equivalents of Tf₂O needed here. Therefore, a different explanation was sought. Taking a closer look at the ¹H NMR spectrum reveals the close resemblance of this side-product to the parent nitride, see Figure 52. A crystallisation attempt yielded the structure of [ReN(P=N=P)(MeCN)]OTf. This finding is unexpected, since it does not match with the ¹H NMR spectroscopy of our side-product. Furthermore, MeCN is not regularly used in the synthesis glovebox used within this work. Its formation however indicates that the chloride of nitride complex **3**^{Cl} is labile and can be substituted, i.e. with a triflate. A LIFDI mass of the side product showed indeed a major peak at 706.1 m/z, which corresponds to [ReN(OTf)(P=N=P)] (**11**) (calculated mass 706.1 m/z). Assignment of this neutral species as side product is in line with the NMR spectra, the resemblance to **3**^{Cl}, and the observed solubility. Furthermore, the addition of excess (nHe₄N)Cl to a sample of **11** in C₆H₆ results in qualitative regeneration of **3**^{Cl}, confirming the anion-exchange from chloride to triflate to form **11**. Notably, Dr. I. Scheibel reported the exchange from chloride to cyanide.⁷⁹

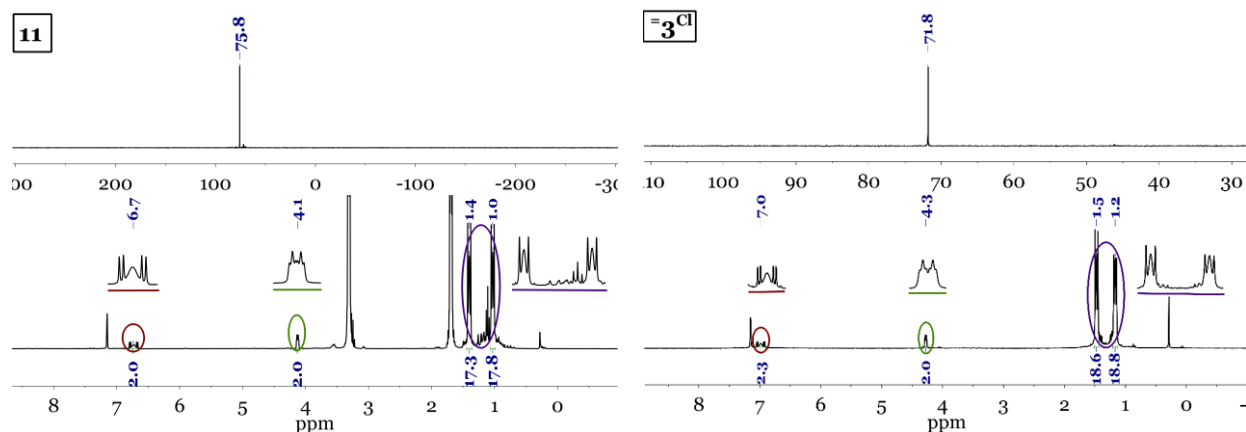
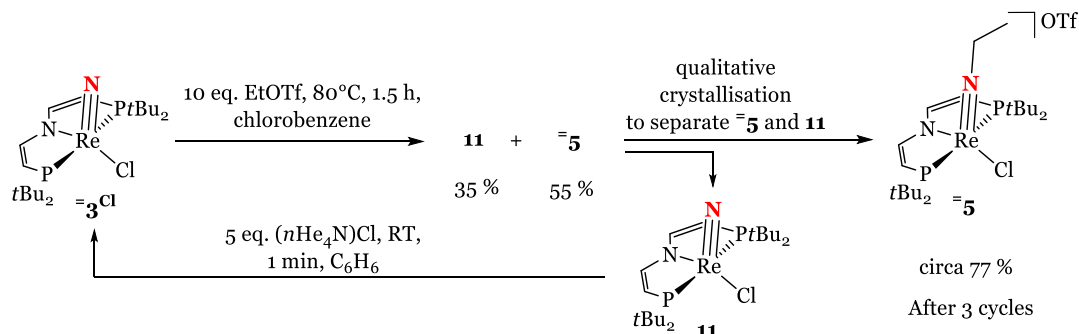


Figure 52. Left: NMR spectra of **11** in C_6D_6 : $^{31}P\{^1H\}$ NMR (top), 1H NMR (bottom). Right: NMR spectra of $=\mathbf{3}^{Cl}$ in C_6D_6 : $^{31}P\{^1H\}$ NMR (top), 1H NMR (bottom).

The saturated imido **5** was synthesised in up to 80 % yield without the mentioning of a repeatedly observed side-product. It cannot be fully excluded if some anion exchange occurs, but it is for sure less prominent in comparison to the unsaturated platform. This difference is likely the result of different reaction conditions between ethylation of $\mathbf{3}^{Cl}$ or $=\mathbf{3}^{Cl}$, since for the latter either large excess of EtOTf or higher reaction temperatures are needed, which will both favour anion exchange. Furthermore, it can be stated that nitride **11** is clearly not capable of ethylation, since no $[Re(NCH_2CH_3)(OTf)(P=N=P)]OTf$ is formed. This is in line with weaker donor properties of triflate compared to chloride, as reflected in their respective *Lever parameters* (-0.22 V (Cl^-) vs. $+0.13$ V (OTf^-))⁶⁴ or *ligand donor properties* (15.05 ± 0.29 kcal mol⁻¹ (Cl^-) 15.75 ± 0.29 kcal mol⁻¹ (OTf^-), see Section II.2.8 for details),¹⁹¹ making the nitride less nucleophilic.

Since the reverse reaction of **11** to $=\mathbf{3}^{Cl}$ by addition of excess chloride proved successful, ethylation was examined in presence of $(nHe_4N)Cl$ to increase the imido yield. However, several C_T -symmetric products were formed besides **5** as judged by the $^{31}P\{^1H\}$ NMR spectrum. Upon deprotonation these do not form **6**. As alternative strategy, ethylation was performed in a repetitive approach, where after each run, **11** was separated from **5** and reacted with $(nHe_4N)Cl$. Subsequent extraction with pentane affords clean $=\mathbf{3}^{Cl}$, which can be recycled for the reaction sequence (see Scheme 58). It was noted that during ethylation of $=\mathbf{3}^{Cl}$, some protonated nitride $[\mathbf{9}^{Cl}]^+$ is formed, which upon addition of $(nHe_4N)Cl$ also reacts to $=\mathbf{3}^{Cl}$. In this reaction, the chloride can be assumed to act as a base. Via this repetitive synthesis route, which was done three times, **5** was isolated in 77 % yield. The theoretical maximum after three runs is only

slightly higher (82 %). Although the material and time consumption of this approach is substantial, the yield of **=5** is higher.



Scheme 58. Repetitive ethylation, separation, and chlorination cycles to increase the overall yield of the ethylation from **=3Cl** to **=5** by recycling the side-product **11**.

To circumvent formation of **11**, experiments were initiated with Meerwein salts (OEt₃)BF₄ or (OEt₃)BAR^F₂₄, of which the first one contained significant traces of water, leading to quantitative protonation of the nitride. Upon reaction of **=3Cl** with the BAR^F₂₄ salt, a ³¹P{¹H}NMR peak at 86.9 ppm was observed, which is basically identical to **=5**, that could not be isolated (likely due to its Et₂O solubility). Deprotonation of the mixture resulted in partial formation of **=6** as proven by ³¹P{¹H} NMR spectroscopy (*vide infra* for characterisation of **=6**), proving that [Re(NCH₂CH₃)Cl(P=N=P)]BAR^F₂₄ was formed, accompanied by side-products. Due to challenging purification of the crude imido mixture, the synthesis of **=5** using (OEt₃)BAR^F₂₄ was not further pursued.

Upon establishing the unsaturated ethyl imido species, the electrochemistry of nitrido (⁼**3**) and imido (⁼**5**) can be compared. The nitrides are irreversibly reduced at very cathodic potential ($E_p \approx -3.4$ V (**3Cl**, Table A2), $E_p \approx -3.1$ V (**=3Cl**)²⁰⁶, both at $\nu = 0.1$ Vs⁻¹), whereas the imido reveals a much milder potential for the first reduction ($E_p \approx -1.8$ V at $\nu = 0.1$ Vs⁻¹ (**5**, Table A23), $E_{1/2} \approx -1.3$ V (**=5**, Table A22)). This represents a striking shift (by circa 40 kcal mol⁻¹), taking into account that both species are formal Re(V), and the ethyl-group is assumed to be redox-inactive (thereby rendering the reductions at least in the saturated case metal-based).

=5 was deprotonated with an excess NEt₃ in chlorobenzene to form [Re(NCHCH₃)Cl(P=N=P)] (**=6**). ³¹P{¹H} NMR spectroscopy revealed full conversion after 24 h and the appearance of two peaks at $\delta^{31P\{^1H\}} = 34.1$ and 33.2 ppm, which couple via ³¹P-¹H HMBC spectroscopy to two ethyl-fragment containing C_s-symmetric species. Between these species, only the ethyl-peaks seem to be in a different chemical environment, as their chemical shift deviates ($\Delta\delta \approx 0.3$ ppm), in

contrast to the overlapping backbone protons ($\Delta\delta \approx 0-0.1$ ppm). Since in LIFDI mass spectroscopy only one main peak is found at 620.3 m/z, the reaction mixture is explained by formation of two isomers of **6** as present in solution, which was shown before for the saturated analogue **6**. Deprotonation of the imido ligand of **5** leads to an azavinylidene ligand with a formal N-C double bond that hinders rotation: one isomer has the methyl group pointing towards the ligand and *vice versa*.

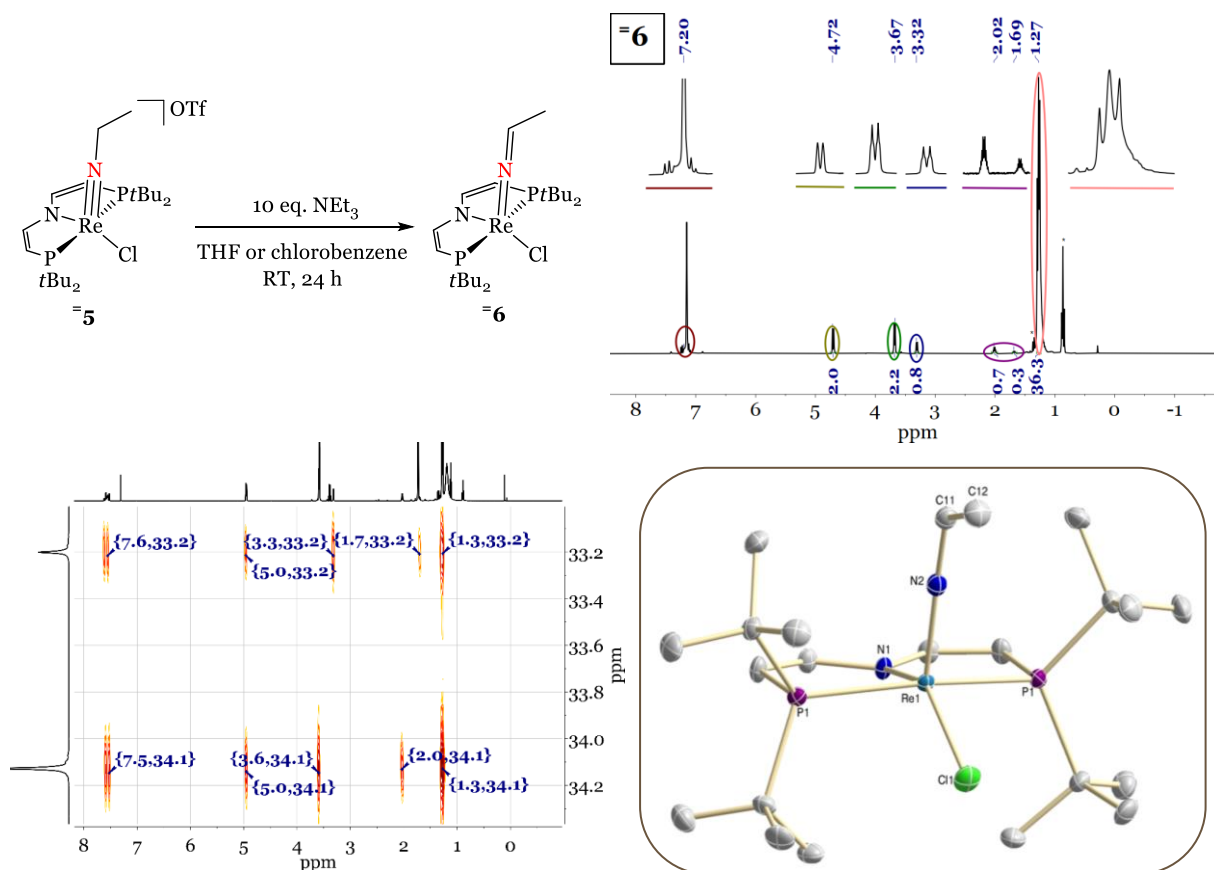


Figure 53. Top left: Deprotonation of **5** with NEt_3 yields **6** in quantitative amounts. Top right: ^1H NMR spectrum of **6** in C_6D_6 . Bottom left: ^{31}P - ^1H HMBC of **6** in d_8 -THF. Bottom right: ORTEP plot of **6** with anisotropic displacement parameters drawn at the 50% probability level. Hydrogen atoms are omitted for clarity. Selected bond lengths (\AA) and angles (deg.): Re-Cl1: 2.3718(9), Re-N2: 1.794(3), Re-N1: 2.011(3), Re-P1(#): 2.4114(15), N1-C11: 1.268(5), P1-Re-P1#: 160.60(3), N1-Re-N2: 109.01(13), N1-Re-Cl1: 144.77(9), N2-C11-C12: 122.6(4), $\tau_5 = 0.26$.

Single crystals for XRD could be grown from a saturated pentane solution,ⁿ and show a distorted square pyramidal coordination geometry around the Re-centre ($\tau_5 = 0.26$).¹⁷¹ Compared to imido **5**, the Re- N_{imido} bond is elongated (1.680(5) \AA for **5** and 1.794(3) \AA for **6**) and the $\text{N}_{\text{imido}}\text{-C}$ bond is shortened (1.449(7) \AA for **5** and 1.268(5) \AA for **6**), in agreement with a lower bond

ⁿ XRD performed by Dr. C. Würtele.

order between $N_{\text{imido-C}}$ upon deprotonation. Comparing this structure to the saturated PNP-ligand analogue **6**, especially the coordination geometry strikes the eye. The τ_5 value of **6** is 0.45, which is mainly the result of the increased $N_{\text{amide-Re-Cl}}$ angle ($144.77(9)^\circ$ (**6**) compared to $135.07(15)^\circ$ (**6**)). The ligand-bite angle is barely touched: P-Re-P decreases from $162.01(5)^\circ$ (**6**) upon desaturation to $160.60(3)^\circ$ (**6**). Since the $N_{\text{amide,P=N=P}}$ is a weaker trans-donor compared to $N_{\text{amide,PNP}}$, this increases the angles of the chloride with respect to the ligand, likely favourable due to decreased strain of the proximity to the *tert*-butyl moieties.

At RT in solution, both isomers of **6** are present (ratio circa 1:3), indicating that the isomerisation rate is slower compared to the timescale of NMR. It was noted that in most solvents, a set of *tert*-butyl moieties appeared broad in the ^1H and $^{13}\text{C}\{^1\text{H}\}$ NMR spectra (e.g. at $\delta^1_{\text{H}} = 1.3$ ppm in Figure 54, right). This could indicate that at RT, the NMR time scale is close to the isomerisation rate. Therefore, we measured VT-NMR of **6** in d_8 -THF to 60°C . However, instead of additional broadness, as expected in case the increasing temperature would allow the isomerisation rate to come closer to the experimental conditions, the *tert*-butyl moiety sharpens. The same behaviour was observed when **6** was heated in d_8 -toluene to 95°C . This indicates that the isomerisation rate is clearly lower as can be examined with straightforward NMR spectroscopy. The observed broadness at RT is attributed to additional dynamic processes.

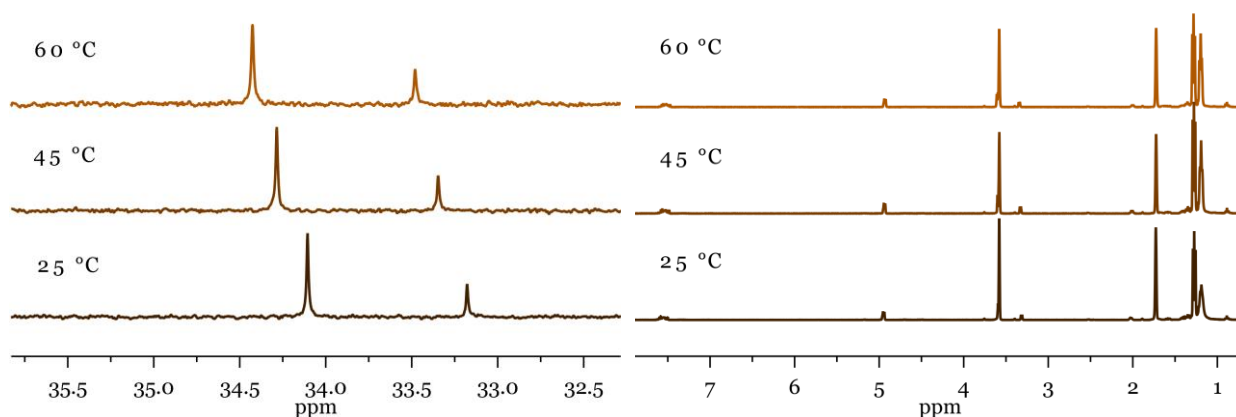


Figure 54. VT-NMR of **6** in d_8 -THF. Left: $^{31}\text{P}\{^1\text{H}\}$ NMR spectra, right: ^1H NMR spectra.

4.3. Electrochemical MeCN release of [ReCl(NCHCH₃)(P=N=P)]

After establishing the synthesis of **6**, we measured its electrochemical behaviour as isolated species, and in presence of base and (*n*He₄N)Cl, analogous to **6**. CV of **6** reveals two main oxidations. A reversible oxidation at $E_{1/2} = -0.28$ V, that is assigned to the Re(IV/III)-couple and subsequently, an irreversible oxidation at $E_p = 0.45$ V at $\nu = 0.1$ Vs⁻¹. This second oxidation is accompanied by a small feature slightly more anodic at $E_p = 0.61$ V, that however quickly decreases at higher ν . Therefore, it is most likely a follow up product of the second oxidation in an *ECE*-pathway. In addition, an irreversible reduction with a multi-electron character is found at $E_p = -2.58$ V at $\nu = 0.1$ Vs⁻¹ (Figure A36). **6** shows a far more negative one-electron reduction ($E_p = -3.14$ V, $\nu = 0.1$ Vs⁻¹), and considering the multi-electron character of this reduction of **6**, we attribute this to (P=N=P)-ligand reduction.

Towards electrochemical MeCN release, the CV of **6** was examined in presence of different bases, of which first DBU was tried. However, addition of DBU directly lead to a colour change from blue to violet and the appearance of several new oxidation waves. Likely, DBU reacts with **6** prior to oxidation, and DBU was not examined further. Upon addition of an excess of NEt₃ (>10 eq.) to the CV of **6**, the first reduction becomes irreversible, shifts cathodically by circa 0.02 V, and its current increases by circa 40-50 %. This is in line with an *ECE*-mechanism where NEt₃ deprotonates [**6**]⁺, forming a species that is further oxidised at these potentials. When fewer equivalents are added, two features appear without current increase that slowly merge upon increased NEt₃ concentration. This likely indicates that NEt₃ is just strong enough to deprotonate [**6**]⁺. Since for deprotonation of saturated [**6**]⁺ stronger bases are needed, the unsaturated analogue is a stronger acid; the resulting negative charge might be better stabilised over the conjugated system. The subsequent addition of 20 eq. of (*n*He₄N)Cl results in a strong cathodic shift (0.1 V) and a current decrease of 110-120 % of the original height of the one-electron transfer of **6**. A second prominent feature is observed at $E_p = +0.08$ V ($\nu = 0.1$ Vs⁻¹). Furthermore, in the reductive trace a promising appearance of reductive waves around $E_p = -0.9$ V, is observed close to the first reduction of [ReCl₃(P=N=P)] (**8**) ($E_p = -0.90$ V, *vide infra*). This behaviour was reproduced five times. Combining an *ECE*-mechanism with the fact that the current is essentially unchanged between the first oxidation of **6** before and after base and chloride addition, the first oxidation should not be sufficient to release MeCN. Indeed, when CPE was performed at the peak potential of the first wave ($E_{appl.} = -0.27$ V), neither MeCN nor **8** were formed as judged by GC and NMR spectroscopy, respectively. The crude NMR spectroscopy showed a low-intensity mixture of at least four diamagnetic and one paramagnetic species, but the reaction outcome was not examined further.

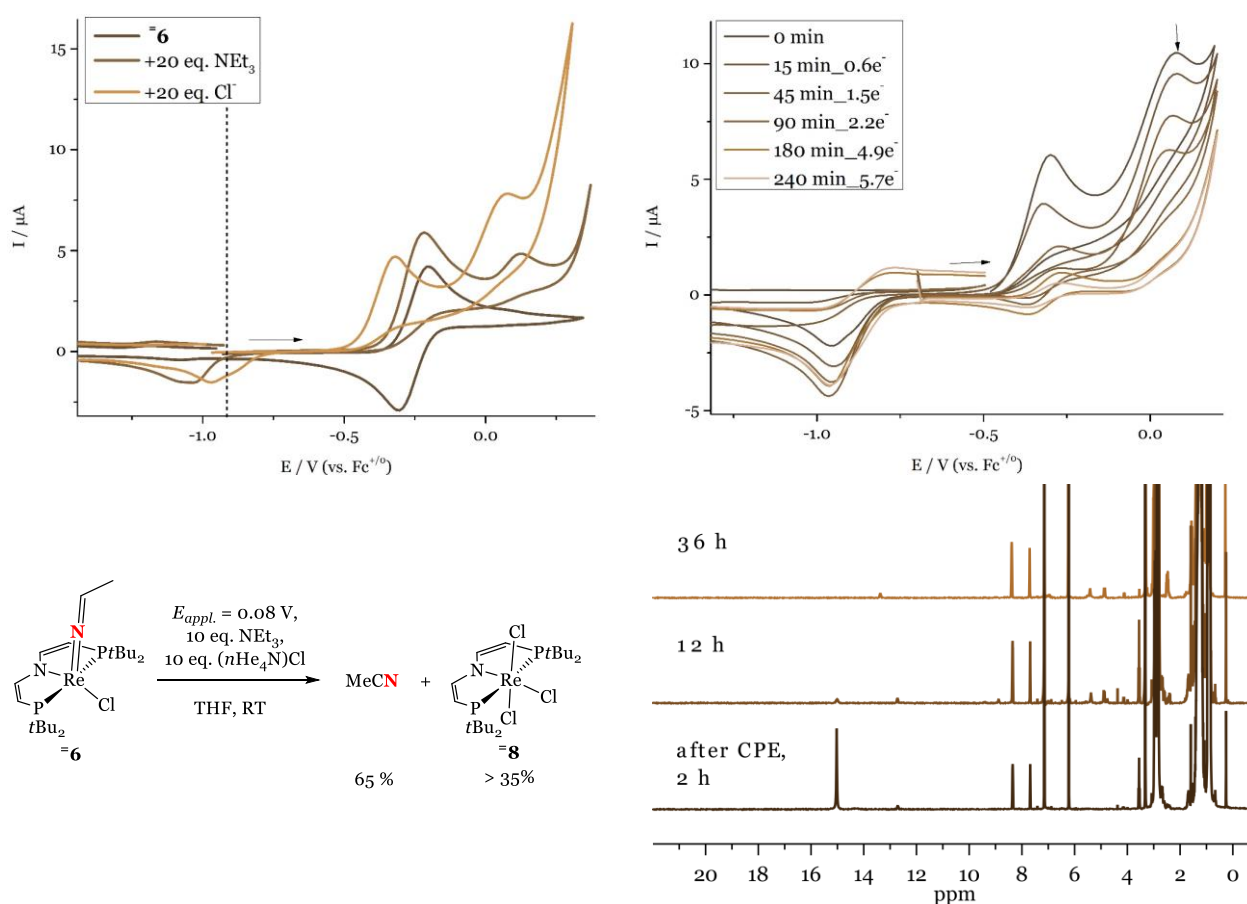


Figure 55. Top left: CV of the Re(IV/III)-oxidation of **6** at $\nu = 0.1 \text{ Vs}^{-1}$ in presence of 10 eq. NEt₃ and subsequently 10 eq. (nHe₄N)Cl in THF with 0.2 M (nBu₄N)PF₆. The dashed line indicates is the Re(VI/III) reduction of **8**. Top right: CPE of the previous mixture at $E_{\text{appl.}} = 0.08 \text{ V}$ with the total transfer of 5.7 electrons per Re in this specific example. Bottom left: Electrochemical oxidation of **6** to release acetonitrile and form **8**. Bottom right: ¹H NMR series after CPE at $E_{\text{appl.}} = 0.08 \text{ V}$ after 2 h (where **8** ($\delta^{\text{H}} = 15 \text{ ppm}$) was quantified, see Figure A38), and the decomposition of **8** after time.

Instead, CPE was performed at $E_{\text{appl.}} = +0.08 \text{ V}$ as envisioned to be the sufficient potential to release MeCN (Figure 55). Over the course of circa 4 h of CPE, the colour changes from light blue via orange to green and circa 5.5 electrons are needed to fully oxidise all features at this potential, as averaged by several runs. In a separate experiment, we confirmed that only 1 electron is transferred when isolated **6** is electrolysed at this potential. In the reductive region, a feature at $E_p = -0.95 \text{ V}$ ($\nu = 0.1 \text{ Vs}^{-1}$) rises that resembles the reduction of **8**, which reaches a maximum after circa 1.5 h and decreases afterwards. After CPE, the volatiles are separated and examined by GC, showing the release of MeCN in circa 65 % yield (averaged from 4 runs of 55 %, 77 %, 67 % and 58 %). The crude inorganic fraction was examined by ¹H NMR spectroscopy, revealing the presence of **8** in 35 % yield at its initial measurement. Both results represent a significant optimisation compared to **6**, where no Re-complex could be identified and less MeCN was obtained. Yet, this system is not without its challenges that are discussed in the next paragraphs.

First, we examine the CPE as monitored by CV. Although less electrons are transferred compared to **6**, the required electrons for full conversion (averaged to ≈ 5.5) still represent an over-oxidation to release MeCN and form **=8**. It was considered if the additives itself are being oxidised at this potential, yet the potentials of both base and chloride source are far more anodic compared to the CPE potential, see Appendix A2. In the CV traces of the CPE, it becomes evident that after the transfer of ≈ 2 -3 electrons, a reversible oxidation is observed at $E_{1/2} = -0.35$ V. Further oxidation will decompose this species, which might be a source for the additionally transferred electrons. The Re-product **=8** is oxidised at $E_{1/2} = +0.33$ V and is therefore excluded to account for this new oxidation. In an attempt to identify the corresponding species, the coordination of MeCN was tested by adding increasing equivalents MeCN to **=1^{Cl}** and measuring CV. The irreversible oxidation of **=1^{Cl}** at $E_p = -0.05$ V becomes reversible upon addition of MeCN and shifts anodically to a potential of $E_{1/2} = -0.29$ V. This is in close proximity of the observed oxidation during CPE and could indicate formation of $[\text{ReCl}_2(\text{P}=\text{N}=\text{P})(\text{MeCN})]$. In a separate experiment, we performed CPE until three electrons were transferred, and added 5 eq. *t*BuNC to the inorganic fraction. Yet, no additional MeCN is formed during this experiment, which discards a significant relevance of MeCN coordination. The formation of such a Re(III) compound would also be more reasonable if less electrons were transferred as expected.

Additionally, the stability of the inorganic product should be discussed, as only 35 % yield of **=8** was observed by ¹H NMR spectroscopy. Intriguingly, whilst quantifying, **=8** decreases over the course of hours (see Figure 55). As the yield thereby depends on the time between the end of CPE and quantification by NMR, we consider 35 % a lower limit. The decomposition of **=8** is not accompanied by precipitation. By NMR spectroscopy, no main decomposition product is observed, only several low-intense paramagnetic species. We found by a separate CV study (*vide infra*) that **=8** is not stable in presence of $(\text{HNet}_3)^+$, which will be formed during CPE. This likely account for some of the decomposition. To examine the stability of this Re^{IV}-species in more detail, separately synthesised **=8** was assessed by NMR spectroscopy and CV under several conditions: i.e. in the presence of a clear excess of $(n\text{He}_4\text{N})\text{Cl}$ or electrolyte. The results of these experiments are not consistent and puzzling. ¹H NMR spectroscopy in *d*₈-THF shows that **=8** is stable in the presence of electrolyte and chloride source for at least 24 h. Even though this experiment was not performed in presence of an internal standard, no substantial decrease is observed (Figure 56). Only after a couple of days in solution, the colour changes to red and **=8** decomposes (this behaviour is well understood, namely the formation of **12**, and presented in Section II.4.5). This result is in strong contrast to the measurement of isolated **=8** under CV conditions (Section II.4.5 for the discussion of the CV of **=8**), where the timescale of decomposition is faster, as shown in Figure 56. After 60 min, a colour change from green to

yellow is observed, all waves of **8** decrease and a new, reversible reduction is observed. NMR spectroscopy of such a mixture shows a mixture of para- and diamagnetic species with a main, unknown feature at 48 ppm in the $^3\text{P}\{^1\text{H}\}$ NMR spectrum. This behaviour was also observed using freshly dried THF. Since the same batch of **8** and electrolyte were used for both stability experiments, we can only speculate about the quality of the THF as the origin of these differences. Both the d_8 -THF for NMR spectroscopy and THF for electrochemistry are dried over Na/K, although the latter is pre-dried via a solvent purification system. For future examination, it should be considered to examine **8** in freshly dried THF that was not in contact with the SPS. Notably, the involvement of residual water in all the decomposition as here described is rather unlikely, since the product of **8** and traces of water is known (compound **12**, *vide infra*), which was not observed neither by NMR-spectroscopy nor CV.

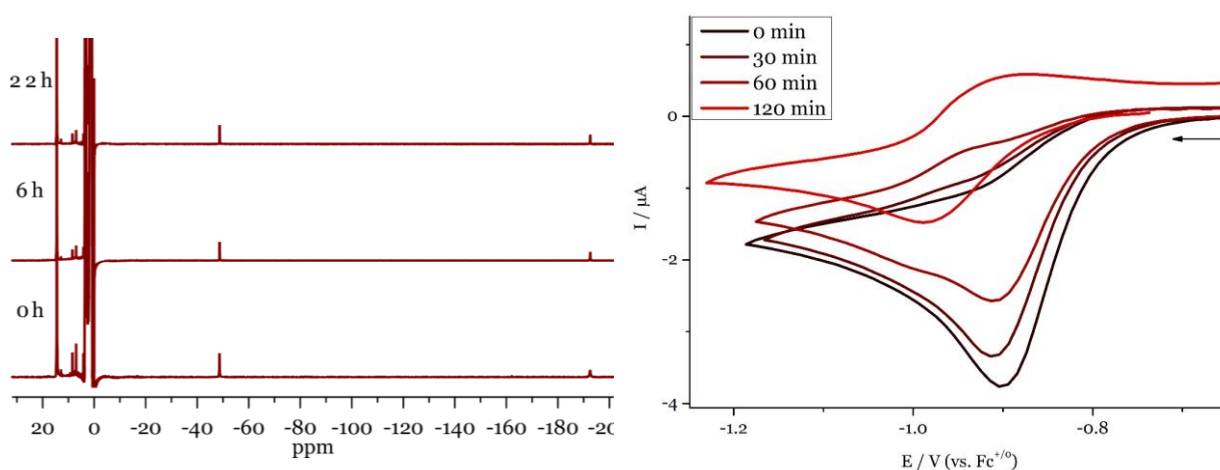


Figure 56. Left: ^1H NMR spectra over time of **8** in d_8 -THF with 0.2 M $(n\text{Bu}_4\text{N})\text{PF}_6$ and 5 eq. $(n\text{He}_4\text{N})\text{Cl}$. **8** has signals at +15, -48 and -192 ppm. Right: CV of the Re(IV/III) reduction of **8** in THF with 0.2 M $(n\text{He}_4\text{N})\text{PF}_6$.

A method to obtain a more reliable yield on **8** would be quantification via CV at an early stage of CPE, where barely any conversion and hopefully barely any decomposition has taken place. Therefore, we performed CPE of **6** in presence of chloride and base after transfer of only 10 % of the theoretically expected 3 electrons. Scanning negative first, CPE under these conditions forms a species with a reductive feature at $E_p = -0.93$ V at $\nu = 0.1$ Vs $^{-1}$. When this mixture is allowed to stand, full decomposition is observed within circa 3-4 h. Due to its similarity to the Re(IV/III) reduction of **8**, it was initially interpreted to be the same feature. Via the *Randles-Ševčík* equation (3) as valid at RT,¹⁷⁴ the peak current was recalculated to the concentration of **8** (D of **8** = $7.5 \cdot 10^{-6}$ cm 2 s $^{-1}$ as determined via DOSY NMR spectroscopy), see Section IV.6.4 for details.

$$i_{p,c} = 2.69e^5 * n^{\frac{3}{2}} * A * D^{\frac{1}{2}} * \nu^{\frac{1}{2}} * c \quad (3)$$

Yet, this method showed a **=8** yield of circa 24 % as reproduced twice, although at this stage maximum 10 % could be reached. In addition, the reduction after CPE also does not show the quasi-reversible character as was shown for the isolated compound (see Section II.4.5), which is certainly expected in the presence of excess chloride. This yield discrepancy would vanish if the reduction of **=8** became a multi-electron character after CPE. If the Re(IV) compound for instance appears as a two-electron wave, the yield would reduce to circa 9 %, which would be indicative of almost quantitative formation of **=8**. During CPE, $(\text{HNEt}_3)^+$ is formed that could be envisioned to induce an *ECE*-mechanism for e.g. (P=N=P)-ligand reduction of **=8**. Therefore, we measured CV of **=8** in presence of $(\text{HNEt}_3)\text{Cl}$. This reveals the loss of the initial reversibility as is observed after CPE, see Figure 57, yet without a current increase. In fact, the current drops slightly, and after stirring of this mixture for 30 min, the current is halved, which indicates fast decomposition (faster than isolated **=8**). This provides an explanation for decomposition of **=8** after CPE, although the timescales are substantially different. A possible multi-electron character of **=8** could not be justified, and therefore this CV method is inappropriate to quantify the yield of **=8**. In future research, one could add some of isolated **=8** to this reaction mixture after 10 % conversion, to check for its appearance in combination with all reagents and intermediates during electrochemical MeCN release.

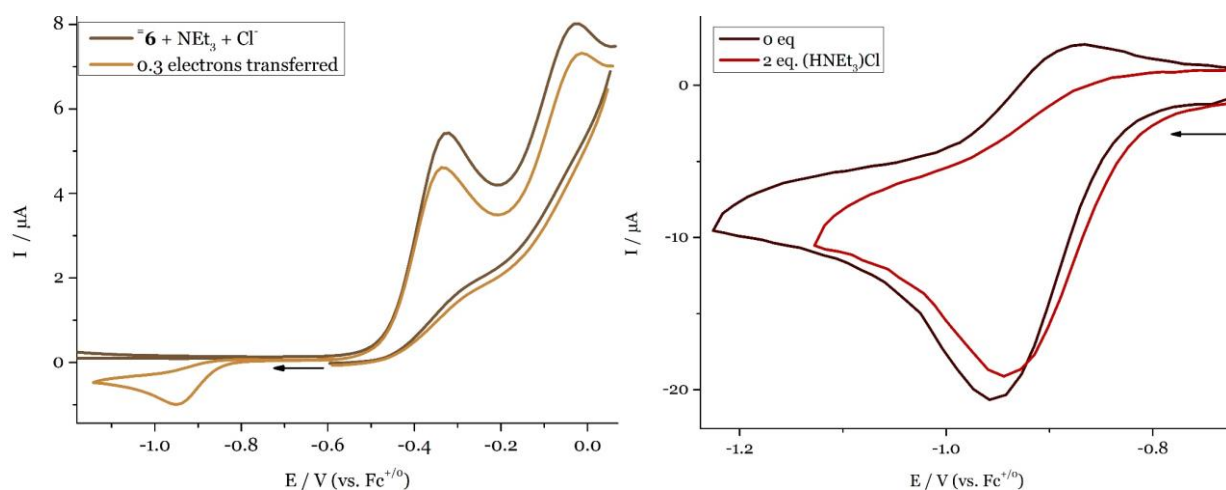


Figure 57. Left: CV before and after the transfer of 0.3 electrons during CPE of **=6** and 20 eq. of NEt_3 and 20 eq. of $(\text{nHe}_4\text{N})\text{Cl}$ in THF with 0.2 M $(\text{nBu}_4\text{N})\text{PF}_6$, $\nu = 0.1 \text{ Vs}^{-1}$. Right: CV of **=8** in presence of 2 eq. of $(\text{HNEt}_3)\text{Cl}$ in THF with 0.2 M $(\text{nBu}_4\text{N})\text{PF}_6$, $\nu = 2.0 \text{ Vs}^{-1}$.

Despite the challenges around quantifying the formation of **=8** after electrochemical MeCN release, it is easily stated that the P=N=P-ligand platform performs superior over the saturated analogue, as at least a Re-fragment was obtained combined with a higher MeCN yield. This different behaviour is attributed to the different ligand stabilities under the applied conditions:

the oxidative potential in combination with excess base will induce ligand PCET reactions that are unfavourable for the saturated ligand platform.

4.4. Chemical MeCN release of [ReCl(NCHCH₃)(P=N=P)]

For the newly established unsaturated **6**, its performance regarding chemical MeCN release is also of interest. Therefore, we reacted it with 2.0 eq. of NCS in C₆D₆, upon which the colour changed from blue to dark brown. By ¹H NMR spectroscopy, formation of MeCN and **8** was observed in circa 65 % and 50 % yield respectively, as averaged from four runs (amongst one run with 10 mg **6**), accompanied by the appearance of two equivalents of protonated *H*-NCS, see Figure 58.

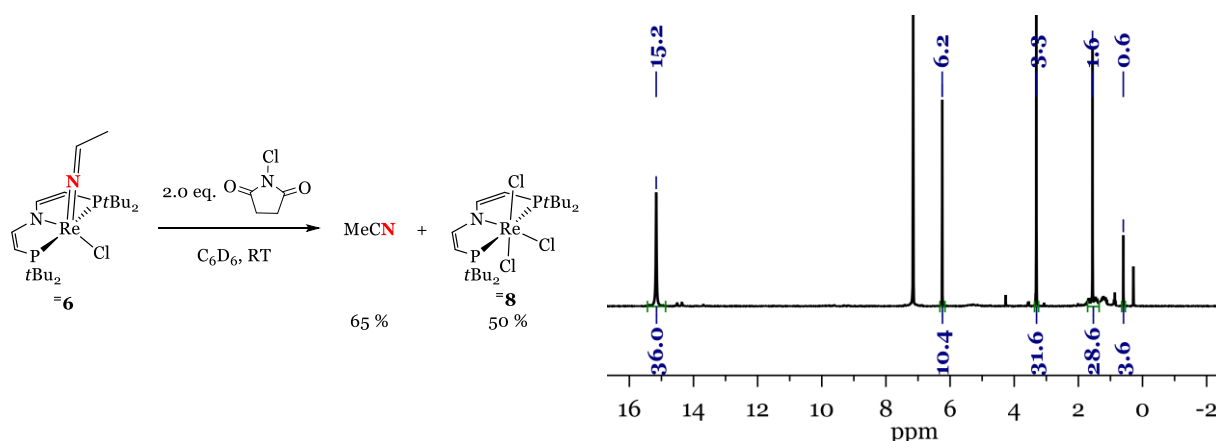


Figure 58. Left: Chemical oxidation of **6** to release acetonitrile and form **8**. Right: ¹H NMR after reaction between **6** and 2.0 eq. of NCS with 1,3,5-trimethoxybenzene as standard showing formation of **8** ($\delta^1_{\text{H}} = 15.2$ ppm), MeCN ($\delta^1_{\text{H}} = 0.6$ ppm), and *H*-NCS ($\delta^1_{\text{H}} = 1.6$ ppm).

For **6**, slightly more MeCN was found upon chemical release (80 %), but significantly more of the Re-product (93 %).⁷⁹ One source of diminished yield on the Re-side could lie in the accurateness of the stoichiometry between **6** and NCS, since already a slight excess of the latter results in decomposition of **8**. Although the colour remains green when **8** and NCS react in a separate experiment, a new paramagnetic compound is observed by ¹H NMR spectroscopy with relatively sharp peaks at +13.7 and -30.9 ppm. These integrate in a 36:2 ratio, and most likely indicate the formation of a C_{2v}-symmetric species, where the second backbone peak must be shifted extreme or broadened. Besides unreacted NCS, also the product of chloride-transfer *N*-succinimide is observed. After three days, this species is converted into a C_s-symmetric species, judged by the appearance of two similarly integrating peaks at +14.5 and +14.8 ppm assigned to *tert*-butyl moieties. Multiple small paramagnetic features hinder the allocation of backbone features to this final compound. In both product compositions, the ³¹P{¹H} spectrum remains

blank, excluding substantial redox chemistry to occur during this decomposition. Of the final C_s -symmetric compound, LIFDI mass was measured showing a main peak at 752.0 m/z, that could not be assigned to any realistic species because of the high mass. In future research, LIFDI mass spectroscopy should be performed directly after this first compound is formed. In initial experiments, **8** seems stable in presence of (excess) NCS, potentially reflecting the higher Lewis acidity in =**8** upon desaturation of the pincer backbone. Either way, the decomposition products from this separate experiment are found when chemically releasing MeCN from =**6**, yet in small amounts that do not account for the missing 50 % on the mass balance. The remaining fate on the Re-side could not be clarified.

4.5. Synthesis and CV analysis of [ReCl₃(PNP)] and [ReCl₃(P=N=P)]

The product of the (electro)chemical release of MeCN from **6** or =**6** in presence of chloride source, is either the six-coordinate Re(IV) [ReCl₃(PNP)] (**8**) or [ReCl₃(P=N=P)] (=8) respectively. In order to recognise their presence in CV, we synthesised and electrochemically characterised both complexes. A synthesis pathway towards **8** was developed and published by Dr. I. Scheibel, which relied on NCS as chloride source and oxidant in DCM at -40 °C. Formation of **8** was observed via this route, yet not in a pure fashion. Therefore, a different synthesis pathway was developed inspired by Dr. J. Abbenseth, who found **8** as main product upon reaction of **1**^{Cl} with PCl₃. Because of the toxicity of PCl₃, the new synthesis route is not an optimisation, yet provides **8** in a reproducible and clean way with a yield of 64 %. To access =8, we reacted **8** with an excess of TBP as PCET-reagent at 50 °C, upon which new features are formed in the ¹H NMR spectrum, matching a C_{2v} -symmetric compound (Figure 59). After work up, clean formation of =8 was confirmed by LIFDI mass and elemental analysis. For a Re(IV)-compound and in comparison to **8**, its ¹H NMR peaks at +15.2, -51.7, and -194.6 ppm are very sharp. Sharp resonances of a paramagnetic compound in NMR spectroscopy usually indicates fast electron relaxation.²⁰⁷ Even though EPR spectroscopy was not examined for this Re(IV)-species, it is likely not successful because of this fast electron relaxation.

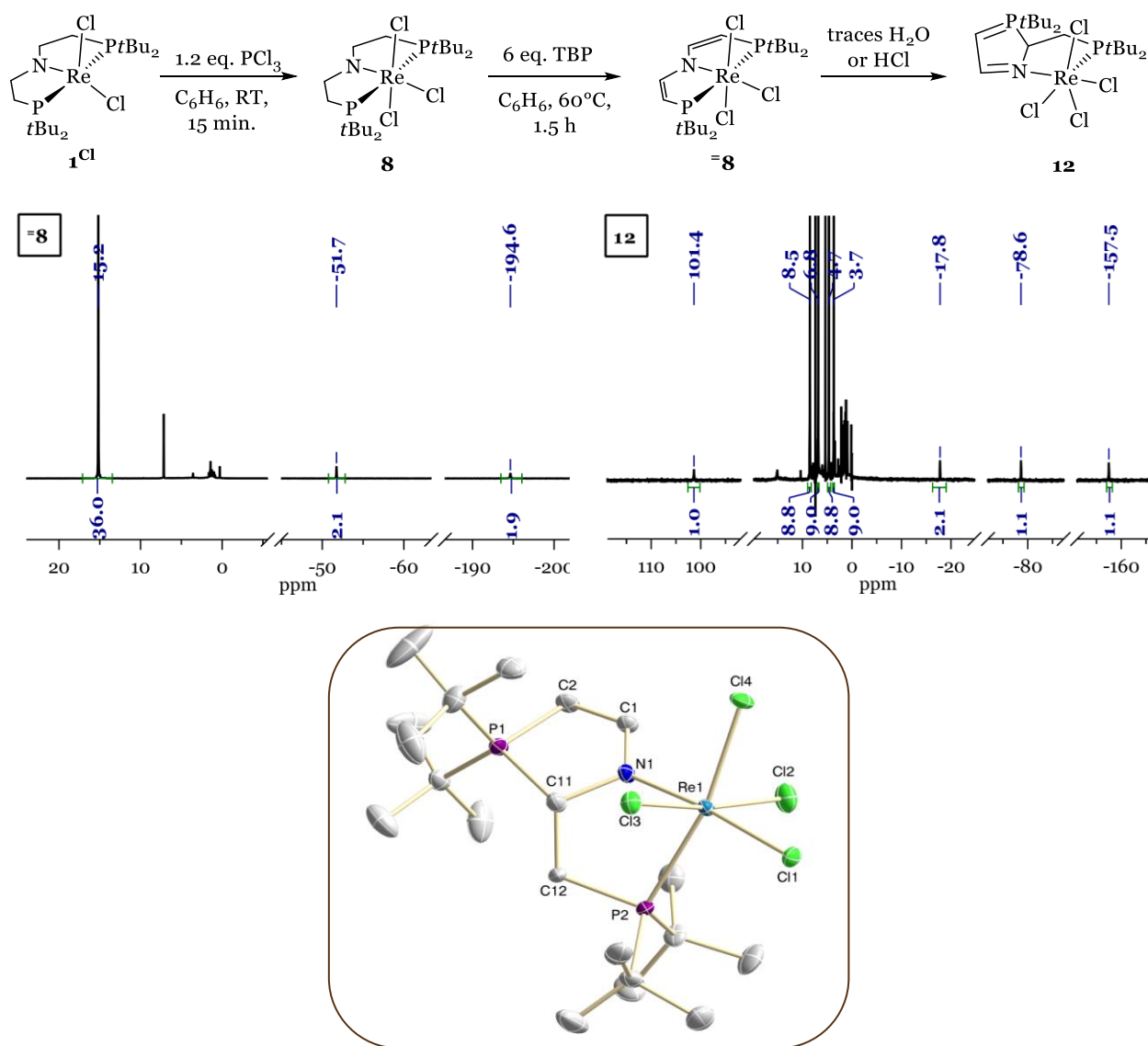


Figure 59. Top: Alternative synthesis of **8**, its dehydrogenation to =**8** and subsequent reaction with water of HCl to **12**. Middle left: ¹H NMR spectrum of =**8** in C₆D₆. Middle right: ¹H NMR spectrum of **12** in C₆D₆. Bottom: ORTEP plot of **12** with anisotropic displacement parameters drawn at the 50% probability level. Hydrogen atoms are omitted for clarity. Selected bond lengths (Å) and angles (deg.): Re-Cl₁: 2.3745(8), Re-Cl₂: 2.3254(10), Re-Cl₃: 2.3583(9), Re-Cl₄: 2.4042(8), Re-N₁: 2.043(3), Re-P₂: 2.5349(8), C₁-C₂: 1.359(5), C₁₁-C₁₂: 1.522(5), N₁-Re-Cl₁: 174.34(8), Cl₂-Re-Cl₃: 171.62(3), P₂-Re-Cl₄: 167.38(3).

In attempts to examine =**8** by XRD, red crystals were obtained after a couple of days (in contrast to the green colour of the complex), that offered a surprising structure: a 6-coordinate Re-compound where the P=N=P-ligand is cyclised via P-C bond formation to form azaphosphole **12**, which is the formal HCl-adduct of =**8** (Figure 59). Indeed, the ¹H NMR spectrum measured from the crystals shows a *C₁*-symmetric compound with four *tert*-butyl and four backbone peaks, one integrating to 2 protons. Analogous to =**8**, the peaks are strongly paramagnetically shifted, yet sharp. By XRD, a distorted octahedral coordination is observed, with angles around Re of

about 170°. In the now bidentate ligand, single protonation of the backbone can be confirmed, as there is single bond character between C11 and C22, and double bond character between C1 and C2. The formation of this species is likely initiated by protonation of the carbon adjacent to phosphorous, upon which cyclising occurs via a nucleophilic attack of the opposite phosphorous atom. The positive charge from protonation is balanced by coordination of a chloride ion, which must come from decomposition of other Re-species.

12 is likely formed via reaction of **=8** with residual traces of water in the crystallisation attempt. Even when using NaK-dried C₆H₆, **12** is the only product after circa 1 week in solution. Deliberate addition of water to **=8** also leads to (unselective) formation of **12**, and a selective synthesis pathway is found upon reaction of **=8** with HCl in Et₂O. The formation of this highly unusual species displays the high water-sensitivity of this compound and a possible general breakdown pathway for the (P=N=P)-ligand. Since **12** is a Re(IV)-compound, this maybe more often occurring decomposition pathway is not easily recognised. Therefore, we tried to reduce it with 1 eq. of CoCp₂, to find the corresponding Re(III) diamagnetic ³¹P NMR-signals. This reaction however lead to an untraceable mixture of products.

Since both in the basic CV of **=8** and the (electro)chemical MeCN release, decomposition of **=8** was determined, the formation of **12** in these experiments was hypothesised. Via chemical MeCN release, we learned that new products are formed when **=8** is in presence of excess NCS (a reagent that could potentially offer the extra chloride for **12**). However, the ¹H NMR traces of these new species do not match with **12** as they represent a symmetric species. Furthermore, decomposition of **=8** was observed in the CV set up (Figure 56) to (amongst others) a species with a reversible reduction at $E_{1/2} = -0.95$ V. Yet, **12** is reduced at $E_p = -1.07$ V and -1.20 V at $\nu = 0.1$ Vs⁻¹ (Figure A41), that remain irreversible up to $\nu = 2.0$ Vs⁻¹, even if only the first reduction is scanned. An oxidation is observed at $E_p = 0.95$ V, that becomes quasi-reversible from $\nu = 0.5$ Vs⁻¹ onwards. The reductive behaviour of **12** is distinctly different from the decomposition product of **=8** in the CV set up and its presence can therefore be ruled out.

Both trichloride complexes show a reduction at mild potentials ($E_p = -1.10$ V (**8**), $E_p = -0.91$ V (**=8**)) attributed to the Re(IV/III) reduction, that is irreversible at $\nu = 0.1$ Vs⁻¹. This reduction must be coupled to chloride loss (via an *EC*^{Cl}-mechanism), as the following reductive trace is identical to their 5-coordinate dichloride congeners, see Chapter II.1 and II.3. In case of **8**, no reversibility was observed up to $\nu = 2.0$ Vs⁻¹. The coupled chemical reaction was confirmed by the addition of up to 40 eq. of (*n*He₄N)Cl at $\nu = 2.0$ Vs⁻¹, which induces a cathodic shift of 0.02 V, yet without an increase of reversibility. This indicates that chloride loss from **8** must be

significantly fast and more extreme conditions would be necessary to probe the kinetics of this chemical reaction. For this Re(IV/III)-reduction, no differences are observed between measuring in a N₂ or Ar atmosphere, which substantiates the finding by NMR-spectroscopy in Chapter II.1 that N₂-coordination is not relevant on the Re(III)-stage.

For **8**, the first reduction shows quasi-reversible behaviour by having the onset of a return peak at 2.0 Vs⁻¹. At 20 Vs⁻¹ the ratio $i_{p,f}/i_{p,r}$ is 1.6 and the most reliable $E_{1/2}$ that is determined, represents an upper limit ($E_{1/2} < -0.90$ V). This reversibility indicates that the chloride loss at the unsaturated platform is slower, which could either have an electronic or steric reason. The latter could be examined via structural comparison of the ligand bite angles, however in the series **8** / **8** or **1**^{Cl} / **1**^{Cl}, XRD structures are only available of the saturated congener. In the next best series, small differences are observed between the pincer bite angles: P-Re-P [°]: 156.16(7) for **3**^{Cl} vs. 155.11(13) for **3**^{Cl}, and 161.62(3) for **1**^I vs. 158.12(4) for **1**^I, which rules out steric reasons. More realistically is an electronic reason, since chloride is a donating ligand towards the more Lewis acidic Re-centre in the case of the P=N=P-ligand. In line with the observed onset of reversibility of **8**, probing the first reduction in presence of (nHe₄N)Cl results in an increased reversibility even at low scan rates (Figure 60, $\nu = 0.05$ Vs⁻¹). However, over the course of the experiment, **8** decomposes, as elaborated in Section II.4.3. Therefore, this chloride titration was not studied in detail. In future research, a thoroughly prepared experiment carried out in minimal amount of time could gain chloride dissociation kinetics for **8**. A first estimate of chloride loss is obtained via peak shift analysis according equation (4),¹⁷⁴ where k_f represents the rate constant for chloride loss from [ReCl₃(P=N=P)]⁻. Plotting $E_{p,c}$ vs. $\ln(\nu^{-1})$ (Figure A40) leads to a chloride loss of circa 14 s⁻¹, which represents an upper limit in line with only the upper limit $E_{1/2}$ that we can derive.

$$E_{p,c} = E_{1/2} - 0.78 \frac{RT}{F} + \frac{RT}{2F} \ln \left(\frac{RTk_f}{F} \right) - \frac{RT}{2F} \ln \left(\frac{1}{\nu} \right) \quad (4)$$

Scanning oxidative first reveals a reversible oxidation for **8** at $E_{1/2} = 0.33$ V. For **8**, this oxidation is quasi-reversible at $E_p = 0.05$ V at $\nu = 0.1$ Vs⁻¹ and is followed by a small re-reduction in the cathodic trace at $E_p = -0.26$ V (Figure 60). This represents a product of the oxidation of **8** after an EC-mechanism, since this feature becomes less prominent at higher scan rates and the oxidation approaches reversibility ($i_{p,f}/i_{p,r} = 1.14$ ($\nu = 0.1$ Vs⁻¹) 1.04 ($\nu = 2.0$ Vs⁻¹)). The possibility of solvent coordination can be ruled out since it is not observed for the less electron dense metal centre of **8**, where it would be more likely. This EC-mechanism upon oxidation of **8** remains therefore unassigned.

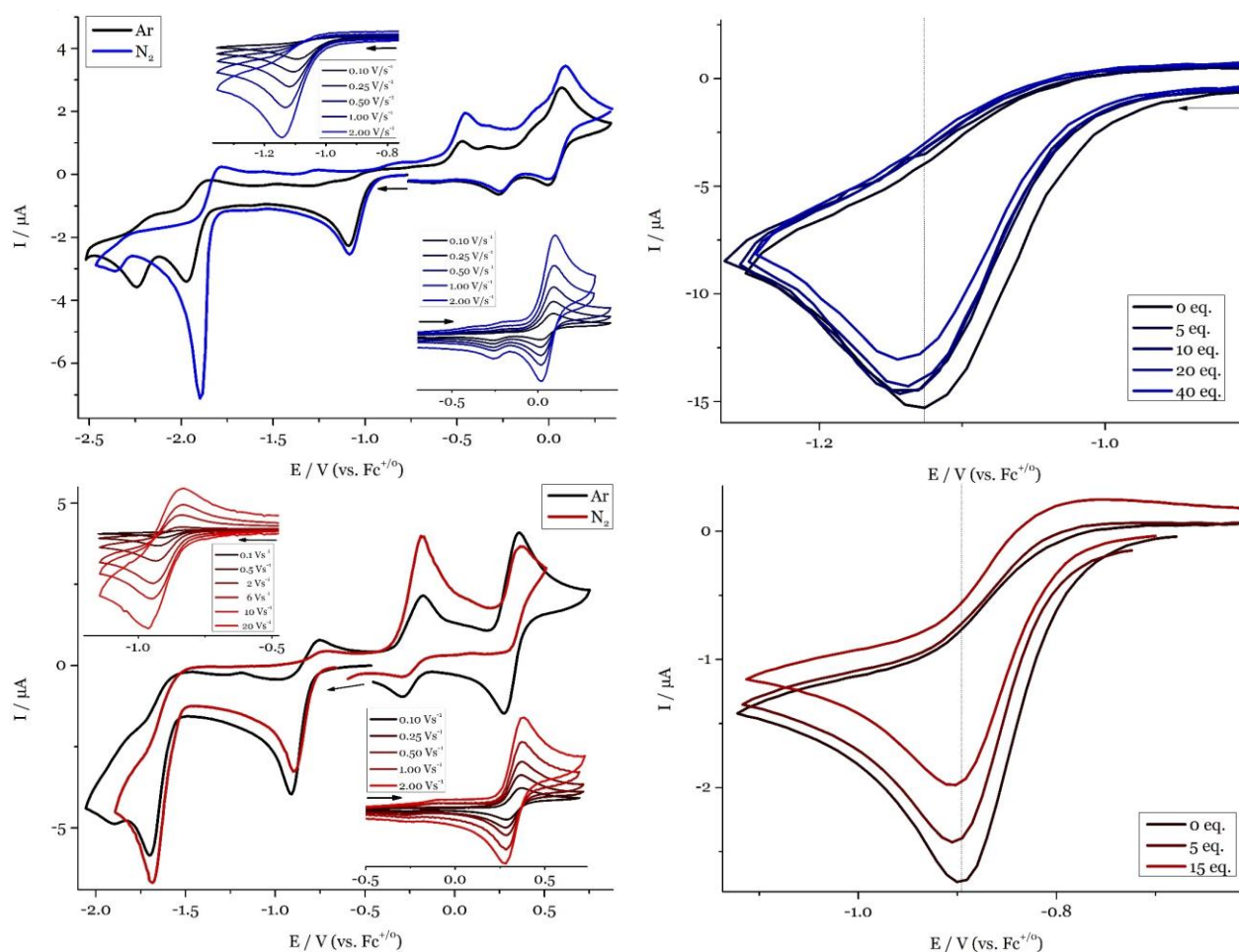


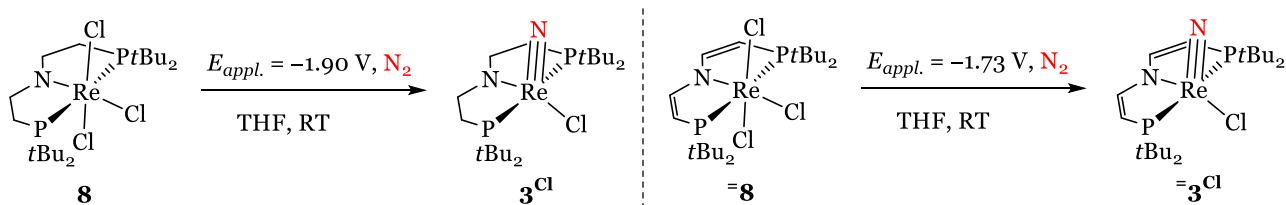
Figure 60. Top: CV of 1.0 mM **8** in THF with 0.2 M (nBu₄N)PF₆. Top left: Comparison of **8** under N₂ and Ar at $\nu = 0.1 \text{ Vs}^{-1}$. Inset top left: zoom of the first reduction under Ar. Inset bottom right: the first oxidation under Ar. Top right: first reduction of **8** in presence of different equivalents of (nHe₄N)Cl, $\nu = 2.0 \text{ Vs}^{-1}$. Bottom: CV of 1.0 mM **=8** in THF with 0.2 M (nBu₄N)PF₆. Bottom left: Comparison of the CV of **=8** under Ar or N₂ at $\nu = 0.1 \text{ Vs}^{-1}$. Inset top left: zoom of the first reduction under Ar. Inset bottom right: the first oxidation under Ar. Bottom right: first reduction of **=8** in presence of different equivalents of (nHe₄N)Cl, $\nu = 0.05 \text{ Vs}^{-1}$.

In general, due to the decreased donor ability of the P=N=P-ligand, the whole spectrum is shifted anodically by circa 0.2 V. We also note that in the CV comparison between **8** and **=8**, no far anodic peak is observed until circa +1.0 V that is assigned to PNP-ligand oxidation in contrast to the several examples as described herein (i.e. **3**^{Cl}/**=3**^{Cl} and **6**/**=6**).

4.6. Electrochemical N₂-splitting from the Re(IV)-platform

As Re-product from (electro)chemical MeCN release, the six-coordinate **8** (accessed only by means of chemical oxidation) or **=8** (accessed via both electro- and electrochemical MeCN release) were found. To connect this reactivity to the N₂-splitting as presented in Chapters II.1

and II.3, the missing link is the electrochemical N₂-splitting from these Re(IV)-platforms. Both reactions were performed as a proof of principle, without several reproductions to precisely quantify the corresponding nitrides **3**^{Cl} and =**3**^{Cl}.



Scheme 59. Electrochemical N₂-splitting in THF from the six-coordinated trichloride platform, either the saturated **8** yielding circa 35 % **3**^{Cl} (left) and unsaturated =**8** yielding traces of =**3**^{Cl} (right).

CPE of **8** at $E_{\text{appl.}} = -1.90 \text{ V}$ results in a colour change from light green via colourless to yellow, accompanied by the transfer of 2.25 electrons per rhenium in circa 3 h. Formation of **3**^{Cl} was proven by ³¹P{¹H} NMR spectroscopy, in circa 35 % yield (Figure 61). In the CPE trace, the Re(IV/III) reduction decreases first and a temporarily discolouration of the solution indicates presence of violet **1**^{Cl}, which is only weakly coloured at low concentrations. CPE of =**8** was performed at $E_{\text{appl.}} = -1.73 \text{ V}$ for 3 h, which results in a colour change from dark green via orange to intense light green, accompanied by a transfer of only 1.4 electrons per rhenium. By ³¹P{¹H} NMR spectroscopy traces of =**3**^{Cl} were observed, of which the yield was not quantified, see Figure 61. This result is not unexpected, since =**8** showed decomposition within a CV or CPE set up, and CPE from Re(III) =**1**^{Cl} also afforded the corresponding nitride in only 15 % yield. The CV traces as measured during CPE already show substantial decomposition after 15 % of the required two electrons for N₂-splitting are transferred. If this reaction is to be quantified in future research, the reaction time (and thereby the presence time of =**8** in the cell) should be decreased by taking fresh sample holders for CPE (which increases the current passed per second compared to the used and slightly fouled ones), and/or by applying a stronger overpotential. Nevertheless, both reactions prove electrochemical N₂-splitting from **8** and =**8**.

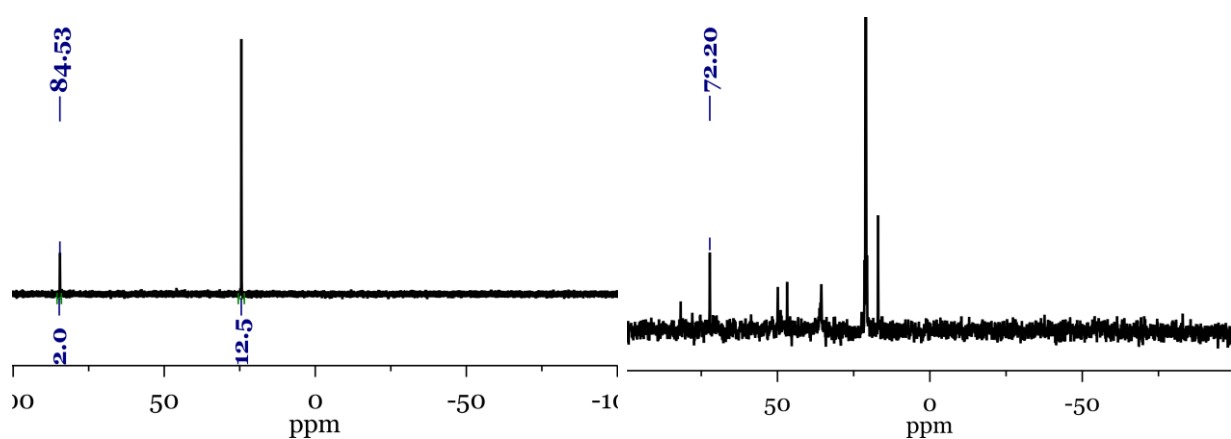


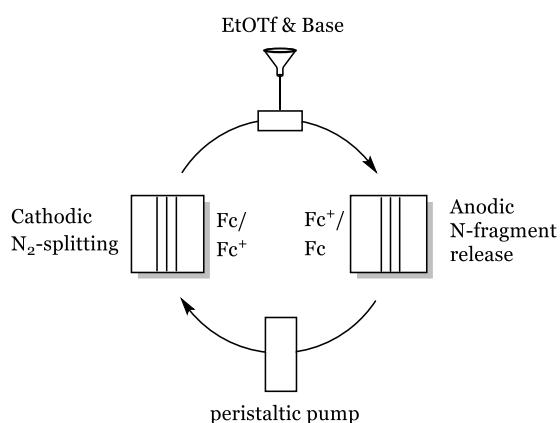
Figure 61. $^{31}\text{P}\{^1\text{H}\}$ NMR spectra after CPE of **8** to form $\mathbf{3}^{\text{Cl}}$ (peak at 84.5 ppm) (left), and $\mathbf{8}$ to form $\mathbf{=3}^{\text{Cl}}$ (peak at 72.2 ppm) (right). PPh_3O (peak at 24.2 ppm) was added as standard for nitride quantification, which was not performed in case of $\mathbf{=3}^{\text{Cl}}$, since only traces are observed.

II.5: N₂-splitting in a flow cell

Parts of this Chapter are published in: 'Implementierung einer Flow-Zelle in die elektrochemische Stickstoffspaltung', C.M.G.K. von Petersdorff-Campen, 2020, Bachelorthesis, Georg-August-Universität Göttingen.

The electrochemical N₂-splitting, C-N bond functionalisation and subsequent MeCN release starting from the (un)saturated platform [ReCl_{2/3}(P(=)N(=)P)] can only move closer towards a catalytic future if the separate reactions are carried out at isolated reaction sites, preventing all incompatible reagents to directly react with each other. Initially, separating the reductive N₂-splitting and the oxidative MeCN-release could be envisioned in a regular CPE set up, where both reactions occur and the transport of the corresponding Re-species occurs via a membrane or porous filter. Considering the saturated platform, the applied potentials of oxidative MeCN release ($E_{appl.} = -0.3$ V from **6**) and reductive N₂-splitting ($E_{appl.} = -1.9$ V from **8**, respectively) would allow that the required Re-species are not reacting at the opposite electrode: reduction of **6** is at very negative potentials ($E_p = -3.1$ V) and **8**, which would be the starting platform of choice, is first oxidised at $E_{1/2} = 0.05$ V. Yet, the C-N bond functionalisation should also be incorporated (which is a rather slow reaction), and complicates the one CPE cell set up. Furthermore, intermediates (such as **1^{Cl}** during N₂-splitting), might not be compatible with these potentials. It should be stated that EtOTf is first reduced starting from > -2.5 V in 1,2-difluorobenzene (see Appendix A2), and it is imagined to be at least partially compatible with electrochemical N₂-splitting. A solution can be found in a flow cell set up, where both reactions are separated and coupled to a separate reaction vessel where the electrophilic ethylation is performed, as very simply sketched in Scheme 60. As counter reaction, Fc oxidation and re-reduction is envisioned, that can occur at high concentrations, to ensure that there are no limitations from the counter electrode side. A cyclic flow could be generated from a peristaltic pump.

It is noted that the simple sketch of this envisioned flow cell set up disregards many challenges, for instance many compatibility questions, i.e. formation of MeCN & N₂-splitting, EtOTf & THF, excess Cl⁻ ions & N₂-splitting, just to name some. Addressing those is beyond the scope of this work. As final part of this thesis, a flow cell set up was explored for the N₂-splitting reduction. In general, the diamagnetic nitride result of such a reaction is easier to quantify compared to the MeCN release reaction. As found in Chapter II.4, the unsaturated platform is performing better for the MeCN release, giving at least some of **8**. Yet, we perform test reactions on **1^{Cl}** in THF, as high nitride yields were obtained.



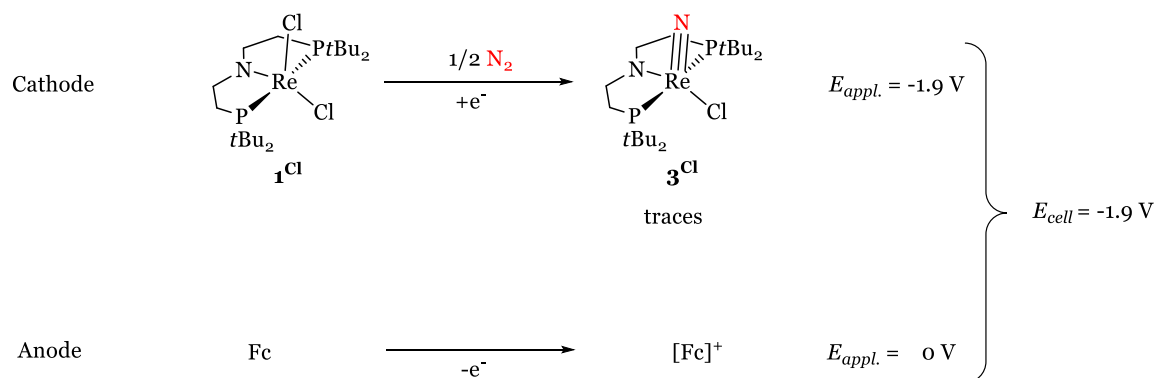
Scheme 60. Schematic set up of the Re-mediated N_2 -splitting and oxidative MeCN release, coupled via a separate reaction vessel where the chemical C-N bond formation reagents are injected.



Figure 62. Flow cell set up with the syringe pump as used for initial attempts of electrochemical N_2 -splitting from $\mathbf{1}^{Cl}$. From left to right comes first the syringe pump with a solution of $\mathbf{1}^{Cl}$ (purple, back) and a solution of Fc (yellow, front) in THF. The syringes are connected via PTFE tubes to the stainless steel entrances of the flow cell. The flow cell is connected via crocodile clamps to the potentiostat. After flowing passed the electrodes, the solutions are gathered in the attached vials on the right.

First, we recognised that the commercially obtained flow cell was made from mainly two materials that are not compatible with most organic solvents (EPDM, CPVC), and had to be modified to a PTFE set up, which is extensively described in Section IV.4.2. Meanwhile, we wanted to correlate the flow rates with conversion via UV-vis spectroscopy for a simple test system, either using the $[Fc]^{+/0}$ couple in organic solvents or $[Fe(CN_6)]^{2-/3-}$ in water. Yet, we encountered several obstacles that hampered a decent study at this point. Amongst the problems are mainly the facts that we a) explored graphite electrodes for most test runs that required high overpotentials to observe some current density, and b) the presence of stainless steel entrances of the flow cell as described in Section IV.4.2, which strangely proved incompatible with $[Fc]^+$.

Despite lacking information about the flow rate/conversion correlation, we explored a first attempt for dinitrogen activation in the flow cell set up in the MBraun glovebox under a N_2 atmosphere, as depicted in Figure 62 and Scheme 61. Instead of a peristaltic pump, a syringe pump was used for these initial tests, since its handling proved easier.



Scheme 61. Reactions examined in the flow cell: electrochemical N_2 -splitting from $\mathbf{1}^{Cl}$ into $\mathbf{3}^{Cl}$ at the cathode and Fc oxidation at the anode, with an overall cell potential of $E_{cell} = -1.9 V$.

We confirmed that both $\mathbf{1}^{Cl}$ and $\mathbf{3}^{Cl}$ are stable while flowing through the stainless steel entrances of the flow cell, as judged from identical UV-vis traces before and after a run through the flow cell. Afterwards, we charged the syringes with separate solutions of $\mathbf{1}^{Cl}$ and Fc, and applied a flowrate of 0.04 mL min^{-1} . This corresponds to a dwell time for the Re-species at the electrode surface of circa $7/8$ times lower compared to a classic steady state CPE experiment. An anion-exchange membrane was applied to secure charge compensation and to prevent Fc^+ migrating in the cathode frame to oxidise $\mathbf{1}^{Cl}$. Based on literature examples, we got the impression that large overpotentials were required,¹²³ and CPE was initially examined at a large overpotential of $E_{appl.} = -3.0 V$ vs. the Ag-wire (which very roughly corresponds to $-3.4 V$ vs. $Fc^{+/0}$). Although the colour of the Re-containing solution changed promisingly to orange, no $\mathbf{3}^{Cl}$ was found by NMR spectroscopy. Instead, it showed a mixture of at least 7 unknown species. Supported by full conversion of $\mathbf{1}^{Cl}$ in this attempt, a modest overpotential was explored next at $E_{appl.} = -1.6 V$ vs. the Ag-wire (which very roughly corresponds to $\approx -2.0 V$ vs. $Fc^{+/0}$). The colour on the Re-side changed to yellow, accompanied by a current density of $\approx 1.6 \text{ mA cm}^{-2}$. In the $^{31}P\{^1H\}$ NMR spectrum we observe a feature at 84.2 ppm, which matches to formation of $\mathbf{3}^{Cl}$, as shown in Figure 63. The nitride is formed alongside many other species as judged by the appearance of many signals in the $^{31}P\{^1H\}$ NMR spectrum, and was not quantified. The main species is found at 80 ppm, which based on its chemical shift corresponds to a Re(I) or Re(V)-species. Unfortunately, the mixture of compounds hinder clear allocation of $\mathbf{3}^{Cl}$ via 1H NMR spectroscopy: with a very optimistic eye, the backbone features at 3.10 and 3.69 ppm might be

recognised, yet also clearly obscured by other peaks. Surprisingly, the ^1H NMR spectrum of the cathodic side shows the presence of Fc, which was not expected based on the anion-exchange membrane. Besides, paramagnetic species must be present, judged from the appearance of broad features in the range of -5 to -11 ppm. Via LIFDI mass spectroscopy, no clear feature for the nitride was observed, although the region is obscured by other features at 598 m/z and 594 m/z (calculated for $\mathbf{3}^{\text{Cl}}$ is 596 m/z). Although the outcome now only relies on one method, we believe it is a promising start for future research.

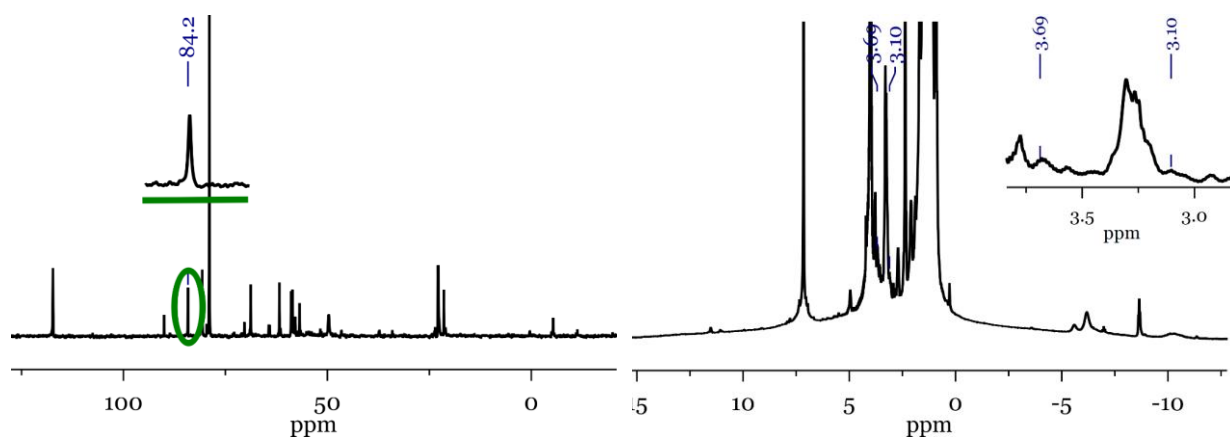


Figure 63. NMR spectroscopy of electrochemical N_2 -splitting in a flow cell at roughly $E_{\text{appl.}} = -2.0$ V vs. $\text{Fc}^{+/0}$ with a flow rate of 0.04 mL min^{-1} . Left: $^{31}\text{P}\{^1\text{H}\}$ NMR, right: ^1H NMR.

III Conclusion and Outlook

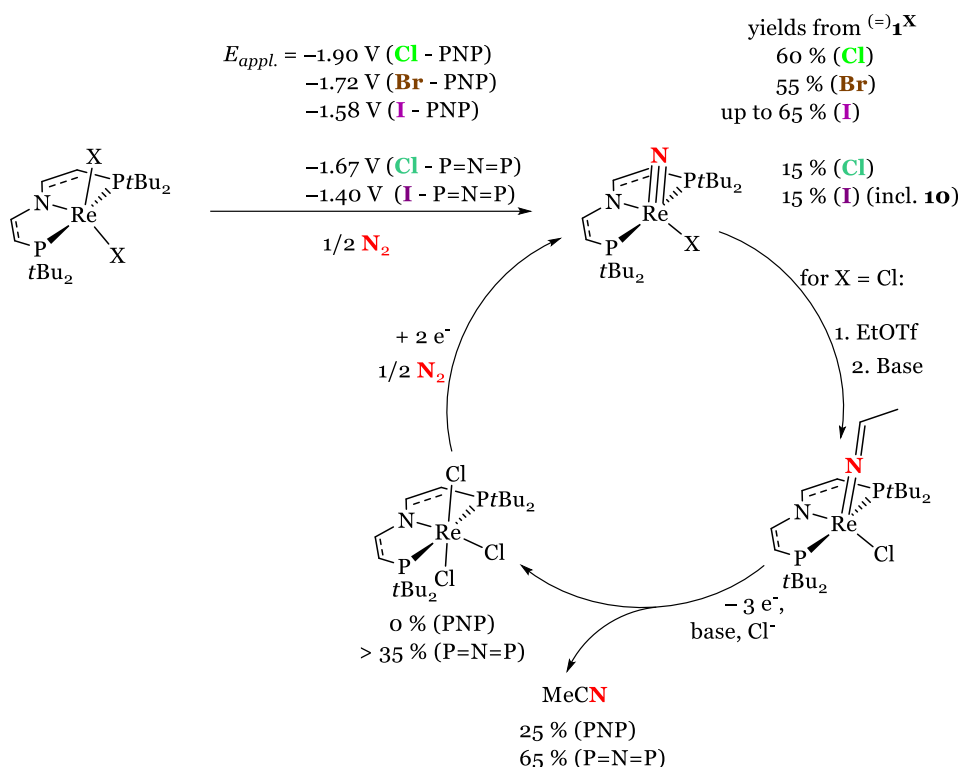
III.1. Conclusion

Several topics were addressed within this work: electrochemical N₂-splitting into terminal nitrides, mechanistic examinations from the five-coordinate starting platforms into the nitrides, and the electrochemical release of N₂-derived MeCN. A brief summary and the most important conclusions of each topic is highlighted.

First, we showed successful electrochemical N₂-splitting from flagship compound [ReCl₂(PNP)] into the well-defined terminal nitride [ReNCl(PNP)] in 60 % yield based on rhenium and 50 % faradaic yield. We could expand this platform to the bromide and iodide congeners that showed electrochemical N₂-splitting with similar nitride yields. From the chloride and iodide platform bearing the unsaturated P=N=P-platform, the corresponding nitrides were also accessed electrochemically, yet in significant detrimental yields, see Scheme 62. With regard to the required N₂-splitting reduction potential, we identify two trends: 1) going down the halide group, electrochemical access to the nitrides becomes more favourable by circa 0.15 V per halide. This is attributed to the weaker electron donating properties going to the heavier halide ligand. Furthermore, 2) changing the PNP for the P=N=P-ligand allows for an approx. 0.2 V more positive applied potential, due to the diminished N_{Amide} π-donation from this unsaturated ligand. Within the established series, electrochemical nitride formation from =**1** is at the most benign potential. In general, we can conclude that the exchange of halide ligands within a ligand backbone series has virtually no effect on the efficiency of N₂-splitting, in contrast to desaturation of the ligand backbone.

As a second main topic, we extensively examined the mechanism of (electro)chemical N₂-splitting by spectroscopic and voltammetric techniques. First, we examined the reduction profile for (=)**1**^X under Ar, always revealing two reductions, attributed to an *ECE*-mechanism of initial Re^{III/II} reduction ([ReX₂(P(=)N(=)P)]^{0/-}), coupled to halide loss, and the subsequent Re^{II/I} reduction of [ReX(P(=)N(=)P)]^{0/-} (X= Cl, Br and I). The potential difference between these reductions show two trends: 1) it becomes larger down the halide group (E_{p,c,1}-E_{p,c,2} = 0.30 V (**1**^{Cl}), 0.43 (**1**^{Br}), and 0.60 (**1**^I)), and 2) smaller when going from the PNP to the P=N=P ligand (E_{p,c,1}-E_{p,c,2} = 0.16 V (= **1**^{Cl}), and 0.37 (= **1**^I)). The latter might indicate that the second reduction is partially ligand based, which would then be favoured for the conjugated P=N=P-ligand. The reductively induced halide loss was quantified for the (=)**1**^{Cl} and **1**^I platforms, showing values between ≈ 10²-10⁴ s⁻¹. This is substantially higher compared to platforms bearing only monodentate or less electron donating ligands, as showcased in Section II.1.5. We consider the

pincer ligand instrumental to favour halide loss, with most emphasis on the strong N_{amide} -metal electron donation unique for the herein examined pincer platforms.



Scheme 62. Graphical overview of some important findings within this work.

The mechanism of N_2 -splitting was examined starting from 1^{Cl} . We found a fast number of elemental steps that form the dinuclear N_2 -bridging intermediate $[(\text{ReCl}(\text{PNP}))_2(\mu\text{-N}_2)]$, that follow an $EC^{N_2}CC^{Cl}EC^{dim.}$ -mechanism. N_2 -coordination is at the Re(II) stage with dramatically improved dinitrogen affinity compared to its oxidised Re(III) precursor 1^{Cl} . Notably, for all platforms there exist indications that the oxidation state for N_2 -coordination is Re(II), i.e. the disappearance of the $[\text{ReX}(\text{P}(=\text{N})(=\text{N})\text{P})^{0/-}]$ reduction when measuring CV under N_2 instead of under Ar. Binding of the π -accepting N_2 ligand to $[\text{ReCl}(\text{N}_2)(\text{PNP})]$ leads to immediate further reduction to Re(I) due to *potential inversion*, followed by a comproportionation type reaction with the Re(III) precursor to reach the N_2 -bridged dinuclear compound. DFT calculations stated that considerable N_2 -activation is not achieved prior to formation and subsequent splitting of 2^{Cl} . It is reasonable to assume that the accessibility of the more stable Re(I) is instrumental to avoid Re(II) decay pathways. Furthermore, two reduction equivalents are stored on the metal in this manner, thereby avoiding unfavourable one-electron reduction of N_2 . Based on the similar

CV traces between $\mathbf{1}^{\text{Br}}$ and $\mathbf{1}^{\text{Cl}}$, this mechanism is also assumed as the main pathway for the bromide congener.

Regarding the iodide platform $\mathbf{1}^{\text{I}}$, the CV trace appears dramatically different: the two for N_2 -splitting effective reductions are deconvoluted, instead of potentially inverted, as is the case for $\mathbf{1}^{\text{Br}}$ and $\mathbf{1}^{\text{Cl}}$. The appearance of two isolated waves and their v -dependency lead us to expand our N_2 -splitting model and to include two co-existing pathways. First, a comparable two electron reduction / comproportionation pathway is followed, although discrimination between the order of N_2 -coordination of iodide loss (i.e. $EC^{\text{N}_2}C^{\text{I}}EC^{\text{dim}}$ or $EC^{\text{I}}C^{\text{N}_2}EC^{\text{dim}}$) is not possible due to faster and more favourite iodide loss compared to chloride. In addition, longer lifetimes for Re(II) species allow for direct dimerization in a one electron / dimerization pathway.

These series of elemental steps yield dinuclear intermediate $\mathbf{2}^{\text{X}}$. For $\mathbf{2}^{\text{Cl}}$, its characterisation was completed within the context of this work and $\mathbf{2}^{\text{Br}}$ and $\mathbf{2}^{\text{I}}$ were spectroscopically characterised. Going down the group, paramagnetic contributions towards the magnetic ground state increase, as indicated by the more paramagnetically shifted ^1H NMR spectroscopic features, the absence of heteronuclear NMR for $\mathbf{2}^{\text{I}}$, and the larger chemical shift differences by VT-NMR. The lifetime of $\mathbf{2}^{\text{X}}$ increases slightly down the group, and they are instable with respect to N_2 -splitting, which quantitatively represents the slowest reaction in overall N_2 -splitting.

An extended mechanistic study regarding the platforms bearing the unsaturated $\text{P}=\text{N}=\text{P}$ is not reasonable, based on the low nitride yield via electrochemical N_2 -splitting. For $=\mathbf{1}^{\text{Cl}}$, we explored different solvents (Et_2O , fluorobenzene, 1,2-difluorobenzene, THF), yet leading to the same mediocre results. Upon both chemical and electrochemical N_2 -splitting on $=\mathbf{1}^{\text{I}}$, we also found nitride [$\text{ReNI}(\text{N}(\text{CHCHPtBu}_2)(\text{CHCHPHtBu}))$] ($\mathbf{10}$), which is the product of $=\mathbf{3}^{\text{I}}$ and isobutene loss, leaving a direct P-H bond. We believe that this reactivity is favoured for the $(\text{P}=\text{N}=\text{P})$ -platform.

In search for an explanation for the low yields on this platform, we can argue on three aspects: 1) we found that the $=\mathbf{1}^{\text{Cl}}$ platform is instable under a N_2 atmosphere (less pronounced) and in presence of Cl^- (more pronounced). For this latter, a chloride induced disproportionation type reactivity was proposed that ultimately forms [$\text{ReCl}_3(\text{P}=\text{N}=\text{P})$]. The overall uphill process might play a decomposing role during electrolysis, due to longer reaction time compared to chemical N_2 -splitting. In contrast, this was not observed for $=\mathbf{1}^{\text{I}}$ (initial iodide coordination is likely more uphill due to steric reasons), indicating this proposed reactivity plays only a minor role as general pathway of decreased nitride yield from the $\text{P}=\text{N}=\text{P}$ -platform. 2) Likely more attributing to the

overall low yield is the stronger anodic shift of the second reduction compared to the first reduction of $[\text{ReX}_2(\text{P}=\text{N}=\text{P})]$, which could cause overreductions that lead to decomposition. 3) In addition, we identified for =1^{Cl} that at the Re(II) stage, two decomposition pathways could compete with N_2 -splitting, amongst one with a bimolecular nature. This can be especially unfavourable for electrochemical reduction, where high local Re(II) concentrations are expected.

Next, we focused on the electrochemical MeCN release, which was successful upon performing oxidative electrolysis of **6** in presence of DBU and Cl^- -source. Yet, the yield in acetonitrile was low, and only a mixture of several unknown Re-compounds was found instead of the expected $[\text{ReCl}_3(\text{PNP})]$. Based on the large charge excess that is needed for full conversion, we attribute PNP-backbone reactivity under oxidative conditions to unselective decomposition. Within this work, we propose for 1^{Cl} that the ligand oxidation, as usually found at potentials > 0.6 V, shifts substantially anodically in presence of base indicative of PCET reactivity. Therefore, we synthesised the P=N=P bearing analogue =6 , and oxidative electrolysis affords MeCN in circa 65 % and =8 in minimally 35 % yield. The latter value is a lower limit, as this compound suffers from decomposition in solution. Amongst the decomposition products of =8 we could isolate a structure with a surprising cyclised ligand-backbone (**12**). Yet, this compound is not involved in decomposition of =8 in the electrochemical set up and the fate of that decomposition remains unsolved. The CV of both (=)8 show an irreversible Re(IV/III) reduction, which is coupled to chloride loss, and continue cathodically precisely identical to (=)1^{Cl} . As a proof of principle, electrochemical N_2 -splitting from both trichloride platforms into the corresponding nitrides was shown.

From considering both the reductive N_2 -splitting and oxidative MeCN, we can now emphasise even more the challenges towards a catalytic future for this platform. From the starting platform bearing the PNP-ligand, we find good nitride yields via electrochemical N_2 -activation, but an unselective mixture of Re-products in oxidative MeCN release attributed to ligand backbone oxidation. This latter problem is (partly) circumvented by using the unsaturated P=N=P ligand, yet electrochemical N_2 -splitting from these platforms is associated with low yields.

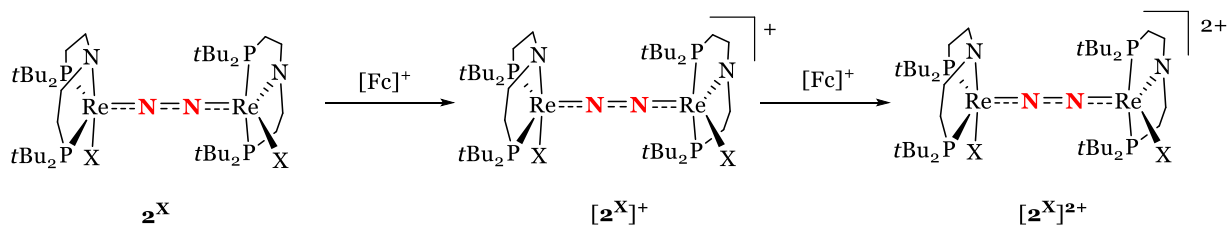
The aim of electrifying this stoichiometric cycle of N_2 -splitting and MeCN release is achieved, and key findings towards the design of future (electro)chemical molecular N_2 -splitting complexes or catalysts were extracted.

III.2. Outlook

If this system would be continued, several aspects can still be examined.

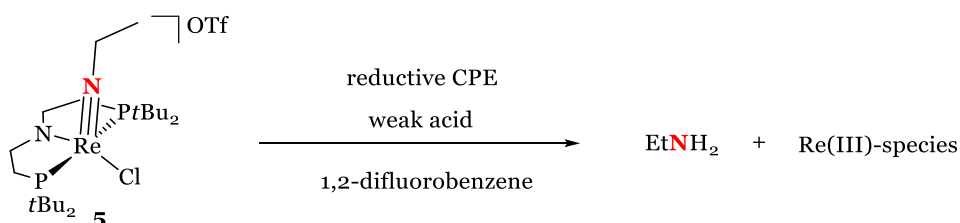
Regarding electrochemical nitrile release, an alternative nitrile should be examined compared to MeCN from a very practical point of view. The release of MeCN is detected via GC chromatography, and it is found to run very close to all low-boiling solvents that can be present in the electrolysis solvent, box atmosphere, or GC room atmosphere (i.e. acetone for cleaning, see Section IV.3 for more details). Yet, not many organotriflates (RCH₂OTf) compounds are commercially available. To increase the scope of used compounds and relief the quantification method, we could explore activation of **3^{Cl}** following the strategy from Cummins: first react the nitrile with Me₃SiOTf, upon which it is activated for less strong electrophiles, i.e. acid chlorides,¹⁵⁰ that usually have a large variety of possible R-groups.

It would be very interesting to take a closer look into the end-on N₂-bridging **2^X** complexes. Due to their very limited RT-stability and decreased purity, no SQUID magnetometry is possible, and many questions regarding their electronic description and electrochemistry remain. Although their electrochemical properties could be examined by low temperature CV, the easiest solution would be to sequentially oxidise this δ⁴π¹⁰ system to its single (δ⁴π⁹) and double (δ⁴π⁸) positively charged complex series. Series like this (in various electronic configurations), were discussed in Section I.1.4.3. Although the lifetime of **2^I** is the longest, **2^{Cl}** is obtained in a spectroscopically high yield. Therefore, the chloride system is preferred and based on reliable δ⁴π¹⁰ systems (see Section II.2.8), oxidation with a [Fc]⁺-salt is sufficient to access this series (Scheme 63). Especially interesting would be to follow the reductive trace of either oxidised dimer: hopefully, the concentration of the re-reduced **2^X** species at the electrode surface is high enough to unequivocally conclude if the small cathodic feature in the CVs of **1^X** can be assigned to **2^X** (as hypothesised in Section II.2.8).



Scheme 63. Envisioned sequential twofold oxidation of **2^X** to its putative δ⁴π⁹ and δ⁴π⁸ congener.

A main conclusion from this work is the incompatibility of either ligand platform with both electrochemical reductive N₂-splitting and oxidative MeCN release. To move into a forward direction, there are several possibilities. Either the ligand platform is changed or the envisioned reactivity is modified to make it compatible with either the reductive or the oxidative chemistry. To follow up on this latter, Pickett provides an interesting alternative approach as exemplified in Scheme 26 in Section I.2.2.2. Instead of oxidising the N-C bond of an imido fragment to e.g. MeCN, they showed the release of amines upon reduction in presence of acid.¹³⁸ Such an approach is currently under investigation within our research group for [ReBr₃(HPNP^{Pr})]. It is possible that the same approach is feasible for our system. A key reaction is shown in Scheme 64, imagined to start from imido **5**. In order for this reaction to be successful, the reduction of **5** should be coupled to protonation to the amido ligand, and a subsequent cycle of reduction-protonation releases the amine. As initial experiment, it is proposed to titrate weak acids into a solution of **5** and measure CV: successful protonation can be assumed if the irreversible reduction of **5** at $E_p = -1.84$ V (see Chapter II.4) shifts and increases in current. Notably, this potential leaves us still with a choice between some acids before competing HER occurs.¹⁰⁹ If in this manner an electrochemical reductive C-N fragment release can be established, it even has a promise to be catalytic, combining reductive N₂-splitting, C-N bond formation via reaction with alkyltriflates and reductive amine release. Initially, competing reduction of EtOTf seems problematic, but the far cathodic potential (> -2.5 V, see Appendix A2) is well beyond the reduction of **5** and the N₂-splitting potential for **1**^{Cl}. This latter would only be formed if additional Cl⁻ ions are added, but alternative Re(III) species such as [ReCl(OTf)(PNP)] likely operate in the same potential range. It is very likely that the backbone will get protonated, which shifts the reduction potentials cathodically, but there is still a potential window to perform CPE more reductive until reduction of EtOTf or competing HER occurs.



Scheme 64. Proposed amine release from reductive CPE of **5** in presence of protons.

The other main possibility is to modify the ligand platform towards a more robust system, stable against both reductive and oxidative conditions. A promising strategy for increased stability would be to install a phenyl-linkage in the backbone, as outlined in Figure 64. A modification of such a platform was used to synthesise a Re(V) nitride (not originating from N₂) and its

corresponding N-C bond formation using CO by Ison.²⁰⁸ Due to the increased steric demand in the backbone, it is unlikely to isolate the *tert*-butyl substituted phosphorous platform. Instead, *iso*-propyl substituted phosphorus can be synthesised and therefore a Re(IV) starting platform is envisioned similar to $[\text{ReCl}_3(\text{PNP}^{i\text{Pr}})]$, as described in Section I.1.4. The extended conjugated system in the backbone can also introduce ligand-based electrochemistry that can shift the redox potentials. Studies within our group with a modification of this ligand already show good results regarding N_2 -splitting and subsequent functionalisation.

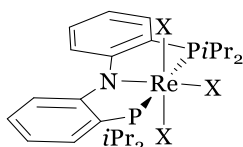


Figure 64. Proposed ligand modification for future research.

IV Experimental Section

IV.1. General working techniques

All chemical reactions were performed under an inert atmosphere (either Ar 5.0 or N₂ 5.0 from *Linde*) as obtained either via a Schlenkline or upon working within an MBraun Glovebox. The temperature within this latter proved to fluctuate between 25 and 30 °C. All glassware was cleaned first in KOH/iso-propanol and subsequently in HCl baths, washed with demineralised water and pre-heated at 115 °C or heated with a heat gun whilst applying vacuum. At the Schlenkline, solvents were transferred via over-condensation or via a stainless-steel cannula. Filtration was performed using pre-heated PTFE tubing to which a Whatmann Glasfiberfilter (GF/B, 25 mm) is attached with PTFE-band or with a pre-heated small piece of this filter within a pipette. Small-scale chemical reactions (≤ 5 mg) were performed in a J-Young NMR tube.

IV.2. Chemicals and purification methods

All solvents were purchased in HPLC quality (*Sigma Aldrich/Merck*), and dried using an MBRAUN Solvent Purification System. All deuterated solvents were acquired from *Eurio-Top GMBH*. Solvents THF, *d*₈-THF, *d*₈-toluene, C₆H₆, C₆D₆, and Et₂O were dried over NaK for one week, over-condensed, and degassed prior to use. CH₂Cl₂, CD₂Cl₂, Chlorobenzene, fluorobenzene, 1,2-difluorobenzene, and NEt₃ were dried by stirring over CaH₂ for two weeks and subsequent over-condensing (when NaK- or CaH₂-dried non-deuterated solvents are required, it is specified in the experimental information). Demineralised water was used, which was de-oxygenated by bubbling Ar through.

The following Re-compounds were synthesised according to their literature procedure: [Re(MeCN)Cl₃(PPh₃)₂],^{169,170} [Re(MeCN)Br₃(PPh₃)₂],^{169,170}, [ReCl₂(PNP)] (**1**Cl),⁷⁹ [ReCl₂(P=N=P)] (=1Cl),⁷¹ [ReI₂(P=N=P)] (=1I),¹⁶⁸ [ReCl(NCH₂CH₃)(PNP)]OTf (**5**),⁷⁹ [ReCl(NCHCH₃)(PNP)](**6**),⁷⁹ and [ReCl(NCHCH₂)(PNP)]OTf (**7**).⁷⁹ 1 M Na/Hg was prepared by addition of Hg (0.292 mL, 4 g) to Na (6.7 mg, 0.292 mol) in the glovebox, upon which Na/Hg is formed. 2,4,6-tri-*tert*-butylphenoxy radical was synthesised as adapted from a published procedure by Mayer and coworkers.²⁰⁹ In a typical run, 2,4,6-tri-*tert*-butylphenol (1.25 g) was dissolved in C₆D₆ (80 mL), NaOH (15 mL, 1 M) was added, and the mixture was degassed by freeze pump thaw cycles. To the frozen reaction mixture, K[Fe(CN)₆] (3.9 g, 2.5 eq.) was added and it was allowed to warm to room temperature and stirred for 2 h. Subsequently, the organic phase was decanted, and the water phase was washed with pentane (3 x 10 mL). The solvents were removed *in vacuo*, and the product was extracted with pentanes. Pentane was removed *in*

vacuo and lyophilisation yielded 2,4,6-tri-*tert*-butylphenoxy as dark blue solid in circa 90 % yield. $(\text{OEt}_3)\text{BAr}^{\text{F}_{24}}$ was synthesised by allowing equimolar mixtures of $(\text{OEt}_3)\text{BF}_4$ and $\text{NaBAr}^{\text{F}_{24}}$ to react in DCM for 1 h, after which it was extracted with Et_2O and dried extensively. $(n\text{Bu}_4\text{N})\text{BAr}^{\text{F}_{24}}$ was synthesised according to a modified procedure based on the published one by Geiger²¹⁰: $(n\text{Bu}_4\text{N})\text{Cl}$ (3.3 g, 12 mmol, 1.1 eq.) was dissolved in a methanol-water mixture (2:1, 15 mL) and are added dropwise to a solution of $\text{NaBAr}^{\text{F}_{24}}$ (10 g, 11.1 mmol, 1 eq.) in a methanol-water mixture (2:1, 30 mL). Directly, a lot of white precipitation was observed. The suspension was stirred for 15 minutes, and added dropwise to water (30 mL). The precipitate was filtered-off, dissolved in DCM (20 mL) and washed several times with water and Brine solution until minor yellow colouration was removed. Subsequently, the reaction mixture was dried over MgSO_4 . This suspension was filtered-off and from the filtrate, the volatiles were removed *in vacuo*. The so obtained white solid was further dried at 90 °C overnight. $(n\text{Bu}_4\text{N})\text{BAr}^{\text{F}_{24}}$ was obtained as dry and clean solid as judged by a clean blank CV in THF and no water-peak in its IR-spectrum in 65 % yield (8.6 g, 7.8 mmol). $(\text{PPN})\text{N}_3$ was synthesised according to the procedure as described by Dr. M. Scheibel.²¹¹ $[\text{Fc}]\text{BAr}^{\text{F}_{24}}$ was synthesised upon reaction of equimolar amounts of $\text{NaBAr}^{\text{F}_{24}}$ and $[\text{Fc}]\text{PF}_6$ in DCM for circa 1 h. Subsequent evaporation of the solvents *in vacuo*, extraction with Et_2O and drying afforded the dark blue $[\text{Fc}]\text{BAr}^{\text{F}_{24}}$.

TMS-N_3 was distilled at 140 °C at 1 atm Ar and stored over 3 Å moll sieves in the freezer. EtOTf was distilled at 115 °C at 1 atm Ar and stored in the freezer. Fc, NCS, and Fc^* were sublimed at 0.020 mbar at 40 °C, 80 °C, and 105 °C mbar, respectively. $(n\text{Bu}_4\text{N})\text{PF}_6$, $(n\text{Bu}_4\text{N})\text{Cl}$, $(n\text{He}_4\text{N})\text{Cl}$, $(n\text{He}_4\text{N})\text{Br}$, and $(n\text{He}_4\text{N})\text{I}$ were extensively dried at 0.020 mbar at 80°C, 85°C, 85°C, 85°C, 95°C, respectively and the absence of water was judged based on the absence of OH-bands in the IR spectrum. For $(n\text{He}_4\text{N})\text{I}$, the presence of Br^- (≈ 2 ppm) and Cl^- (≈ 8 ppm), and for $(n\text{Bu}_4\text{N})\text{PF}_6$ the presence of Cl^- (≈ 2 ppm) was determined via elemental analysis. DBU was degassed and stored over moll sieves. Silanised silica and Celite were heated to 150 °C for 1-2 weeks at 0.020 mbar. PPh_3 , PPh_3O , $\text{P}(\text{O}(\text{Si}(\text{CH}_3)_3)_3$, $\text{Co}(\text{Cp}^*)_2$, $[\text{Co}(\text{Cp}^*)_2]\text{PF}_6$, $\text{Cr}(\text{Cp}^*)_2$, KHMDS , hexamethylbenzene, 1,3,5-trimethoxybenzene, AgOTf , 2,4,6-tri-*tert*-butylphenol, $\text{K}_3[\text{Fe}(\text{CN})_6]$, $(\text{OEt}_3)\text{BF}_4$, $\text{NaBAr}^{\text{F}_{24}}$, were deoxygenated by applying vacuum and subsequently used as commercially obtained. HCl in Et_2O , Tf_2O , and $^{15}\text{N}_2$ (98 %) were used as commercially obtained.

IV.3. Analytical methods

Cyclic voltammetry (CV)

CV was measured on several potentiostats: a Gamry 600 reference for the N₂-measurements for Chapter II.1 and II.3 (the data for **1^{Cl}**), a Gamry 1010E for the N₂-measurements in Chapter II.2, II.3 (the data for **1^I**), the MeCN release in Chapter II.4, and the Flow Cell chemistry in Chapter II.5. All data were it is explicitly mentioned that it is under an Ar atmosphere were measured on a Metrohm PGSTAT101. For Gamry, electrochemistry was recorded using the Gamry software, and for Metrohm, the software Nova 2.0 or 2.1 was used.

CV was measured in a three-neck-cell with a RE (Ag-wire, *ChemPur*, 99.999 %), CE (Pt-wire) and a WE electrode (glassy carbon disk, A = 0.020 cm², *IJ Cambria*) in the main compartment. The three-neck cell was usually charged with solvent and 0.2 M (*n*Bu₄N)PF₆. All CVs were compensated for the remaining internal Resistance (iR-compensation) by circa 90-95 % of the uncompensated resistance value. Referencing was performed by addition of an internal reference, either during the whole measurement (i.e. for reagent titration) or only at the end of the measurement. Compounds that were regularly used as internal reference include Fc, Fc*, acetylFc, and [Co(Cp*)₂]PF₆.

Throughout this work, redox features are assigned as being reversible, which in this context relates to electrochemical reversibility: where the electron transfer is faster than mass transport of the redox-active species to the electrode. To judge if a feature is reversible, the following four criteria were taken into account: the peak to peak separation ΔE_p (a theoretical maximum exists of 0.059 V for a 1 electron transfer at RT), the ratio between the forward and reverse peak current $i_{p,f}/i_{p,r}$ (around 1.0), a linear relationship between the square root of ν and the $i_{p,f}$, and a constant $E_{p,f}$ with increasing ν .

These four criteria all have their possible error marges. Both the criterion of the peak-to-peak separation, and the relationship between $E_{p,f}$ and ν , can suffer extremely from an insufficient iR-compensation or by remaining resistance upon using the relatively non-conducting solvent THF. To reduce this problem, the electrolyte concentration was usually increased from the commonly used 0.1 M to 0.2 M, which lowers the resistance from 6000-7000 Ω to 2500-3000 Ω . Nevertheless, even for Fc & Fc*, ΔE_p values are found in the range of 0.08 V at low ν (< 0.5 Vs⁻¹), which is therefore considered to be sufficient to still judge a feature as reversible. The criterion $i_{p,f}/i_{p,r}$ was found to depend on the reverse point of the CV measurement after the forward wave.

When a sufficient wide potential range (> 0.5 V) after the forwards peak is chosen before returning the CV sweep, the baseline for the reverse wave can be read off precisely. However, either when there is a following redox feature in proximity or to acquire data for digital simulation, the CV is quickly reversed after scanning through the forward wave. The baseline for the reverse wave is less accurate and thereby the determination of $i_{p,r}$. Usually, the $i_{p,r}$ was found too small, making $i_{p,f}/i_{p,r}$ too large. A linear relationship between $i_{p,f}$ and $v^{1/2}$ is throughout this work found for most redox transfers. It is however not a selective criterion for an electrochemical reversible process, since it can also hold for electrochemical quasi- or irreversibility, and indicates that electron transfer occurs on a freely-diffusing species in solution (in contrast to an adsorbed species).¹⁷⁴

When the four criteria are met with taking the errors of the measurement into account as described above, a feature is assigned as reversible. Those features that are not reversible are either quasi-reversible or irreversible, which can either indicate their electron transfer is slower compared to mass transport or when the redox event is coupled to a chemical reaction. In case of the latter situation, they also (partially) lose their reverse CV response and show a moderate shift of $E_{p,f}$ with changing v to more harsh potentials (cathodic for a reductive event, anodic for an oxidative event). The classification quasi-reversible is used within this work when there is a v -regime where the criteria for reversibility are (almost) met.

Cyclic voltammetry (CV)

The CVs of **6** were simulated with the DigiElch8 software from ElchSoft

Controlled Potential Electrolysis (CPE)

CPE was performed in a three-neck-cell where all three electrodes were separated in different compartments with sample holders (*IJ Cambria*, with a Vycor glass tip), see Figure 65. These sample holders are soaked in for at least 3-4 days (more usually a couple of weeks) in 0.1 M of electrolyte in the CPE solvent. In a usual run, the RE (a Ag-wire) was placed in a 6 mm diameter sample holder to one side, and the CE (for Chapter II.1-3 a simple Pt-wire was used, in Chapter II.4&5 a spiral Pt-wire was used for a higher contact area (*IJ Cambria*)) was placed in a 9 mm diameter sample holder. For the WE, in Chapter II.1 a 1x1x3 cm (l * w * h) glassy carbon foam (3000C, 6.35 mm thickness, 0.05 gcm⁻³, 96.5 % porosity) was used that was connected via a graphite rod (*C3-analysentechnik*). However, this set up is very fragile and could in future be re-applied when using a different cell (H-cell approach) and/or by connecting via a Pt-wire. From Chapter II.2 and onwards, CPE was performed using a 100 mm glassy carbon rod (type 2, *Alfa*

Aesar). Next to the CPE WE, a glassy carbon disk electrode was placed to record CVs for CPE monitoring and potential determination. Since both CV and CPE electrodes are made out of glassy carbon, the potential is believed to be rather constant. At the start of CPE, a sacrificial redox agent is placed in the CE compartment (in case of reductive CPE, a sacrificial reductant and vice versa). As sacrificial reductant, a clear excess of 2-3 spatula tips of Fc are added. $[\text{Fc}]\text{PF}_6$ is more soluble than $[\text{Fc}^*]\text{PF}_6$, explaining why Fc was used. For oxidative CPE in Chapter II.4, first $[\text{Fc}]\text{PF}_6$ was used as sacrificial oxidant, that however shows a low solubility. The solution in the sample holder had to be replaced several times, initially leading to very long CPE times, after which it was replaced for the better soluble $[\text{Fc}]\text{BARF}_{24}$. When CPE was performed overnight, septa were placed over the sample holders to prevent evaporation of the solvent. For the CPE solution, 0.1 M electrolyte is usually used and no iR-compensation was applied because of the sample holders that add too much noise if iR-compensation is applied. The potential for CPE was determined by CV versus the Ag-wire and later recalculated versus $\text{Fc}^{+/0}$, either by addition of an internal standard or by transferring peak potential knowledge from earlier CV measurements. If nothing else is stated, CPE was performed until all redox waves at the CPE potential are sufficiently low ($< 0.5 \mu\text{A}$). CPE was controlled either via Gamry or Nova software on a Gamry or Metrohm potentiostat, respectively. In the first case, the current versus time integration was done automatically, in the second it was done by Origin. After CPE, PPh_3O was directly added for quantification and the three neck cell was rinsed properly. The sample was concentrated and analysed by $^3\text{P}\{^1\text{H}\}$ NMR spectroscopy.



Figure 65. Typical CPE set up with the three electrode as compartmented via the sample holders. The additional septa on the sample holders are only used when long measurements are performed (> 5 h) to prevent solvent evaporation.

Elemental analysis

Elemental analysis were obtained from the *Analytisches Labor* at the *Georg-August-University Göttingen* using an Elementar Vario EL 3 analyser.

Gas Chromatography

Gas chromatography was measured on an Agilent Technologies 7890A GC System. The column was a DB-5MS 30 m x 0.25 m, 0.25 μm (Agilent), and we applied the following method: 30 $^{\circ}\text{C}$ for 5 min, then 65 $^{\circ}\text{C}/\text{min}$ to 250 $^{\circ}\text{C}$, which is hold for 5 minutes. Despite the low starting temperature, MeCN basically shows no retention time, and comes already after 1.8 minutes alongside all low-boiling solvents, such as acetone (often used to rinse the GC), pentane or Et_2O . A different column was tested, where MeCN however appeared in the tail of THF, hindering its quantification. Therefore, the quantification experiments were well prepared by ensuring on the one side that no pentane or Et_2O is present in the THF and on the other hand that no acetone is used parallel in the GC analysis room. In a typical experiment, up to five blank runs are needed to get a sufficiently clean background. A calibration curve was measured for MeCN in THF, where the small peak in the background with the same retention time was subtracted (see Figure 66), just as was done for the real samples.

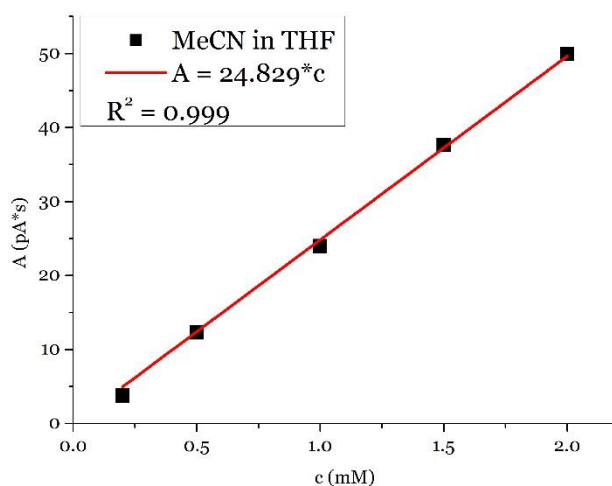


Figure 66. Calibration curve of MeCN in THF by GC Chromatography, with subtraction of the small background peak with the same retention time as MeCN.

IR-spectroscopy

IR-spectroscopy was measured on a Bruker Alpha FT-IR-Spectrometer with a Pt ATR-Module.

EPR-spectroscopy

EPR-spectroscopy was measured on a magnettech MiniScope MS400 Benchtop machine at RT.

Karl-Fischer Titration

The water-content of the solvents as presented in Chapter II.3 was determined with a C20 Karl-Fischer-Titrator from Mettler Toledo.

Mass Spectroscopy

Mass Spectroscopy was recorded by the Mass Spectroscopy department of the *Institute of Organic and Biomolecular Chemistry* of the *Georg-August-University Göttingen*. A soft ionisation technique was used: liquid-injected field desorption ionisation (LIFDI-MS) on a JEOL AccuTOF JMS-T100GCV.

NMR Spectroscopy

NMR spectroscopy was recorded on a Bruker Avance III 300, Avance III 400, or Avance 500 spectrometer (with broadband cryoprobe) and referenced to the residual solvent signals (C₆D₆: $\delta^1\text{H} = 7.16$ ppm, $\delta^{13}\text{C} = 128.4$ ppm, *d*₈-THF: $\delta^1\text{H}$: 3.58 ppm, 1.72 ppm, $\delta^{13}\text{C} = 67.6$ ppm, 25.31 ppm. CD₂Cl₂: $\delta^1\text{H} = 5.32$ ppm, $\delta^{13}\text{C} = 53.8$ ppm, *d*₈-toluene: $\delta^1\text{H} = 2.08, 6.79, 7.01, 7.09$). ³¹P NMR, ¹⁴N NMR, and ¹⁵N NMR chemical shifts are reported relative to external phosphoric acid and nitromethane standards, respectively ($\delta^{31}\text{P} = 0.0$ ppm, $\delta^{14}\text{N} = 0.0$ ppm, $\delta^{15}\text{N} = 0.0$ ppm). Signal multiplicities are abbreviated as: s (singlet), d (doublet), t (triplet), m (multiplet). The ¹H-³¹P coupling constants are read off from the outer sides of the multiplet.

³¹P{¹H} NMR quantification method

For most of the nitride yield determination after CPE, we relied on quantification via ³¹P{¹H} NMR spectroscopy. Either because the nitride could not be separated from the electrolyte, or in some cases side-products are formed that overlap with the nitride. In both cases, no free ¹H NMR peak of the nitride is available for quantification. As reference, PPh₃O was usually chosen; since it is non-coordinating in comparison to PPh₃. Long measurement times were secured at an NMR machine with a broad band observe probe head, as especially suitable for heteronuclei. To make quantitative ³¹P{¹H} NMR spectroscopy the most reliable, we took care of the following: sufficient relaxation time was ensured by setting d1 to approx. 20 seconds, since the T1 times of prototype nitride **3**^{Cl} and standard PPh₃O were determined via inversion recovery to be circa 0.3

and circa 3 seconds, respectively. To prevent signal modifications by Nuclear Overhauser Effect (NOE) build up during proton decoupling, an ‘inverse gated’ decoupling sequence was applied with decoupling only during acquisition time. After measuring, the spectra were phase- and baseline corrected. In some cases, when yield determination via ^1H NMR spectroscopy was possible (i.e. chemical N_2 -splitting into $\mathbf{3}^{\text{Br}}$), both nuclei were used, yielding to similar reaction outcomes (within 5%), which verifies the here used quantification methods.²¹²

UV-vis Spectroscopy

UV-vis spectra are recorded on a Cary 300 UV-vis spectrometer from Agilent.

UV-vis Spectroelectro (UV-vis SEC)

A 1-mm thin layer UV-vis cell with a Pt mesh WE, a Pt disk ($A = 0.071 \text{ cm}^2$) CE, and a Ag-wire RE was used for SEC. UV-vis data were recorded with a BWTEK ExemplarLS, which is connected in to the cuvette cell via fibre optics. Electrochemistry was measured on a Gamry 600.

IV.4. Special equipment

4.1 High-pressure electrochemical equipment

Electrochemistry under high N_2 pressures was measured in a Parr Reactor with electrochemical feedthroughs (see Figure 67) The design of this set up was inspired mainly by the reported example by Shaw.²¹³ The feedthrough cables were obtained from Bax Engineering, which use PTFE as sealing-material. On both sides of the sealing, their length is 300 mm and their maximum electrochemical values are 9 A and 600 V. While designing this electrochemistry autoclave, several constraints were considered. To prevent side-reactions with the analyte or solvent vapours inside the autoclave, only inert materials came into question, for which we chose Teflon and glass material. The dimensions and weight of the autoclave were determined by the constraints of large chamber of the Mbraun Glovebox (maximal 27 cm height and 25 kg maximum load on a point area). Yet, a sufficient large autoclave provides the possibility for up-scaling experiments in future research. A compromise was found in a 300 mL autoclave, with a total height of 25 cm and a load of 11 kg, that can host electrochemical cells as low as 2 mL total volume. Inside the Parr reactor, we placed a PTFE inlet with lid, which has holes in different sizes (6x3 mm, 1x6 mm and 1x9 mm) to guide the electrodes and prevent them from touching each other. The PTFE inlet is equipped with a glass vial where the electrolyte solution is placed

in. Four electrochemical feedthrough cables were chosen as minimal requirement for a CPE experiment (CE, RE, WE, and CPE WE). In a future design, more than four electrochemical feedthrough cables would be more beneficial, in case of damage or to position several WE's in the autoclave to prevent time-intensive polishing.

In a typical CV experiment, the three electrodes (a 3 mm outer diameter WE, a 6 mm outer diameter Platinum CE, and a Ag-wire pseudo RE) are attached to the feedthrough wires via an insulating screw joint, and carefully brought into the PTFE inlet (CE via the 6 mm hole, WE via the 3 mm hole and Ag-wire via the 9 mm hole). Inside the MBraun Glovebox, the connections are checked by measuring a CV, after which the autoclave is tightened. Subsequently, the autoclave is brought outside of the MBraun Glovebox and attached to a pre-flushed tubing connected to the N₂-gas bottle. To remove the last parts of O₂, both the tap of N₂-gas towards the autoclave and a direct outlet next to it are opened simultaneously, to create a N₂-outflow. After flowing N₂ like this for 10-20 seconds, the gas attachment is considered O₂-free. At each different pressure step, the system is stirred for 5 minutes to allow the system to become in equilibrium. De-pressurising is done via one of the two outlets. In case of a CPE experiment, a 50 mm glassy carbon rod was used as CPE WE, since the 100 mm rod does not fit to the inner dimensions of the autoclave.

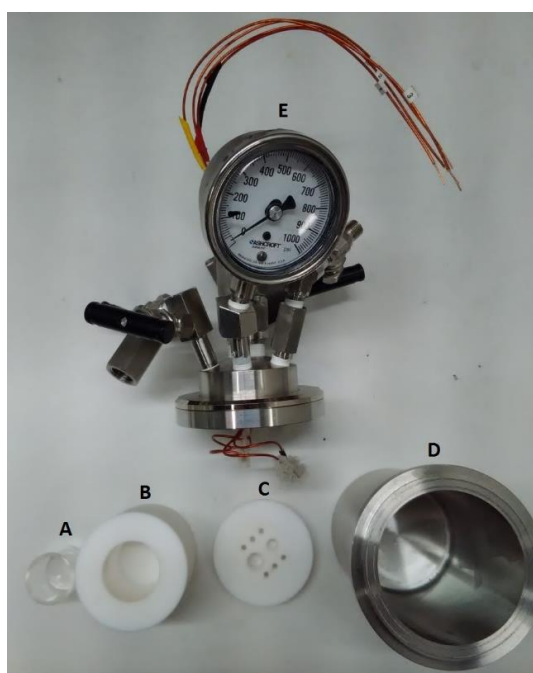


Figure 67. Parr reactor electrochemistry setup containing A: glass inlet, B: PTFE inlet, C: PTFE inlet lid, D: Parr Reactor bottom part, E: Parr Reactor top part with four electrochemical feedthrough cables.

4.2 Flow Cell

4.2.1 Flow Cell modifications

A flow cell was commercially obtained in form of the 1x1 C-flow flow cell from *C-tech innovation*. In general, this flow cell consists of two cell frames that are separable with a membrane, where in each, a half-cell reaction (anodic or cathodic) can occur. For each cell frame, a solution can enter, flow over an electrode and leave the frame on the other side. The electrode is connected to current collectors, which are connected to the potentiostat. A reference electrode (a wire with maximum diameter of 1 mm) can be placed in either compartments. We found out that both the gaskets to tight the electrode, the membrane, and the frames, just as the cell frames itself are constructed from materials that find no compatibility with organic solvents as THF (ethylene propylene diene monomer (EPDM), a synthetic rubber, or chlorinated Polyvinylchloride (CPVC), respectively). In order to use this flow cell, we had to change several components to a THF-compatible material, with polytetrafluoroethylene (PTFE) as most likely candidate. Therefore, we exchanged the O-rings, electrode and membrane gaskets, and the cell frames to PTFE, each with its own complications. Most complications arise from the hardness of PTFE, which is in the medium range (Shore Hardness *D55*), and therefore not suitable when specifically either a hard or a soft material is required. Regarding the O-rings on the cell frame that keep the solution, we acquired PTFE O-rings (*Dichtelemente Arcus* 40.87 x 3.53 mm and 50.47 x 2.62 mm). Although they initially function, some leaking around these O-rings occurs already after a limited number of experiments (and especially when the membrane gaskets are applied), likely because PTFE is a too hard material to be bend for prolonged times. They likely need to be exchanged frequently. For the membrane and electrode gaskets, we explored PTFE plates of 1.0 and 0.5 mm, which showed severe leaking. Here, the PTFE is too hard to be sufficiently pressable as needed for a gasket. In comparison, the EPDM that was commercially used here has a Shore Hardness of *A20-85*, which is tremendously weaker. More successful was the use of expanded PTFE (ePTFE plates of 1 mm or 1.5 mm, *VTE Industrietechnik*), especially as material for the electrode gaskets. For the membrane gaskets, small liquid leaks around the O-rings were observed. Fortunately, when the right membrane material is used (see Section IV.4.2.3), sufficient tightness was obtained without using any membrane gaskets.

Most challenging was to optimise the cell frame, which was done by the *Werkstätten der Universität Göttingen*. Although the CPVC was successfully replaced by PTFE, this material proved too soft (in comparison, CPVC has a Shore Hardness of *D82*). The flow in- and outlets cannot find enough grip to construct a tight connection. To overcome this problem to do our initial studies, stainless steel entrances were fixed in the PTFE cell frames. However, all solutions

have to pass these steel inlets, which is problematic for chemical compatibility (as was found for $[\text{Fc}]\text{PF}_6$). In future research, these inlets should also be constructed from PTFE. Nevertheless, with these changes, we ended up with a THF compatible flow cell, as shown in Figure 68.

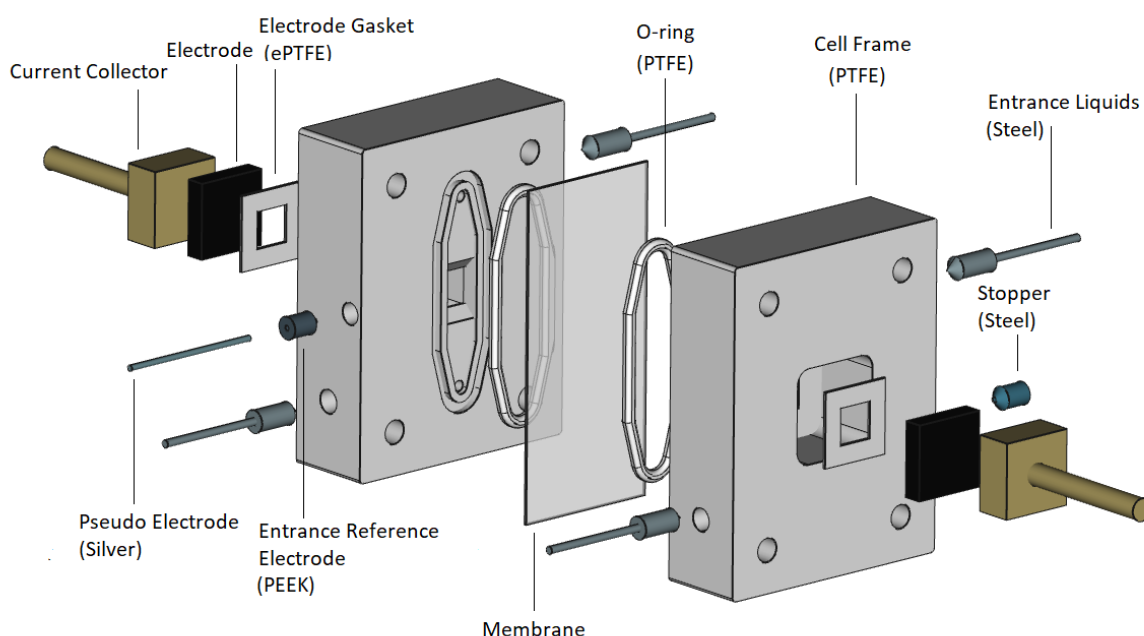


Figure 68. Sliced visualisation of the THF compatible, adapted flow cell as explored within this work. Picture made by C. von Petersdorff-Campen.²¹⁴

4.2.2 Electrodes

The flow cell as described above fits electrodes with 20x20 mm dimensions that reduce by the cell frame to a 10x10 mm active electrochemical surface. For our first purpose (N_2 -splitting on $\mathbf{1}^{\text{Cl}}$ in a flow cell), we wanted to mimic the CPE conditions, by choosing electrode materials as analogous to ‘normal’ CPE conditions. Therefore, a Glassy Carbon plate (25x25 mm, type 2, *Alfa Aeser*, 3 mm thickness) was required and cut with a diamond cutter to circa 20x20 mm, used as WE. As CE, a 19x19 mm Pt plate (99.95 % Fein Platin Blech, *Götze Gold*, 1.0 mm thickness) was used. As pseudo-reference electrode, a Ag-wire with 1.0 mm diameter was used (*ChemPur*, 99.999 %), that was placed in the cell frame with the WE attached. The original flow cell had graphite plates as WE or CE, that were explored in initial pre-studies to parallelly oxidise Fc or $[\text{Fe}(\text{CN})_6]^{2-}$ and reduce $[\text{Fc}]\text{PF}_6$ or $[\text{Fe}(\text{CN})_6]^{3-}$. The required overpotentials were however very large, and it is not advised to continue using these electrodes.

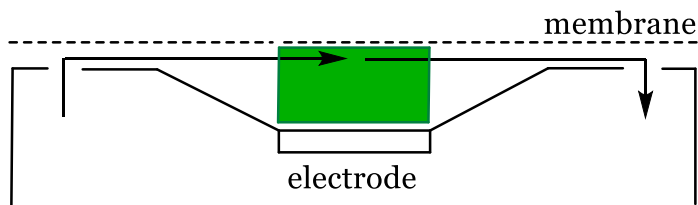
4.2.3 Membranes

In case the redox species of interest are inert to the potential applied to the opposite electrode, an undivided flow cell can be applied without any separating membrane material.²¹⁵ For our initial case, we couple reduction of $\mathbf{1}^{\text{Cl}}$ at the cathode to oxidation of Fc at the anode. The oxidation potential of $\mathbf{1}^{\text{Cl}}$ ($E_{1/2} = -0.48$ V) is incompatible with the applied oxidation potential required to oxidise Fc, and therefore a membrane has to be inserted. Three categories of membranes come in question for us: cation-exchange membranes (CEM), anion-exchange membranes (AEM), and neutral nanoporous materials. Well known is the material Nafion® as CEM, which is based on polysulfonic groups that are anionic enable to shuttle cations. Within the context of this work, Nafion (Nafion 115, *Ion Power*) was explored in THF (showing quick swelling that makes it leaky) and in some initial water studies using LiClO_4 as electrolyte. Although in this latter case the Nafion should behave well, we needed very high potentials to only obtain a minimal current response. This is attributed to the unfavoured graphite electrodes that were initially used (as described in Section IV.4.2.2), or to insufficient pre-treatment. Its incompatibility with THF is a discarding argument for our main study anyway. In organic solvents, where usually larger electrolytes are needed, the use of AEM is widely accepted,²¹⁶ where the charge carrier in our case is PF_6^- . We therefore ordered a wide range of AEM materials (Fumasep® FAP-450, FAAM-15, FAS-50, *FumaTech BWT*). However all were basically incompatibility with THF, leading to leaking membranes. To overcome this problem, we ordered a PEEK-reinforced AEM (Fumasep® FAA-3-PK-130, *FumaTech BWT*), which proved sufficiently stable. Fortunately, when using this membrane, no membrane gaskets are needed to make the flow cell tight. Inspired by the literature, a third class of membranes was considered, namely neutral, nanoporous materials as used by Manthiram for N_2 -splitting in a flow cell set up using lithium, as described in Section I.2.1.3.¹²³ We were able to obtain a sample of this exact material (DRQ-175A206A, *DARAMIC*). Initial experiments with this material proved it to have too large pores (both when 1 or 3 layers of this material are used), as judged by the generation of too much current. The exact composition of the nanoporous separator and the PEEK reinforced AEM is not known.

4.2.4 Flow rates

In general, two types of flow movements are known: laminar and turbulent flow. Since laminar flow is associated with a controlled and constant flow that can be mathematically described, this condition is aimed for. In order to qualitatively describe the flow type, the Reynolds number (Re) can be calculated, which is an expression of the ratio between the inertial and viscous forces a solution experiences when flowing through a certain dimension. Below a certain value interval

for Re , the flow can be considered laminar. For our flow cell, we simplified the system by taking the cubic area above the electrode (as highlighted in green in Scheme 65), for which the mathematic description for a rectangular duct to calculate Re is known.



Scheme 65. Schematic representation of the square area above the electrode for which the Reynolds number was calculated. The arrows indicate the solvent flowing in and subsequent out of the cell frame.

The Reynolds number for a rectangular duct can be described via equation 5, where v_{flow} accounts for the flow rate [$m^3 s^{-1}$], d for the characteristic length of the space through which the solution [m], A for the surface area [m^2], and η_{kin} for the kinematic viscosity of the solvent [$m^2 s^{-1}$]²¹⁷:

$$Re = \frac{v_{flow} * d}{\eta_{kin} * A} \quad (5)$$

With a flow rate of 0.04 mL min^{-1} , a kinematic viscosity for THF of $5.2 \cdot 10^{-7} \text{ m}^2 \text{ s}^{-1}$,²¹⁸ and the dimensions of the space in front of the electrode ($l \times b \times h$: $10.2 \times 10.2 \times 4.8 \text{ mm}$), Re is calculated as shown in equation 6.

$$Re = \frac{(6.7 * 10^{-10}) * (6.5 * 10^{-3})}{(5.4 * 10^{-7}) * (4.9 * 10^{-5})} = 0.16 \quad (6)$$

In literature, the area for the transition between laminar and turbulent flow is between 1500-2800.²¹⁹ Since the Re -value is far below this range, we have a laminar flow. With this confirmed laminar flow, we can also calculate the dwell time of a Re -species at the surface of the electrode at circa 12 min (which is an order of magnitude lower as for steady state CPE electrochemical N_2 -splitting).

IV.5. Syntheses of Rhenium compounds

[ReBr₂(PNP)] (**1^{Br}**)

[ReBr₃(PPh₃)₂(MeCN)] (550 mg, 555 μmol, 1.0 eq), HPNP (200 mg, 554 μmol; 1.1 eq) and NEt₃ (101 mg, 1.01 mmol, 2 eq.) were suspended in THF (40 mL) and refluxed for 4 h, which is accompanied by a colour change towards brown. After evaporation *in vacuo*, the residue is extracted with freshly degassed benzene (3 x 10 mL), concentrated, and lyophilized, resulting in a brown-white solid. After extensive washing with pentanes, and lyophilisation from benzene, remaining PPh₃ is off-sublimed for 48 h at 80 °C at 30 mTorr. The title compound is obtained as brown solid in 81 % yield (320 mg, 450 μmol), which is sufficiently pure for most syntheses. Further purification is done by crystallisation from toluene by layering with diethyl ether.

¹H NMR (300 MHz, C₆D₆, [ppm]): δ = 0.78 (m, 4H, NCH₂), 1.83 (A₁₈XX'A'₁₈, N = |³J_{HP} + ⁵J_{HP}| = 12.1 Hz, 36 H, P(C(CH₃)₃)₂), 2.74 (m, 4H, PCH₂). ¹³C NMR (125.8 MHz, C₆D₆, [ppm]): δ = 33.2 (s, P(C(CH₃)₃)₂), 42.8 (t, N = |²J_{AX} + ³J_{A,X'}| = 13.7 Hz, PCH₂), 60.2 (t, N = |¹J_{AX} + ³J_{A,X'}| = 15.6 Hz, P(C(CH₃)₃)₂), 111.3 (t, N = |²J_{AX} + ⁴J_{A,X'}| = 8.3 Hz, NCH₂). ³¹P{¹H} NMR (121.5 MHz, C₆D₆, [ppm]): δ = -109.5 (s, P(C(CH₃)₃)₂). **E.A.** calcd. for C₂₀H₄₄Br₂NP₂Re (%): C, 34.00; H, 6.28; N, 1.98. Found: C, 34.27; H, 6.17; N, 1.88. **LIFDI-MS** (THF, [m/z]): 707.1 (100 %, [M]⁺), calcd. 707.1. **UV-vis** (λ_{max}, THF, [nm]): 312 (ε = 5320 L mol⁻¹ cm⁻¹), 388 (ε = 857 L mol⁻¹ cm⁻¹), 540 (ε = 257 L mol⁻¹ cm⁻¹).

[ReI₂(PNP)] (**1^I**)

In comparison to the published route by Dr. J. Abbsenseth,¹⁶⁸ the second benzene extraction was performed over Celite. Subsequent washings with pentane and lyophilisation (from benzene) afforded the title compound in circa 85 % yield. The obtained E.A. was slightly deviating (C too high), which is attributed to minor presence of **1^{Cl}**.

E.A. calcd. for C₂₀H₄₄I₂NP₂Re (%): C, 30.01; H, 5.54; N, 1.75. Found: C, 30.98; H, 5.69; N, 1.75.

[ReBrCl(PNP)] (1^{BrCl}) (as spectroscopically found)

In a young NMR tube **1^{Cl}** (5 mg, 8.4 μmol) and **1^{Br}** (6.1 mg, 8.6 μmol) were dissolved in THF and $^{31}\text{P}\{^1\text{H}\}$ NMR spectroscopy was measured that proved formation of **1^{BrCl}** ($\delta^{31\text{P}\{^1\text{H}\}} = -81$ ppm) in about 50 % spectroscopic yield. Heating to 60 °C has no influence on the spectroscopic yield. Since isolation was not possible, only *in situ* spectroscopic characterization is performed.

^1H NMR (300 MHz, C_6D_6 , [ppm]): $\delta = 1.40$ (m, 2 H, backbone) 1.63 ($\text{A}_9\text{XX}'\text{A}'_9$, $^3\text{J}_{\text{AX}} = 11.8$ Hz, 18 H, $\text{P}(\text{C}(\text{CH}_3)_3)$), 1.71 ($\text{A}_9\text{XX}'\text{A}'_9$, $^3\text{J}_{\text{AX}} = 12.2$ Hz, 18 H, $\text{P}(\text{C}(\text{CH}_3)_3)$), 1.89 (m, 2 H, backbone), 1.95 (m, 2 H, backbone), 2.79 (m, 2 H, backbone). **$^{31}\text{P}\{^1\text{H}\}$ NMR**: (121.5 MHz, C_6D_6 , [ppm]) $\delta = -80.5$ (s, $\text{P}(\text{C}(\text{CH}_3)_3)_2$). **LIFDI-MS**: (THF, [m/z]): 661.2 (100 %, M^+), calcd. 661.1.

[ReClI(PNP)] (1^{ClI}) (as spectroscopically found)

In a NMR Young tube, **1^I** (5.0 mg, 6.2 μmol) and **1^{Cl}** (3.5 mg, 5.7 μmol) were dissolved in THF, upon which no new peak was formed. Heating to 60 °C overnight resulted in the appearance of a new feature by $^{31}\text{P}\{^1\text{H}\}$ NMR spectroscopy ($\delta^{31\text{P}\{^1\text{H}\}} = -118$ ppm), indicating formation of **1^{ClI}**. No ^1H NMR spectrum was recorded.

$^{31}\text{P}\{^1\text{H}\}$ NMR (300 MHz, THF, [ppm]): -118 . **LIFDI-MS** (THF, [m/z]) 709.1 (100 %, $[\text{M}]^+$), calcd. 709.1.

Synthesis attempts to [ReCl₂(P=NP)] (1^{Cl})

From CPE: **1^{Cl}** (1.8 mg; 3 μmol), NEt_3 (4.2 μL , 30 μmol) and 0.2 M ($n\text{Bu}_4\text{N}$) PF_6 electrolyte solution in THF were added to the electrolysis cell. The solution was electrolysed for 1.5 h at -0.4 V and the colour changed from violet via red to yellow. THF was evaporated *in vacuo* and redissolved in d_8 -THF for NMR spectroscopic analysis.

From chemical oxidation: **1^{Cl}** (5.0 mg, 8.1 μmol), NEt_3 (5.6 μL , 41 μmol), and $[\text{Fc}^*]\text{BARF}_{24}$ (29 mg, 24.3 μmol) were combined in an NMR tube and d_8 -THF (0.5 μL) was added. Within a couple of minutes, the solution changed from purple to dark green and the solution was analysed by NMR spectroscopy.

[{ReCl(PNP)}₂(μ-N₂)] (2^{Cl})

Degassed THF (0.5 mL) was vacuum transferred to a mixture of **1^{Cl}** (5.0 mg, 8.1 μmol) and Na/Hg (1 M, 125 mg, 1.1 eq.), and placed under a N₂-atmosphere at -30 °C. The mixture was shaken vigorously for 3-5 minutes while cooling in a -30 °C bath, resulting in a colour change from violet to deep red, indicating formation of the title compound. This species was not isolable and was further characterised *in situ* with a maximum yield of 74 % by ¹H NMR spectroscopy. For kinetic analysis, full conversion of the starting material was secured by ¹H NMR spectroscopy where the main side-product in the mixture was **3^{Cl}**. For the ¹⁵N labelled dimer complex, the same procedure was carried out under a ¹⁵N₂ atmosphere.

¹H NMR (400 MHz, THF-*d*₈, -20 °C, [ppm]): δ -16.48 to -16.53 (m, 2 H, XCHH), -12.46 to -12.56 (m, 2 H, XCHH), 0.38 to 0.50 (m, 2 H, XCHH), 0.50 to 0.90 (broad, 18 H, PC(CH)₃)₃), 3.25 to 3.43 (m, 36 H, PC(CH)₃)₃), 3.59 (m, 2 H, XCHH, overlapping with THF-*d*₈), 3.72 to 3.94 (m, 18 H, PC(CH)₃)₃), 4.06 to 4.16 (m, 2 H, XCHH), 8.60 to 8.71 (m, 2 H, XCHH), 10.49 to 10.62 (m, 2H, XCHH). **¹⁵N NMR** (50.7 MHz, THF-*d*₈, -30 °C, [ppm]): δ = 211.1 (s, ReN₂Re) **³¹P{¹H}** **NMR** (161 MHz, THF-*d*₈, -20 °C, [ppm]): δ 16.98 (d, ²J_{PP} = 235.8 Hz, P(C(CH₃)₃)₂), -120.20 (d, ²J_{PP} = 234.5 Hz, P(C(CH₃)₃)₂). **UV-vis** (λ_{max}, THF, -30 °C, [nm]): 375, 533.

[{ReBr(PNP)}₂(μ-N₂)] (2^{Br})

Degassed THF (0.5 mL) was vacuum transferred to a mixture of **1^{Br}** (5.0 mg, 7.1 μmol) and Na/Hg (1 M, 120 mg, 1.1 eq), and placed under a N₂-atmosphere at -30 °C. The mixture was shaken vigorously for 3-5 minutes while cooling in a -30 °C cooling bath, resulting in a colour change from violet to deep red, indicating formation of the title compound. This species was not isolable and was further characterised *in situ* by NMR spectroscopy. For the ¹⁵N labelled dimer complex, the same procedure was carried out under a ¹⁵N₂ atmosphere.

¹H NMR (400 MHz, THF-*d*₈, -30 °C, [ppm]): δ -20.27 to -20.13 (m, 2 H, XCHH), -19.4 (s, 2H, XCHH), -0.60 (broad, Δ_{1/2} = 823 Hz, 18 H, PC(CH)₃)₃), 3.75 (broad, overlapping with **3^{Br}** 18 H, PC(CH)₃)₃), 4.01 (broad, Δ_{1/2} = 43 Hz, 18 H, PC(CH)₃)₃), 4.26 (broad, Δ_{1/2} = 29 Hz, 18 H, PC(CH)₃)₃), 4.58 to 4.71 (m, 2 H, XCHH), 5.25 to 5.39 (m, 2 H, XCHH), 9.3 (s, 2 H, XCHH), 11.56 to 11.77 (m, 2 H, XCHH), 15.4 (s, 2 H, XCHH), 16.96 to 17.18 (m, 2 H, XCHH). **¹⁵N NMR** (50.7 MHz, THF-*d*₈, -30 °C, [ppm]): δ = 219.6 (s, ReN₂Re) **³¹P{¹H}** **NMR** (161 MHz, THF-*d*₈, -30 °C, [ppm]): δ -12.1 (d, ²J_{PP} = 227.8 Hz, P(C(CH₃)₃)₂), -159.1 (d, ²J_{PP} = 227.4 Hz, P(C(CH₃)₃)₂). **UV-vis** (λ_{max}, THF, -30 °C, [nm]): 342, 386, 545.

[{ReI(PNP)}₂(μ-N₂)] (2^I)

Degassed *d*₈-THF (0.45 mL) was vacuum transferred to a mixture of **1^I** (5.0 mg, 6.3 μmol) and Co(Cp*)₂ (2.5 mg, 6.5 μmol, 1.05 eq.), and placed under a N₂-atmosphere at -30 °C. The mixture was shaken vigorously for 3-5 minutes while cooling in a -30 °C cooling bath, resulting in a colour change from green to deep red, indicating formation of the title compound. This species was not isolable and was further characterised *in situ* by NMR spectroscopy.

¹H NMR (400 MHz, THF-*d*₈, -30 °C, [ppm]): δ -25.1 (s, 2 H, XCHH), -20.7 (s, 2 H, XCHH), -1.1 (broad, 18 H, PC(CH)₃)₃), 3.83 (overlapping signals, broad, 2x18 H, PC(CH)₃)₃), 4.3 (broad, 18 H, PC(CH)₃)₃), 7.4 (s, 2 H, XCHH), 10.8 (s, 2 H, XCHH), 13.4 (s, 2 H, XCHH), 16.4 (s, 2 H, XCHH), 17.6 (s, 2 H, XCHH), 21.1 (s, 2 H, XCHH). **UV-vis** (λ_{max}, THF, -30 °C, [nm]): 343, 399, 553.

[ReNCI(PNP)] (3^{Cl})

From N₂, electrochemical reduction from [ReCl₂(PNP)]: **1^{Cl}** (1.8 mg, 3.0 μmol) and 3 mL 0.2 M (nBu₄N)PF₆ electrolyte solution in THF were added to the electrolysis cell. The solution was electrolysed for 2 h at the peak potential of the first reduction feature obtained by CV, resulting in a colour change from purple to brown to yellow. Integration of the current versus time plot gave a charge corresponding to 1.2 mol e⁻ per mol Re. At the end of electrolysis, PPh₃O was added as internal standard via a stock solution (7.2 μmol), the solution was evaporated and re-dissolved in THF (0.5 mL). The solution was analysed by ³¹P{¹H} NMR. **3^{Cl}** was obtained in circa 60% yield by ³¹P{¹H} NMR integration, see Figure A5.

From N₂, electrochemical reduction from [ReCl₂(PNP)] in the flow cell: in a vial, **1^{Cl}** (6.0 mg, 9.8 μmol) was dissolved in 5 mL 0.1 M (nBu₄N)PF₆ electrolyte solution in THF. In another vial, Fc (circa 9 mg, circa 50 μmol) was dissolved in 5 mL 0.1 M (nBu₄N)PF₆ electrolyte solution in THF. Both solutions were transferred to the syringes of the syringe pump, which were connected to 'PTFE straight connectors (Reichelt CT GmbH)' as attached to the stainless steel inlets of the flow cell. The syringe pump was started at 0.04 mL min⁻¹, parallel to a CPE at -1.6 V vs. the Ag-wire, which represents a slight over potential for electrochemical N₂-reduction on **1^{Cl}**. After circa 1 h, a first drop of a yellow solution was observed on the outcome side of the Re-containing fraction. After the syringes are emptied, they were refilled with 2 mL of THF and started again at the same flow rate to recover (most of) the Re-species that still resides in the flow cell.

Afterwards, the volatiles are evaporated *in vacuo* and the remaining solid is extracted with pentane, and analysed by $^{31}\text{P}\{^1\text{H}\}$ NMR spectroscopy, revealing trace presence of $\mathbf{3}^{\text{Cl}}$.

From N_2 , electrochemical reduction from $[\text{ReCl}_3(\text{PNP})]$: $\mathbf{8}$ (2.0 mg, 3.0 μmol) and 3 mL THF with 0.1 M $(n\text{Bu}_4\text{N})\text{PF}_6$ were added to the electrolysis cell. The solution was electrolysed for 3 h at a potential slightly more cathodic of the second reduction feature obtained by CV, resulting in a colour change from green via colourless to yellow. Integration of the current versus time plot gives a charge corresponding to 2.25 mol e^- per mol Re. At the end of electrolysis, PPh_3O was added as internal standard (3.6 mg, 13.2 μmol), the solution was evaporated, re-dissolved in THF (0.5 mL) and analysed by $^{31}\text{P}\{^1\text{H}\}$ NMR. $\mathbf{3}^{\text{Cl}}$ was obtained in 35 % yield by $^{31}\text{P}\{^1\text{H}\}$ NMR integration.

$[\text{ReNCl}(\text{P}=\text{N}=\text{P})]$ ($=\mathbf{3}^{\text{Cl}}$)

*From N_2 , electrochemical reduction from $[\text{ReCl}_2(\text{P}=\text{N}=\text{P})]$ in THF at 1.0 mM: $=\mathbf{1}^{\text{Cl}}$ (2.6 mg, 4.2 μmol) and 4 mL 0.2 M $(n\text{Bu}_4\text{N})\text{PF}_6$ electrolyte solution in THF were added to the electrolysis cell. The solution was electrolysed for 2 h at the peak potential of the first reduction feature obtained by CV, resulting in a colour change from light brown to green. Integration of the current versus time plot gives a charge corresponding to 1.2 mol e^- per mol Re. At the end of electrolysis, THF was removed *in vacuo*, and the resulting light green solid was re-dissolved in 0.6 mL of THF and PPh_3O (4.5 mg, 16.2 μmol) was added, and analysed by $^{31}\text{P}\{^1\text{H}\}$ NMR. $=\mathbf{3}^{\text{Cl}}$ was obtained in 22 % yield by $^{31}\text{P}\{^1\text{H}\}$ NMR integration, see Figure A27. The title compound can also be removed from the electrolyte by pentane extraction, without loss of product. Reproduction led to yields of 17, 13, and 15 %, as generally averaged as a yield in $=\mathbf{3}^{\text{Cl}}$ via CPE of 15 %.*

*From N_2 , electrochemical reduction from $[\text{ReCl}_2(\text{P}=\text{N}=\text{P})]$ in 1,2-difluorobenzene, THF, fluorobenzene, and Et_2O at 2.8 mM: $=\mathbf{1}^{\text{Cl}}$ (4.0 mg, 6.5 μmol) and 3.2 mL electrolyte solution (0.1 M $(n\text{Bu}_4\text{N})\text{PF}_6$ (1,2-difluorobenzene, THF, fluorobenzene), or 0.1 M $(n\text{Bu}_4\text{N})\text{BAR}^{\text{F}}_{24}$ (Et_2O)) in the solvent were added to the electrolysis cell. The solution was electrolysed for 160, 170, 100, 120 min, respectively, at the peak potential of the first reduction feature obtained by CV. Integration of the current versus time plot gives a charge corresponding to 0.8, 1.1, 0.9, 0.9 mol e^- per mol Re. At the end of electrolysis, the solvent was removed *in vacuo*, and the resulting solid was re-dissolved in 0.6 mL of THF and PPh_3O was added, and analysed by $^{31}\text{P}\{^1\text{H}\}$ NMR. $=\mathbf{3}^{\text{Cl}}$ was obtained in 4, 11, 8, 4 % yield, respectively, by $^{31}\text{P}\{^1\text{H}\}$ NMR integration.*

From N_2 , electrochemical reduction from $[ReCl_3(P=N=P)]$: **8** (2.6 mg, 4.0 μ mol) and 2 mL THF with 0.1 M (*n*Bu₄N)PF₆ were added to the electrolysis cell. The solution was electrolysed for 3 hours slightly more cathodic of the second reduction feature obtained by CV, resulting in a colour change from dark green via orange to intensely coloured green. Integration of the current versus time plot gave a charge corresponding to 1.4 mol e⁻ per mol Re. At the end of electrolysis, PPh₃O was added as internal standard (3.4 mg, 12.5 μ mol), the solution was evaporated, extracted with Et₂O, evaporated, re-dissolved in THF (0.5 mL) and analysed by ³¹P{¹H} NMR. Traces of **3^{Cl}** were found and not quantified.

[ReNBr(PNP)] (**3^{Br}**)

From N_2 , chemical reduction: Degassed THF-*d*₈ (0.45 mL) was vacuum-transferred to a mixture of **1^{Br}** (5.0 mg, 7.1 μ mol, 1.0 eq) and reductant (Co(Cp^{*})₂: 3.6 mg, 7.8 μ mol, 1.1 eq.; Na/Hg (1 M): 119 mg, 8.8 μ mol, 1.2 eq.) in a J-Young NMR tube and placed under an N₂-atmosphere at -30 °C. The mixture was shaken vigorously upon which the colour gradually changed from purple to red to dark yellow. After 30 min at RT, 1,3,5-trimethoxybenzene was added and the spectroscopy yield was obtained by integration of non-overlapping ¹H NMR-signals of **3^{Br}** vs. the standard (maximum 80 % for Na/Hg (Figure A8) based on two individual yields of 76 % and 85 %, 45 % for Co(Cp^{*})₂ (Figure A8), based on two individual yields of 35 % and 55 %). **3^{Br}** was not isolated via this route.

From N_2 , electrochemical reduction: **1^{Br}** (2.1 mg, 3.1 μ mol) and 3 mL THF with 0.1 M (*n*Bu₄N)PF₆ were added to the electrolysis cell. The solution was electrolysed for 2 h at the peak potential of the first reduction feature obtained by CV, resulting in a colour change from violet to red to brown/yellow. Integration of the current versus time plot gave a charge corresponding to 1.20 mol e⁻ per mol Re. The electrolysis solution was concentrated to a pale yellow solution. PPh₃O (7.2 μ mol) was added via a stock solution as an internal standard and the solution was measured by ³¹P{¹H} NMR. The title compound **3^{Br}** was obtained in 57 % yield by ³¹P{¹H} NMR integration, see Figure A8.

From azide: To a solution of **1^{Br}** (10.3 mg; 0.015 mmol; 1.0 eq) in C₆H₆ (4 mL) was added a mixture of TMSN₃ (4.0 mg; 0.035 mmol; 2.5 eq) in C₆H₆ (1 mL) whilst stirring. The mixture was allowed to stir for 15 minutes and gradually changed colour to orange, after which the solvents were removed *in vacuo*. Upon re-dissolving in C₆H₆ (1 mL), KHMDS (1.4 mg, 0.007 mmol, 0.5 eq.) was added to obtain a brown suspension. After 15 minutes stirring, the volatiles were

evaporated *in vacuo*, and the product was extracted with pentanes (5 x 2 mL). After evaporation and lyophilisation (C₆H₆), the title compound is obtained in 89 % yield (8.33 mg, 0.013 mmol).

¹H NMR (300 MHz, C₆D₆, [ppm]): δ = 1.22 (A₉XX'A'₉, ³J_{AX} = 13.3 Hz, 18 H, P(C(CH₃)₃), 1.37 (m, 2 H, P(CH₂)₂ overlapping), 1.41 (A₉XX'A'₉, ³J_{AX} = 13.6 Hz, 18 H, P(C(CH₃)₃), 1.60 (m, ABCDXX'D'C'B'A', N = |²J_{AX} + ⁴J_{A,X'}| = 32.7 Hz, 2 H, P(CH₂)₂), 3.05 (m, ²J_{HH} = 10.8 Hz, ³J_{HH} = 5.3 Hz, 2 H, N(CH₂)₂), 3.62 (m, ABCDXX'D'C'B'A', N = |³J_{AX} + ⁴J_{A,X'}| = 31.6 Hz, ²J_{HH} = 10.6 Hz, ³J_{HH} = 7.6 Hz, ³J_{HH} = 1.7 Hz, 2 H, N(CH₂)₂). **¹³C NMR** (75.5 MHz, C₆D₆, [ppm]): δ = 25.7 (t, AXX'A', N = |¹J_{AX} + ³J_{A,X'}| = 22.7 Hz, P(CH₂)), 29.2 (A₃XX'A'₃, N = |²J_{AX} + ⁴J_{A,X'}| = 4.4 Hz, P(C(CH₃)₂), 29.4 (A₃XX'A'₃, N = |²J_{AX} + ⁴J_{A,X'}| = 3.5 Hz, P(C(CH₃)₂), 35.9 (t, AXX'A', N = |¹J_{AX} + ³J_{A,X'}| = 15.8 Hz, P(C(CH₃)₂), 36.9 (t, AXX'A', N = |¹J_{AX} + ³J_{A,X'}| = 22.0 Hz, P(C(CH₃)₂), 71.9 (t, AXX'A', N = |²J_{AX} + ³J_{A,X'}| = 7.3 Hz, N(CH₂)₂). **¹⁵N{¹H} NMR** (50.7 MHz, C₆D₆, [ppm]): δ = 375.0 (s, ReN) **³¹P{¹H} NMR** (121.5 MHz, C₆D₆, [ppm]): δ = 83.0 (s, P(C(CH₃)₃)₂). **E.A.** calcd. for C₂₀H₄₄IN₂P₂Re (%): C, 37.50; H, 6.92; N, 4.37. Found: C, 37.79, H, 6.92; N, 3.87. **LIFDI-MS** (THF, [m/z]): 640.1 (100 %, [M]⁺), calcd. 640.1. **UV-vis:** (λ_{max}, THF; RT, [nm]) 296 (ε = 3605 L mol⁻¹ cm⁻¹), 395 (ε = 567 L mol⁻¹ cm⁻¹), 478 (ε = 204 L mol⁻¹ cm⁻¹).

[ReNI(PNP)] (**3**^I)

From N₂, chemical reduction: Degassed THF (0.45 mL) was vacuum-transferred to a mixture of **1**^I (5.0 mg, 6.3 μmol, 1.0 eq) and reductant (Co(Cp^{*})₂: 2.4 mg, 7.3 μmol, 1.2 eq.; Cr(Cp^{*})₂: 2.3 mg, 7.1 μmol, 1.1 eq.; Na/Hg (1 M): 104 mg, 7.7 μmol, 1.2 eq.) in a J-Young NMR tube and placed under an N₂-atmosphere. After thawing of the solvent the mixture was shaken vigorously upon which the colour gradually changed from dark brown via red to light brown. After 30 min at RT internal standard was added. The spectroscopic yield of the title compound was obtained by integration of a PNP-ligand backbone ¹H NMR signal or the ³¹P{¹H} NMR peak *vs.* the internal standard or (58 % for Cr(Cp^{*})₂ (see Figure A10) based on two individual yields of 58 % and 58 %, 60 % for Co(Cp^{*})₂ (see Figure A10) based on four individual yields of 60 %, 60 %, 57 % and 63 %, 30 % for Na/Hg (see Figure A10) based on two individual yields of 41 % and 20 %). **3**^I was not isolated via this route.

From N₂, electrochemical reduction, two routes: **1**^I (2.1 mg, 3.1 μmol) and 3 mL 0.2 M (nBu₄N)PF₆ solution were added to the electrolysis cell. The solution was electrolysed for 1.5 h to 2 h in separate experiments both at the peak potential of the first reduction feature obtained by CV, and at the peak potential of the second reduction feature. This was accompanied by a

colour change from green to red orange to brown. Integration of the current versus time plot gave a charge corresponding to 1.07 mol e⁻ per mol Re for electrolysis at the first peak and 1.10 mol e⁻ per mol Re for electrolysis at the second peak. The electrolysis solution was concentrated to a pale yellow solution. PPh₃O (7.2 μmol) was added via a stock solution as an internal standard and the solution was measured by ³¹P{¹H} NMR. The title compound (**3**¹) was obtained in 50 % yield for electrolysis on the first reduction peak and in 65 % yield for electrolysis on the second reduction peak by ³¹P{¹H} NMR integration, see Figures A9.

From azide: To a solution of **1**¹ (40.0 mg, 0.05 mmol, 1.0 eq) in THF (4 mL) was added a mixture of TMSN₃ (13 mg, 0.11 mmol, 2.3 eq) in THF (1 mL) whilst stirring. A direct colour change to light orange was observed, after which the reaction mixture was allowed to stir for 15 minutes. KHMDS (10 mg, 0.05 mmol, 1.0 eq) was added, to obtain a brown suspension. After 15 minutes stirring, THF was evaporated *in vacuo* to obtain a sticky brown solid, which was washed three times with pentanes (2 mL each time). Extraction with benzene (3 x 2 mL) and subsequent lyophilisation afforded the title compound in 87 % yield (29.8 mg; 0.043 mmol). Alternatively, the base can be circumvented: To a solution of **1**¹ (10.0 mg, 0.013 mmol, 1.0 eq) in THF (1.5 mL) was added a mixture of TMSN₃ (1.4 mg, 0.13 mmol, 1 eq) in THF (1 mL) whilst stirring. A colour change to light orange was observed over the course of 2 h, after which the volatiles were evaporated *in vacuo*. The resulting solid was washed with pentane and extracted three consecutive times with Et₂O. Lyophilisation afforded the title compound in 70 % yield (6.0 mg; 0.009 mmol).

¹H NMR (300 MHz, C₆D₆, [ppm]): δ = 1.21 (A₉XX'A', ³J_{AX} = 13.5 Hz, 18 H, P(C(CH₃)₃)₂), 1.40 (2 H, P(CH₂)₂ overlapping), 1.4 (A₉XX'A', ³J_{AX} = 13.5 Hz, 18 H, P(C(CH₃)₃)₂), 1.60 (ABCDXX'D'C'B'A', N = |²J_{AX} + ⁴J_{A,X'}| = 32.3 Hz, 2 H, P(CH₂)₂), 3.05 (ABCDXX'D'C'B'A', N = |³J_{AX} + ⁴J_{A,X'}| = 26.6 Hz, 2 H, N(CH₂)₂), 3.58 (ABCDXX'D'C'B'A', N = |³J_{AX} + ⁴J_{A,X'}| = 30.6 Hz, 2 H, N(CH₂)₂). ¹³C NMR (125.8 MHz, C₆D₆, [ppm]): δ = 25.9 (AXX'A', N = |¹J_{AX} + ³J_{A,X'}| = 22.5 Hz, P(CH₂)), 29.2 (A₃XX'A₃', N = |²J_{AX} + ⁴J_{A,X'}| = 1.6 Hz, P(C(CH₃)₂), 29.4 (A₃XX'A₃', N = |²J_{AX} + ⁴J_{A,X'}| = 1.7 Hz, P(C(CH₃)₂), 35.9 (AXX'A', N = |¹J_{AX} + ³J_{A,X'}| = 16.3 Hz, P(C(CH₃)₂), 36.9 (AXX'A', N = |¹J_{AX} + ³J_{A,X'}| = 22.4 Hz, P(C(CH₃)₂), 71.5 (AXX'A', N = |²J_{AX} + ³J_{A,X'}| = 7.3 Hz, N(CH₂)). ¹⁵N{¹H} NMR (50.7 MHz, C₆D₆, [ppm]): δ = 380.6 (ReN). ³¹P{¹H} NMR (121.5 MHz, C₆D₆, [ppm]): δ = 81.5 (s, P(C(CH₃)₃)₂). **E.A.** calcd for C₂₀H₄₄IN₂P₂Re (%): C, 34.93; H, 6.45; N, 4.07. Found: C, 34.93, H, 6.03; N, 3.47. **LIFDI-MS** (THF, [m/z]): 688.1 (100 %, [M]⁺), calculated 688.2. **UV-vis:** (λ_{max}, THF; RT, [nm]) 302 (ε = 3100 L mol⁻¹ cm⁻¹), 403 (ε = 578 L mol⁻¹ cm⁻¹), 481 (ε = 298 L mol⁻¹ cm⁻¹).

[ReNI(P=N=P)] (=3^I)

From N₂, chemical reduction: Degassed *d*₈-THF (0.45 mL) was vacuum-transferred to a mixture of =1^I (10.0 mg, 12.6 μmol, 1.0 eq) and reductant (Cr(Cp^{*})₂: 4.5 mg, 13.8 μmol, 1.1 eq, Co(Cp)₂: 2.4 mg, 12.5 μmol, 2.5 eq. (only 4.0 mg =1^I was used in case of reduction with cobaltocene)) in a J-Young NMR tube and placed under an N₂-atmosphere. After thawing of the solvent, the mixture was shaken vigorously. After 30 min at RT, 1,3,5-trimethoxybenzene was added via a stock solution. The spectroscopic yield of the title compound was obtained by integration of a PNP-ligand backbone ¹H NMR signal *vs.* the internal standard or (maximum 43 % for Cr(Cp^{*})₂, 20 % for Co(Cp^{*})₂). In case of reduction under a ¹⁵N₂ atmosphere, Cr(Cp^{*})₂ was used as reductant. =3^I was not isolated via this route. In case of reduction via Cr(Cp^{*})₂, it was accompanied by formation of [ReNI(N(CHCHPh*t*Bu)₂)(CHCHPh*t*Bu)] (**10**), which shares a similar solubility and cannot be separated.

From N₂, electrochemical reduction: =1^I (4.0 mg, 5.0 μmol) and 2.5 mL 0.1 M (nBu₄N)PF₆ solution were added to the electrolysis cell. The solution was electrolysed for 1.5 h at the peak potential of the first reduction feature as obtained by CV. This was accompanied by a colour change from dark brown to dark green. Integration of the current versus time plot gives a transferred charge corresponding to 1.2 electrons per Re. The solution was evaporated and PPh₃O was added (4.1 mg, 0.015 mmol). Based on ³¹P{¹H} NMR spectroscopic integration, the title compound is found in circa 12 % yield, as averaged between 10 %, 14 %, and 10% yield. =3^I was accompanied by **10** (which is present in circa 5 % yield).

From azide: To a solution of =1^I (15.0 mg, 0.019 mmol, 1 eq.) in THF (2 mL) was added TMSN₃ (12.4 μL, 0.094 mmol, 5 eq.) in THF (1 mL) whilst stirring. It was stirred for 2 h, upon which a colour change towards light orange was observed. The volatiles were evaporated *in vacuo*, washed with pentane (2 x 1 mL) and extracted with Et₂O. The title compound was obtained as orange solid in 85 % yield (11 mg, 0.016 mmol).

¹H NMR (500 MHz, C₆D₆, [ppm]): δ = 1.18 (A₉XX'A', ³J_{AX} = 13.4 Hz, 18 H, P(C(CH₃)₃)₂), 1.49 (A₉XX'A', ³J_{AX} = 14.2 Hz, 18 H, P(C(CH₃)₃)₂), 1.60 (ABCDXX'D'C'B'A', N = |²J_{AX} + ⁴J_{A,X'}| = 32.3 Hz, 2 H, P(CH₂)₂), 4.3 (ABXX'B'A', N = |³J_{AX} + ⁴J_{A,X'}| = 10.3 Hz, ³J_{HH} = 6.2 Hz, 2 H, P(CH)₂), 6.9 (ABXX'B'A', N = |³J_{AX} + ⁴J_{A,X'}| = 42.6 Hz, ³J_{HH} = 6.2 Hz, 2 H, P(CH)₂) ¹³C NMR (125.8 MHz, C₆D₆, [ppm]): δ = 28.7 (broad s, P(C(CH₃)₂), 29.3 (broad s, P(C(CH₃)₂), 35.5 (t, AXX'A', N = |²J_{AX} + ⁴J_{A,X'}| = 21.4 Hz, P(C(CH₃)₂), 37.4 (t, AXX'A', N = |¹J_{AX} + ³J_{A,X'}| = 24.0 Hz, P(C(CH₃)₂), 92.9 (t, AXX'A', N = |¹J_{AX} + ³J_{A,X'}| = 41.2 Hz, P(CH)₂), 169.4 (t, AXX'A', N = |²J_{AX} + ³J_{A,X'}| = 13.6 Hz, N(CH)₂). ¹⁵N{¹H} NMR (50.7 MHz, C₆D₆, [ppm]): δ = 370.2 (s, ReN) ³¹P{¹H} NMR (202.5

MHz, C₆D₆, [ppm]): δ = 70.5 (s, P(C(CH₃)₃)₂). **E.A.** calcd for C₂₀H₄₄IN₂P₂Re (%): C, 35.14; H, 5.90; N, 4.10. Found: C, 35.82, H, 5.77; N, 4.00. **LIFDI-MS** (THF, [m/z]): 684.0 (100 %, [M]⁺), calculated 684.1.

[ReNBr(^HPNP)]Br (**4^{Br-Br}**)

After reaction of **1^{Br}** (10.0 mg, 0.014 mmol, 1.0 eq) in C₆H₆ (4 mL) with TMS-N₃ (8.1 mg, 0.070 mmol, 5.0 eq) in C₆H₆ (1 mL) (see Section II.2.3), crude NMR reveals the presence of **4^{Br-Br}** in about 40% yield. This species was not isolated and is only characterised *in situ*.

¹H NMR (300 MHz, C₆D₆, [ppm]): δ = 1.14 (A₉XX'A'₉, ³J_{AX} = 14.4 Hz, 18 H, P(C(CH₃)₃), 1.24 (overlapping with nitride **3^{Br}**, 18 H, P(C(CH₃)₃), 1.98 (m, 2 H, P(CH₂)₂), 2.72 (m, 2 H, N(CH₂)₂), 4.01 (m, 2 H, N(CH₂)₂), 9.65 (broad, NH, 1 H). The missing signal for a P(CH₂)₂-group, is likely overlapping within the *tert*-butyl resonances **³¹P{¹H} NMR** (121.5 MHz, C₆D₆, [ppm]): δ = 70.0 (s, P(C(CH₃)₃)₂). **High resolution ESI-MS** (THF, [m/z]): 641.1779 (100 %, [M]⁺), calcd. 641.1776.

[ReNI(^HPNP)]I (**4^{I-I}**)

To a mixture of TMS-N₃ (18 mg, 156 μ mol, 6.8 eq.) in THF at 0 °C was added **1^I** (19 mg, 24 μ mol, 1.0 eq) in THF over the course of 5 minutes. A direct colour change to orange was observed and after removal of the volatiles *in vacuo*, a pink solid was obtained.

¹H NMR (300 MHz, CD₂Cl₂, [ppm]): δ = 1.46 (A₉XX'A'₉, ³J_{AX} = 15.0 Hz, 18 H, P(C(CH₃)₃)₂), 1.61 (A₉XX'A'₉, ³J_{AX} = 14.6 Hz, 18 H, P(C(CH₃)₃)₂), 2.3 (2 H, P(CH₂)₂, m), 2.59-2.79 (m, overlapping P(CH₂)₂ and N(CH₂)₂, 4 H), 4.28 (m, N(CH₂)₂, 2 H), 7.37 (broad, NH, 1 H). **³¹P{¹H} NMR** (121.5 MHz, CD₂Cl₂, [ppm]): δ = 69.0 (s, P(C(CH₃)₃)₂). **LIFDI-MS** (THF, [m/z]): 689.1 (100 %, [M]⁺), calcd. 689.2.

[Re(NCH₂CH₃)Cl(P=N=P)] (=5)

Quick synthesis, low yield: EtOTf (5 μ L, 6.8 mg, 38.3 μ mol, 1.1 eq) was added to a solution of **=3** (20.5 mg, 34.6 μ mol) in chlorobenzene (5 mL). Full conversion was obtained either after 22 h at 80 °C, or by using 10 eq. of EtOTf and a reaction time of 48 h at RT or 1.5 h at 80 °C, all accompanied by a colour change towards darker red. After solvent removal *in vacuo*, it was re-

dissolved in THF (3 mL) and layered with excess Et₂O (10 mL) to crystallise out the title compound after 3-4 hours at -40 °C as red solid in 55 % yield.

Slow synthesis, higher yield: EtOTf (60 mg, 335 μmol, 10 eq.) was added to a solution of =**3**^{Cl} (20 mg, 33.8 μmol) in chlorobenzene (0.5 mL) and the mixture was heated to 80 °C. After full conversion, the volatiles were removed *in vacuo*, re-dissolved in THF and layered with Et₂O. After 4-5 hours at -40 °C, red precipitation was formed and filtered off. The filtrate was evaporated, re-dissolved in C₆H₆ and reacted with circa 5 eq. of (nHe₄N)Cl (22 mg, 58 μmol), upon which =**3**^{Cl} was re-formed. The nitride was again reacted with EtOTf as described above. The quantity of =**3**^{Cl} was not determined, yet estimated. In the second and third run, crystallisation was substantially slower due to lower concentrations of =**5**. After three runs, all fractions of =**5** were combined using CH₂Cl₂, and dried to yield =**5** in 77 % (20 mg, 26 μmol).

¹H NMR (400 MHz, CD₂Cl₂, [ppm]): δ = 1.27 (A₉XX'A'₉, N = |³J_{HP} + ⁵J_{HP}| = 15.27 Hz, 18 H, PC(CH₃)₃), 1.43 (t, ³J_{HH} = 7.06 Hz, 3 H, NCH₂CH₃), 1.49 (A₉XX'A'₉, N = |³J_{HP} + ⁵J_{HP}| = 15.51 Hz, 18 H, PC(CH₃)₃), 2.99 (q, ³J_{HH} = 6.94 Hz, 2 H, NCH₂CH₃), 5.34 (PCH, overlapping with CD₂Cl₂), 7.99 (ABXX'A'B', N = |²J_{AX} + ⁴J_{AX'}| = 36.20 Hz, ³J_{AB} = 6.51 Hz, 2 H, NCH), ¹³C NMR (100 MHz, CD₂Cl₂, [ppm]): δ = 12.2 (s, NCH₂CH₃), 28.7 (s, P(C(CH₃)₂)), 30.1 (A₃XX'A'₃, N = |²J_{AX} + ⁴J_{AX'}| = 1.9 Hz, P(C(CH₃)₂)), 69.2 (s, NCH₂CH₃), 99.1 (t, AXX'A', N = |¹J_{AX} + ³J_{AX'}| = 21.3 Hz, PCH), 172.6 (t, AXX'A', N = |²J_{AX} + ³J_{AX'}| = 5.3 Hz, NCH), ¹⁹F NMR (376 MHz, CD₂Cl₂, [ppm]): δ = -78.8 (s, CF₃), ³¹P{¹H} NMR (162.0 MHz, CD₂Cl₂, [ppm]): δ = 87.0 (s, P^tBu₂). E.A. calcd. for C₂₃H₄₅ClN₂P₂ReSO₃F₃ (%): C, 35.86; H, 5.89; N, 3.64. Found: C, 35.74, H, 5.73; N, 3.46. LIFDI-MS (THF, [m/z]): 621.4 (100 %, [M]⁺), calcd. 621.2.

[Re(NCHCH₃)Cl(PNP)] (**6**)

To a solution of **5** (3 mg, 3.9 μmol, 1 eq.) in C₆D₆ (0.5 mL) in a NMR Young Tube was added DBU (0.6 μL, 3.9 μmol, 1 eq) via a Hamilton syringe. The colour directly changed towards orange and NMR spectroscopy revealed quantitative conversion towards the title compound.¹⁵¹

[Re(NCHCH₃)Cl(P=N=P)] (=6)

NEt₃ (11.4 μL, 89 μmol, 10 eq.) was added to a solution of =**5** (6.9 mg, 8.9 μmol, 1.0 eq.) in chlorobenzene (CaH₂ dried), and stirred for 1 day at RT accompanied by a colour change to dark blue. The solvent was removed *in vacuo*. After extraction with pentanes (3 x 5 mL), and

subsequent lyophilisation from benzene, the title compound was obtained as green solid in 87 % yields.

^1H NMR (500 MHz, d_8 -THF, [ppm]): 1.19 (broad, overlapping isomer 1 and 2, $\text{PC}(\text{CH}_3)_3$) 1.28 (m, overlapping isomer 1 and 2, $\text{PC}(\text{CH}_3)_3$) 1.70 (m, NCHCH_3 , isomer 2, 1 H, $^3J_{\text{HH}} = 5.5$ Hz), 2.03 (m, NCHCH_3 , isomer 1, 1 H, $^3J_{\text{HH}} = 5.4$ Hz), 3.31 (dt, NCHCH_3 , isomer 2, 3 H, $^5J_{\text{HP}} = 1.7$ Hz, $^3J_{\text{HH}} = 5.4$ Hz), 3.60 (m, NCHCH_3 , overlapping with d_8 -THF, isomer 1, 3 H), 4.95 (m, PCH , isomer 1, 1 H, $^3J_{\text{HH}} = 6.5$ Hz), 4.96 (m, PCH , isomer 2, 1 H, $^3J_{\text{HH}} = 6.3$ Hz), 7.55 (m, NCH , isomer 1, 1 H, $^3J_{\text{HH}} = 6.5$ Hz), 7.58 (m, NCH , isomer 2, 1 H, $^3J_{\text{HH}} = 6.3$ Hz) (300 MHz, C_6D_6 , [ppm]): 1.27 (overlapping isomer 1 and 2, $\text{PC}(\text{CH}_3)_3$), 1.69 (m, NCHCH_3 , isomer 1, $^4J_{\text{HP}} = 22.4$ Hz, $^3J_{\text{HH}} = 5.5$ Hz), 2.02 (m, NCHCH_3 , isomer 2, $^4J_{\text{HP}} = 22.3$ Hz, $^3J_{\text{HH}} = 5.5$ Hz), 3.32 (dt, NCHCH_3 , isomer 1, $^5J_{\text{HP}} = 1.4$ Hz, $^3J_{\text{HH}} = 5.5$ Hz), 3.69 (dt, NCHCH_3 , isomer 2, $^5J_{\text{HP}} = 1.5$ Hz, $^3J_{\text{HH}} = 5.5$ Hz), 4.72 (d, PCH , overlapping isomer 1 and 2, $^3J_{\text{HH}} = 6.4$ Hz), 7.22 (m, NCH , overlapping with C_6D_6 , overlapping isomer 1 and 2) **^{13}C NMR** (125.8 MHz, d_8 -THF, [ppm]): $\delta = 5.1$ (s, NCHCH_3 , isomer 1), 8.4 (s, NCHCH_3 , isomer 2), 29.2 (broad, $\text{P}(\text{C}(\text{CH}_3)_2)$), 30.6 (t, $\text{P}(\text{C}(\text{CH}_3)_2)$), 30.9 (t, $\text{P}(\text{C}(\text{CH}_3)_2)$, isomer 2), 34.7 (t, $\text{P}(\text{C}(\text{CH}_3)_2)$, isomer 2) 35.9 (t, $\text{P}(\text{C}(\text{CH}_3)_2)$, isomer 1), 39.3 (m, $\text{P}(\text{C}(\text{CH}_3)_2)$ isomer 1 and 2), 103.3 (t, PCH , isomer 1), 103.8 (t, PCH , isomer 2), 151.2 (t, NCHCH_3 , isomer 2), 151.9 (t, NCHCH_3 , isomer 1), 170.9-171.1 (m, NCH , isomer 1 and 2) **$^3\text{P}\{^1\text{H}\}$ NMR** (162.0 MHz, d_8 -THF, [ppm]): $\delta = 34.1$ (s, $\text{P}(\text{C}(\text{CH}_3)_3)$, isomer 1) 32.2 (s, $\text{P}(\text{C}(\text{CH}_3)_3)$, isomer 2) **E.A.** calcd for $\text{C}_{22}\text{H}_{44}\text{ClN}_2\text{P}_2\text{Re}$ (%): C, 42.61; H, 7.15; N, 4.52. Found: C, 42.59, H, 7.08; N, 4.37. **LIFDI-MS** (THF, [m/z]): 620.3 (100 %, [M]⁺), calculated 620.2.

[$\text{ReCl}_3(\text{PNP})$] (**8**)

As alternative to the published procedure of the title compound, a more-reproducible synthesis procedure was found: To **1**^{Cl} (15.2 mg, 24.8 μmol) in NaK-dried C_6H_6 (0.5 mL) was added PCl_3 (0.75 mL of a 0.04 M stock solution in C_6H_6). After stirring for 15 minutes, the resulting green suspension is filtered and the volatiles removed *in vacuo*. After re-dissolving in C_6H_6 (0.2 mL) and addition of pentanes (5 mL), the precipitate is filtered off and lyophilised. The title compound is obtained as green solid in 64 % yield (10.3 mg, 16.0 μmol)

^1H NMR (300 MHz, C_6D_6 , [ppm]) : $\delta = 10.7$ (s, LWHH = 175 Hz), -15.8 (s, LWHH = 275 Hz). **E.A.** calcd. for $\text{C}_{20}\text{H}_{44}\text{Cl}_3\text{NP}_2\text{Re}$ (%): C 36.78; H 6.79; N 2.14. Found: C 36.73; H 7.10; N 2.36. Mass spectroscopy was identical to the previous published spectrum.

[ReCl₃(P=N=P)] (=8)

8 (15.3 mg, 0.023 mmol) and 2,4,6-tri-*tert*-butylphenoxy radical (33.9 mg, 0.12 mmol, 5.4 eq.) were combined in NaK dried C₆H₆. After heating at 60 °C for 1.5 h, the solvents were evaporated *in vacuo*. After extensive washing with pentane, and lyophilisation (C₆H₆), the title compound is obtained in 70% yield (10.6 mg, 0.016 μmol).

¹H NMR (300 MHz, C₆D₆, [ppm]) : δ = 15.2 ppm (s, LWHH = 7.5 Hz, 36), -51.7 (s, LWHH = 14.8 Hz, 2 H), -194.6 (s, LWHH = 30.3 Hz, 2 H). **E.A.** calcd. for C₂₀H₄₀Cl₃NP₂Re (%): C 37.01; H 6.21; N 2.16. Found: C 36.66; H 6.29; N 1.96. **LIFDI-MS** (Toluene, [m/z]): 648.1 (100 %, [M]⁺), calcd. 648.1.

[ReNI(N(CHCH₂P^tBu₂)(CHCHP^tBu₂))OTf (9^I-OTf)

To =**3^I** (3.0 mg, 4.4 μmol) in C₆H₆ was added HOTf (0.4 μL, 4.4 μmol, 1 eq.), directly leading to a colour change from orange to brown. The volatiles were evaporated *in vacuo*, and re-dissolved in C₆D₆. NMR spectroscopy showed quantitative conversion to the title compound.

¹H NMR (500 MHz, C₆D₆, [ppm]): δ = 0.96 (d, ²J_{HP} = 15.2, 9 H, P(C(CH₃)(CH₃)₂), 1.08 (d, ²J_{HP} = 15.1, 9 H, P(C(CH₃)(CH₃)₂), 1.20 (overlapping d, ²J_{HP} = 15.2, 18 H, P(C(CH₃)(CH₃)₂), 3.37 (dd, ²J_{HH} = 21.3 Hz, ³J_{HP} = 7.3 Hz, 1 H PCHHCH), 4.24 (dd, ²J_{HH} = 21.3 Hz, ³J_{HP} = 7.5 Hz, 1 H PCHHCH), 6.00 (m, ³J_{HH} = 6.6 Hz, 1 H, PCHCH), 8.05 (m, 1 H, NCHCH), 9.29 (d, ³J_{HP} = 20.9 Hz, 1H, NCHCH₂). ¹³C NMR (125.8 MHz, C₆D₆, [ppm]): δ = 28.0 (s, PC(CH₃)₂), 28.3 (s, PC(CH₃)₂), 28.6 (s, PC(CH₃)₂), 28.9 (s, PC(CH₃)₂), 35.5 (d, ²J_{CP} = 18.8 Hz, PC(CH₃)₂), 35.8 (d, ¹J_{CP} = 15.8 Hz, PC(CH₃)₂), 37.6 (m, PC(CH₃)₂), 38.1 (m, PC(CH₃)₂), 40.55 (d, ¹J_{CP} = 23.0 Hz, PCH₂CH), 126.6 (d, ¹J_{CP} = 32.6 Hz, PCHCH), 163.3 (s, NCHCH), 200.8 (s, NCHCH₂). ¹⁹F NMR (470.7 Hz, C₆D₆, [ppm]): -77.8 (s, (OSO₂CF₃)⁻) ³¹P{¹H} NMR (202.5 MHz, C₆D₆, [ppm]): δ = 70.2 (d, ²J_{PP} = 135.8 Hz, 1 P, P(C(CH₃)₂) 72.5 (d, ²J_{PP} = 135.9 Hz, 1 P, P(C(CH₃)₂)

[ReNI(N(CHCHP^tBu₂)(CHCHP^hBu)) (10)

Compound **10** is formed upon (electro)chemical reduction of =**1^I** accompanied by =**3^I**. Similar solubility properties hinders its isolation, therefore **10** is spectroscopically characterised in presence of =**3^I**.

¹H NMR (500 MHz, C₆D₆, [ppm]): 1.14 (m, overlapping with a *tert*-butyl moiety of =**3**^I, 9 H, P(C(CH₃)₃)₂), 1.30 (d, ³J_{HP} = 17.0 Hz, 9 H, PH(C(CH₃)₃)), 1.46 (d, ³J_{HP} = 14.5 Hz, 9 H, P(C(CH₃)₃)₂), 4.38 (m, ³J_{HH} = 6.2 Hz, 1 H, PCHCH), 4.41 (m, ³J_{HH} = 6.2 Hz, 1 H, PCHCH), 5.72 (dd, ¹J_{HP} = 356 Hz, ³J_{HP} = 7.1 Hz, 1 H, PH(C(CH₃)₃)), 6.81 (dd, ³J_{HP} = 21.6 Hz, ³J_{HH} = 6.1 Hz, 1 H, NCHCH), 6.87 (dd, ³J_{HP} = 18.4 Hz, ³J_{HH} = 6.1 Hz, 1 H, NCHCH). **¹⁵N{¹H} NMR** (50.7 MHz, C₆D₆, [ppm]): δ = 364.3 (s, ReN). **³¹P{¹H} NMR** (202.5 MHz, C₆D₆, [ppm]): δ = 46.1 (d, ²J_{PP} = 152.2, 1 P, PH(C(CH₃)₃)) 73.8 (d, ²J_{PP} = 152.2, 1 P, P(C(CH₃)₃)₂). **³¹P NMR** (202.5 MHz, C₆D₆, [ppm]): δ = 46.1 (d, ¹J_{HP} = 357 Hz, ²J_{PP} = 152.2, 1 P, PH(C(CH₃)₃)) 73.8 (d, ²J_{PP} = 152.2, 1 P, P(C(CH₃)₃)₂). **LIFDI-MS** (THF, [m/z]): 628.1 (100 %, [M]⁺), calculated 628.1.

[ReN(OTf)(P=N=P)] (**11**)

In the quick synthesis of =**5**, **11** was found in circa 35 % and could be isolated upon removal of =**5** via crystallization in THF/Et₂O. The mother liquid was evaporated *in vacuo* and washed with pentanes. A sufficiently pure fraction of **11** is obtained via this method.

¹H NMR (300 MHz, C₆D₆, [ppm]): δ = 1.03 (A₉XX'A'₉, ³J_{AX} = 14.52 Hz, 18 H, P(C(CH₃)₃)₂), 1.40 (A₉XX'A'₉, ³J_{AX} = 14.92 Hz, 18 H, P(C(CH₃)₃)₂), 4.13 (m, ³J_{HH} = 6.41 Hz, ²J_{HP} = 4.65 Hz, P(CH₂)₂, 2 H), 6.73 (m, N(CH₂)₂, 2 H). **³¹P{¹H} NMR** (121.5 MHz, C₆D₆, [ppm]): δ = 75.8 (s, P(C(CH₃)₃)₂). **LIFDI-MS** (THF, [m/z]): 706.1 (100 %, [M]⁺), calcd. 706.2.

12

To =**8** (3 mg, 4,7 μmol) was added excess of HCl (0.1 mL of 0.2 M) in C₆H₆ which resulted in a colour change from green to red. Upon degassing of the solution, red precipitation is observed. Extraction with THF and subsequent washing with pentane yielded **12** in circa 80 % yield.

¹H NMR (300 MHz, C₆D₆, [ppm]) : δ = 101.4 (s, LWHH = 52 Hz, 1 H), 8.5 (s, LWHH = 8.4 Hz, 9 H), 6.8 (s, LWHH = 5.9 Hz, 9 H), 4.7 (s, LWHH = 8.2 Hz, 9 H), 3.7 (s, LWHH = 5.3 Hz, 9 H), -17.8 (s, LWHH = 26 Hz, 2 H), -78.6 (s, LWHH = 27.0 Hz, 1 H), -157.5 (s, LWHH = 26 Hz, 1 H).

IV.6. Electrochemical, kinetic and various experiments

6.1 Chapter II.1.

NMR kinetic measurement for N₂ splitting of **2^{Cl}** into **3^{Cl}**

[{ReCl(PNP)}₂(μ-N₂)] (**2^{Cl}**) was prepared as described in the synthesis section with addition of a capillary containing P(OSi(CH₃)₃)₃ as internal standard. For kinetic analysis, full conversion of the starting material was secured judged by ¹H NMR spectroscopy at -30 °C. The main side-product in the mixture was **3^{Cl}**. Conversion of **2^{Cl}** was followed at -15 °C, -10 °C, -5 °C, -2.5 °C, 0 °C, 2.5 °C, 5 °C, and 7.5 °C by ¹H NMR spectroscopy over two half-lives and each run was repeated at least twice. The so obtained rate constants were combined via Eyring analysis, using equation 7:

$$\ln\left(\frac{k}{T}\right) = -\frac{\Delta H^\ddagger}{R} * \frac{1}{T} + \ln\left(\frac{k_B}{h}\right) + \frac{\Delta S^\ddagger}{R} \quad (7)$$

With temperature T [K], activation enthalpy ΔH[‡] [kJ mol⁻¹], gas constant R [J mol⁻¹ K⁻¹], Boltzmann constant k_B [m² kg s⁻² K⁻¹], Planck constant h [m² kg s⁻¹], and the activation entropy ΔS[‡] [J mol⁻¹ K⁻¹]. The resulting Eyring analysis is presented in Section II.1.1.

NMR experiments of **1^{Cl}** at high pressures and with added chloride

*NMR spectroscopy of **1^{Cl}** at increased pressure.*

Complex **1^{Cl}** (6.0 mg; 9.7 μmol) was dissolved in THF-*d*₈ (0.3 mL) in a high-pressure NMR tube and degassed via 3 freeze-pump-thaw cycles. 3.8 bars of N₂ or Ar were applied and NMR spectra were measured between +25 °C and -95 °C. With no evidence of N₂ coordination, this experiment provides an estimate for the upper limit for the equilibrium constant of N₂ binding to **1^{Cl}**. From a signal-to-noise ratio of 3:1, a detection limit of approx. 0.5 mM of putatively formed [ReCl₂(N₂)(PNP)] could be estimated. The upper limit of *K*_{Eq} is determined according equation 8:

$$K_{eq} = \frac{[ReCl_2(N_2)(PNP)]}{[ReCl_2(PNP)] * [N_2]} \quad (8)$$

$[ReCl_2(PNP)]_{starting} = 32.3 \text{ mM}$

$[N_2]_{starting} = 3.8 * 6.4 \text{ mM} = 24.3 \text{ mM}^{198}$

$[ReCl_2(PNP)]_{Lower \text{ limit}} \sim 31.8 \text{ mM}$

$[N_2]_{Lower \text{ limit}} \sim 23.8 \text{ mM}$

$[ReCl_2(N_2)(PNP)]_{Upper \text{ limit}} \sim 0.5 \text{ mM}$

$K_{eq} < 0.66 \text{ M}^{-1}$

From this calculation, K_{eq} is assumed to be approx. below 1 M^{-1} .

NMR stability tests for 1^{Cl}

1^{Cl} (5.0 mg, 8.1 μmol) was dissolved in THF-*d*₈ (0.5 mL) in a J-Young tube and measured under Ar. The sample was degassed via 3 freeze-pump-thaw cycles and backfilled with N₂. The stability under N₂ was monitored via NMR spectroscopy. To examine the stability against chloride, (*n*Bu₄N)Cl (11.0 mg; 40.5 μmol ; 5 eq.) was added forming a suspension and NMR spectroscopy was measured in regular time distances.

Electrochemical experiments for 1^{Cl} and 3^{Cl}

Chloride concentration dependence under N₂ and Ar for 1^{Cl}.

1^{Cl} (2.4 mg; 4.0 μmol) was dissolved in 4 mL of a 0.2 M solution of (*n*Bu₄N)PF₆ in THF and a small amount of Fc* was added as an internal reference. In sequence, a total of 1, 2, 5, 10, 20 eq. of (*n*Bu₄N)Cl was added as solid. After each chloride addition, CVs for the first reduction feature under N₂ and the first two reduction features for Ar were recorded.

Chloride concentration dependence for 3^{Cl}.

3^{Cl} (1.8 mg; 3.0 μmol) was dissolved in 3 mL of a 0.2 M solution of (*n*Bu₄N)PF₆ in THF and a small amount of Fe* was added as an internal reference. 1 eq. of (*n*He₄N)Cl was added as solid. After and before the chloride addition, CVs for the first oxidation feature were recorded.

N₂ pressure dependence of 1^{Cl}.

The electrochemistry autoclave as described in Section IV.4.1 was charged with **1^{Cl}** (3.0 mg; 4.9 μmol), 5 mL of a 0.2 M (*n*Bu₄N)PF₆ solution in THF, and a pipette tip of Fc under a N₂ atmosphere. The reactor was sealed and an initial 1 atm N₂ CV at a scan rate of 0.1 Vs⁻¹ was recorded. The pressure of the reactor was increased to 3 atm, the solution was stirred for 5 minutes, and a CV at a scan rate of 0.1 Vs⁻¹ was recorded. The process was repeated for total N₂

pressures of 5, 7, 9, and 11 atm. The pressure was then reduced and CVs were recorded at each of the pressures.

Rhenium concentration dependence under N₂ and Ar.

A stock solution of **1^{Cl}** was prepared by dissolving **1^{Cl}** (14.7 mg, 23.8 μmol) in a 1.0 mL solution of 0.2 M (*n*Bu₄N)PF₆ in THF. Aliquots of this stock solution were added to a 5 mL solution of 0.2 M (*n*Bu₄N)PF₆ in THF, with a spatula tip of Fc as an electrochemical reference, to afford solutions of 0.5, 1.0, 2.0, and 4.0 mM **1^{Cl}**. CVs for both the first reduction feature (as well as the first 2 reduction features under Ar) were recorded

6.2 Chapter II.2:

UV-vis Spectroelectrochemistry of **1^{Cl}, **1^{Br}**, **1^I****

Circa 5 mL of a 4.0 mM THF solution of **1^X** was prepared with 0.2 M (*n*Bu₄N)PF₆ and circa 0.4 mL was transferred to a 1 mm path SEC UV-vis cuvette for each single experiment. The cuvette was equipped with a Pt-mesh WE, a Pt Disk (*A* = 0.071 cm²) CE, and a Ag-wire pseudo-RE. By measuring a CV of **1^X**, the CPE potential was determined being at the onset of the first reduction wave (See Figure A15). In a separate experiment, a **1^X**-solution was electrolysed at this potential to determine after what time the highest concentration of dimer **2^X** was observed based on absorption in the simultaneously measured UV-vis. UV-vis SEC was performed by doing a CPE for the pre-determined time, after which UV-vis measurement started and measured every 10 seconds to monitor the decay of **2^X** into **3^X**, with a total experiment time of 15 minutes to get a final absorbance. Each measurement was repeated three times. To analyse the slightly wobbly data, kinetics were derived from 3 wavelengths close to the absorption maximum of **2^X** (See Figure A15). The half-life of **2^X** was derived from a plot of $\ln((A_t - A_f)/(A_0 - A_f))$ vs time, where *A_t* is the absorbance at time *t*, *A_f* the final absorbance, and *A₀* the absorbance at the start (directly after CPE was stopped).

Electrochemical experiments for **1^{Br}**

Bromide concentration dependence under N₂ and Ar.

1^{Br} (2.1 mg; 3.0 μmol) was dissolved in 3 mL of a 0.2 M solution of (*n*Bu₄N)PF₆ in THF and a small amount of Fc* was added as an internal reference. In sequence, a total of 0, 20, 40, 60, and 80 eq. of (*n*He₄N)Br was added. After each bromide addition, CVs for the first reduction features under N₂ and Ar were recorded.

N₂ pressure dependence of 1^{Br}.

The electrochemistry autoclave as described in Section IV.4.1 was charged with **1^{Br}** (2.9 mg, 4.1 μmol), 4 mL of a 0.2 M (*n*Bu₄N)PF₆ solution in THF, and a pipette tip of Fc under a N₂ atmosphere. The reactor was sealed and an initial 1 atm N₂ CV at a scan rate of 0.1 Vs⁻¹ was recorded. The pressure of the reactor was increased to 3 atm, the solution was stirred for 5 minutes, and a CV at a scan rate of 0.1 Vs⁻¹ was recorded. The process was repeated for total N₂ pressures of 1, 3, 5, 7, 9, and 11 atm.

Rhenium concentration dependence under N₂ and Ar.

For N₂: A stock solution of **1^{Br}** was prepared by dissolving **1^{Br}** (16.0 mg, 22.5 μmol) in a 0.9 mL solution of 0.2 M (*n*Bu₄N)PF₆ in THF. Aliquots of this stock solution were filled up to 5 mL solution using THF with 0.2 M (*n*Bu₄N)PF₆, with a spatula tip of Fc as an electrochemical reference, to afford solutions of 0.5, 1.0, 2.0, 3.0, and 4.0 mM **1^{Br}**.

Chloride concentration dependence for 3^{Br}.

3^{Br} (1.9 mg, 3.0 μmol) was dissolved in 3 mL of a 0.2 M solution of (*n*Bu₄N)PF₆ in THF and a small amount of [Co(Cp*)₂]PF₆ was added as an internal reference. 1, 2 and 5 eq. of (*n*Bu₄N)Br was added as solid. After and before the chloride addition, CVs for the first oxidation feature were recorded.

NMR experiments of 1^I at high pressures and with added iodide and electrolyte*NMR spectroscopy of 1^I at increased pressure.*

Complex **1^I** (10.8 mg, 9.7 μmol) was dissolved in THF-*d*₈ (0.45 mL) in a high-pressure NMR tube and degassed via 3 freeze-pump-thaw cycles. 3.8 bars of N₂ or Ar were applied and NMR spectra were measured between +25 °C and -95 °C. With no evidence of N₂ coordination, this experiment provides an estimate for the upper limit for the equilibrium constant of N₂ binding to **1^{Cl}**. From a signal-to-noise ratio of 3:1, a detection limit of approx. 0.7 mM of putatively formed [ReCl₂(N₂)(PNP)] could be estimated. *K_{eq}* was determined according equation 9:

$$K_{eq} = \frac{[ReI_2(N_2)(PNP)]}{[ReI_2(PNP)] * [N_2]} \quad (9)$$

$$[ReI_2(PNP)]_{starting} = 30.0 \text{ mM}$$

$$[N_2]_{starting} = 3.8 * 6.4 \text{ mM} = 24.3 \text{ mM}^{198}$$

$$[ReI_2(PNP)]_{Lower \text{ limit}} \sim 29.3 \text{ mM}$$

$$[N_2]_{Lower \text{ limit}} \sim 23.6 \text{ mM}$$

$$[ReI_2(N_2)(PNP)]_{Upper \text{ limit}} \sim 0.7 \text{ mM}$$

$$K_{eq} < 1.0 \text{ M}^{-1}$$

NMR stability tests for 1^I

1^I (2.1 mg, 3 μmol) was dissolved in THF-*d*₈ (0.5 mL) in a J-Young tube and measured under Ar. The sample was degassed via 3 freeze-pump-thaw cycles and backfilled with N₂. The stability under N₂ was monitored via NMR spectroscopy over 48 h. To examine the stability against iodide, (*n*He₄N)I (150.0 mg; 0.311 mmol; 25 eq) was added to **1^I** (10.8 mg, 0.012 μmol) and NMR spectroscopy was measured in regular time distances. Besides an initial upfield shift, no changes are observed. The same upfield shield could be achieved when (*n*Bu₄N)PF₆ (120 mg, 0.310 μmol , 50 eq.) was added to **1^I** (4.8 mg, 6 μmol) and examined by NMR spectroscopy.

Electrochemical experiments for 1^I*Iodide concentration dependence under N₂ and Ar.*

1^I (1.9 mg, 2.4 μmol) was dissolved in 3 mL of a 0.2 M solution of (*n*Bu₄N)PF₆ in THF and a small amount of [Co(Cp*)₂]PF₆ was added as an internal reference and stirred 30 minutes to fully dissolve the reference. In sequence, a total of 20, 40, 60, 80 eq. of (*n*He₄N)I was added as solid. After each iodide addition, CVs for the first 3 reduction features under N₂ as well as the first two reduction features for Ar were recorded. After reproducing this experiment 5-6 times and averaging the peak potentials, one experiment was measured without the addition of a reference suitable for simulation and the peaks were referenced on the determined values.

N₂ pressure dependence of 1^I.

The electrochemistry autoclave as described in Section IV.4.1 was charged with **1^I** (3.2 mg; 4.0 μmol), 4 mL of a 0.2 M (*n*Bu₄N)PF₆ solution in THF, and a pipette tip of Fc under a N₂ atmosphere. The reactor was sealed and an initial 1 atm N₂ CV at a scan rate of 0.1 Vs⁻¹ was recorded. The pressure of the reactor was increased to 3 atm, the solution was stirred for 5 minutes, and a CV at a scan rate of 0.1 Vs⁻¹ was recorded. The process was repeated for total N₂ pressures of 1, 3, 5, 7, 9, and 11 atm.

Rhenium concentration dependence under N₂ and Ar.

A stock solution of **1^I** was prepared by dissolving **1^I** (12.0 mg, 15.0 μmol) in a 0.25 mL solution of 0.2 M (*n*Bu₄N)PF₆ in THF. Aliquots of this stock solution were added to a 3 mL solution of 0.2 M (*n*Bu₄N)PF₆ in THF, with a spatula tip of Fc as an electrochemical reference, to afford solutions of 0.5, 1.0, 2.0, 3.0 for both atmospheres and in addition for Ar: 3.5 mM, for N₂: 4.0 mM **1^I**. CVs for the first three reduction features for N₂, and for the first two reduction features for Ar were recorded.

6.3 Chapter II.3

(Electro)chemical stability tests*Chemical stability tests for $=1^{Cl}$*

$=1^{Cl}$ (5.0 mg, 8.1 μmol) was dissolved in THF (0.5 mL) in J-Young tube under Ar and the stability was monitored by NMR spectroscopy over time. The sample was degassed by three freeze-pump-thaw cycles and backfilled with N_2 and the stability was monitored by NMR spectroscopy over time. To examine the stability in the presence of chloride, a sample with $=1^{Cl}$ in THF was prepared analogue as described above, just with added ($n\text{Bu}_4\text{N}$)Cl (11.0 mg, 40.5 μmol , 5.0 eq.). The mixture was examined by NMR spectroscopy over time and after 15 h, the solvent was changed for C_6D_6 to examine ^1H NMR spectroscopy. To check for the chloride induced disproportionation, a sample was prepared of $=8$ (2 mg, 3.1 μmol) and ($n\text{He}_4\text{N}$)Cl (1.5 mg, 3.8 μmol , 1.2 eq.) in d_8 -THF. After measuring ^1H NMR spectroscopy, $=1^{Cl}$ (1.9 mg, 3.1 μmol , 1 eq.) was added and another ^1H NMR spectrum was measured.

Chemical stability tests for $=1^I$

$=1^I$ (4.0 mg, 5.0 μmol , 1 eq.), and ($n\text{He}_4\text{N}$)I (9.1 mg, 25.1 μmol , 5 eq.) were dissolved in d_8 -THF (0.5 mL) in a J-Young tube under Ar and the stability was monitored by NMR spectroscopy over time.

Electrochemical stability tests for $=3^{Cl}$

$=3^{Cl}$ (1.8 mg, 3.0 μmol) and 3.0 mL of a 0.1 M ($n\text{Bu}_4\text{N}$)PF₆ solution in THF with addition of ($n\text{He}_4\text{N}$)Cl (1.2 mg, 3.0 μmol , 1.0 eq.) were combined in the electrolysis cell. CPE was performed at $E_{\text{appl.}} \approx -1.7$ V for 100 min to mimic the N_2 -splitting CPE conditions. A total of 0.1 electrons per Re-centre were transferred. After CPE, the nitride was extracted away from the electrolyte by pentane and analysed by NMR spectroscopy.

Electrochemical experiments for $=1^{Cl}$ *Chloride concentration dependence under Ar.*

$=1^{Cl}$ (2.5 mg; 4.0 μmol) was dissolved in 4 mL of a 0.2 M solution of ($n\text{Bu}_4\text{N}$)PF₆ in THF and a small amount of Fc^* was added as an internal reference. In sequence and quickly, a total of 0, 10, 20 eq. of ($n\text{Bu}_4\text{N}$)Cl was added as solid to examine the first reduction by CV at $v = 0.5, 1, 2, 3, 4, 5$ Vs⁻¹ and a total of 0, 1, 2, 5, 10 and 20 eq. to examine the whole reductive area by CV at $v = 0.5$ Vs⁻¹.

N₂ pressure dependence of =1^{Cl}.

The electrochemistry autoclave as described in Section IV.4.1 was charged with =1^{Cl} (2.5 mg, 4.0 μmol), 4 mL of a 0.2 M (*n*Bu₄N)PF₆ solution in THF, and a pipette tip of Fc* as electrochemical reference under a N₂ atmosphere. The reaction was sealed and pressurised with N₂ to obtain CVs at 1, 3, 5, 7, 9, and 11 bars. At 11 bars, the system was allowed to stay for 45 minutes, while regular CVs were measured. After depressurising the reaction was transferred back into the glovebox and the reaction mixture was analysed by ³¹P{¹H} NMR spectroscopy.

Rhenium concentration dependence under N₂ and Ar.

A stock solution of =1^{Cl} was prepared by dissolving =1^{Cl} (15.3 mg, 25.0 μmol) in a 1.0 mL solution of 0.2 M (*n*Bu₄N)PF₆ in THF. Aliquots of this stock solution were added to a 5 mL solution of 0.2 M (*n*Bu₄N)PF₆ in THF, with a spatula tip of Fc as an electrochemical reference, to afford solutions of 0.5, 1.0, 2.0, 3.0 and 4.0 mM. CVs for the first two reduction features under Ar were recorded.

Attempt to form NH₄⁺ from 3^I and =3^I using SmI₂/H₂O

In two separate Young-flasks was weighted **3^I** (4.9 mg, 7.3 μmol, 1 eq.) and =**3^I** (4.2 mg, 6.1 μmol, 1 eq.), were weighted and to both was added SmI₂ in THF (0.73 mL and 0.61 mL of a 0.1 M solution, respectively). Then, degassed H₂O (13 μL, 0.73 mmol, 100 eq. and 11 μL, 0.61 mmol, 100 eq.) was added via a Hamilton syringe, while the solution was stirring. In both cases, a direct colour change to red and a strong gas evolution was observed. After 1h stirring, the by then orange solution was evaporated overnight to remove most of the H₂O. The flasks were brought into the box, and the orange solid was suspended in *d*₈-THF. NMR spectroscopy revealed the exclusive presence of **4^I-I** and =**3^I**, respectively, and no traces of NH₄I formation.

6.4 Chapter II.4.

Electrochemical MeCN release from **6**

To a solution of **6** (1.9 mg, 3 μ mol, 1.0 eq.) in THF (3 mL) with 0.1 M (*n*Bu₄N)PF₆, was added DBU (4.5 μ L, 30 μ mol, 10 eq.) and (*n*He₄N)Cl (11.7 mg, 29.9 μ mol, 10 eq.) upon which the characteristic oxidative double features were obtained in CV. CPE was performed at $E_{appl.} = -0.3$ V for circa 3 h after which in repetitive experiments 7.0, 5.8, and 8.5 electrons were transferred per rhenium, accompanied by a colour change from brown via green to orange. After electrolysis, the solution was transferred to a young-flask, and the three-neck cell, the electrodes and the sample holders were rinsed with maximum 1 mL THF. From this young flask, the volatiles were vacuum transferred to a separate flask. Subsequently, its volume was measured as necessary for MeCN yield determination and an aliquot was taken for GC chromatography. MeCN yield was determined at 20 % and 32 %, as averaged to 25 %. The subsequent inorganic fraction was dissolved and analysed by NMR spectroscopy.

Electrochemical MeCN release from **5**

To a solution of **5** (2.1 mg, 2.7 μ mol, 1.0 eq.) in THF (3 mL) with 0.1 M (*n*Bu₄N)PF₆, was added DBU (2.0 μ L, 13.5 μ mol, 5 eq.), and (*n*He₄N)Cl (6.1 mg, 15.6 μ mol, 5.8 eq.). CPE was performed at $E_{appl.} = -0.3$ V, leading to a colour change towards brown and a transfer of 7.2 electrons per rhenium to fully oxidise the features at the CPE potential. After CPE, the same work up as described in 'electrochemical MeCN release from **6**', was performed, yielding an MeCN yield of circa 15 %.

Electrochemical MeCN release from =6****

To a solution of =**6** (2.4 mg, 3.9 μ mol, 1.0 eq) in THF (3 mL) with 0.1 M (*n*Bu₄N)PF₆ was added NEt₃ (5.4 μ L, 3.9 mg, 39 μ mol, 10 eq.) and (*n*He₄N)Cl (15.0 mg, 38.5 μ mol, 9.8 eq.). CPE was performed at the second feature at $E_{appl.} = +0.08$ V for circa 4 h. During CPE, the colour changes from light blue via orange to green and in successive experiment, 5.7, 7.2, 5.1, 4.9, and 5.8 electrons are needed to fully oxidise the oxidative features at the CPE potential. After CPE, the same work up as described in 'electrochemical MeCN release from **6**' was performed, yielding an MeCN yield in subsequent runs of 55 %, 77 %, 67 %, and 58 %. To the inorganic fraction, 2.3 mg 1,3,5-trimethoxybenzene was added as standard to determine the yield of =**8**. As described in Section II.4.3, =**8** suffers from decomposition. The highest yield in =**8** was found to be 36 %.

Chemical MeCN release from =6

To =6 (3 mg, 4.8 μmol , 1.0 eq) was added NCS (1.3 mg, 9.7 μmol , 2.0 eq.) and C_6D_6 (0.4 mL). Directly, a colour change to brown was observed and the reaction was allowed to stir 3-4 h. In most runs, both 1,3,5-trimethoxybenzene and hexamethylbenzene were added as standard and yield in MeCN and =8 was determined by ^1H NMR spectroscopy. Next to these small runs, also a large scale experiment was performed with 10 mg of =6. In successive runs, MeCN was found in 65, 56, 55, 66 and 66 % yield, and =8 in 46, 50, and 45 % yield. Less runs were used for quantification of the inorganic product, since sometimes too much NCS was added, leading to decomposition of =8 (Section II.4.4).

Attempts to quantify =8 electrochemically upon oxidation of (=6)

To a solution of =6 (1.8 mg, 3.0 μmol) in THF (3 mL) with 0.1 M ($n\text{Bu}_4\text{N}$)PF₆ in a CPE set up was added NEt_3 (7.7 μL , 60 μmol , 20 eq.) and ($n\text{He}_4\text{N}$)Cl (29 mg, 60 μmol , 20 eq.). A CV was measured in the reductive direction. CPE was performed at $E_{\text{appl.}} = +0.08$ V vs. $\text{Fc}^{+/0}$ until a charge of 87 mC was transferred, corresponding to 0.3 electrons (10 % conversion of the starting material). Again, a reductive scan was made, and the current was determined of the new reductive feature at -0.95 V at $v = 0.1$ Vs^{-1} .

To quantify the amount of =8, we used the Randles-Ševčík equation (10) as described at 25 °C:¹⁷⁴

$$i_{p,c} = 2.69e^5 * n^{\frac{3}{2}} * A * D^{\frac{1}{2}} * v^{\frac{1}{2}} * c \quad (10)$$

$$i_{p,c} = 1.12 \cdot 10^{-6} \text{ A}$$

$$n = 1$$

$$A = 0.02 \text{ cm}^2$$

$$D = 7.5 \cdot 10^{-6} \text{ cm}^2\text{s}^{-1} \text{ (as determined via DOSY NMR)}$$

$$v = 0.1 \text{ Vs}^{-1}$$

Via this procedure a reproduced concentration of =8 of $2.5 \cdot 10^{-7}$ mol L^{-3} was found, which corresponds to a yield of approx. 25 %. This exceeds the theoretical maximum of only 10 % conversion.

Chloride titration of 8

A solution was prepared of 8 (2.0 mg, 3.0 μmol , 1 eq.) in 3 mL THF with 0.2 M ($n\text{Bu}_4\text{N}$)PF₆ and a spatula tip of Fc^* . By CV, the first wave was measured at $v = 0.1, 0.25, 0.5, 1.0,$ and 2.0 Vs^{-1} . ($n\text{He}_4\text{N}$)Cl was added in subsequent amounts: 5 eq. (+5.4 mg), 11 eq. (+6.6 mg), 20 eq. (+12.7 mg), 40 eq. (+26.6 mg) and 100 eq. (89.6 mg). At the latter condition, 70 % current reduction

was observed likely indicating some decomposition. The data was therefore not further analysed (although it still has no onset for reversibility). At each condition, the before mentioned scan rates were scanned, including the internal reference.

Chloride titration of =8****

A solution was prepared of =**8** (1.2 mg, 2.0 μmol , 1 eq.) in 2 mL THF with 0.2 M ($n\text{Bu}_4\text{N}$)PF₆ and a spatula tip of Fc*. By CV, the first wave was measured at $v = 0.1, 0.25, 0.5, 1.0, \text{ and } 2.0 \text{ Vs}^{-1}$. ($n\text{He}_4\text{N}$)Cl was added in subsequent amounts: 5 eq. (+4.4 mg) and 15 eq. (+14.6 mg). At each condition, the before mentioned scan rates were scanned, including the internal reference.

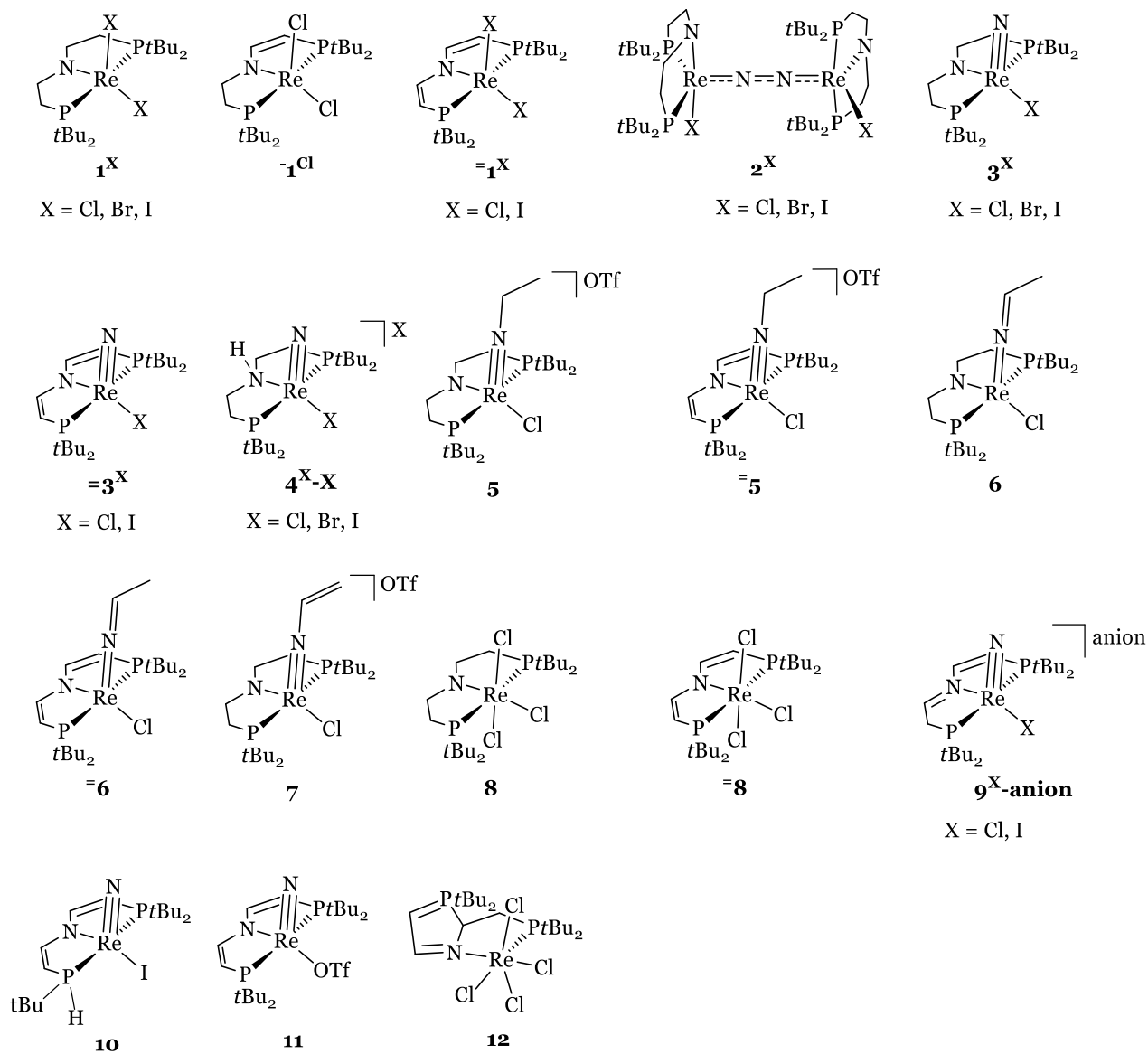
Stability of =8** in presence of electrolyte and chloride source**

By NMR spectroscopy: In a NMR Young tube, =**8** (2 mg, 3.1 μmol , 1.0 eq) was dissolved in d_8 -THF and a ¹H NMR spectrum was measured. ($n\text{He}_4\text{N}$)Cl (6.3 mg, 5.2 eq) was added, and ¹H NMR spectra were measured after 10 min, 2h, 6h, and 24h. Subsequently, ($n\text{Bu}_4\text{N}$)PF₆ (38.7 mg, 100 μmol , 32 eq.) was added and NMR spectra were measured directly, after 6 h and 22 h. No decomposition was observed.

By CV: In the three-neck cell, =**8** (1.4 mg, 2 μmol) was dissolved in 2.3 mL THF with 0.2 M ($n\text{Bu}_4\text{N}$)PF₆ and a spatula tip of Fc was added. In regular time distances, CV of the Re(IV/III) reduction of =**8** was measured, showing current decrease accompanied by colour change to yellow. From different runs, the time for full decomposition was in the range of 120 min – 240 min. In attempting to perform a chloride titration into this CV mixture, similar decomposition was found (not significantly accelerated by addition of ($n\text{He}_4\text{N}$)Cl).

V Appendix

A1. Graphical overview of all *used* or *aimed for* rhenium complexes.



A2. pKa-values and Redox potentials of reagents/solvents used in this work

For most reagents, a redox potential measured in acetonitrile is literature-known. Redox potentials in THF were determined for those reagents whose redox-behaviour was of interest (e.g. different bases for MeCN release in Chapter II.4). Usually, these reagents appear irreversible and can foil the working electrode in such a way that no referencing is possible afterwards. Therefore, the reversible wave of the respective reference compound (Fc* for reductive-, and [Co(Cp*)₂]PF₆ for oxidative reagents) was scanned first, before the redox wave of the reagent of interest was examined. Notably, the onset of a wave can lay up to 0.3 V before the E_p , which was taken into account when choosing a reagent.

Table A1. pKa values and self-determined redox potentials of reagents used within this work.

Reagent / Solvent	E_p / V ($v = 0.1 \text{ V s}^{-1}$) ^a	$E_{1/2}$ / V^a	Solvent window	pKa (THF)
Proton sponge	0.09			11.6
NEt ₃	0.49			14.0
TMG	0.80			17.0
DBU	0.73			18.1
EtOTf	< -2.5 ^b			
Cl ⁻	0.82			
Br ⁻	0.02			
I ⁻	-0.40			
[Cr(Cp) ₂] ⁺⁰		-1.10		
[Cr(Cp*)(C ₆ H ₆)] ⁺⁰		-1.20		
[Co(Cp) ₂] ⁺⁰		-1.32		
Fluorobenzene			-3.1 to +1.1 V	
1,2-difluorobenzene			-2.8 to +1.2 V	
Et ₂ O			-2.8 to +1.3 V	

^a in THF with 0.1 M or 0.2 M (*n*Bu₄N)PF₆. ^a in 1,2-difluorobenzene with 0.1 M (*n*Bu₄N)PF₆. From -2.5 V onwards current increase is observed compared to the blank.

A3. Figures and tables of chapter II.1.

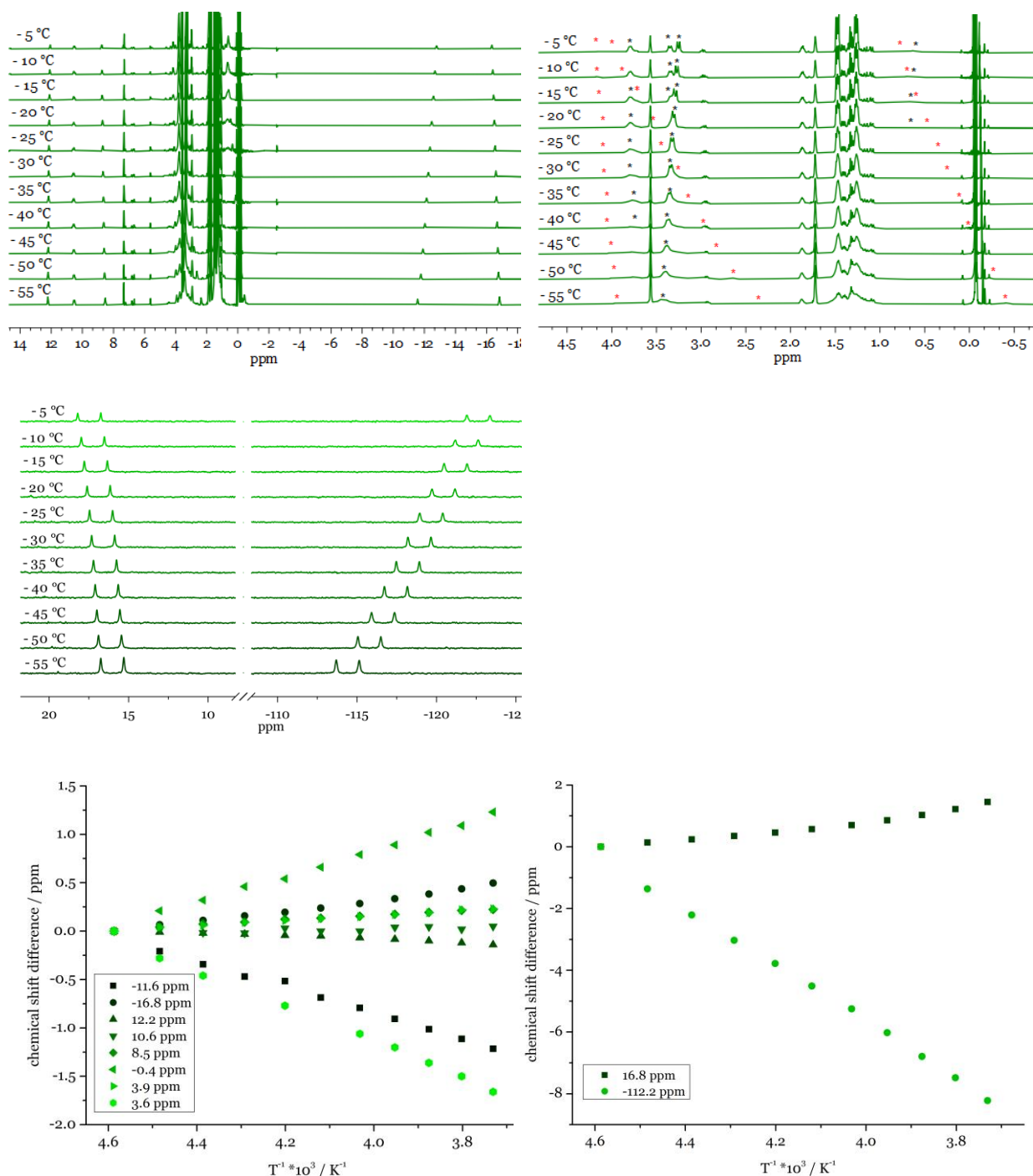


Figure A1. VT-NMR of **2^{Cl}** in *d*₈-THF from -55°C to -5°C . Top left: ^1H NMR spectrum. Top right: ^1H NMR spectrum, zoom of the *tert*-butyl region. *Tert*-butyl and PNP-backbone peaks are indicated with a black and red asterisk, respectively. Middle: $^{31}\text{P}\{^1\text{H}\}$ NMR spectrum. Bottom left: Chemical shift difference vs. $T^{-1}\cdot 10^3$ for the CH_2 -backbone signals. Bottom right: Chemical shift difference vs. $T^{-1}\cdot 10^3$ for the phosphorous signals. For the last two mentioned figures: a positive shift indicates an upfield shift and the values in the legend refers to the shift at -30°C .

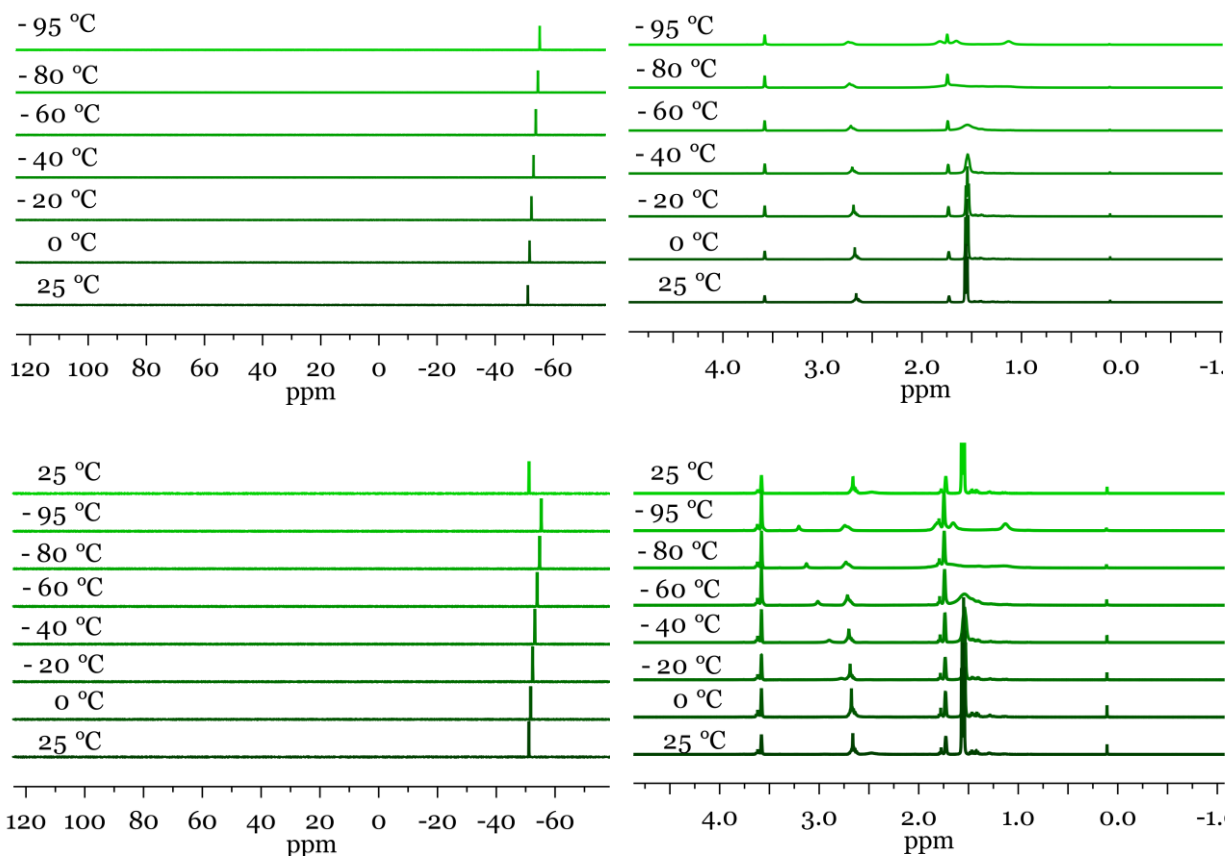


Figure A2. NMR spectroscopy of 1^{Cl} under N_2 or Ar (4 atm) in d_8 -THF from RT to $-95\text{ }^\circ\text{C}$ (and back to $25\text{ }^\circ\text{C}$ in case of Ar). Top left: N_2 , $^{31}\text{P}\{^1\text{H}\}$ NMR. Top right: N_2 , ^1H NMR. Bottom left: Ar, $^{31}\text{P}\{^1\text{H}\}$ NMR. Bottom right: Ar, ^1H NMR.

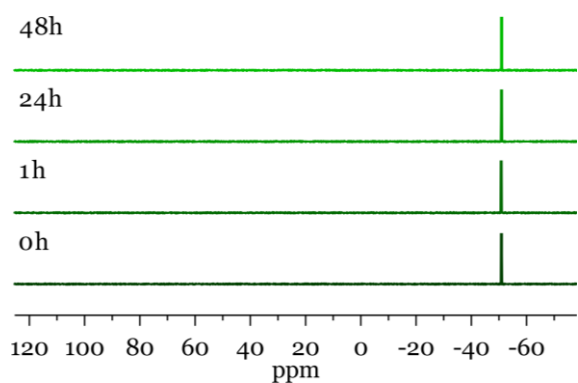


Figure A3. $^{31}\text{P}\{^1\text{H}\}$ NMR spectra of 1^{Cl} under N_2 in THF with 5 eq. of $(n\text{Bu}_4\text{N})\text{Cl}$ over the course of 48 h.

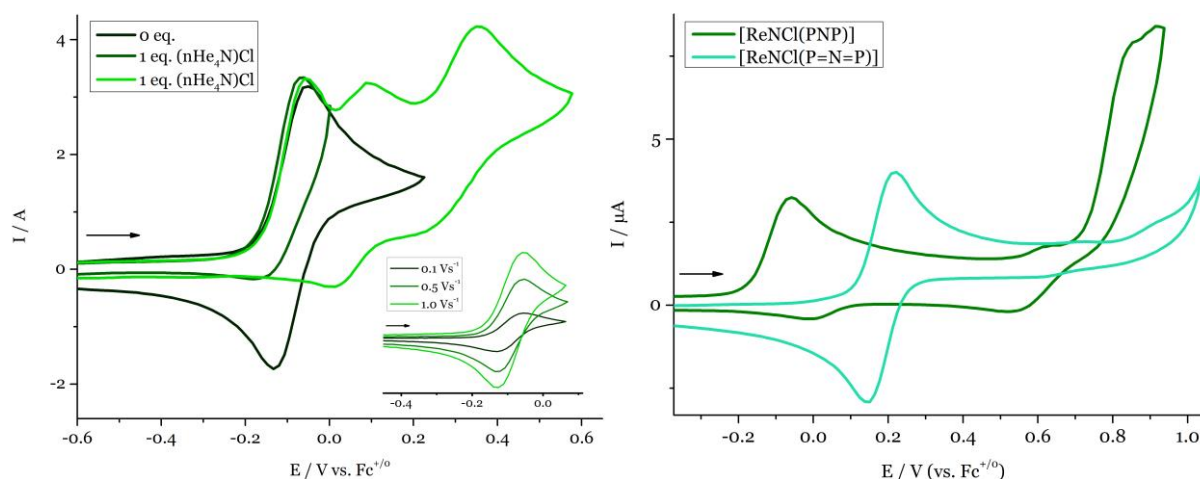


Figure A4. Left: CV of 3^{Cl} in THF with 0.2 M $(n\text{Bu}_4\text{N})\text{PF}_6$, and addition of 1 eq. of $(n\text{He}_4\text{N})\text{Cl}$. Inset: first oxidation without additives. Right: CV comparison of 3^{Cl} (green) and 3^{Cl} (turquoise) in THF with 0.2 M $(n\text{Bu}_4\text{N})\text{PF}_6$.

Table A2. CV Peak analysis of 3^{Cl} in THF.

3^{Cl}	v / Vs^{-1}	$E_{1/2}$ /V	$i_{\text{pf}}/i_{\text{pr}}$	E_{pf} /V	ΔE_{p} /V		v / Vs^{-1}	E_{pf} /V	i_{pf} / μA
1 st Ox	0.1	-0.09	1.27	-0.053	0.081	1 st red ^a	0.1	-3.390	6.5
	0.5	-0.09	1.18	-0.053	0.076				
	1.0	-0.09	1.14	-0.055	0.073				
2 nd Ox.	0.1	0.69	4.68	0.852	0.331				

^a no reverse wave

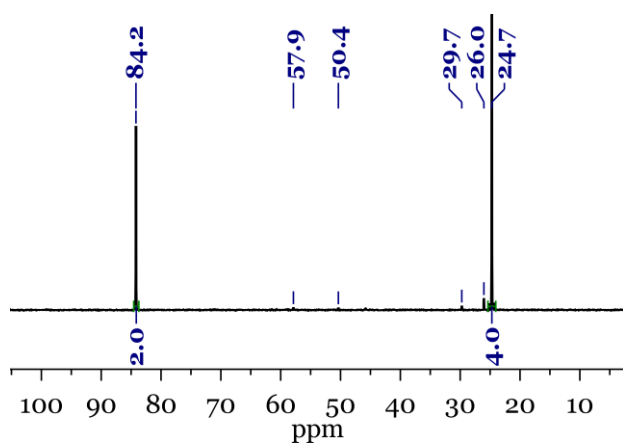


Figure A5. $^{31}\text{P}\{^1\text{H}\}$ NMR spectrum of 3^{Cl} (84.2 ppm) as obtained via CPE of 1^{Cl} at $E_{\text{appl.}} = -1.90$ V in THF with 0.2 M $(n\text{Bu}_4\text{N})\text{PF}_6$ with addition of 7.2 μmol PPh_3O (24.7 ppm) for quantification.

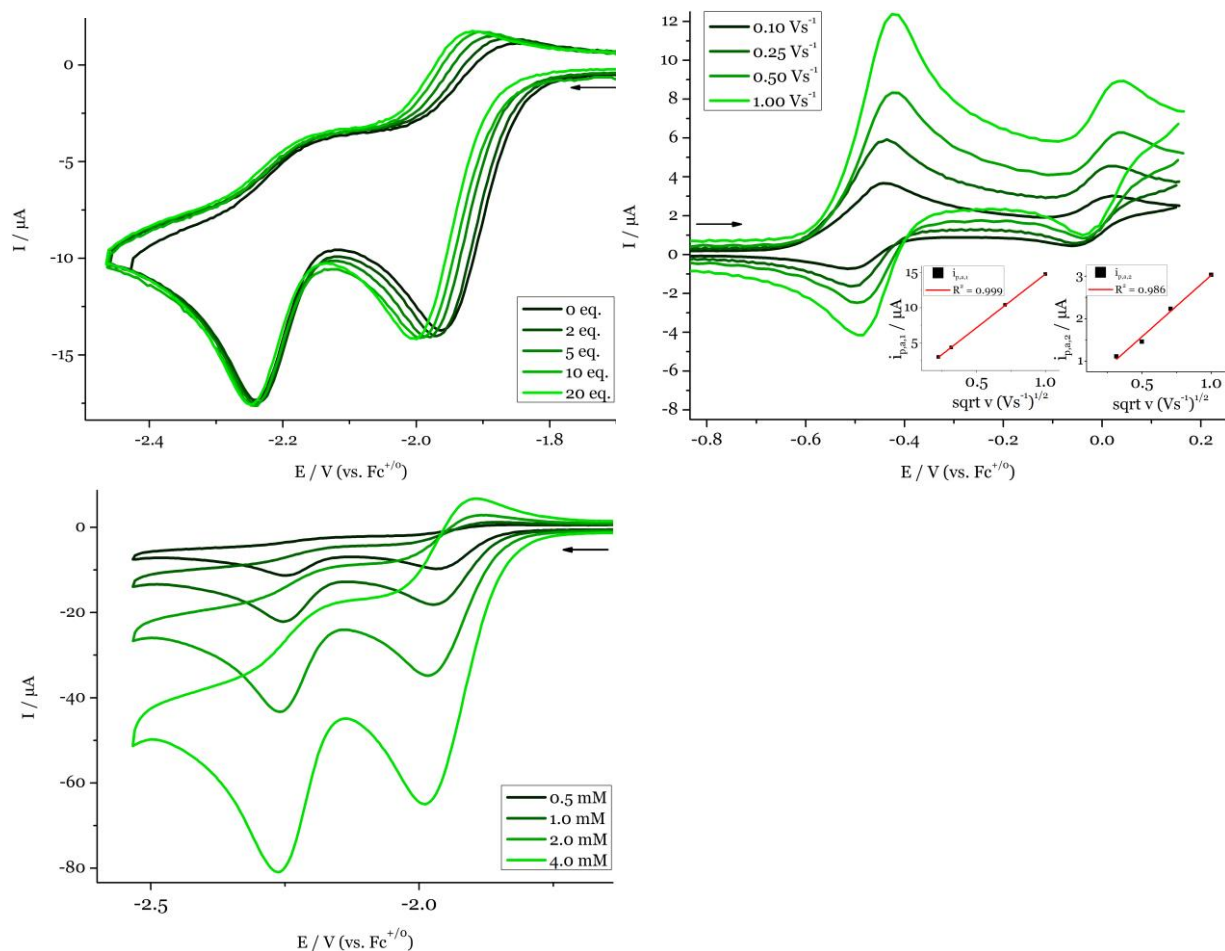


Figure A6. Top left: CV of the first and second reduction of 0.8 mM $\mathbf{1}^{\text{Cl}}$ in THF with 0.2 M $(n\text{Bu}_4\text{N})\text{PF}_6$ in presence of 0-20 eq. of $(n\text{Bu}_4\text{N})\text{Cl}$, $v = 0.1 \text{ Vs}^{-1}$ (measurement performed on a WE with $A = 0.071 \text{ cm}^2$ instead of the commonly used $A = 0.020 \text{ cm}^2$). Top right: CV of the oxidative area of 1.0 mM $\mathbf{1}^{\text{Cl}}$ in THF with 0.2 M $(n\text{Bu}_4\text{N})\text{PF}_6$. Inset left: plot of $i_{p,a,1}$ versus the square root of v . Inset right: plot of $i_{p,a,2}$ versus the square root of v . Bottom left: Concentration dependence of the first and second reduction of $\mathbf{1}^{\text{Cl}}$ in THF with 0.2 M $(n\text{Bu}_4\text{N})\text{PF}_6$, $v = 0.1 \text{ Vs}^{-1}$.

Table A3. CV Peak analysis of $\mathbf{1}^{\text{Cl}}$ under Ar.

$\mathbf{1}^{\text{Cl}}$	v / Vs^{-1}	E_{pf} / V	i_{pf} / μA		v / Vs^{-1}	$E_{1/2}$ / V	i_{pf}/i_{pr}	E_{pf} / V	ΔE_p / V
$\mathbf{1}^{\text{st}}$ red ^a	0.05	-1.957	3.2	$\mathbf{1}^{\text{st}}$ ox	0.05	-0.48	1.54	-0.441	0.073
	0.10	-1.962	4.6		0.10	-0.48	1.43	-0.440	0.075
	0.25	-1.968	7.0		0.50	-0.48	1.64	-0.442	0.079
	0.50	-1.982	10.1		1.00	-0.48	1.61	-0.439	0.084
	1.00	-1.997	14.1		0.10	-0.02	1.20	0.021	0.082
$\mathbf{2}^{\text{nd}}$ red ^b	2.00	-2.016	18.5	0.25	-0.01	1.36	0.020	0.074	
	3.00	-2.022	22.3	0.50	-0.01	1.33	0.038	0.078	
	0.10	-2.240	4.7	1.00	0.00	1.34	0.037	0.075	
	0.25	-2.256	7.3						
	0.75	-2.272	12.3						
	1.00	-2.280	13.9						

^a – no prominent reverse wave visible. The small onset of a reverse wave is further analysed in Table A4.

^b – no reverse wave.

Table A4. CV Peak analysis of the first reduction of $\mathbf{1}^{\text{Cl}}$ in presence of different equivalents of $(n\text{Bu}_4\text{N})\text{Cl}$ under Ar, $v = 0.1 \text{ Vs}^{-1}$.

$\mathbf{1}^{\text{Cl}}$ $(n\text{Bu}_4\text{N})\text{Cl}$ / eq.	$E_{1/2}$ /V	$i_{\text{pf}}/i_{\text{pr}}$	E_{pf} /V	ΔE_{p} /V
0	-1.902	3.12	-1.965	0.127
1	-1.921	2.55	-1.978	0.114
5	-1.934	2.20	-1.984	0.097
10	-1.948	1.93	-1.993	0.091
20	-1.962	1.75	-2.004	0.083

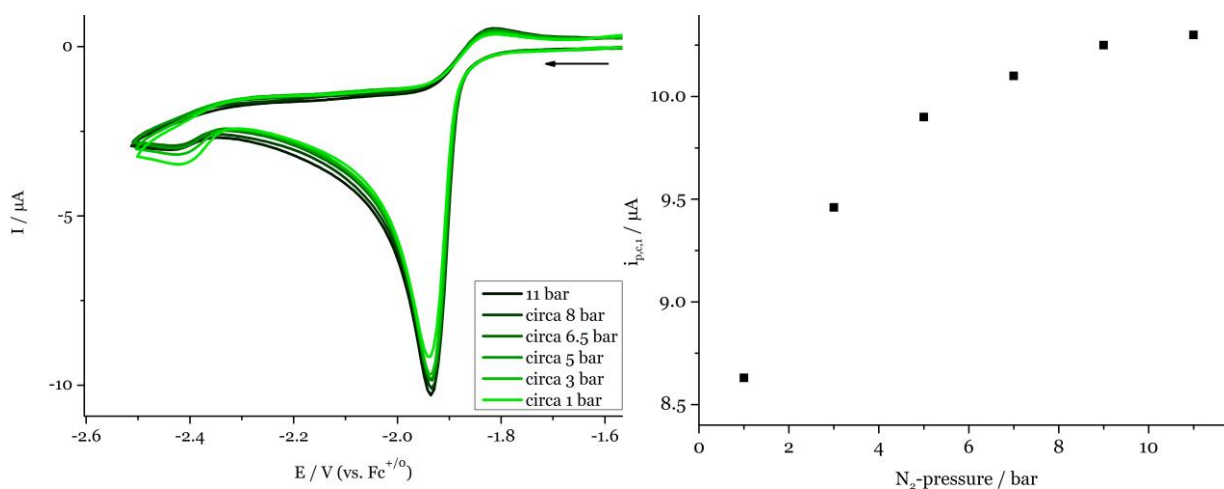


Figure A7. Left: N_2 -pressure dependence of 1.0 mM $\mathbf{1}^{\text{Cl}}$ in THF with 0.2 M $(n\text{Bu}_4\text{N})\text{PF}_6$, depressurising from 11-1 bars. Right: Plot of the peak current of the first reduction feature of $\mathbf{1}^{\text{Cl}}$ versus 1 to 11 bars of N_2 pressure.

Table A5. CV Peak analysis of $\mathbf{1}^{\text{Cl}}$ under N_2 .

$\mathbf{1}^{\text{Cl}}$	v / Vs^{-1}	$E_{1/2}$ /V	$i_{\text{pf}}/i_{\text{pr}}$	E_{pf} /V	ΔE_{p} /V	v / Vs^{-1}	E_{pf} /V	i_{pf} / μA
1 st red	0.05 ^a	-	-	-1.893	-	2 nd red ^a	0.05	1.8
	0.10 ^a	-	-	-1.900	-		0.10	2.2
	0.25	-1.87	4.66	-1.924	0.103	0.25	-2.389	2.8
	0.50	-1.89	3.98	-1.958	0.139	0.50	-2.415	2.9
	1.00	-1.90	3.03	-1.983	0.166	1.00	-2.437	2.1
	1.50	-1.91	2.61	-2.007	0.185	1.50 ^b	-	-

^a – no reverse wave. ^b – no clear feature visible.

Table A6. CV Peak analysis of the first reduction of $\mathbf{1}^{\text{Cl}}$ in presence of different equivalents of $(n\text{Bu}_4\text{N})\text{Cl}$ under N_2 , $v = 0.1 \text{ Vs}^{-1}$. These data were measured several times within this work and by cooperation partners and averaged values were used as guidelines for the digital simulation.⁷⁰

$\mathbf{1}^{\text{Cl}}$ $(n\text{Bu}_4\text{N})\text{Cl}$ / eq.	$E_{1/2}$ /V	$i_{\text{pf}}/i_{\text{pr}}$	E_{pf} /V	ΔE_{p} /V
0	-	-	-1.894	-
5	-1.85	4.20	-1.899	0.087
10	-1.87	3.37	-1.914	0.099
20	-1.88	2.85	-1.929	0.102

A4. Figures and tables of chapter II.2.

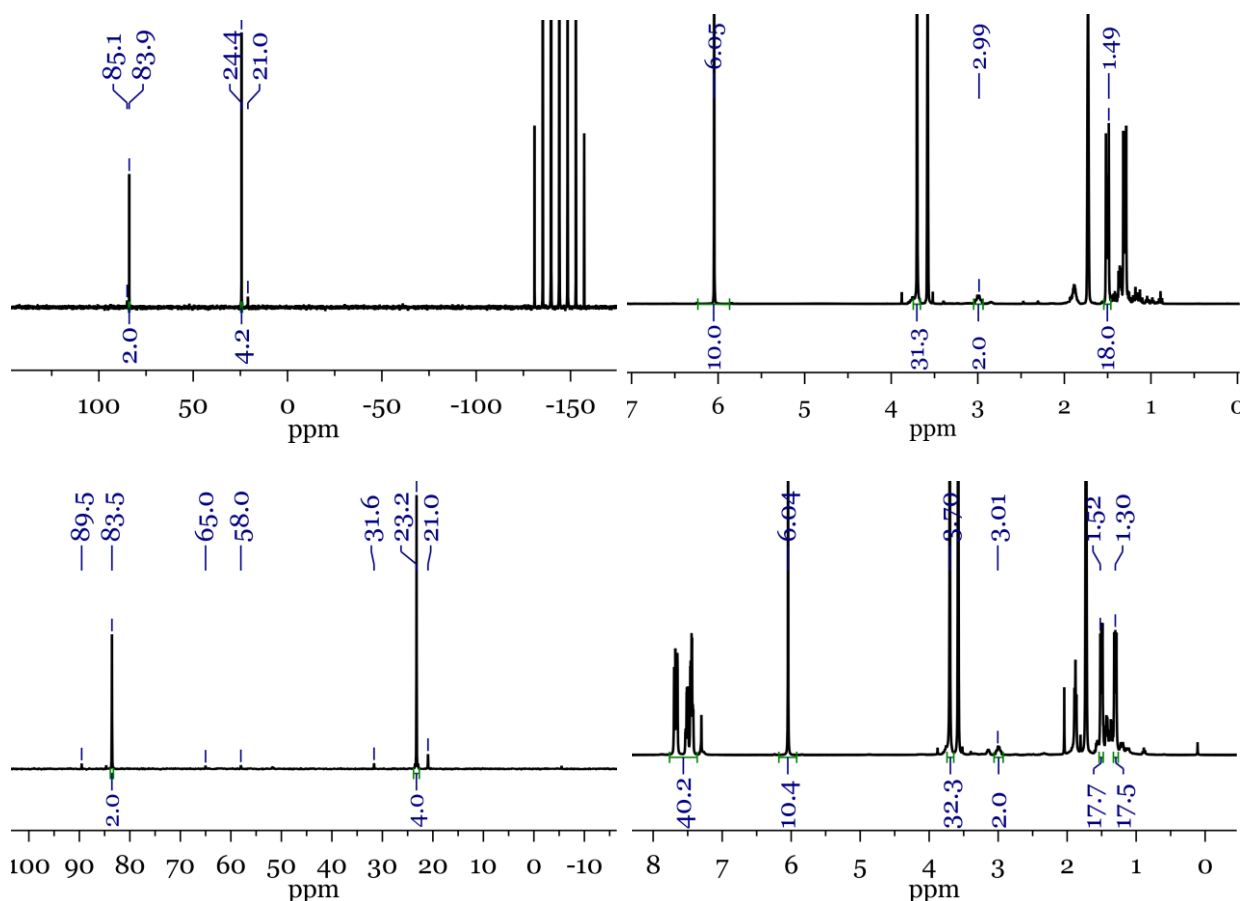


Figure A8. NMR spectroscopy for the quantification of 3^{Br} ($\delta^{31\text{P}\{^1\text{H}\}} = 83.9$ ppm) as formed via (electro)chemical reduction of 1^{Br} . Top left: $^{31}\text{P}\{^1\text{H}\}$ -NMR spectrum obtained via CPE with addition of $7.2 \mu\text{mol}$ PPh_3O as standard ($\delta^{31\text{P}\{^1\text{H}\}} = 24.4$ ppm) used for yield determination (57 %). Top right: using Na/Hg as reductant with addition of $19.8 \mu\text{mol}$ hexamethylbenzene as standard ($\delta^{\text{H}} = 6.1$ and 3.7 ppm) used for yield determination (81 %). Bottom: using $\text{Co}(\text{Cp}^*)_2$ as reductant with addition of $12.3 \mu\text{mol}$ 1,3,5-trimethoxybenzene and $9.6 \mu\text{mol}$ PPh_3O as standard used for yield determination (56 % via both ^1H and ^{31}P NMR spectroscopy). Left: $^{31}\text{P}\{^1\text{H}\}$ NMR. Right: ^1H NMR.

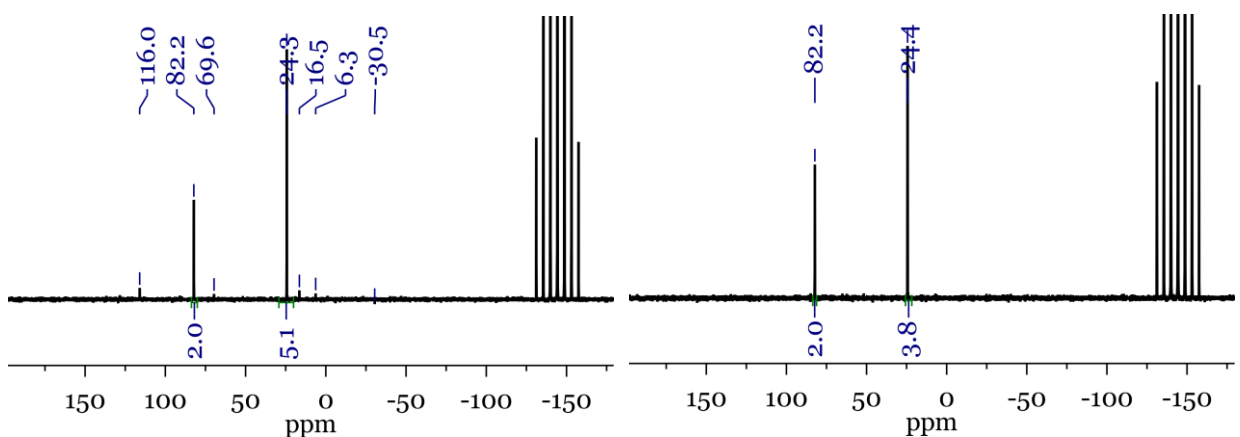


Figure A9. Left: $^{31}\text{P}\{^1\text{H}\}$ -NMR spectrum of 3^{I} obtained via CPE at $E_{\text{appl.}} = -1.58$ V with addition of $7.2 \mu\text{mol}$ PPh_3O as standard for yield determination (47 %). Right: $^{31}\text{P}\{^1\text{H}\}$ -NMR spectrum of 3^{I} obtained via CPE at $E_{\text{appl.}} = -1.72$ V with addition of $7.2 \mu\text{mol}$ PPh_3O as standard for yield determination (64 %).

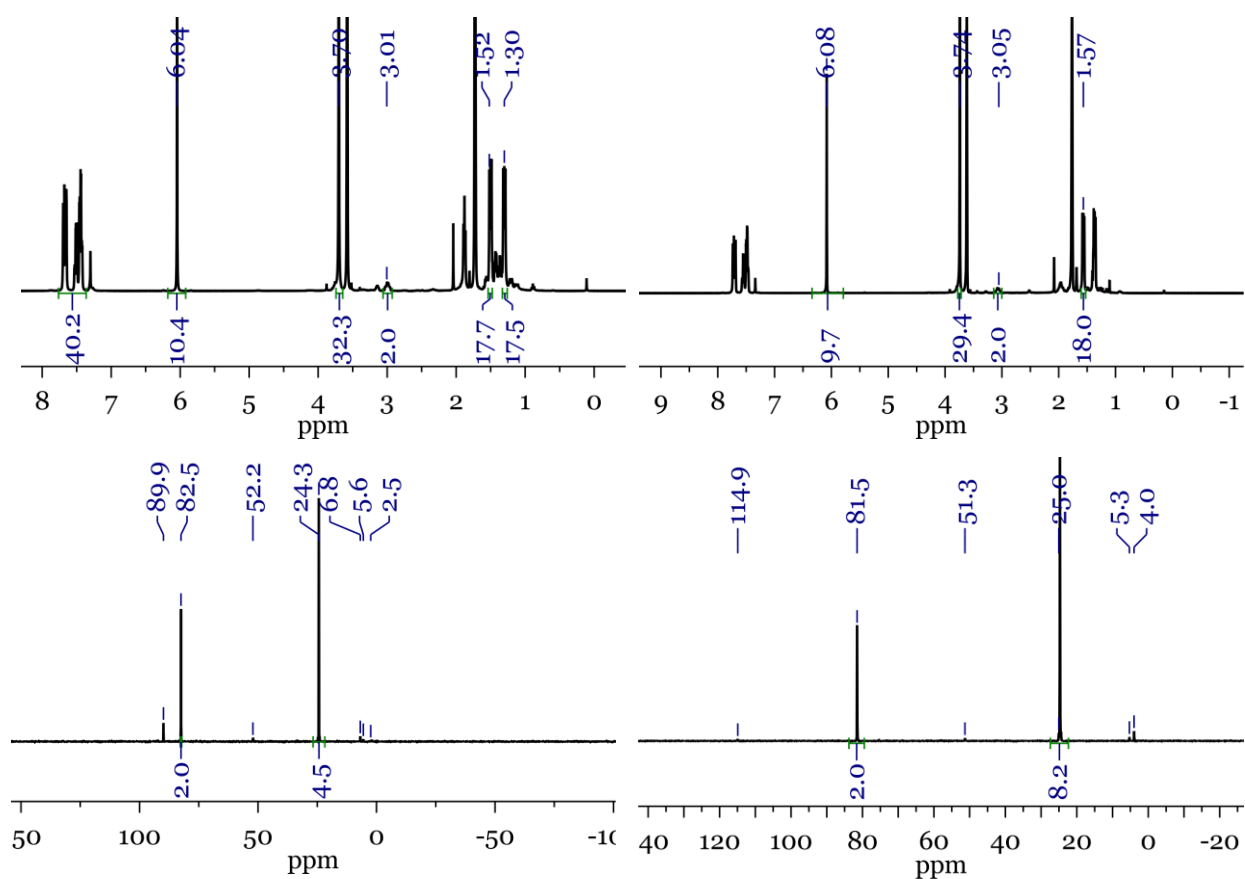


Figure A10. NMR spectroscopy for the quantification of **3^I** ($\delta^{31\text{P}\{^1\text{H}\}} = 82$ ppm) as formed via chemical reduction of **1^I**. Top: $\text{Cr}(\text{Cp}^*)_2$ as reductant with addition of $9.6 \mu\text{mol}$ PPh_3O and $12.3 \mu\text{mol}$ 1,3,5-trimethoxybenzene as standards (58 % via $^{31}\text{P}\{^1\text{H}\}$ -NMR and 61 % via ^1H -NMR). Top left: $^{31}\text{P}\{^1\text{H}\}$ -NMR. Top right: ^1H -NMR. Bottom left: $^{31}\text{P}\{^1\text{H}\}$ -NMR spectrum from $\text{Co}(\text{Cp}^*)_2$ as reductant with addition of $32.3 \mu\text{mol}$ PPh_3O as standard (63 % via $^{31}\text{P}\{^1\text{H}\}$ -NMR). Bottom right: $^{31}\text{P}\{^1\text{H}\}$ -NMR spectrum from Na/Hg as reductant with addition of $12.6 \mu\text{mol}$ PPh_3O as standard (41 % via $^{31}\text{P}\{^1\text{H}\}$ -NMR).

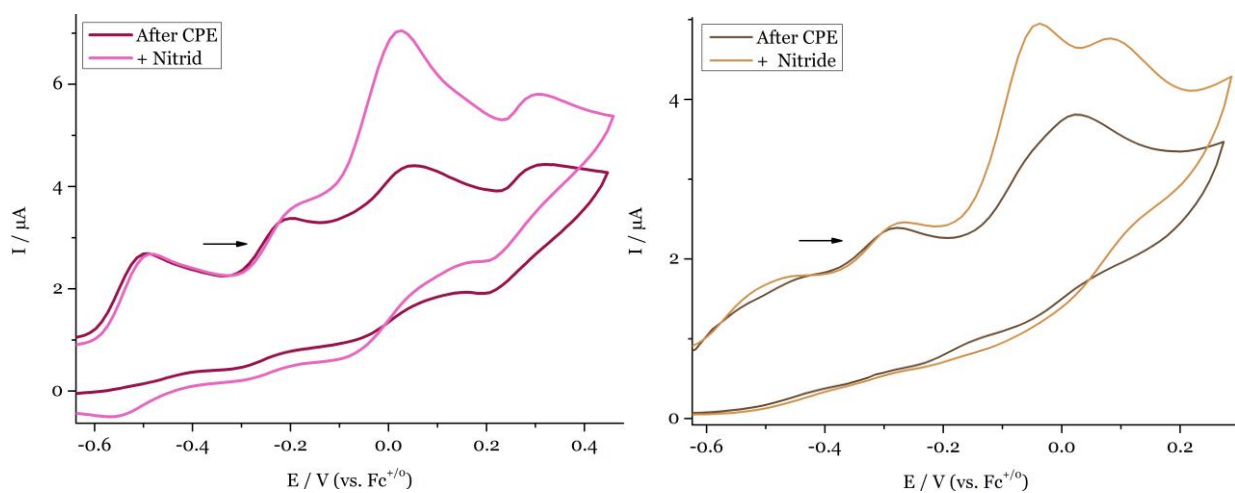


Figure A11 Left: CV of the oxidative region after CPE of **1^{Br}** and addition of **3^{Br}**. Right: CV of the oxidative region after CPE of **1^I** and addition of **3^I**.

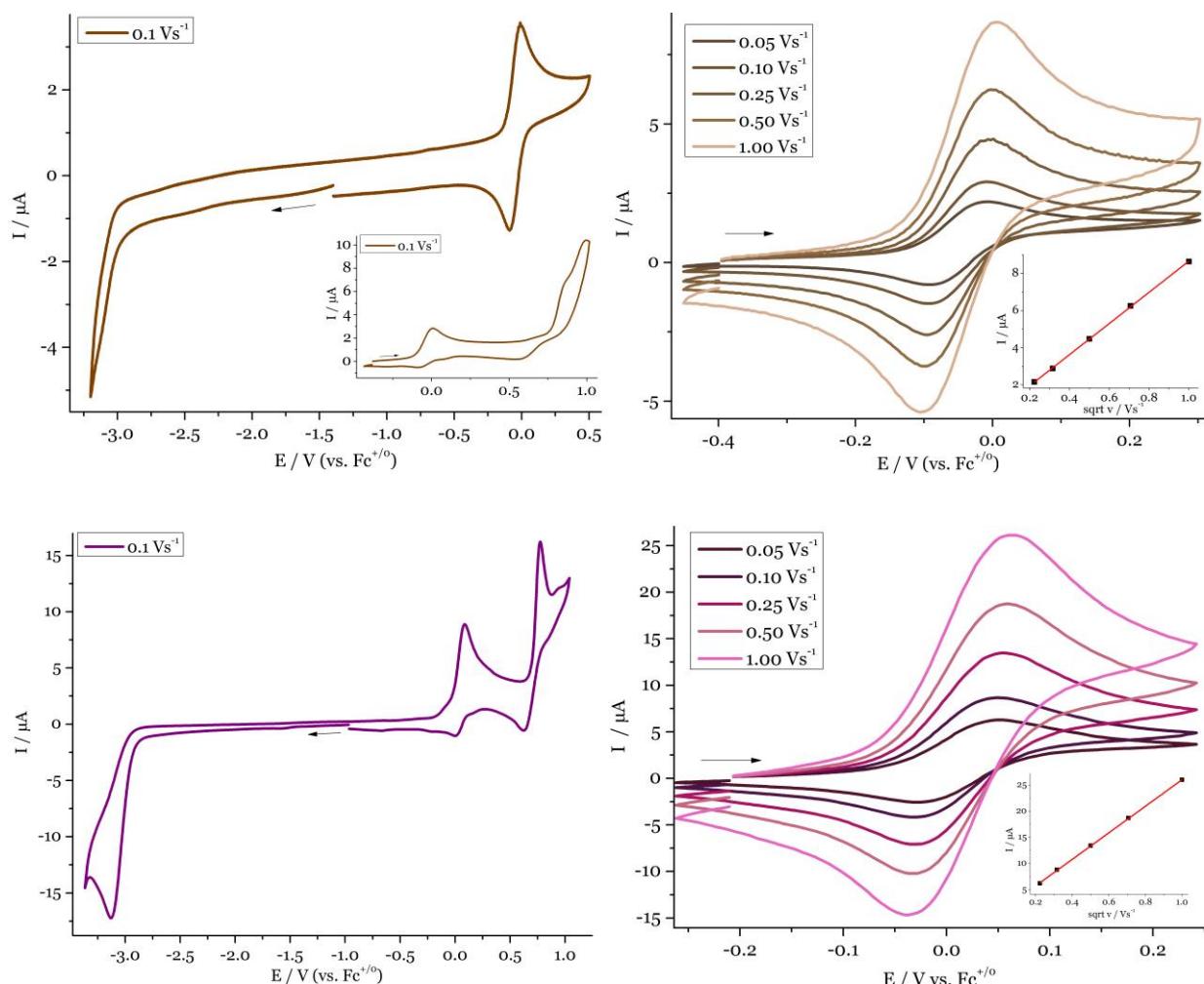


Figure A12. CV in THF with 0.2 M (*n*Bu₄N)PF₆ measured under N₂. Top Left: CV of 1 mM of **3^{Br}**. Inset: full oxidative region. Top right: first oxidation of **3^{Br}**. Inset: plot of *i*_{p,a} vs. *v*^{1/2}. Bottom left: CV of 2 mM of **3^I**. Bottom right: first oxidation of **3^I**. Inset: plot of *i*_{p,a} vs. *v*^{1/2}.

Table A7. CV Peak analysis of **3^{Br}** and **3^I**

3^{Br}	<i>v</i> / Vs ⁻¹	<i>E</i> _{1/2} /V	<i>i</i> _{pf} / <i>i</i> _{pr}	<i>E</i> _{pf} /V	ΔE_P	3^I	<i>v</i> / Vs ⁻¹	<i>E</i> _{1/2} /V	<i>i</i> _{pf} / <i>i</i> _{pr}	<i>E</i> _{pf} /V	ΔE_P
1 st Ox	0.05	-0.05	1.11	-0.007	0.086	0.05	0.01	1.07	0.050	0.075	
	0.10	-0.05	1.11	-0.007	0.086	0.10	0.01	0.96	0.050	0.082	
	0.25	-0.05	1.08	-0.003	0.093	0.25	0.01	1.00	0.054	0.086	
	0.50	-0.05	1.04	0.001	0.099	0.50	0.01	1.03	0.054	0.091	
	1.00	-0.05	1.06	0.006	0.111	1.00	0.01	0.99	0.58	0.102	
2 nd Ox	0.10	0.682	6.24	0.840	0.317	0.10	0.701	2.31	0.773	0.151	
1 st red						0.10	- ^a	-	-3.122	-	
						0.50	- ^a	-	-3.187	-	
						1.00	- ^a	-	-3.224	-	

^a no reverse wave

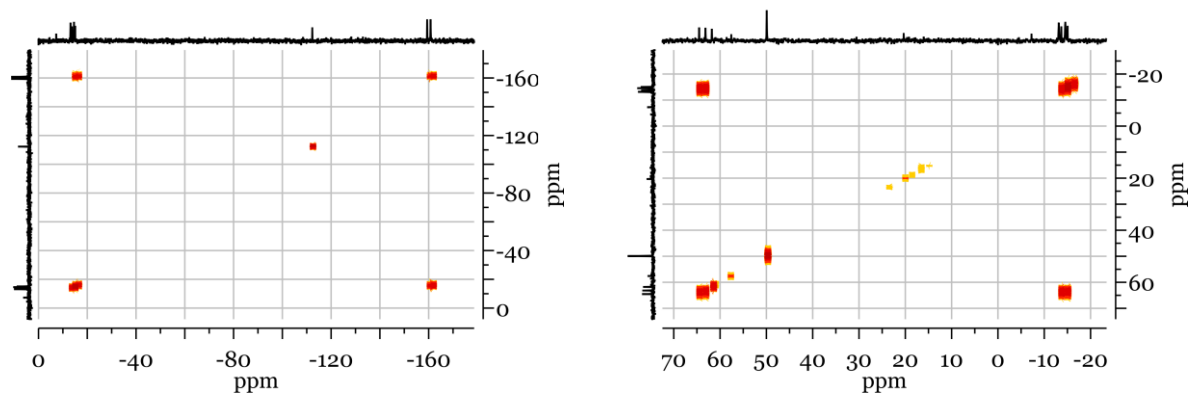


Figure A13. ^{31}P - ^{31}P COSY spectrum of the solution after reduction of 1^{Br} in d_8 -THF at -75°C . Left: region from 0 to -180 ppm showing 2^{Br} . Right: region of -30 to $+70$ ppm.

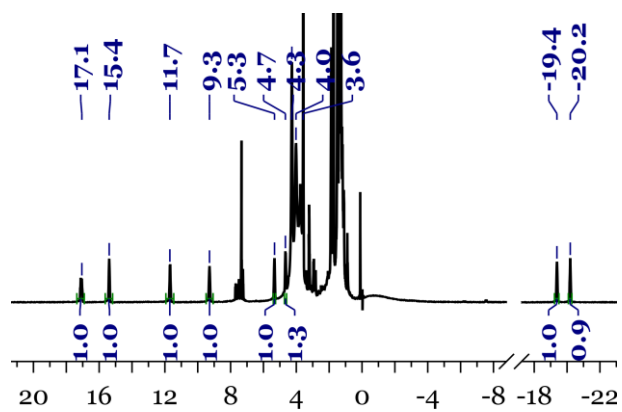


Figure A15. ^1H NMR spectroscopy of 2^{Br} in d_8 -THF at -30°C .

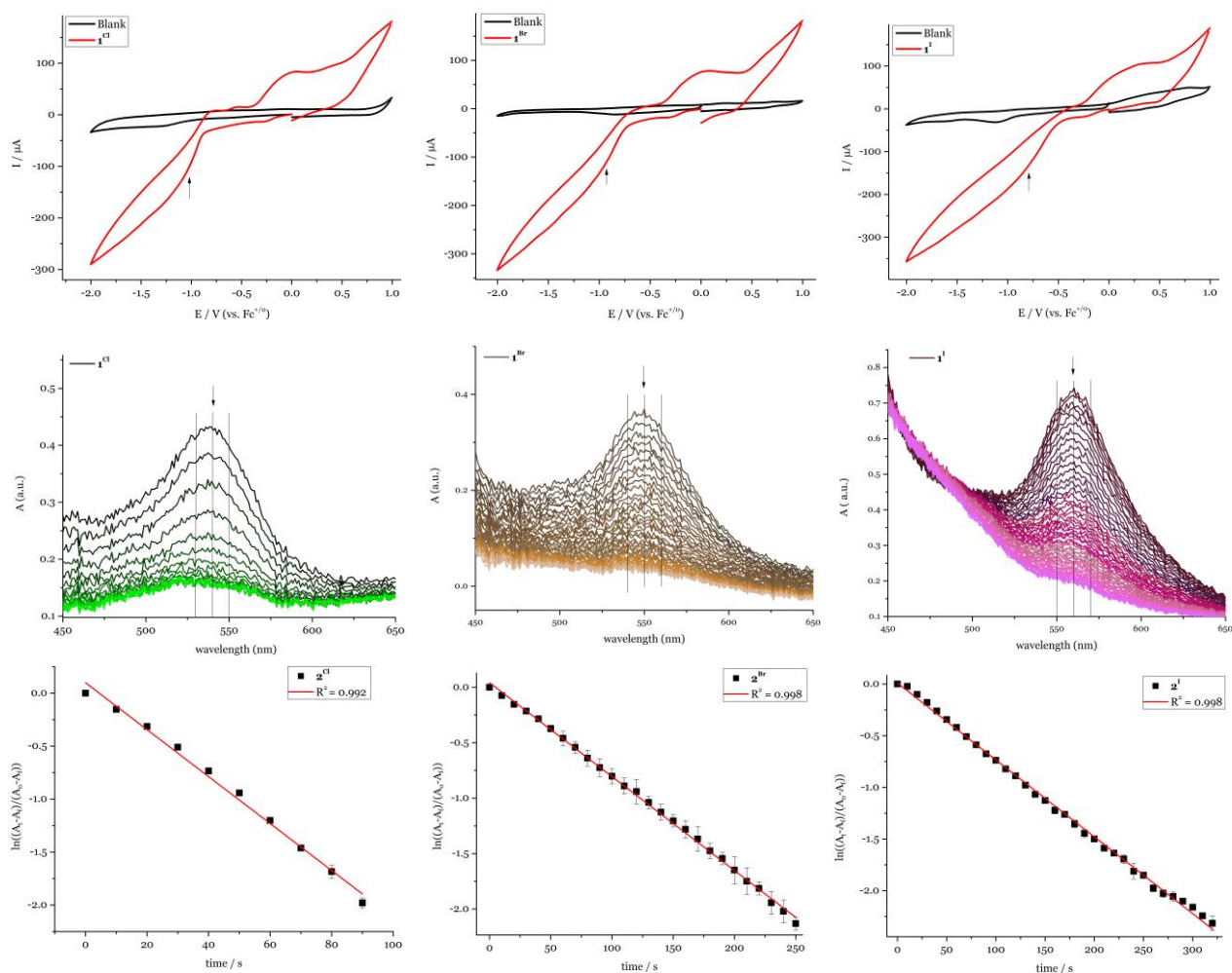


Figure A15. Top: CV traces of blank solutions and 1^{X} -solutions, to determine the CPE potential for the UVvis SEC experiments. Top left: 1^{Cl} , CPE at $E_{\text{appl.}} = -1.0$ V vs. Ag-wire. Top middle: 1^{Br} , CPE at $E_{\text{appl.}} = -0.9$ V vs. Ag-wire. Top right: 1^{I} , CPE at $E_{\text{appl.}} = -0.8$ V vs. Ag-wire. Middle: UV-vis traces of the decay of 2^{X} with the three lines on which the decay was measured to cancel the noise from the data. Each line represent 10 seconds reaction time. Middle left: 2^{Cl} , Middle middle: 2^{Br} , Middle right: 2^{I} . Bottom: An exemplary plot of $\ln((A_t - A_f)/(A_0 - A_f))$ vs. time of 2^{X} to abstract the half-life time. Bottom left: 2^{Cl} , bottom middle: 2^{Br} , bottom right: 2^{I} .

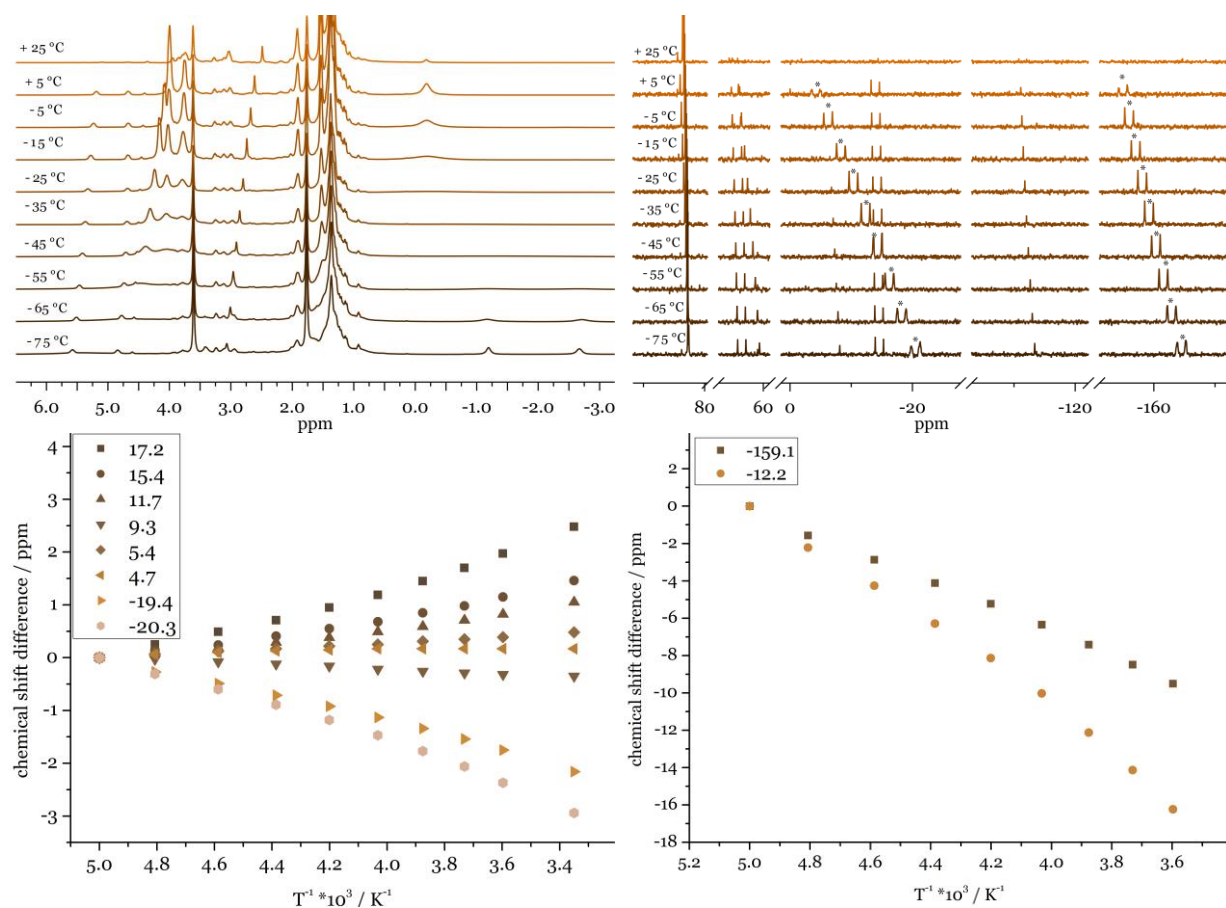


Figure A16. VT-NMR of 2^{Br} in d_8 -THF from -75°C to $+25^\circ\text{C}$. Top left: ^1H NMR spectrum, zoom of the *tert*-butyl region. Top right: $^{31}\text{P}\{^1\text{H}\}$ NMR spectrum. 2^{Br} is indicated with an asterisk. Bottom left: Chemical shift difference vs. $T^{-1} \cdot 10^3$ for the CH_2 -backbone signals. Bottom right: Chemical shift difference vs. $T^{-1} \cdot 10^3$ for the phosphorous signals. For the two last mentioned figures: a positive shift indicates an upfield shift and the values in the legend refers to the chemical shift at -30°C .

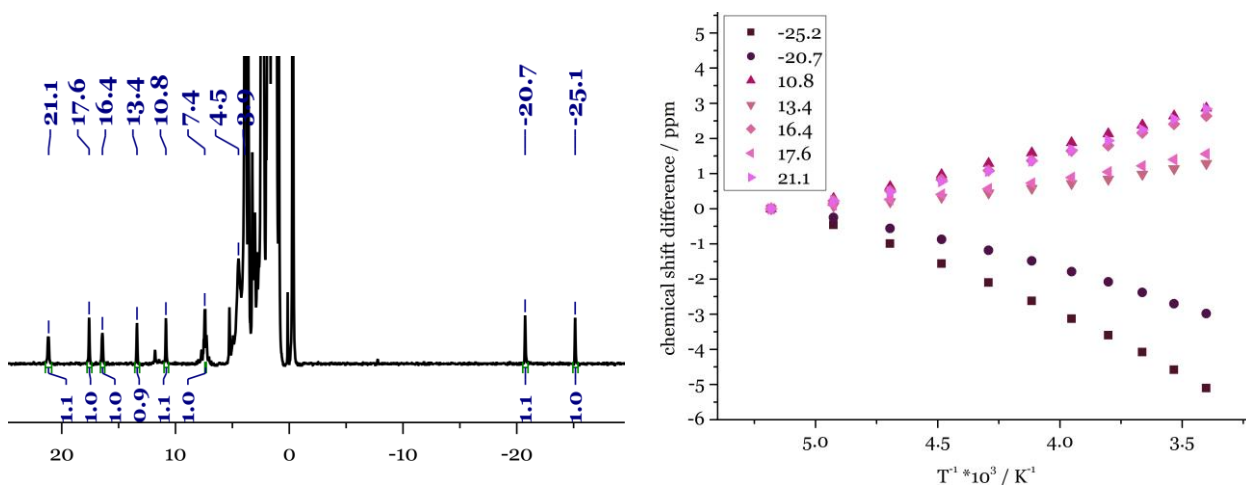


Figure A17. Left: ^1H NMR spectroscopy of 2^{I} in d_8 -THF at -30°C . Right: Chemical shift difference vs. $T^{-1} \cdot 10^3$ for the CH_2 -backbone signals extracted from VT-NMR of 2^{I} in d_8 -THF from -75°C to $+25^\circ\text{C}$. A positive shift indicates an upfield shift and the values in the legend refers to the chemical shift at -30°C .

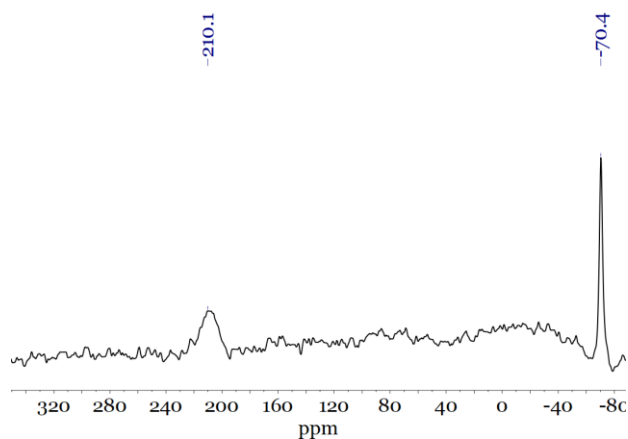


Figure A18. ^{14}N NMR spectrum of 2^{Cl} in d_8 -THF at -30°C . The signal at -70.4 ppm is dissolved N_2 .

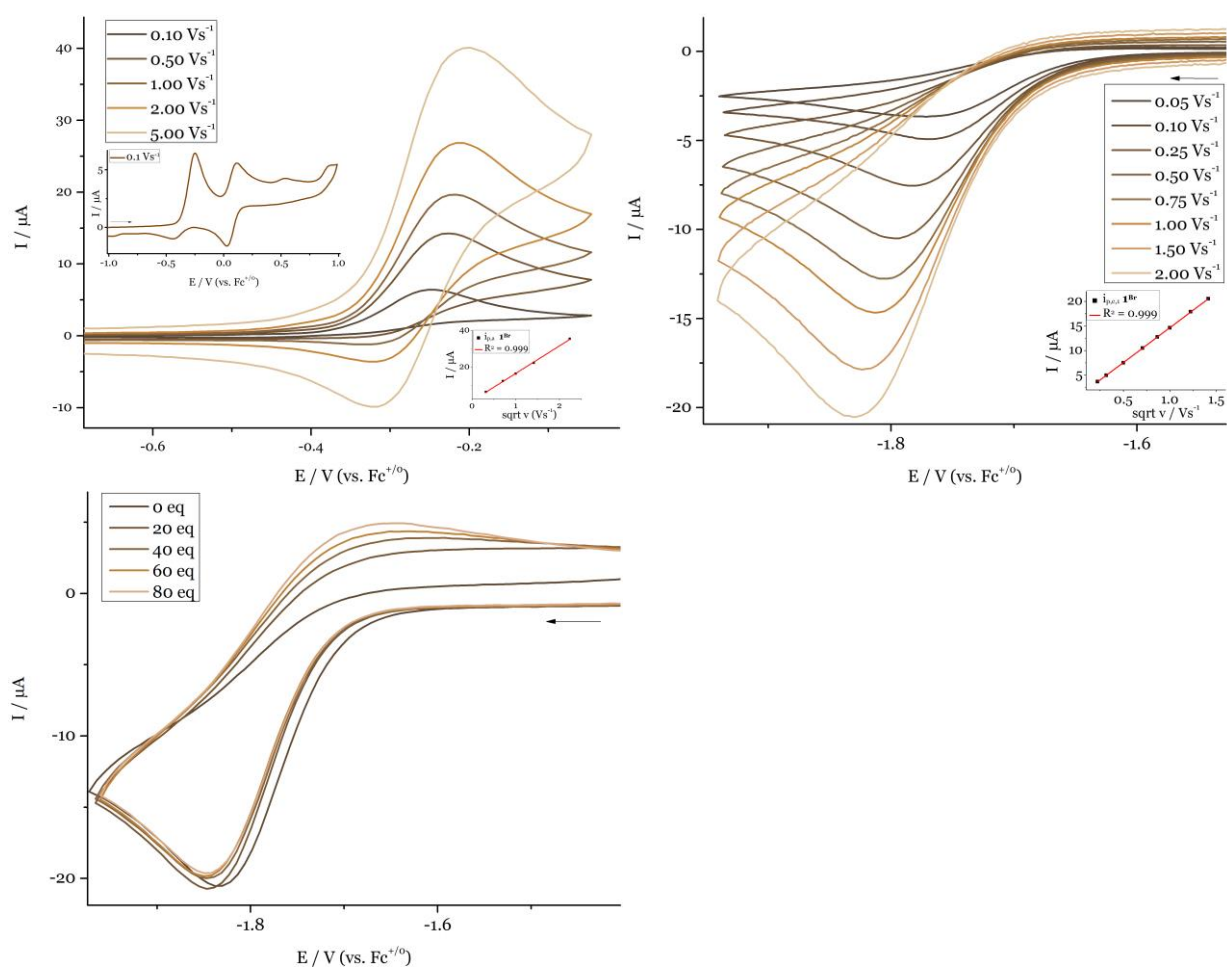


Figure A19. CV data of 1.0 mM 1^{Br} solutions in THF with 0.2 M $(n\text{Bu}_4\text{N})\text{PF}_6$ under Ar. Top left: v -dependent data of the first oxidation wave and the whole oxidative area at $v = 0.1$ Vs^{-1} . Inset: plot of $i_{\text{p},\text{a},1}$ vs. $v^{1/2}$. Top right: v -dependent data of the first reduction wave of a 1.0 mM solution. Inset: plot of $i_{\text{p},\text{c},1}$ vs. $v^{1/2}$. Bottom left: first reductive wave with addition of 0 - 80 eq. of $(n\text{He}_4\text{N})\text{Br}$, $v = 2.0$ Vs^{-1} .

Table A8. CV Peak analysis of $\mathbf{1^{Br}}$ under Ar.

$\mathbf{1^{Br}}$	$E_{1/2}$ /V	i_{pf}/i_{pr}	E_{pf} /V	ΔE_P /V	$E_{1/2}$ /V	i_{pf}/i_{pr}	E_{pf} /V	ΔE_P /V
v / Vs^{-1}								
0.05	1 st Red ^a	b	-1.770		2 nd Red	b	-2.199	
0.10		b	-1.776			b	-2.214	
0.25		b	-1.788			b	-2.233	
0.50		b	-1.803			b	-2.252	
0.75		b	-1.820			b	-2.263	
1.00		b	-1.828			b	-2.272	
2.00		b	-1.839			b	-2.287	
	1 st Ox				2 nd Ox			
0.10		b	-0.246		+0.082	1.86	+0.126	0.088
0.50		b	-0.266		+0.083	1.18	+0.129	0.093
1.00	-0.276	3.1	-0.216	115	+0.080	1.14	+0.131	0.102
2.00	-0.267	2.3	-0.212	111	+0.081	1.05	+0.134	0.105
5.00	-0.260	1.9	-0.201	117				

^a The peak potential of the 1st reduction of the different scan rates represents the average of six runs with a standard deviation around 0.025 V. ^b no reverse wave.

Table A9. Referencing v-dependent data of $\mathbf{1^{Br}}$ under Ar and N₂ using Fc* as reference compound.

$\mathbf{1^{Br}}$	v / Vs^{-1}	E_p / V						
		0.05	0.10	0.25	0.5	0.75	1.0	2.0
$E_p, \text{Ar} / \text{V}$		-1.777	-1.782	-1.795	-1.808	-1.822	-1.835	-1.846
		-1.769	-1.777	-1.795	-1.811	-1.829	-1.838	-1.847
		-1.748	-1.750	-1.765	-1.784	-1.804	-1.818	-1.828
		-1.743	-1.751	-1.761	-1.778	-1.794	-1.804	-1.815
		-1.811	-1.822	-1.832	-1.839	-1.851	-1.862	-1.872
		-1.770	-1.771	-1.782	-1.797		-1.811	-1.829
$E_p, \text{N}_2 / \text{V}$		-1.751	-1.757	-1.776	-1.802	-1.826	-1.838	-1.852
			-1.718	-1.735	-1.752	-1.776		-1.802
		-1.744	-1.747	-1.758	-1.781	-1.826		
		-1.712	-1.739	-1.761	-1.778	-1.801		
		-1.728	-1.741	-1.758	-1.776	-1.798	-1.813	-1.824
		-1.696	-1.709	-1.718		-1.737	-1.755	-1.779
Averaged								
$E_p, \text{Ar} / \text{V}$		-1.770	-1.776	-1.788	-1.803	-1.820	-1.828	-1.839
(st.dev)		(22)	(24)	(24)	(20)	(20)	(19)	(18)
$E_p, \text{N}_2 / \text{V}$		-1.726	-1.735	-1.751	-1.778	-1.794	-1.802	-1.814
(st. dev)		(20)	(17)	(19)	(16)	(31)	(35)	(27)

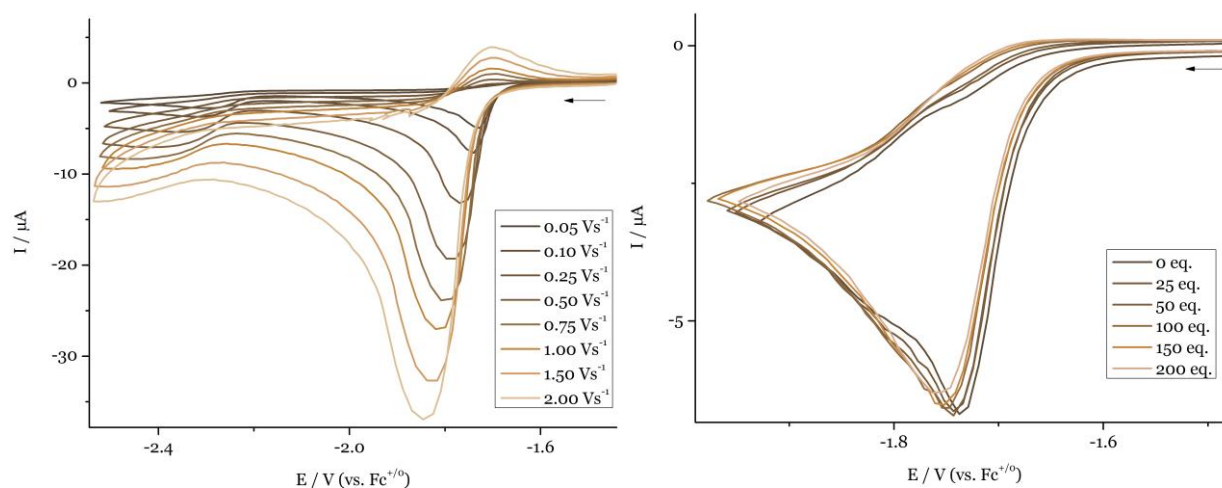
**Figure A20.** CV data of 1.0 mM $\mathbf{1^{Br}}$ solutions in THF with 0.2 M $(n\text{Bu}_4\text{N})\text{PF}_6$ under N_2 . Left: v-dependent data of the reduction area. Right: first reductive wave with addition of 0-200 eq. of $(n\text{He}_4\text{N})\text{Br}$, $v = 0.1 \text{ Vs}^{-1}$.

Table A10. CV Peak analysis of **1^{Br}** under N₂.

1^{Br}	$E_{1/2}$ /V	i_{pf}/i_{pr}	E_{pf} /V	ΔE_P /V	$E_{1/2}$ /V	i_{pf}/i_{pr}	E_{pf} /V	ΔE_P /V
v / Vs^{-1}								
0.05	<i>1st Red^a</i>	b	-1.726		<i>2nd Red</i>	b	-2.286	
0.10		b	-1.735			b	-2.306	
0.25		b	-1.751			b	-2.343	
0.50		b	-1.778			b	-2.370	
0.75	-1.758	25.5	-1.794	121		b	-2.380	
1.00	-1.759	8.6	-1.802	130				
2.00	-1.767	9.0	-1.814	152				

^a The peak potential of the 1st reduction of the different scan rates represent the average of six runs with a standard deviation around 0.025 V. ^b no reverse wave.

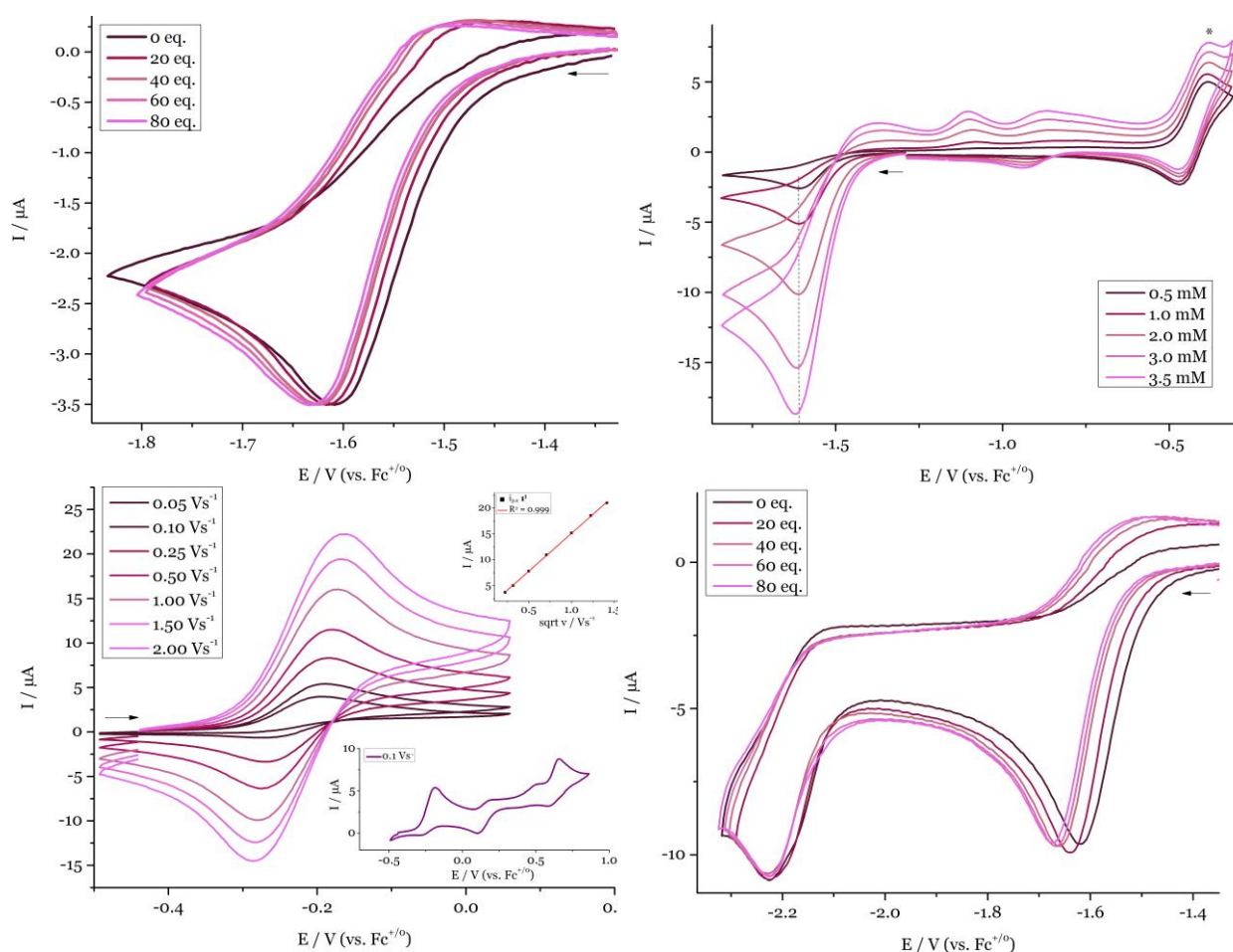


Figure A21. CV data of **1** in THF with 0.2 M (nBu₄N)PF₆ under Ar. Fc* is indicated with an asterisk. Top left: first reduction wave of a 0.8 mM solution with 0–80 eq. of (nHe₄N)I, $v = 0.1 \text{ Vs}^{-1}$. Top right: concentration dependence of the first reductive wave from 0.5 mM to 3.5 mM. Bottom left: oxidative area of a 1.0 mM solution. Inset: plot of $i_{p,a,1}$ vs. $v^{1/2}$. Bottom right: first two reduction waves of a 0.8 mM solution with 0–80 eq. of (nHe₄N)I, $v = 0.1 \text{ Vs}^{-1}$.

Table A11. CV Peak analysis of **1^I** under Ar.

1^I	$E_{1/2}$ /V	i_{pf}/i_{pr}	E_{pf} /V	ΔE_P /V	$E_{1/2}$ /V	i_{pf}/i_{pr}	E_{pf} /V	ΔE_P /V
v / Vs⁻¹								
0.05	<i>1st Red^a</i>	b	-1.598		<i>2nd Red</i>	b	-2.234	
0.10		b	-1.609			b	-2.235	
0.25		b	-1.621			b	-2.243	
0.50		b	-1.633		-2.194	3.65	-2.257	0.122
1.00		b	-1.648		-2.206	4.28	-2.269	0.144
1.50		b	-1.656		-2.207	3.17	-2.278	0.143
2.00		b	-1.662		-2.209	3.44	-2.286	0.154
3.00		b	-1.672					
	<i>1st Ox</i>				<i>2nd Ox</i>			
0.05		b	-0.192			b	+0.645	
0.10	-0.231	3.07	-0.187	0.089		b	+0.655	
0.25	-0.227	1.41	-0.184	0.085		b	+0.679	
0.50	-0.228	1.11	-0.180	0.095		b	+0.699	
1.00	-0.227	1.05	-0.173	0.108		b	+0.720	
1.50	-0.225	0.99	-0.168	0.115		b	+0.733	
2.00	-0.225	1.02	-0.164	0.122		b	+0.743	

^a The peak potential of the 1st reduction of the different scan rates represent the average of 6 runs with a standard deviation around 0.015 V. ^b no reverse wave.

Section A4.1 Referencing challenges for iodide titrations on **1^I**

To probe whether reduction of **1^I** is coupled to iodide loss, it was aimed to titrate in increasing equivalents of (*n*He₄N)I. Nicewicz reported the value for I⁻ oxidation to be at $E_p = -0.14$ V in acetonitrile.²²⁰ In THF however, I⁻ oxidation occurs at circa -0.4 V, which is too close to the commonly used Fe^{III/II} oxidation couple of Fc* for referencing of the CVs ($E_{1/2} = -0.427$ V). At high iodide concentrations (≥ 0.04 M), the I⁻ oxidation shifts more anodically and merges into the Fc* oxidation (see Figure A21). In search for another referencing possibility, we first tried coordination compounds that have a reversible oxidation or reduction wave more electronegative as I⁻ oxidation, and more electropositive as the reduction of **1^I** ($E_p = -1.61$ V, $\nu = 0.1$ Vs⁻¹). Starting with other Cp-ring containing compounds as possible reference, we found the current of the reference decreased upon increasing halide concentration, as exemplified for Cr(Cp)₂ in Figure A21, which was reproduced multiple times. The cathodic potential shift on **1^I** as showed in this example varied for each measurement and is not trustworthy. We attribute this current decrease to partial decomposition, maybe due to slow iodide coordination or Cp for I substitution. Clearly, these compounds are not inert and therefore not suitable as reference compounds. In addition to this behaviour, when exploring Co(Cp)₂, a current decrease on **1^I** upon initial addition of this reference compound was observed, attributed to partial reduction of **1^I**.

For next attempts, we turned away from Cp ligands towards coordination compounds containing bulky ligands and being coordinatively unsaturated to hopefully obtain more inert complexes. We synthesised [Co(tpy)₂](PF₆)₂ (tpy = 2,2':6',2''-terpyridine),²²¹ [Fe(PDI)(CO)₂] (PDI = 2,6-

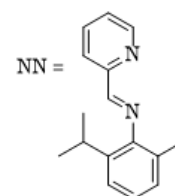
bis[1-(2,6-diisopropylphenylimino)methyl]pyridine),²²² [Ni(NN)₂] (NN = 2,6-bis(1-methylethyl)-N-(2-pyridinylmethylene)phenylamine, and is depicted in Table A11)²²³ according to their literature procedures and [Fe(acac)₃] (acac = acetylacetonate) was commercially obtained. However, all compounds proved either to be not inert or reversible enough. The reduction of [Fe(acac)₃] is only reversible at low ν , due to reversible loss of a acac ligand. In case of [Co(tpy)₂](PF₆)₂, small reduction features at $E_p = -1.33$ V and -1.69 V appear directly after addition of **1**^I, and over time the current of the reference decreases. The redox features of [Ni(NN)] completely disappear upon addition of **1**^I, likely due to its reactive character. Finally, the oxidation of [Fe(PDI)CO₂] becomes irreversible upon addition of (nHe₄N)I, attributed to iodide coordination.

As final attempt, stable RE systems were explored based on both silver and Fc. In case of silver, a stable Ag^{+/0} was aimed for by dissolving 1.0 mM AgPF₆ (AgNO₃ is not soluble in THF) in a Ag-wire loaded sample holder. After soaking in the SH for 1-2 days in the dark, this Ag^{+/0}/Ag RE was tested on the titration of (nHe₄N)Cl into a solution of **1**^{Cl}: for this experiment both the potential shift and the increased reversibility are quantified. As shown in Figure A21, this RE is not stable, since the peak potential shifts too large and the reverse wave barely increases. To improve its stability, the Ag⁺ concentration should have likely been increased. Overall, most promising is the RE based on a solution of both 4 mM Fc and 4 mM [Fc]BAR₂₄.²²⁴ In the chloride titration experiment on **1**^{Cl}, we do observe the expected increased reversibility and a cathodic peak potential shift, although the latter is less extended compared to the reference experiment. In addition, the absolute referencing was repeatedly off: it shows an E_p of -1.95 V at $\nu = 0.1$ Vs⁻¹, which is about 0.05 V too electropositive. The same behaviour was observed in the initial attempts to use this Fc^{+/0} RE for **1**^I. Therefore, we discarded this possibility for referencing the iodide titration of **1**^I.

Table A12. Overview of the explored referencing methods for referencing I⁻ titration of **1**^I.

Coordination compound or method ^a	Potential / V
Ag ^{+/0} (1 mM)	+0.20
Fc ^{+/0} (4 mM)	0.00
[Fe(PDI)(CO) ₂]	-0.47
[Cr(Cp) ₂] ^{+/0}	-1.10
[Co(tpy) ₂] ^{2+/+}	-1.10
[Ni(NN) ₂]	-1.18
[Cr(Cp*)(C ₆ H ₆)] ^{+/0}	-1.20
[Fe(acac) ₃]	-1.24
[Co(Cp) ₂] ^{+/0}	-1.32
[Co(Cp*) ₂] ^{+/0}	-1.84

^a abbreviations, see text.



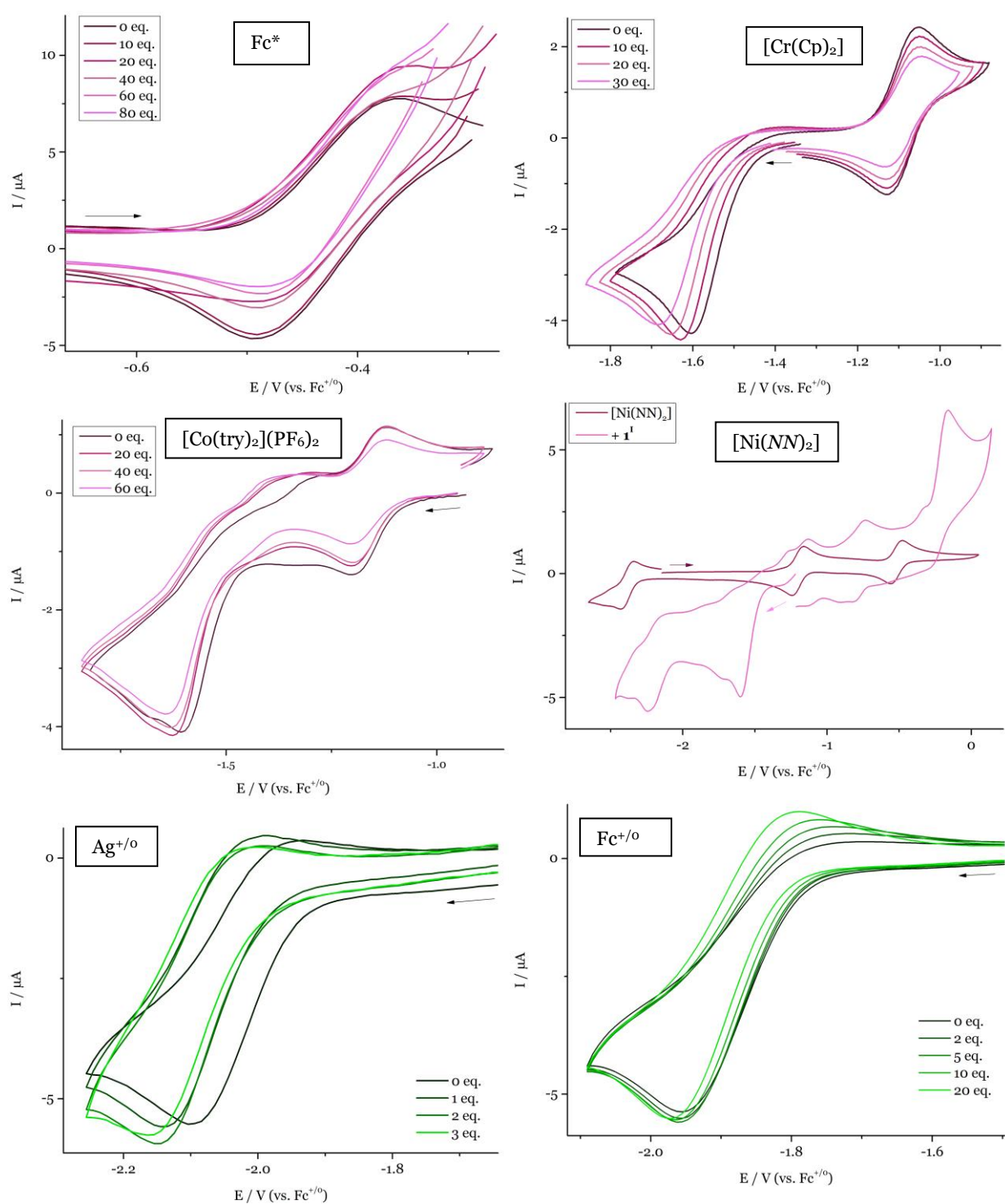


Figure A21. Different reference compounds or methods aiming for referencing the iodide titration to 1^I , all data under Ar containing 0.2 M $(n\text{Bu}_4\text{N})\text{PF}_6$ in THF. Top left: Fc^* in iodide titration of 1^I . Top right: $[\text{Cr}(\text{Cp})_2]$ in iodide titration of 1^I . Middle left. $[\text{Co}(\text{trp})_2](\text{PF}_6)_2$ in iodide titration of 1^I . Middle right: $[\text{Ni}(\text{NN})_2]$ and 1^I . Bottom left: $\text{Ag}^{+/0}$ RE in chloride titration of 1^{Cl} . Bottom right: $\text{Fc}^{+/0}$ RE in chloride titration of 1^{Cl} . Abbreviations are found in the text of Section A4.1.

Expanding our potential window in looking for references, we assessed the possibility of $[\text{Co}(\text{Cp}^*)_2]\text{PF}_6$ to be a reference compound, having a reduction at $E_{1/2} = -1.84$ V, clearly more electronegative as **1**^I. Fortunately, this reference proved stable, showing barely any current varieties. In Figure A22 a experiment under N_2 is shown, where the current of the reference does decrease upon increasing equivalents of iodide. However, this current decrease is fairly parallel to the iodide-induced decrease of the second reduction feature: the base-line corrected current of the second reduction of **1**^I is decreased by circa 1.2, 0.5, 0.8, 0.5, 1.4 μA from 0 to 150 eq. of $(n\text{He}_4\text{N})\text{I}$ at $v = 0.1$ Vs^{-1} , whereas the peak current of the reference is decreased by circa 0.9, 0.6, 0.7, 0.6, 1.4 μA . The peak potential of the reverse peak of the reference was not always analysed easy leading to a certain noisiness in the experiment, it was reproduced at least five times, see Table A12 for these data under an Ar- and in Table A13 under a N_2 atmosphere. After determining the average peak potential value and its standard deviation, these values were transferred to a CV without added $[\text{Co}(\text{Cp}^*)_2]\text{PF}_6$.

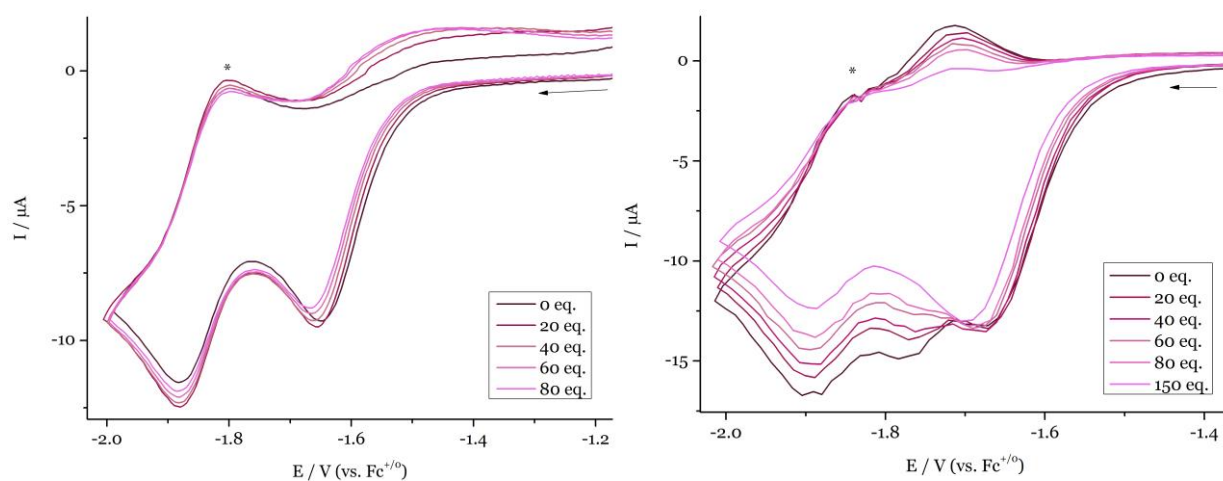


Figure A22. Iodide titration of a 0.8 mM solution of **1**^I containing 0.2 M $(n\text{Bu}_4\text{N})\text{PF}_6$ in THF using $[\text{Co}(\text{Cp}^*)_2]\text{PF}_6$ as reference, marked with an asterisk. $v = 1.0$ Vs^{-1} . Measured under a Ar (left) or N_2 (right) atmosphere.

Table A13. Peak shifts upon iodide titration on **1**¹ as referenced using [Co(Cp*)₂]PF₆, under Ar, reproduced several times.

1 ¹	eq. (nHe ₄ N)I										
	0	20	40	60	80	0	20	40	60	80	
v / V _S ⁻¹						v / V _S ⁻¹					
0.10	-1.621	-1.636	-1.645	-1.645	-1.654	0.25	-1.637	-1.647	-1.651	-1.659	-1.658
	-1.616	-1.627	-1.627	-1.629	-1.633		-1.660	-1.667	-1.668	-1.673	-1.676
	-1.616	-1.626	-1.632	-1.631	-1.637		-1.653	-1.647	-1.658	-1.667	-1.666
	-1.632	-1.637	-1.645	-1.650	-1.654		-1.644	-1.655	-1.658	-1.658	-1.659
	-1.624	-1.634	-1.637	-1.646	-1.651						
	-1.647	-1.658	-1.669	-1.675	-1.681						
	-1.647	-1.647	-1.655	-1.658	-1.663						
	-1.634	-1.645	-1.654	-1.655	-1.658						
0.50	-1.639	-1.644	-1.652	-1.657	-1.662	1.00	-1.649	-1.656	-1.662	-1.664	-1.668
	-1.642	-1.644	-1.650	-1.650	-1.652		-1.661	-1.666	-1.672	-1.673	-1.679
	-1.649	-1.657	-1.661	-1.667	-1.669		-1.659	-1.665	-1.664	-1.668	-1.670
	-1.646	-1.652	-1.658	-1.659	-1.665		-1.684	-1.687	-1.693	-1.694	-1.701
	-1.657	-1.658	-1.660	-1.663	-1.665		-1.664	-1.670	-1.670	-1.675	-1.677
2.00	-1.652	-1.666	-1.671	-1.673	-1.678	3.00	-1.666	-1.674	-1.679	-1.681	-1.684
	-1.674	-1.682	-1.686	-1.687	-1.692		-1.681	-1.687	-1.688	-1.691	-1.692
	-1.674	-1.675	-1.678	-1.675	-1.682		-1.678	-1.680	-1.683	-1.683	-1.684
	-1.700	-1.702	-1.705	-1.710	-1.712		-1.704	-1.712	-1.712	-1.713	-1.718
	-1.677	-1.678	-1.678	-1.683	-1.687		-1.681	-1.685	-1.690	-1.691	-1.694
shifts /V (st.dev)											
	20 eq.	40 eq.	60 eq.	80 eq.							
0.10	9(3)	16(4)	20(5)	26(6)							
0.25	8(3)	10(4)	16(4)	16(3)							
0.50	4(3)	10(4)	13(5)	16(6)							
1.00	5(1)	9(3)	11(2)	16(3)							
2.00	5(5)	8(6)	10(7)	15(7)							
3.00	6(2)	8(3)	10(3)	12(4)							

Table A15. Peak shifts upon iodide titration on **1¹** as referenced using [Co(Cp^{*})₂]PF₆, under N₂, reproduced several times.

1¹	eq. (nHe ₄ N)I										
	0	40	60	80	100	0	40	60	80	100	
v / V _s ⁻¹						v / V _s ⁻¹					
0.10	-1.597	-1.602	-1.602	-1.609	-1.612	0.25	-1.611	-1.617	-1.614	-1.621	-1.630
	-1.582	-1.590	-1.592	-1.594	-1.599		-1.594	-1.604	-1.605	-1.610	-1.614
	-1.618	-1.626	-1.630	-1.631			-1.637	-1.638	-1.648	-1.655	
	-1.594	-1.598	-1.604	-1.607	-1.615		-1.609	-1.614	-1.622	-1.621	-1.630
	-1.575	-1.580	-1.584	-1.588	-1.586		-1.587	-1.591	-1.594	-1.603	-1.602
	-1.618	-1.622	-1.626	-1.629	-1.633		-1.629	-1.634	-1.637	-1.639	-1.648
0.50	-1.622	-1.629	-1.632	-1.633	-1.643	1.0	-1.639	-1.640	-1.648	-1.652	-1.658
	-1.606	-1.610	-1.615	-1.619	-1.623		-1.618	-1.622	-1.625	-1.631	-1.634
	-1.649	-1.660	-1.667	-1.669			-1.671	-1.671	-1.674	-1.689	
	-1.628	-1.635	-1.635	-1.640	-1.641		-1.644	-1.648	-1.655	-1.656	-1.664
	-1.600	-1.602	-1.602	-1.610	-1.617		-1.613	-1.616	-1.621	-1.627	-1.629
	-1.644	-1.649	-1.649	-1.651	-1.659		-1.655	-1.658	-1.659	-1.659	-1.666
2.0	-1.646	-1.650	-1.653	-1.662	-1.671	3.0	-1.671	-1.676	-1.681	-1.692	-1.694
	-1.642	-1.642	-1.647	-1.650	-1.654		-1.650	-1.650	-1.656	-1.659	-1.661
	-1.697	-1.708	-1.712	-1.715			-1.678	-1.682	-1.689	-1.691	-1.700
	-1.668	-1.671	-1.679	-1.680	-1.689		-1.644	-1.645	-1.647	-1.651	-1.653
	-1.629	-1.630	-1.638	-1.645	-1.645		-1.692	-1.693	-1.700	-1.703	-1.708
	-1.681	-1.685	-1.687	-1.692	-1.694						
shifts /V (st.dev)											
	40 eq.	60 eq.	80 eq.	100 eq.							
0.10	9(2)	12(1)	17(3)	20(2)							
0.25	9(3)	14(3)	19(2)	25(3)							
0.50	9(5)	12(4)	18(4)	22(5)							
1.00	7(3)	12(4)	18(4)	24(2)							
2.00	9(3)	14(3)	18(5)	20(6)							
3.00	8(3)	12(5)	16(6)	21(5)							

Table A15. Referencing v-dependent data of **1^I** under Ar and N₂ using Fc* as reference compound.

1^I	v / Vs ⁻¹							
	0.05	0.10	0.25	0.5	0.75	1.0	2.0	3.0
E _p , Ar / V	-1.591	-1.600	-1.611	-1.623	-1.633	-1.639	-1.647	-1.664
	-1.632	-1.640	-1.650	-1.661	-1.670	-1.674	-1.689	-1.695
	-1.574	-1.586	-1.598	-1.614	-1.619	-1.625	-1.640	-1.655
	-1.592	-1.601	-1.615	-1.626	-1.634	-1.640	-1.656	-1.664
	-1.602	-1.609	-1.624	-1.637	-1.644	-1.655	-1.669	-1.678
	-1.599	-1.609	-1.627	-1.634		-1.652	-1.668	-1.675
E _p , N ₂ / V	-1.587	-1.593	-1.610	-1.632	-1.653	-1.670	-1.680	
	-1.569	-1.580	-1.590	-1.609	-1.619	-1.628	-1.648	-1.655
	-1.605	-1.612	-1.635	-1.635	-1.653	-1.668	-1.664	
	-1.587	-1.603	-1.620	-1.620	-1.640	-1.653		
	-1.584	-1.595	-1.611	-1.622	-1.642	-1.650		
	-1.588	-1.599	-1.616	-1.628	-1.639	-1.646		
Averaged								
	E _p , Ar / V (st.dev)	-1.598 (17)	-1.608 (16)	-1.621 (16)	-1.633 (15)	-1.640 (17)	-1.648 (15)	-1.662 (16)
E _p , N ₂ / V (st.dev)	-1.585 (11)	-1.595 (10)	-1.612 (13)	-1.626 (9)	-1.641 (11)	-1.650 (14)	-1.664 (13)	

Table A16. CV Peak analysis of **1^I** under N₂.

1^I	v / Vs ⁻¹	E _{1/2} / V	i _{pf} /i _{pr}	E _{pf} / V	ΔE _P / V	E _{1/2} / V	i _{pf} /i _{pr}	E _{pf} / V	ΔE _P / V
	0.05	b		-1.585		-1.691	0.60	-1.734	0.059
	0.10	b		-1.595		-1.683	0.60	-1.736	0.072
	0.25	b		-1.612		-1.693	0.88	-1.739	0.057
	0.50	b		-1.626		-1.689	^c	-1.747	0.068
	1.00	b		-1.650		-1.700	^c	-1.725	0.063
	2.00	b		-1.664		-1.703	^c	-1.724	0.059
	3.00	b				-1.706	^c	-1.733	0.062
		3 th Red		3 th Red					
	0.05	b		-2.194					
	0.10	b		-2.202					
	0.25	b		-2.219					
	0.50	b		-2.230					
	1.00	b		-2.250		b		-2.35	
	2.00	b		-2.263		b		-2.36	
	3.00	b		-2.265		b		-2.37	
		1 st Ox		2 nd Ox					
	0.05	-0.203	1.10	-0.161	0.082				
	0.10	-0.203	1.09	-0.160	0.085	b		+0.686	
	0.25	-0.203	1.06	-0.164	0.080				
	0.50	-0.204	1.02	-0.160	0.087	b		+0.712	
	1.00	-0.200	1.04	-0.157	0.082	b		+0.728	
	2.00					b		+0.741	

^a The peak potential of the 1st reduction of the different scan rates represent the average of six runs with a standard deviation around 0.015 V. ^b no reverse wave. ^c due to the close proximity of both reductions, no baseline drawing is possible.

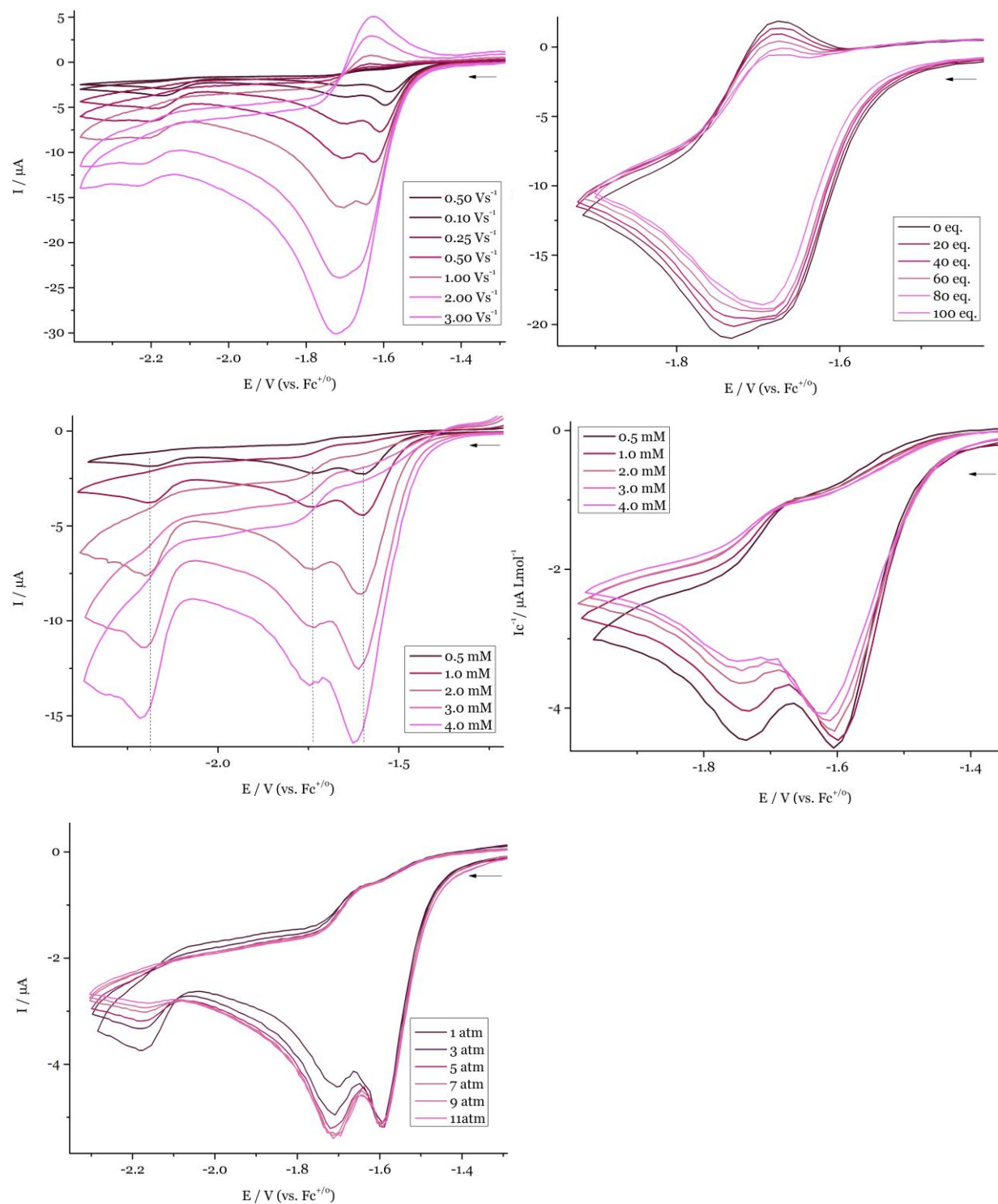


Figure A22. CV data of **1^I** in THF with 0.2 M (*n*Bu₄N)PF₆ under an N₂ atmosphere. Top left: scan rate dependent data of the whole reductive area. Top right: First two reduction waves of a 0.8 mM solution with 0-100 eq. of (*n*He₄N)I, $\nu = 2.0 \text{ Vs}^{-1}$. Middle left: concentration dependence of the whole reductive area from 0.5 mM to 4.0 mM, $\nu = 0.1 \text{ Vs}^{-1}$. Middle right: concentration normalised data of the first two reduction waves, $\nu = 0.1 \text{ Vs}^{-1}$. Bottom left: N₂-pressure dependent data of the whole reductive area of a 1.0 mM solution, $\nu = 0.1 \text{ Vs}^{-1}$.

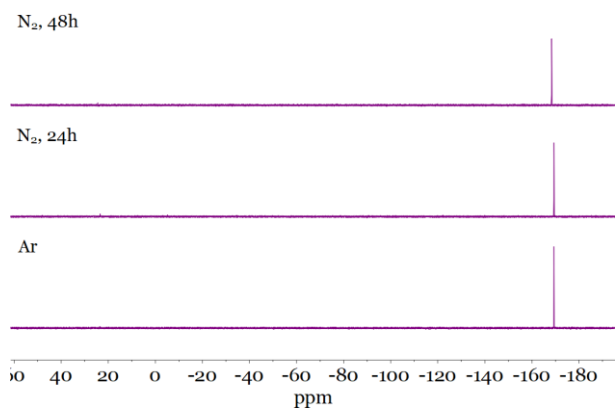


Figure A23. $^{31}\text{P}\{^1\text{H}\}$ NMR spectra of **1^I** under N_2 in THF over 48 h.

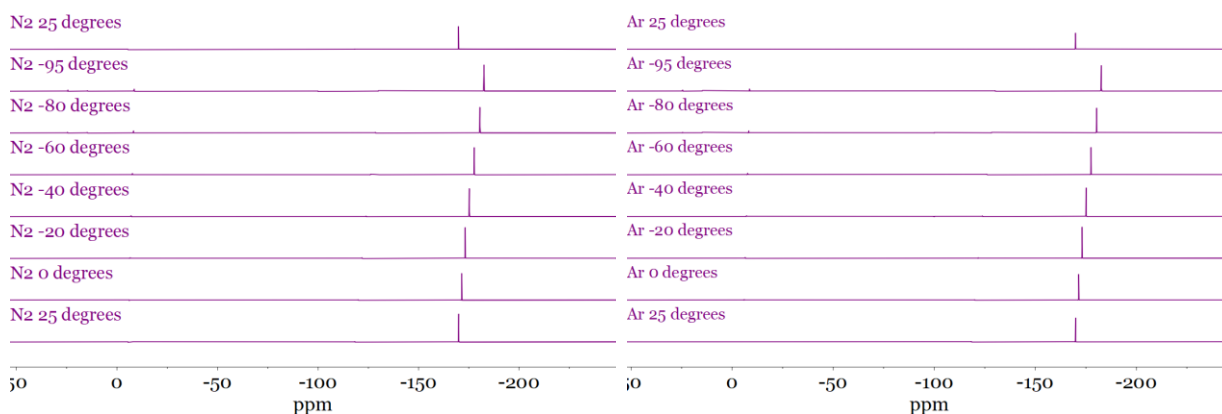


Figure A24. $^{31}\text{P}\{^1\text{H}\}$ NMR spectroscopy of **1^I** under N_2 or Ar (4 atm) in d_8 -THF from RT to $-95\text{ }^\circ\text{C}$ (and back to $25\text{ }^\circ\text{C}$). Left: N_2 . Right: Ar.

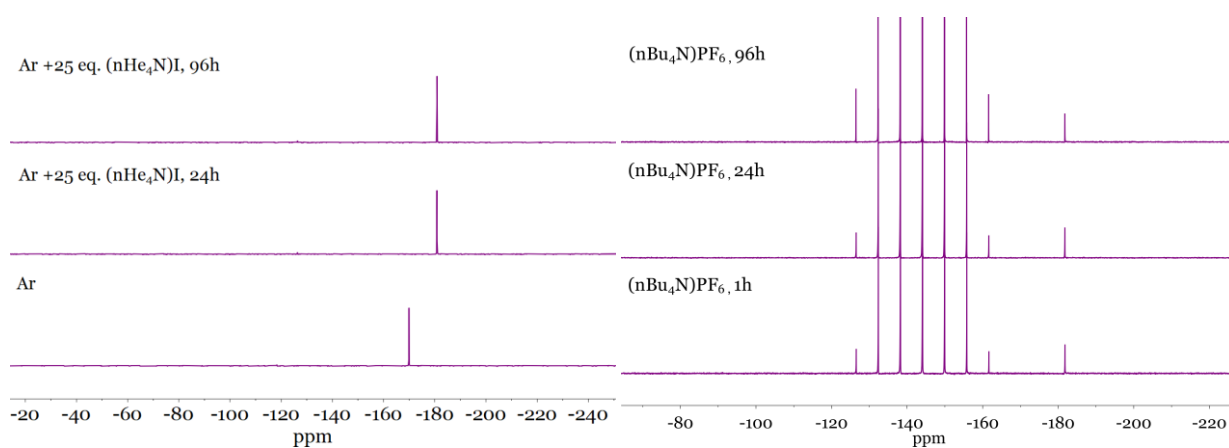


Figure A25. $^{31}\text{P}\{^1\text{H}\}$ NMR spectra of **1^I** under Ar in THF 25 eq. of $(n\text{He}_4\text{N})\text{I}$ over the course of 96 h (left) or 50 eq. $(n\text{Bu}_4\text{N})\text{PF}_6$ (right). Upon addition of the iodide source, an upfield shift of circa 10 ppm is observed, which is only due to the presence of ions, as proven by a similar upfield shift from -170 to -180 ppm upon addition of electrolyte.

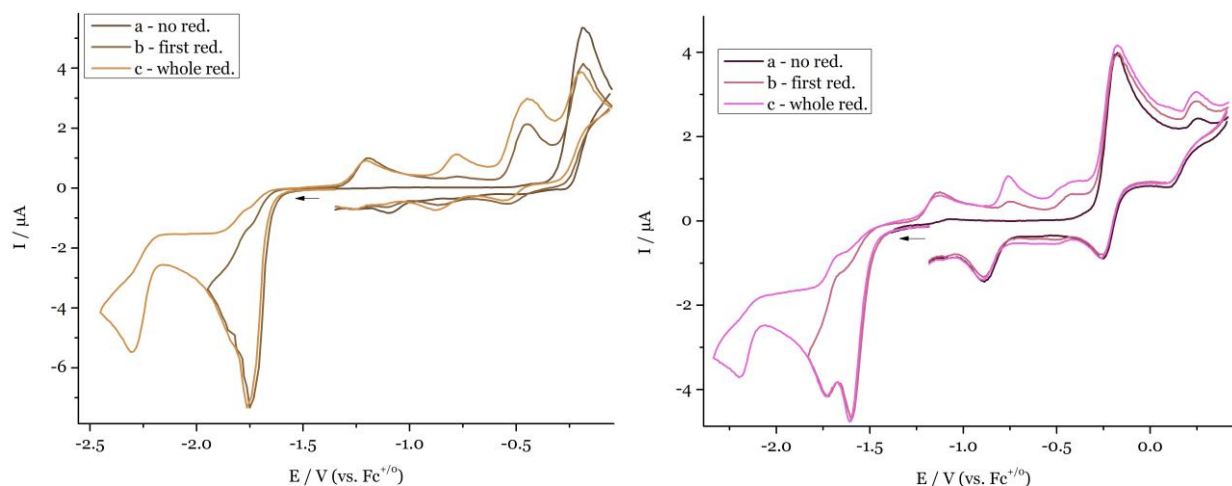


Figure A26 CV of a 1.0 mM solution of $\mathbf{1}^X$ in THF with 0.2 M $(n\text{Bu}_4\text{N})\text{PF}_6$ under an N_2 atmosphere. Measured three ranges, scanning through: a) only the oxidative area, b) the first reductive area, then the oxidative area, c) the whole reductive area, then the oxidative area. Left: $\mathbf{1}^{\text{Br}}$. Right: $\mathbf{1}^{\text{I}}$.

A5. Figures and tables of chapter II.3.

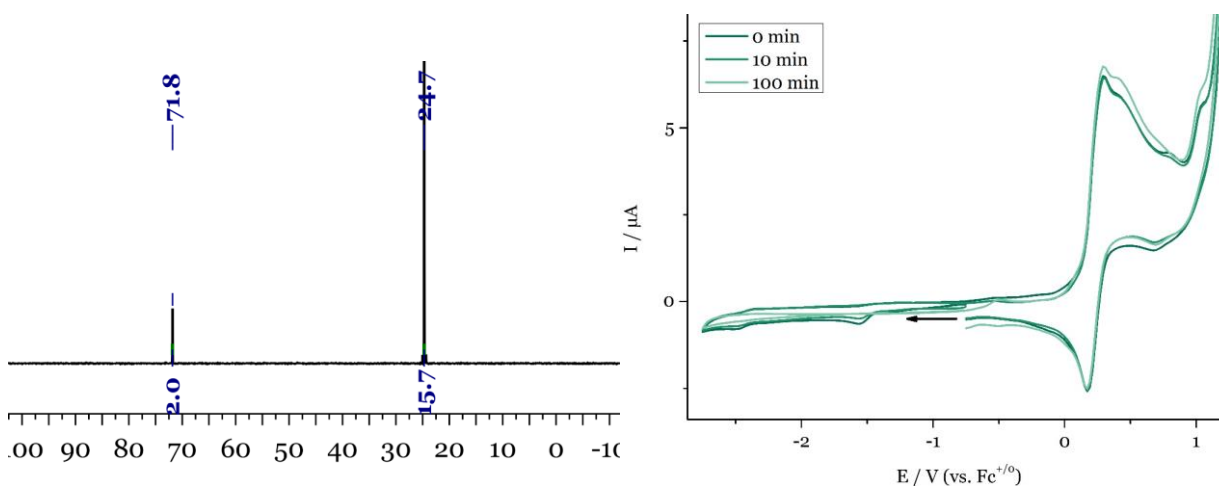


Figure A27. Left: $^{31}\text{P}\{^1\text{H}\}$ -NMR spectrum of $\mathbf{3}^{\text{Cl}}$ obtained via electrochemical reduction of $\mathbf{1}^{\text{Cl}}$ (1.0 mM) in THF at $E_{\text{appl.}} = -1.67\text{ V}$ with addition of 16.2 μmol PPh_3O as internal standard (signal at 24.7 ppm) used for yield determination (22%). Right: CPE of $\mathbf{3}^{\text{Cl}}$ at $E_{\text{appl.}} = -1.67\text{ V}$ in THF with 0.1 M $(n\text{Bu}_4\text{N})\text{PF}_6$ in presence of 1 eq. of $(n\text{He}_4\text{N})\text{Cl}$ for 100 min to check the stability of the nitride. The small, irreversible anodic feature at $E_p = +0.42\text{ V}$ is tentatively attributed to some contamination of the GC electrode, since from the same nitride, THF and electrolyte batch, CVs without this feature were obtained.

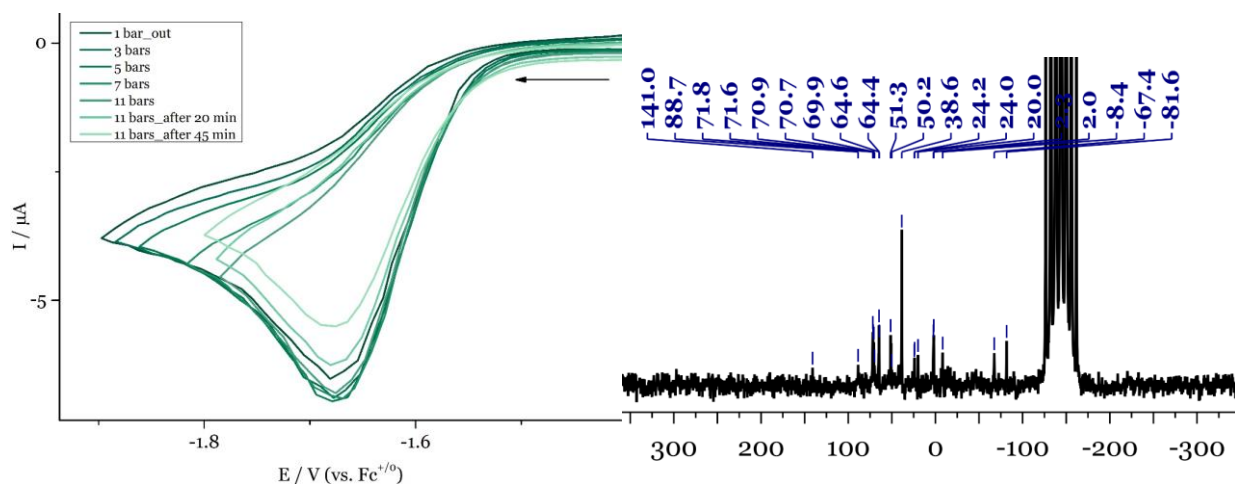


Figure A28. Left: CV of 1.2 mM $[1]Cl$ in THF with 0.2 M $(nBu_4N)PF_6$ at increasing pressures of N_2 . Right: $^{31}P\{^1H\}$ NMR spectrum of the reaction mixture of $[1]Cl$ in THF after measuring CV of at increasing N_2 pressures and remaining at 11 bars for 45 minutes and subsequent depressurising.

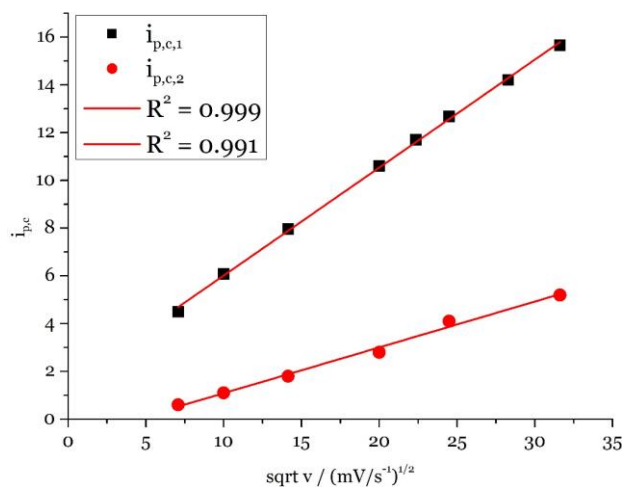


Figure A29. Plot of $i_{p,c,1}$ (black) and $i_{p,c,2}$ of $[1]Cl$ vs. $v^{1/2}$. The baseline for the second feature is hard to set; therefore this fitting has more uncertainty.

Table A17. CV Peak analysis of $[1]Cl$ under Ar.

$[1]Cl$	v / Vs^{-1}	E_{pf} / V	i_{pf} / μA		v / Vs^{-1}	E_{pf} / V	i_{pf} / μA
1 st red ^a	0.05	-1.726	4.5	2 nd red ^a	0.05	-1.948	0.6
	0.10	-1.750	6.1		0.10	-1.951	1.1
	0.20	-1.775	8.0		0.20	-1.968	1.7
	0.60	-1.827	12.7		0.60	-2.024	3.5
	0.80	-1.851	14.2		0.80	-2.050	4.3
	1.00	-1.861	15.7		1.00	-2.069	5.1

^a – no reverse wave.

Table A18. CV Peak analysis of the first reduction of =**1**^{Cl} in presence of different equivalents of (nBu₄N)Cl under Ar.

= 1 ^{Cl} , 0.5 Vs ⁻¹	<i>E</i> _{1/2} /V	<i>i</i> _{pf} / <i>i</i> _{pr}	<i>E</i> _{pf} /V	ΔE_p /V	= 1 ^{Cl} , 1.0 Vs ⁻¹	<i>E</i> _{1/2} /V	<i>i</i> _{pf} / <i>i</i> _{pr}	<i>E</i> _{pf} /V	ΔE_p /V
(nBu ₄ N)Cl / eq.									
0	-	-	-1.826	-	-	-	-	-1.922	-
10	-1.74	8	-1.834	0.19	-1.78	2.4	-1.929	0.28	
20	-1.75	3.7	-1.837	0.17	-1.80	1.9	-1.934	0.27	

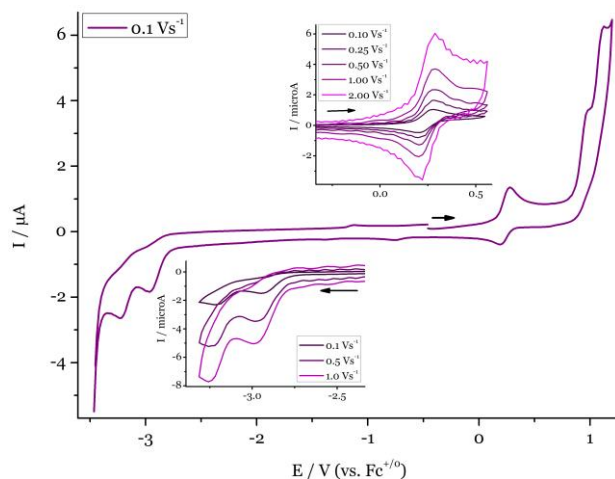


Figure A30. CV of =**3**^I in THF with 0.2 M (nBu₄N)PF₆. Top inset: first oxidation. Bottom inset: reductive area.

Table A19. CV Peak analysis of =**3**^I.

= 3 ^I	<i>v</i> / Vs ⁻¹	<i>E</i> _{1/2} /V	<i>i</i> _{pf} / <i>i</i> _{pr}	<i>E</i> _{pf} /V	ΔE_p /V	<i>v</i> / Vs ⁻¹	<i>E</i> _{pf} /V	<i>i</i> _{pf} /μA
1 st Ox	0.10	0.24	1.06	0.279	0.082	1 st red ^a	0.10	-2.965
	0.25	0.24	1.04	0.282	0.083		0.25	-2.954
	0.50	0.24	1.06	0.284	0.079		0.50	-2.969
	1.00	0.24	1.04	0.288	0.088		1.00	-2.981
	2.00	0.25	1.18	0.287	0.070			
						2 nd red ^a	0.10	-3.215
							0.50	-3.251
							1.00	-3.255
						2 nd ox ^a	0.10	0.979
						3 th ox ^a	0.10	1.120
								2.33

^a no reverse wave

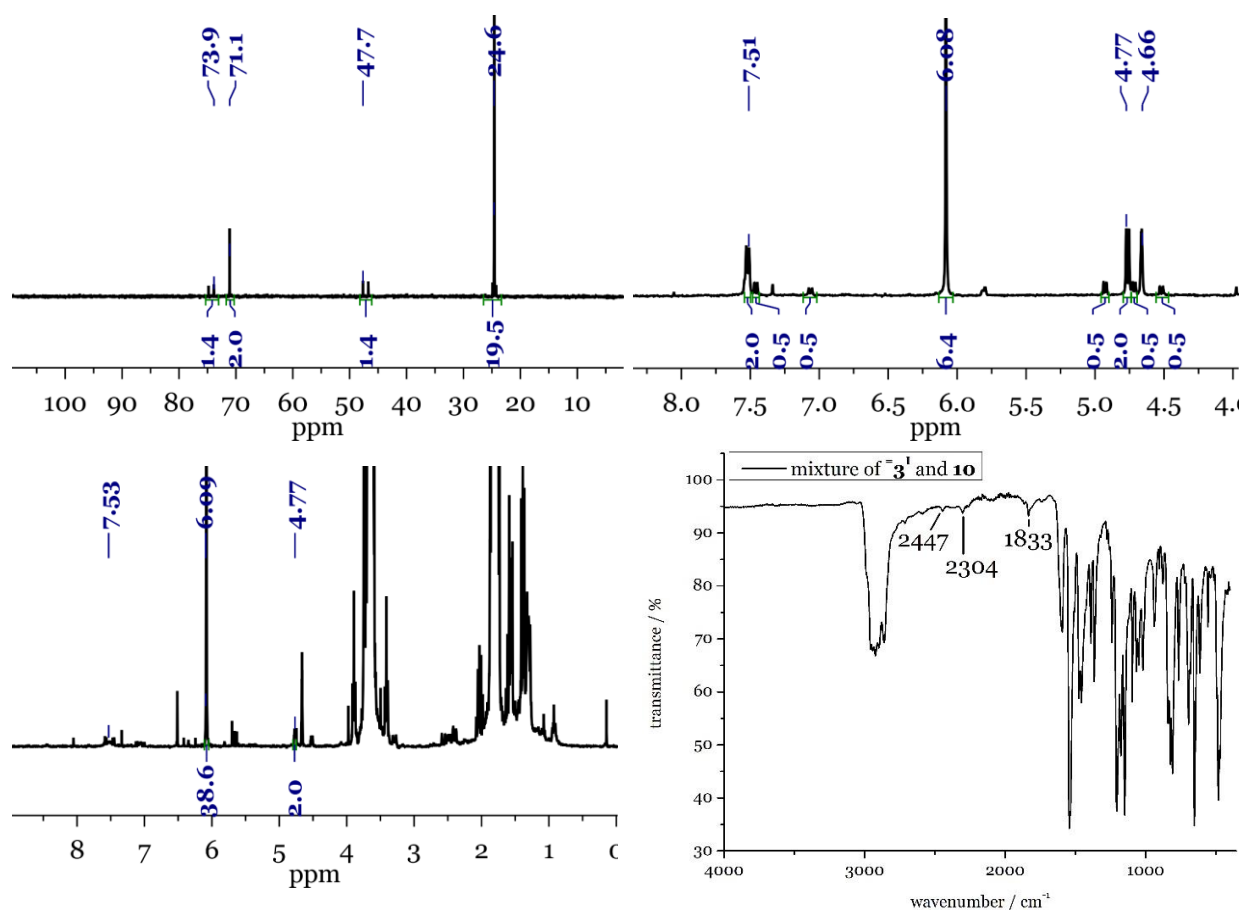


Figure A31. Top left: $^{31}\text{P}\{^1\text{H}\}$ -NMR spectrum of $=\mathbf{3}^{\text{I}}$ and $\mathbf{10}$ obtained via electrochemical reduction in THF at $E_{\text{appl.}} = -1.41$ V with addition of $15.1 \mu\text{mol}$ PPh_3O as standard (signal at 24.6 ppm) used for yield determination of $=\mathbf{3}^{\text{I}}$ (14 %). Top right: ^1H -NMR spectrum of the product mixture obtained via reduction in THF using $\text{Co}(\text{Cp})_2$ with addition of $13.1 \mu\text{mol}$ 1,3,5-trimethoxybenzene as standard (signal at 6.1 ppm) used for yield determination of $=\mathbf{3}^{\text{I}}$ (20 %). Bottom left: ^1H -NMR spectrum of the product mixture containing $=\mathbf{3}^{\text{I}}$ obtained via reduction in THF using $\text{Cr}(\text{Cp}^*)_2$ with addition of $11.6 \mu\text{mol}$ 1,3,5-trimethoxybenzene as standard (signal at 6.1 ppm) used for yield determination of $=\mathbf{3}^{\text{I}}$ (43 %). In addition, $\mathbf{10}$ is found in 21 % yield and the unknown C_{2v} -symmetric side-product in 10.5 % yield, as discussed in Section II.3.4. Bottom right: ATR IR spectrum of a mixture of $=\mathbf{3}^{\text{I}}$ and $\mathbf{10}$.

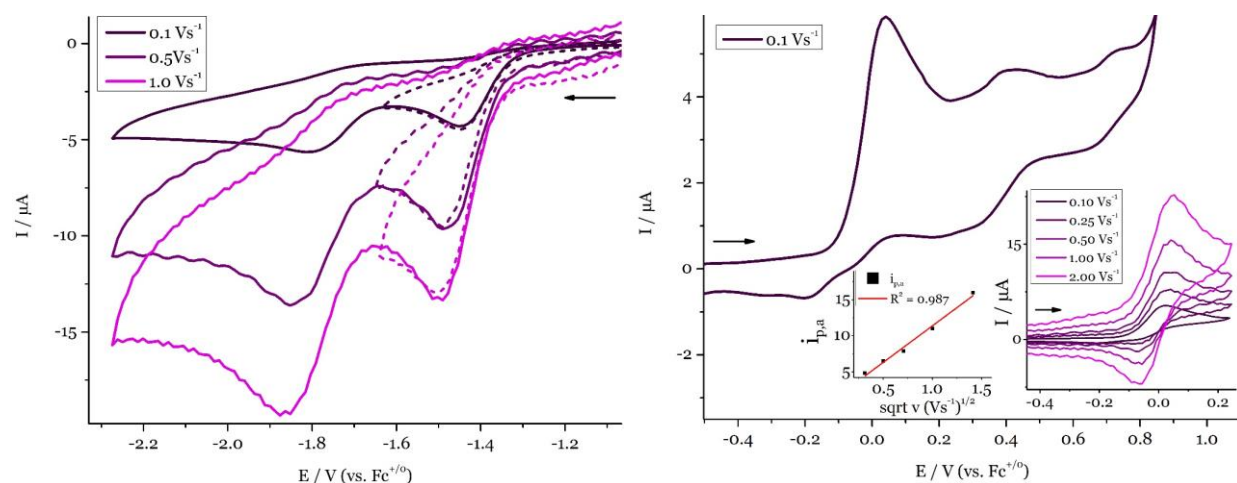


Figure A32 CV of $1.0 \text{ mM } =\mathbf{1}^{\text{I}}$ in THF with $0.2 \text{ M } (\text{nBu}_4\text{N})\text{PF}_6$ under Ar. Left: v -dependence of the reductive area. Right: oxidative area at $v = 0.1 \text{ Vs}^{-1}$. Right inset: first oxidation. Left inset: plot of $i_{p,a}$ vs. $v^{1/2}$.

Table 20 CV Peak analysis of $=\mathbf{1}^{\text{Cl}}$ under Ar.

$=\mathbf{1}^{\text{I}}$	v / Vs^{-1}	$E_{1/2}$ /V	$i_{\text{pf}}/i_{\text{pr}}$	E_{pf} /V	ΔE_p /V		v / Vs^{-1}	E_{pf} /V	i_{pf} / μA
1 st Ox	0.10 ^a	-	-	0.025	-	1 st red ^a	0.10	-1.44	3.7
	0.25	-0.02	2.16	0.032	0.10		0.50	-1.49	7.6
	0.50	-0.02	1.49	0.041	0.11		1.00	-1.50	10.3
	1.00	-0.01	1.34	0.042	0.10				
	2.00	-0.01	1.28	0.049	0.11	2 nd red ^a	0.10	-1.81	2.8
							0.50	-1.85	7.7
							1.00	-1.86	10.8

^a – no reverse wave.

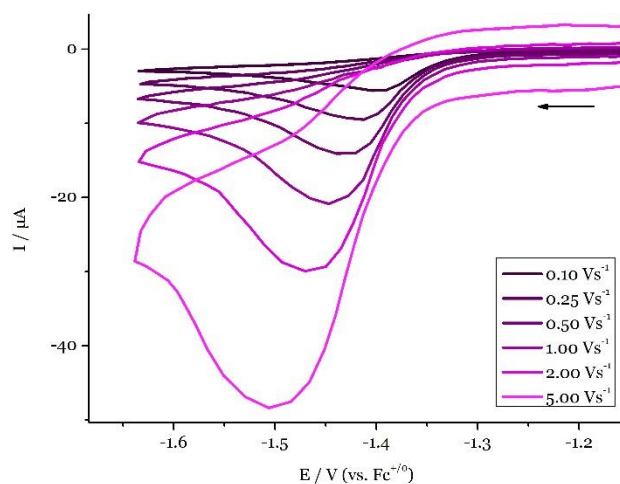


Figure A33. v -dependence of the first reduction feature of 1.0 mM $=\mathbf{1}$ in THF with 0.2 M $(n\text{Bu}_4\text{N})\text{PF}_6$ under N_2 .

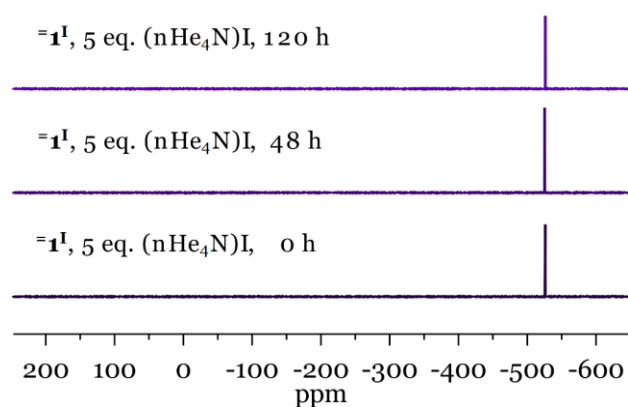


Figure A34 $^{31}\text{P}\{^1\text{H}\}$ NMR spectra of $=\mathbf{1}$ in THF with 5.0 eq. of $(n\text{He}_4\text{N})\text{I}$ under N_2 directly after mixing, after 48 and 120 h.

A6. Figures and tables of chapter II.4.

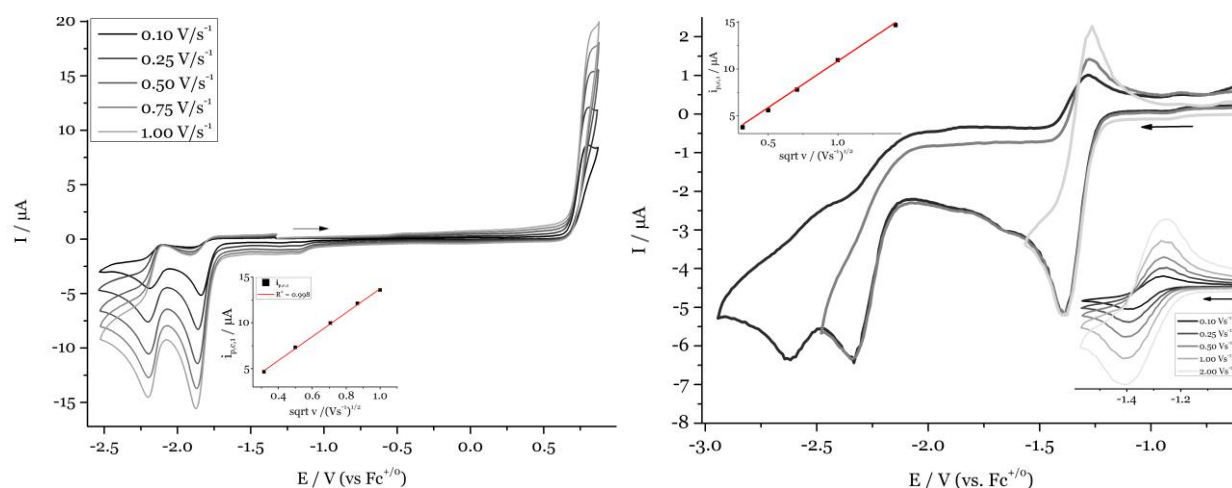


Figure A35. Left: CV of **5** in THF with 0.2 M (*n*Bu₄N)PF₆. Inset: plot of *i*_{p,c,1} vs. *v*^{1/2}. Right: CV of **5** in THF with 0.1 M (*n*Bu₄N)PF₆. Inset top left: plot of *i*_{p,c,1} vs. *v*^{1/2}. Inset bottom right: *v*-dependency of the first reduction.

Table A21. CV Peak analysis of **5**.

5	<i>v</i> / Vs ⁻¹	<i>E</i> _{pf} /V	<i>i</i> _{pf} /μA		<i>v</i> / Vs ⁻¹ ₁	<i>E</i> _{1/2} /V	<i>i</i> _{pf} / <i>i</i> _{pr}	<i>E</i> _{pf} /V	Δ <i>E</i> _p /V
1 st Ox ^a	0.10	0.800	8.5	2 nd red	0.10	-2.14	1.61	-2.190	0.108
	0.25	0.809	11.		0.25	-2.15	1.51	-2.202	0.097
	0.50	0.832	14.2		0.50	-2.15	1.38	-2.198	0.093
	0.75	0.847	16.1		0.75	-2.15	1.26	-2.198	0.097
	1.00	0.840	17.3		1.00	-2.15	1.25	-2.202	0.103
1 st red ^a	0.10	-1.840	4.7						
	0.25	-1.860	7.3						
	0.50	-1.866	10.0						
	0.75	-1.869	12.1						
	1.00	-1.873	13.6						

^a no reverse wave

Table A22. CV Peak analysis of **5**.

5	<i>v</i> / Vs ⁻¹	<i>E</i> _{1/2} /V	<i>i</i> _{pf} / <i>i</i> _{pr}	<i>E</i> _{pf} /V	Δ <i>E</i> _p ^b /V		<i>v</i> / Vs ⁻¹	<i>E</i> _{pf} /V	<i>i</i> _{pf} /μA
1 st red	0.10	-1.33	1.27	-1.391	0.126	2 nd red ^a	0.10	-2.345	3.6
	0.25	-1.33	1.18	-1.389	0.126		0.50	-2.399	8.8
	0.50	-1.33	1.23	-1.402	0.138		1.00	-2.419	12.2
	1.00	-1.34	1.08	-1.407	0.144	3 th red ^a	0.10	-2.624	2.1
	2.00	-1.33	1.06	-1.400	0.146		0.50	-2.722	2.7
							1.00	-2.766	3.9

^a no reverse wave. ^b The Δ*E*_p of Fc present within the measurement has similar values, indicating iR-compensation was not sufficient, and this wave is classified as reversible.

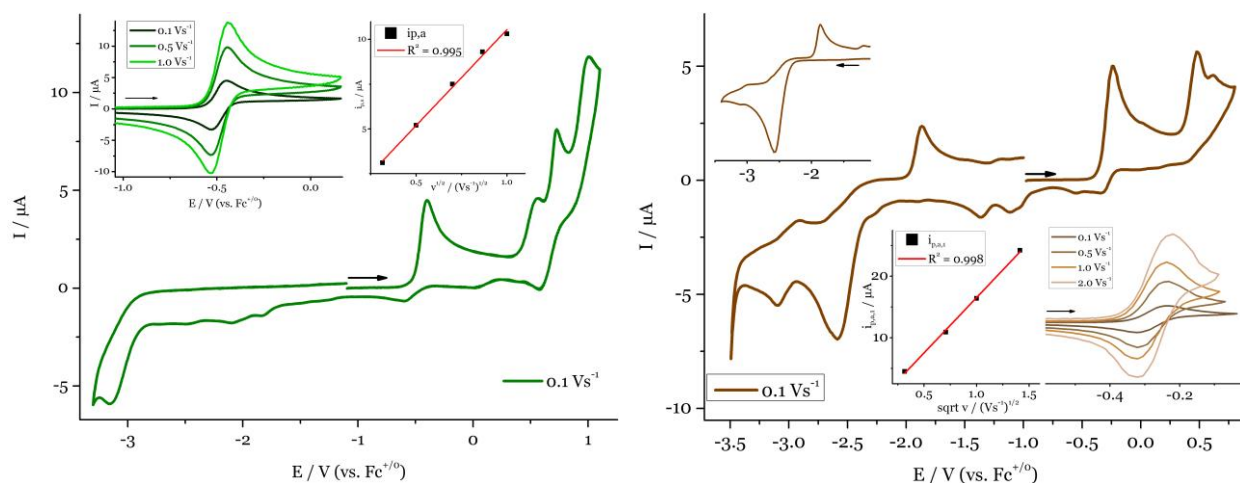


Figure A36. Left: CV of **6** in THF with 0.2 M (*n*Bu₄N)PF₆. Inset top left: v -dependence of the first oxidation. Inset top right: plot of $i_{p,a,1}$ vs. $v^{1/2}$. Right: CV of **=6** in THF with 0.2 M (*n*Bu₄N)PF₆. Inset bottom right: scan rate dependence of the first oxidation. Inset bottom right: plot of $i_{p,a,1}$ vs. $v^{1/2}$. Inset top left: CV of the cathodic region, $v = 0.1 \text{ Vs}^{-1}$.

Table A23. CV Peak analysis of **6**.

6	v / Vs^{-1}	$E_{1/2}$ / V	i_{pf}/i_{pr}	E_{pf} / V	ΔE_p / V		v / Vs^{-1}	E_{pf} / V	i_{pf} / μA
1 st ox	0.1	-0.49	1.02	-0.448	0.081	2 nd ox ^a	0.1	0.504	3.5
	0.5	-0.49	1.04	-0.443	0.090		0.5	0.553	5.8
	1.0	-0.49	1.04	-0.442	0.090		1.0	0.576	9.5
3 th ox	0.1	0.61	2.47	0.672	0.127	4 th ox ^a	0.1	0.948	4.8
	0.5	0.65	4.46	0.753	0.204		0.5	0.979	9.1
	1.0	0.69	4.18	0.811	0.249		1.0	0.996	12.6
						1 st red ^a	0.1	-3.14	6.6

^a no reverse wave

Table A24. CV Peak analysis of **=6**.

=6	v / Vs^{-1}	$E_{1/2}$ / V	i_{pf}/i_{pr}	E_{pf} / V	ΔE_p / V		v / Vs^{-1}	E_{pf} / V	i_{pf} / μA
1 st ox	0.1	-0.28	1.00	-0.236	0.085	2 nd ox ^a	0.1	0.447	3.52
	0.5	-0.28	1.15	-0.234	0.086		0.5	0.500	9.65
	1.0	-0.28	1.09	-0.237	0.085		1.0	0.499	14.1
	2.0	-0.27	1.06	-0.219	0.105		2.0	0.533	20.1
						3 th ox ^a	0.1	0.612	0.9
						1 st red ^a	0.1	-2.573	7.7
							0.5	-2.621	17.3
							1.0	-2.635	26.2
							2.0	-2.681	32.6

^a no reverse wave

Table A25. CV Peak analysis of **7**.

7	v / Vs^{-1}	E_{pf} /V	i_{pf} / μA		v / Vs^{-1}	E_{pf} /V	i_{pf} / μA
1 st Ox ^a	0.10	0.833	3.5	1 st red ^a	0.1	-1.380	1.5
	0.25	0.843	5.3		0.5	-1.398	2.7
	0.50	0.856	6.9		1.0	-1.405	3.6
	1.00	0.864	8.8		2.0 ^b	-1.415	4.9
					3.0 ^b	-1.431	5.8

^a no reverse wave. ^b The data are wobbly and therefore not depicted in the Figure showing the CV of **7**.

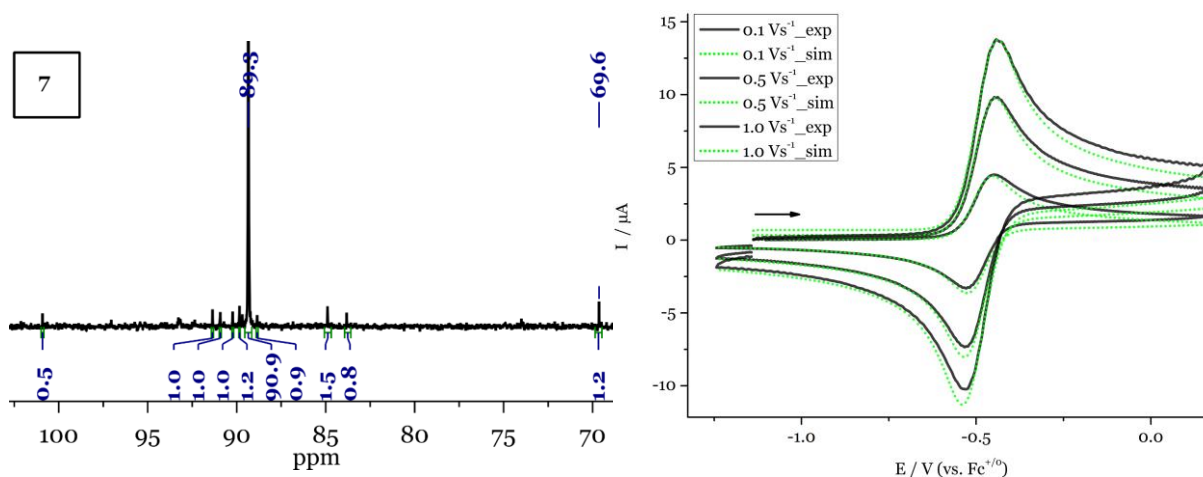


Figure A37. Left: $^{31}P\{^1H\}$ NMR spectrum of the best batch of **7** as obtained via this route within this work (circa 90 % purity). Right: Simulation of the Re(IV/III) oxidation of **6** at $v = 0.1, 0.5, 1.0 Vs^{-1}$. Parameters used: $A = 0.020 cm^2$, $D_{6/6^+} = 8.5 \cdot 10^{-6} cm^2 s^{-1}$ (an estimation based on the complexes examined within this work), $R_u = 500 \Omega$, $CdL = 7^*10^{-7} F$, $E_{1/2} = -0.49 V$, $\alpha = 0.5$, $k_s = 0.03 cm^2 s^{-1}$.

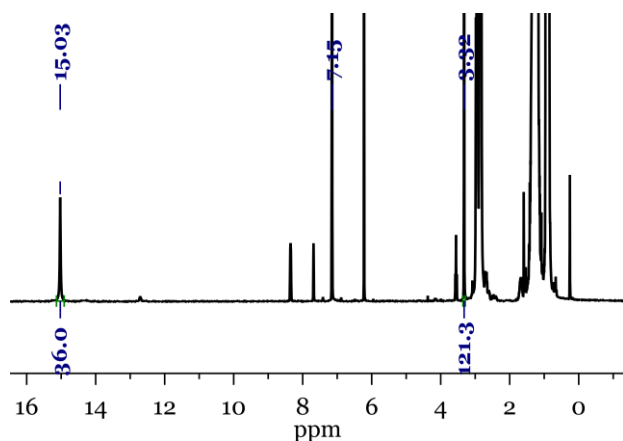


Figure A38. 1H NMR of the crude inorganic fraction after CPE of **6** at $E_{appl.} = +0.08 V$ in C_6D_6 with 1,3,5-trimethoxybenzene as standard.

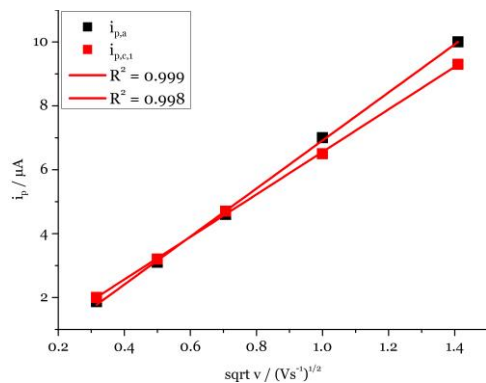


Figure A39. Plot of $i_{p,a}$ vs. $v^{1/2}$ and $i_{p,c,1}$ vs. $v^{1/2}$ of **8** in THF with 0.2 M (nBu₄N)PF₆.

Table A26. CV Peak analysis of **8**, data here enlisted as collected under Ar.

8	v / Vs ⁻¹	E_{pf} /V	i_{pf} /μA		v / Vs ⁻¹	$E_{1/2}$ /V	i_{pf}/i_{pr}	E_{pf} /V	ΔE_P /V
1 st red ^a	0.10	-1.096	2.0	1 st ox	0.10	0.05	1.14	0.089	0.080
	0.25	-1.107	3.2		0.25	0.05	1.08	0.089	0.077
	0.50	-1.118	4.7		0.50	0.05	1.05	0.091	0.078
	1.00	-1.131	6.5		1.00	0.06	1.04	0.095	0.076
	2.00	-1.143	9.3		2.00	0.06	1.04	0.098	0.081
2 nd red	0.10	-1.970	2.4						
	0.25	-1.986	3.6						
	0.50	-2.000	4.9						
	1.00	-2.009	7.0						
	2.00	-2.028	9.6						
3 th red	0.10	-2.244	1.5						
	0.25	-2.258	2.2						
	0.50	-2.269	3.7						
	1.00	-2.279	5.9						
	2.00	-2.290	8.0						

^a no reverse wave

Table A27. CV Peak analysis of **8** in presence of different equivalents of (nHe₄N)Cl, data here enlisted as collected under N₂.

8	v / Vs ⁻¹	E_{pf} /V				
		0	5	10	20	40
(nHe ₄ N)Cl / eq.						
1 st red	0.1	-1.075	-1.083	-1.086	-1.092	-1.094
	1.0	-1.107	-1.114	-1.119	-1.125	-1.128
	2.0	-1.126	-1.132	-1.138	-1.340	-1.344

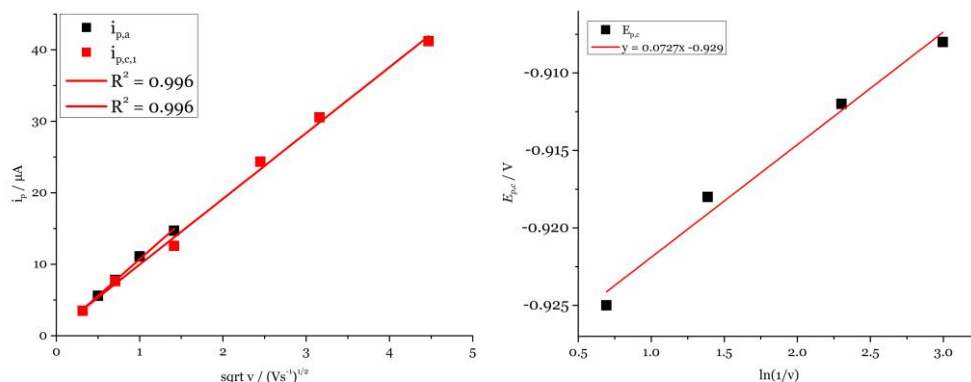


Figure A40. Left: Plot of $i_{p,a}$ vs. $v^{1/2}$ and $i_{p,c,1}$ vs. $v^{1/2}$ of **8** in THF with 0.2 M ($n\text{Bu}_4\text{N}$)PF₆. Right: Peak shift analysis of the $E_{p,c,1}$ of **8**, plotting $E_{p,c}$ vs. $\ln(1/v)$. Only the peak potentials of the low scan rates are considered, where the wave still appears fully irreversible. For the analysis in Section II.4.5, $E_{1/2} = -0.896$ V is used.

Table A28. CV Peak analysis of **8**, data here enlisted as collected under Ar.

8	v / Vs^{-1}	$E_{1/2}$ /V	i_{pf}/i_{pr}	E_{pf} /V	ΔE_P /V	v / Vs^{-1}	E_{pf} /V	i_{pf} / μA
1 st red	0.10 ^a			-0.910		2 nd red ^a	0.05	-1.694
	0.50 ^a			-0.925			0.10	-1.699
	2.00	-0.883	3.12	-0.934	0.102		0.25	-1.711
	6.00	-0.892	1.97	-0.947	0.110		0.50	-1.728
	10.0	-0.891	1.73	-0.950	0.118		1.00	-1.745
	20.0	-0.899	1.63	-0.963	0.131			
1 st ox	0.10	0.330	1.09	0.371	0.083	3 th red ^a	0.05	
	0.25	0.326	1.10	0.369	0.086		0.10	-1.894
	0.50	0.328	1.08	0.373	0.090		0.25	-1.900
	1.00	0.329	1.09	0.375	0.092		0.50	-1.923
	2.00	0.329	1.05	0.382	0.107		1.00	-1.938

^a no reverse wave

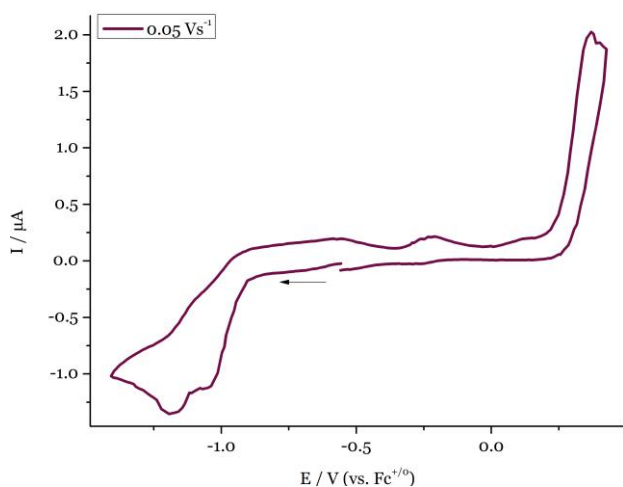


Figure A41. CV of 0.3 mM **12** in THF with 0.2 M ($n\text{Bu}_4\text{N}$)PF₆, $v = 0.05$ Vs^{-1} .

Table A29. CV Peak analysis of **12**.

12	v / Vs^{-1}	E_{pf} /V	i_{pf} / μA		v / Vs^{-1}	$E_{1/2}$ /V	i_{pf}/i_{pr}	E_{pf} /V	ΔE_P /V
1 st red ^a	0.05	-1.044	0.93	1 st ox	0.10 ^a			0.336	
	0.10	-1.066	1.24		0.50	0.336	2.45	0.388	0.104
					1.00	0.340	1.94	0.391	0.102
2 nd red ^a	0.05	-1.186	0.2						
	0.10	-1.201	0.34						

^a no reverse wave.

A7. Crystallographic Details

A7.1 General crystallographic experimental details^o

Suitable single crystals for X-ray structure determination were selected from the mother liquor under an inert gas atmosphere and transferred in protective perfluoro polyether oil on a microscope slide. The selected and mounted crystals were transferred to the cold gas stream on the diffractometer. The diffraction data were obtained at 100 K on a Bruker D8 three circle diffractometer, equipped with a PHOTON 100 CMOS detector and an INCOATEC microfocus source with Quazar mirror optics (Mo-K α radiation, $\lambda = 0.71073 \text{ \AA}$).

The data obtained were integrated with SAINT and a semi-empirical absorption correction from equivalents with SADABS was applied. The structure was solved and refined using the Bruker SHELX 2014 software package.^{225–228} All non-hydrogen atoms were refined with anisotropic displacement parameters. All C-H hydrogen atoms were refined isotropically on calculated positions by using a riding model with their Uiso values constrained to 1.5 Ueq of their pivot atoms for terminal sp³ carbon atoms and 1.2 times for all other carbon atoms.

^o All XRD measurements were performed by Dr. J. Abbenseth, Dr. M. Otte, and Dr. C. Würtele and supervised by Dr. C. Würtele.

A7.2 Crystallographic Details of **1^{Br}**

Table A30. Crystal data and structure refinement for **1^{Br}**

Identification code	mo_CW_PW_RvA_160418_2_om_a	
Empirical formula	C ₂₀ H ₄₄ Br ₂ NP ₂ Re	
Formula weight	706.52	
Temperature	101(2) K	
Wavelength	0.71073 Å	
Crystal system	Monoclinic	
Space group	P2 ₁ /n	
Unit cell dimensions	a = 8.2636(2) Å	α = 90°
	b = 13.4057(4) Å	β = 93.221(2)°
	c = 22.8310(6) Å	γ = 90°
Volume	2525.21(12) Å ³	
Z	4	
Density (calculated)	1.858 Mg/m ³	
Absorption coefficient	8.110 mm ⁻¹	
F(000)	1384	
Crystal size	0.173 x 0.077 x 0.050 mm ³	
Crystal shape and color	Needle, clear intense brown	
Theta range for data collection	2.345 to 28.337°	
Index ranges	-10 ≤ h ≤ 11, -17 ≤ k ≤ 17, -30 ≤ l ≤ 30	
Reflections collected	72189	
Independent reflections	6284 [R(int) = 0.1161]	
Completeness to theta = 25.242°	100.0 %	
Refinement method	Full-matrix least-squares on F ²	
Data / restraints / parameters	6284 / 0 / 247	
Goodness-of-fit on F ²	1.039	
Final R indices [I > 2σ(I)]	R ₁ = 0.0341, wR ₂ = 0.0516	
R indices (all data)	R ₁ = 0.0592, wR ₂ = 0.0566	
Largest diff. peak and hole	1.044 and -1.648 eÅ ⁻³	

A7.3 Crystallographic Details of **3^{Br}**

Table A31. Crystal data and structure refinement for **3^{Br}**.

Identification code	JA_RvA_260718_3_a	
Empirical formula	C ₂₀ H ₄₄ BrN ₂ P ₂ Re	
Formula weight	640.62	
Temperature	100(2) K	
Wavelength	0.71073 Å	
Crystal system	Orthorhombic	
Space group	Pbca	
Unit cell dimensions	a = 17.1032(4) Å	α = 90°
	b = 15.5203(4) Å	β = 90°
	c = 18.8077(5) Å	γ = 90°
Volume	4992.4(2) Å ³	
Z	8	
Density (calculated)	1.705 Mg/m ³	
Absorption coefficient	6.605 mm ⁻¹	
F(000)	2544	
Crystal size	0.226 x 0.124 x 0.106 mm ³	
Crystal shape and color	Plate, clear intense brown	
Theta range for data collection	2.166 to 25.409°.	
Index ranges	-20 ≤ h ≤ 20, -18 ≤ k ≤ 18, -22 ≤ l ≤ 22	
Reflections collected	148440	
Independent reflections	4602 [R(int) = 0.1307]	
Completeness to theta = 25.242°	100.0 %	
Refinement method	Full-matrix least-squares on F ²	
Data / restraints / parameters	4602 / 15 / 257	
Goodness-of-fit on F ²	1.019	
Final R indices [I > 2σ(I)]	R1 = 0.0225, wR2 = 0.0346	
R indices (all data)	R1 = 0.0385, wR2 = 0.0376	
Largest diff. peak and hole	0.739 and -0.661 eÅ ⁻³	

A7.4 Crystallographic Details of 3'

Table A32. Crystal data and structure refinement for 3'

Identification code	CW_RvA_200418_a	
Empirical formula	C ₂₀ H ₄₄ IN ₂ P ₂ Re	
Formula weight	687.61	
Temperature	102(2) K	
Wavelength	0.71073 Å	
Crystal system	Orthorhombic	
Space group	Pbca	
Unit cell dimensions	a = 17.2431(7) Å	α = 90°
	b = 15.4644(7) Å	β = 90°
	c = 18.8491(8) Å	γ = 90°
Volume	5026.2(4) Å ³	
Z	8	
Density (calculated)	1.817 Mg/m ³	
Absorption coefficient	6.199 mm ⁻¹	
F(000)	2688	
Crystal size	0.303 x 0.217 x 0.215 mm ³	
Crystal shape and color	Block, clear intense yellow	
Theta range for data collection	2.362 to 28.343°	
Index ranges	-22 ≤ h ≤ 22, -20 ≤ k ≤ 20, -25 ≤ l ≤ 25	
Reflections collected	87608	
Independent reflections	6248 [R(int) = 0.1376]	
Completeness to theta = 25.242°	100.0 %	
Refinement method	Full-matrix least-squares on F ²	
Data / restraints / parameters	6248 / 3 / 269	
Goodness-of-fit on F ²	1.063	
Final R indices [I > 2σ(I)]	R1 = 0.0377, wR2 = 0.0611	
R indices (all data)	R1 = 0.0666, wR2 = 0.0682	
Largest diff. peak and hole	1.287 and -1.305 eÅ ⁻³	

A7.5 Crystallographic Details of 4^I-I

Table A33. Crystal data and structure refinement for 4^I-I.

Identification code	mo_CW_RvA_250418_2_om_a	
Empirical formula	C ₂₀ H ₄₅ I ₂ N ₂ P ₂ Re	
Formula weight	815.52	
Temperature	106(2) K	
Wavelength	0.71073 Å	
Crystal system	Monoclinic	
Space group	C2/c	
Unit cell dimensions	a = 29.3983(10) Å	α = 90°
	b = 14.5529(4) Å	β = 112.287(2)°
	c = 14.2548(5) Å	γ = 90°
Volume	5643.0(3) Å ³	
Z	8	
Density (calculated)	1.920 Mg/m ³	
Absorption coefficient	6.617 mm ⁻¹	
F(000)	3120	
Crystal size	0.123 x 0.108 x 0.036 mm ³	
Crystal shape and color	Plate, clear yellow	
Theta range for data collection	2.404 to 26.426°	
Index ranges	-36<=h<=36, -18<=k<=18, -17<=l<=17	
Reflections collected	44265	
Independent reflections	5797 [R(int) = 0.0425]	
Completeness to theta = 25.242°	99.9 %	
Refinement method	Full-matrix least-squares on F ²	
Data / restraints / parameters	5797 / 0 / 260	
Goodness-of-fit on F ²	1.039	
Final R indices [I>2sigma(I)]	R1 = 0.0215,	wR2 = 0.0453
R indices (all data)	R1 = 0.0280,	wR2 = 0.0474
Largest diff. peak and hole	2.467 and -1.210 eÅ ⁻³	

A7.6. Crystallographic Details of $\mathbf{5}$

Table A34. Crystal data and structure refinement for $\mathbf{5}$.

Identification code	JA_RvA_030919	
Empirical formula	$\text{C}_{23}\text{H}_{45}\text{ClF}_3\text{N}_2\text{O}_3\text{P}_2\text{ReS}$	
Formula weight	770.26	
Temperature	100(2) K	
Wavelength	0.71073 Å	
Crystal system	Triclinic	
Space group	P-1	
Unit cell dimensions	$a = 13.0607(14)$ Å	$\alpha = 65.990(3)^\circ$
	$b = 14.8030(16)$ Å	$\beta = 89.823(4)^\circ$
	$c = 17.4321(18)$ Å	$\gamma = 87.660(4)^\circ$
Volume	$3075.8(6)$ Å ³	
Z	4	
Density (calculated)	1.663 Mg/m ³	
Absorption coefficient	4.254 mm ⁻¹	
F(000)	1544	
Crystal size	0.182 x 0.160 x 0.055 mm ³	
Crystal shape and color	Block, clear intense red	
Theta range for data collection	2.216 to 26.508°.	
Index ranges	-16 ≤ h ≤ 16, -18 ≤ k ≤ 18, -21 ≤ l ≤ 18	
Reflections collected	122549	
Independent reflections	12653 [R(int) = 0.1480]	
Completeness to theta = 25.242°	99.6 %	
Refinement method	Full-matrix least-squares on F ²	
Data / restraints / parameters	12653 / 96 / 706	
Goodness-of-fit on F ²	1.009	
Final R indices [I > 2σ(I)]	R1 = 0.0370,	wR2 = 0.0698
R indices (all data)	R1 = 0.0696,	wR2 = 0.0809
Largest diff. peak and hole	2.201 and -1.270 eÅ ⁻³	

A7.7. Crystallographic Details of **6**

Table A35. Crystal data and structure refinement for **6**.

Identification code	mo_CW_RvA_221019_0m_a	
Empirical formula	C ₂₂ H ₄₄ ClN ₂ P ₂ Re	
Formula weight	620.18	
Temperature	100(2) K	
Wavelength	0.71073 Å	
Crystal system	Tetragonal	
Space group	P4 ₂ /mbc	
Unit cell dimensions	a = 15.3251(7) Å	α = 90°
	b = 15.3251(7) Å	β = 90°
	c = 22.4403(11) Å	γ = 90°
Volume	5270.3(5) Å ³	
Z	8	
Density (calculated)	1.563 Mg/m ³	
Absorption coefficient	4.845 mm ⁻¹	
F(000)	2496	
Crystal size	0.159 x 0.100 x 0.067 mm ³	
Crystal shape and color	Plate, clear intense green	
Theta range for data collection	2.613 to 30.528°	
Index ranges	-21 ≤ h ≤ 21, -21 ≤ k ≤ 21, -28 ≤ l ≤ 32	
Reflections collected	173871	
Independent reflections	4123 [R(int) = 0.1085]	
Completeness to theta = 25.242°	99.9 %	
Refinement method	Full-matrix least-squares on F ²	
Data / restraints / parameters	4123 / 0 / 142	
Goodness-of-fit on F ²	1.076	
Final R indices [I > 2σ(I)]	R1 = 0.0266,	wR2 = 0.0477
R indices (all data)	R1 = 0.0398,	wR2 = 0.0514
Largest diff. peak and hole	1.032 and -1.172 eÅ ⁻³	

A7.7 Crystallographic Details of 12

Table A35. Crystal data and structure refinement for **12**.

Identification code	mo_CW_RvA_290819_om_a	
Empirical formula	C ₂₇ H ₄₉ Cl ₄ NP ₂ Re	
Formula weight	777.61	
Temperature	100(2) K	
Wavelength	0.71073 Å	
Crystal system	Monoclinic	
Space group	P2 ₁ /c	
Unit cell dimensions	a = 12.2642(5) Å	α = 90°
	b = 15.5206(7) Å	β = 91.632(2)°
	c = 16.5211(7) Å	γ = 90°
Volume	3143.5(2) Å ³	
Z	4	
Density (calculated)	1.643 Mg/m ³	
Absorption coefficient	4.325 mm ⁻¹	
F(000)	1564	
Crystal size	0.221 x 0.136 x 0.055 mm ³	
Crystal shape and color	Plate, dark brown	
Theta range for data collection	2.426 to 28.379°	
Index ranges	-16 ≤ h ≤ 16, -20 ≤ k ≤ 20, -22 ≤ l ≤ 22	
Reflections collected	92832	
Independent reflections	7859 [R(int) = 0.0761]	
Completeness to theta = 25.242°	99.9 %	
Refinement method	Full-matrix least-squares on F ²	
Data / restraints / parameters	7859 / 102 / 360	
Goodness-of-fit on F ²	1.059	
Final R indices [I > 2σ(I)]	R ₁ = 0.0291,	wR ₂ = 0.0509
R indices (all data)	R ₁ = 0.0478,	wR ₂ = 0.0565
Largest diff. peak and hole	1.259 and -1.138 eÅ ⁻³	

VI References

- (1) Singh, D.; Buratto, W. R.; Torres, J. F.; Murray, L. J. Activation of Dinitrogen by Polynuclear Metal Complexes. *Chem. Rev.* **2020**, *120* (12), 5517–5581. <https://doi.org/10.1021/acs.chemrev.0c00042>.
- (2) Jia, H. P.; Quadrelli, E. A. Mechanistic Aspects of Dinitrogen Cleavage and Hydrogenation to Produce Ammonia in Catalysis and Organometallic Chemistry: Relevance of Metal Hydride Bonds and Dihydrogen. *Chem. Soc. Rev.* **2014**, *43* (2), 547–564. <https://doi.org/10.1039/c3cs60206k>.
- (3) Benson, S. W. Bond Energies. *J. Chem. Educ.* **1965**, *42*, 502–518.
- (4) Shilov, A. E. Catalytic Reduction of Molecular Nitrogen in Solutions. *Russ. Chem. Bull.* **2003**, *52* (12), 2555–2562. <https://doi.org/10.1023/B:RUCB.0000019873.81002.60>.
- (5) Einsle, O.; Rees, D. C. Structural Enzymology of Nitrogenase Enzymes. *Chem. Rev.* **2020**, *120* (12), 4969–5004. <https://doi.org/10.1021/acs.chemrev.0c00067>.
- (6) Rutledge, H. L.; Tezcan, F. A. Electron Transfer in Nitrogenase. *Chem. Rev.* **2020**, *120* (12), 5158–5193. <https://doi.org/10.1021/acs.chemrev.9b00663>.
- (7) Ertl, G. Reactions at Surfaces: From Atoms to Complexity (Nobel Lecture). *Angew. Chemie - Int. Ed.* **2008**, *47* (19), 3524–3535. <https://doi.org/10.1002/anie.200800480>.
- (8) Masero, F.; Perrin, M. A.; Dey, S.; Mougel, V. Dinitrogen Fixation: Rationalizing Strategies Utilizing Molecular Complexes. *Chem. - A Eur. J.* **2020**, 1–38. <https://doi.org/10.1002/chem.202003134>.
- (9) Appl, M. Ammonia, 1. Introduction. *Ullmann's Encycl. Ind. Chem.* **2012**, 263–285. <https://doi.org/10.1002/14356007.a02>.
- (10) Van Der Ham, C. J. M.; Koper, M. T. M.; Hetterscheid, D. G. H. Challenges in Reduction of Dinitrogen by Proton and Electron Transfer. *Chem. Soc. Rev.* **2014**, *43* (15), 5183–5191. <https://doi.org/10.1039/c4cs00085d>.
- (11) Allen, B. A. D.; Senoff, C. V. Nitrogenopentammineruthenium (II) Complexes. *Chem. Commun.* **1965**, No. 24, 621–622.
- (12) Jones, B. https://sites.chem.utoronto.ca/chemistry/jbj_videos/bert_allen.php.
- (13) Leigh, G. J. Bert Allen and the First Complex of Dinitrogen. *Can. J. Chem.* **2011**, *83* (4), 277–278.
- (14) Bottomley, F.; Nyburg, S. C. Molecular Nitrogen as a Ligand: The Crystal Structure of Nitrogenpentammineruthenium(II) Dichloride. *Chem. Commun.* **1966**, 23 (24), 897–898. <https://doi.org/10.1039/C19660000897>.
- (15) Chatt, J.; Dilworth, J. R.; Richards, R. L. Recent Advances in the Chemistry of Nitrogen Fixation. *Chem. Rev.* **1978**, *78* (6), 589–625. <https://doi.org/10.1021/cr60316a001>.
- (16) Klopsch, I.; Yuzik-Klimova, E. Y.; Schneider, S. Functionalization of N₂ by Mid to Late Transition Metals via N–N Bond Cleavage. *Top. Organomet. Chem.* **2017**, *60*, 71–112. https://doi.org/10.1007/3418_2016_12.
- (17) Harrison, D. F.; Weissberger, E.; Taube, H. Binuclear Ion Containing Nitrogen as a Bridging Group. *Science* **1969**, *3812*, 320–322.
- (18) Treitel, I. M.; Flood, M. T.; Marsh, R. E.; Gray, H. B. Molecular and Electronic Structure of μ -Nitrogen-Decaamminediruthenium(II). *J. Am. Chem. Soc.* **1969**, *91* (23), 6512–6513. <https://doi.org/10.1021/ja01051a070>.
- (19) Nishibayashi, Y. *Nitrogen Fixation*; 2017. <https://doi.org/10.1201/9780429445651-41>.
- (20) Forrest, S. J. K.; Schluschaß, B.; Yuzik-Klimova, E. Y.; Schneider, S. Nitrogen Fixation via Splitting into Nitrido Complexes. *Chem Rev* **2021**, *Accepted*.
- (21) Chatt, J.; Fay, R. C.; Richards, R. L. Preparation and Characterisation of the Dinuclear Dinitrogen Complex, Trichloro- μ -Dinitrogenbis(Tetrahydrofuran{chlorotetrakis[Dimethyl(Phenyl)Phosphine]Rhenium(I)}chromium(III)). *Inorg. Phys. Theor.* **1971**, 702–704.
- (22) Mercer, M. Crystal Structure of a Dinuclear Dinitrogen Complex: Tetrachloro{chlorotetrakis[Dimethyl(Phenyl)Phosphine]Rhenium(I)}- μ -Dinitrogen-Methosymolybdenum(V)-Methanol-Hydrochloric Acid. *Dalton* **1974**, 1637–1640.
- (23) Mercer, M.; Crabtree, R. H.; Richards, R. L. A μ -Dinitrogen Complex with a Long N–N Bond. X-Ray Crystal Structure of [(PMe₂Ph)₄CiReN₂MoCl₄(OMe)]. *J. Chem. Soc. Chem. Commun.* **1973**, 1 (21), 808–809. <https://doi.org/10.1039/C39730000808>.
- (24) Curley, J. J.; Cook, T. R.; Reece, S. Y.; Müller, P.; Cummins, C. C. Shining Light on Dinitrogen Cleavage: Structural Features, Redox Chemistry, and Photochemistry of the Key Intermediate Bridging Dinitrogen Complex. *J. Am. Chem. Soc.* **2008**, *130* (29), 9394–9405. <https://doi.org/10.1021/ja8002638>.
- (25) Schluschaß, B.; Abbenseth, J.; Demeshko, S.; Finger, M.; Franke, A.; Herwig, C.; Würtele, C.; Ivanovic-Burmazovic, I.; Limberg, C.; Telser, J.; et al. Selectivity of Tungsten Mediated Dinitrogen Splitting: Vs. Proton Reduction. *Chem. Sci.* **2019**, *10* (44), 10275–10282. <https://doi.org/10.1039/c9sc03779a>.
- (26) Abbenseth, J.; Oudsen, J. P. H.; Venderbosch, B.; Demeshko, S.; Finger, M.; Herwig, C.; Würtele, C.; Holthausen, M. C.; Limberg, C.; Tromp, M.; et al. Examination of Protonation-Induced Dinitrogen Splitting

- by in Situ EXAFS Spectroscopy. *Inorg. Chem.* **2020**, *59* (19), 14367–14375. <https://doi.org/10.1021/acs.inorgchem.0c02134>.
- (27) Ferguson, R.; Solari, E.; Floriani, C.; Osella, D.; Ravera, M.; Re, N.; Chiesi-Villa, A.; Rizzoli, C. Stepwise Reduction of Dinitrogen Occurring on a Divanadium Model Compound: A Synthetic, Structural, Magnetic, Electrochemical, and Theoretical Investigation on the $[V=N=N=N](N^+)$ [$n = 4-6$] Based Complexes. *J. Am. Chem. Soc.* **1997**, *119* (42), 10104–10115. <https://doi.org/10.1021/ja971229q>.
- (28) Ferguson, R.; Solari, E.; Floriani, C.; Chiesi-Villa, A.; Rizzoli, C. Fixation and Reduction of Dinitrogen by Vanadium(II) and Vanadium(III): Synthesis and Structure of Dinitrogenmesitylvanadium Complexes. *Angew. Chemie - Int. Ed.* **1993**, *32*, 396–397.
- (29) Nazzareno, R.; Rosi, M.; Sgamellotti, A.; Floriani, C.; Solari, E. A Theoretical Study of Dinitrogen Activation by Vanadium(II) and Vanadium(III): Ab Initio Calculations on Various Model Compounds. *Inorg. Chem.* **1994**, *33* (19), 4390–4397. <https://doi.org/10.1021/ic00097a030>.
- (30) Bezdek, M. J.; Guo, S.; Chirik, P. J. Terpyridine Molybdenum Dinitrogen Chemistry: Synthesis of Dinitrogen Complexes That Vary by Five Oxidation States. *Inorg. Chem.* **2016**, *55* (6), 3117–3127. <https://doi.org/10.1021/acs.inorgchem.6b00053>.
- (31) Hirotsu, M.; Fontaine, P. P.; Epshteyn, A.; Zavalij, P. Y.; Sita, L. R. Dinitrogen Activation at Ambient Temperatures: New Modes of H_2 and $PhSiH_3$ Additions for an “End-on-Bridged” $[Ta(IV)]_2(\mu-H_1:H_1-N_2)$ Complex and for the Bis(μ -Nitrido) $[Ta(V)(\mu-N)]_2$ Product Derived from Facile $N\equiv N$ Bond Cleavage. *J. Am. Chem. Soc.* **2007**, *129* (30), 9284–9285. <https://doi.org/10.1021/ja072248v>.
- (32) Fontaine, P. P.; Yonke, B. L.; Zavalij, P. Y.; Sita, L. R. Dinitrogen Complexation and Extent of N-N Activation within the Group 6 “End-On-Bridged” Dinuclear Complexes, $\{(H_5-C_5Me_5)M[N(i-Pr)C(Me)N(i-Pr)]\}_2(\mu-H_1:H_1-N_2)$ ($M = Mo$ and W). *J. Am. Chem. Soc.* **2010**, *132* (35), 12273–12285. <https://doi.org/10.1021/ja100469f>.
- (33) Keane, A. J.; Yonke, B. L.; Hirotsu, M.; Zavalij, P. Y.; Sita, L. R. Fine-Tuning the Energy Barrier for Metal-Mediated Dinitrogen $N\equiv N$ Bond Cleavage. *J. Am. Chem. Soc.* **2014**, *136* (28), 9906–9909. <https://doi.org/10.1021/ja505309j>.
- (34) Hirotsu, M.; Fontaine, P. P.; Zavalij, P. Y.; Sita, L. R. Extreme $N\equiv N$ Bond Elongation and Facile N-Atom Functionalization Reactions within Two Structurally Versatile New Families of Group 4 Bimetallic “Side-on-Bridged” Dinitrogen Complexes for Zirconium and Hafnium. *J. Am. Chem. Soc.* **2007**, *129* (42), 12690–12692. <https://doi.org/10.1021/ja0752989>.
- (35) Fryzuk, M. D.; Haddad, T. S.; Mylvaganam, M.; McConville, D. H.; Rettig, S. J. End-On Versus Side-On Bonding of Dinitrogen to Dinuclear Early Transition-Metal Complexes. *J. Am. Chem. Soc.* **1993**, *115* (7), 2782–2792. <https://doi.org/10.1021/ja00060a028>.
- (36) Fryzuk, M. D.; Haddad, T. S.; Rettig, S. J. Reduction of Dinitrogen by a Zirconium Phosphine Complex To Form a Side-On-Bridging N_2 Ligand. Crystal Structure of $\{[(Pr)_2PCH_2SiMe_2]_2N\}ZrCl\}_2(\mu-H_2:H_2-N_2)$. *J. Am. Chem. Soc.* **1990**, *112* (22), 8185–8186. <https://doi.org/10.1021/ja00178a063>.
- (37) Bobadova-Parvanova, P.; Wang, Q.; Morokuma, K.; Musaev, D. G. How Many Methyl Groups in $\{(H_5-C_5Me_n)Zr\}_2(M_2, H_2, H_2-N_2)$ Are Needed for Dinitrogen Hydrogenation? A Theoretical Study. *Angew. Chemie - Int. Ed.* **2005**, *44* (43), 7101–7103. <https://doi.org/10.1002/anie.200501371>.
- (38) Pool, J. A.; Bernskoetter, W. H.; Chirik, P. J. On the Origin of Dinitrogen Hydrogenation Promoted by $[(H_5-C_5Me_4H)Zr]_2(M_2, H_2, H_2-N_2)$. *J. Am. Chem. Soc.* **2004**, *126* (44), 14326–14327. <https://doi.org/10.1021/ja045566s>.
- (39) Pool, J. A.; Lobkovsky, E.; Chirik, P. J. Hydrogenation and Cleavage of Dinitrogen to Ammonia with a Zirconium Complex. *Nature* **2004**, *427*, 527–530. <https://doi.org/10.1038/nature02311.1>.
- (40) Sanner, R. D.; Manriquez, J. M.; Marsh, R. E.; Bercaw, J. E. Structure of μ -Dinitrogen-Bis(Bis(Pentamethylcyclopentadienyl)Dinitrogenzirconium(II)), $\{(H_5-C_5(CH_3)_5)ZrN_2\}_2N_2$. *J. Am. Chem. Soc.* **1976**, *98* (26), 8351–8357. <https://doi.org/10.1021/ja00442a007>.
- (41) Manriquez, J. M.; Bercaw, J. E. Preparation of a Dinitrogen Complex of Bis(Pentamethylcyclopentadienyl)Zirconium(II). Isolation and Protonation Leading to Stoichiometric Reduction of Dinitrogen to Hydrazine. *J. Am. Chem. Soc.* **1974**, *96* (19), 6229–6230. <https://doi.org/10.1021/ja00826a071>.
- (42) Laplaza, C. E.; Cummins, C. C. Dinitrogen Cleavage by a Three-Coordinate Molybdenum(III) Complex. *Science* **1995**, *268* (5212), 861–863. <https://doi.org/10.1126/science.268.5212.861>.
- (43) Laplaza, C. E.; Johnson, M. J. A.; Peters, J. C.; Odom, A. L.; Kim, E.; Cummins, C. C.; George, G. N.; Pickering, I. J. Dinitrogen Cleavage by Three-Coordinate Molybdenum(III) Complexes: Mechanistic and Structural Data. *J. Am. Chem. Soc.* **1996**, *118* (36), 8623–8638. <https://doi.org/10.1021/ja960574x>.
- (44) Tsai, Y. C.; Johnson, M. J. A.; Mindiola, D. J.; Cummins, C. C.; Klooster, W. T.; Koetzle, T. F. A Cyclometalated Resting State for a Reactive Molybdenum Amide: Favorable Consequences of β -Hydrogen

- Elimination Including Reductive Cleavage, Coupling, and Complexation [6]. *J. Am. Chem. Soc.* **1999**, *121* (44), 10426–10427. <https://doi.org/10.1021/ja9917464>.
- (45) Chisholm, M. H.; Cotton, F. A.; Frenz, B. A.; Reichert, W. W.; Shive, L. W.; Stults, B. R. The Molybdenum-Molybdenum Triple Bond. 1. Hexakis(Dimethylamido)Dimolybdenum and Some Homologues: Preparation, Structure, and Properties. *J. Am. Chem. Soc.* **1976**, *98* (15), 4469–4476. <https://doi.org/10.1021/ja00431a024>.
- (46) Bruch, Q. J.; Connor, G. P.; McMillion, N. D.; Goldman, A. S.; Hasanayn, F.; Holland, P. L.; Miller, A. J. M. Considering Electrocatalytic Ammonia Synthesis via Bimetallic Dinitrogen Cleavage. *ACS Catal.* **2020**, *10* (19), 10826–10846. <https://doi.org/10.1021/acscatal.0c02606>.
- (47) Cui, Q.; Musaev, D. G.; Svensson, M.; Sieber, S.; Morokuma, K. N₂ Cleavage by Three-Coordinate Group 6 Complexes. W(III) Complexes Would Be Better Than Mo(III) Complexes. *J. Am. Chem. Soc.* **1995**, *117* (49), 12366–12367. <https://doi.org/10.1021/ja00154a052>.
- (48) Solari, E.; Silva, C. Da; Iacono, B.; Hesschenbrouck, J.; Rizzoli, C.; Scopelliti, R.; Floriani, C. Photochemical Activation of the N≡N Bond in a Dimolybdenum-Dinitrogen Complex: Formation of a Molybdenum Nitride. *Angew. Chemie - Int. Ed.* **2001**, *40* (20), 3907–3909. [https://doi.org/10.1002/1521-3773\(20011015\)40](https://doi.org/10.1002/1521-3773(20011015)40).
- (49) Shih, K. Y.; Kempe, R.; Schrock, R. R. Synthesis of Molybdenum Complexes That Contain Silylated Triamidoamine Ligands. A μ -Dinitrogen Complex, Methyl and Acetylide Complexes, and Coupling of Acetylides. *J. Am. Chem. Soc.* **1994**, *116* (19), 8804–8805. <https://doi.org/10.1021/ja00098a048>.
- (50) Mindiola, D. J.; Meyer, K.; Cherry, J. P. F.; Baker, T. A.; Cummins, C. C. Dinitrogen Cleavage Stemming from a Heterodinuclear Niobium/Molybdenum N₂ Complex: New Nitridoniobium Systems Including a Niobazene Cyclic Trimer. *Organometallics* **2000**, *19* (9), 1622–1624. <https://doi.org/10.1021/om000159k>.
- (51) Hebden, T. J.; Schrock, R. R.; Takase, M. K.; Müller, P. Cleavage of Dinitrogen to Yield a (t-BuPOCOP)Molybdenum(IV) Nitride. *Chem. Commun.* **2012**, *48* (13), 1851–1853. <https://doi.org/10.1039/c2cc17634c>.
- (52) Arashiba, K.; Eizawa, A.; Tanaka, H.; Nakajima, K.; Yoshizawa, K.; Nishibayashi, Y. Catalytic Nitrogen Fixation via Direct Cleavage of Nitrogen-Nitrogen Triple Bond of Molecular Dinitrogen under Ambient Reaction Conditions. *Bull. Chem. Soc. Jpn.* **2017**, *90* (10), 1111–1118. <https://doi.org/10.1246/bcsj.20170197>.
- (53) Tanabe, Y.; Sekiguchi, Y.; Tanaka, H.; Konomi, A.; Yoshizawa, K.; Kuriyama, S.; Nishibayashi, Y. Preparation and Reactivity of Molybdenum Complexes Bearing Pyrrole-Based PNP-Type Pincer Ligand. *Chem. Commun.* **2020**, *56* (51), 6933–6936. <https://doi.org/10.1039/d0cc02852e>.
- (54) Liao, Q.; Cavallé, A.; Saffon-Merceron, N.; Mézailles, N. Direct Synthesis of Silylamine from N₂ and a Silane: Mediated by a Tridentate Phosphine Molybdenum Fragment. *Angew. Chemie - Int. Ed.* **2016**, *55* (37), 11212–11216. <https://doi.org/10.1002/anie.201604812>.
- (55) Connelly, N. G.; Geiger, W. E. Chemical Redox Agents for Organometallic Chemistry. *Chem. Rev.* **1996**, *96* (2), 877–910. <https://doi.org/10.1021/cr940053x>.
- (56) Liao, Q.; Saffon-Merceron, N.; Mézailles, N. N₂ Reduction into Silylamine at Tridentate Phosphine/Mo Center: Catalysis and Mechanistic Study. *ACS Catal.* **2015**, *5* (11), 6902–6906. <https://doi.org/10.1021/acscatal.5b01626>.
- (57) Ashida, Y.; Arashiba, K.; Nakajima, K.; Nishibayashi, Y. Molybdenum-Catalysed Ammonia Production with Samarium Diiodide and Alcohols or Water. *Nature* **2019**, *568* (7753), 536–540. <https://doi.org/10.1038/s41586-019-1134-2>.
- (58) Gunanathan, C.; Milstein, D. Metal-Ligand Cooperation by Aromatization-De aromatization: A New Paradigm in Bond Activation and “Green” Catalysis. *Acc. Chem. Res.* **2011**, *44* (8), 588–602. <https://doi.org/10.1021/ar2000265>.
- (59) Ritleng, V.; Yandulov, D. V.; Weare, W. W.; Schrock, R. R.; Hock, A. S.; Davis, W. M. Molybdenum Triamidoamine Complexes That Contain Hexa-Tert-Butylterphenyl, Hexamethylterphenyl, or p-Bromohexaisopropylterphenyl Substituents. An Examination of Some Catalyst Variations for the Catalytic Reduction of Dinitrogen. *J. Am. Chem. Soc.* **2004**, *126* (19), 6150–6163. <https://doi.org/10.1021/ja0306415>.
- (60) Arashiba, K.; Miyake, Y.; Nishibayashi, Y. A Molybdenum Complex Bearing PNP-Type Pincer Ligands Leads to the Catalytic Reduction of Dinitrogen into Ammonia. *Nat. Chem.* **2011**, *3* (2), 120–125. <https://doi.org/10.1038/nchem.906>.
- (61) Doyle, L. R.; Wooles, A. J.; Jenkins, L. C.; Tuna, F.; McInnes, E. J. L.; Liddle, S. T. Catalytic Dinitrogen Reduction to Ammonia at a Triamidoamine-Titanium Complex. *Angew. Chemie - Int. Ed.* **2018**, *57* (21), 6314–6318. <https://doi.org/10.1002/anie.201802576>.
- (62) Lv, Z. J.; Huang, Z.; Zhang, W. X.; Xi, Z. Scandium-Promoted Direct Conversion of Dinitrogen into Hydrazine Derivatives via N-C Bond Formation. *J. Am. Chem. Soc.* **2019**, *141* (22), 8773–8777.

- <https://doi.org/10.1021/jacs.9b04293>.
- (63) Pfeil, M.; Engesser, T. A.; Koch, A.; Junge, J.; Krahmer, J.; Näther, C.; Tucek, F. Oligodentate Phosphine Ligands with Phospholane End Groups: New Synthetic Access and Application to Molybdenum-Based Synthetic Nitrogen Fixation. *Eur. J. Inorg. Chem.* **2020**, 2020 (15–16), 1437–1448. <https://doi.org/10.1002/ejic.201901068>.
- (64) Lever, A. B. P. Electrochemical Parametrization of Metal Complex Redox Potentials, Using the Ruthenium(III)/Ruthenium(II) Couple To Generate a Ligand Electrochemical Series. *Inorg. Chem.* **1990**, 29 (6), 1271–1285. <https://doi.org/10.1021/ic00331a030>.
- (65) Lever, A. B. P. Electrochemical Parametrization of Rhenium Redox Couples. *Inorg. Chem.* **1991**, 30 (9), 1980–1985. <https://doi.org/10.1021/ic00009a008>.
- (66) Silantyev, G. A.; Förster, M.; Schluschaß, B.; Abbenseth, J.; Würtele, C.; Volkmann, C.; Holthausen, M. C.; Schneider, S. Dinitrogen Splitting Coupled to Protonation. *Angew. Chemie - Int. Ed.* **2017**, 56 (21), 5872–5876. <https://doi.org/10.1002/anie.201701504>.
- (67) Schluschaß, B. *N₂ Splitting and Functionalization in the Coordination Sphere of Tungsten*; 2020.
- (68) Katayama, A.; Ohta, T.; Wasada-Tsutsui, Y.; Inomata, T.; Ozawa, T.; Ogura, T.; Masuda, H. Dinitrogen-Molybdenum Complex Induces Dinitrogen Cleavage by One-Electron Oxidation. *Angew. Chemie - Int. Ed.* **2019**, 58 (33), 11279–11284. <https://doi.org/10.1002/anie.201905299>.
- (69) Klopsch, I.; Finger, M.; Würtele, C.; Milde, B.; Werz, D. B.; Schneider, S. Dinitrogen Splitting and Functionalization in the Coordination Sphere of Rhenium. *J. Am. Chem. Soc.* **2014**, 136 (19), 6881–6883. <https://doi.org/10.1021/ja502759d>.
- (70) Lindley, B. M.; Van Alten, R. S.; Finger, M.; Schendzielorz, F.; Würtele, C.; Miller, A. J. M.; Siewert, I.; Schneider, S. Mechanism of Chemical and Electrochemical N₂ Splitting by a Rhenium Pincer Complex. *J. Am. Chem. Soc.* **2018**, 140 (25), 7922–7935. <https://doi.org/10.1021/jacs.8b03755>.
- (71) Wätjen, F. *Rhenium and Osmium PNP Pincer Complexes for Nitrogen Fixation and Nitride Transfer*; 2019.
- (72) van Alten, R. S.; Wätjen, F.; Demeshko, S.; Miller, A. J. M.; Würtele, C.; Siewert, I.; Schneider, S. (Electro-)Chemical Splitting of Dinitrogen with a Rhenium Pincer Complex. *Eur. J. Inorg. Chem.* **2020**, 1402–1410. <https://doi.org/10.1002/ejic.201901278>.
- (73) Kinauer, M.; Scheibel, M. G.; Abbenseth, J.; Heinemann, F. W.; Stollberg, P.; Würtele, C.; Schneider, S. [IrCl₂(N(CHCHPtBu)₂)₂]-: A Versatile Source of the Ir(PNP) Pincer Platform. *Dalt. Trans.* **2014**, 43 (11), 4506–4513. <https://doi.org/10.1039/c3dt53304b>.
- (74) Abbenseth, J.; Diefenbach, M.; Bete, S. C.; Würtele, C.; Volkmann, C.; Demeshko, S.; Holthausen, M. C.; Schneider, S. A Square-Planar Osmium(II) Complex. *Chem. Commun.* **2017**, 53 (40), 5511–5514. <https://doi.org/10.1039/c7cc01569k>.
- (75) Scheibel, M. G.; Askevold, B.; Heinemann, F. W.; Reijerse, E. J.; De Bruin, B.; Schneider, S. Closed-Shell and Open-Shell Square-Planar Iridium Nitrido Complexes. *Nat. Chem.* **2012**, 4 (7), 552–558. <https://doi.org/10.1038/nchem.1368>.
- (76) Bruch, Q. J.; Lindley, B. M.; Askevold, B.; Schneider, S.; Miller, A. J. M. A Ruthenium Hydrido Dinitrogen Core Conserved across Multielectron/Multiproton Changes to the Pincer Ligand Backbone. *Inorg. Chem.* **2018**, 57 (4), 1964–1975. <https://doi.org/10.1021/acs.inorgchem.7b02889>.
- (77) Askevold, B.; Khusniyarov, M. M.; Kroener, W.; Gieb, K.; Müller, P.; Herdtweck, E.; Heinemann, F. W.; Diefenbach, M.; Holthausen, M. C.; Vieru, V.; et al. Square-Planar Ruthenium(II) Complexes: Control of Spin State by Pincer Ligand Functionalization. *Chem. - A Eur. J.* **2015**, 21 (2), 579–589. <https://doi.org/10.1002/chem.201404282>.
- (78) Lagaditis, P. O.; Schluschaß, B.; Demeshko, S.; Würtele, C.; Schneider, S. Square-Planar Cobalt(III) Pincer Complex. *Inorg. Chem.* **2016**, 55 (9), 4529–4536. <https://doi.org/10.1021/acs.inorgchem.6b00369>.
- (79) Klopsch, I. *N₂ Splitting and Functionalization in the Coordination Sphere of Rhenium*; 2016.
- (80) Schendzielorz, F.; Finger, M.; Abbenseth, J.; Würtele, C.; Krewald, V.; Schneider, S. Metal-Ligand Cooperative Synthesis of Benzonitrile by Electrochemical Reduction and Photolytic Splitting of Dinitrogen. *Angew. Chemie Int. Ed.* **2019**, 58 (3), 830–834. <https://doi.org/10.1002/anie.201812125>.
- (81) Keane, A. J.; Farrell, W. S.; Yonke, B. L.; Zavalij, P. Y.; Sita, L. R. Metal-Mediated Production of Isocyanates, R₃EN=C=O from Dinitrogen, Carbon Dioxide, and R₃ECl. *Angew. Chemie - Int. Ed.* **2015**, 54 (35), 10220–10224. <https://doi.org/10.1002/anie.201502293>.
- (82) Miyazaki, T.; Tanaka, H.; Tanabe, Y.; Yuki, M.; Nakajima, K.; Yoshizawa, K.; Nishibayashi, Y. Cleavage and Formation of Molecular Dinitrogen in a Single System Assisted by Molybdenum Complexes Bearing Ferrocenyldiphosphine. *Angew. Chemie - Int. Ed.* **2014**, 53 (43), 11488–11492. <https://doi.org/10.1002/anie.201405673>.
- (83) Kunkely, H.; Vogler, A. Photolysis of Aqueous [(NH₃)₅Os(μ-N₂)Os(NH₃)₅]⁵⁺: Cleavage of Dinitrogen by

- an Intramolecular Photoredox Reaction. *Angew. Chemie - Int. Ed.* **2010**, *49* (9), 1591–1593. <https://doi.org/10.1002/anie.200905026>.
- (84) Bruch, Q. J.; Connor, G. P.; Chen, C. H.; Holland, P. L.; Mayer, J. M.; Hasanayn, F.; Miller, A. J. M. Dinitrogen Reduction to Ammonium at Rhenium Utilizing Light and Proton-Coupled Electron Transfer. *J. Am. Chem. Soc.* **2019**, *141* (51), 20198–20208. <https://doi.org/10.1021/jacs.9b10031>.
- (85) Weber, J. E.; Hasanayn, F.; Fataftah, M.; Mercado, B. Q.; Crabtree, R. H.; Holland, P. L. Electronic and Spin-State Effects on Dinitrogen Splitting to Nitrides in a Rhenium Pincer System. *Inorg. Chem.* **2021**, <https://doi.org/10.1021/acs.inorgchem.0c03778>. <https://doi.org/10.1021/acs.inorgchem.0c03778>.
- (86) Chalkley, M. J.; Drover, M. W.; Peters, J. C. Catalytic N₂-to-NH₃(or -N₂H₄) Conversion by Well-Defined Molecular Coordination Complexes. *Chem. Rev.* **2020**, *120* (12), 5582–5636. <https://doi.org/10.1021/acs.chemrev.9b00638>.
- (87) Chatt, J.; Pearman, A. J.; Richards, R. L. The Reduction of Mono-Coordinated Molecular Nitrogen to Ammonia in a Protic Environment. *Nature* **1975**, *253* (5486), 39–40. <https://doi.org/10.1038/253039bo>.
- (88) Chatt, J.; Pearman, A. J.; Richards, R. L. Conversion of Dinitrogen in Its Molybdenum and Tungsten Complexes into Ammonia and Possible Relevance to the Nitrogenase Reaction. *J. Chem. Soc. Dalton Trans.* **1977**, No. 19, 1852–1860. <https://doi.org/10.1039/DT9770001852>.
- (89) Chatt, J.; Richards, R. L. The Reactions of Dinitrogen in Its Metal Complexes. *J. Organomet. Chem.* **1982**, *239* (1), 65–77. [https://doi.org/10.1016/S0022-328X\(00\)94103-2](https://doi.org/10.1016/S0022-328X(00)94103-2).
- (90) Pickett, C. J. The Chatt Cycle and the Mechanism of Enzymic Reduction of Molecular Nitrogen. *J. Biol. Inorg. Chem.* **1996**, *1* (6), 601–606. <https://doi.org/10.1007/S007750050099>.
- (91) Ashida, Y.; Nishibayashi, Y. Catalytic Conversion of Nitrogen Molecule into Ammonia Using Molybdenum Complexes under Ambient Reaction Conditions. *Chem. Commun.* **2021**, *57* (10). <https://doi.org/10.1039/D0CC07146C>.
- (92) Reiners, M.; Baabe, D.; Münster, K.; Zaretzke, M. K.; Freytag, M.; Jones, P. G.; Coppel, Y.; Bontemps, S.; Rosal, I. del; Maron, L.; et al. NH₃ Formation from N₂ and H₂ Mediated by Molecular Tri-Iron Complexes. *Nat. Chem.* **2020**, *12* (8), 740–746. <https://doi.org/10.1038/s41557-020-0483-7>.
- (93) Shilov, A. E. Catalytic Reduction of Dinitrogen in Protic Media: Chemical Models of Nitrogenase. *J. Mol. Catal.* **1987**, *41* (1–2), 221–234. [https://doi.org/10.1016/0304-5102\(87\)80030-5](https://doi.org/10.1016/0304-5102(87)80030-5).
- (94) Yandulov, D. V.; Schrock, R. R. Catalytic Reduction of Dinitrogen to Ammonia at a Single Molybdenum Center. *Science* **2003**, *301*, 76–79.
- (95) Lindley, B. M.; Appel, A. M.; Krogh-Jespersen, K.; Mayer, J. M.; Miller, A. J. M. Evaluating the Thermodynamics of Electrocatalytic N₂ Reduction in Acetonitrile. *ACS Energy Lett.* **2016**, *1* (4), 698–704. <https://doi.org/10.1021/acsenergylett.6b00319>.
- (96) Anderson, J. S.; Rittle, J.; Peters, J. C. Catalytic Conversion of Nitrogen to Ammonia by an Iron Model Complex. *Nature* **2013**, *501* (7465), 84–87. <https://doi.org/10.1038/nature12435>.
- (97) Hodge, S. A.; Tay, H. H.; Anthony, D. B.; Menzel, R.; Buckley, D. J.; Cullen, P. L.; Skipper, N. T.; Howard, C. A.; Shaffer, M. S. P. Probing the Charging Mechanisms of Carbon Nanomaterial Polyelectrolytes. *Faraday Discuss.* **2014**, *172*, 311–325. <https://doi.org/10.1039/c4fd00043a>.
- (98) Chalkley, M. J.; Del Castillo, T. J.; Matson, B. D.; Roddy, J. P.; Peters, J. C. Catalytic N₂-to-NH₃ Conversion by Fe at Lower Driving Force: A Proposed Role for Metallocene-Mediated PCET. *ACS Cent. Sci.* **2017**, *3* (3), 217–223. <https://doi.org/10.1021/acscentsci.7b00014>.
- (99) Schild, D. J.; Drover, M. W.; Oyala, P. H.; Peters, J. C. Generating Potent C-H PCET Donors: Ligand-Induced Fe-to-Ring Proton Migration from a Cp*FeIII-H Complex Demonstrates a Promising Strategy. *J. Am. Chem. Soc.* **2020**, *142* (44), 18963–18970. <https://doi.org/10.1021/jacs.0c09363>.
- (100) Kolmar, S. S.; Mayer, J. M. SmI₂ (H₂O)_n Reduction of Electron Rich Enamines by Proton-Coupled Electron Transfer. *J. Am. Chem. Soc.* **2017**, *139* (31), 10687–10692. <https://doi.org/10.1021/jacs.7b03667>.
- (101) Chalkley, M. J.; Peters, J. C. Relating N–H Bond Strengths to the Overpotential for Catalytic Nitrogen Fixation. *Eur. J. Inorg. Chem.* **2020**, *2020* (15–16), 1353–1357. <https://doi.org/10.1002/ejic.202000232>.
- (102) Arashiba, K.; Kanega, R.; Himeda, Y.; Nishibayashi, Y. Electrochemical Reduction of Samarium Triiodide into Samarium Diiodide. *Chem. Lett.* **2020**, *49* (10), 1171–1173. <https://doi.org/10.1246/CL.200429>.
- (103) Hochman, G.; Goldman, A. S.; Felder, F. A.; Mayer, J. M.; Miller, A. J. M.; Holland, P. L.; Goldman, L. A.; Manocha, P.; Song, Z.; Aleti, S. Potential Economic Feasibility of Direct Electrochemical Nitrogen Reduction as a Route to Ammonia. *ACS Sustain. Chem. Eng.* **2020**, *8* (24), 8938–8948. <https://doi.org/10.1021/acssuschemeng.0c01206>.
- (104) McPherson, I.; Zhang, J. Can Electrification of Ammonia Synthesis Decrease Its Carbon Footprint? *Joule* **2020**, *4* (1), 12–14. <https://doi.org/10.1016/j.joule.2019.12.013>.
- (105) Ostermann, N.; Siewert, I. Electrochemical N₂ Splitting at Well-Defined Metal Complexes. *Curr. Opin. Electrochem.* **2019**, *15*, 97–101. <https://doi.org/10.1016/j.coelec.2019.04.024>.

- (106) Pickett, C. J.; Talarmin, J. Electrosynthesis of Ammonia. *Nature* **1985**, *317* (6038), 652–653. <https://doi.org/10.1038/317652ao>.
- (107) Chalkley, M. J.; Del Castillo, T. J.; Matson, B. D.; Peters, J. C. Fe-Mediated Nitrogen Fixation with a Metallocene Mediator: Exploring p Ka Effects and Demonstrating Electrocatalysis. *J. Am. Chem. Soc.* **2018**, *140* (19), 6122–6129. <https://doi.org/10.1021/jacs.8b02335>.
- (108) Del Castillo, T. J.; Thompson, N. B.; Peters, J. C. A Synthetic Single-Site Fe Nitrogenase: High Turnover, Freeze-Quench ⁵⁷Fe Mössbauer Data, and a Hydride Resting State. *J. Am. Chem. Soc.* **2016**, *138* (16), 5341–5350. <https://doi.org/10.1021/jacs.6b01706>.
- (109) McCarthy, B. D.; Martin, D. J.; Rountree, E. S.; Ullman, A. C.; Dempsey, J. L. Electrochemical Reduction of Brønsted Acids by Glassy Carbon in Acetonitrile-Implications for Electrocatalytic Hydrogen Evolution. *Inorg. Chem.* **2014**, *53* (16), 8350–8361. <https://doi.org/10.1021/ic500770k>.
- (110) Sherbow, T. J.; Thompson, E. J.; Arnold, A.; Saylor, R. I.; Britt, R. D.; Berben, L. A. Electrochemical Reduction of N₂ to NH₃ at Low Potential by a Molecular Aluminum Complex. *Chem. - A Eur. J.* **2019**, *25* (2), 454–458. <https://doi.org/10.1002/chem.201804454>.
- (111) Pospíšil, L.; Bulíčková, J.; Hromadová, M.; Gál, M.; Civiš, S.; Cihelka, J.; Tarábek, J. Electrochemical Conversion of Dinitrogen to Ammonia Mediated by a Complex of Fullerene C₆₀ and γ-Cyclodextrin. *Chem. Commun.* **2007**, No. 22, 2270–2272. <https://doi.org/10.1039/b701017f>.
- (112) Zhang, L.; Chen, G. F.; Ding, L. X.; Wang, H. Advanced Non-Metallic Catalysts for Electrochemical Nitrogen Reduction under Ambient Conditions. *Chem. - A Eur. J.* **2019**, *25* (54), 12464–12485. <https://doi.org/10.1002/chem.201901668>.
- (113) McPherson, I. J.; Sudmeier, T.; Fellowes, J.; Tsang, S. C. E. Materials for Electrochemical Ammonia Synthesis. *Dalt. Trans.* **2019**, *48* (5), 1562–1568. <https://doi.org/10.1039/c8dt04019b>.
- (114) Qing, G.; Ghazfar, R.; Jackowski, S. T.; Habibzadeh, F.; Ashtiani, M. M.; Chen, C. P.; Smith, M. R.; Hamann, T. W. Recent Advances and Challenges of Electrocatalytic N₂ Reduction to Ammonia. *Chem. Rev.* **2020**, *120* (12), 5437–5516. <https://doi.org/10.1021/acs.chemrev.9b00659>.
- (115) Zhang, L.; Cong, M.; Ding, X.; Jin, Y.; Xu, F.; Wang, Y.; Chen, L.; Zhang, L. A Janus Fe-SnO₂ Catalyst That Enables Bifunctional Electrochemical Nitrogen Fixation. *Angew. Chemie* **2020**, *132* (27), 10980–10985. <https://doi.org/10.1002/ange.202003518>.
- (116) Choi, J.; Suryanto, B. H. R.; Wang, D.; Du, H. L.; Hodgetts, R. Y.; Ferrero Vallana, F. M.; MacFarlane, D. R.; Simonov, A. N. Identification and Elimination of False Positives in Electrochemical Nitrogen Reduction Studies. *Nat. Commun.* **2020**, *11* (1), 1–10. <https://doi.org/10.1038/s41467-020-19130-z>.
- (117) Andersen, S. Z.; Čolić, V.; Yang, S.; Schwalbe, J. A.; Nielander, A. C.; McEnaney, J. M.; Enemark-Rasmussen, K.; Baker, J. G.; Singh, A. R.; Rohr, B. A.; et al. A Rigorous Electrochemical Ammonia Synthesis Protocol with Quantitative Isotope Measurements. *Nature* **2019**, *570* (7762), 504–508. <https://doi.org/10.1038/s41586-019-1260-x>.
- (118) Greenlee, L. F.; Renner, J. N.; Foster, S. L. The Use of Controls for Consistent and Accurate Measurements of Electrocatalytic Ammonia Synthesis from Dinitrogen. *ACS Catal.* **2018**, *8* (9), 7820–7827. <https://doi.org/10.1021/acscatal.8b02120>.
- (119) Weekes, D. M.; Salvatore, D. A.; Reyes, A.; Huang, A.; Berlinguette, C. P. Electrolytic CO₂ Reduction in a Flow Cell. *Acc. Chem. Res.* **2018**, *51* (4), 910–918. <https://doi.org/10.1021/acs.accounts.8b00010>.
- (120) Ren, S.; Joulié, D.; Salvatore, D.; Torbensen, K.; Wang, M.; Robert, M.; Berlinguette, C. P. Molecular Electrocatalysts Can Mediate Fast, Selective CO₂ Reduction in a Flow Cell. *Science* **2019**, *365* (6451), 367–369. <https://doi.org/10.1126/science.aax4608>.
- (121) Jiang, C.; Nichols, A. W.; Walzer, J. F.; Machan, C. W. Electrochemical CO₂ Reduction in a Continuous Non-Aqueous Flow Cell with [Ni(Cyclam)]²⁺. *Inorg. Chem.* **2020**, *59* (3), 1883–1892. <https://doi.org/10.1021/acs.inorgchem.9b03171>.
- (122) Kani, N. C.; Prajapati, A.; Collins, B. A.; Goodpaster, J. D.; Singh, M. R. Competing Effects of PH, Cation Identity, H₂O Saturation, and N₂ Concentration on the Activity and Selectivity of Electrochemical Reduction of N₂ to NH₃ on Electrodeposited Cu at Ambient Conditions. *ACS Catal.* **2020**, *10* (24), 14592–14603. <https://doi.org/10.1021/acscatal.0c04864>.
- (123) Lazouski, N.; Chung, M.; Williams, K.; Gala, M. L.; Manthiram, K. Non-Aqueous Gas Diffusion Electrodes for Rapid Ammonia Synthesis from Nitrogen and Water-Splitting-Derived Hydrogen. *Nat. Catal.* **2020**, *3* (5), 463–469. <https://doi.org/10.1038/s41929-020-0455-8>.
- (124) Andersen, S. Z.; Statt, M. J.; Bukas, V. J.; Shapel, S. G.; Pedersen, J. B.; Krempel, K.; Saccoccio, M.; Chakraborty, D.; Kibsgaard, J.; Vesborg, P. C. K.; et al. Increasing Stability, Efficiency, and Fundamental Understanding of Lithium-Mediated Electrochemical Nitrogen Reduction. *Energy Environ. Sci.* **2020**, *13* (11), 4291–4300. <https://doi.org/10.1039/d0ee02246b>.
- (125) Bezdek, M. J.; Chirik, P. J. Expanding Boundaries: N₂ Cleavage and Functionalization beyond Early

- Transition Metals. *Angew. Chemie - Int. Ed.* **2016**, *55* (28), 7892–7896.
<https://doi.org/10.1002/anie.201603142>.
- (126) Lv, Z.-J.; Wei, J.; Zahng, W.-X.; Chen, P. C.; Deng, D.; Shi, Z.-J.; Xi, Z. Direct Transformation of Dinitrogen: Synthesis of N-Containing Organic Compounds via N-C Bond Formation. *Natl. Sci. Rev.* **2020**, *7*, 1564–1583.
- (127) Kim, S.; Loose, F.; Chirik, P. J. Beyond Ammonia: Nitrogen-Element Bond Forming Reactions with Coordinated Dinitrogen. *Chem. Rev.* **2020**, *120* (12), 5637–5681.
<https://doi.org/10.1021/acs.chemrev.9b00705>.
- (128) Tanaka, H.; Sasada, A.; Kouno, T.; Yuki, M.; Miyake, Y.; Nakanishi, H.; Nishibayashi, Y.; Yoshizawa, K. Molybdenum-Catalyzed Transformation of Molecular Dinitrogen into Silylamine: Experimental and DFT Study on the Remarkable Role of Ferrocenyldiphosphine Ligands. *J. Am. Chem. Soc.* **2011**, *133* (10), 3498–3506. <https://doi.org/10.1021/ja109181n>.
- (129) Allcock, H. R.; Honeyman, C. H.; Manners, I.; Morrissey, C. T. Synthesis of Polyphosphazenes with Controlled Molecular Weight and Polydispersity, 1995.
- (130) Welz, E.; Krummenacher, I.; Engels, B.; Braunschweig, H. Reduction At Boron. *Science* **2018**, *359* (February), 896–900.
- (131) Légaré, M. A.; Bélanger-Chabot, G.; Rang, M.; Dewhurst, R. D.; Krummenacher, I.; Bertermann, R.; Braunschweig, H. One-Pot, Room-Temperature Conversion of Dinitrogen to Ammonium Chloride at a Main-Group Element. *Nat. Chem.* **2020**, *12* (11), 1076–1080. <https://doi.org/10.1038/s41557-020-0520-6>.
- (132) Volpin, M. E.; Shur, V. B.; Kudryavtsev, R. V.; Prodayko, L. A. Amine Formation in Molecular Nitrogen Fixation: Nitrogen Insertion into Transition Metal-Carbon Bonds. *Chem. Commun.* **1968**, 1038–1040.
- (133) Chatt, J.; Heath, G. A.; Leigh, G. J. The Formation of a Nitrogen to Carbon Bond in a Reaction of a Dinitrogen Complex. *J. Chem. Soc. Chem. Commun.* **1972**, *0* (8), 444–445.
<https://doi.org/10.1039/C39720000444>.
- (134) McWilliams, S. F.; Broere, D. L. J.; Halliday, C. J. V.; Bhutto, S. M.; Mercado, B. Q.; Holland, P. L. Coupling Dinitrogen and Hydrocarbons through Aryl Migration. *Nature* **2020**, *584* (7820), 221–226.
<https://doi.org/10.1038/s41586-020-2565-5>.
- (135) Chatt, B. J.; Head, R. A.; Leigh, G. J.; Pickett, C. J.; Fixation, N.; Sciences, M. Mechanism of Alkylation and Acylation of Dinitrogen Co-Ordination to Molybdenum and Tungsten. **1977**, 1638–1647.
- (136) Pickett, J.; Leigh, G. J. Towards a Nitrogen-Fixing Cycle : Electrochemical Reduction of a Hydrazido-Complex of Molybdenum(o) Dinitrogen Complex. *J.C.S. Chem. Comm.* **1981**, No. 3, 1033–1035.
- (137) Fairhurst, S. A.; Hughes, D. L.; Ibrahim, S. K.; Abasq, M.; Talarmin, J.; Queiros, M. A.; Fonseca, C. A.; Pickett, C. J. Ligand-Centred Chemistry of Molybdenum Organoimides. Formation of C-C Bonds. *Dalt. Trans.* **1995**, 1973–1984.
- (138) Alias, Y.; Ibrahim, S. K.; Queiros, M. A.; Fonseca, A.; Talarmin, J.; Volant, F.; Pickett, C. J. Electrochemistry of Molybdenum Imides: Cleavage of Molybdenum-Nitrogen Triple Bonds to Release Ammonia or Amines. *J. Chem. Soc. - Dalt. Trans.* **1997**, No. 24, 4807–4815. <https://doi.org/10.1039/a705441f>.
- (139) Hughes, D. L.; Ibrahim, S. K.; Macdonald, C. J.; Ali, H. M.; Pickett, C. J. Electrosynthesis of Amino Acids from a Molybdenum Nitride via Nitrogen-Carbon and Carbon-Carbon Bond Formation Reactions Involving Imides and Nitrogen Ylides: X-Ray Structure of Trans-[MoCl(NCHCO₂Me)(Ph₂PCH₂CH₂PPh₂)₂]*CH₂Cl₂. *Chem. Commun.* **1992**, 1762–1763.
- (140) Andino, J. G.; Mazumder, S.; Pal, K.; Caulton, K. G. New Approaches to Functionalizing Metal-Coordinated N₂. *Angew. Chemie - Int. Ed.* **2013**, *52* (18), 4726–4732. <https://doi.org/10.1002/anie.201209168>.
- (141) Ishida, Y.; Kawaguchi, H. Nitrogen Atom Transfer from a Dinitrogen-Derived Vanadium Nitride Complex to Carbon Monoxide and Isocyanide. *J. Am. Chem. Soc.* **2014**, *136* (49), 16990–16993.
<https://doi.org/10.1021/ja510317h>.
- (142) Eikey, R. A.; Abu-Omar, M. M. Nitrido and Imido Transition Metal Complexes of Groups 6–8. *Coord. Chem. Rev.* **2003**, *243* (1–2), 83–124. [https://doi.org/10.1016/S0010-8545\(03\)00048-1](https://doi.org/10.1016/S0010-8545(03)00048-1).
- (143) Connor, G. P.; Mercado, B. Q.; Lant, H. M. C.; Mayer, J. M.; Holland, P. L. Chemical Oxidation of a Coordinated PNP-Pincer Ligand Forms Unexpected Re-Nitroxide Complexes with Reversal of Nitride Reactivity. *Inorg. Chem.* **2019**, *58* (16), 10791–10801. <https://doi.org/10.1021/acs.inorgchem.9b01075>.
- (144) Schendzielorz, F. S.; Finger, M.; Volkmann, C.; Würtele, C.; Schneider, S. A Terminal Osmium(IV) Nitride: Ammonia Formation and Ambiphilic Reactivity. *Angew. Chemie - Int. Ed.* **2016**, *55* (38), 11417–11420.
<https://doi.org/10.1002/anie.201604917>.
- (145) Brazdil, J. F. Acrylonitrile. *Ullmann's Encycl. Ind.Chem.* **2012**, 1–8.
- (146) Cardoso, D. S. P.; Šljukić, B.; Santos, D. M. F.; Sequeira, C. A. C. Organic Electrosynthesis: From Laboratorial Practice to Industrial Applications. *Org. Process Res. Dev.* **2017**, *21* (9), 1213–1226.
<https://doi.org/10.1021/acs.oprd.7b00004>.

- (147) Hussain, W.; Leigh, G. J.; Pickett, C. J. Stepwise Conversion of Dinitrogen Co-Ordinated to Molybdenum into an Amine and an Imido-Complex. Relevance to the Reactions of Nitrogenase. *J. Chem. Soc. Chem. Commun.* **1982**, No. 13, 747–748. <https://doi.org/10.1039/C39820000747>.
- (148) Figueroa, J. S.; Piro, N. A.; Clough, C. R.; Cummins, C. C. A Nitridoniobium(V) Reagent That Effects Acid Chloride to Organic Nitrile Conversion: Synthesis via Heterodinuclear (Nb/Mo) Dinitrogen Cleavage, Mechanistic Insights, and Recycling. *J. Am. Chem. Soc.* **2006**, *128* (3), 940–950. <https://doi.org/10.1021/ja056408j>.
- (149) Sceats, E. L.; Figueroa, J. S.; Cummins, C. C.; Loening, N. M.; Van Der Wel, P.; Griffin, R. G. Complexes Obtained by Electrophilic Attack on a Dinitrogen-Derived Terminal Molybdenum Nitride: Electronic Structure Analysis by Solid State CP/MAS ¹⁵N NMR in Combination with DFT Calculations. *Polyhedron* **2004**, *23*, 2751–2768. <https://doi.org/10.1016/j.poly.2004.08.010>.
- (150) Curley, J. J.; Sceats, E. L.; Cummins, C. C. A Cycle for Organic Nitrile Synthesis via Dinitrogen Cleavage. *J. Am. Chem. Soc.* **2006**, *128* (43), 14036–14037. <https://doi.org/10.1021/ja066090a>.
- (151) Klopsch, I.; Kinauer, M.; Finger, M.; Würtele, C.; Schneider, S. Conversion of Dinitrogen into Acetonitrile under Ambient Conditions. *Angew. Chemie - Int. Ed.* **2016**, *55* (15), 4786–4789. <https://doi.org/10.1002/anie.201600790>.
- (152) Klopsch, I.; Schendzielorz, F.; Volkmann, C.; Würtele, C.; Schneider, S. Synthesis of Benzonitrile from Dinitrogen. *Zeitschrift für Anorg. und Allg. Chemie* **2018**, *644* (17), 916–919. <https://doi.org/10.1002/zaac.201800181>.
- (153) Guru, M. M.; Shima, T.; Hou, Z. Conversion of Dinitrogen to Nitriles at a Multinuclear Titanium Framework. *Angew. Chemie - Int. Ed.* **2016**, *55* (40), 12316–12320. <https://doi.org/10.1002/anie.201607426>.
- (154) Shima, T.; Hu, S.; Luo, G.; Kang, X.; Luo, Y.; Hou, Z. Dinitrogen Cleavage and Hydrogenation by a Trinuclear Titanium Polyhydride Complex. *Science* **2013**, *340* (6140), 1549–1552. <https://doi.org/10.1126/science.1238663>.
- (155) Song, J.; Liao, Q.; Hong, X.; Jin, L.; Mézailles, N. Conversion of Dinitrogen into Nitrile: Cross Metathesis of N₂-Derived Molybdenum Nitride with Alkynes. *Angew. Chemie* **2021**, <https://doi.org/10.1002/anie.202015183>. [https://doi.org/10.1016/0009-2509\(62\)87032-8](https://doi.org/10.1016/0009-2509(62)87032-8).
- (156) Mason, J. Nitrogen Nuclear Magnetic Resonance Spectroscopy in Inorganic, Organometallic, and Bioinorganic Chemistry. *Chem. Rev.* **1981**, *81* (3), 205–227. <https://doi.org/10.1021/cr00043a001>.
- (157) Chatt, J.; Leigh, G. J.; Mingos, D. M. P. Configurations of Some Complexes of Rhenium, Ruthenium, Osmium, Rhodium, Iridium, and Platinum Halides with Mono(Tertiary Phosphines) and Mono(Tertiary Arsines). *J. Am. Chem. Soc. Phys. Org. Chem.* **1969**, 1963–1969.
- (158) Bendix, J.; Meyer, K.; Weyhermüller, T.; Bill, E.; Metzler-Nolte, N.; Wieghardt, K. Nitridocyanometalates of CrV, MnV, and MnVI. *Inorg. Chem.* **1998**, *37* (8), 1767–1775. <https://doi.org/10.1021/ic971377h>.
- (159) Rittle, J.; McCrory, C. C. L.; Peters, J. C. A 106-Fold Enhancement in N₂-Binding Affinity of an Fe₂(μ-H)₂core upon Reduction to a Mixed-Valence FeII/FeIstate. *J. Am. Chem. Soc.* **2014**, *136* (39), 13853–13862. <https://doi.org/10.1021/ja507217v>.
- (160) Prokopchuk, D. E.; Wiedner, E. S.; Walter, E. D.; Popescu, C. V.; Piro, N. A.; Kassel, W. S.; Bullock, R. M.; Mock, M. T. Catalytic N₂ Reduction to Silylamines and Thermodynamics of N₂ Binding at Square Planar Fe. *J. Am. Chem. Soc.* **2017**, *139* (27), 9291–9301. <https://doi.org/10.1021/jacs.7b04552>.
- (161) Roncari, E.; Mazzi, U.; Seeber, R.; Zanello, P. Electrochemical Investigation on the Phosphine Rhenium Complexes [ReCl₃(PMe₂Ph)₃] and [ReCl₄(PMe₂Ph)₂] in an Aprotic Medium. *J. Electroanal. Chem.* **1982**, *132*, 221–231.
- (162) Huang, T.; Rodriguez, T. M.; Gruninger, C. T.; Kurtz, D. A.; Jordan, A. M.; Chen, C. H.; Dempsey, J. L. Electrosynthetic Route to Cyclopentadienyl Rhenium Hydride Complexes Enabled by Electrochemical Investigations of Their Redox-Induced Formation. *Organometallics* **2020**, *39* (10), 1730–1743. <https://doi.org/10.1021/acs.organomet.0c00049>.
- (163) Kirchoff, J. R.; Heineman, W. R.; Deutsch, E. Technetium Electrochemistry. 4.1 Electrochemical And Spectroelectrochemical Studies On The Bis(Tertiary Phosphine Or Arsine (d))Rhenium(Iii) Complexes Trans-[Red₂x₂]⁺(x = Cl, Br). Comparison With The Technetium(Iii) Analogues. *Inorg. Chem.* **1987**, *26* (19), 3108–3113. <https://doi.org/10.1021/ic00266a010>.
- (164) Trans, D.; Chatt, J.; Hussain, W.; Leigh, G. J.; Ali, H. M.; Pickett, C. J.; Rankin, D. A. The Preparation and Properties of Some Diphosphines R₂PCH₂CH₂PR₂ (R = Alkyl of Aryl) and of Their Rhenium(I) Dinitrogen Derivatives. *J. Chem. Soc. Dalt. Trans.* **1985**.
- (165) Bazhenova, T. A.; Shilov, A. E. Nitrogen Fixation in Solution. *Coord. Chem. Rev.* **1995**, *144* (C), 69–145. [https://doi.org/10.1016/0010-8545\(95\)01139-G](https://doi.org/10.1016/0010-8545(95)01139-G).
- (166) Fergusson, J. E.; Heveldt, P. F. Tertiary Phosphine Complexes of Rhenium: A Spectroscopic Study. *J. inorg.*

- nucl. Chem.* **1976**, *38*, 2231–2237.
- (167) Abbenseth, J.; Diefenbach, M.; Hinz, A.; Alig, L.; Würtele, C.; Goicoechea, J. M.; Holthausen, M. C.; Schneider, S. Oxidative Coupling of Terminal Rhenium Pnictide Complexes. *Angew. Chemie - Int. Ed.* **2019**, *58* (32), 10966–10970. <https://doi.org/10.1002/anie.201905130>.
- (168) Abbenseth, J. *Synthesis of Terminal Transition Metal Pnictide Complexes by Activation of Small Molecules*; 2019.
- (169) Chatt, J.; Rowe, G. A. Complex Compounds of Tertiary Phosphines and a Tertiary Arsine with Rhenium(V), Rhenium(III), and Rhenium(II). *Pure Appl. Chem.* **1961**, *16*, 4019–4033.
- (170) Rouschias, G.; Wilkinson, G. The Preparation and Reactions of Trihalogeno(Alkanonitrile)Bis(Triphenylphosphine)Rhenium(III) Complexes. *JACS* **1967**, No. 993–1000.
- (171) Addison, A. W.; Rao, T. N.; Reedijk, J.; van Rijn, J.; Verschoor, G. C. Synthesis, Structure, and Spectroscopic Properties of Copper(II) Compounds Containing Nitrogen-Sulphur Donor Ligands; the Crystal and Molecular Structure of Aqua[1,2-Bis(N-Methylbenzimidazol-2'-Yl)-2,3-Dithiaheptane]Copper(II) Perchlorate. *J. Chem. Soc. Dalt. Trans.* **1984**, No. 1, 1349–1356.
- (172) Reid, S. M.; Neuner, B.; Schrock, R. R.; Davis, W. M. Synthesis of Rhenium Complexes That Contain the [(C₆F₅NCH₂CH₂)₃N] ³⁻ Ligand. *Organometallics* **1998**, *17* (18), 4077–4089. <https://doi.org/10.1021/om980220+>.
- (173) Connor, G. P.; Mercado, B. Q.; Lant, H. M. C.; Mayer, J. M.; Holland, P. L. Chemical Oxidation of a Coordinated PNP-Pincer Ligand Forms Unexpected Re-Nitroxide Complexes with Reversal of Nitride Reactivity. *Inorg. Chem.* **2019**, *58* (16), 10791–10801. <https://doi.org/10.1021/acs.inorgchem.9b01075>.
- (174) Zanello, P. Inorganic Electrochemistry: Theory, Practice and Application. In *Chapter 2*; 2003.
- (175) Huss, A. S.; Curley, J. J.; Cummins, C. C.; Blank, D. A. Relaxation and Dissociation Following Photoexcitation of the (μ-N₂)[Mo(N[t-Bu]Ar)₃]₂ Dinitrogen Cleavage Intermediate. *J. Phys. Chem. B* **2013**, *117* (5), 1429–1436. <https://doi.org/10.1021/jp310122x>.
- (176) Mohammad, H. A. Y.; Grimm, J. C.; Eichele, K.; Mack, H. G.; Speiser, B.; Novak, F.; Quintanilla, M. G.; Kaska, W. C.; Mayer, H. A. C-H Oxidative Addition with a (PCP)Ir(III)-Pincer Complex. *Organometallics* **2002**, *21* (26), 5775–5784. <https://doi.org/10.1021/om020621w>.
- (177) Kinauer, M. *Transient and Stable Terminal Imido Complexes of Iridium*; 2019.
- (178) Bauer, J.; Braunschweig, H.; Hörl, C.; Radacki, K.; Wahler, J. Synthesis of Zwitterionic Cobaltocenium Borate and Borate-Alkene Derivatives from a Borole-Radical Anion. *Chem. - A Eur. J.* **2013**, *19* (40), 13396–13401. <https://doi.org/10.1002/chem.201302201>.
- (179) Krzystek, J.; Kohl, G.; Hansen, H. B.; Enders, M.; Telser, J. Combining HFEPR and NMR Spectroscopies to Characterize Organochromium(III) Complexes with Large Zero-Field Splitting. *Organometallics* **2019**, *38* (9), 2179–2188. <https://doi.org/10.1021/acs.organomet.9b00158>.
- (180) Martin, B.; Autschbach, J. Temperature Dependence of Contact and Dipolar NMR Chemical Shifts in Paramagnetic Molecules. *J. Chem. Phys.* **2015**, *142* (5). <https://doi.org/10.1063/1.4906318>.
- (181) Martin, B.; Autschbach, J. Erratum: Temperature Dependence of Contact and Dipolar NMR Chemical Shifts in Paramagnetic Molecules (Journal of Chemical Physics (2015) 142 (054108)). *J. Chem. Phys.* **2016**, *145* (4), 2015–2016. <https://doi.org/10.1063/1.4959030>.
- (182) Bleaney, B. Nuclear Magnetic Resonance Shifts in Solution Due to Lanthanide Ions. 1972, pp 91–100.
- (183) Eyring, G.; Curry, B.; Mathies, R.; Broek, A.; Lugtenburg, J. Direct Measurement of the Electron Susceptibility Anisotropy in Paramagnetic Complexes Using High-Field Deuterium NMR. *J. Am. Chem. Soc.* **1980**, No. 5, 5392–5393.
- (184) Domaille, P. J.; Harlow, R. L.; Ittel, S. D.; Peet, W. G. NMR Spectra of Paramagnetic Group 8 Complexes of Bis(Pyridylimino)Isoindoline. *Inorg. Chem.* **1983**, *22* (26), 3944–3952. <https://doi.org/10.1021/ic00168a024>.
- (185) Saupe, A. Recent Results in the Field of Liquid Crystals. *Angew. Chemie Int. Ed. English* **1968**, *7* (2), 97–112. <https://doi.org/10.1002/anie.196800971>.
- (186) Damjanović, M.; Samuel, P. P.; Roesky, H. W.; Enders, M. NMR Analysis of an Fe(i)-Carbene Complex with Strong Magnetic Anisotropy. *Dalt. Trans.* **2017**, *46* (16), 5159–5169. <https://doi.org/10.1039/c7dt00408g>.
- (187) Raghavan, P. MOMENTS. *At. Data Nucl. Data Tables* **1989**, *42* (2), 189–291.
- (188) Pletcher, D. *A First Course in Electrode Processes*; 2008.
- (189) Al-Salih, T. I.; Pickett, C. J. Electron-Transfer Reactions in Nitrogen Fixation. Part 1. The Electrosynthesis of Dinitrogen, Hydride, Isocyanide, and Carbonyl Complexes of Molybdenum: Intermediates, Mechanisms and Energetics. *J. Chem. Soc. Dalt. Trans.* **1985**, 1255–1264.
- (190) Fagnou, K.; Lautens, M. Halide Effects in Transition Metal Catalysis. *Angew. Chemie - Int. Ed.* **2002**, *41* (1), 26–47. [https://doi.org/10.1002/1521-3773\(20020104\)41](https://doi.org/10.1002/1521-3773(20020104)41).
- (191) Difranco, S. A.; Maciulis, N. A.; Staples, R. J.; Batrice, R. J.; Odom, A. L. Evaluation of Donor and Steric

- Properties of Anionic Ligands on High Valent Transition Metals. *Inorg. Chem.* **2012**, *51* (2), 1187–1200. <https://doi.org/10.1021/ic202524r>.
- (192) Greco, G. E.; Schrock, R. R. Synthesis, Structure, and Electrochemical Studies of Molybdenum and Tungsten Dinitrogen, Diazenido, and Hydrazido Complexes That Contain Aryl-Substituted Triamidoamine Ligands. *Inorg. Chem.* **2001**, *40* (16), 3861–3878. <https://doi.org/10.1021/ic001123n>.
- (193) Peters, J. C.; Cherry, J. P. F.; Thomas, J. C.; Baraldo, L.; Mindiola, D. J.; Davis, W. M.; Cummins, C. C. Redox-Catalyzed Binding of Dinitrogen by Molybdenum N-Tert-Hydrocarbylanilide Complexes: Implications for Dinitrogen Functionalization and Reductive Cleavage. *J. Am. Chem. Soc.* **1999**, *121* (43), 10053–10067. <https://doi.org/10.1021/ja991435t>.
- (194) Askevold, B.; Friedrich, A.; Buchner, M. R.; Lewall, B.; Filippou, A. C.; Herdtweck, E.; Schneider, S. Reactivity of Iridium(I) PNP Amido Complexes toward Protonation and Oxidation. *J. Organomet. Chem.* **2013**, *744*, 35–40. <https://doi.org/10.1016/j.jorganchem.2013.04.022>.
- (195) Wise, C. F.; Agarwal, R. G.; Mayer, J. M. Determining Proton-Coupled Standard Potentials and X-H Bond Dissociation Free Energies in Nonaqueous Solvents Using Open-Circuit Potential Measurements. *J. Am. Chem. Soc.* **2020**, *142* (24), 10681–10691. <https://doi.org/10.1021/jacs.0c01032>.
- (196) Fischer, K.; Wilken, M. Experimental Determination of Oxygen and Nitrogen Solubility in Organic Solvents up to 10 MPa at Temperatures between 298 K and 398 K. *J. Chem. Thermodyn.* **2001**, *33* (10), 1285–1308. <https://doi.org/10.1006/jcht.2001.0837>.
- (197) Stenutz, R. <http://www.stenutz.eu/chem/> accessed August 2020.
- (198) Battino, R. IUPAC Solubility Data Series, Volume 10: Nitrogen and Air. *Pergamon Press., Oxford*; 1981.
- (199) Schneck, F.; Finger, M.; Tromp, M.; Schneider, S. Chemical Non-Innocence of an Aliphatic PNP Pincer Ligand. *Chem. - A Eur. J.* **2017**, *23* (1), 33–37. <https://doi.org/10.1002/chem.201604407>.
- (200) Kühnl, O. *Phosphorous-31 NMR Spectroscopy*; 2008.
- (201) Kessler, J. A.; Iluc, V. M. Ni(II) Phosphine and Phosphide Complexes Supported by a PNP-Pyrrole Pincer Ligand. *Dalt. Trans.* **2017**, *46* (36), 12125–12131. <https://doi.org/10.1039/c7dt02784b>.
- (202) Hinrichsen, S.; Schnoor, A. C.; Grund, K.; Flöser, B.; Schlimm, A.; Näther, C.; Krahmer, J.; Tuczek, F. Molybdenum Dinitrogen Complexes Facially Coordinated by Linear Tridentate PEP Ligands (E = N or P): Impact of the Central e Donor in: Trans -Position to N₂. *Dalt. Trans.* **2016**, *45* (37), 14801–14813. <https://doi.org/10.1039/c6dt02316a>.
- (203) Abbenseth, J.; Delony, D.; Neben, M. C.; Würtele, C.; de Bruin, B.; Schneider, S. Interconversion of Phosphinyl Radical and Phosphinidene Complexes by Proton Coupled Electron Transfer. *Angew. Chemie - Int. Ed.* **2019**, *58* (19), 6338–6341. <https://doi.org/10.1002/anie.201901470>.
- (204) Leto, I.; Kütt, A.; Kaljurant, I.; Room, E.-I.; Rodima, T. Koppel, I. A. Bronstedt Acidity of Neutral and Cationic Acids in Nonaqueous Solvents: Recent Developments.
- (205) Tabassum, S.; Sereda, O.; Reddy, P. V. G.; Wilhelm, R. Hindered Brønsted Bases as Lewis Base Catalysts. *Org. Biomol. Chem.* **2009**, *7* (19), 4009–4016. <https://doi.org/10.1039/b908899g>.
- (206) Becker, J. C. *Rhenium-Vermittelte N₂-Funktionalisierung*; 2017.
- (207) Satterlee, J. D. Fundamental Concepts of NMR in Paramagnetic Systems. Part II: Relaxation Effects. *Concepts Magn. Reson.* **1990**, *2* (3), 119–129. <https://doi.org/10.1002/cmr.1820020302>.
- (208) Lambic, N. S.; Sommer, R. D.; Ison, E. A. High-Valent Nitridorhenium(v) Complexes Containing PNP Ligands: Implications of Ligand Flexibility. *Dalt. Trans.* **2018**, *47* (3), 758–768. <https://doi.org/10.1039/c7dt03615a>.
- (209) Manner, V. W.; Markle, T. F.; Freudenthal, J. H.; Roth, J. P.; Mayer, J. M. The First Crystal Structure of a Monomeric Phenoxy Radical: 2,4,6-Tri-Tert-Butylphenoxy Radical. *Chem. Commun.* **2008**, *246* (2), 256–258. <https://doi.org/10.1039/b712872j>.
- (210) Nafady, A.; Costa, P. J.; Calhorda, M. J.; Geiger, W. E. Electrochemical Oxidation of CoCp(CO)₂: Radical-Substrate Reaction of a 17 e⁻/18 e⁻ Pair and Production of a Unique Dimer Radical. *J. Am. Chem. Soc.* **2006**, *128* (51), 16587–16599. <https://doi.org/10.1021/ja0653775>.
- (211) Scheibel, M. *Metal-Nitrogen Multiple Bonds with Square-Planar Group 9 Transition Metal PNP Pincer Complexes*; 2014.
- (212) Bharti, S. K.; Roy, R. Quantitative ¹H NMR Spectroscopy. *TrAC - Trends Anal. Chem.* **2012**, *35*, 5–26. <https://doi.org/10.1016/j.trac.2012.02.007>.
- (213) Dutta, A.; Roberts, J. A. S.; Shaw, W. J. Arginine-Containing Ligands Enhance H₂ Oxidation Catalyst Performance. *Angew. Chemie - Int. Ed.* **2014**, *53* (25), 6487–6491. <https://doi.org/10.1002/anie.201402304>.
- (214) von Petersdorff-Campen, C. M. G. K. *Implementierung Einer Flow-Zelle in Die Elektrochemische Stickstoffspaltung*; 2020.
- (215) Pletcher, D.; Green, R. A.; Brown, R. C. D. Flow Electrolysis Cells for the Synthetic Organic Chemistry

- Laboratory. *Chem. Rev.* **2018**, *118* (9), 4573–4591. <https://doi.org/10.1021/acs.chemrev.7b00360>.
- (216) Shin, S. H.; Yun, S. H.; Moon, S. H. A Review of Current Developments in Non-Aqueous Redox Flow Batteries: Characterization of Their Membranes for Design Perspective. *RSC Adv.* **2013**, *3* (24), 9095–9116. <https://doi.org/10.1039/c3ra00115f>.
- (217) https://www.engineeringtoolbox.com/reynolds-number-d_237.html.
- (218) Das, B.; Roy, M.; Hazra, D. Densities and Viscosities of the Binary Aqueous Mixtures of Tetrahydrofuran and 1,2-Dimethoxyethane at 298, 308 and 318 K. *Indian J. Chem. Technol.* **1994**, *01* (2), 93–97.
- (219) Tosun, I.; Uner, D.; Ozgen, C. Communications: Critical Reynolds Number for Newtonian Flow in Rectangular Ducts. *Ind. Eng. Chem. Res.* **1988**, *27* (10), 1955–1957. <https://doi.org/10.1021/ie00082a034>.
- (220) Roth, H. G.; Romero, N. A.; Nicewicz, D. A. Experimental and Calculated Electrochemical Potentials of Common Organic Molecules for Applications to Single-Electron Redox Chemistry. *Synlett* **2016**, *27* (5), 714–723. <https://doi.org/10.1055/s-0035-1561297>.
- (221) Constable, E. C.; Harris, K.; Housecroft, C. E.; Neuburger, M.; Zampese, J. A. Turning {M(Tpy)₂}ⁿ⁺ Embraces and CH $\cdots\pi$ Interactions on and off in Homoleptic Cobalt(II) and Cobalt(III) Bis(2,2':6',2''-Terpyridine) Complexes. *CrystEngComm* **2010**, *12* (10), 2949–2961. <https://doi.org/10.1039/c002834g>.
- (222) Russell, S. K.; Milsmann, C.; Lobkovsky, E.; Weyhermüller, T.; Chirik, P. J. Synthesis, Electronic Structure, and Catalytic Activity of Reduced Bis(Aldimino)Pyridine Iron Compounds: Experimental Evidence for Ligand Participation. *Inorg. Chem.* **2011**, *50* (7), 3159–3169. <https://doi.org/10.1021/ic102186q>.
- (223) Lu, C. C.; Bill, E.; Weyhermüller, T.; Bothe, E.; Wieghardt, K. Neutral Bis(α -Iminopyridine)Metal Complexes of the First-Row Transition Ions (Cr, Mn, Fe, Co, Ni, Zn) and Their Monocationic Analogues: Mixed Valency Involving a Redox Noninnocent Ligand System. *J. Am. Chem. Soc.* **2008**, *130* (10), 3181–3197. <https://doi.org/10.1021/ja710663n>.
- (224) Baron, R.; Kershaw, N. M.; Donohoe, T. J.; Compton, R. G. Electrochemistry in Tetrahydrofuran and at Low Temperature: Protocol, Procedures and Methods. *J. Phys. Org. Chem.* **2009**, *22* (12), 1136–1141. <https://doi.org/10.1002/poc.1574>.
- (225) Bruker ACS INC., M. W. U. APEX3 V2016.9-0 (Saint/SADABS/SHELXT/SHELXL). 2016.
- (226) Sheldrick, G. M. *Acta Cryst.* **2015**, *A71*, 3.8.
- (227) Sheldrick, G. M. *Acta Cryst.* **2015**, *C71*, 3–8.
- (228) Sheldrick, G. M. *Acta Cryst.* **2008**, *A64*, 112–122.

VII Curriculum Vitae

Name: Richt Sieteke van Alten
Nationality: Dutch
Place of birth: Dokkum (NL)
Date of birth: 03-06-1993

Education

2016 – present Graduate Student
Georg-August University, Göttingen (DE)
Institute for Inorganic Chemistry
Research Group of Prof. Dr. S. Schneider

2014 – 2016 Master Nanomaterials: Chemistry and Physics
University of Utrecht (NL)
Organic Chemistry and Catalysis
Thesis title: 'A study towards alkyl substituted diphosphine ligands with an envisioned redox non-innocent character'

2010 – 2014 Bachelor Chemistry,
University of Utrecht (NL)
Organic Chemistry and Catalysis
Thesis title: 'A study towards the catalytic ability of different Fe-complexes in oxidation chemistry'

Internships

2016 Erasmus internship
Leibniz Institute for Catalysis, Rostock (DE)
Research topic: 'Valorization of CO₂ as C₁ building block for hydroformylation and hydrogen reactions'.

2013 Erasmus exchange semester
Technische Universität München (DE)

Conference and research school participations and contributions

2019: International Conference of Inorganic Chemistry (IT): poster
2019: Ferrocene Colloquium (DE): talk (best talk award)
2019: Electrochemical Approaches to Chemical Synthesis (DE)
2018: Netherlands Chemistry and Catalysis Conference (NL): talk
2018: Niedersächsisches Katalyse Symposium (DE): poster
2017: Nord Deutsches Doktoranden Kolloquium (DE): talk (best talk award)
2017: Instrumental Methods in Electrochemistry (GB)

Publication list

‘Mechanism of Chemical and Electrochemical N₂-splitting by a Rhenium Pincer Complex’ Brian M. Lindley, Richt S. van Alten, Markus Finger, Florian Schendzielorz, Christian Würtele, Alexander J.M. Miller, Inke Siewert and Sven Schneider, *JACS*, **2018**, *140*, 25, 7922-7935.

‘(Electro)-chemical Splitting of Dinitrogen with a Rhenium Pincer Complex’ Richt S. van Alten, Florian Wätjen, Serhiy Demeshko, Alexander J.M. Miller, Christian Würtele, Inke Siewert and Sven Schneider, *EuroJIC*, **2020**, 1402-1410.
